Dissertation zur Erlangung des Doktorgrades
der Fakultät für Chemie und Pharmazie
der Ludwig-Maximilians-Universität München

Hemithioindigo-based Molecular Switches, Motors and Machines
–
Tracing, Transmission and Modulation of Molecular Motions at the Nanoscale

Benjamin Lukas Regen-Pregizer

aus
Stuttgart, Deutschland
2023

Erklärung

Diese Dissertation wurde im Sinne von § 7 der Promotionsordnung vom 28. November 2011 von Herrn Prof. Dr. Henry Dube betreut.

Eidesstattliche Versicherung

Diese Dissertation wurde eigenständig und ohne unerlaubte Hilfe erarbeitet.

München, den .....22.08.2023..... .....

Benjamin Lukas Regen-Pregizer

Dissertation eingereicht am:	22.08.2023
1. Gutachter:	Prof. Dr. Henry Dube
2. Gutachter:	Prof. Dr. Konstantin Karaghiosoff
Mündliche Prüfung am:	26.09.2023

Acknowledgements

This work was carried out between July 2019 and September 2023 in the group of *Prof. Dr. Henry Dube* at the faculty for chemistry and pharmacy of the Ludwig-Maximilians-University (LMU) Munich and the department of chemistry and pharmacy of the Friedrich-Alexander-University (FAU) Erlangen-Nuremberg.

Firstly, I want to thank *Prof. Dr. Henry Dube* for the possibility to pursue my dissertation in his research group and the very warm welcome, plenty of formal and informal discussions about work, chemistry, science, research and many other aspects of life. I am especially grateful for the always encouraged attitude of standing up for and advocating my very own opinion.

Secondly, I want to express my thankfulness to *Prof. Dr. Konstantin Karaghiosoff* for accepting my request undertaking the second referee of my thesis and all other members of my defense committee, who were *Prof. Dr. Norbert Jux*, *Prof. Dr. Franz Bracher*, *Prof. Dr. Markus Heinrich* and *Prof. Dr. Silvija Markic*.

Next, I want to thank *Dr. Harald Maid*, *Christian Placht*, *Mike Seyfarth*, *Holger Wohlfahrt*, *Dr. Peter Mayer*, *Carrie Louis*, *Margarete Dzialach*, *Sofia Rohde*, *Martina Sonntag*, *Robert Panzer*, *Corina England* and all other employes from the LMU and FAU who supported me during my work at the respective institution.

Furthermore, I want to thank all my collaboration partners and students who were *Dr. Ani Özcelik*, *Lilli Reissenweber*, *Aila Rothweiler*, *Konstantin Kublik*, *Sylvia Sabine Heberl*, *Georg Fickenscher*, *Viridiana Velazquez Castillo*, *Baolin Zhao*, *Antony George*, *Hyoungwon Park*, *Dr. Evgeny Kataev*, *Prof. Dr. Andrey Turchanin*, *Prof. Dr. rer. nat. Marcus Halik*, *Prof. Dr. Jörg Libuda*.

My deep gratitude is expressed to all my wonderful colleagues at the LMU and FAU. This goes to *Dr. Edgar Uhl* for being a wonderful boulder buddy, music enthusiast and collector of a library of facial emotions. *Dr. Kerstin Grill* for another great boulder buddy, giving me such a warm welcome and always having an open ear for all my questions and personal stories. *Dr. Christian Petermayer* for having the most extensive do it yourself attitude I have ever seen, unconditionally cooperativity and entertaining attitude. *Maximilian Sacherer* for our everlasting and most intensive lab partner relationship I have ever been in and for loving life the same way *Vicky Leandros* probably does. *Lilli Reissenweber* for being such a great benchbuddy, nights out buddy and my most talented master student. *Laura Köttner* for sharing a bench with me and always being up for activities of all sorts. *Fabien Kohl* for his strongest support of the bullshit playlist. *Dr. Stefan Thumser* for always being *Esteban* and his very supportive attitude, which is why he became my lab superhero. *Dr. Nicolai Bach* for being the one moving from Munich to Erlangen with me. *Dr. Aaron Gerwien* for great weekends, ski trips and great tinker attitude.

Frederik Gnannt for fun night activities and cigarettes. *Manuel Valentin* for your awesome pasta cooking skills. *Dr. Roland Wilcken* for your original down-to-earth attitude towards life. *Matthias Fröhling* for your relaxed attitude. *Dr. Thomas* Bartelmann, *Elias Ciekalski*, *Sven Waldmannstetter*, *Sofia Gracheva*, *Pavel Shelyganov*, *Verena Josef*, *Max Zitzmann*, *Dr. Pronay Biswas* and all other lab friends, colleagues and co-workers along the way.

Additionally, I want to thank all previous members of the *Dube* group who helped shaping this marvellous atmosphere between all PhD students during great but also tough times. *Dr. Manuel Güntner*, *Dr. Sandra Wiedbrauk*, *Dr. Ludwig Huber*, *Dr. Monika Schildhauer* and *Florian Kink* I unfortunately never worked with you but appreciate what you helped create.

In the end I want to thank my family for their support especially during stressful times, without your help I would have never ended up where I am now. Thank you, *Susanne Regen*, for your thesis writing/birthday advents calendar and all the support I have received until this day during my whole life. Thank you, *Dieter Pregizer*, for your aid with formal corrections and support throughout my life. Thank you, *Lara Regen-Pregizer* and *Jonathan Regen-Pregizer* for support with thesis writing/birthday advents calendar and always having my back and being great siblings.

I would also like to thank my grandparents *Otto* and *Elsbeth Regen* as well as *Robert* and *Elsbeth Pregizer* who were always there for me.

I want to thank *Marie Lisa Sailer* and *Laura Sturm* for sharing a very significant part of life with me. I am deeply grateful I have met you.

In the end I want to thank all other family members, friends, and people I forgot to mention explicitly but have supported me in any conceivable way during my thesis work or helped shaping the person I have become.

List of Publications

Parts of this Ph.D. thesis have been published as research articles

"A Photochemical Method to Evidence Directional Molecular Motions"

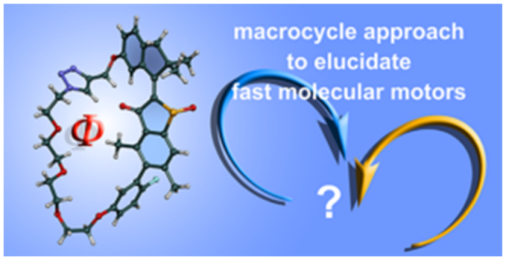

Benjamin Lukas Regen-Pregizer, Ani Ozcelik, Peter Mayer, Frank Hampel, Henry Dube, *Nat. Commun.* **2023**, *14*, 4595. doi:10.1038/s41467-023-40190-4; and *ChemRxiv.* Preprint. **2022**. doi: 10.26434/chemrxiv-2022-4th46

"Defining Unidirectional Motions and Structural Reconfiguration
in a Macrocyclic Molecular Motor"

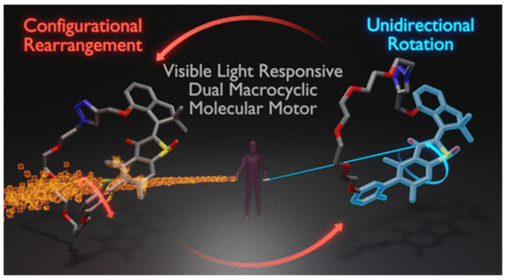

Benjamin Lukas Regen-Pregizer, Henry Dube, *J. Am. Chem. Soc.* **2023**, *145*, 13081-13088. doi: 10.1021/jacs.3c01567

Parts of this thesis have been presented at a scientific conference

"A Photochemical Method to Determine Directionality of Molecular Motions", Benjamin Lukas Regen-Pregizer, Ani Ozcelik, Peter Mayer, Frank Hampel, Henry Dube, *28th PhotoIUPAC* **2022**, Amsterdam.

Contributions

[I]*Georg Fickenscher*	Experiments with **11** on a Co_3O_4 (111) surface.
[II]*Viridiana Velazquez Castillo*	Fluorescence and binding measurements of **11**.
[III]*Sylvia Heberl*	Synthesis of molecular motor **15e**.
[IV]*Laura Köttner*	Provided a sample of photoswitch **10**.
[V]*Dr. Ani Özcelik*	Quantum yield measurements of **15h**, **33**, **51** and **56** with the improved setup.
[VI]*Dr. Stefan Thumser*	Introduction to and guidance for theoretical descriptions.
[VII]*Dr. Peter Mayer*	Solving of crystal structures **33**-*Z*-**I**, **33**-*E*-**II**, **33**-*Z*-**II** and **51**-***E***.
[VIII]*Dr. Frank Hampel*	Solving of crystal structure **15h**-*Z*.
[IX]*Christian Placht*	Recording of low temperature NMR measurements.
[X]*Dr. Harald Maid*	Recording of 1D and 2D NMR spectra.
[XI]*Claudia Ober*	Recording of 1D and 2D NMR spectra.
[XII]*Margarete Dzialach*	Mass spectrometry measurements.
[XIII]*Sonja Kosak*	Mass spectrometry measurements.
[XIV]*Dr. Werner Spahl*	Mass spectrometry measurements.

Abbreviations

AlO_x	aluminium oxide
APPI	atmospheric pressure photoionization
ATP	adenosine triphosphate
BINAP	([1,1′-Binaphthalene]-2,2′-diyl)bis(diphenylphosphane)
a.u.	arbitrary unit
°C	degree Celsius
cw	clockwise
ccw	counterclockwise
d	doublet (NMR spectroscopy)
DFT	density functional theory
DBI	double bond inversion
δ	chemical shift (NMR spectroscopy)
E	double bond configuration
ECD	electronic circular dichroism
EDG	electron donating group
EI	electron ionization
equiv.	equivalent(s)
ESPT	excited state proton transfer
ESI	electron spray ionization
EWG	electron withdrawing group
FAU	Friedrich-Alexander-Universität (University of Erlangen–Nuremberg)
FET	field-effect transistor
Fmoc	9-fluorenylmethoxycarbonyl
h	hour(s)
HI	hemiindigos
HPLC	high performance liquid chromatography
HR-MS	high resolution mass spectrometry

HTI	hemithioindigo
Hz	Hertz (s^{-1}, NMR spectroscopy)
IC	internal conversion
ISC	intersystem crossing
IR	infrared (spectroscopy)
${}^{X}J_{YZ}$	coupling constant between nuclei Y and Z and number of bonds X in between (NMR spectroscopy)
K	kelvin
k	kilo (10^3)
kcal	kilocalories
L	liter
LMU	Ludwig-Maximilians-Universität (Ludwig Maximilian University of Munich)
λ	wavelength
M	mega
M	helicity
m	mili (10^{-3})
m	multiplet (NMR spectroscopy)
m	medium (IR spectroscopy)
μ	mikro (10^{-6})
M	molarity (mol L^{-1})
[M]	molecule (mass spectrometry)
Mol	mole ($6.02 \cdot 10^{23}$)
min	minute(s)
m/z	mass/charge ratio (mass spectrometry)
NOE	nuclear *Overhauser* effect
NOESY	nuclear *Overhauser* effect spectroscopy
NMR	nuclear magnetic resonance
P	helicity
PA	phosphonic acid

PEG	poly ethylene glycol
PSS	photostationary state
q	quartet (NMR spectroscopy)
QY Φ	quantum yield
ROE	Rotating-frame *Overhauser* effect
R	stereodescriptor
R_a	stereodescriptor (axial chirality)
R_f	retardation factor
S	stereodescriptor
S_a	stereodescriptor (axial chirality)
SAM	self-assembled monolayer
s	singlet (NMR spectroscopy)
s	strong (IR spectroscopy)
s	second(s)
t	triplet (NMR spectroscopy)
TDBI	thermal double bond inversion
THI	thermal helix inversion
TLC	thin layer chromatography
UV	ultraviolet
$\tilde{\nu}$	wavenumber
vis	visible
VT	variable temperature
w	weak (IR spectroscopy)
Z	double bond configuration

“Unfortunately, it seems to be much easier to condition human behavior and to make people conduct themselves in the most unexpected and outrageous manner, than it is to persuade anybody to learn from experience, as the saying goes; that is, to start thinking and judging instead of applying categories and formulas which are deeply ingrained in our mind, but whose basis of experience has long been forgotten and whose plausibility resides in their intellectual consistency rather than in their adequacy to actual events.”

“Personal Responsibility Under Dictatorship” 1964

Hannah Arendt

(1906–1975)

Table of contents

1. Summary

1.1. HTI-based switch modified for surface attachment

The first part of this work is concerned with the design of molecular photoswitches for surface attachment. A high yielding five step synthetic route for hemithioindigo (HTI) based phosphonic acid (PA) self-assembled monolayer (SAM) monomer HTI PA **2** was developed. This monomer can be covalently bound to aluminium oxide (AlO_x) surfaces forming true monolayers as shown in Figure Ib which will be examined in collaboration with *Prof. Dr. Marcus Halik* and *Prof. Dr. Andrey Turchanin*.

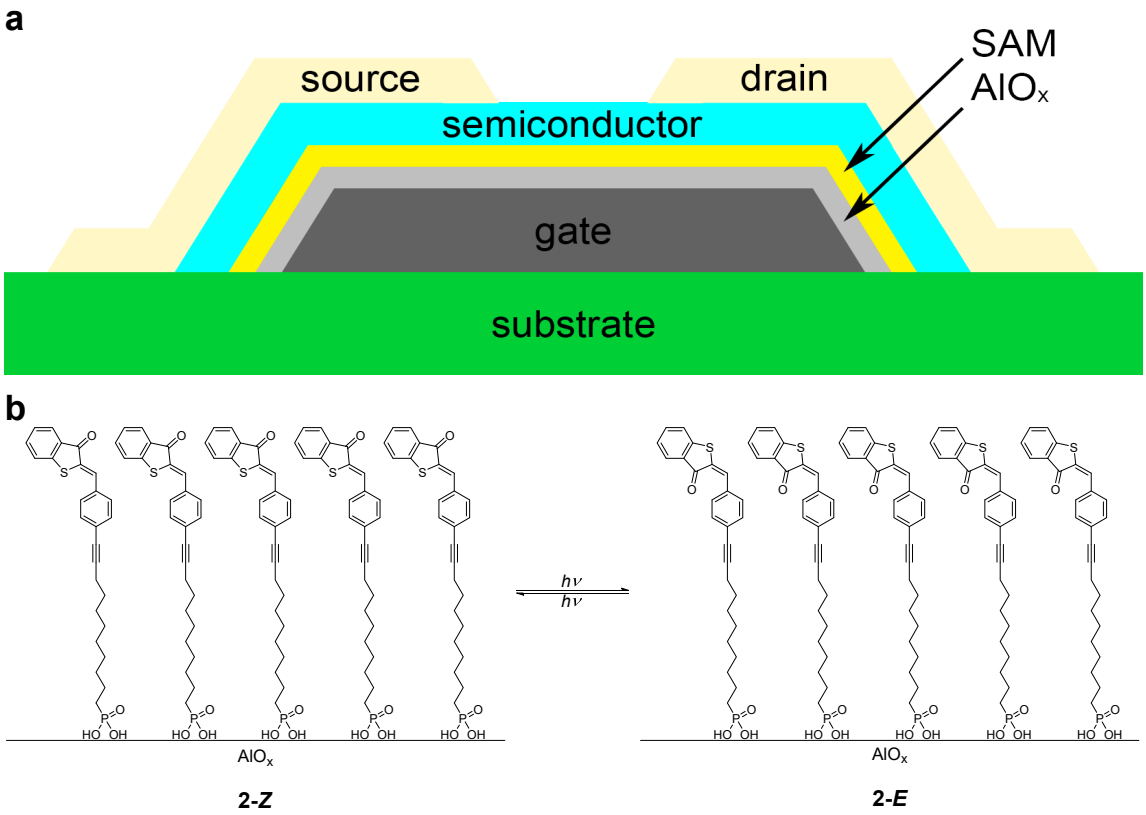

Figure I Design of a potential HTI-based self-assembled monolayer (HTI SAM) **2** based field-effect transistor (FET). **a** Schematic FET design displaying gate (dark grey), source and drain (light yellow) electrodes as well as substrate (green), aluminium oxide (AlO_x) layer (light grey), SAM (yellow) and semiconductor layer (turquoise). **b** Illustration of envisioned HTI-based AlO_x SAM design showing switching between *Z*-isomers (left) and *E*-isomers (right).

These monolayers could potentially be utilized for a first solely visible light modulated MoS_2-based field-effect transistor (FET) design illustrated in Figure Ia. Since this is work in progress, further experiments are necessary characterizing possible devices for applications to complete this study.

1.2. HTI-based switch with fluorescence response

In the second part of this work a fluorescent HTI-based photoswitch **11** has been synthesized in one step shown in Figure II for photoswitching on a $Co_3O_4(111)$ surface in the group of *Prof. Dr. Jörg Libuda* by *Georg Fickenscher*[I] but unfortunately no photoswitching on the surface has been observed. Furthermore, photoswitch **11** could be utilized as a potential guest for a fluorescence enhancing host system developed in the group of *Dr. Evgeny Kataev* and will be tested by *Viridiana Velazquez Castillo*[II] in the near future.

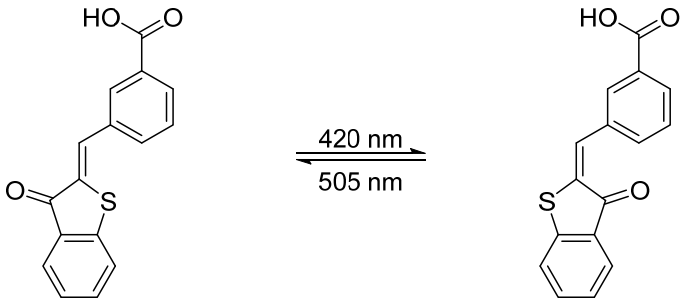

11-*Z* **11**-*E*

Figure II Overview of synthetically obtained conformational *Z*-isomers and photochemically obtained metastable *E*-isomer of **11**.

1.3. Modifying electronics of HTI-based molecular motors

In the third part of this thesis a series of six HTI molecular motors based on the initial design by *Guentner et al*. shown in Figure III were synthesized and examined upon electronic influence on kinetics of the thermal ratcheting step, thermodynamic stability of isomers and photophysical properties. During this study direct observation of detailed geometrical information about the *E*-configuration of metastable *E*-(*S*)-(*M*)-intermediate were obtained for the first time using *in situ* low temperature irradiation 2D nuclear magnetic resonance (NMR) spectroscopy. Additionally, a prospective acid sensitive functionalization has been synthesized for which the rotational cycle appears to be tunable *in situ* by addition of acid.

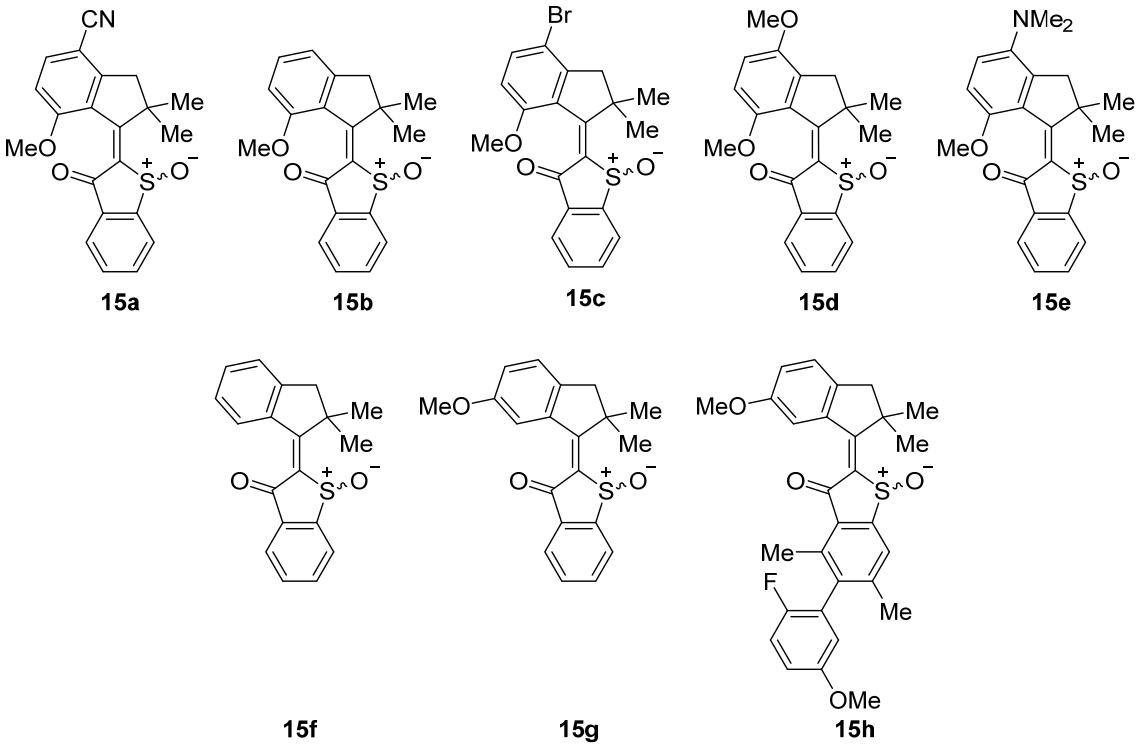

Figure III Overview of all HTI-based molecular motors **15a**–**15h** investigated for electronic influence on the motor cycle.

It has been shown during this study that the contribution from electronics to the thermal helix inversion (THI) is rather limited when compared to the influence originating from steric hindrance. Taken together, these results provide necessary information for designing novel optimized HTI-based motors which can find applications in future integrated molecular machinery with biological, medicinal, or material uses. Since this is work in progress, further already planned experiments are necessary to complete this study.

1.4. Evidencing fast directional molecular motions
A photochemical method

In the fourth part of this thesis a photochemical method was developed, enabling to evidence fast light-induced molecular motions experimentally using a synthetic approach schematically illustrated in Figure IV. Commonly, ultrafast motions for molecules such as **15f** for which intermediates are either not observable using standard analytical methods – or not even present – are attempted to be resolved by ultrafast transient techniques such as transient absorption spectroscopy, or theoretical predictions. However, these methods do rarely deliver detailed experimental geometrical information about configuration of intermediates or fail completely in cases where no observable high-energy intermediates are present. To this end, a synthetically based approach is presented embedding the molecular structure of interest into macrocyclic framework **33**. Through connecting the rotating part with a biaryl axis which is linked to the other end of the molecule with a covalently attached flexible linker all possible motions, clockwise (cw) and counterclockwise (ccw) can be observed.

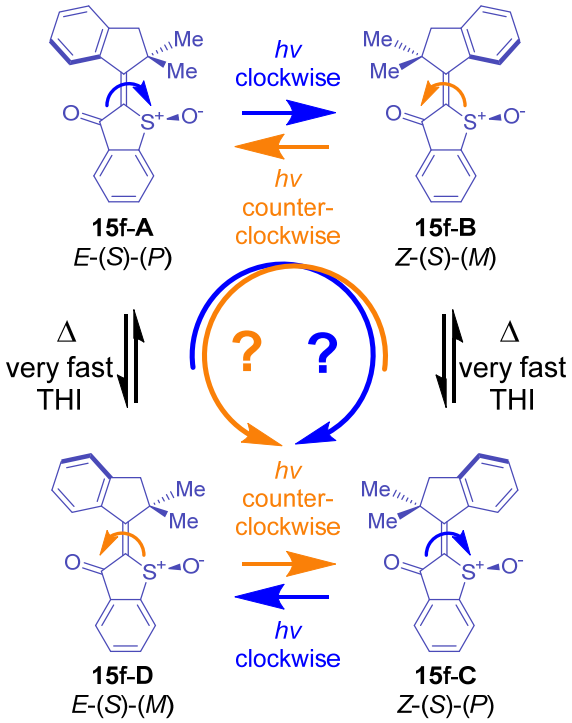

Figure IV Determining directionality of very fast light-powered molecular motors *via* direct experimental evidence can be very challenging since it involves observation of short-lived intermediates. In the case of overcrowded alkene motors, such as the depicted HTI-based system **15f**, this requires tracing of thermal helix inversion (THI). Structural lability resulting from reduced steric interactions do enable different feasibly rotation directions, namely clockwise (cw) rotation illustrated with blue arrows, or counterclockwise (ccw) rotation illustrated with orange arrows. A preferred rotation direction according to the initial helical twist has been assumed but not yet demonstrated. Adapted with minor format modifications from *Nat. Commun.* **2023**, *14*, 4595 licensed under CC BY 4.0.[1]

The plane of the terminal aryl should be as perpendicular as possible to the system of interest providing enough flexibility for both directions, namely the clockwise and counterclockwise movements. This was achieved through increasing steric bulk in *ortho*-positions of the biaryl axis. Consequently, the light-induced 360° rotation in the unrestricted system is now limited to two separate ~180° rotation-photoequilibria in the restricted macrocyclic system shown in Figure V. This allows to measure quantum yields (QYs) Φ for the clockwise and counterclockwise rotation in case of *e.g.* a molecular motor leading to values attributable to both directions. In other words, a thorough quantification of all possible involved rotational movements induced by light was feasible. After taking the macrocyclization effect into account, comparison of QYs to the corresponding unrestricted system delivered a direct prediction of unidirectionality according to best matching values. All QY measurements were repeated for verification by *Dr. Ani Özcelik*[V].

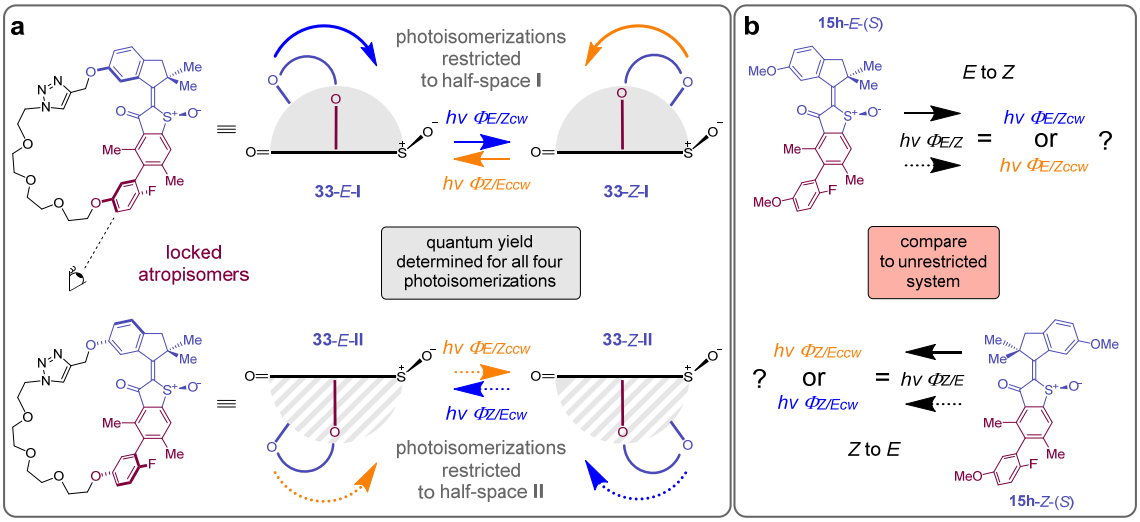

Figure V Determining of very fast molecular motor directionalities. **a** Setup for macrocyclic embedding **33** of very fast molecular motions including the motor of interest (blue), a biaryl moiety (purple), and a linking chain (black). Motions are restricted to either half-space **I** (grey, solid arrows) or **II** (dashed grey, dotted arrows) with respect to the sulfoxide oxygen by locked atropisomers. Individual measurement of quantum yields (QYs) Φ for all four possible photoisomerization directions allows to determine QYs for the cw rotation (blue arrows) and ccw (orange arrows). **b** These QYs can then be assigned to their respective counterparts in the unrestricted non-macrocyclic system **15h** (black arrows) allowing to predict its motion direction. Adapted with minor format modifications from *Nat. Commun.* **2023**, *14*, 4595 licensed under CC BY 4.0.[1]

This method does at least offer the possibility to make the distinction between a motor and a switch determining a preferred directionality if differences in QY for the respective directions are small. However, if QY differences of clockwise and counterclockwise motions are large enough it is possible to determine a semi-quantitative high or low degree of unidirectionality.

What is more, this methodology can also be extended to fast molecular motions without any high energy intermediates present since it does not rely on the observation of configurations but can instead trace back a motion to its starting state.

1.5. Structural reconfiguration of macrocyclic molecular motors Defining unidirectional motions

In the fifth and last part of this thesis a macrocyclic molecular motor system is presented shown in Figure VI which consists of an enlarged revolving door section with an integrated switchable biaryl axis, which is stable during motor operation at ambient temperatures and below. Through precise adjustment of the biaryl axis barrier *via* steric overcrowding and integration into the revolving door, two independent atropisomer configurations can be obtained which are each part of a different unidirectional cycle. Enlargement of the covalent linker enables movement of the biaryl – hence the respective revolving door – independent from its macrocyclic connecting tether. This defines the point of rotation during motor operation to be outside of the biaryl fragment.

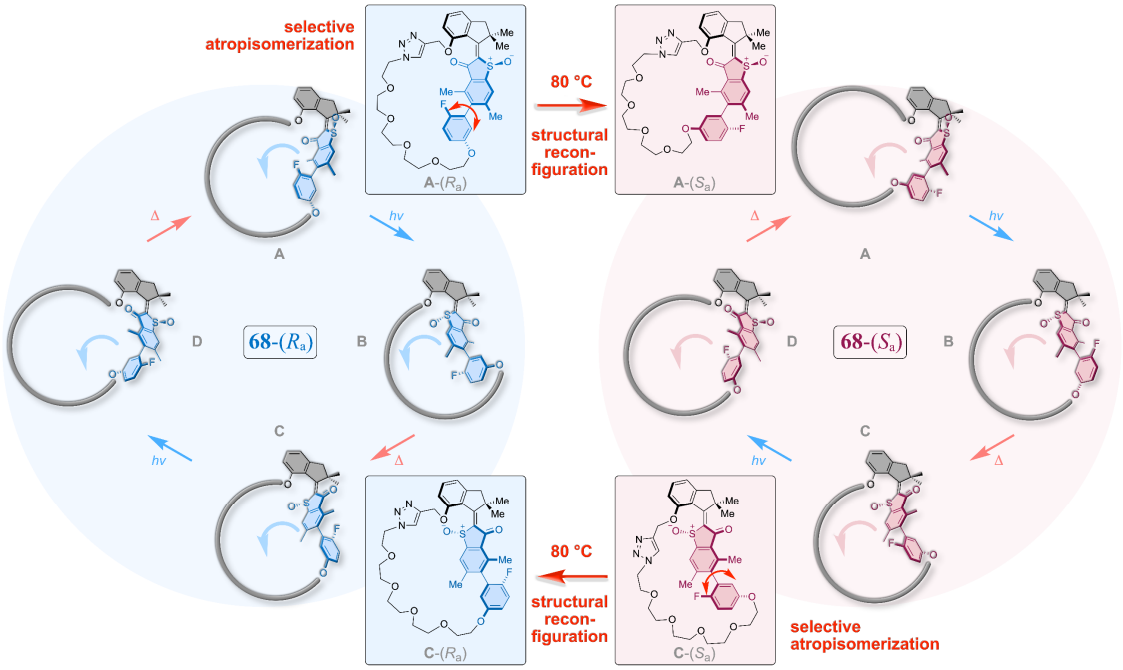

Figure VI Structural reconfiguration combines macrocyclic molecular motor cycle of **68**-(R_a) with **68**-(S_a). Independent rotation of enlarged revolving doors (blue and red highlighted structures) with identical directionality is achieved in **68**-(R_a) (blue) and **68**-(S_a) (red) within the same macrocyclic framework under illumination with visible light at ambient temperatures. The macrocyclic environment of the embedded molecular motor can be switched from **A**-(R_a) to **A**-(S_a) and from **C**-(S_a) to **C**-(R_a) at elevated temperatures *via* selective atropisomerization, namely structural reconfiguration. Adapted with minor format modifications from *J. Am. Chem. Soc.* **2023**, 145, 13081–13088 licensed under CC BY-NC-ND 4.0. Copyright © 2023 The Authors. Published by American Chemical Society.[2]

Furthermore, these two individual revolving door elements rotate in the same direction fueled by their respective motor units with highly selective interconversion possible at specific positions in each cycle *via* atropisomerization at elevated temperatures. In this way, an orthogonal stimulus introduces another

level of control for the unidirectional rotating revolving door which abrogates the conjunct motion leading to a sole single bond rotation along the biaryl axis, flipping its configuration. During this structural reconfiguration step, the point of rotation lies inside the revolving door, more specifically in the middle of the biaryl axis. Afterwards, the resulting reconfigured macrocycle can again be operated employing the enlarged revolving door again at ambient temperatures and below. The motor rotation mechanism was only affected slightly from this design with respect to operational speed, or wavelength dependency demonstrating two entirely functional unidirectional molecular motor cycles within one macrocyclic machine.

2. Introduction

2.1. Preface

Life – in its present form on planet earth – mainly exists because of an immense variety of nanomachinery operating on a molecular scale sustaining a multitude of vital functions.[3,4] These range from replication of genetic information involved in the continuity and evolution of life,[5] to cargo transport through kinesin proteins,[6] to adenosine triphosphate (ATP) synthesis[7–9] perpetuating a plethora of processes in living organisms.[10] In view of the relevance of these striking machinery for the existence of mankind, humans strived to mimic these imposing biological machines by developing artificial ones or coming forth with new concepts. This led to the emergence of a relatively young field engaged with the development of artificial molecular machines for which the Nobel prize in Chemistry has been awarded in 2016 to *Jean-Pierre Sauvage*, *Sir J. Fraser Stoddart*, and *Bernard L. Feringa*.[11–13]

These complex molecular machines can be broken down or compared to much simpler units such as the thermally activated rotors, brakes and gears or the actively-driven, *i.e*. light-powered switches, pumps, motors and the recently added photogears.[14–16] For the actively-powered entities, an energy input is necessary for operation. To this end, a variety of stimuli have been proposed comprising chemical and thermal ones or electromagnetic radiation. Visible light is arguably amongst the ideal stimuli to date because of its high spatio-temporal resolution and non-destructive nature.[17–20] Thus, with visible light and thermal excitation as the two only stimuli utilized for responsive molecules within this work, these will also be mainly focused on during this prelude. However, despite molecular machine exploration being a young area of research, photochromism has already been described as early as 1867 by *Fritzsche,*[21] who reported on anthracene dimerization upon sunlight exposure which paved the way towards control of molecular structures with light. In contrast to this, the first anthropogenic molecular motor has just been developed in 1999 by *Feringa*.[22]

This work focuses on actively visible light-powered molecular switches, motors and machines and theory as well as insightful examples concerning these compound classes will be elaborated and discussed in detail in the following chapter.

2.2. Photochemistry

The field of photochemistry examines the interactions between electromagnetic radiation in the range of 100–2500 nm – which corresponds to energies between 11.0–286.0 kcal mol^{-1} – and physical matter.[23,24] This correlates with chemical bond energies, which lie between 2.0–9500.0 kcal mol^{-1} for

hydrogen bonds at the lower end and ionic bonds as the strongest ones.[25] These so-called photoreactions range from simple reactions like homolytic bond cleavage forming radicals or isomerization reactions between two species[26] to catalytic reactions[27] to highly complex transformations forming natural products.[28] Natural occurring processes make use of photochemical reactions in vital life sustaining mechanisms, such as photosynthesis, isomerization reactions of retinal involved in human visual perception, as well as the synthesis of vitamin D by sunlight in the human body.

The basis of all photochemical processes is the absorption of a photon possessing a certain energy. In the case of the visible light spectrum, the human eye does perceive this absorption as a color resulting from the removal of a fraction from the sunlight spectrum. This frequency band from the sun which would be observed as white is reflected to the human eye without the absorbed part of the spectrum resulting in a color corresponding to the mixture of the remaining wavelengths, see chapter 2.3.1. The molecular part responsible for photon absorption and the resulting observed color is called chromophore. This concept in terms of absorbed and emitted energies is straightforwardly illustrated by the *Jabłoński* diagram, shown in Figure 1. The electronic ground state S_0 of a molecule can be excited with a photon of energy λ corresponding to the difference between the electronic ground state, typically in the lowest vibrational state S_0v_0, and the corresponding electronically excited state, typically in a vibrationally excited state S_1v_x, it transitions to in a process called absorption.

It must be noted that not all transitions have equal probability to occur. Each combination of electronic and vibronic state can be represented using a wavefunction and transitions where overlap between the initial and the excited state wavefunction is maximal have greater probability to arise. In other words, the probability for a transition is proportional to the square of the integral overlap between the initial and the excited state wave function, called the *Franck-Condon* principle. In a classical sense, the movement of the nuclei in a molecule are very slow relative to the timescale of the absorption process (see Table 1) with the result that the former can be assumed stationary. With this assumption in mind, it becomes clear why excitations are depicted vertically in energy vs. reaction coordinate diagrams (see Figure 5), since changes in geometry are linked to changes in nuclei coordinates. As a result, excitations and de-excitations usually occur as vibronic transitions which means that they are usually accompanied with a simultaneous change in electronic and vibrational state of the molecule. In other words, the most probable transitions are usually the ones which involve excitation to a different vibrational state of the excited electronic state with respect to the vibrational state of the electronic ground state where the excitation occurred from and *vice versa*. This does furthermore also explain the occurrence of shifts to longer wavelengths, leading to an energy loss between absorption and fluorescence or phosphorescence emission. This loss originates from the fact that absorptive and emissive processes have the highest probability to occur from the lowest vibrational state of a given electronic state, because of timescale differences of involved processes (see also Table 1 below). Since this results in an energy difference

between absorption and emission energy originating from vibrational relaxation, a wavelength shift between absorption and emission spectra can be observed, called *Stokes* shift.

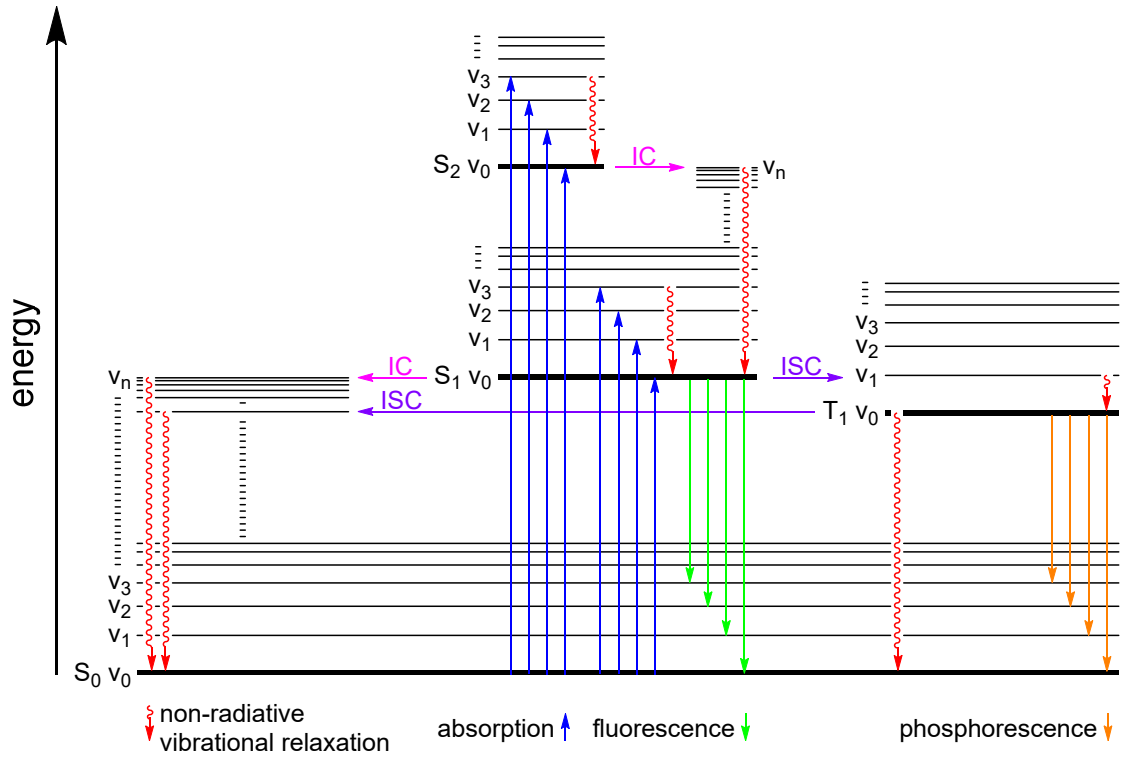

Figure 1 *Jabłoński* energy diagram depicting photophysical processes from excitation *via* absorption (blue) to various modes of de-excitation, namely fluorescence (green), phosphorescence (orange) and non-radiative vibrational relaxation (red). Internal conversion (IC) is depicted in pink and intersystem crossing (ISC) in purple. Only the first three electronic singlet states S_0–S_2, the first triplet state T_1 and the first four vibrational states v_1–v_3 are explicitly considered for excitation and de-excitation processes for reason of clarity.

From the excited vibrational state in the electronically excited state $S_{\geq 1}v_{\geq 1}$ relaxation occurs to the lowest vibrational mode $S_{\geq 1}v_0$ dissipating the corresponding energy as heat. From this lowest mode, multiple possibilities for de-excitation pathways exist. First, internal conversion (IC) can occur without energy loss to an isoelectronic higher vibrational mode of the electronic ground state $S_0v_{\geq 1}$ followed by non-radiative vibrational de-excitation. Secondly, de-excitation to the electronic ground state in an emissive fashion while spin multiplicity is maintained can occur resulting in emission of a photon corresponding to the energy difference between the two states, which is called fluorescence. Thirdly, intersystem crossing (ISC) involving a change in spin multiplicity to a triplet state with a longer lifetime can occur, resulting in delayed de-excitation *via* spin multiplicity altering emission called phosphorescence. From this triplet state, ISC to a vibrational mode $v_{\geq 1}$ of the S_0 ground state followed by non-radiative vibrational relaxation is also possible. Furthermore, these processes are also possible for higher electronic states $S_{>1}$ but omitted here for clarity.

The timescale on which the photophysical processes depicted in the *Jabłoński* energy scheme occur can be found in Table 1. From this table, *Kasha's* rule can be derived by comparing the timescale between vibrational relaxation and the fastest radiative emissive process, namely fluorescence. Comparing these numbers, it becomes clear that as a rule of thumb vibrational relaxation to the lowest excited state vibrational mode of a given multiplicity does always occur faster than any radiative de-excitation process.

Table 1 Average timescales for processes involved in the *Jabłoński* energy diagram describing the radiative and non-radiative interaction of light and physical matter.

isomer	timescale in s	radiative process
absorption	10^{-15}	yes
nuclei movement period	10^{-14}–10^{-13}	no
internal conversion (IC)	10^{-14}–10^{-9}	no
vibrational relaxation	10^{-12}–10^{-10}	no
intersystem crossing (ISC) (S→T)	10^{-12}–10^{-6}	no
intersystem crossing (ISC) (T→S)	10^{-9}–10^{-1}	no
fluorescence	10^{-10}–10^{-7}	yes
phosphorescence	10^{-6}–10^{5}	yes

While all the above-mentioned photophysical processes lead back to the initial ground state geometry, all photochemical-based nanomachinery exist in at least two different molecular states. Namely the global thermodynamic stable minimum and at least one metastable local minimum. These geometries represent different chemical species and can be interconverted by conformational changes, bond breaking or forming processes, and redox processes. To understand these photochemical reactions – involving two or more species – a slightly more elaborated model needs to be applied, which is explained in the following chapter.

2.3. Photoswitches

Molecular photoswitches are molecules that can be isomerized between at least two states in a reversible manner, with a minimum of one isomerization process occurring in response to light irradiation. Typical photoreactions are *Z* to *E* and *E* to *Z* double bond isomerizations as observed in stilbenes,[29] azobenzenes,[26] diazocines,[30] arylhydrazones,[31] indigos,[32] thioindigos,[32] hemiindigos (HIs),[32] hemithioindigos (HTIs),[32,33] iminothioindoxyls,[34] and indirubins[35] or ring-opening and -closing reactions observed in spiropyranes,[36,37] spirooxazines,[36] diarylethenes,[38,39] norbornadienes,[40–42] donor-acceptor *Stenhouse* adducts (DASA),[43,44] dihydroazulenes,[45,46] fulgides,[47,48] and fulgimides.[49] For examples of each of the above-mentioned photoswitch classes see Figure 2 and 3 respectively, except for indigoid-based photoswitches which are discussed in more detail in chapter 2.3.2.

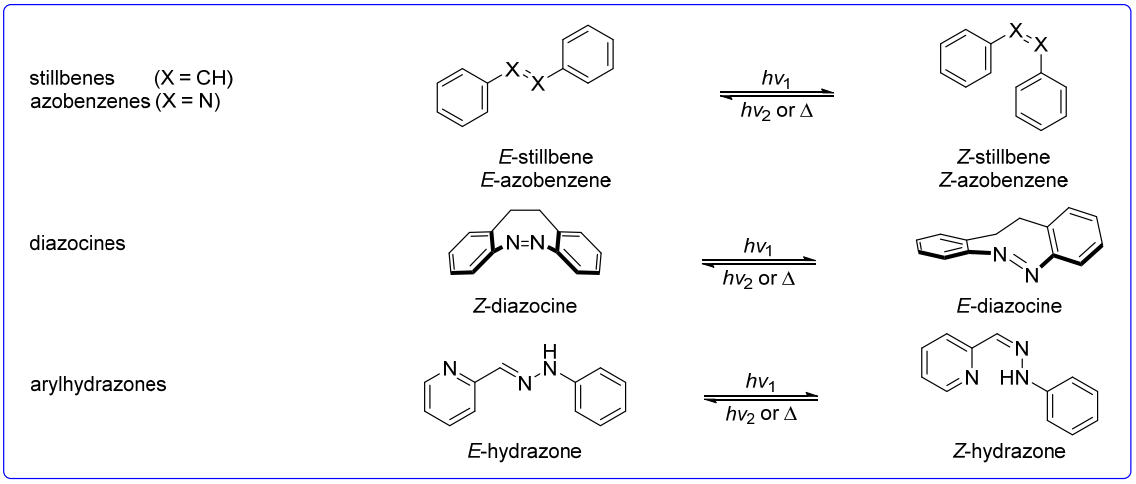

Figure 2 Various photoswitch compound classes exhibiting *E* to *Z* and reverse phototisomerizations (blue frame). Examples for *E* to *Z* and *Z* to *E* phototisomerizations of stilbenes,[29] azobenzenes,[26] diazocines,[30] and arylhydrazones.[31]

Photoswitches which undergo ring-opening and -closing reactions (Figure 3 red frame) do usually display stronger differences in absorption spectra because of severely changed electronics between isomers but only little geometry change. The other compound class of switches which undergo *E* to *Z* and reverse isomerizations (Figure 2 blue frame) exhibit much larger geometrical changes, but less pronounced absorption spectra change since electronic differences are not that pronounced. Hence, molecular nanomachinery design does commonly rely on the use of the latter because significant conformational changes are ideally suited to induce further geometry changes at the molecular scale.

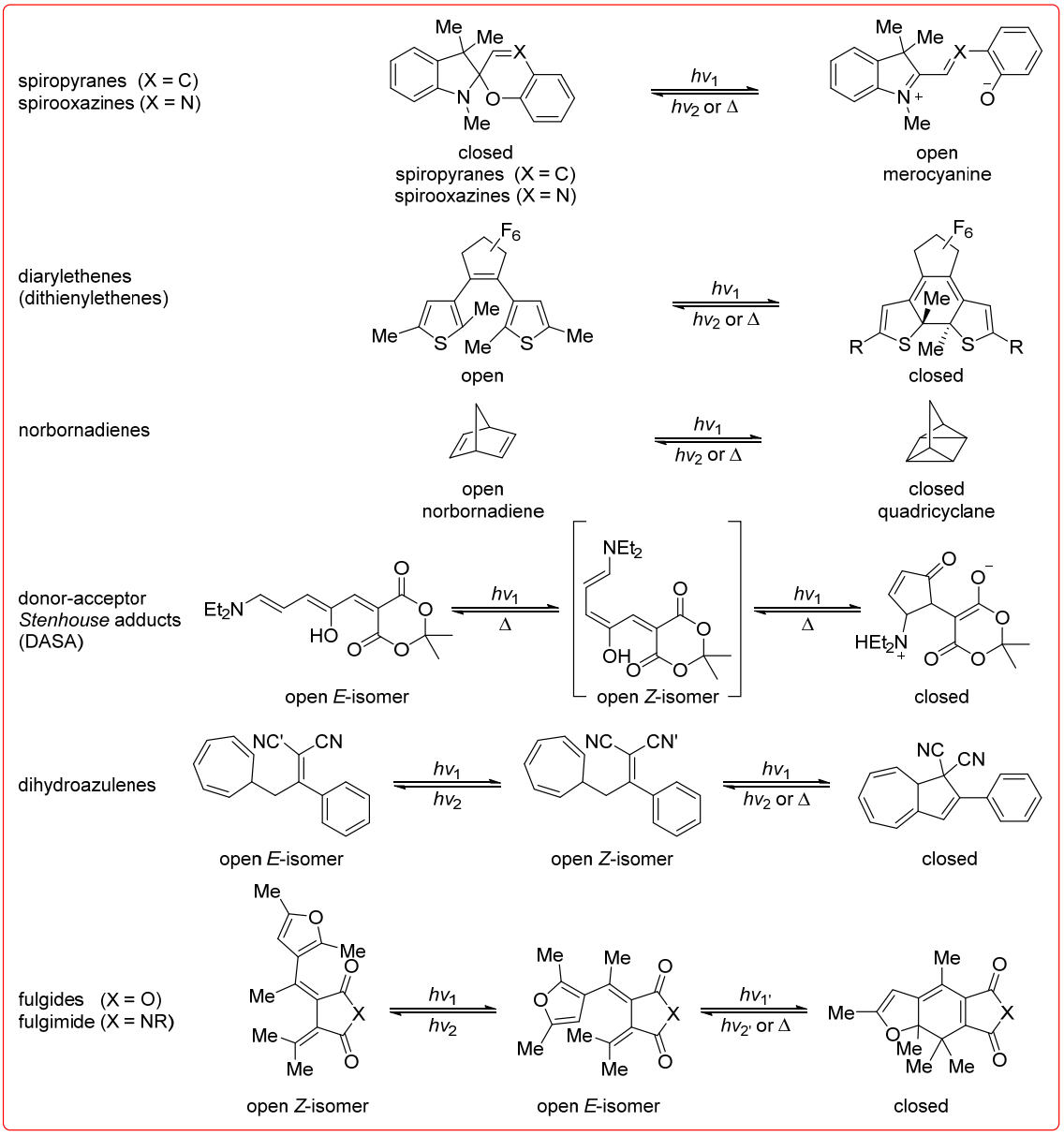

Figure 3 Various photoswitch compound classes exhibiting ring-opening and -closing reactions (red frame). Examples for ring-opening and -closing reactions of spiropyranes,[36,37] spirooxazines,[36] diarylethenes,[38,39] norbornadienes,[40–42] donor-acceptor *Stenhouse* adducts (DASA),[43,44] dihydroazulenes,[45,46] fulgides,[47,48] and fulgimides.[49]

2.3.1. Photoswitching theory

As stated above, photoswitches are molecules able to isomerize between at least two states upon irradiation with light of a specific wavelength. These two isomers **A** and **B** are usually photochromic compounds with different absorption spectra as depicted for an idealized photoswitch in Figure 4. The difference between the absorption maxima is one factor determining the performance of a photoswitch

resulting in easier distinction between the two states and enhanced addressability of each state with the corresponding wavelength.

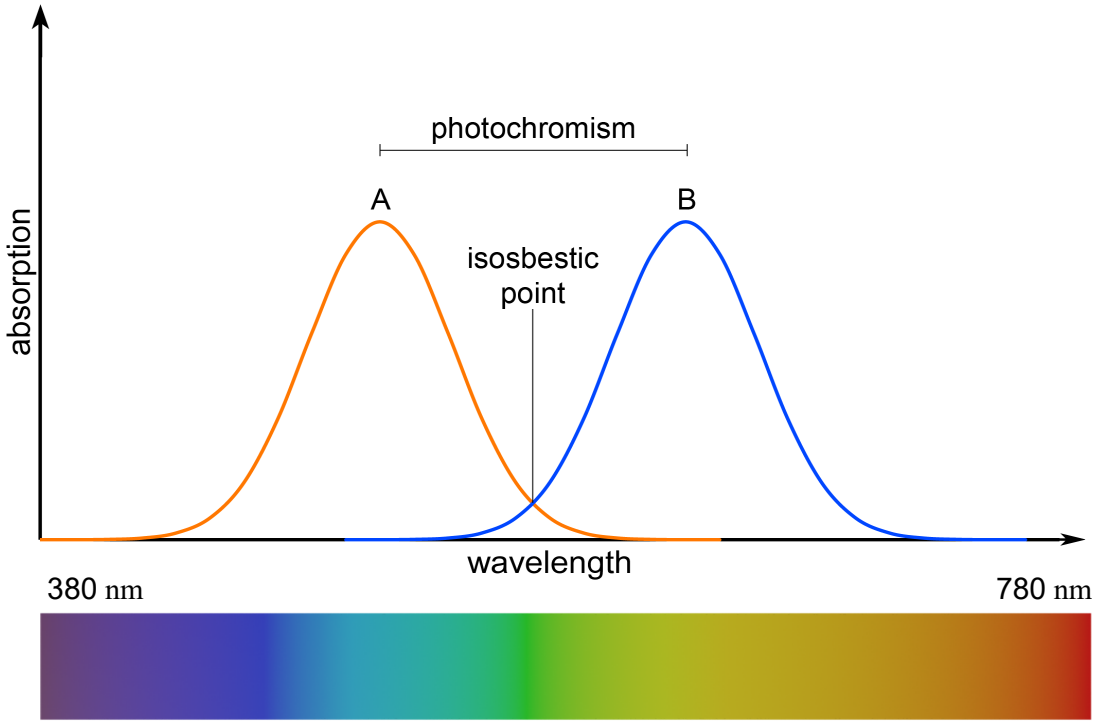

Figure 4 Absorption spectra of an idealized two state photoswitch. The orange spectrum represents isomer **A** and the blue spectrum isomer **B**. The difference between the two absorption spectra is called photochromism.

Photochromism is defined as the overall difference between two distinct absorption spectra. For the ideal photoswitch in Figure 4 this means isomer **A** does appear orange since the blue part of the visible light spectrum is absorbed, reflecting a mixture of the other colors resulting in an orange-colored compound. For isomer **B** this would be blue because of absorbing the red fraction from the Vis spectrum. Hence, the difference between the orange and blue spectra of isomers **A** and **B** respectively is called photochromism.

During the process of photon absorption, the photoswitch reaches an excited state which can decay back to the ground state in a non-radiative or emissive process such as fluorescence or phosphorescence. However, this behavior is also observed for non-switching chromophores. What characterizes a switching molecule is that there is at least one additional metastable ground state present. The electronic states depicted in the *Jabłoński* energy scheme shown in Figure 1 represent potential energy surfaces defined by moleculelar geometry and energy as depicted in a simplified 2D energy diagram shown in Figure 5. Basic concepts such as *Gibbs* energy of activation $\Delta G^{\ddagger}$ and the *Gibbs* energy ΔG are illustrated

as the energy difference between the metastable state and the transition state (TS) in between or the ground state and the metastable state respectively.

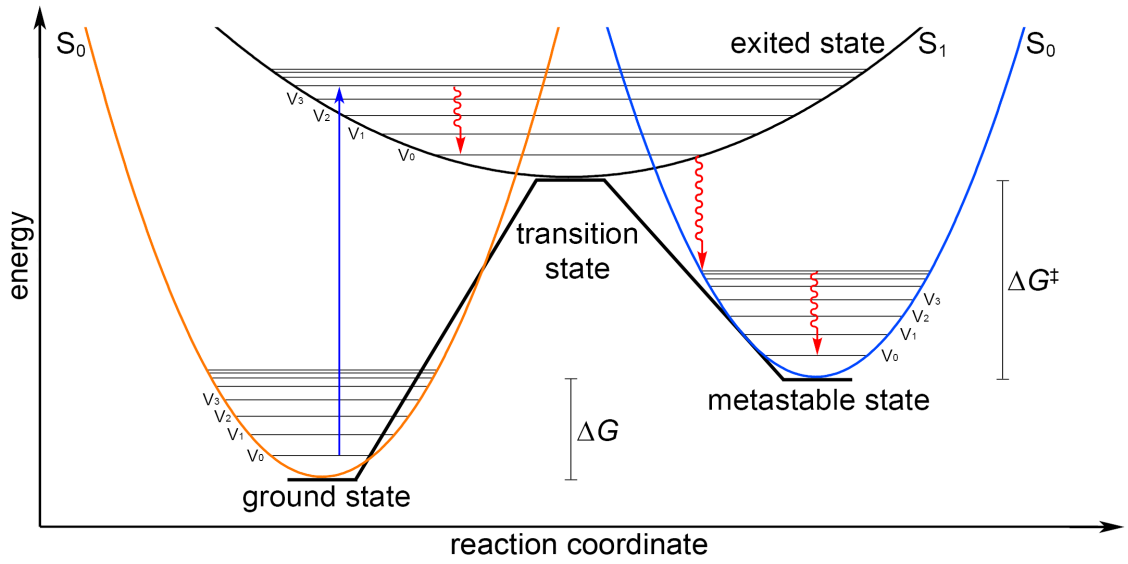

Figure 5 Simplified photoswitching energy scheme. Illustrated are the ground state (orange), the metastable state (blue) and the excited state (black) of an imaginary photoswitch. The *Gibbs* energy of activation $\Delta G^{\ddagger}$ and the *Gibbs* energy ΔG are illustrated within the energy scheme as well as the photoswitching process *via* absorption (blue arrows) and vibrational relaxation (red arrows) from the ground state to the metastable state *via* the excited state.

After the absorption of a photon, a molecule in the ground state S_0 is excited to a higher singlet state, *e.g.* S_1, with excitation into higher electronic states $S_{>1}$ being also possible but omitted here for clarity. From the excited vibronic states $S_1v_{>0}$, non-radiative de-excitation to the lowest vibrational excited state S_1v_0 occurs from which in turn de-excitation happens resulting in decay of the excited state S_1 back to the ground state S_0, which is known as *Kasha's* rule. This is depicted exemplarily for the isomerization from the global thermodynamic vibrational ground state minimum S_0v_0 (orange) to the metastable vibrational ground state minimum S_1v_0 (blue) in Figure 5. However, since two ground states are accessible – the metastable and the global thermodynamic stable ground state – it is possible, that according to the intersections between the excited and the ground state potential surface – called conical intersections – a de-excitation in either of the two is possible. A conical intersection is defined as one or multiple points on two different electronic potential energy surfaces with degenerated wave functions. In other words, a conical intersection allows the funneling between excited $S_{>0}$ and ground states S_0. In this context a photophysical process is characterized by a reaction back to the initial starting geometry before photon absorption and a photochemical process by a reaction to a different molecular geometry. The photochemical process represents the incident of photoswitching.

Choosing an adequate energy quantity for excitation *i.e*. wavelength, does influence the photostationary state (PSS), which is defined as the wavelength dependent equilibrium composition between two or more isomers. However, this is only a result of the different photochromism of the respective isomer and not depending on the process after photon absorption if *Kasha's* rule is not violated. Furthermore, the quantum yield (QY) of a given photophysical or photochemical process is also not wavelength dependent since non-radiative relaxation to the lowest excited state does occur before any geometry inducing or radiative relaxation, which is known as the *Kasha-Vavilov* rule.

This theoretical explanation of photoswitching is the foundation of a variety of photochemical transformations which can become considerably more complex for systems with more possible metastable states or intermediates leading to a sizeable number of possible pathways. However, photodriven switches, molecular motors and more elaborated molecular machinery as well as their non-photodriven counterparts can usually be described by means of energy schemes based on this simplified concept.

2.3.2. Indigoid-based photoswitches

Indigo as a dye has been known to human civilizations for millenia with the oldest trace found in 6000-year-old cotton fabrics in the ancient Andes in the north of Peru.[50] However, it took until 1883 for *Adolf von Baeyer*[51] to first synthesized indigo artificially and elucidated its structure for which he got *i.a*. awarded the nobel prize in chemistry 1905. Plain unsubstituted indigo is unfortunately a very limited photoswitch since it undergoes rapid excited state proton transfer (ESPT) resulting in very efficient de-excitation back to the global thermodynamic ground state minimum.[52] This can be circumvented effectively by introducing residues on the nitrogen atoms allowing the observation of *E*/*Z*-photoisomerization.[53–56] Furthermore, thioindigo was first synthesized by *Paul Friedländer* in 1906,[57] but it took until 1942 for *Stearns*[58] followed by *Wyman* in 1951[59] and *Rogers* in 1957[60] to report upon its photochromic properties. The half indigo or thioindigo derivatives hemiindigo and hemithioindigo have both also been known as synthetic dyes described by *Adolf von Baeyer*[51] and *Paul Friedländer*[57] respectively, but their photoswitching behavior were only reported in 1961 for hemithioindigo and 1970 for hemiindigo by *Mostoslavskii*.[61,62] More recently, iminothioindoxyl was presented as a novel indigo-based photoswitch compound class,[34] aurones were investigated,[63] indirubin was modified in order to serve as a photoswitch,[35] as well as the more distant rhodanine photoswitches were utilized for photopharmacology.[64] Parent compounds for all the above-mentioned indigo-based photoswitches are shown in orange framed Figure 6.

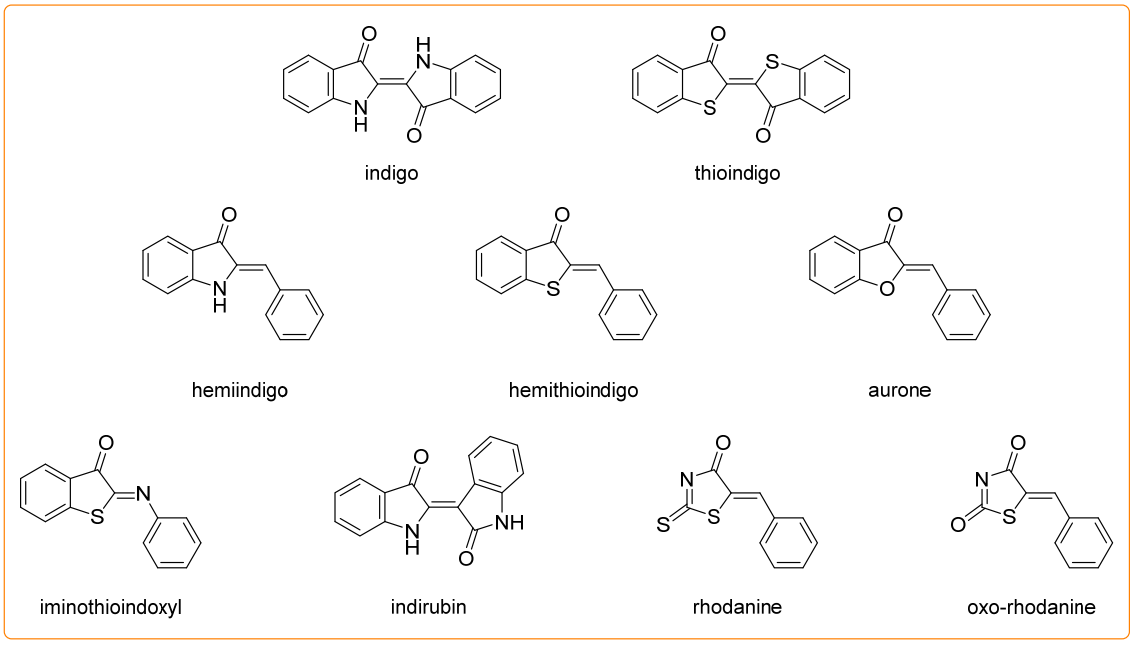

Figure 6 Structures of parent unsubstituted indigo, thioindigo, hemiindigo, hemithioindigo, aurone, iminothioindoxyl, indirubin, rhodamine, and oxo-rhodanine photoswitches.

Among indigoid-based photoswitches especially HIs and HTIs benefit from red-shifted absorption, near quantitative switching, very long half-lives of metastable states up to thousands of years at 25 °C, high fatigue resistance,[65] pronounced visible light photochromism close to the biooptical window starting at >700 nm[20] and high QYs in both directions.[32,53,66] Switching of the commonly thermodynamic stable *Z*-isomer to the usually metastable *E*-isomer (see orange framed Figure 7) can be achieved by irradiation with visible light around 400 nm while the reverse reaction occurs using wavelengths around 500 nm or through supplying thermal energy. Owed to these properties applications of HI, HTI, and other indigoid-based photoswitches range from photopharmacology,[64,67–73] as a result of their red light addressability,

allowing for deeper skin penetration of the utilized irradiation wavelength,[74] to sensing,[75–77] information processing,[78,79] and material science.[80,81]

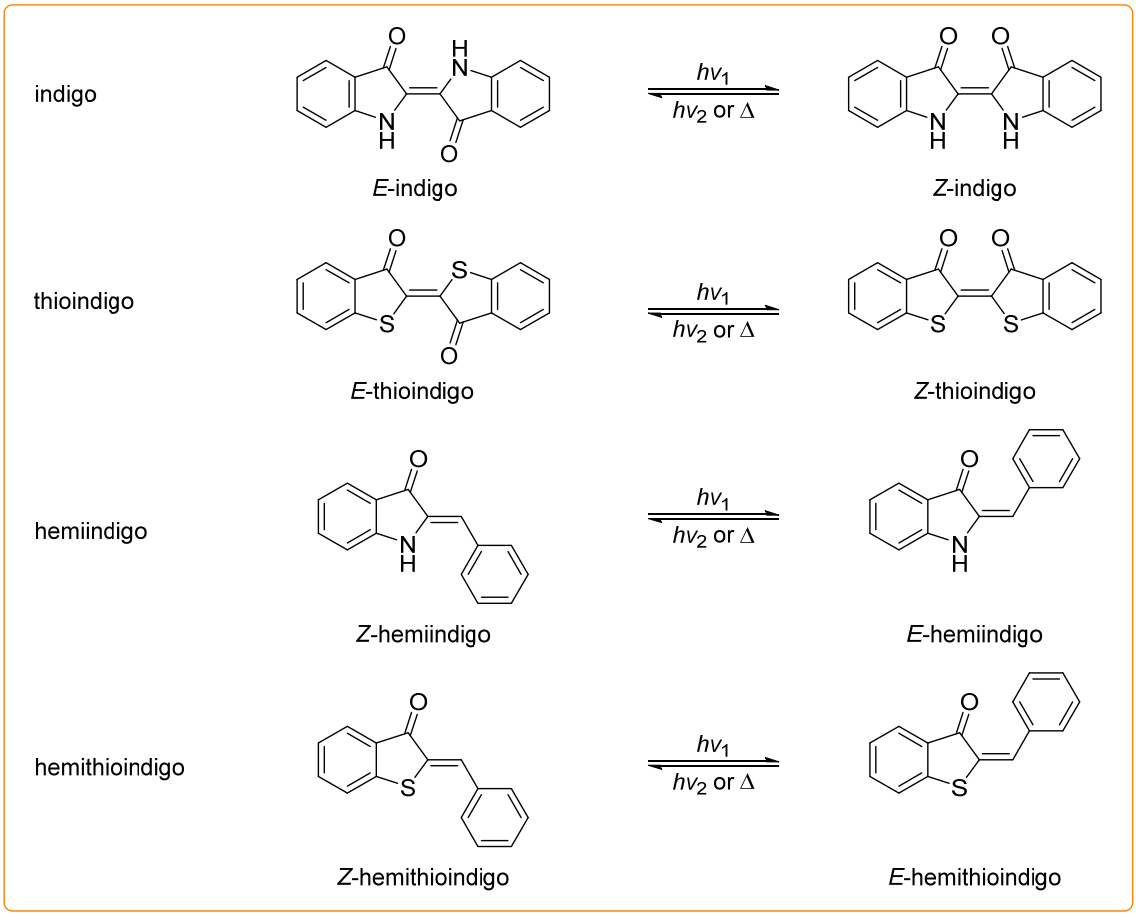

Figure 7 Examples of *E*- and *Z*-isomers of indigoid-based parent photoswitches, namely indigo, thioindigo, hemiindigo, and hemithioindigo.

In recent years, indigo-based photoswitches have been developed with respect to heterocyclic substituents,[66,82,83] diaryl substituents,[79,80,84] novel unprecedented isomerization reactions,[84–86] host-guest encapsulation or molecular tweezers,[75–77,87] alternative connectivity,[35,86] tuning of photoswitching behavior or thermal stability,[88–93] all-red-light photoswitching,[94] and reversible photochemical bond formation reactions[95] to name only a few recent developments.

2.4. From switches to molecular motors

The first notion of artificial molecular machines was made by *Richard Feynman* in his famous 1960 lecture "There's Plenty of Room at the Bottom".[96] Only half a century later the Nobel Prize got awarded for the "Design and synthesis of molecular machines".[11–13] While photochromism has already been described as early as 1867, developing the first unidirectional rotating artificial molecular motor took more than another 130 years. The first unidirectional rotary motion has been reported by *Kelly et al.*[97] in 1999 capable of a 120° directional rotation based on their molecular ratchet designs.[98–101] The same year *Feringa* published the first unidirectional 360° continuous rotary motion of an overcrowded alkene motor[22] based on the more promising light switchable overcrowded alkene double bond connected architecture.[102,103] In the time since, a huge variety of molecular nanomachinery has been devised.[14,104–107]

Molecular photoswitches are molecules existing in at least two different states which can be selectively addressed and reversibly interconverted in at least one direction stimulated by light. In contrast to molecular motors – which are discussed in chapter 2.4.2.1 and 2.4.2.2 – the work performed by switches is undone upon their returning to their initial state or by continued switching. This is a result of the forwards and backwards reactions undoing all work performed along one direction. In other words, forwards and backwards motions occur in a mirror-symmetric fashion with equal probabilities.

Molecular motors are defined as a subclass of molecular machines which can convert energy into directional molecular motion. In contrast to molecular switches, rotating motors reach the initial state during their rotation cycle *via* a *net* pathway oriented in one direction only. Their motion follows one pathway without the proceeding of the respective reverse or backwards reaction which allows to utilize molecular motors to drive a respective coupled system continuously away from its thermodynamic equilibrium.[104–106] This is illustratively explained in biological molecular motors such as the ATP synthase which forms ATP along an energetically uphill pathway driven by a downhill concentration gradient.[6] This biological fuel is then used *i.e.* to unidirectionally drive the kinesin motor along microtubules.[7–9]

Noteworthily, two classes of directional motors can be found in nature namely linear motors including myosin,[108] kinesin,[109,110] and dynein,[111] and rotary motors represented by ATP synthase,[112] V-ATPase,[113] and flagellar motors.[114] With more and more biologically machines discovered, their relevance for organic life became significantly more apparent, leading to the ever-increasing scientific question if these machines can be artificially recreated.[115,116]

Performing directed motions against ever-present inherent forces in solution such as random Brownian motion or ground state vibrations requires additional energy input not inherently present in the thermal

bath. This challenge has been overcome by the design of chemically,[107] electrically[117] or light-powered molecular motors.[14] Since this work solely discusses purely light- and thermally-powered switches and motors, the following examples of molecular machinery are also exclusively based on these stimuli.

2.4.1. Linear directional molecular motions

To achieve directed linear transport several fundamental requirements and conditions need to be met. Firstly, the moving unit must be associated to the track in some way. Secondly, a directionality greater than 50% is to be given to call it a directed motion. Thirdly, the motion should be repetitive. Fourthly, the moving entity should end up in its initial position without undoing the work performed, or in other words should reach its initial state along one direction of the trajectory without a backwards movement. Lastly, the movement should ideally occur as long as the energetic input stimulus is present and without additional interference from outside of the system.

The first artificial molecular walker of this sort was reported by *Leigh* in 2010 migrating along a track shown in Figure 8.[118,119] The operational mechanism consists of reversible orthogonal dynamic covalent chemistry, namely a hydrazone and a disulfide exchange reaction which are locked under basic and acidic conditions respectively while alternating the conditions enable the movement of the walker.

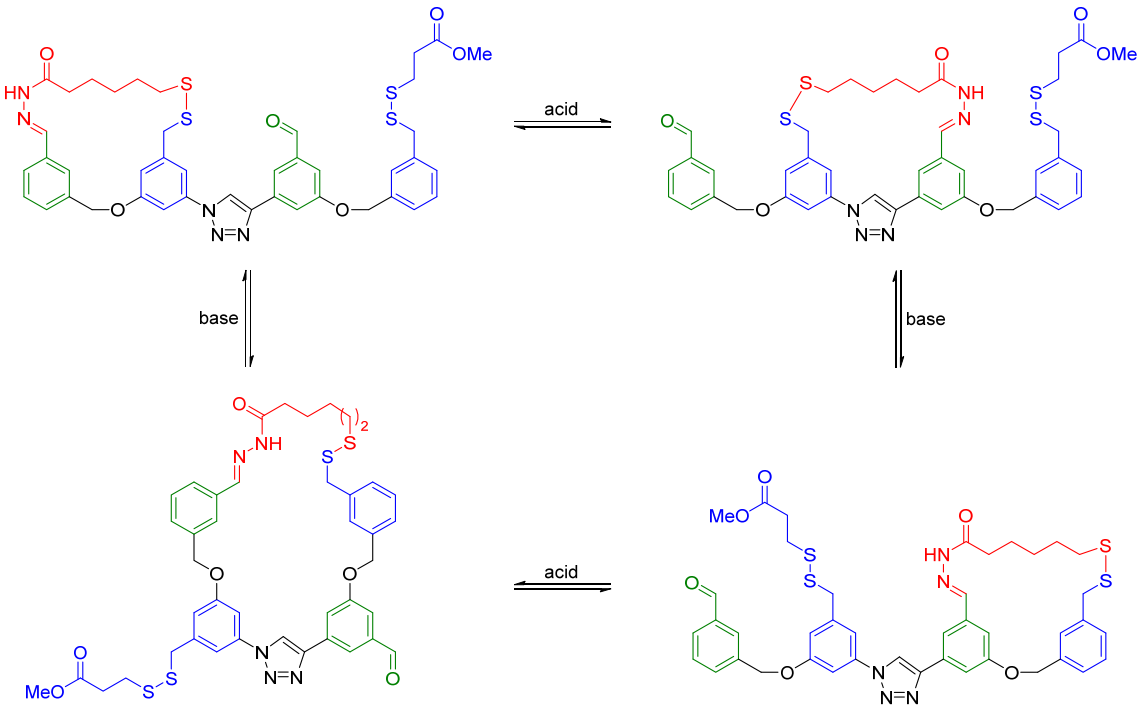

Figure 8 First example of an artificial linear translational small molecule published by *Leigh* in 2010.[118,119] Reversible reactions are used moving the molecular walker in one direction. However, continuous movement halts after a few cycles since an equilibrium distribution is reached.

However, after some cycles a steady-state equilibrium distribution is reached representing the global energetic minimum resulting in no *net* movement of the walker anymore. Directionality in this system is a result of the nonsymmetric and out-of-equilibrium starting point, which reaches equilibrium resulting in a non-continuous directional movement. This system was further elaborated including a photochemical *E*/*Z*-isomerization favoring one position of the track over the other as a result of spatial proximity using a stilbene.[120] Later, the concept of directed linear motion was developed even further, resulting in the design of a rotaxane-based peptide synthesizing machine by *Leigh* in 2013,[121] an artificial molecular pump by *Stoddart* in 2015[122] and light-powered directed linear motion in 2015 by *Credi*[123] to name just a few recent advancements.

2.4.2. Rotary directional molecular motors

Besides chemically driven linear moving motor systems, chemically fueled rotating motors do also exist. Generally, these rotary systems are based on chemically fueled single bond rotations, catenane-based circular motions or light-fueled double bond rotations. Furthermore, double bond rotation systems can be classified into symmetric and asymmetric designs.

2.4.2.1. Single bond rotation based designs

A molecular motor based on single bond rotation was initially conceptualized for a non-repetitive unidirectional 120° rotation[97] by *Kelly* in 1999 and further elaborated in 2003 but still lacked directionality[124] until an operational biaryl-based design was presented in 2005 by *Feringa*, which is shown in Figure 9. A series of deprotection and lactonization followed by asymmetric lactone reduction, protection and oxidation reactions drive the rotor fragment of the biaryl in one direction. After 180° rotation, this sequence is repeated leading to a full directional 360° rotation,[125] enabled by the advancement in atroposelective synthesis.[126,127]

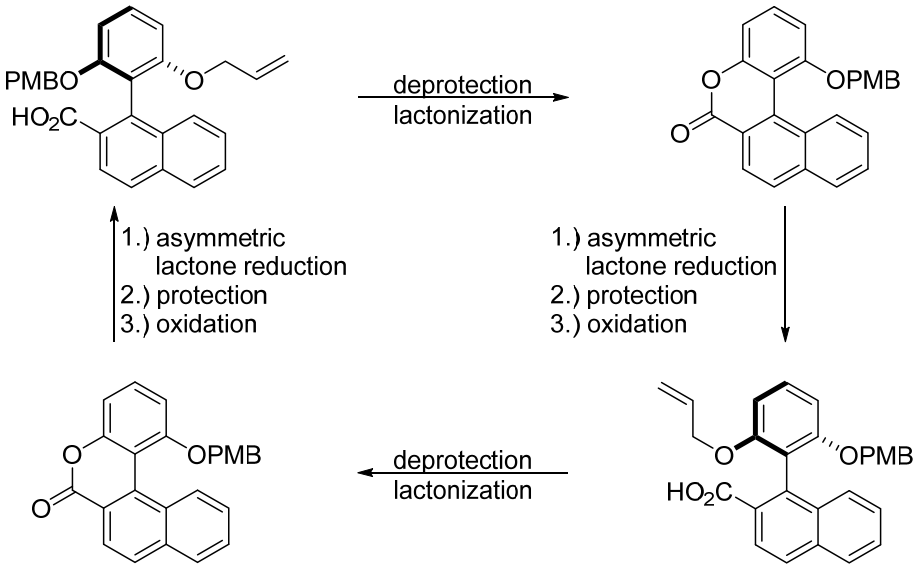

Figure 9 Atropisomerization-based molecular motor developed in 2005 by *Feringa*.[125] Starting from the top left structure, deprotection followed by lactonization leads to the bicyclic ring system on the top right side. An asymmetric ring-opening reaction leads to a continuous rotation of the biaryl and is followed by protection group addition and oxidation furnishing the bottom right molecule. The initial state can be regenerated repeating these steps *via* the bottom left configuration leading to a full directional 360° rotation.

In related systems developed subsequently, unidirectional 360° rotation around a single bond has also been achieved utilizing a palladium redox cycle in 2016,[128] and an improved lactone-based design with quantitative directionality in 2020[129] by *Feringa* or anhydride formation and hydrolysis for an autonomous fueled directional rotation by *Leigh* in 2022.[130]

2.4.2.2. Double bond rotation based designs

Control of molecular ratcheting mechanisms – explained in more detail below – which subsequently lead to the emergence of rotary directional molecular motions was first inherited from theory into molecular designs in 2003 from a catenane rotary motor system developed by *Zerbetto*.[131,132] Even though they are not double bond rotation based designs, these systems paved the way for ratcheting mechanisms which most double bond rotary motors are based upon. Ratcheting on a molecular scale is defined as a process which – below a specific temperature – only proceeds in one direction. This is attributed to a significantly higher energy barrier of the backwards process leading to a reaction progressing to completion without entering a thermal equilibrium. In other words, by introduction of asymmetry in the molecule an asymmetric kinetic barrier is realized as well, which does – in conjunction with energy input – lead to directional *net* equilibration.[133–135] This development lead to the first autonomous chemically driven fully unidirectional catenane-based motor system[136] in 2016 shown in

Figure 10, which was improved with respect to previous systems that did not allow autonomous operation.[131,137]

In this [2]catenane-based system, through removal of the red 9-fluorenylmethoxycarbonyl (Fmoc) groups the blue benzyl amide macrocycle is transported in a clockwise fashion towards the next green station on the track. Key to unidirectional motion in this design is the increased reaction rate for attachment of the bulky red stopper groups at the far end, where the small blue ring is not present, while cleavage is independent from the blue macrocycle position. Therefore, this design does lead to an overall unidirectional net motion of the small amide macrocycle around the large macrocycle in a clockwise fashion as depicted in Figure 10. Rotational movement of the catenane occurs as long as chemical fuel – responsible for protecting group cleavage and attachment – is provided to the system.

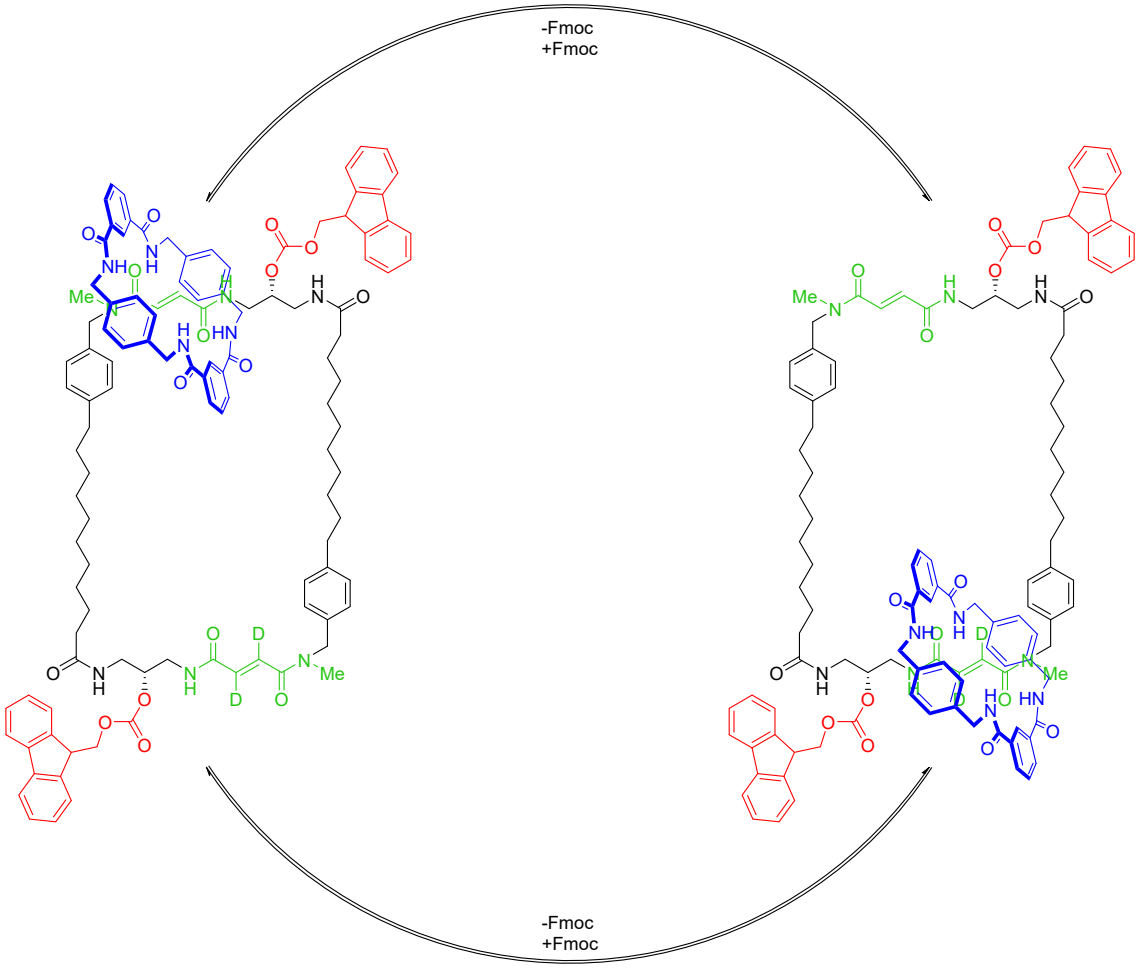

Figure 10 First autonomous chemically driven [2]catenane motor reported by *Leigh* in 2016.[136] Key for the operating mechanism of this motor is that attachment of the 9-fluorenylmethoxycarbonyl (Fmoc) protection group is faster for the position further away from the cyclic benzylic amide while cleavage is not influenced by the position of the blue ring. This leads to a *net* rotation of the benzylic amide ring in a clockwise direction from the non-deuterated to the deuterated station and to the non-deuterated position again.

Another motor system based on a two-stroke motor sequence was developed by *Lehn* in 2014 shown in Figure 11.[138] Starting from a (*P*)-helical isomer (top left) a photoisomerization establishes helix inversion to (*M*)-helicity (top right) which can subsequently isomerize back to the initial (*P*)-helicity *via* nitrogen inversion or ring inversion leading to the same isomer. From this point onwards the 180° rotation can be repeated leading to a full unidirectional 360° cycle.

A four-stroke version of the imine-based motor shown in Figure 11 has also been developed by exchanging the *tert*-butyl group with a naphthalene residue and desymmetrization of the seven membered ring, leading to a repeated ring inversion sequence with four different steps instead of two mirror symmetric ones.[138,139] The full cycle does then consist of a classical 360° rotation cycle involving four intermediates interconverted by two identical sequences of a photochemical step followed by a thermal one. This rotation cycle is similar to what is observed for overcrowded alkenes or thioindigo-based motors. Another motor following a different isomerization trajectory than the conventional rotary motions can be found in the four-stroke motor trajectory developed by *Haberhauer* in 2011,[140] and *Gerwien et al*. in 2018[141] and 2019.[142] For reasons of clarity *E*- and *Z*-stereodescriptors are used without brackets and all other stereodescriptors are set in brackets in the following isomer descriptions.

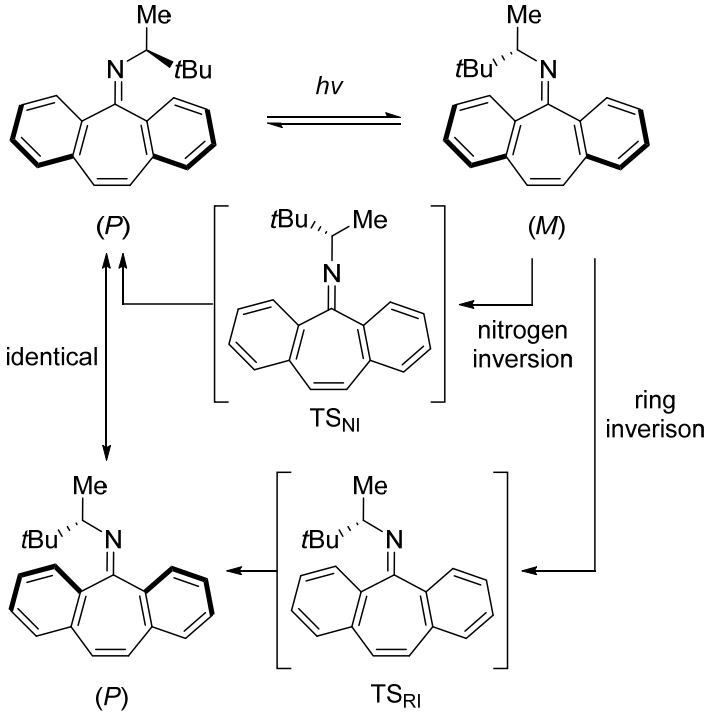

Figure 11 Two stroke unidirectional imine-based molecular motor developed by *Lehn* in 2014.[138] This motor cycle is based on four intermediates during the rotation. After photoisomerization to (*M*)-configuration, nitrogen inversion (NI) or ring inversion (RI) *via* transition state NI (TS_{NI}) or transition state RI (TS_{RI}) respectively leads back to the initial state. However, only half of the cycle is shown with the two (*P*)-configurations on the left side being identical.

Before a ratcheting mechanism was recognized as the key step for unidirectional rotation in the catenane-based motor system by *Zerbetto*,[131,132] the original overcrowded alkene-based motor was developed.[22] Molecular motors based on rotation around double bonds represent the compound class of photochemical driven molecular motors, which are utilized in systems elaborated upon in this work as well. The first system of this compound class is represented by the overcrowded alkene motor **57** published in 1999 by the *Feringa* group based on a symmetrical design shown in Figure 12.[22] In this system unidirectional rotation around a double bond is achieved leading from an *E*-(*P*)-(*P*)-configuration to the corresponding *Z*-(*M*)-*(M*)-isomer upon photoisomerization followed by a thermal helix inversion (THI) to the *Z*-(*P*)-(*P*)-configuration concluding the first 180° directional rotation. From this point onwards, the remaining 180° can be accomplished repeating these two isomerization steps in the same order *via E*-(*M*)-*(M*)-configuration leading to a fully unidirectional 360° rotation. Key for this rotation mechanism is the steric overcrowding in the fjord region – the region in close proximity to the double bond – which leads to destabilization of the (*M*)-(*M*)-helical isomers. This enables THI to the stable (*P*)-(*P*)-configuration before thermal back isomerization of the double bond occurs, which would represent a backwards motion along the reverse trajectory, diminishing unidirectionality. Helix inversions from (*M*)-(*M*)- to (*P*)-(*P*)-configurations – also known as the ratcheting steps – are crucial in this mechanism because they ensure directionality by progressing to completion, without entering a thermal equilibrium under normal conditions. Without this ratcheting mechanism, the motor would only function as a mere photoswitch, since photoisomerization occurs in both directions.

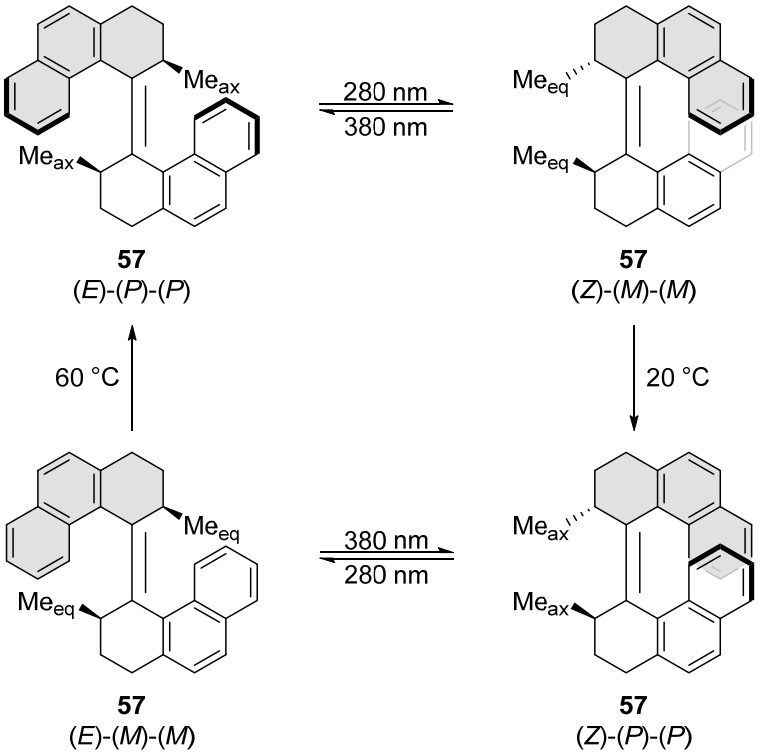

Figure 12 First unidirectional rotating artificial molecular motor **57** based on a symmetrical design comprised of two ratcheting steps published in 1999 by *Feringa*.[22] Starting from an *E*-(*P*)-(*P*)-configuration, in a first photoisomerization a *Z*-(*M*)-*(M)*-isomer is accessed which subsequently isomerizes to a *Z*-(*P*)-(*P*)-geometry finishing the first 180° degree of the unidirectional rotation cycle. These steps can be repeated leading to a complete directional 360° rotation *via* the *E*-(*M*)-*(M)*-configuration.

In a subsequently designed non symmetric system, the operational wavelength is pushed towards the visible region and the barriers for the thermal ratcheting steps are harmonized resulting in a more uniform rotary motion.[143] Throughout the following years a plethora of alternative designs were developed including sophisticated concepts like reversal of rotation direction,[144] self-locking,[145] coupled motion,[146] speed modulation,[147,148] chirality transfer,[149–151] energy transfer,[152] combining a rotaxane with a molecular motor[153] and many more.[16]

The first HTI-based molecular motor **15d** featuring fully visible light operationality was developed by *Güntner et al.* in 2015,[154] shown in Figure 13, featuring the same rotation mechanism as the overcrowded alkene based motor shown in Figure 12. Starting from the global thermodynamic minimum *Z*-(*S*)-(*P*)-configuration, photoisomerization initiates rotation to the metastable *E*-(*S*)-(*M*)-isomer. The overcrowded fjord region around the double bond destabilizes this *M*-helicity, promoting complete helix inversion to the metastable *E*-(*S*)-(*P*)-conformation in a thermal ratcheting step at temperatures significantly lower than those necessary for back-isomerization to *E*-(*S*)-(*M*), which would diminish unidirectionality. This ratcheting mechanism is key to the 100% unidirectionality achieved in double bond rotation based molecular motors. After the first 180° rotation, photoisomerization to *Z*-(*S*)-(*M*)

followed by another helix inversion step to *Z*-(*S*)-(*P*) concludes the second 180° rotation, and taken together lead to an overall unidirectional 360° rotation.

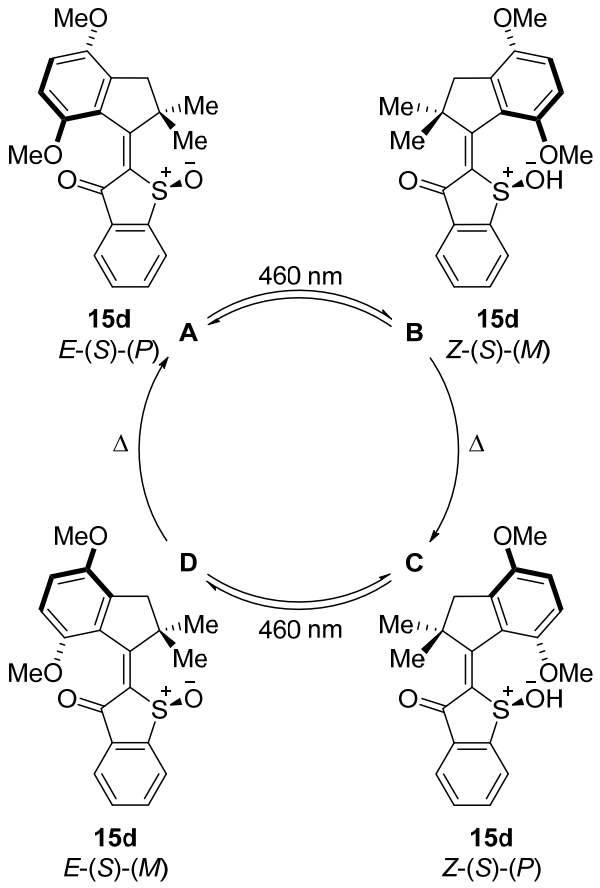

Figure 13 First HTI-based molecular motor **15d** operated by visible light exclusively developed by *Güntner et al.* in 2015.[154] Operational mechanism starts from the global thermodynamic minimum configuration *Z*-(*S*)-(*P*) = **C**, which is converted to the corresponding metastable configuration *E*-(*S*)-(*M*) = **D** *via* photoisomerization with 460 nm light. Metastable configuration **D** isomerizes quickly to the metastable *E*-(*S*)-(*P*)-isomer = **A** – usually more stable than *E*-(*S*)-(*M*) and *Z*-(*S*)-(*M*) – finishing the first 180° of the rotation cycle. Configuration **A** can in turn be photoisomerized with 460 nm light to *Z*-(*S*)-(*M*) = **B** which inverts helicity again leading to the initial configuration *Z*-(*S*)-(*P*) = **C**, concluding the unidirectional 360° rotation. All thermal steps are operational at temperatures above −80 °C.

Noteworthily, the *Z*-(*S*)-(*M*) to *Z*-(*S*)-(*P*) isomerization is much quicker than the corresponding *E*-(*S*)-(*M*) to *E*-(*S*)-(*P*) helix inversion. Therefore, the *Z*-(*S*)-(*M*) configuration was not observable in the original study. Subsequent investigations enabled observation of the elusive *Z*-(*S*)-(*M*)-configuration for the same motor structure through transient absorption spectroscopy[155] and *via* chemical modifications of the motor structure, decelerating the rotation.[156] To introduce chirality into the HTI core-chromophore, leading to introduction of two additional metastable states and thus facilitating unidirectional rotation, three modifications are necessary. Firstly, a stable asymmetric element needs to

be present which is implemented *via* oxidation of the sulphur to a sulfoxide. Secondly, the stilbene moiety needs to be rigidified which is achieved through fusion of the ring to the double bond. Thirdly, increasing steric loading in the fjord region is necessary to reduce reactivity of metastable states. Additionally, this destabilizes one helicity with respect to the other in conjunction with the stereocenter.

More recently, molecular motors based on HTI and other indigoid scaffolds have also emerged as actively-powered building blocks and frameworks for more elaborate molecular architecture in this field. Some of these concepts which use indigoid-based systems for building advanced nanomachinery range from advanced molecular motor designs[141,142] to development of active mechanical threading[157] or transmission of directional rotation,[158–160] to catalytic applications[161] to a rotation cycle containing a high energy intermediate.[162]

2.5. Macrocyclic molecular motor based artificial molecular machines

Besides switches and molecular motors, a variety of alterations and other molecular machine concepts have been put forward.[16,105,106] Among them are molecular information ratchets,[163–166] energy ratchets,[167] compartmentalized rotaxanes[121,153,168] or catenanes,[131,14,136,137] oxidation state controlled switches,[169–171] brakes,[98,172] molecular shuttles,[169,173] pumps,[122,123,174] gears,[175–184] or the recently developed photogears,[85,185–189] to name only a few more concepts. With this work being focused on switches, motors and especially implementation of motors into more elaborated molecular machinery, these concepts will not be elaborated any further. The development of macrocyclic molecular motor embeddings built in this work are explained therefore more comprehensively in the following.

One of the biggest challenges in creating functional molecular machinery is harnessing the above-mentioned directional motion to perform work at the nanoscale and this has only been started to be tapped in artificial molecular machine designs. To this end, one powerful approach has been macrocyclic embedding of molecular motor units.[2,157–159,190–194] Two main design concepts are frequently employed for macrocyclizations, either attaching a macrocycle somewhere on the motor[145,195] (Figure 14a) or connecting rotor and stator of the molecular motor[1,2,157–160,190,192–194] (Figure 14b). Macrocyclic embeddings can be separated into different functional units which are termed rotor, stator and covalent linker part shown in Figure 14. Cyclic structures can be obtained through two different approaches. The rotor or stator unit can be extended upon a macrocyclic unit, or the rotor and stator can be interconnected forming a macrocycle containing all functional units of the motor. All herein presented work is based on the latter approach.

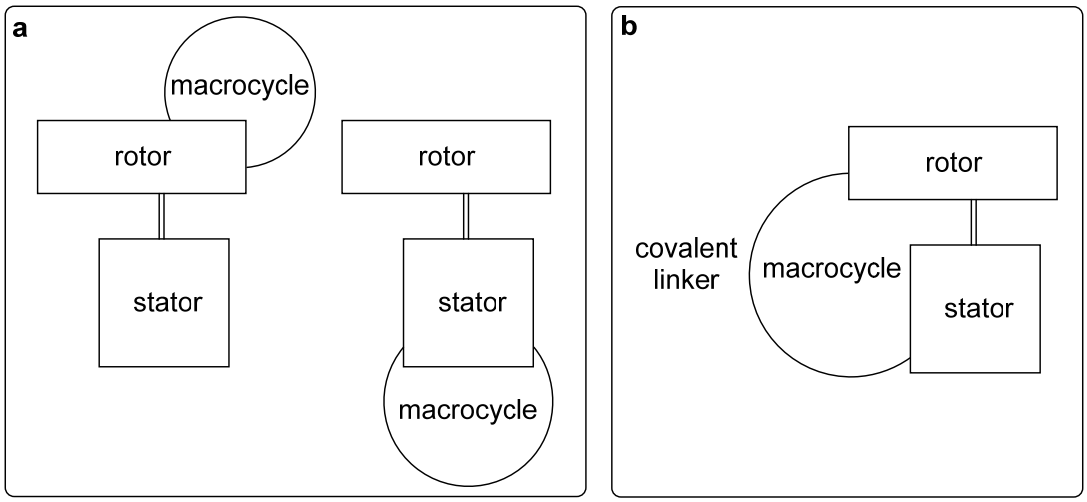

Figure 14 Simplified depiction of a macrocyclic embeddings illustrating the rotor, stator and covalent linker subunits in a macrocyclization approach. Macrocyclization of molecular motors can be achieved *via* two different ways, either by (**a**) addition of a macrocycle to the rotor or stator of the motor or (**b**) interconnecting the rotor and stator. Further functional units such as biaryl axes or threads can be included but are not required.

For HTI-based molecular motors, the indanone unit is usually referred to as the rotor, the benzothiophenone as the stator and the interconnecting chain as the covalent linker. Noteworthily, the basis for the assignment of rotor and stator is not as straightforward as it appears. Naturally, the heavier unit would be considered the stator part with respect to inertia of mass, but physical concepts of the macroscopic world such as conservation of mass do not translate unaltered to the nanoscale. Furthermore, switching these terms would not result in any change of concept or predictions made for macrocyclic embedded molecular motors previously or within this work. For simplicity and comparability to previous reports, the terminology of rotor and stator are kept as initially assigned and shown in Figure 14, neglecting inertia of mass when the rotor becomes heavier than the stator.

The concept of driving a system out of equilibrium using a molecular motor has been shown very vividly by the concept put forward by the *Giuseppone* group[190] in 2015 shown in Figure 15 and was elaborated between 2017–2022.[190,191,193,196] Winding of **59** leads to contraction of a gel which as a macroscopic effect, represents an example of work performed by a molecular motor.

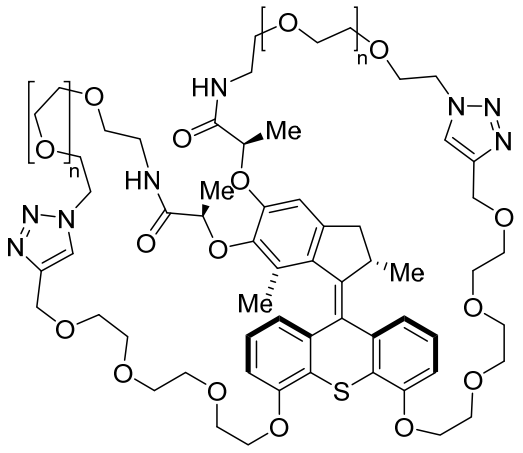

59
n = 107, 237

Figure 15 System **59** capable to perform molecular winding developed in 2015 by *Giuseppone*.[190] Winding of the macrocycle chains around the motor core does lead to the contraction of a gel, which – as a macroscopic effect – represents an example of work performed by a molecular motor.

Further concepts of macrocyclic embeddings connecting rotor and stator parts of molecular motors are displayed in Figure 16. Among these are the 2021 cation binding macrocyclic motor **61** representing a photoswitchable motorized host-guest system,[192] the 2022 strain modulated alkyl chain macrocycle **62** influencing the rotation cycle characteristics,[194] and the 2022 molecular winding design **63**,[193] all developed by *Feringa*. The most recent molecular design **63** in Figure 16 can drive a motor coupled chemical equilibrium from an equilibrated state to an energetically higher non-equilibrated state by means of light. In this example, the linker is wound around the core leading to a distribution with the

coiled state most populated, which resembles a system out of equilibrium.[193] This coiling around the motor core continues until no more windings can be formed as a result of the now limited length of the chains.

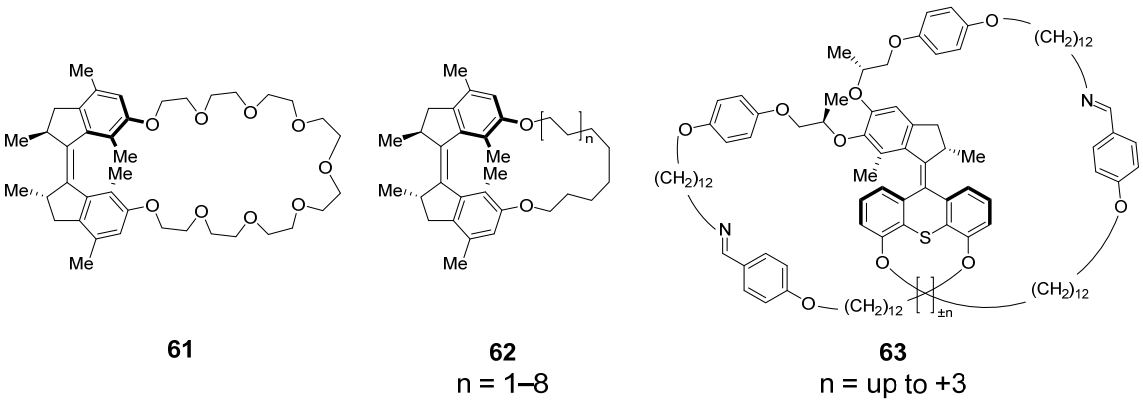

Figure 16 Exemplary selected examples illustrating the relevance of macrocyclic molecular motors. A cation binding macrocycle **61** was reported in 2021,[192] followed by a strain modulated series of molecular motors **62** in 2022[194] and a system able to undergo molecular winding **63** in 2022[194] all developed in the *Feringa* group. Windings denoted with + represent rotations of the system according to motor rotation direction and − against motor rotation direction (theoretically only accessible through thermal processes).

In the systems put forward by the *Dube* group shown in Figure 17 a biaryl unit as in **64** and **65** by *Uhl et al.* in 2018[159] and 2020,[158] an additional thread as in **66** developed by *Bach et al.* in 2022[157] or a shifted biaryl axis in **67** by *Reißenweber et al.* in 2024[160] were incorporated into the HTI-based macrocyclic molecular motor embeddings. This allows for more elaborated functions such as transmission or acceleration of motion, molecular threading, and directionality reversal. Furthermore, systems **64**–**66** do have a revolving door functional unit incorporated which is moving through the macrocycle during motor rotation. This feature provides an additional handle for diversification enabling the creation of more complex functions and trajectories within the motor cycle.

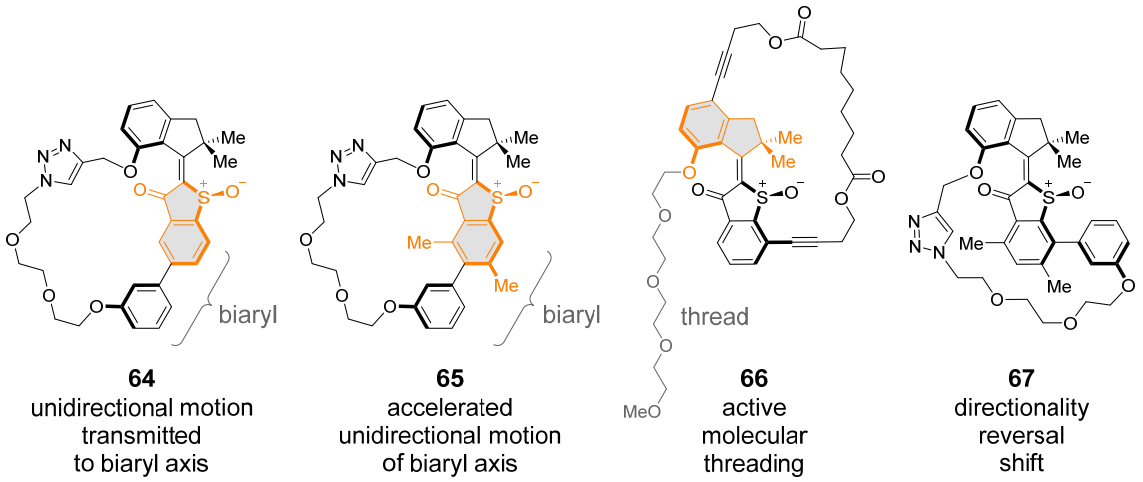

Figure 17 HTI-based macrocyclic molecular motor embeddings **64**, **65**, **66**, and **67** developed between 2018–2024 in the *Dube* group, demonstrating unprecedented actively-powered actions at the nanoscale. The revolving door units are highlighted in orange. Systems **64** and **65** developed by *Uhl et al.* in 2018 and 2020, enable the transmission of unidirectional rotation onto a passive receiver unit and their respective acceleration[158,159] and system **66** reported by *Bach et al.* in 2022 showing the first actively-powered molecular threading event at the nanoscale.[157] Most recently, a 120° shifted biaryl axis was incorporated into **67** inducing directionality reversal of the motor rotation.[160] Adapted with minor format modifications from *J. Am. Chem. Soc.* **2023**, 145, 13081–13088 licensed under CC BY-NC-ND 4.0. Copyright © 2023 The Authors. Published by American Chemical Society.[2]

These systems allow transfer of unidirectional motion from the motor core to a remote passive receiver. For macrocyclic **64** the circular motor rotation is transmitted to a distant biaryl unit. The advanced system **65** enables acceleration of the corresponding biaryl receiver rotation by several orders of magnitude with respect to the non-cyclic system. Macrocycle **66** introduced the concept of active mechanical threading at the nanoscale through a strand which can be repetitively pulled through the macrocycle. The most recent example **67** enables reversal of rotation directionality. All macrocycles except **67** follow the rotary cycle shown in Figure 13. This unidirectional rotation is used to execute functions, which are elaborated further in chapters 6 and 7. As illustrated with these examples, interconnecting rotor and stator is the most straightforward way to transfer generated motion to another position within the molecule, while other macrocyclization approaches do not allow for such simple transfer of the generated work.

3. HTI switch modified for surface attachment

3.1. Aim

Manipulating molecules on surfaces benefits from possibilities such as studying single molecule behavior,[197,198] excitation *via* electron tunneling,[197–199] defined spatial arrangement of molecular functions,[200] and the possibility of coherently behaving molecules,[201] to name only a few.[202,203] Visible-light-responsive machines are particularly interesting to study on surfaces since a second orthogonal stimulus, *i.e.* nondamaging visible light can be utilized to induce changes.[204–210] However, a severe limitation is defining the positioning of molecules on the surface. Designing structures standing orthogonal on a surface often fails, resulting in molecules being positioned in all sorts of flat orientations covering as much surface area as possible but avoiding upright positions.

Various attempts of designing HTIs for surface attachment were made, such as using *tert*-butylthiol groups in **1** for metal surfaces synthesized from *Hoffmann et al.* shown in Figure 18.[211,212] However, difficulties in applying the compounds on the surface as well as the position for subsequent analysis turned out to be the biggest pitfalls. The rational design of upright standing molecules and especially molecular functional systems is apparently significantly more challenging than adding anchor groups onto a nanomachine and applying it onto a surface.

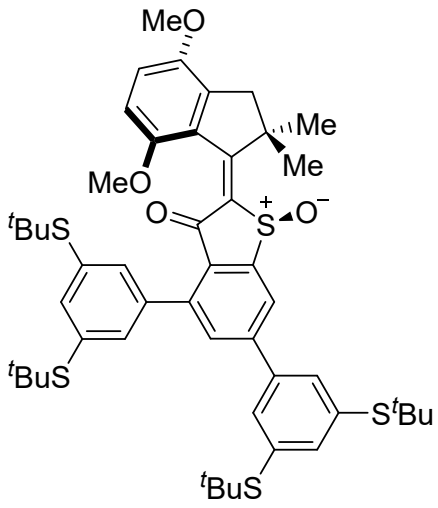

1

Figure 18 First HTI-based molecular motor **1** modified for surface attachment.

Both issues regarding application and upright positioning can be circumvented utilizing self-assembled monolayers (SAMs).[202,203,213–215] More precisely, using phosphonic acid (PA) monolayers which can be covalently linked to an aluminium oxide (AlO_x) surface foster orientation of molecules in the same direction as shown in Figure 19b. Furthermore, using covalently anchored molecules on a surface

generates genuine monolayers because excess molecules accumulating in additional layers can be removed in a washing step.

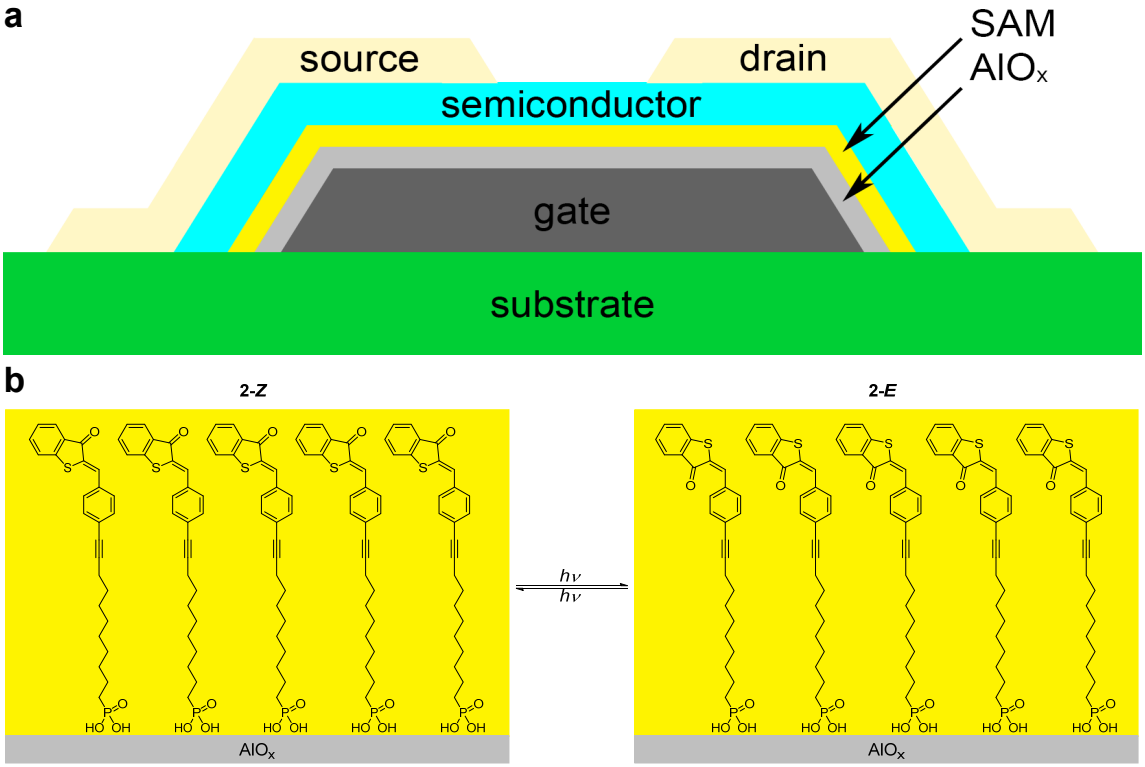

Figure 19 Design of a potential HTI-based self-assembled monolayer (HTI SAM) **2** based field-effect transistor (FET). **a** Schematic FET design displaying gate (dark grey), source and drain (light yellow) electrodes as well as substrate (green), aluminium oxide (AlO_x) layer (light grey), SAM (yellow) and semiconductor layer (turquoise). **b** Illustration of envisioned HTI-based AlO_x SAM design showing switching between **2**-*Z*-isomers (left) and **2**-*E*-isomers (right).

For reasons of simplicity, a literature-known two-state switch was chosen for monolayer functionalization, testing the upright positioning of HTI functionalized SAMs of **2** on an AlO_x surface. The versatility of these SAMs made them attractive constituents of applications in various fields with one of them being field-effect transistors (FETs).[216–218] Being utilized as a part of FET hybrid dielectrics shown schematically in Figure 19a, SAMs are promising candidates for FET modulation when functionalized with HTIs owed to the large change in dipole moment after visible-light-triggered switching which showed strong FET modulation in previous designs.[219–221]

3.2. Synthesis

The HTI switch **2** was prepared for surface attachment according to a previously known literature procedure[90] starting from commercially available benzenethiol **3** and 4-bromobenzaldehyde **6** shown in Figure 20. Addition of bromoacetic acid to benzenethiol **3** furnished phenylthioacetic acid **4** in 97% yield, which was cyclized through *in situ* formation of the acid chloride followed by intramolecular *Friedel-Crafts* acylation leading to benzothiophenone **5** in quantitative yield according to literature.[154,222] Condensation with 4-bromobenzaldehyde **6** gave access to the *para*-bromine substituted HTI derivative **7** in moderate 34% yield onto which diethyl 10-undecyn-1-ylphosphonate **8** was attached utilizing *Sonogashira* cross-coupling giving protected precursor **9** in excellent yield of 94%. Deprotection of the phosphonate **9** to the corresponding final phosphonic acid **2** in 87% was achieved with bromotrimethylsilane in dichloromethane.

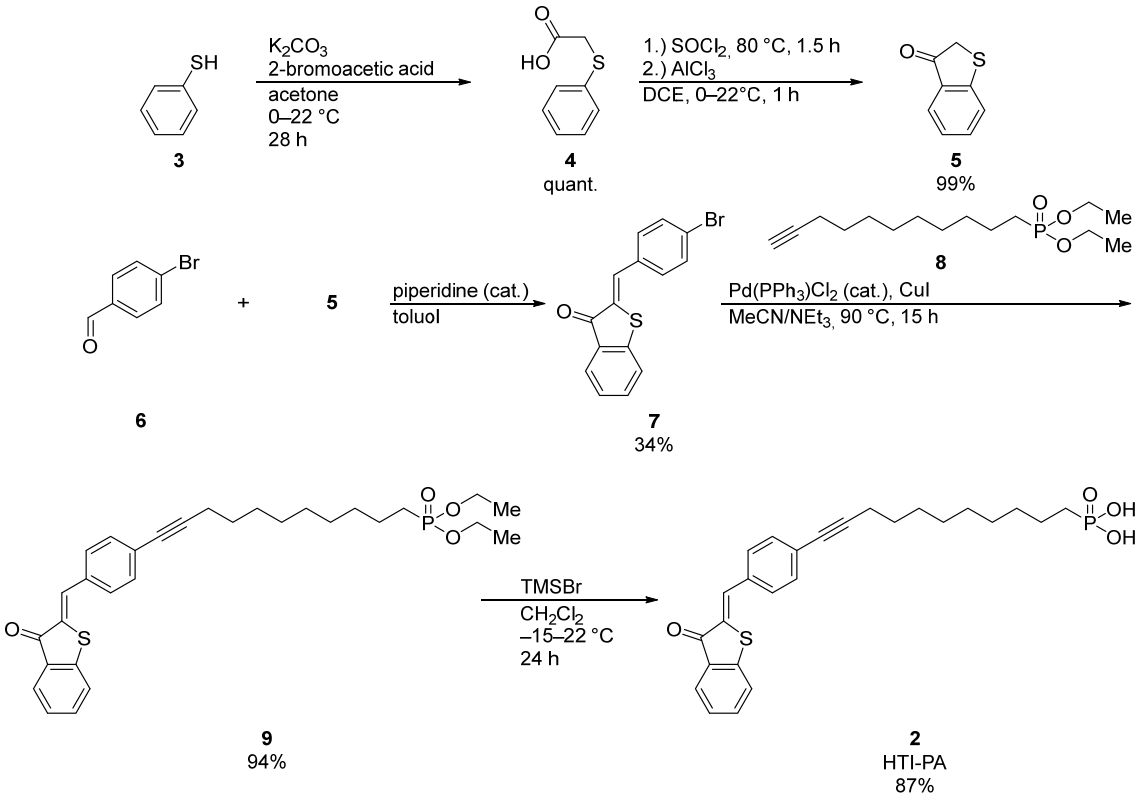

Figure 20 Synthesis of HTI functionalized SAM monomer HTI-PA **2** starting from commercially available starting materials benzenethiol **3** and 4-bromobenzaldehyde **6**. Benzothiophenone **5** was synthesized through *Friedel-Crafts* acylation *via* **4**. HTI derivative **7** was condensed from 4-bromobenzaldehyde **6** and benzothiophenone **5** followed by *Sonogashira* cross-coupling with **8** yielding the phosphonate **9** which furnished the final phosphonic acid (PA) **2** through deprotection.

With the literature-known condensation procedure for HTI **7**, the initially drafted synthesis sequence of a *Sonogashira* cross-coupling followed by deprotection of the phosphonate **9** led to the target SAM monomer **2** in the first attempt. The high-yielding synthesis made further optimizations unnecessary.

3.3. Structural and conformational description

3.3.1. Structure in solution

Conformational analysis in solution was set out for next, starting with thermodynamically stable *Z*-isomer obtained from synthesis and for photochemically enriched solution of *E*-isomer shown in Figure 21. Conventionally performed measured NOE for double bond configuration elucidation resulted in no observable signal able to evidence the constitution of the double bond. Crystallization of molecule **2** was challenging because the only solvent the phosphonic acid SAM monomer could be dissolved in was dimethyl sulfoxide. One hint from literature for the parent HTI **7** pointed towards thermodynamically stable isomer being the *Z*-configuration. However, experimental evidence was necessary to determine the structure in solution.

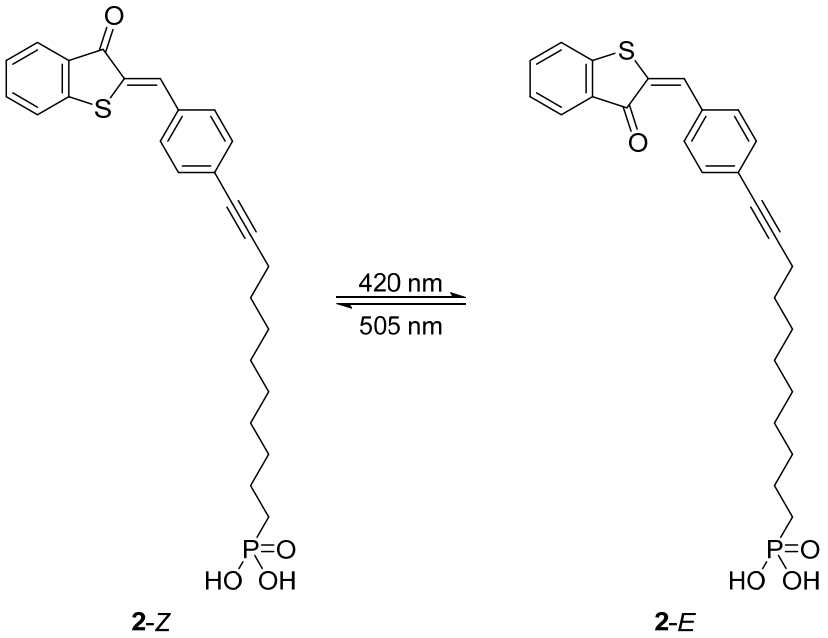

Figure 21 Overview of synthetically obtained conformational *Z*-isomers and photochemically obtained metastable *E*-isomer of **2**.

3.3.2. Elucidating HTI double bond configurations through NMR

Various experimental methodologies are available to determine double bond configurations in solution *via* nuclear magnetic resonance (NMR) spectroscopy, such as direct NOESY (or NOE/ROE) measurements making use of the nuclear *Overhauser* effect (NOE)/rotating-frame *Overhauser* effect (ROE), comparison of ^{1}H or ^{13}C shifts with theoretical predictions or comparing correlating coupling constants. However, in some cases no NOE signal can be observed, and theoretical predictions of chemical shifts are time-consuming and can be misleading. It is therefore noteworthy that coupling

constants as inherent chemical properties are less affected by, *e.g*. heteroatoms, which can shift chemical signals significantly, making them ideal candidates for configuration determinations when all other methods fail.

Vicinal ^{1}H-^{1}H dihedral angles can be described using spin-spin coupling constants $^{3}J_{HH}$ *via* the *Karplus* relationship. This relationship was first described by *Martin Karplus*[223] and has since been used extensively for the determination of dihedral angle torsion for various cases,[224–226] and can be described using general Equation 1.

$$^{3}J(\theta) = A\,cos^{2}(\theta) + B\,cos(\theta) + C \qquad \text{(Eq. 1)}$$

As an example, the dihedral angle of ethane can be described using the following function shown in Equation 2.[227]

$$^{3}J_{HH}(\theta) = 12\,cos^{2}(\theta) - \,cos(\theta) + 2 \qquad \text{(Eq. 2)}$$

Plotting the dihedral angle of ethane against the $^{3}J_{HH}$ coupling constant results in the relationship shown in Figure 22a with the *Newman* projections in Figure 22b depicting the boundary conditions for 0°, 90° and 180° torsion angle.

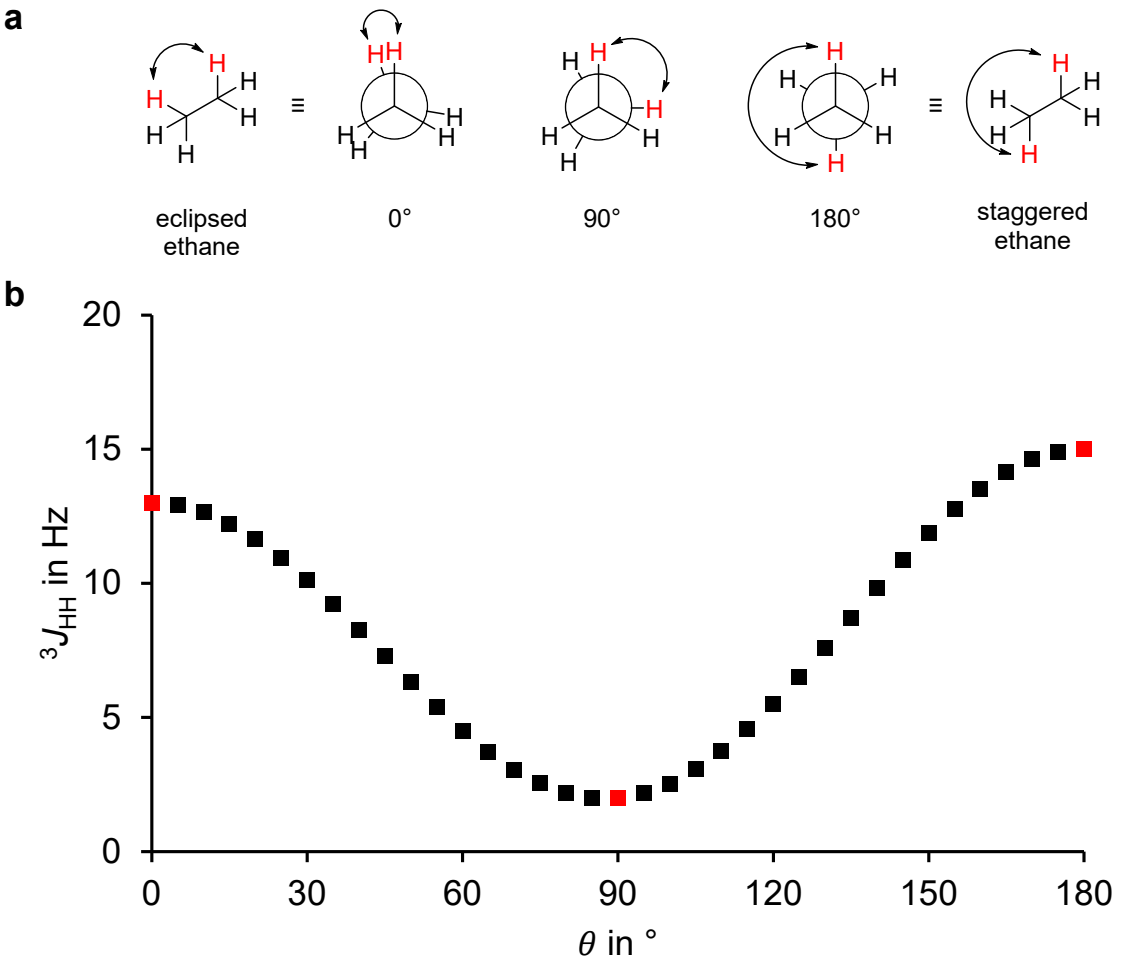

Figure 22 Illustration of the *Karplus* relationship for vicinal $^3J_{HH}$ coupling constants in ethane rotamers. **a** Ethane rotamers shown in *Newman* projection for boundary conditions of maximal orbital overlap in eclipsed (0° dihedral angle) and staggered configuration (180° dihedral angle) and minimal overlap between the staggered and eclipsed configuration (90° dihedral angle). **b** Plotted graph of the *Karplus* relationship in ethane for vicinal $^3J_{HH}$ coupling according to Equation 2 with boundary conditions of 0°, 90° and 180° shown in red.

As a general trend, the observed coupling constant for 90° is close to 0 Hz in contrast to the maximum at a dihedral angle of 180° governed by orbital overlap which is maximal for 0° and 180° and minimal or even non-existing for perpendicular orbitals. Furthermore, the $^3J_{HH}$ *trans* (180° dihedral angle) coupling constant is larger than the $^3J_{HH}$ *cis* (0° dihedral angle) constant making them ideal properties for double bond configuration determination shown in Figure 23.

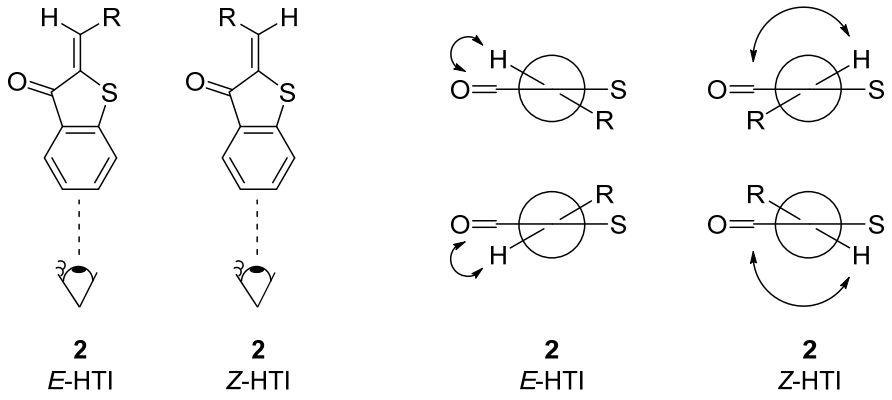

Figure 23 With the blue highlighted structures having dihedral angles close to 0° and the pink highlighted structures close to 180° between the carbonyl and the *β*-proton in **2**.

Spin-spin coupling frequently observed in ^{1}H NMR spectroscopy and widely used for determination of proton positions relative to each other does extend to all active NMR nuclei not just protons. Thus, it is possible to measure $^{3}J_{CH}$ coupling constants using the two-dimensional HSQMBC NMR experiment, yielding coupling constants between ^{1}H and ^{13}C nuclei. More specifically selHSQMBC experiments should be performed since only a small region containing the carbonyl signals of HTIs is required, reducing acquisition time while sensitivity and detection levels are improved at the same time.

The $^{3}J_{CH}$ coupling constants along the double bond are in fact very similar to the already described $^{3}J_{HH}$ couplings with $^{3}J_{CH}$ *trans* > $^{3}J_{CH}$ *cis*. These $^{3}J_{CH}$-values can then be used for determination of the dihedral angle between a proton and a carbonyl across an alkene allowing to identify *E*- and *Z*-conformational isomers.[228,229] According to the *Karplus* relationship, the HTI *E*-isomer having the larger dihedral angle must also have the larger $^{3}J_{CH}$ coupling constant as demonstrated below for a few examples in Table 2. This method allows the determination of double bond conformations independent from solvent and substitution pattern for HTIs within short measuring times (below 60 min on a 600 MHz NMR spectrometer) as well as the possibility to analyze mixtures or solutions containing impurities.

Two experiments with pure *Z*-**2** and an *E*-**2** enriched solutions were conducted confirming the prediction made above, shown in Figure 24 and 25. Since absolute assignments could not be made measuring compound **2** alone, a HTI benchmark set was recorded. Comparing the measured $^{3}J_{CH}$-Values of **2** with related structures for which absolute *E*- and *Z*-configurations were determined using other analysis methods, such as crystallization or NOE measurements enabled determination of double bond configuration in **2**.

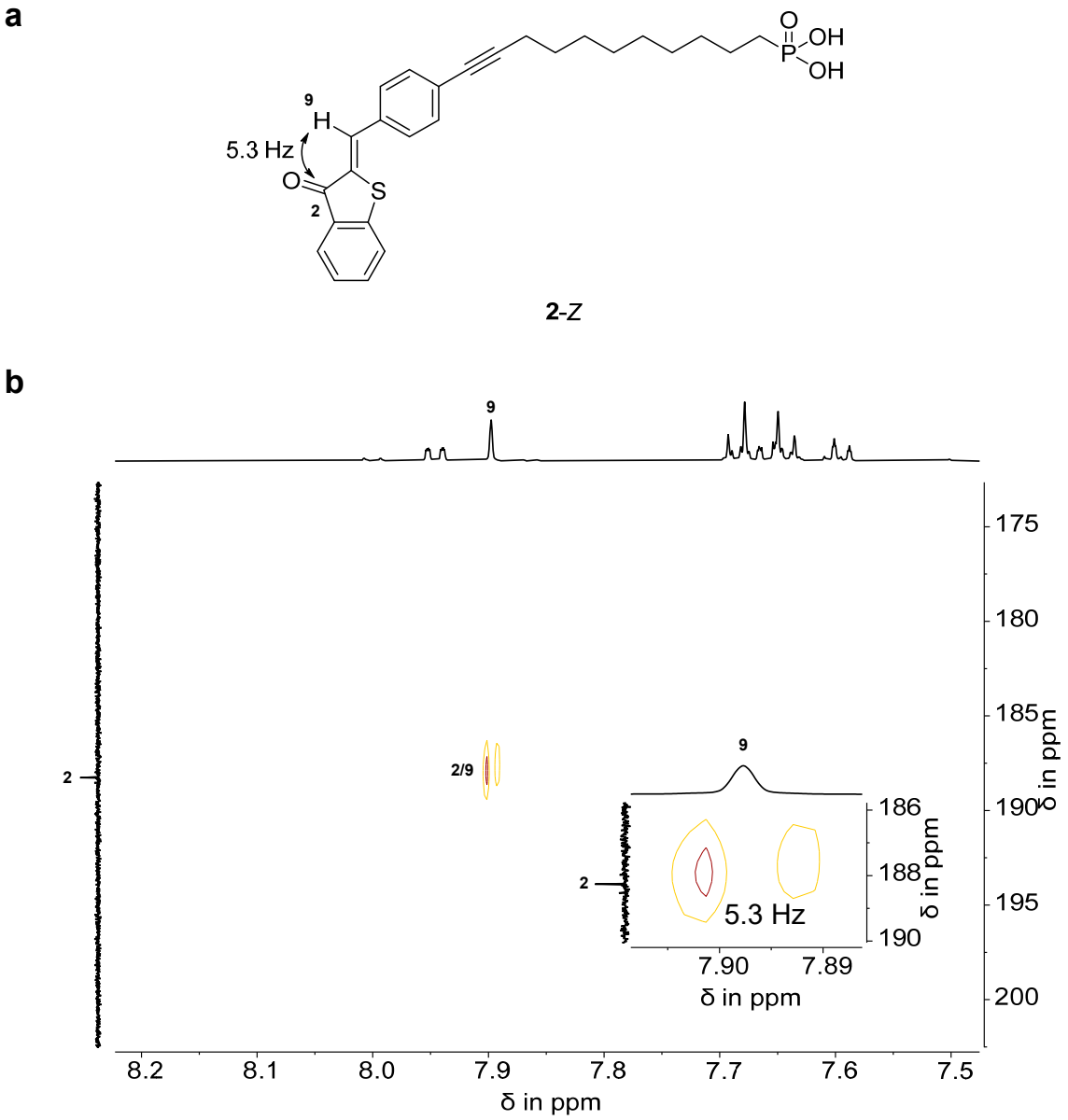

Figure 24 2D selHSQMBC spectrum (601 MHz, dimethyl sulfoxide-*d*6, 25 °C) of a pure (**a**) HTI-PA **2**-*Z*-isomer solution displaying (**b**) 5.3 Hz $^{3}J_{CH}$ coupling between the carbonyl and the *β*-proton.

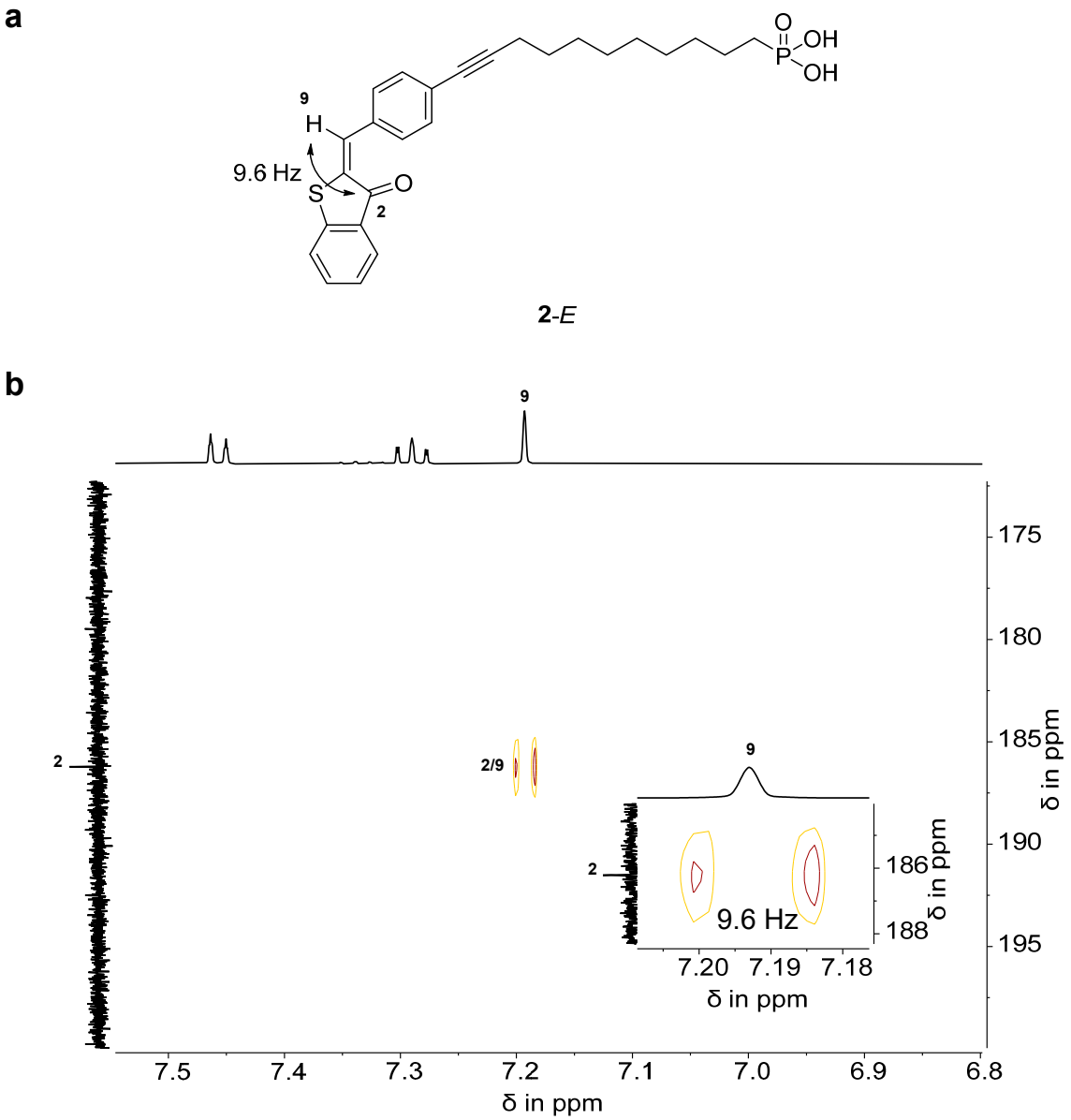

Figure 25 2D selHSQMBC spectrum (601 MHz, dimethyl sulfoxide-d_6, 25 °C) of a (**a**) HTI-PA **2**-*E*-isomer enriched solution displaying (**b**) 9.6 Hz $^3J_{CH}$ coupling between the carbonyl and the *β*-proton.

Measured $^3J_{CH}$ coupling constants confirmed the initial guess of the thermodynamically stable configuration being the *Z*-isomer with a coupling constant of 5.3 Hz in comparison to 9.6 Hz for the *E*-isomer. To compare this observation with some other HTI-based photoswitches, a set of five molecules was measured in different solvents displayed in Figure 26.

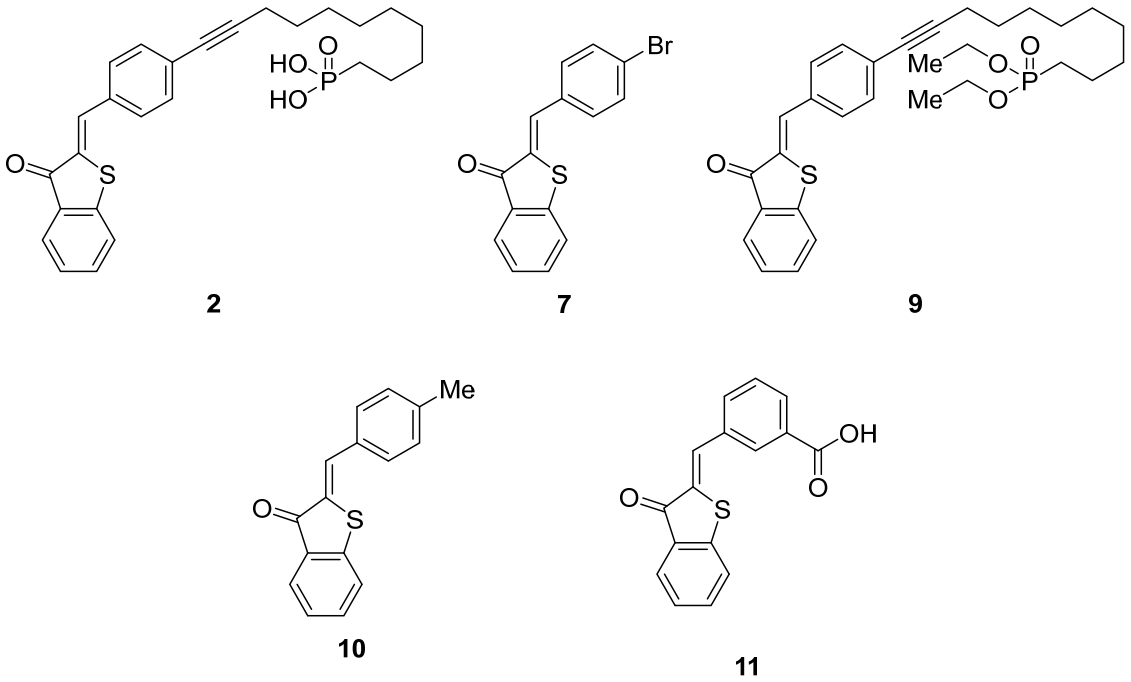

Figure 26 Set of five HTI-based compounds **2**, **7**, **9**, **10**, and **11** for which selHSQMBC measurements were performed in different solvents, recording $^3J_{CH}$ coupling constants among variable molecular functional groups positioned on the stilbene part.

The measured derivatives did confirm the initial assumption $^3J_{CH}$ *trans* > $^3J_{CH}$ *cis* strongly indicating that the Z-isomer is the thermodynamically stable conformation obtained from synthesis of **2** shown in Table 2. For compound **7**, no $^3J_{CH}$ *E*-isomer coupling constant could be obtained in dimethyl sulfoxide since no isomerization was observed from irradiation with wavelengths between 340–600 nm. A sample of **10**[230] was generously provided by *Laura Köttner*.[IV]

Table 2 Examples for $^3J_{CH}$ coupling constants in HTI derivatives **2**, **7**, **9**, **10**, and **11** between the carbonyl and the olefinic proton. Values were determined in [a]dimethylsulfoxide-d_6, [b]toluene-d_8 or [c]dichloromethane-d_2. For compound **7**, no $^3J_{CH}$ *E*-isomer coupling constant was obtained in dimethyl sulfoxide since no isomerization could be observed after irradiation with wavelengths between 340–600 nm. A sample of **10**[230] was generously provided by *Laura Köttner*.[IV]

isomer	$^3J_{CH}$ coupling constant *Z*-isomer in Hz	$^3J_{CH}$ coupling constant *E*-isomer in Hz
2	5.3[a]	9.6[a]
7	5.2[a]	-
7	5.5[c]	9.7[c]
9	5.4[c]	9.5[c]
10[230]	5.4[b]	9.5[b]
11	6.5[a]	9.7[a]

3.4. Thermal isomerization

Isomerization behavior of the thermodynamically metastable state at 22 °C was studied next. A **2**-*E* enriched solution accumulated through irradiation with 420 nm in dimethyl sulfoxide-d_6 was subjected to repeated ^{1}H NMR spectroscopy while the sample was kept at 22 °C recording the thermal isomerization from **2**-*E* to **2**-*Z* shown in Figure 27a. The decay of **2**-*E* shown in Figure 27b can be plotted using Equation 4 shown in chapter 5.6 for a first-order reaction without entering a thermal equilibrium shown in Figure 27c and fitted using a linear regression analysis confirming a first-order reaction. The slope of the fit does translate to a *Gibbs* energy of activation of 21.0 kcal mol^{-1} for the *E*- to *Z*-isomerization process.

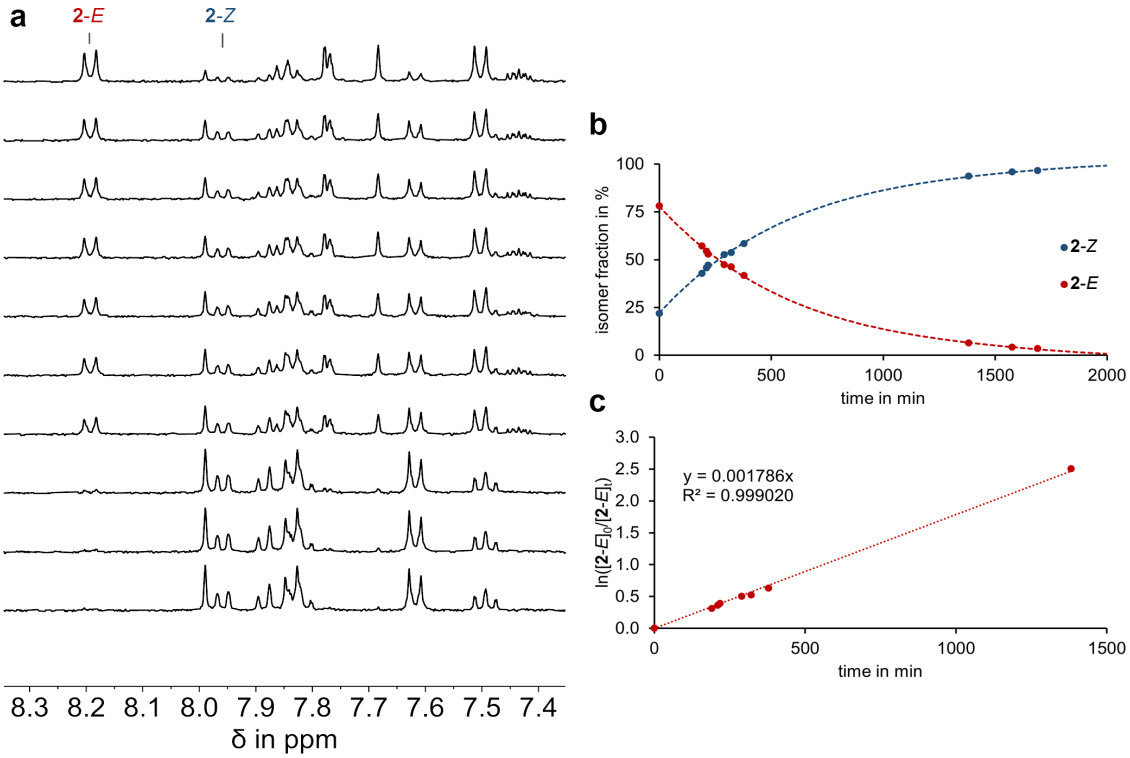

Figure 27 Kinetic analysis of thermal isomerization starting from an **2**-*E* enriched solution at 22 °C. **a** ^{1}H NMR spectra (400 MHz, dimethylsulfoxide-d_6, 25 °C) of **2**-*E* and **2**-*Z* during thermal isomerization of **2**-*E* to **2**-*Z* starting from an **2**-E enriched mixture consisting of 78% **2**-*E* and 22% **2**-*Z* (top spectrum). Spectra were recorded in irregular intervals ordered chronologically from top to bottom. **b** Changing isomer distribution of **2**-*E* (red dots) and **2**-*Z* (blue dots) during thermal conversion at 22 °C. Data were simulated for visual guidance using a fourth-degree polynomial fit shown with color-coded dashed lines. **c** Kinetic evaluation using a first-order rate law without entering a thermal equilibrium provides a linear correlation for the conversion of **2**-*E*. A simulation of the experimental data points using a linear regression fit (dotted red line) leads to a slope of m = 0.001786, translating into a *Gibbs* energy of activation of $\Delta G^{\ddagger}$ = 21.0 kcal mol^{-1}. The absolute energy difference must be at least 1.7 kcal mol^{-1} between thermodynamically stable ground state **2**-*Z* and metastable **2**-*E* under the conservative assumption 5% is not detected from NMR.

3.5. UV-Vis absorption spectra and molar extinction coefficients

Ultraviolet-visible (UV-Vis) absorption spectra of thermodynamically stable **2**-*Z* were measured in dimethyl sulfoxide at 22 °C. Metastable **2**-*E* isomer on the contrary could not be recorded directly, since its half-life of ~6 hours at 22 °C complicates isolation and measurement procedures significantly. Therefore, a solution of pure **2**-*Z* was exposed repetitively to 420 nm LED light until UV-Vis spectra before and after irradiation were identical. This **2**-*E* enriched isomer mixture was then subjected to ^{1}H NMR spectroscopy, determining the *E*- and *Z*-isomer distribution. Spectra of pure *E*-isomer was then obtained *via* subtraction of the pure **2**-*Z* isomer fraction – determined through NMR spectroscopy – from the **2**-*E* enriched solution, followed by re-scaling according to the isosbestic point at 465 nm fitting the pure **2**-*Z* and **2**-*E* enriched spectra. All recorded UV-Vis spectra necessary for this procedure are depicted in Figure 28.

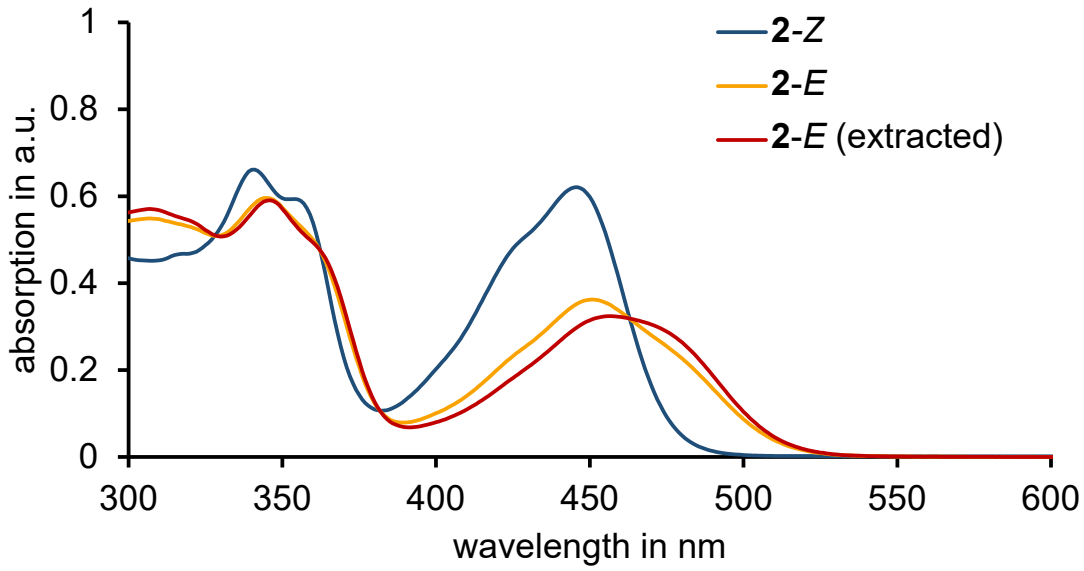

Figure 28 Ultraviolet-visible (UV-Vis) absorption spectra (dimethyl sulfoxide, 22 °C) of isomer **2**-*Z* (blue), 82% **2**-*E* enriched solution (orange) and simulated spectrum of pure **2**-*E* (red) at a concentration of 23 μM.

Molar extinction coefficients displayed in Figure 29 were determined next from the above-mentioned absorption spectra using known concentration of pure and enriched solutions.

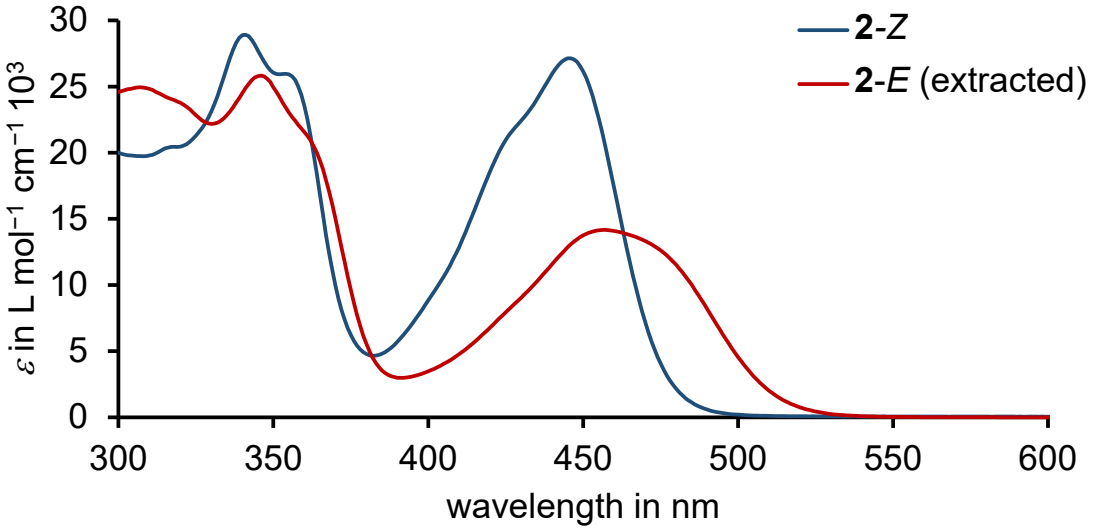

Figure 29 Molar extinction coefficients (dimethyl sulfoxide, 22 °C) of isomer **2**-*Z* (blue) and simulated metastable **2**-*E* (red).

With molar extinction coefficients at hand, photoisomerization behavior as well as PSS analysis and QY measurements could be performed.

3.6. Photostationary state determination

Determination of PSS ratios (shown in Table 3) were carried out for **2** in dimethyl sulfoxide at 22 °C shown in Figure 30a and b using predetermined molar extinction coefficients.

Table 3 Isomer ratios in the PSS determined for **2**-*E*:**2**-*Z* after irradiation with LED light of given wavelengths. Values were determined at 463 nm through UV-Vis absorption spectroscopy at 22 °C in dimethyl sulfoxide solution. Irradiation was stopped after stable PSS ratios were reached.

wavelength in nm	**irradiation time in s**	**2-*E*-isomer in %**	**2-*Z*-isomer in %**
530	125	91	9
515	80	84	16
505	20	94	6
490	20	83	17
470	25	44	56
450	10	11	89
430	10	8	92
405	10	7	93
385	15	27	73
340	25	26	74

3.7. UV–Vis irradiation

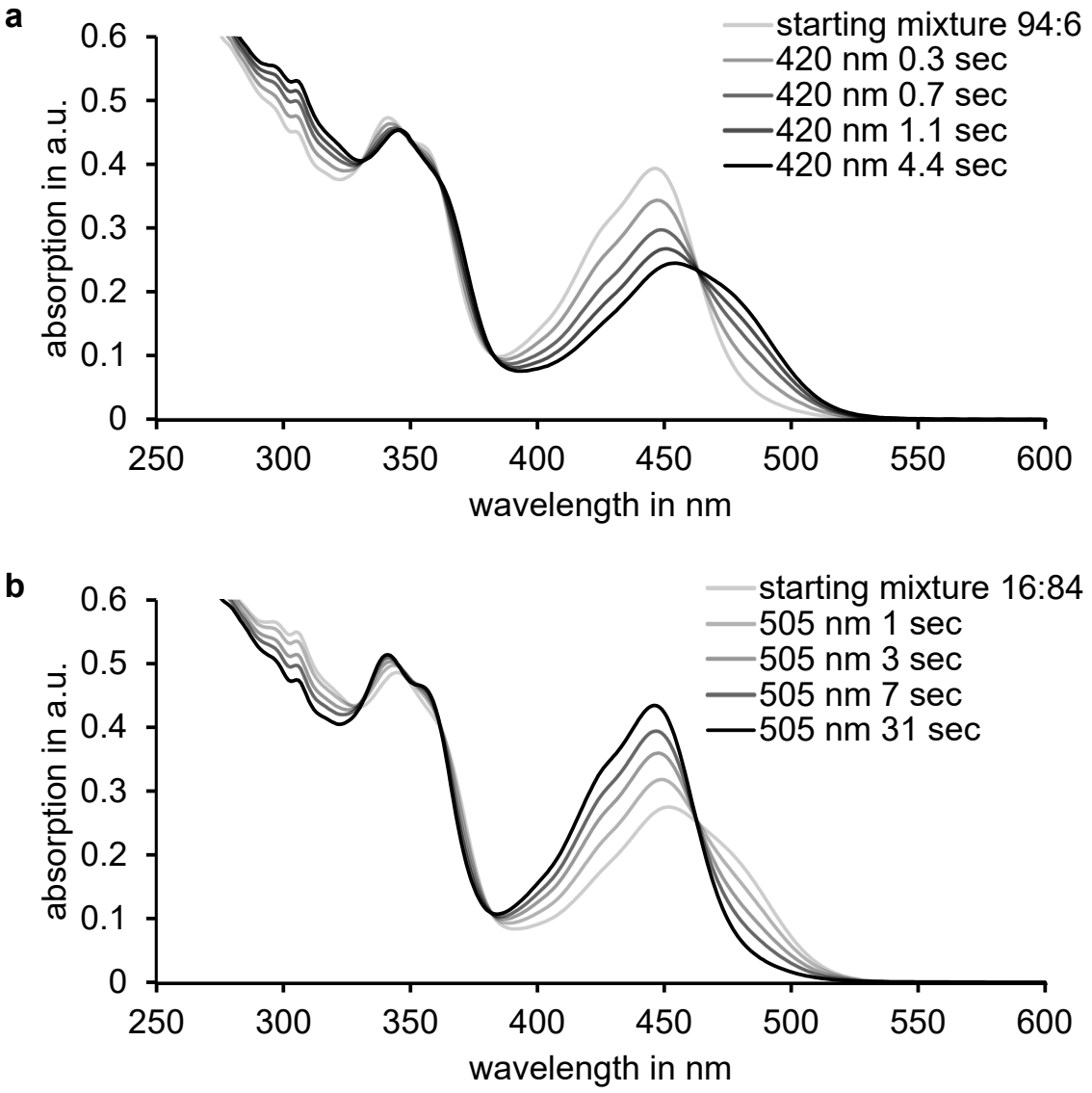

Figure 30 UV-Vis absorption spectra (dimethyl sulfoxide, 22 °C) of HTI **2**. **a** Starting mixture consisting of 6% **2**-*E*-isomer and 94% **2**-*Z*-isomer irradiated with 420 nm light reached the PSS after 4.4 s of irradiation time consisting of 16% *Z*-isomer and 84% *E*-isomer. **b** Starting mixture consisting of 16% *Z*-isomer and 84% *E*-isomer in dimethyl sulfoxide with 505 nm light reached the PSS after 16 s of irradiation time consisting of 94% **2**-*Z*-isomer and 6% **2**-*E*-isomer. Spectra are shown with darker coloured lines indicating longer irradiation time. The ratios were calculated from NMR samples at the PSS.

3.8. Quantum yield determination

Photochemical QYs Φ were measured using the instrumental setup from *E. Riedle*[231] and calculated according to an already established protocol from *Petermayer et al.*[53] Due to short half-life (~6 h) of **2**-*E*, QY measurement had to be performed starting from an **2**-*E* enriched solution instead of utilizing the pure isomer. For this reason, both values for **2**-*E* and **2**-*Z* were determined using a method suitable for mixtures of isomers according to a previously established methodology.[53] Thermal back-isomerization from **2**-*E*- to the **2**-*Z*-isomer during the QY measurement was accounted for by subtracting the thermal isomerization processes using a first-order rate law without entering a thermal equilibrium from the overall measured isomerization processes for each time interval. The calculated isomer concentrations were fitted using fifth-degree polynomials, which were then derived for 0% *E*- or *Z*-isomer respectively calculating the initial slope of the photoreaction shown in Figure 31 and 32.

3.8.1. Quantum yield of 2-*Z*

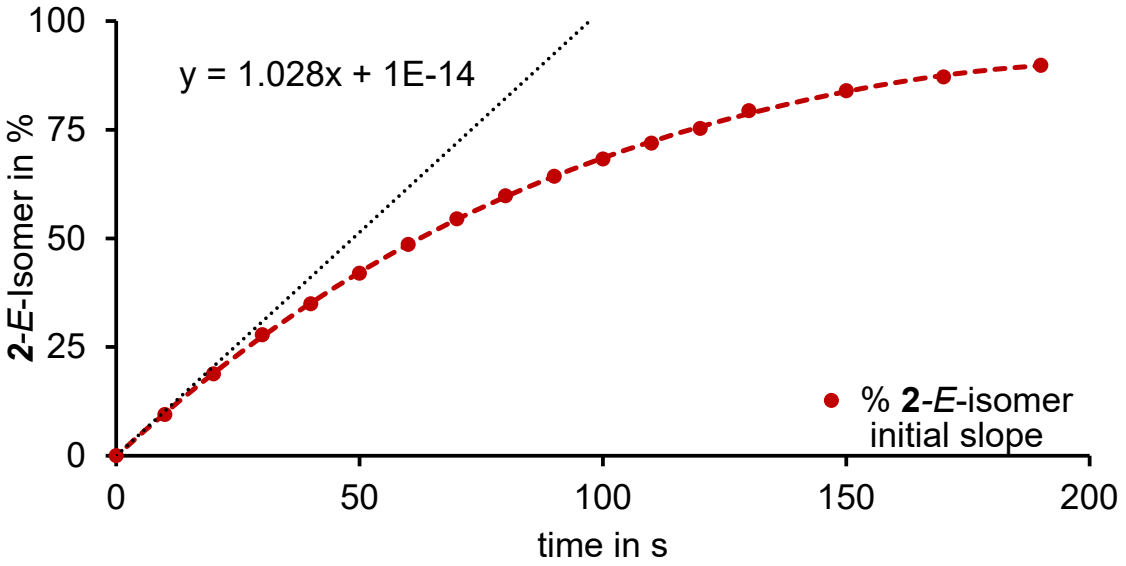

Figure 31 Changing isomer fractions of **2**-*E* (red dots) during photoconversion of **2**-*Z* by 470 nm LED irradiation at 22 °C starting from a solution containing pure **2**-*Z* in dimethyl sulfoxide. Concentrations were determined by means of molar extinction coefficients and the whole photokinetic was fitted using a fifth-degree polynomial (dashed red). Initial slope (dotted black line) of the **2**-*Z* photoconversion was determined by extrapolation of the polynomial fit to 0% **2**-*E*-isomer. A quantum yield (QY) of $\Phi_{Z\rightarrow E}$ = 18.3% was obtained for the **2**-*Z* to **2**-*E* photoisomerization using the initial slope m_0 = 1.028 (black formula).

3.8.2. Quantum yield of 2-*E*

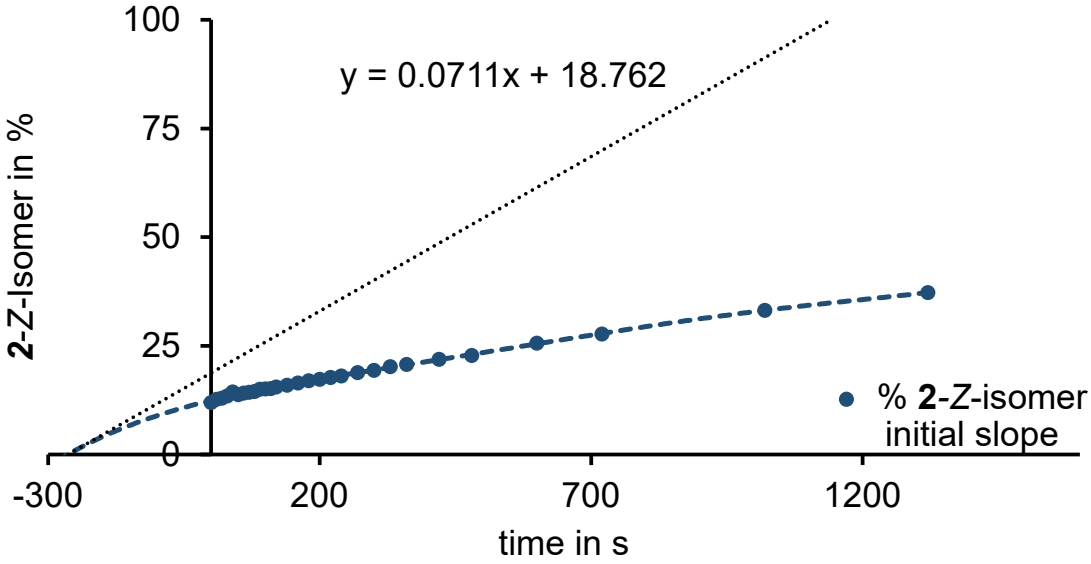

Figure 32 Changing isomer fractions of **2**-*Z* (blue dots) during photoconversion of **2**-*E* by 520 nm LED irradiation at 22 °C starting from an 88% **2**-*E* enriched solution in dimethyl sulfoxide. Concentrations were determined by means of molar extinction coefficients and the whole photokinetic was fitted using a fifth-degree polynomial (dashed blue). Initial slope (dotted black line) of the **2**-*E* photoconversion was determined by extrapolation of the polynomial fit to 0% **2**-*Z*-isomer. A QY of $\Phi_{E\rightarrow Z}$ = 1.2% was obtained for the **2**-*E* to **2**-*Z* photoisomerization using the initial slope m_0 = 0.0711 (black formula).

3.9. Theoretical description

Field-effect transistors are known to be modulated by dipole orientation of the dielectric medium.[219,232,209,210,233] Accountable for observed differences between the *Z*- and *E*-enriched monolayers might therefore be the dipole moments of each state. These were thus simulated using density functional theory (DFT) at the B3LYP-GD3BJ/6-311G(d,p) level of theory for the HTI fragment **12** and the complete phosphonic acid functionalized switch **2**, revealing significant different values for the two states as shown in Figure 33 and 34.

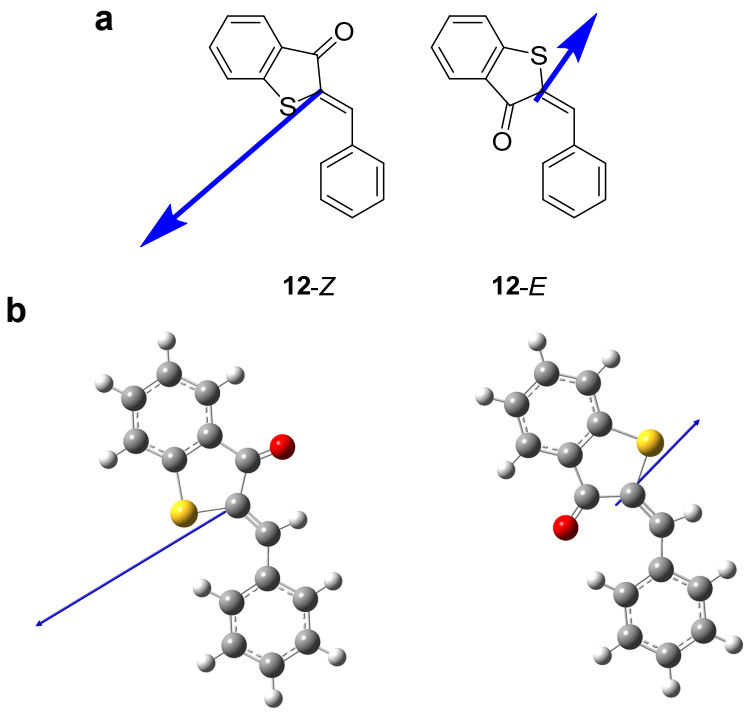

Figure 33 Dipole moment of the HTI fragment **12** simulated at the B3LYP-GD3BJ/6-311G(d,p) level of theory. The *Z*-isomer possesses a dipole moment of 2.4 D and the *E*-isomer of 1.3 D pointing almost in the exact opposite direction. **a** Depiction of the dipole vector with respect to the structural representation of **12**. **b** 3D representation of the dipole vector in **12** obtained from simulations directly.

The simulated dipole vectors point almost perfectly in opposite directions with 2.4 D for the *Z*- and 1.3-D for the *E*-isomer, rendering this HTI switch an ideal candidate for manipulating FETs *via* visible light irradiation. However, the anchoring group containing the phosphonic acid will have an influence on the resulting overall dipole moment which has thus been simulated on the same level of theory for the free acid **2**, shown in Figure 34. As a result of interactions with the surface after covalent attachment of the acid, this is not necessarily the better representation.

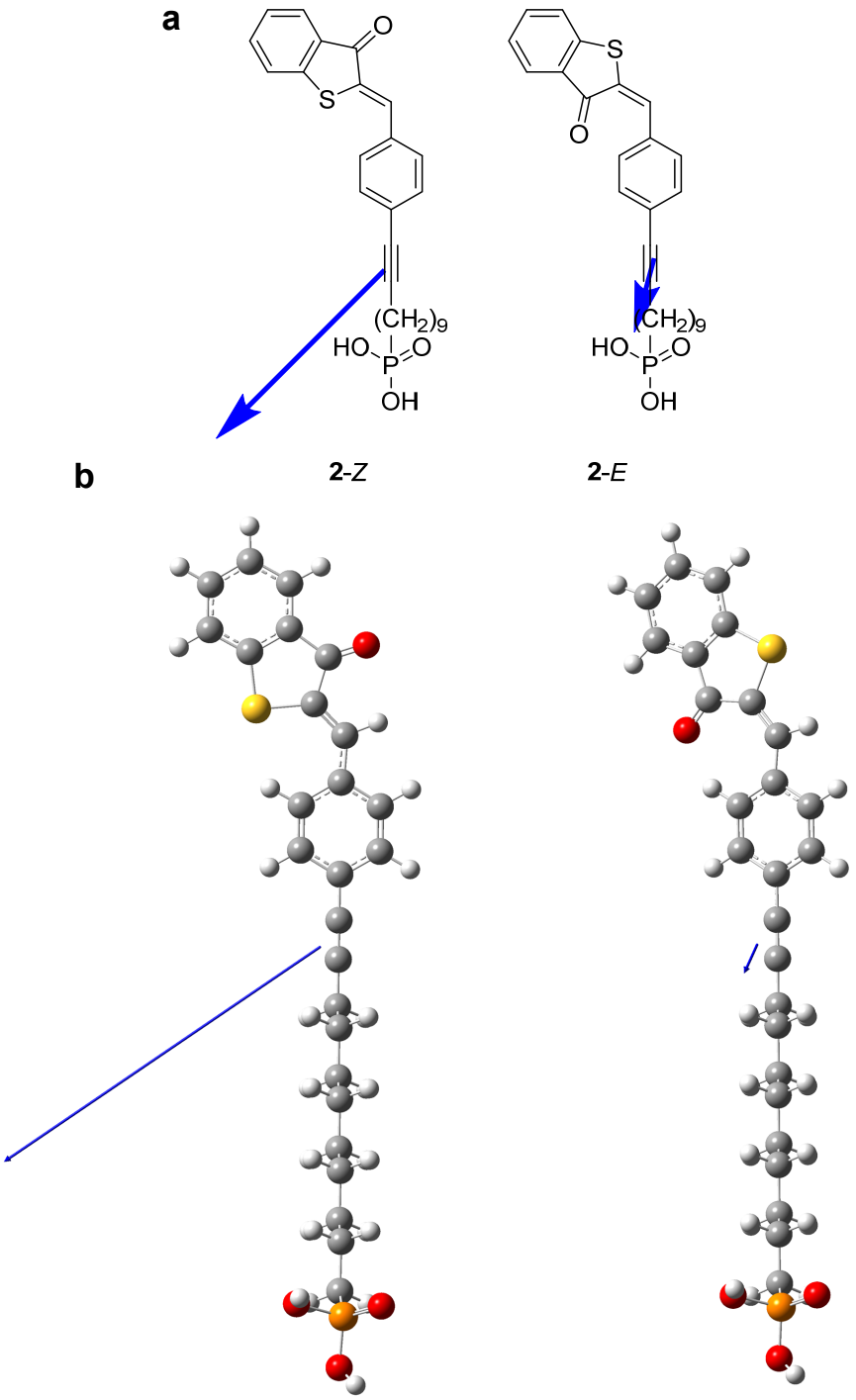

Figure 34 Dipole moment of the phosphonic acid functionalized switch **2** simulated at the B3LYP-GD3BJ/6-311G(d,p) level of theory. The *Z*-isomer possesses a dipole moment of 3.9 D and the *E*-isomer of 0.3 D pointing in identical directions. **a** Depiction of the dipole vector with respect to the structural representation of **2**. **b** 3D representation of the dipole vector in **2** obtained from simulations directly.

The resulting dipole moment for the SAM monomer amounts to 3.9 D for the *Z*- and 0.3 D for the *E*-isomer pointing in similar directions. This is also promising for FET manipulation with a more than 10-fold increase in dipole moment resulting in an on/off behavior from switching.

3.10. Applications

After characterizations of surface-attachable photoswitch **2**, potential applications for material and device applications are examined such as photoswitchable surface wettability, capacitance, and utilization in field-effect transistors. All application-related experiments will be carried out in collaboration with the group of *Prof. Dr. Marcus Halik* and *Prof. Dr. Andrey Turchanin*.

3.11. Conclusion and outlook

In summary, a high-yielding five-step synthetic route for HTI-based PA SAM monomer HTI PA **2** was developed. This monomer can be covalently bound to AlO_x surfaces forming true monolayers as shown in Figure 19b, which will be examined in collaboration with *Prof. Dr. Marcus Halik* and *Prof. Dr. Andrey Turchanin*. This HTI-based SAM has the potential of a first solely visible light modulated MoS_2-based FET device. As a result, a multi-bit memory FET could be obtained which can be stepwise written with 420 nm and stepwise erased with 505 nm. Since this is work in progress, further experiments are necessary characterizing possible devices for applications to complete this study. The reliability, reversibility, dynamic modulation, and fully visible-light-operability of potential future devices could open various potential new possibilities within information storage and processing as well as optoelectronics.

4. HTI Switch with fluorescence response

4.1. Aim

Recently reported[234] fluorescence enhancement using a water-soluble receptor **13** shown in Figure 35 from the *Kataev* group is a promising candidate for sensing applications. A photoswitch with high fluorescence in one state and low in the other plus higher affinity of the high fluorescent state for receptor **13** would be ideally suited for this purpose. To this end, photoswitch **11** was synthesized and characterized.

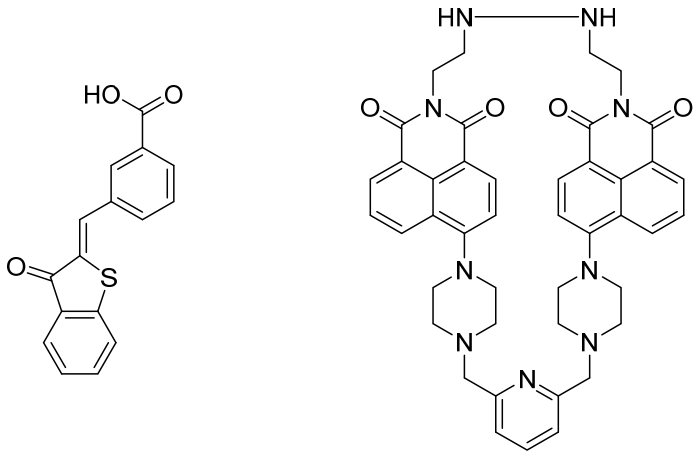

11 **13**

Figure 35 Fluorescent HTI-based photoswitch **11** and water-soluble fluorescence enhancement receptor **13** reported in the *Kataev* group.[234]

In addition to this, carboxylic acid functionalized HTI-based photoswitch **11** is promising for switching on a $Co_3O_4(111)$ surface, which was investigated in collaboration with the *Libuda* group.

4.2. Synthesis

The HTI switch **11** was prepared for surface attachment according to a previously known literature procedure[235] starting from commercially available 3-formylbenzoic acid **14**, see Figure 36. Details for the synthesis of benzothiophenone **5** can be found in chapter 6.3. Condensation of commercially available 3-formylbenzoic acid **14** with benzothiophenone **5** furnished the carboxylic acid functionalized HTI-based photoswitch **11** in 54% yield in one step.

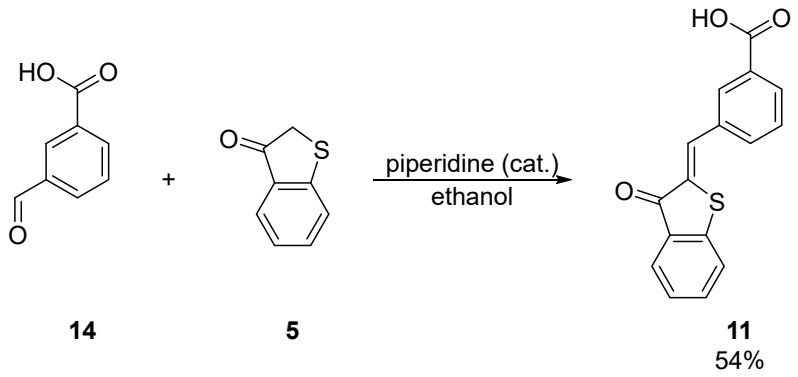

Figure 36 Synthesis of carboxylic acid functionalized HTI-based photoswitch **11** starting from commercially available starting material **14** and benzothiophenone **5**, for which synthesis is described in chapter 5.3.

4.3. Structural and conformational description in solution

Conformations of photoswitch **11** were characterized first in solution at 22 °C shown in Figure 37. Pure solutions of *Z*-isomer in dimethylsulfoxide-d_6 were extensively examined using 1D and 2D NMR spectroscopy. For a detailed ^{1}H and ^{13}C NMR spectroscopic analysis of each isomer see experimental chapter 8.3.

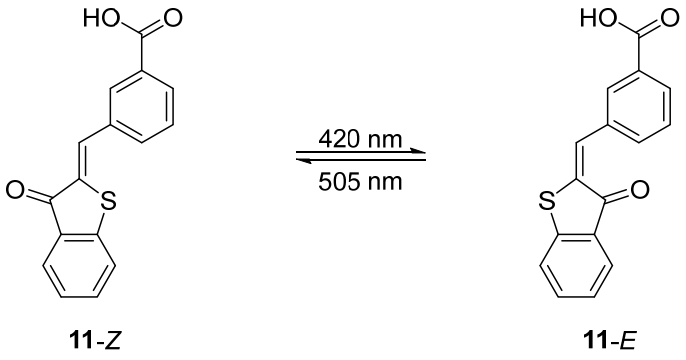

Figure 37 Overview of synthetically obtained conformational *Z*-isomer and photochemically obtained metastable *E*-isomer of **11**.

Proximity of aromatic stilben proton HC13 to aromatic benzothiophenone proton HC9 revealed *Z*-configuration of the central double bond in **11**-*Z*, shown in Figure 38.

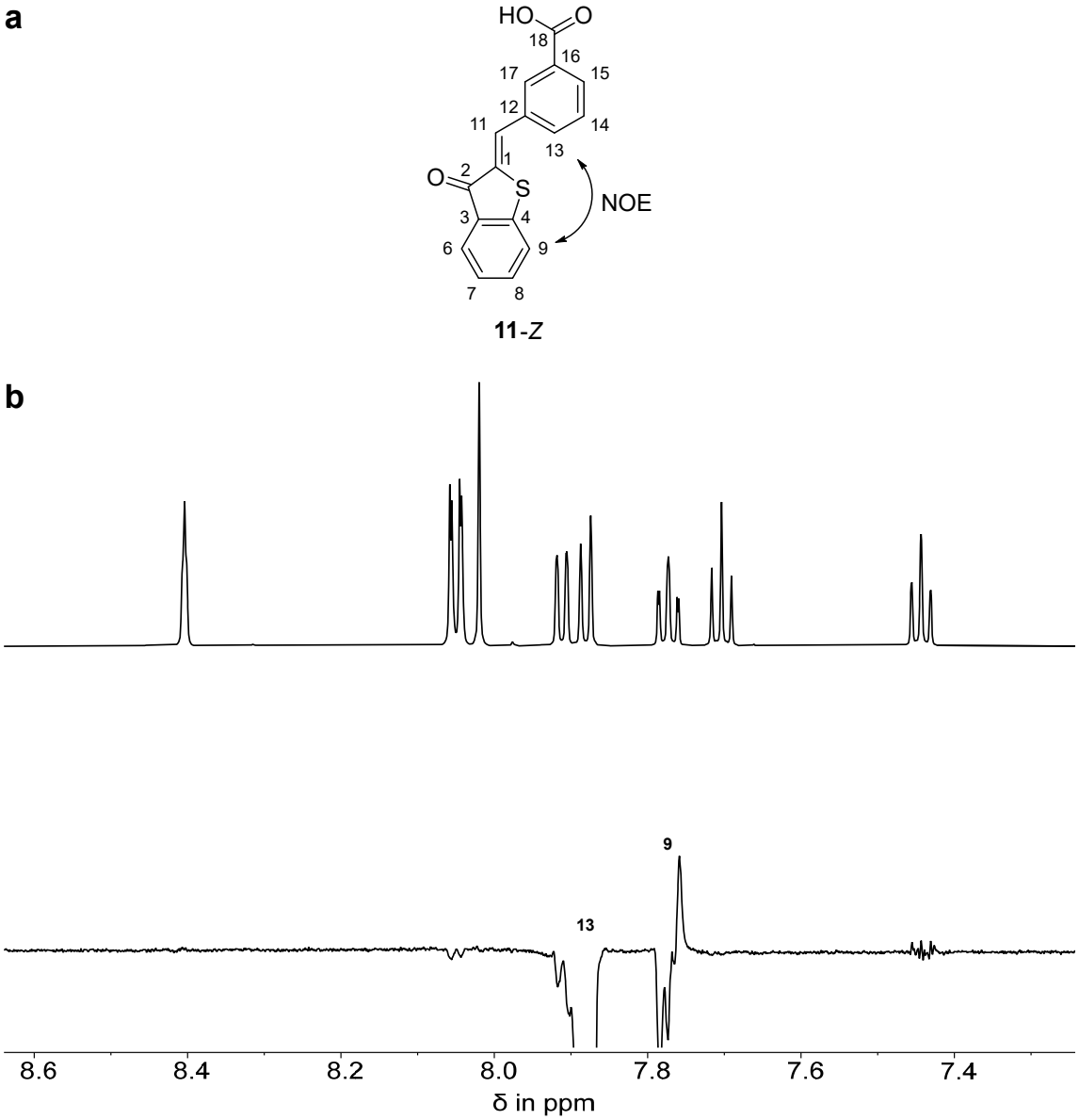

Figure 38 Double bond configuration analysis of isomer **11**-*Z* measured in dimethylsulfoxide-d_6 solution at 25 °C. **a** Structure of **11**-*Z* including arrows depicting observed NOE signals between protons HC13 and HC9. **b** ^{1}H (top) and NOE (bottom) NMR spectra (dimethylsulfoxide-d_6, 600 MHz, 25 °C) of **11**-*Z* display proximity between HC13 and HC9, revealing *Z*-configuration of the double bond.

4.4. Thermal isomerization

Isomerization behavior of the thermodynamically metastable state at 22 °C was set out to be investigated next. A **11**-*E* enriched solution was accumulated through irradiation with 415 nm in dimethyl sulfoxide-d_6 and subjected to repeated ^{1}H NMR spectroscopy while the sample was kept in the dark at 22 °C recording the thermal isomerization from **11**-*E* to **11**-*Z* shown in Figure 39. The decay of **11**-*E* can be plotted as described in chapter 5.6 for a first-order reaction shown in Figure 39 and fitted using a linear regression analysis confirming a first-order reaction. The slope of the fit *m* does translate to a *Gibbs* energy of activation $\Delta G^{\ddagger}$ of 20.5 kcal mol^{-1} for the *E*- to *Z*-isomerization process.

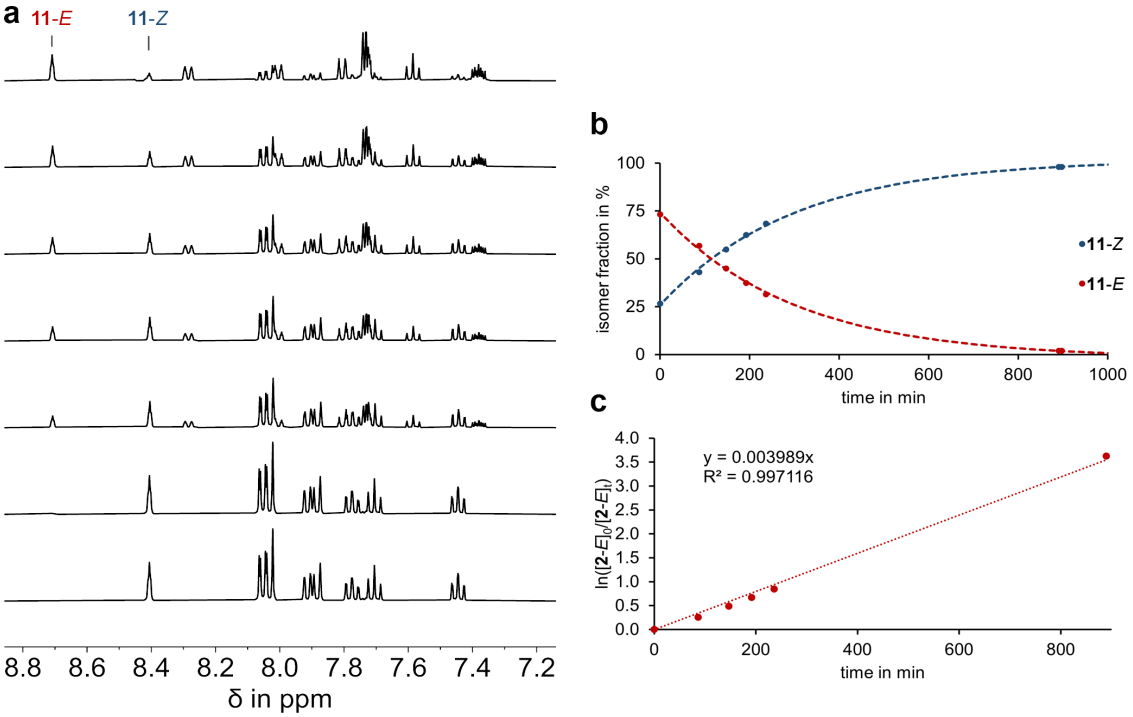

Figure 39 Kinetic analysis of thermal isomerization starting from an **11**-*E* enriched solution at 22 °C. **a** ^{1}H NMR spectra (400 MHz, dimethylsulfoxide-d_6, 25 °C) of **11**-*E* and **11**-*Z* recorded during thermal isomerization of **11**-*E* to **11**-*Z* starting from an **11**-*E* enriched mixture consisting of 73% **11**-*E* and 27% **11**-*Z* (top spectrum). Spectra were recorded in irregular intervals ordered chronologically from top to bottom. **b** Changing isomer distribution of **11**-*E* (red dots) and **11**-*Z* (blue dots) during thermal conversion at 22 °C. Data were simulated for visual guidance using an exponential proportional rate growth or decrease fit shown with color-coded dashed lines. **c** Kinetic evaluation using a first-order rate law without entering a thermal equilibrium provides a linear correlation for the conversion of **11**-*E*. A simulation of the experimental data points using a linear regression fit (dotted red line) leads to a slope of m = 0.003989, translating into a *Gibbs* energy of activation of $\Delta G^{\ddagger}$ = 20.5 kcal mol^{-1}. The absolute energy difference must be at least 1.7 kcal mol^{-1} between thermodynamically stable ground state **11**-*Z* and metastable **11**-*E* under the conservative assumption 5% is not detected from NMR.

4.5. UV-Vis absorption spectra and molar extinction coefficients

Acquisition of UV-Vis absorption spectrum of thermodynamically stable **11**-*Z* was measured in dimethyl sulfoxide at 22 °C shown in Figure 40. Metastable **11**-*E* isomer on the contrary could not be recorded directly, since half-life of ~5 hours at 22 °C complicates isolation and measurement procedures significantly. To this end, the same procedure as already described in chapter 3.4 was applied.

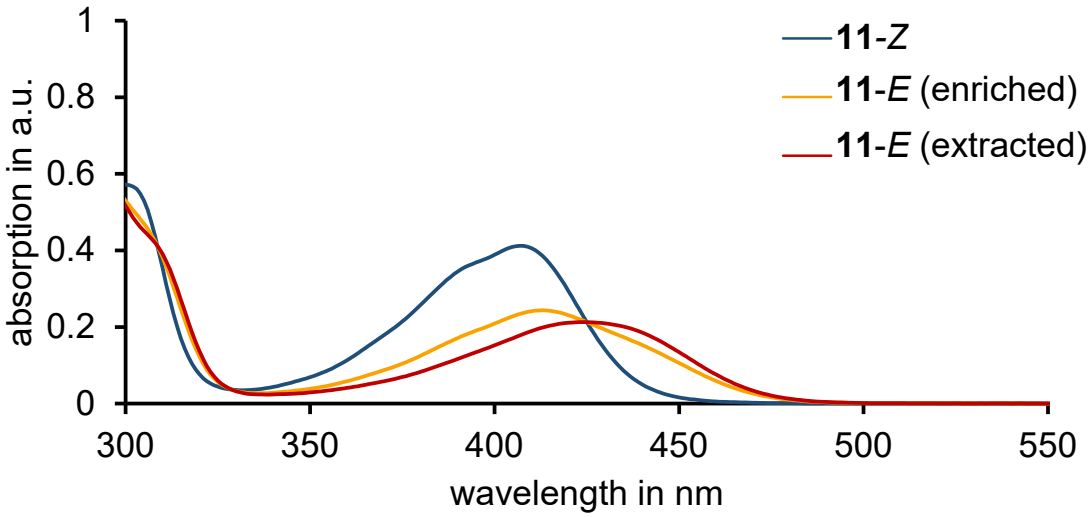

Figure 40 UV-Vis absorption spectra (dimethyl sulfoxide, 22 °C) of isomer **11**-*Z* (blue), 76% **11**-*E* enriched solution (orange) and calculated spectrum of pure **11**-*E* (red) at a concentration of 38 μM.

Molar extinction coefficients displayed in Figure 41 were determined next from the above-mentioned absorption spectra using known concentration of pure and enriched solutions.

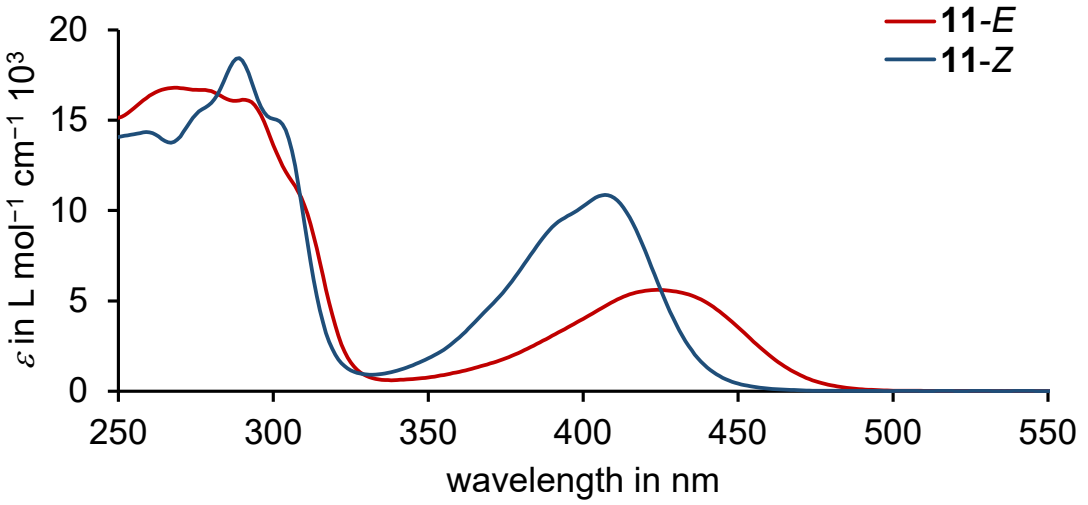

Figure 41 Molar extinction coefficients (dimethyl sulfoxide, 22 °C) of isomer **11**-*Z* (blue) and calculated metastable **11**-*E* (red).

4.6. Fluorescence spectra

4.6.1. Fluorescence spectra of 11-*Z*

Fluorescence emission spectra of **11**-*Z* were measured from pure solutions in various solvents mentioned below for excitation wavelengths of 316, 400 and 453 nm shown in Figure 42–44.

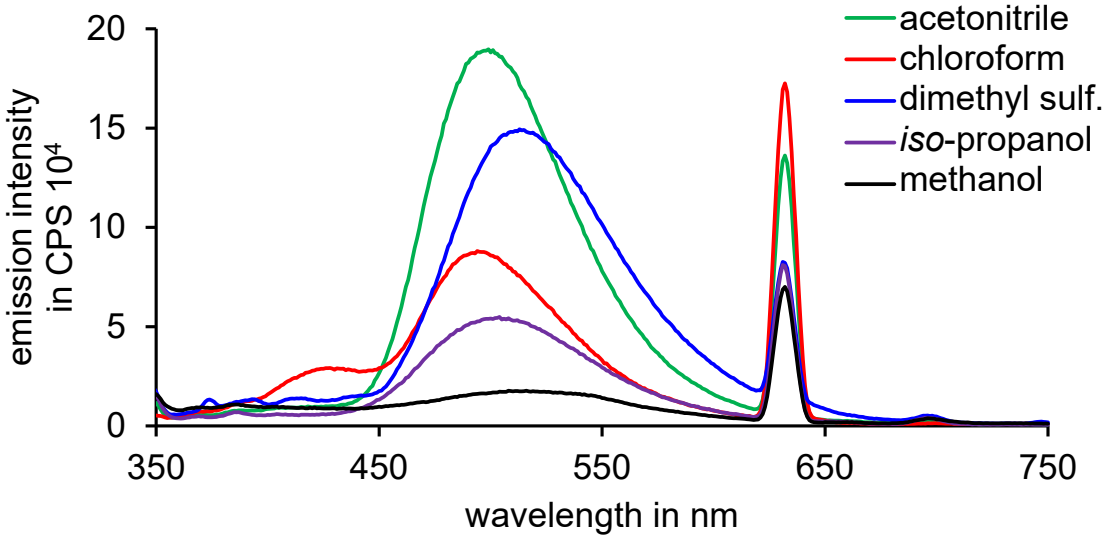

Figure 42 Fluorescence spectra (acetonitrile (green), chloroform (red), dimethyl sulfoxide (blue), *iso*-propanol (purple), methanol (black), 22 °C) of pure isomer **11**-*Z* solutions excited at 316 nm.

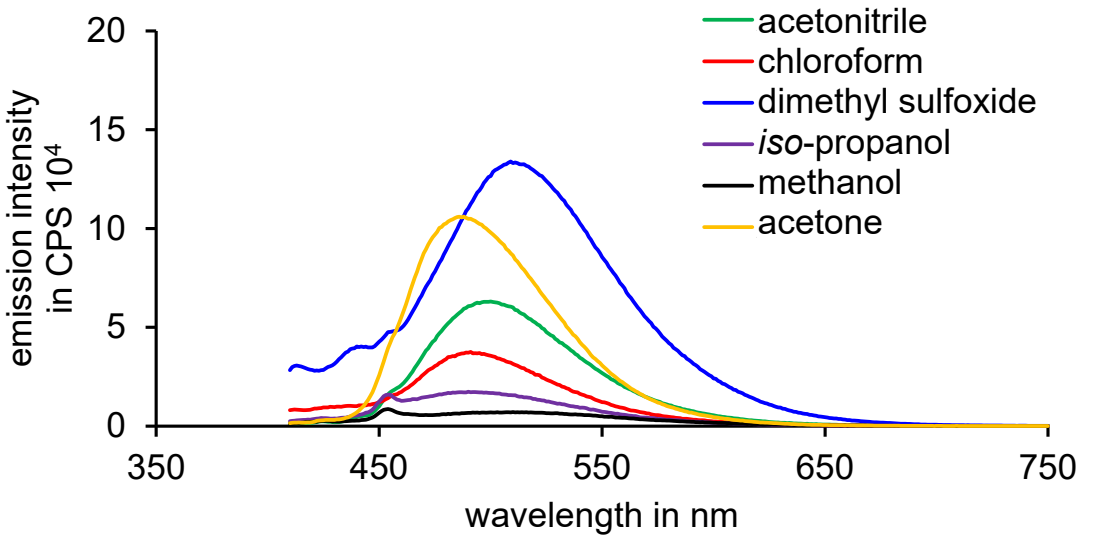

Figure 43 Fluorescence spectra (acetonitrile (green), chloroform (red), dimethyl sulfoxide (blue), *iso*-propanol (purple), methanol (black), acetone (orange), 22 °C) of pure isomer **11**-*Z* solutions excited at 400 nm.

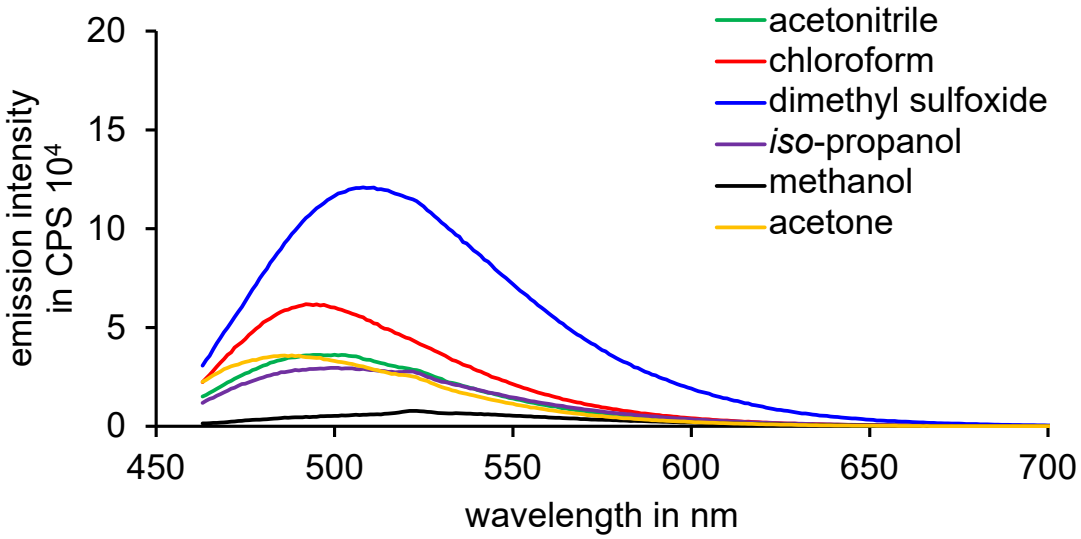

Figure 44 Fluorescence spectra (acetonitrile (green), chloroform (red), dimethyl sulfoxide (blue), *iso*-propanol (purple), methanol (black), acetone (orange), 22 °C) of pure isomer **11**-*Z* solutions excited at 453 nm.

4.6.2. Fluorescence spectra of 11-*E*

Fluorescence emission spectra of **11**-*E* were measured in various solvents mentioned below for excitation wavelengths of 316, 400 and 453 nm shown in Figure 45–47. Since pure solutions of **11**-*E* are challenging to obtain because of the reduced half-life time, see chapter 3.4, mixtures of *Z*- and *E*-isomers were utilized enriched in *E*-isomer to the PSS using a 420 nm LED before each measurement.

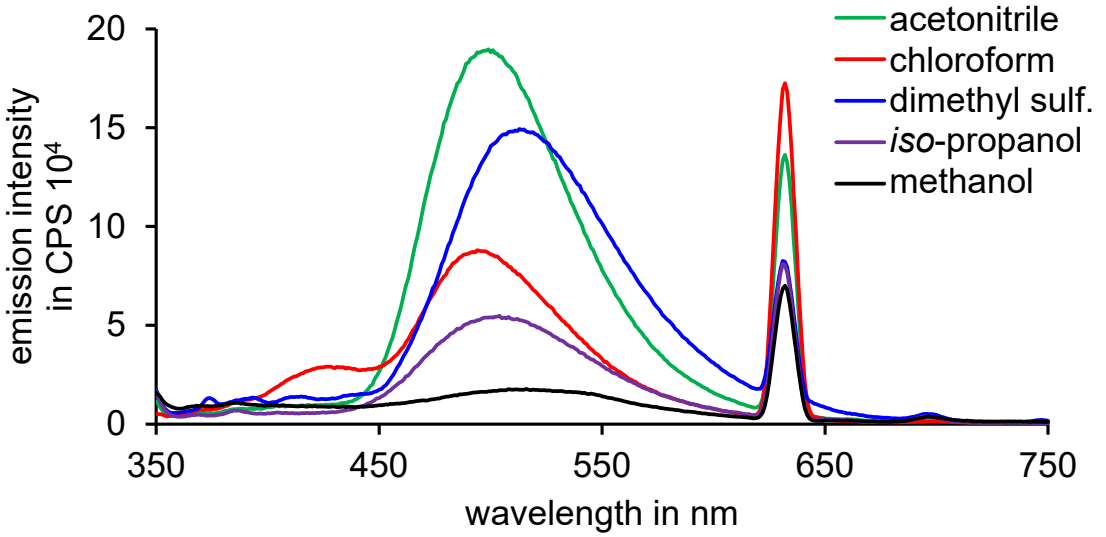

Figure 45 Fluorescence spectra (acetonitrile (green), chloroform (red), dimethyl sulfoxide (blue), *iso*-propanol (purple), methanol (black), 22 °C) of **11**-*E* enriched solutions excited at 316 nm.

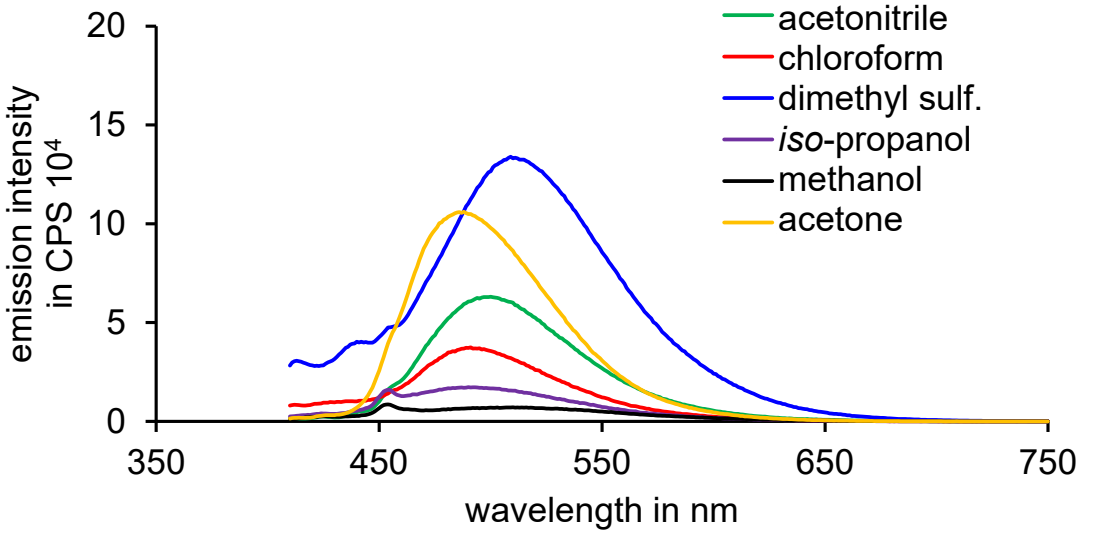

Figure 46 Fluorescence spectra (acetonitrile (green), chloroform (red), dimethyl sulfoxide (blue), *iso*-propanol (purple), methanol (black), acetone (orange), 22 °C) of **11**-*E* enriched solutions excited at 400 nm.

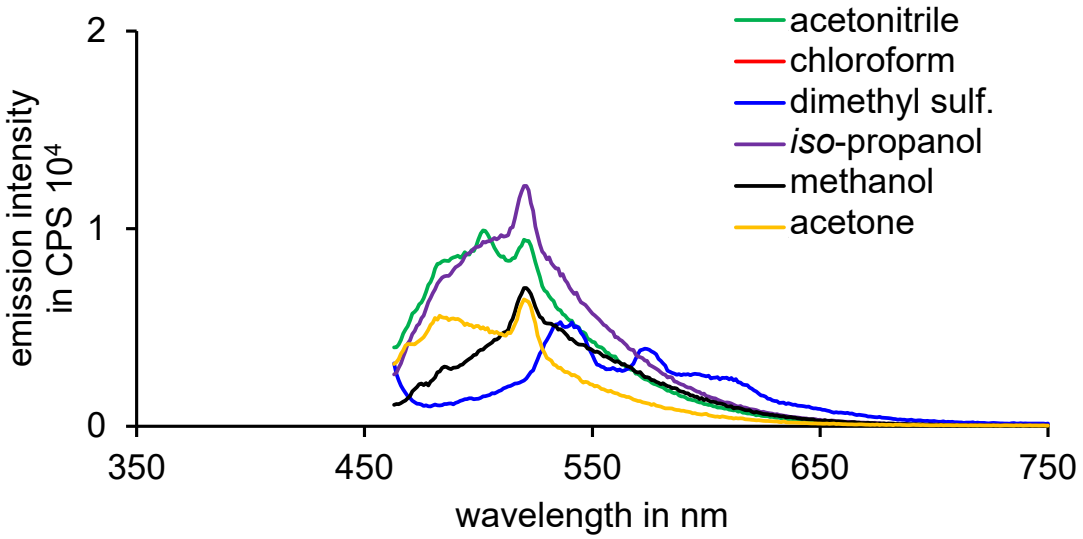

Figure 47 Fluorescence spectra (acetonitrile (green), chloroform (red), dimethyl sulfoxide (blue), *iso*-propanol (purple), methanol (black), acetone (orange), 22 °C) of **11**-*E* enriched solutions excited at 453 nm.

Strong differences between *Z*- and *E*-isomers were observed for the fluorescence spectra after excitation with 453 nm which is promising for fluorescence switching in a host guest system. If bindings constants for the *Z*-isomer are higher than for the *E*-isomer this could result in enhancement of the fluorescence of the *Z*-isomer but not for the *E*-isomer at 453 nm resulting in a turn on/off effect of the emission.

4.7. Applications

After characterizations of fluorescent photoswitch **11**, potential applications for surface attachment and host guest chemistry were examined. All application-related experiments were carried out in collaboration with the group of *Dr. Evgeny Kataev* and *Prof. Dr. Jörg Libuda*.

Preliminary results from the *Libuda* group carried out by *Georg Fickenscher*[I] did unfortunately indicate that no photoswitching occurs after irradiation of **11**-*Z* on a Co_3O_4(111) surface. However, initial experiments in the *Kataev* group by *Viridiana Velazquez Castillo*[II] regarding affinity to a water-soluble receptor show binding constant differences of more than two orders of magnitude and fluorescence modulation with the receptor.

4.8. Conclusion and outlook

Since this is work in progress, further already planned experiments are necessary to complete this study such as determination of PSSs and QYs. Applying photoswitching on a Co_3O_4(111) surface in the group of *Prof. Dr. Jörg Libuda* by *Georg Fickenscher*[I] did unfortunately not result in switching on the surface. Additionally, applications of HTI-based fluorescence switch **11** with fluorescence enhancing receptor **13** will be thoroughly examined in detail in the group of *Dr. Evgeny Kataev* by *Viridiana Velazquez Castillo*[II] in the near future.

5. Modifying electronics of HTI-based molecular motors

5.1. Aim

Light-powered molecular motors account for two decades of research with diversification which advanced into various chemical disciplines and beyond.[236–239] Gaining precise control over molecular motors driven by visible light is one of the cornerstones for the realization of future functional artificial systems powered by non-destructive energy. Currently, there are still considerable efforts to be made to achieve full control over these unidirectional rotating engines. Such as the circumstance that many of the especially thoroughly investigated systems require UV light for operation which limits the applicability in a biological context due to the high energy nature of radiation from this part of the electromagnetic spectrum. Molecular designs based on indigoid chromophores in contrast enable the usage of less destructive light from the visible part of the spectrum but are much less investigated. After full HTI motor mechanism elucidation steric influence upon the rotational cycle was evaluated, but no electronic influence has been systematically studied yet. Some of the more recent concepts which use HTI molecular motors for building advanced nanomachinery range from the development of active mechanical threading[157] or transmission of directional rotation,[159,160,240] to catalytic applications[161] to a rotation cycle containing a high energy intermediate.[162]

To this end, the electronic properties of the motor chromophore based on the first HTI motor system were altered for five molecules **15a–15e** in this work without changing the steric features around the photoisomerizable double bond, rendering the core structure similar to the original system. Combined with a previous study of the influence of steric hindrance around the double bond, upon the rotational mechanism of HTI motors, this allows comparison of the steric and electronic effects separately from each other. With respect to a recently developed chemical method[1] proving unidirectionality for molecular motors which are too fast for conventional analytic methods three more rapidly rotating HTI-based motors **15f–15h** were also investigated in this work.

5.2. Design principles

A series of molecular motors with an electron withdrawing group (EWG) in **15a**, a neutral group in **15b**, and electron donating groups (EDGs) in **15c**, original HTI-based motor **15d** as well as **15e** was designed to investigate electronic effects shown in Figure 48. These substituents were positioned in *para*-position to the methoxy group in the fjord region. Furthermore, motors **15f**, **15g**, and **15h** – for which unidirectionality was predicted experimentally – were included in the series, and are discussed further in chapter 6.

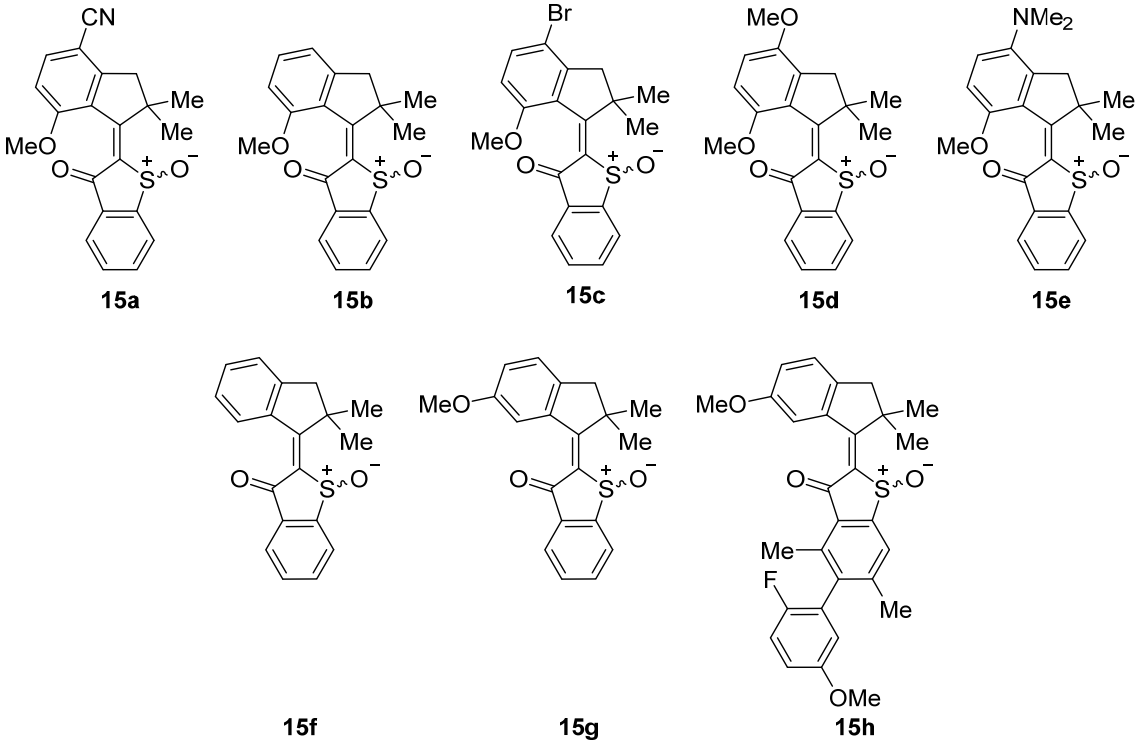

Figure 48 Overview of all HTI-based molecular motors **15a–15h** investigated upon electronic influence from substitution in para-position to the methoxy group in the fjord region. Substituents were sorted from left to right from −M to +M effects in the top row.

5.3. Synthesis of motor series

Molecular motors shown in Figure 48 were synthesized from commercially available starting materials *via* condensation of the respective indanone **16** and benzothiophenone building block **5** or **17**, shown in Figure 49. Details for the synthesis of benzothiophenone building blocks **5** and **17** as well as **18** can be found in chapter 6.3. For more experimental details see chapter 8.5.2 or the literature for details on motors **15d** and **15h**.[1,154] Synthetic procedures towards all herein presented compounds are reported in the experimental chapter 8.4.1 starting from commercially available starting materials. Solely motor **15d** is not reported herein, since a previously in the *Dube* group synthesized sample was used for all experiments.

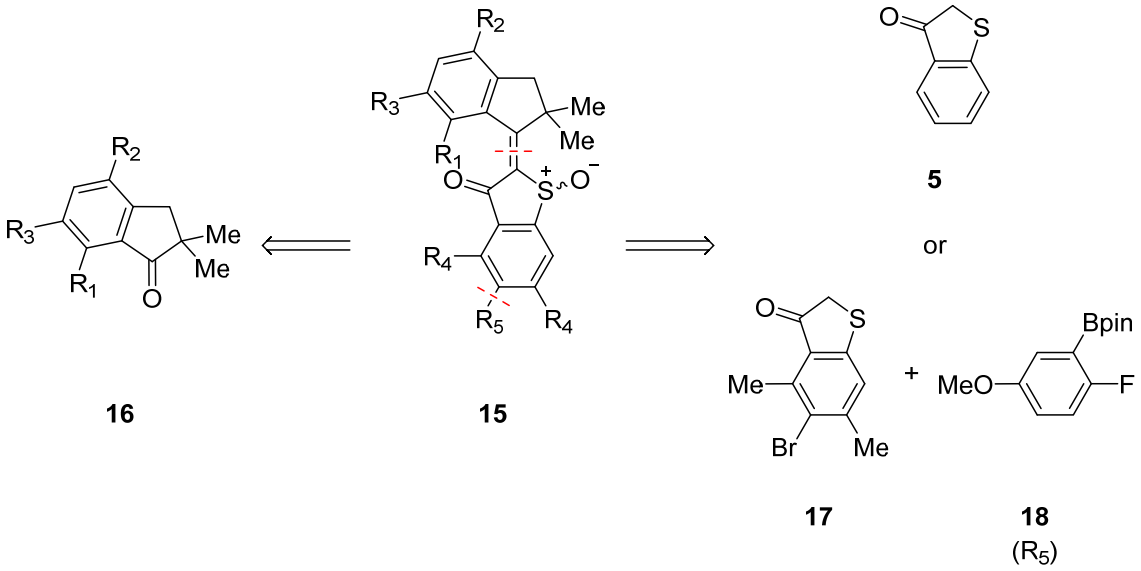

Figure 49 Retrosynthetic analysis of HTI-based molecular motors **15a–15h** illustrated generally for motor **15**. Cleavage along the central double bond and the biaryl axis in **15** lead to indanone rotor building block **16**, benzothiophenone stator **5** or **17**, and aryl **18**.

Substitution patterns of molecular motors **15** and their corresponding starting materials are defined in Table 4. The synthetic procedure for molecular motor **15h** can be found in chapter 6.4 and **15d** in the corresponding literature.[154]

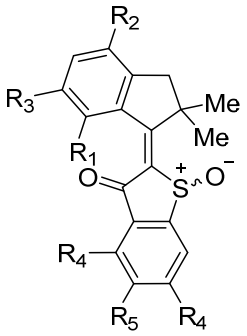

15

Table 4 Substitution patterns of HTI-based molecular motors **15a–15h** and their corresponding starting materials illustrated generally for motor **15**. Substitution pattern of motor **15d** is only listed for completeness but was not synthesized within this work since a sample previously synthesized in the *Dube* group was used for all experiments.

	R_1	R_2	R_3	R_4	R_5
a	OMe	CN	H	H	H
b	OMe	H	H	H	H
c	OMe	Br	H	H	H
d	OMe	OMe	H	H	H
e	OMe	NMe_2	H	H	H
f	H	H	H	H	H
g	H	H	OMe	H	H
h	H	H	OMe	Me	C_7H_6OF

Indanone building blocks **16a–16c** and **16f** were prepared starting from the corresponding commercially available non-methylated indanones **19a–19c** and **19f** through methylation with iodomethane shown in Figure 50. Indanone **16b** and **16c** were synthesized according to a literature procedure.[157,158,241] It is notheworthy, that an exchange of solvent from *N*,*N*-dimethylformamide to tetrahydrofuran yielded **16f** quantitatively which could be beneficial for the methylation of other indanones as well.

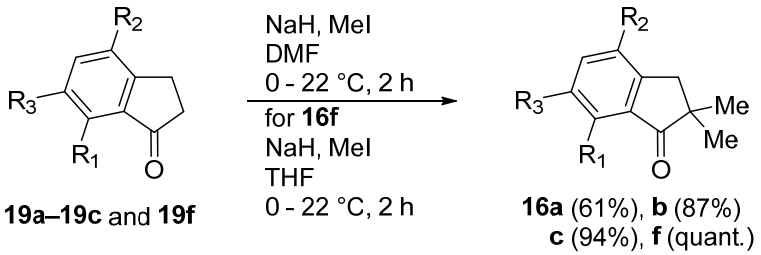

Figure 50 Synthesis of indanone building block **16a–16c** and **16f**. Commercially available starting materials **19a–19c** and **19f** were methylated using iodomethane furnishing the corresponding indanones.

Starting materials **19a** and **16e** were prepared inspired from literature, turning the corresponding brominated indanones **19c** or **16c** into the respective cyano compound **19a** or dimethylamino compound **16e** shown in Figure 51 and 52.[242]

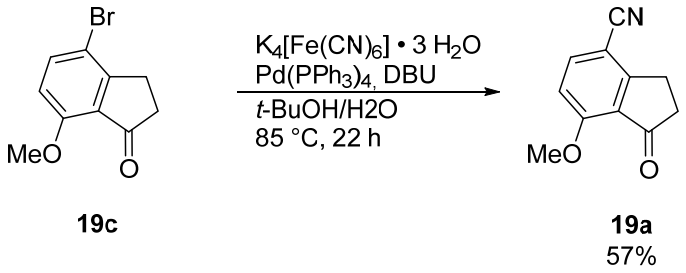

Figure 51 Indanone **19a** was prepared starting from the corresponding brominated indanone **19c** through cyanation using potassium hexacyanidoferrate(II).

Amination of Indanone **16c** was achieved using Buchwald-Hartwig cross coupling chemistry using palladium(II) acetate shown in Figure 52. It is noteworthy that indanone **16c** had to be *di*-methylated in *α*-position to the carbonyl already to furnish **16e**.

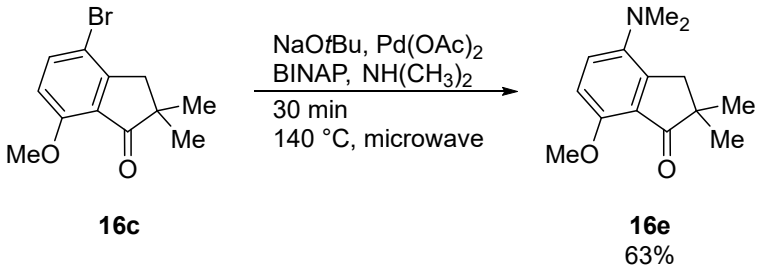

Figure 52 Indanone **16e** was prepared starting from the corresponding brominated and methylated indanone **16c** through amination using *Buchwald-Hartwig* cross coupling chemistry.

The final steps to HTI-based molecular motors **15a–15g** (except **15d**) were carried out *via* condensation of the indanones **16a–16g** with benzothiophenone building block **5** (for **15h** see chapter 6.4) to HTI **20a–20g** followed by direct oxidation of the HTI core without isolation of intermediates shown in Figure 53 inspired from a literature procedure.[158,159] Molecular motor **15e** has been synthesized by *Sylvia Heberl*.[III]

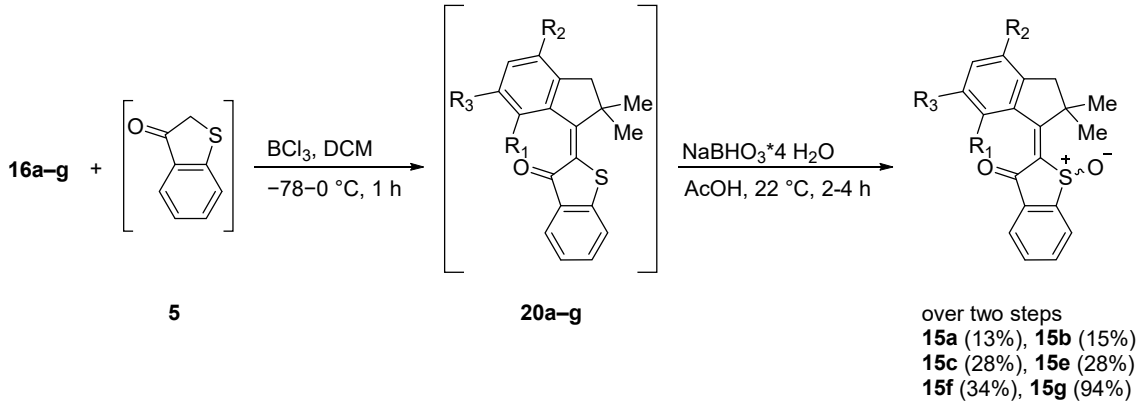

Figure 53 Synthesis of HTI-based molecular motors **15a**–**15g** (except **15d**). Condensation of indanones **16a**–**16g** and benzothiophenone **5** with boron trichloride furnished HTI **20a**–**20g** as a mixture of *E*- and *Z*-isomers which were directly oxidized to the corresponding sulfoxides **15a**–**15g** *via* treatment of the sulfide with an excess of sodium perborate in acetic acid. Structures in brackets were used in the next synthetic transformation without isolation. Molecular motor **15e** has been synthesized by *Sylvia Heberl*.[III]

5.4. Structural and conformational description in solution

All motors presented within this work, follow the unidirectional rotation cycle shown in Figure 54 for **15**. Structures **A** and **C** are thermodynamic or kinetically stable products observed at 22 °C with **C** as the kinetically and **A** the thermodynamically stable one. Structure **D** can usually be found at –90 °C for structures with some steric strain present in the fjord region. If steric strain in that region is reduced, **D** is not observed even at –90 °C anymore. Structure **B** can only be observed at low temperatures if steric load in the fjord region is severely increased.

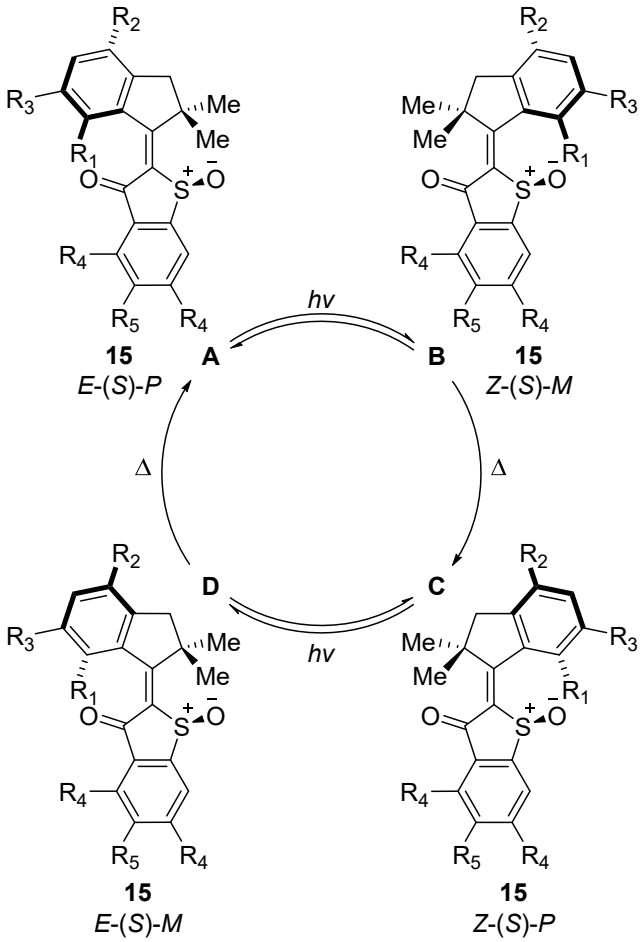

Figure 54 Overview of all conformers of motors **15**, shown according to their occurrence in the motor sequence, consisting of two *E*-isomers (**A** and **D**) and two *Z*-isomers (**B** and **C**) with one stable *P*-helicity (**A** and **C**) at 22 °C and one metastable *M*-helicity (**B** and **D**) for each isomer.

Conformations of molecular motors were characterized first in solution after separation of *E*- and *Z*-isomers stable at 22 °C shown in Figure 55–62. Pure solutions of each isomer in CD_2Cl_2 were extensively examined using 1D, 2D and variable temperature (VT) ^{1}H NMR spectroscopy. For a detailed ^{1}H and ^{13}C spectroscopic analysis of each isomer see chapter 8.4.1. Molecule **15h** and its favored rotation

direction is described in detail in chapter 6. For original motor **15d** and motor **15h** additional experimental details can be found in the corresponding literature.[154,243] Absence of NOE signals in **15g** made the assignment of double bond configuration challenging. An indication for *E*- and *Z*-isomer can be obtained from UV-Vis data when comparisons are made to other motor derivatives.

5.4.1. 15a-*E*-(*S*)-(*P*) = A

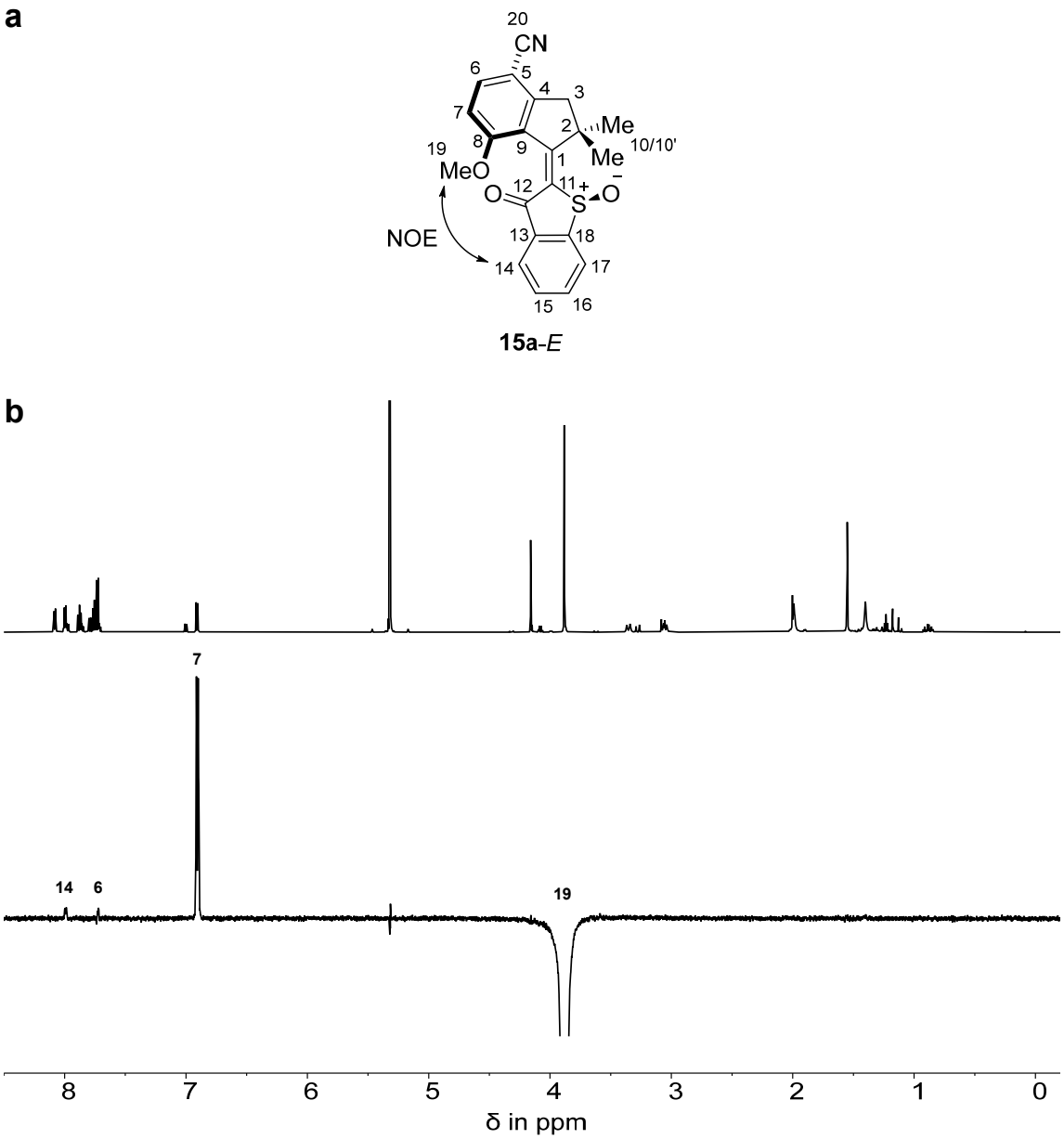

Figure 55 Double bond configuration analysis of **15a**-*E*-(*S*)-(*P*) motor isomer enriched CD_2Cl_2 solution at 25 °C. **a** Structure of **15a**-*E*-(*S*)-(*P*) including arrows depicting observed NOE signals. **b** ^{1}H (top) and NOE (bottom) NMR spectra (600 MHz, CD_2Cl_2, 25 °C) of **15a**-*E*-(*S*)-(*P*) display proximity of H_3C19 to HC14, revealing *E*-configuration of the central double bond.

5.4.2. 15a-*Z*-(*S*)-(*P*) = C

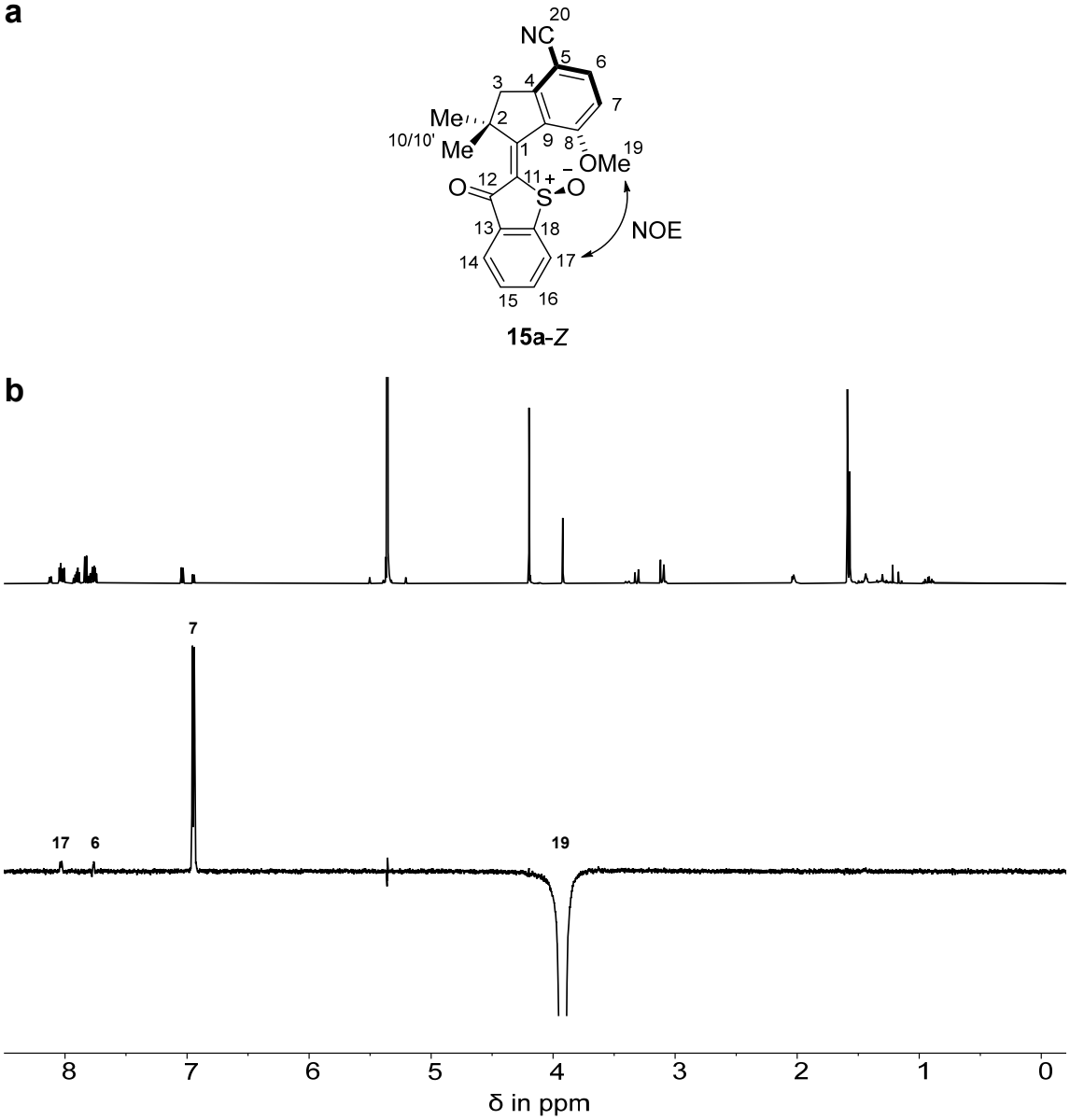

Figure 56 Double bond configuration analysis of **15a**-*Z*-(*S*)-(*P*) motor isomer enriched CD_2Cl_2 solution at 25 °C. **a** Structure of **15a**-*Z*-(*S*)-(*P*) including arrows depicting observed NOE signals. **b** ^1H (top) and NOE (bottom) NMR spectra (600 MHz, CD_2Cl_2, 25 °C) of **15a**-*Z*-(*S*)-(*P*) display proximity of H_3C19 to HC17, revealing *Z*-configuration of the central double bond.

5.4.3. 15c-*E*-(*S*)-(*P*) = A

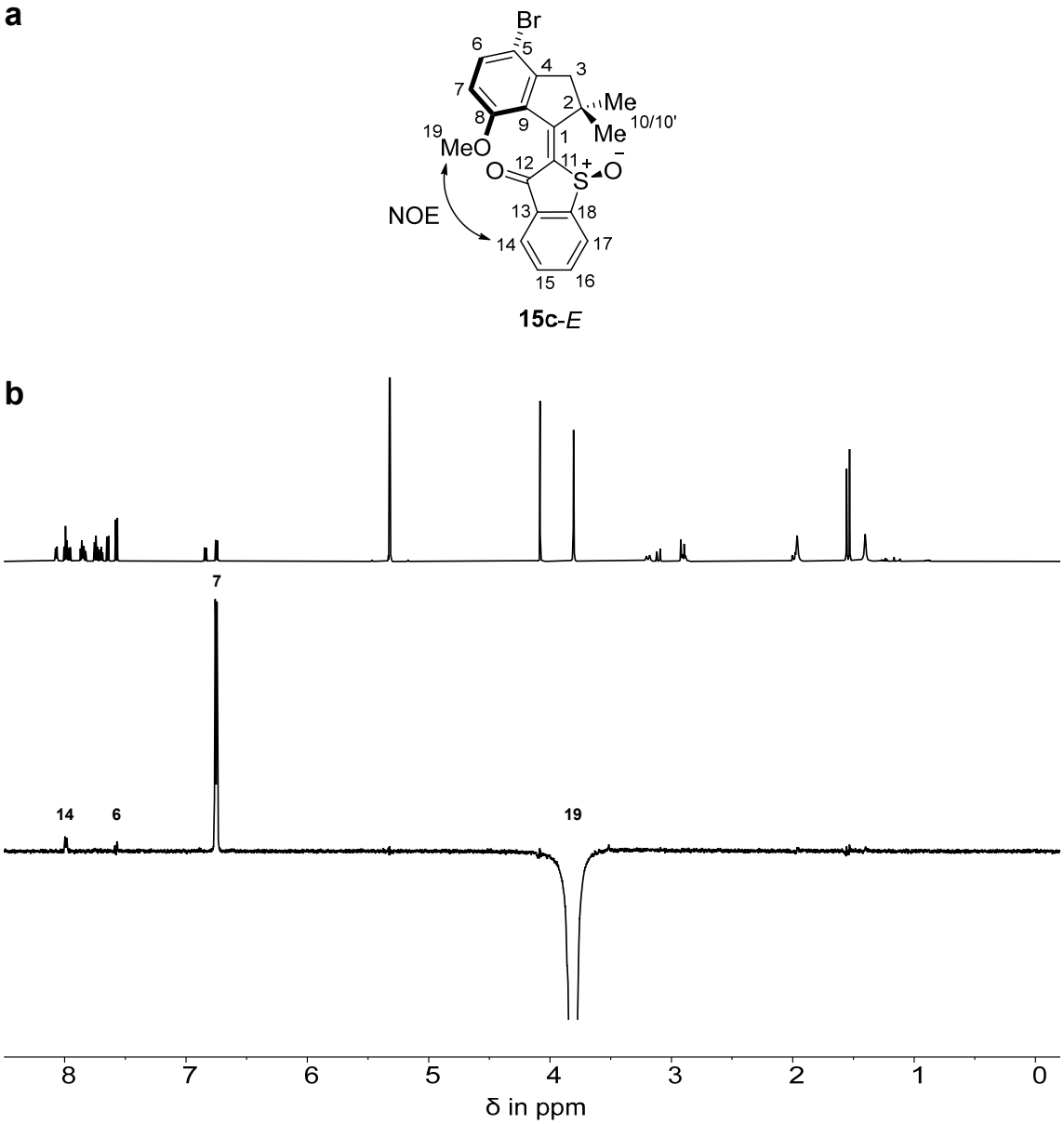

Figure 57 Double bond configuration analysis of **15c**-*E*-(*S*)-(*P*) motor isomer enriched CD_2Cl_2 solution at 25 °C. **a** Structure of **15c**-*E*-(*S*)-(*P*) including arrows depicting observed NOE signals. **b** ^1H (top) and NOE (bottom) NMR spectra (600 MHz, CD_2Cl_2, 25 °C) of **15c**-*E*-(*S*)-(*P*) display proximity of H_3C19 to HC14, revealing *E*-configuration of the central double bond.

5.4.4. 15c-*Z*-(*S*)-(*P*) = C

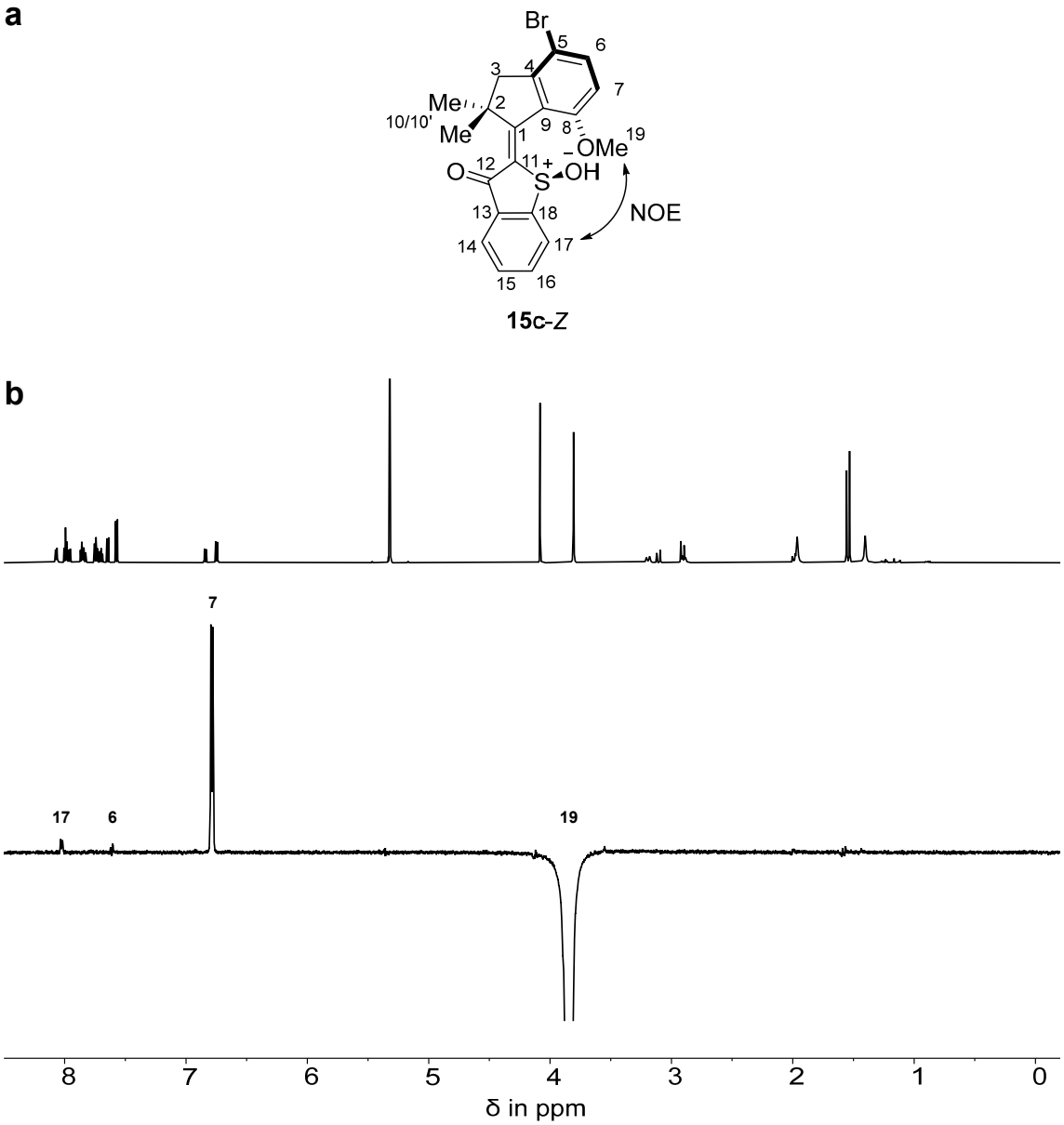

Figure 58 Double bond configuration analysis of **15c**-*Z*-(*S*)-(*P*) motor isomer enriched CD_2Cl_2 solution at 25 °C. **a** Structure of **15c**-*Z*-(*S*)-(*P*) including arrows depicting observed NOE signals. **b** ^1H (top) and NOE (bottom) NMR spectra (600 MHz, CD_2Cl_2, 25 °C) of **15c**-*Z*-(*S*)-(*P*) display proximity of H_3C19 to HC17, revealing *Z*-configuration of the central double bond.

5.4.5. 15e-*E*-(*S*)-(*P*) = A

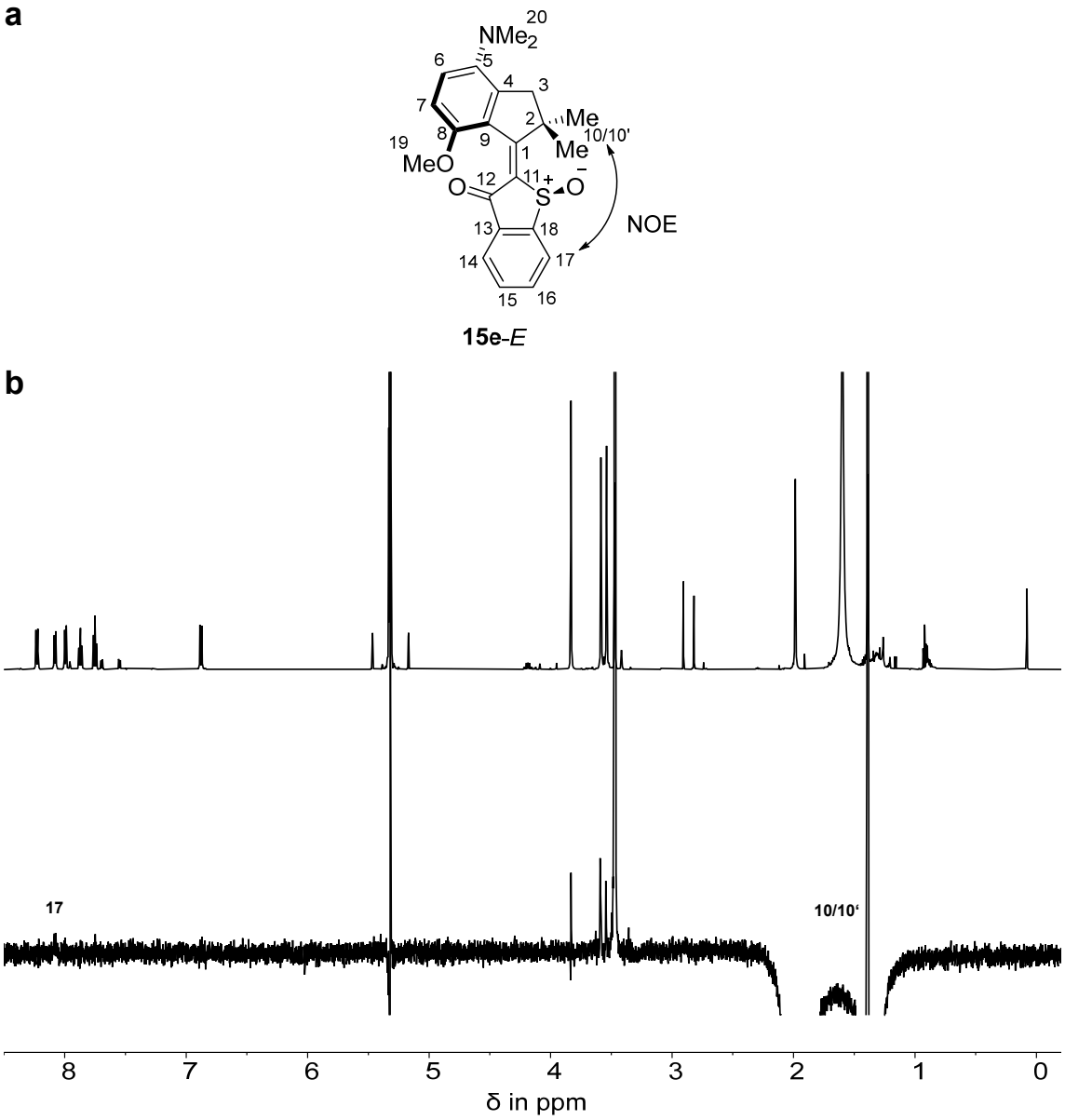

Figure 59 Double bond configuration analysis of **15e**-*E*-(*S*)-(*P*) motor isomer enriched CD_2Cl_2 solution at 25 °C. **a** Structure of **15e**-*E*-(*S*)-(*P*) including arrows depicting observed NOE signals. **b** ^{1}H (top) and NOE (bottom) NMR spectra (600 MHz, CD_2Cl_2, 25 °C) of **15e**-*E*-(*S*)-(*P*) display proximity of H_3C10/H_3C10’ to HC17, revealing *E*-configuration of the central double bond.

5.4.6. 15e-*Z*-(*S*)-(*P*) = C

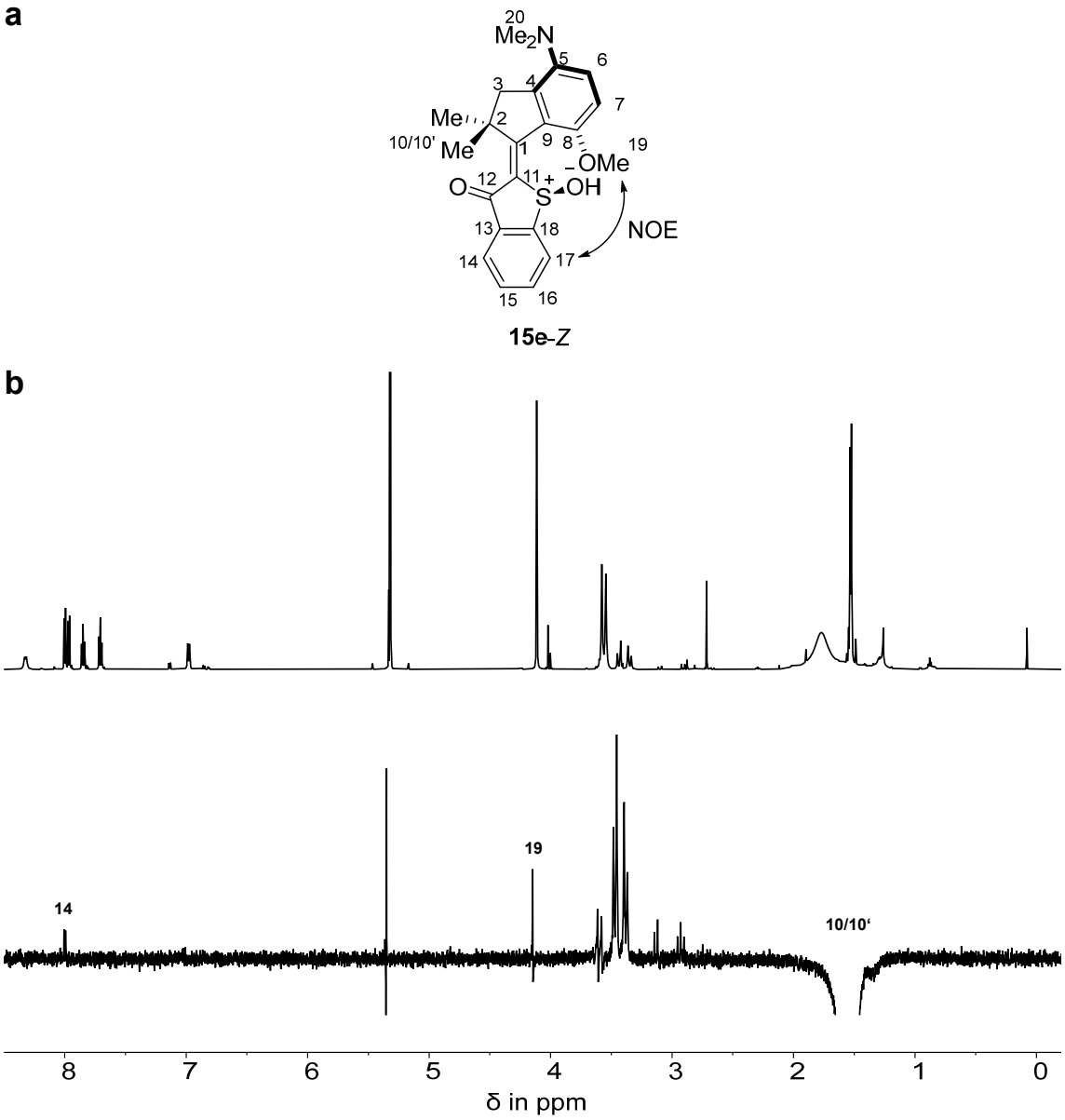

Figure 60 Double bond configuration analysis of **15e**-*Z*-(*S*)-(*P*) motor isomer enriched CD_2Cl_2 solution at 25 °C. **a** Structure of **15e**-*Z*-(*S*)-(*P*) including arrows depicting observed NOE signals. **b** ^1H (top) and NOE (bottom) NMR spectra (600 MHz, CD_2Cl_2, 25 °C) of **15e**-*Z*-(*S*)-(*P*) display proximity of H_3C19 to HC17, revealing *Z*-configuration of the central double bond.

5.4.7. 15f-*E*-(*S*)-(*P*) = A

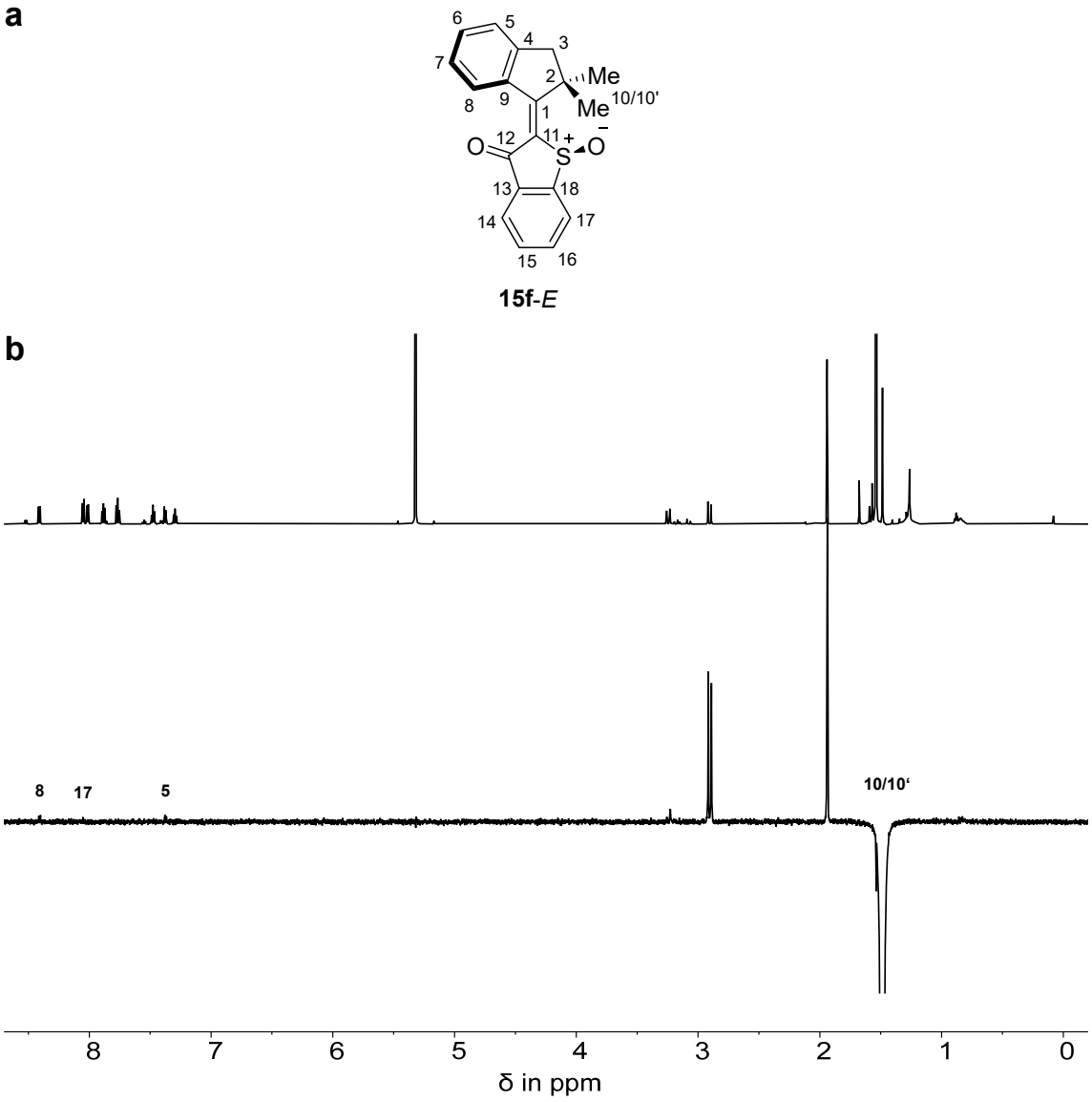

Figure 61 Double bond configuration analysis of **15f**-*E*-(*S*)-(*P*) motor isomer enriched CD_2Cl_2 solution at 25 °C. **a** Structure of **15f**-*E*-(*S*)-(*P*) including arrows depicting observed NOE signals. **b** ^1H (top) and NOE (bottom) NMR spectra (600 MHz, CD_2Cl_2, 25 °C) of **15f**-*E*-(*S*)-(*P*) display proximity of H_3C10/H_3C10' to HC17, revealing *E*-configuration of the central double bond.

5.4.8. 15f-*Z*-(*S*)-(*P*) = C

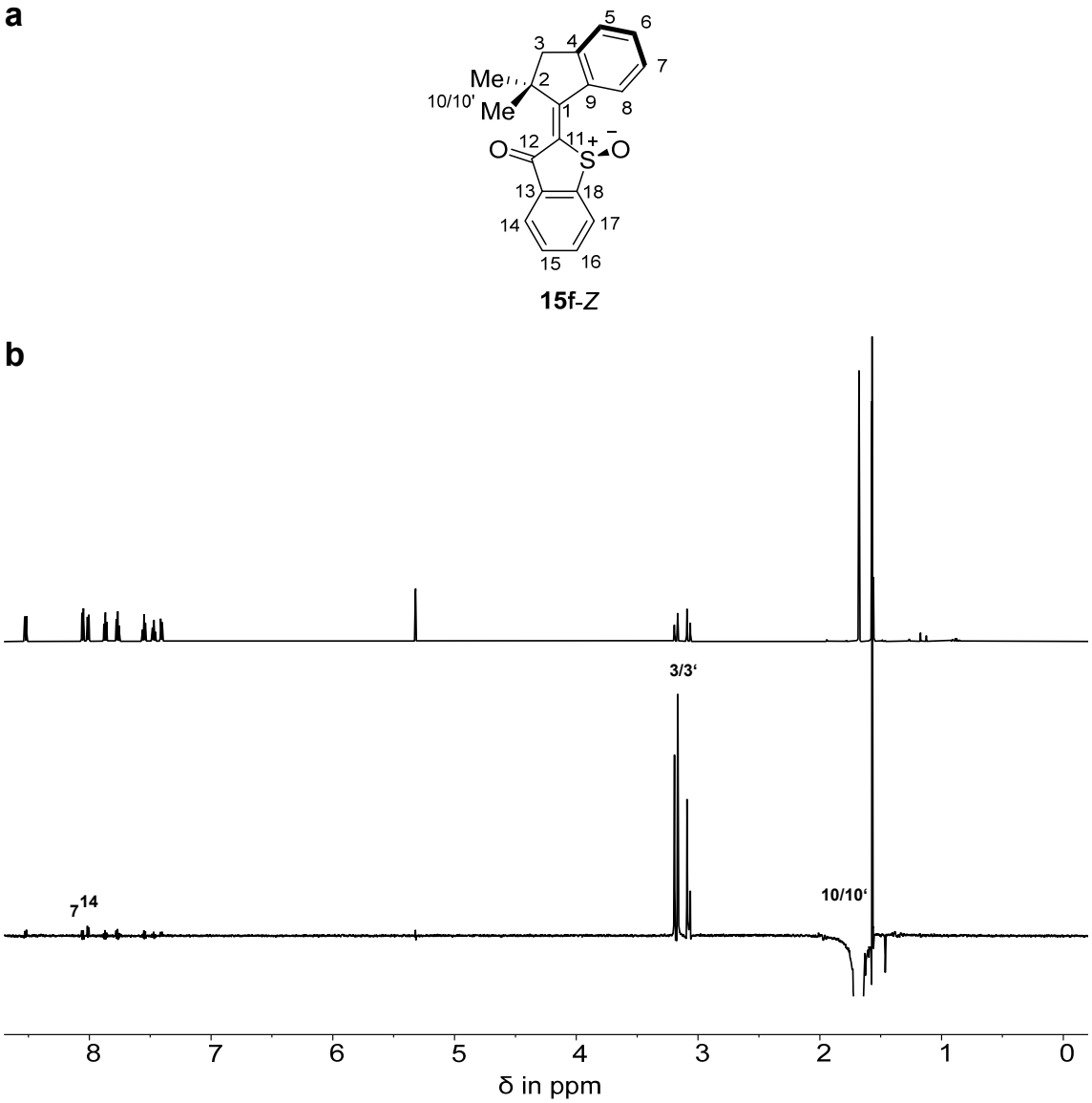

Figure 62 Double bond configuration analysis of **15f**-*E*-(*S*)-(*P*) motor isomer enriched CD_2Cl_2 solution at 25 °C. **a** Structure of **15f**-*E*-(*S*)-(*P*) including arrows depicting observed NOE signals. **b** ^1H (top) and NOE (bottom) NMR spectra (600 MHz, CD_2Cl_2, 25 °C) of **15f**-*E*-(*S*)-(*P*) display proximity of H_3C10/H_3C10' to HC14, revealing *E*-configuration of the central double bond.

5.5. Thermal isomerization at elevated temperatures

The mathematical details for the determination of $\Delta G^{\ddagger}$ and ΔG shown in Figure 63–65 for which results are summarized in Table 5 and 6 can be found in chapter 6.8.

Table 5 Measured *Gibbs* energies of activation $\Delta G^{\ddagger}$ for HTI-based molecular motors **15a**, **15b**, **15c**, and **15d** at 100 °C in toluene-d_8. Configurations utilized as starting points are mentioned in the isomerization process column. [a]Value obtained from literature.[154]

isomerization process	linear regression slope *m*	$\Delta G^{\ddagger}$ in kcal mol^{-1}
15a-*E* → **15a**-*Z*	0.0003779	27.8
15b-*Z* → **15b**-*E*	0.0003701	27.8
15c-*E* → **15c**-*Z*	0.0001972	28.3
15d-*E* → **15d**-*Z*	-	29.5[a]

Table 6 Measured ground state *Gibbs* energy differences ΔG of *E*- and *Z*-isomers for HTI-based molecular motors **15a**, **15b**, **15c**, and **15d** at 100 °C in toluene-d_8. [a]Values obtained from literature.[154]

isomer	ΔG in kcal mol^{-1}
15a-*E*	0.0
15a-*Z*	0.5
15b-*E*	0.0
15b-*Z*	0.7
15c-*E*	0.0
15c-*Z*	0.6
15d-*E*	0.0[a]
15d-*Z*	0.8[a]

5.5.1. Behavior of 15a

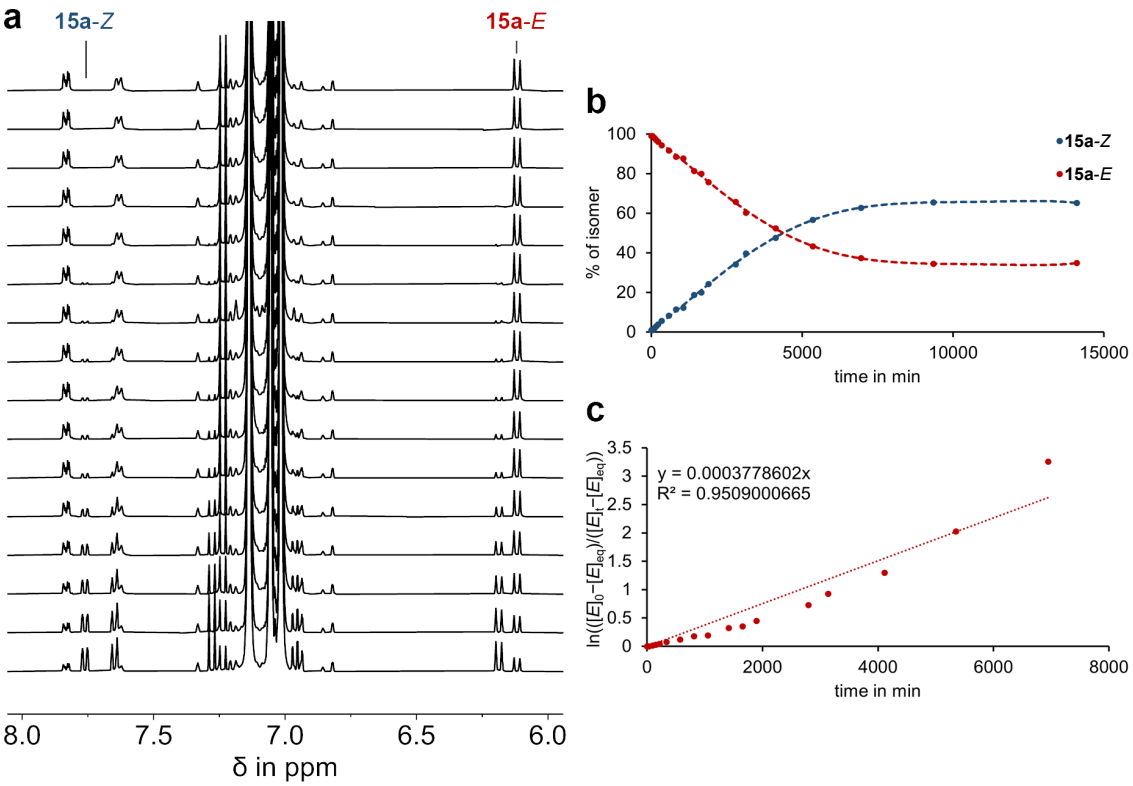

Figure 63 Kinetic analysis of thermal isomerization starting from an **15a**-*E* solution at 100 °C. **a** ^{1}H NMR spectra (400 MHz, toluene-d_8, 25 °C) of racemic **15a**-*E* and **15a**-*Z* during thermal isomerization of **15a**-*Z* to **15a**-*E* starting from a mixture consisting of 99% **15a**-*E* and 1% **15a**-*Z* (top spectrum). Spectra were recorded in irregular intervals ordered chronologically from top to bottom. **b** Changing isomer distribution of **15a**-*E* (red dots) and **15a**-*Z* (blue dots) during thermal conversion at 100 °C until a stable ratio of 65% **15a**-*Z* and 35% **15a**-*E* is reached. Data were simulated for visual guidance using a fourth-degree polynomial fit shown with color-coded dashed lines. **c** Kinetic evaluation using a first-order rate law entering a thermal equilibrium provides a linear correlation for the conversion of **15a**-*E*. A simulation of the experimental data points using a linear regression fit (dotted red line) leads to a slope of $m = 0.0003779$, translating into a *Gibbs* energy of activation of $\Delta G^{\ddagger} = 27.8$ kcal mol^{-1}.

5.5.2. Behavior of 15b

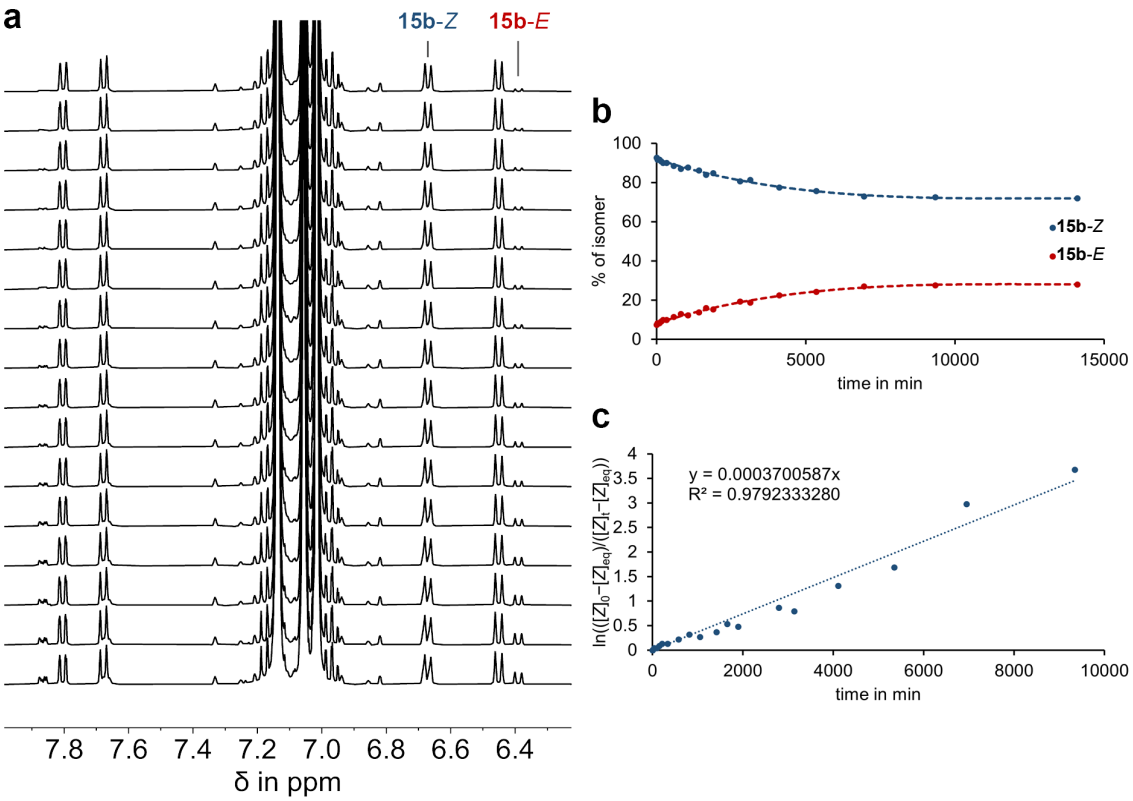

Figure 64 Kinetic analysis of thermal isomerization starting from an **15b**-*Z* enriched solution at 100 °C. **a** ^{1}H NMR spectra (400 MHz, toluene-d_8, 25 °C) of racemic **15b**-*E* and **15b**-*Z* during thermal isomerization of **15b**-*Z* to **15b**-*E* starting from an **15**b-*Z* enriched mixture consisting of 93% **15b**-*Z* and 7% **15b**-*E* (top spectrum). Spectra were recorded in irregular intervals ordered chronologically from top to bottom. **b** Changing isomer distribution of **15b**-*E* (red dots) and **15b**-*Z* (blue dots) during thermal conversion at 100 °C until a stable ratio of 72% **15b**-*Z* and 28% **15b**-*E* is reached. Data were simulated for visual guidance using a fourth-degree polynomial fit shown with color-coded dashed lines. **c** Kinetic evaluation using a first-order rate law entering a thermal equilibrium provides a linear correlation for the conversion of **15b**-*Z*. A simulation of the experimental data points using a linear regression fit (dotted blue line) leads to a slope of m = 0.0003701, translating into a *Gibbs* energy of activation of $\Delta G^{\ddagger}$ = 27.8 kcal mol^{-1}.

5.5.3. Behavior of 15c

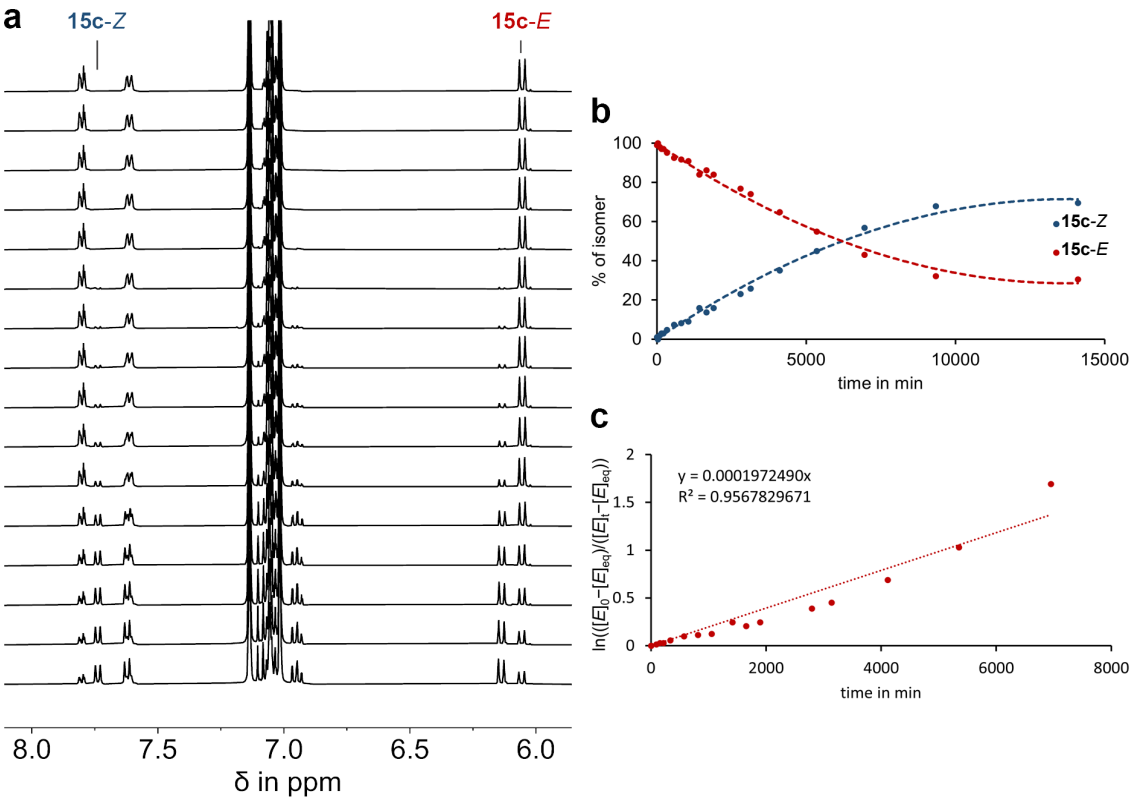

Figure 65 Kinetic analysis of thermal isomerization starting from an **15c**-*E* solution at 100 °C. **a** ^{1}H NMR spectra (400 MHz, toluene-d_8, 25 °C) of racemic **15c**-*E* and **15c**-*Z* during thermal isomerization of **15c**-*Z* to **15c**-*E* starting from a mixture consisting of 99% **15c**-*E* and 1% **15c**-*Z* (top spectrum). Spectra were recorded in irregular intervals ordered chronologically from top to bottom. **b** Changing isomer distribution of **15c**-*E* (red dots) and **15c**-*Z* (blue dots) during thermal conversion at 100 °C until a stable ratio of 70% **15c**-*Z* and 30% **15c**-*E* is reached. Data were simulated for visual guidance using a second-degree polynomial fit shown with color-coded dashed lines. **c** Kinetic evaluation using a first-order rate law entering a thermal equilibrium provides a linear correlation for the conversion of **15c**-*E*. A simulation of the experimental data points using a linear regression fit (dotted red line) leads to a slope of m = 0.0001972, translating into a *Gibbs* energy of activation of $\Delta G^{\ddagger}$ = 28.3 kcal mol^{-1}.

5.6. Low temperature ^{1}H NMR measurements

All motors **15a–15c** and **15e** were subjected to low temperature NMR spectroscopy measurements at −90 °C in order to determine the free *Gibbs* energy of activation $\Delta G^{\ddagger}_{\text{D-A}}$ for the thermal helix inversion (THI) step of the metastable *E*-isomer **D** to the stable *E*-isomer **A**. To this end, solutions of motor **15a–15c**, as well as **15e** and **15e** with 2.0 equiv. TFA in CD_2Cl_2 were prepared in an NMR tube and irradiated *in situ* with a 450 nm UHP LED at −90 °C until the PSS between **A**, **C** and **D** has been reached. At the PSS, irradiation was stopped, and the thermal decay of **D** was measured in appropriate intervals in the dark. From this data, the respective $\Delta G^{\ddagger}_{\text{D-A}}$ values were calculated as described in the following. All low temperature experiments were conducted together with *Christian Placht*.[IX]

THI from **D** to **A** can be described by a first-order rate law allowing to determine a rate constant by fitting the measured data with a linear regression analysis. Inserting the rate constant $k_{(\mathbf{D}\rightarrow\mathbf{A})}$ into the *Eyring* Equation 3 allows determination of $\Delta G^{\ddagger}_{\text{D-A}}$ after rearrangement.

$$k_{(\mathbf{D}\rightarrow\mathbf{A})} = \frac{k_B T}{h}\, e^{\frac{-\Delta G^{\ddagger}}{RT}} \qquad \text{(Eq. 3)}$$

$$T = \text{temperature in K}$$

$$k_B = \textit{Boltzmann}\ \text{constant} = 1.381 \cdot 10^{-23}\ \text{J} \cdot \text{K}^{-1}$$

$$h = \textit{Planck}\ \text{constant} = 6.626 \cdot 10^{-34}\ \text{J} \cdot \text{s}$$

$$R = \text{ideal gas constant} = 8.314\ \text{J} \cdot \text{K}^{-1} \cdot \text{mol}^{-1}$$

Rearranging Equation 3 followed by insertion of $k_{(\mathbf{D}\rightarrow\mathbf{A})}$, temperature of the measurement T and the numerical values for the Boltzmann constant k_B, the *Planck* constant h as well as the ideal gas constant R leads to Equation 4.

$$\Delta G^{\ddagger} = 8.314 \cdot T \cdot \left[23.760 + \ln\left(\frac{T}{k_{(\mathbf{D}\rightarrow\mathbf{A})}}\right)\right] \qquad \text{(Eq. 4)}$$

Additionally, the absolute difference in free *Gibbs* energy between **D** and **A** was estimated using the conservative assumption that 5% residual **D** isomer is not detected with ^{1}H NMR spectroscopy translating to an energy difference of at least 1.1 kcal mol^{-1} at −80 °C.

5.6.1. Behavior of 15a

A solution containing a mixture of **15a**-*E* and **15a**-*Z* in CD_2Cl_2 solution was gradually cooled to −90 °C while ^{1}H NMR spectra were taken at 25 °C, −40 °C, −70 °C and −90 °C to track shifting of signals for each isomer shown in Figure 66a. Subsequently, spectra were recorded in irregular intervals before, during and after irradiation with a 470 nm LED at −90 °C until a maximum of **15a**-*E*-(*S*)-(*M*) = **15a**-**D** is accumulated, shown in Figure 66b ordered chronologically from top to bottom. No signals of intermediate **15a**-*Z*-(*S*)-(*M*) = **15a**-**B** are observed at this temperature which is in agreement with earlier studies on related HTI motors because the *Gibbs* energy of activation for thermal **15a**-**B** to **15a**-**C** conversion is usually smaller than 11.0 kcal mol^{-1}. Thermal isomerization barriers for **15a**-*E*-(*S*)-(*M*) → **15a**-*E*-(*S*)-(*P*) process were calculated at −80 °C from the changing isomer fractions using a first-order rate law without entering a thermal equilibrium since full conversion occurs shown in Figure 67. A linear regression fit translates to a *Gibbs* energy of activation $\Delta G^{\ddagger}$. Annealing and re-irradiation using 470 nm proved that the same PSS was reached and none of the shifting signals were mistaken for another isomer, as shown in Figure 68.

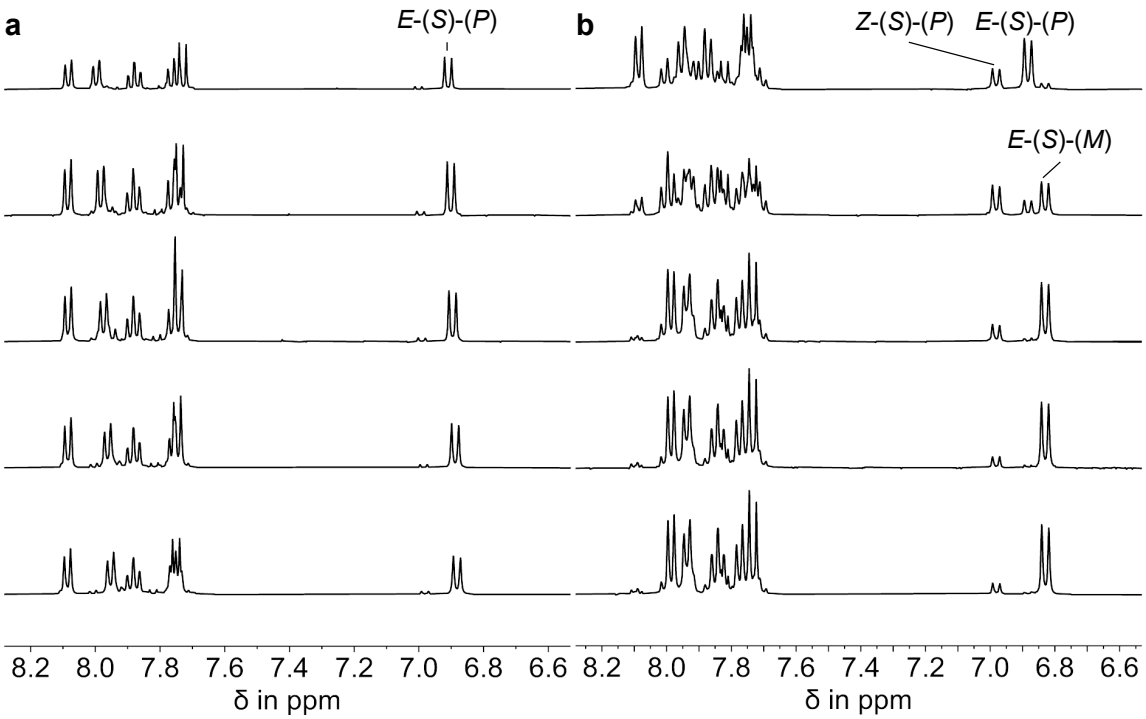

Figure 66 ^{1}H NMR spectra (400 MHz, CD_2Cl_2) of racemic **15a**-*Z* recorded during cooling to −90 °C followed by irradiation with 470 nm light. **a** Stacked NMR spectra of **15a**-*E*-(*S*)-(*P*) at 25 °C, −20 °C, −40 °C, −70 °C and −90 °C from top to bottom. **b** Stacked NMR spectra before, during and after *in situ* irradiation using a 470 nm LED, starting from a **15a**-*E*-(*S*)-(*P*) solution at −90 °C (top). After 52 min a maximum of 80% **15a**-*E*-(*S*)-(*M*) is accumulated with spectra ordered chronologically from top to bottom.

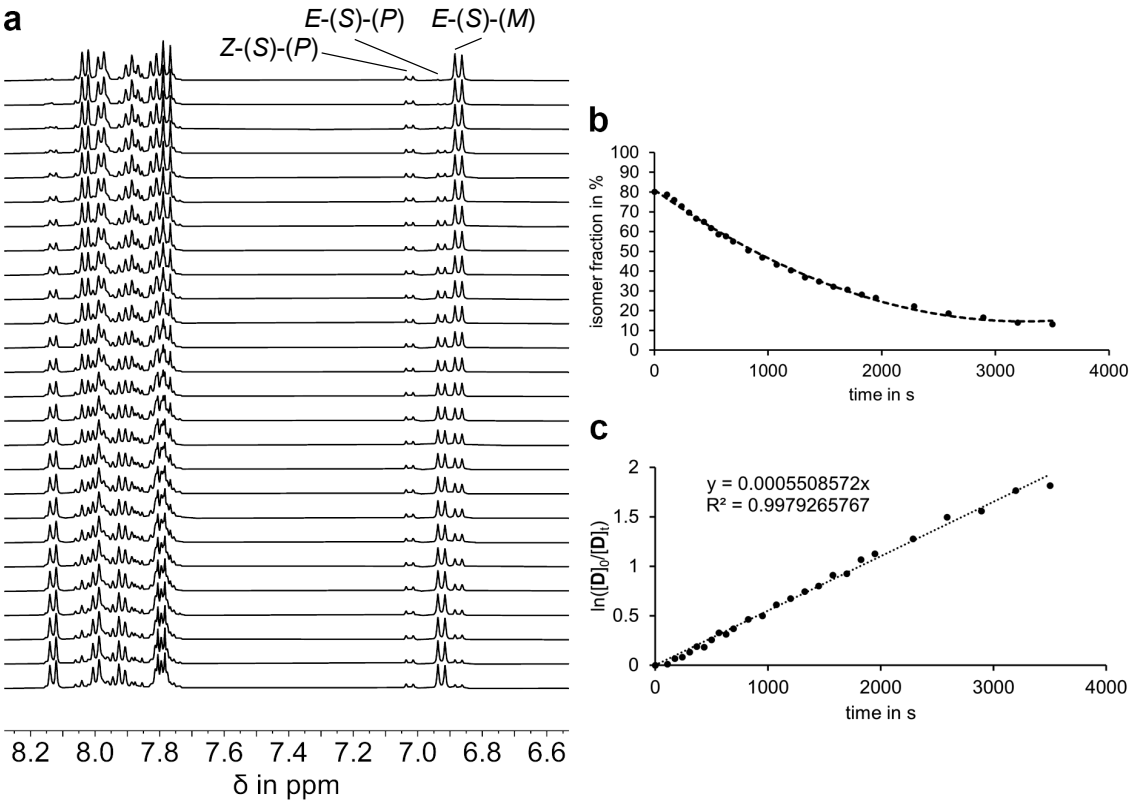

Figure 67 Kinetic analysis of thermal isomerization of racemic **15a**-*E*-(*S*)-(*M*) in CD_2Cl_2 at −90 °C. **a** ^{1}H NMR spectra (400 MHz, CD_2Cl_2, −90 °C) of racemic **15a**-*E*-(*S*)-(*M*), **15a**-*E*-(*S*)-(*P*) and **15a**-*Z*-*S*)-(*P*) during thermal isomerization of **15a**-*E*-(*S*)-(*M*) to **15a**-*E*-(*S*)-(*P*) starting from a mixture consisting of 80% **15a**-*E*-(*S*)-(*M*), 5% **15a**-*E*-(*S*)-(*P*) and 15% **15a**-*Z*-(*S*)-(*P*) (top spectrum). Spectra were recorded in intervals of 60 s and in irregular intervals after 11 min ordered chronologically from top to bottom. **b** Changing isomer fractions during thermal conversion starting from a **15a**-*E*-(*S*)-(*M*) enriched solution comprised of 80% **15a**-*E*-(*S*)-(*M*) (black dots), 5% **15a**-*E*-(*S*)-(*P*) and 15% **15a**-*Z*-(*S*)-(*P*). Data were simulated for visual guidance using a second-degree polynomial fit shown with a dashed line. **c** Kinetic evaluation using a first-order rate law without entering a thermal equilibrium since full conversion of **15a**-*E*-(*S*)-(*M*) to **15a**-*E*-(*S*)-(*P*) occurs, provides a linear correlation for the consumption of **15a**-*E*-(*S*)-(*M*). A simulation of the experimental data points using a linear regression fit (dotted black line) leads to a slope of m = 0.0005509, translating into a *Gibbs* energy of activation of $\Delta G^{\ddagger}$ = 13.3 kcal mol^{-1}.

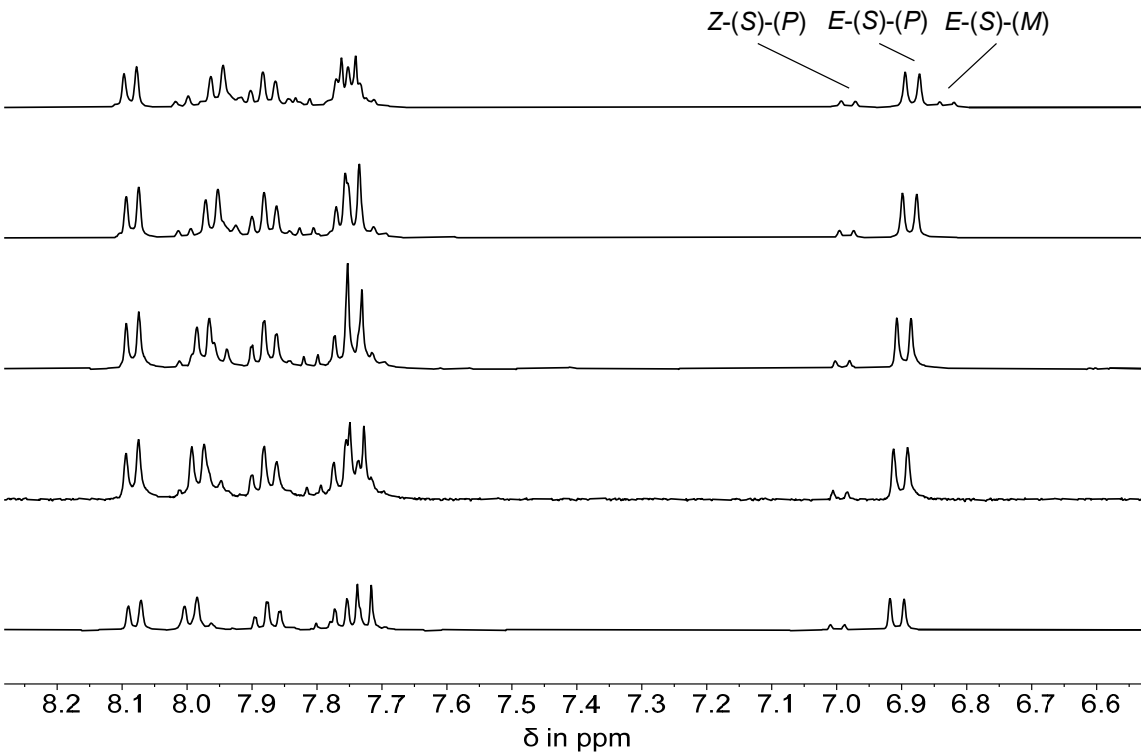

Figure 68 ^{1}H NMR spectra (400 MHz, CD_2Cl_2) measured during annealing of remaining **15a**-*E*-(*S*)-(*M*) after recording thermal isomerization kinetics. Spectra of racemic **15a**-*E*-(*S*)-(*M*), **15a**-*E*-(*S*)-(*P*) and **15a**-*Z*-(*S*)-(*P*) (12:30:57) mixture during thermal annealing from −90 °C (top) to −40 °C (second from the top), −20 °C (second from the bottom) and 25 °C (bottom) showing all **15a**-*E*-(*S*)-(*M*) has been converted to **15a**-*E*-(*S*)-(*P*).

Additionally, since 80% **15a**-*E*-(*S*)-(*M*) could be accumulated, *E*-configuration of this elusive intermediate could be observed for the first time at −90 °C. To this end, protons HC14 and HC15 were assigned as shown in Figure 69. Then the HC14 signal closer to the carbonyl could be assigned as well as shown in Figure 70 and NOE and ROE between H_3C20 and HC14 was measured shown in Figure 71 and 72.

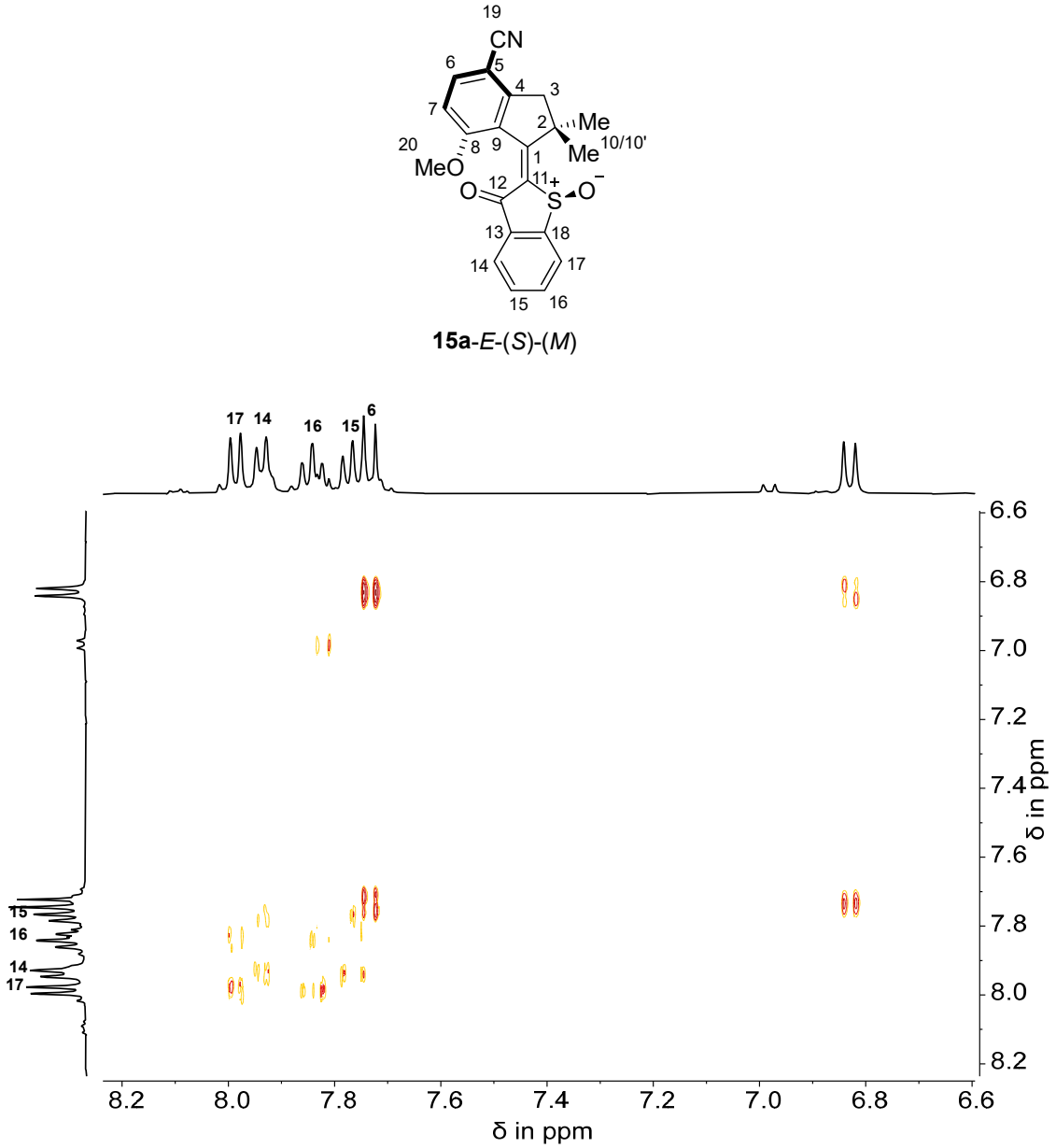

Figure 69 COSY NMR spectrum (CD_2Cl_2, 400 MHz) recorded during continuous *in situ* irradiation using a 450 nm high power LED at −90 °C consisting of 80% **15a**-*E*-(*S*)-(*M*), 5% **15a**-*E*-(*S*)-(*P*) and 15% **15a**-*Z*-(*S*)-(*P*). Indicated are cross peaks between aromatic protons HC14, HC15, HC16 and HC17 revealing the doublets at 7.98 ppm and 7.93 ppm belonging to the protons in *α*-position to the carbonyl and sulfoxide respectively.

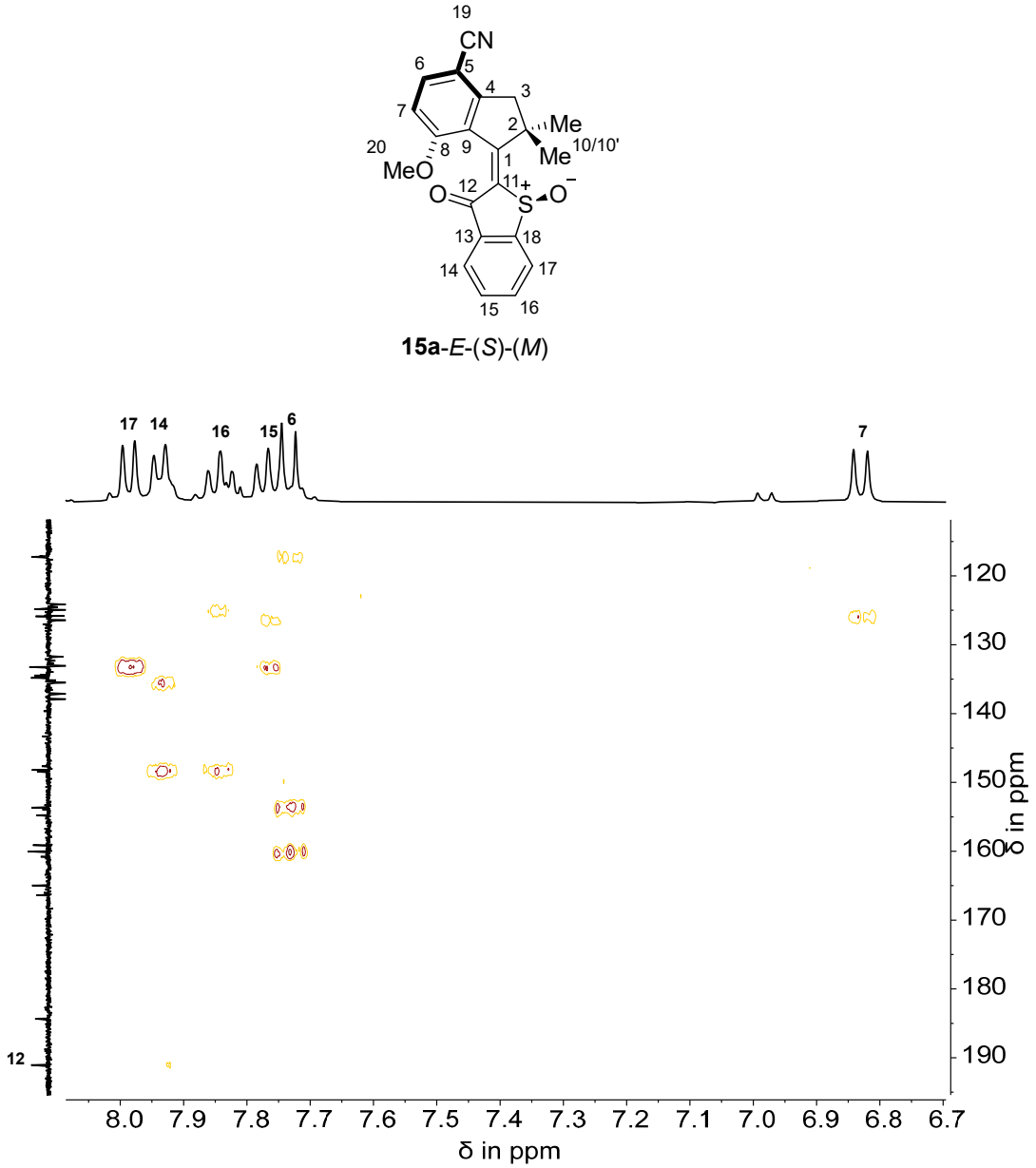

Figure 70 HMBC NMR spectrum (CD_2Cl_2, 400 MHz) recorded during continuous *in situ* irradiation using a 450 nm high power LED at −90 °C consisting of 80% **15a**-*E*-(*S*)-(*M*), 5% **15a**-*E*-(*S*)-(*P*) and 15% **15a**-*Z*-(*S*)-(*P*). Indicated is the cross peak between aromatic proton HC14 and the carbonyl C12 revealing the proton in closer proximity.

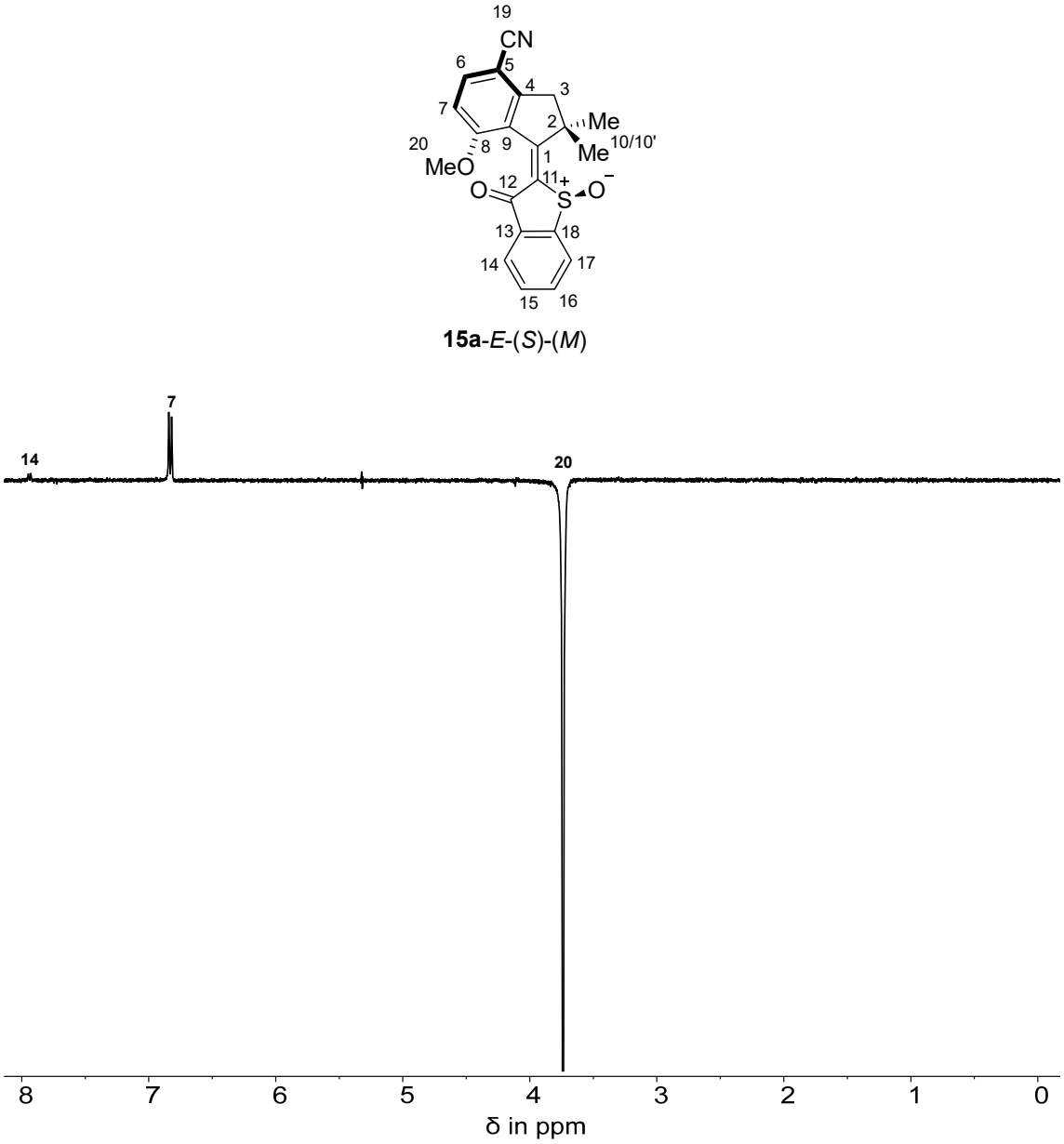

Figure 71 ROE NMR spectrum (CD_2Cl2, 400 MHz) recorded during continuous in situ irradiation using a 450 nm high power LED at −90 °C consisting of 80% **15a**-*E*-(*S*)-(*M*), 5% **15a**-*E*-(*S*)-(*P*) and 15% **15a**-*Z*-(*S*)-(*P*). Negative phase signal displays excitation frequency corresponding to the methoxy group H_3C20 of isomer **15a**-*E*-(*S*)-(*M*). Positive phase signals belong to protons in spatial proximity with intensities depending on distance to the methoxy protons. Marked are signals for aromatic proton HC7 and HC14 revealing *E*-configuration of metastable isomer **15a**-*E*-(*S*)-(*M*).

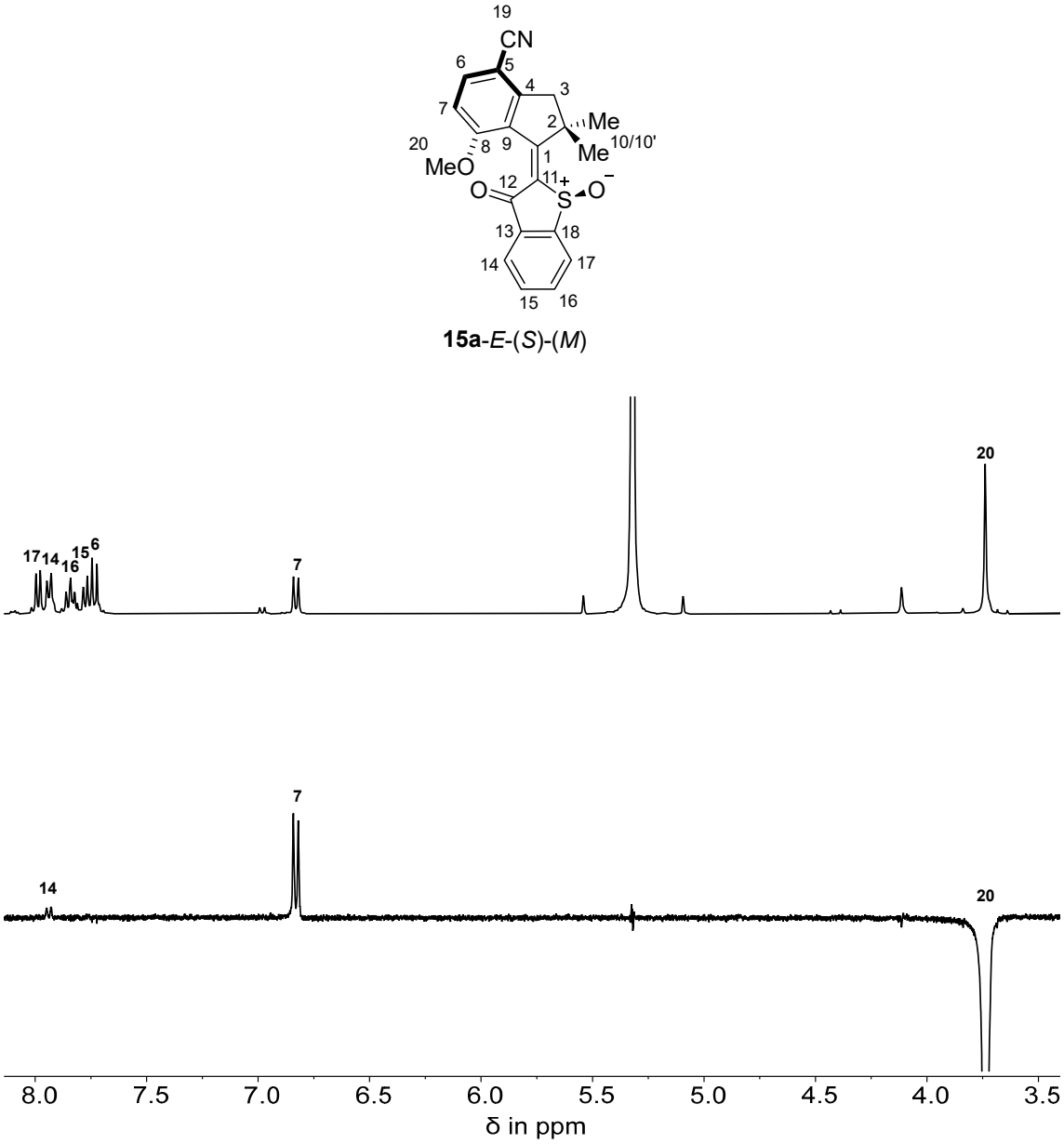

Figure 72 ROE NMR spectrum (CD_2Cl_2, 400 MHz) overlapped with corresponding ^{1}H NMR spectrum recorded during continuous in situ irradiation using a 450 nm high power LED at −90 °C consisting of 80% **15a**-*E*-(*S*)-(*M*), 5% **15a**-*E*-(*S*)-(*P*) and 15% **15a**-*Z*-(*S*)-(*P*). Positive phase signals indicating magnetization transfer to aromatic protons HC7 and HC14 enabling identification of the *E*-configured double bond in metastable isomer **15a**-*E*-(*S*)-(*M*).

5.6.2. Behavior of 15b

A solution containing a mixture of **15b**-*E* and **15b**-*Z* in CD_2Cl_2 solution was gradually cooled to −90 °C while ^{1}H NMR spectra were taken at 25 °C, −40 °C, −70 °C and −90 °C to track shifting of signals for each isomer shown in Figure 73a. Subsequently, spectra were recorded in irregular intervals before, during and after irradiation with a 470 nm LED at −90 °C until a maximum of **15b**-*E*-(*S*)-(*M*) = **15b-D** is accumulated, shown in Figure 73b ordered chronologically from top to bottom. No signals of intermediate **15b**-*Z*-(*S*)-(*M*) = **15b-B** are observed at this temperature which is in agreement with earlier studies on related HTI motors because the *Gibbs* energy of activation for thermal **15b-B** to **15b-C** conversion is usually smaller than 11.0 kcal mol^{-1}. Thermal isomerization barriers for **15b**-*E*-(*S*)-(*M*) → **15b**-*E*-(*S*)-(*P*) process were calculated at −80 °C from the changing isomer fractions using a first-order rate law without entering a thermal equilibrium since full conversion occurs shown in Figure 75. A linear regression fit translates to a *Gibbs* energy of activation $\Delta G^{\ddagger}$. Annealing and re-irradiation using 470 nm proved that the same PSS was reached and none of the shifting signals were mistaken for another isomer, as shown in Figure 74.

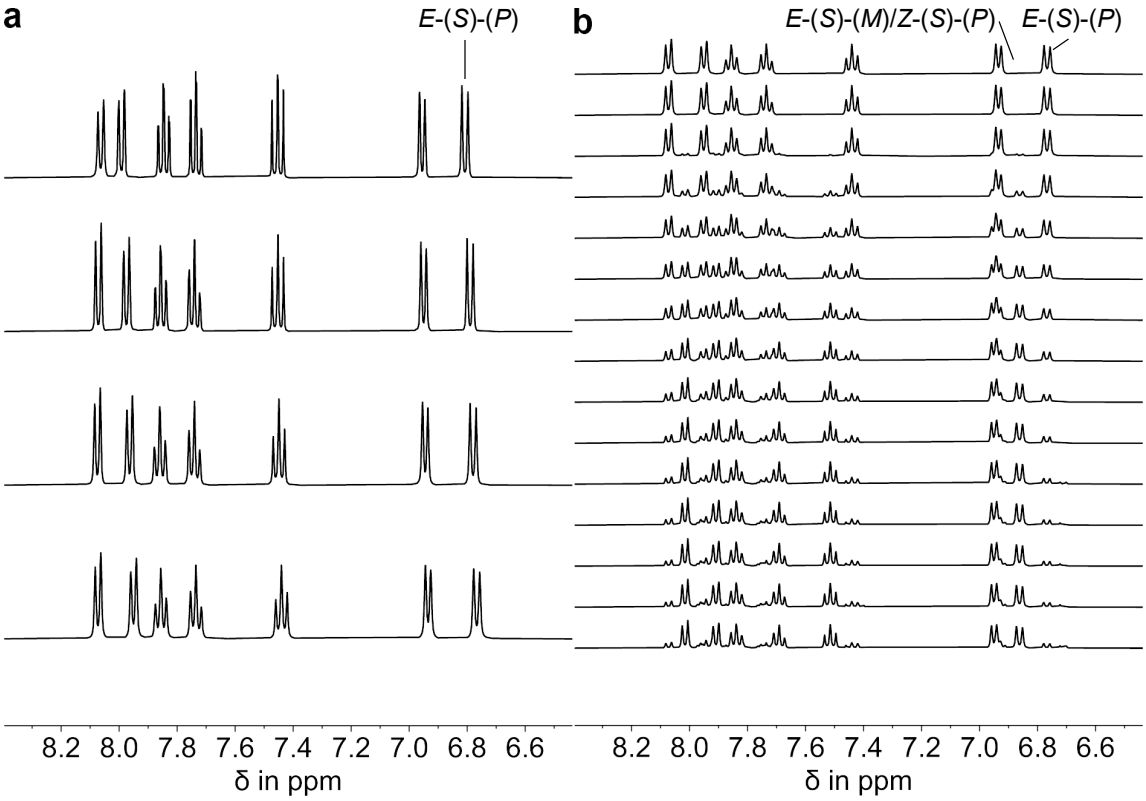

Figure 73 ^{1}H NMR spectra (400 MHz, CD_2Cl_2) of racemic **15b**-*Z* recorded during cooling to −90 °C followed by irradiation with 470 nm light. **a** Stacked NMR spectra of pure **15b**-*E*-(*S*)-(*P*) at 25 °C, −40 °C, −70 °C and −90 °C from top to bottom. **b** Stacked NMR spectra before, during and after *in situ* irradiation using a 470 nm LED, starting from a pure **15b**-*E*-(*S*)-(*P*) solution at −90 °C (top). After 70 min a maximum of 13% **15b**-*E*-(*S*)-(*M*) is accumulated with spectra ordered chronologically from top to bottom.

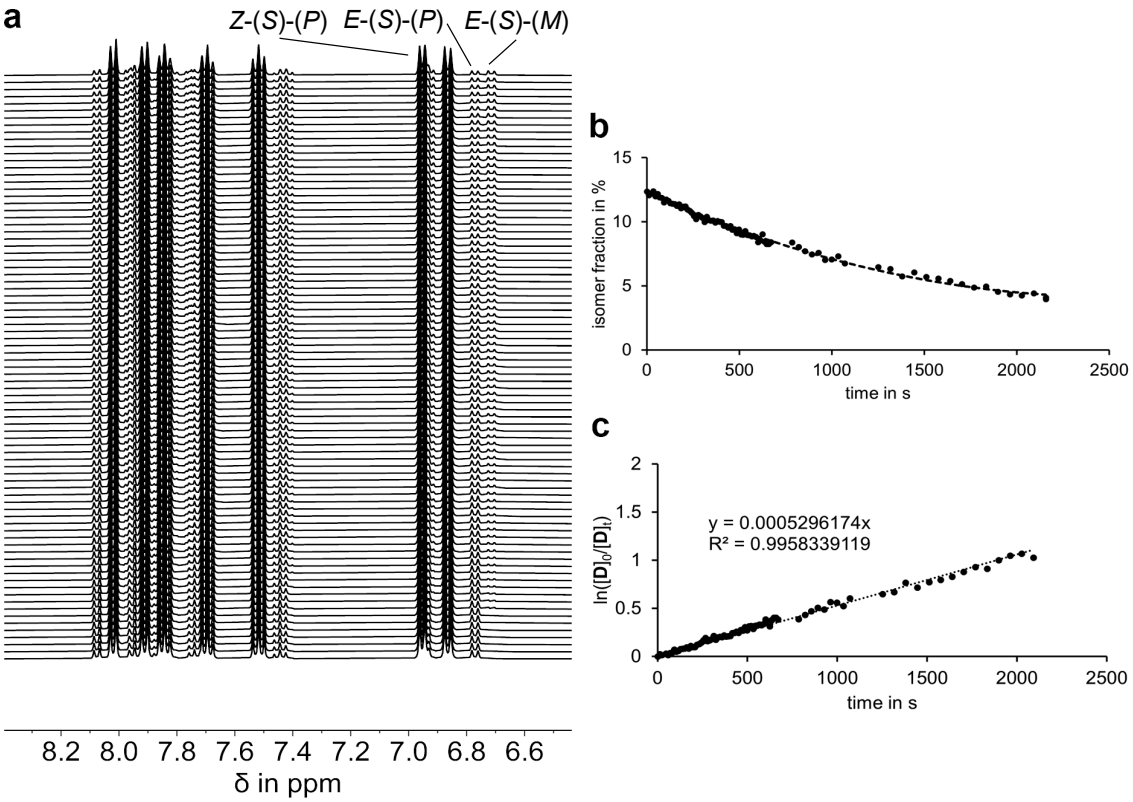

Figure 74 Kinetic analysis of thermal isomerization of racemic **15b**-*E*-(*S*)-(*M*) at −80 °C. **a** ^{1}H NMR spectra (400 MHz, CD_2Cl_2, −80 °C) of racemic **15b**-*E*-(*S*)-(*M*), **15b**-*E*-(*S*)-(*P*) and **15b**-*Z*-*S*)-(*P*) during thermal isomerization of **15b**-*E*-(*S*)-(*M*) to **15b**-*E*-(*S*)-(*P*) starting from a mixture consisting of 13% **15b**-*E*-(*S*)-(*M*), 12% **15b**-*E*-(*S*)-(*P*) and 75% **15b**-*Z*-(*S*)-(*P*) (top spectrum). Spectra were recorded in intervals of 11 s and in irregular intervals after 11 min ordered chronologically from top to bottom. **b** Changing isomer fractions during thermal conversion starting from a **15b**-*E*-(*S*)-(*M*) enriched solution comprised of 13% **15b**-*E*-(*S*)-(*M*) (black dots), 12% **15b**-*E*-(*S*)-(*P*) and 75% **15b**-*Z*-(*S*)-(*P*). Data were simulated for visual guidance using a second-degree polynomial fit shown with a dashed line. **c** Kinetic evaluation using a first-order rate law without entering a thermal equilibrium since full conversion of **15b**-*E*-(*S*)-(*M*) to **15b**-*E*-(*S*)-(*P*) occurs, provides a linear correlation for the consumption of **15b**-*E*-(*S*)-(*M*). A simulation of the experimental data points using a linear regression fit (dotted black line) leads to a slope of $m = 0.0005296$, translating into a *Gibbs* energy of activation of $\Delta G^{\ddagger} = 13.3$ kcal mol^{-1}.

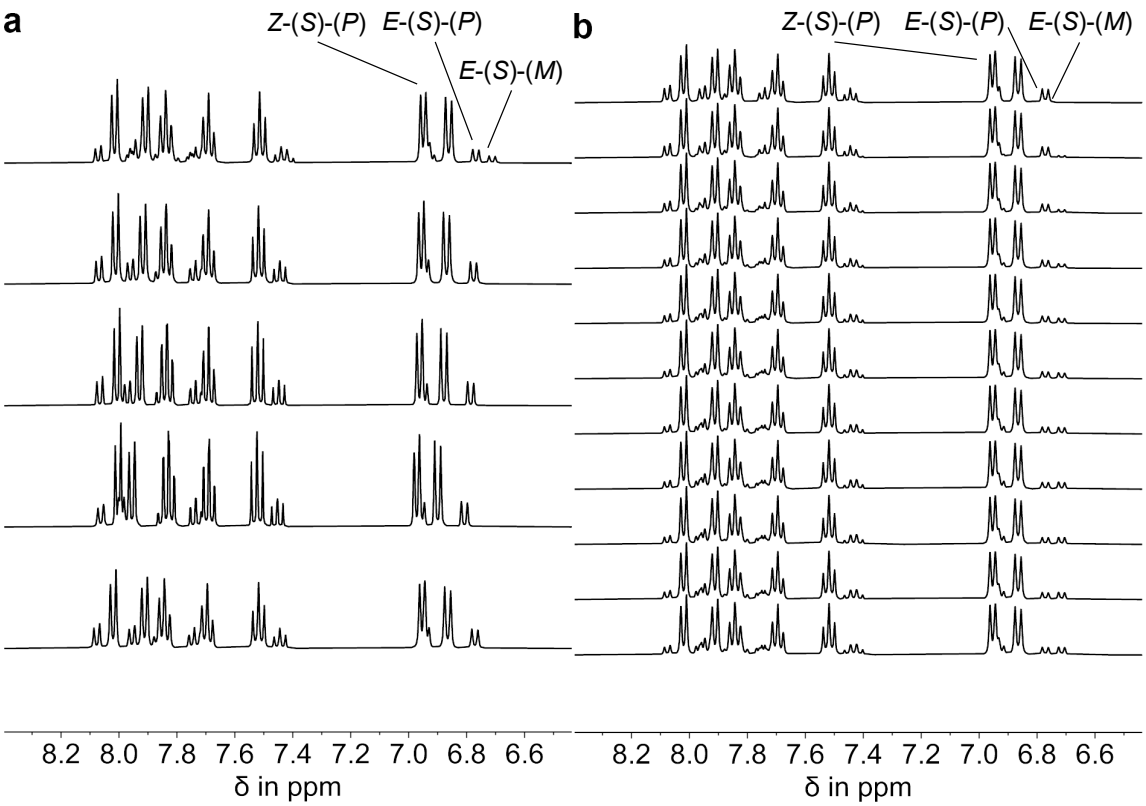

Figure 75 ^{1}H NMR spectra (400 MHz, CD_2Cl_2) measured during annealing of remaining **15b**-*E*-(*S*)-(*M*) after recording thermal isomerization kinetics. **a** Spectra of racemic **15b**-*E*-(*S*)-(*M*), **15b**-*E*-(*S*)-(*P*) and **15b**-*Z*-(*S*)-(*P*) (4:21:75) mixture during thermal annealing from −90 °C (top) to −70 °C (second from the top), −40 °C (third from the top) and 25 °C (second from the bottom). After thermal conversion was finished, the isomer mixture was cooled back to −90 °C ensuring only isomer **15b**-*E*-(*S*)-(*P*) formed from remaining **15b**-*E*-(*S*)-(*M*) (bottom). **b** Racemic mixture of **15b**-*E*-(*S*)-(*P*) and **15b**-*Z*-(*S*)-(*P*) (25:75) measured at −90 °C before (top), after repeated irradiation for 70 min with 470 nm LED. The second irradiation resulted in the same PSS of **15b**-*E*-(*S*)-(*M*), **15b**-*E*-(*S*)-(*P*) and **15b**-*Z*-(*S*)-(*P*) (13:12:75).

5.6.3. Behavior of 15c

A solution containing a mixture of **15c**-*E* and **15c**-*Z* in CD_2Cl_2 solution was gradually cooled to −90 °C while ^{1}H NMR spectra were taken at 25 °C, −40 °C, −70 °C and −90 °C to track shifting of signals for each isomer shown in Figure 76a. Subsequently, spectra were recorded in irregular intervals before, during and after irradiation with a 470 nm LED at −90 °C until a maximum of **15c**-*E*-(*S*)-(*M*) = **15c**-**D** is accumulated, shown in Figure 76b ordered chronologically from top to bottom. No signals of intermediate **15c**-*Z*-(*S*)-(*M*) = **15c**-**B** are observed at this temperature which is in agreement with earlier studies on related HTI motors because the *Gibbs* energy of activation for thermal **15c**-**B** to **15c**-**C** conversion is usually smaller than 11.0 kcal mol^{-1}. Thermal isomerization barriers for **15c**-*E*-(*S*)-(*M*) → **15c**-*E*-(*S*)-(*P*) process were calculated at −80 °C from the changing isomer fractions using a first-order rate law without entering a thermal equilibrium since full conversion occurs shown in Figure 77. A linear regression fit translates to a *Gibbs* energy of activation $\Delta G^{\ddagger}$. Annealing and re-irradiation using 470 nm proved that the same PSS was reached and none of the shifting signals were mistaken for another isomer, as shown in Figure 78.

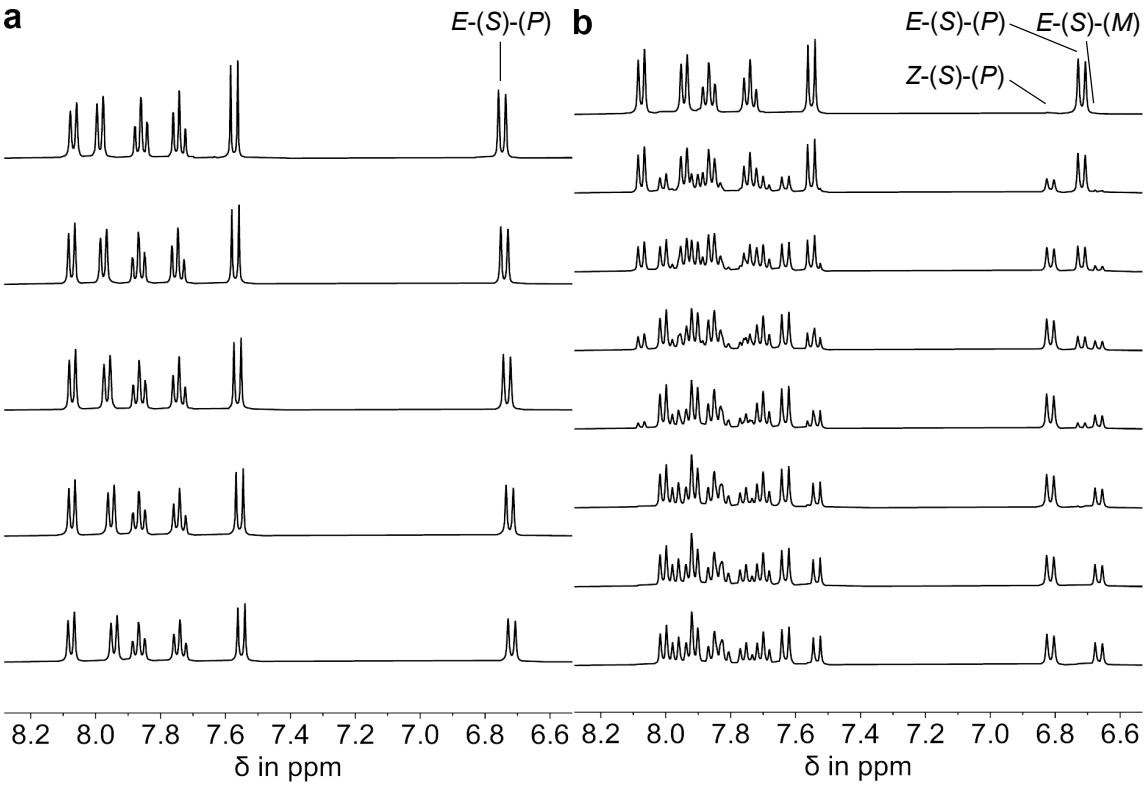

Figure 76 ^{1}H NMR spectra (400 MHz, CD_2Cl_2) of racemic **15c**-*Z* recorded during cooling to −90 °C followed by irradiation with 470 nm light. **a** Stacked NMR spectra of pure **15c**-*E*-(*S*)-(*P*) at 25 °C, −20 °C, −40 °C, −70 °C and −90 °C from top to bottom. **b** Stacked NMR spectra before, during and after *in situ* irradiation using a 470 nm LED, starting from a pure **15c**-*E*-(*S*)-(*P*) solution at −90 °C (top). After 32 min a maximum of 38% **15c**-*E*-(*S*)-(*M*) is accumulated with spectra ordered chronologically from top to bottom.

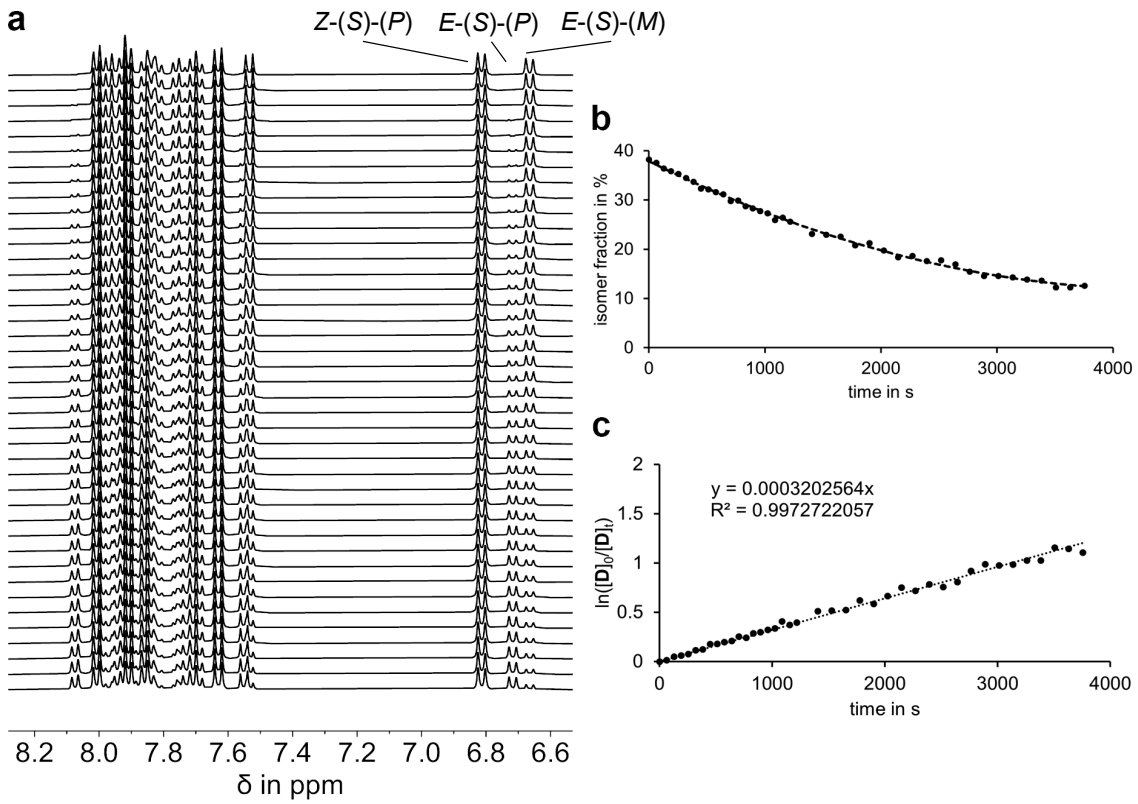

Figure 77 Kinetic analysis of thermal isomerization of racemic **15c**-*E*-(*S*)-(*M*) in CD_2Cl_2 at −90 °C. **a** ^{1}H NMR spectra (400 MHz, CD_2Cl_2, −90 °C) of racemic **15c**-*E*-(*S*)-(*M*), **15c**-*E*-(*S*)-(*P*) and **15c**-*Z*-*S*)-(*P*) during thermal isomerization of **15c**-*E*-(*S*)-(*M*) to **15c**-*E*-(*S*)-(*P*) starting from a mixture consisting of 38% **15c**-*E*-(*S*)-(*M*), 5% **15c**-*E*-(*S*)-(*P*) and 57% **15c**-*Z*-(*S*)-(*P*) (top spectrum). Spectra were recorded in intervals of 60 s and in irregular intervals after 20 min ordered chronologically from top to bottom. **b** Changing isomer fractions during thermal conversion starting from a **15c**-*E*-(*S*)-(*M*) enriched solution comprised of 38% **15c**-*E*-(*S*)-(*M*) (black dots), 5% **15c**-*E*-(*S*)-(*P*) and 57% **15c**-*Z*-(*S*)-(*P*). Data were simulated for visual guidance using a second-degree polynomial fit shown with a dashed line. **c** Kinetic evaluation using a first-order rate law without entering a thermal equilibrium since full conversion of **15c**-*E*-(*S*)-(*M*) to **15c**-*E*-(*S*)-(*P*) occurs, provides a linear correlation for the consumption of **15c**-*E*-(*S*)-(*M*). A simulation of the experimental data points using a linear regression fit (dotted black line) leads to a slope of $m = 0.0003203$, translating into a *Gibbs* energy of activation of $\Delta G^{\ddagger} = 13.5$ kcal mol^{-1}.

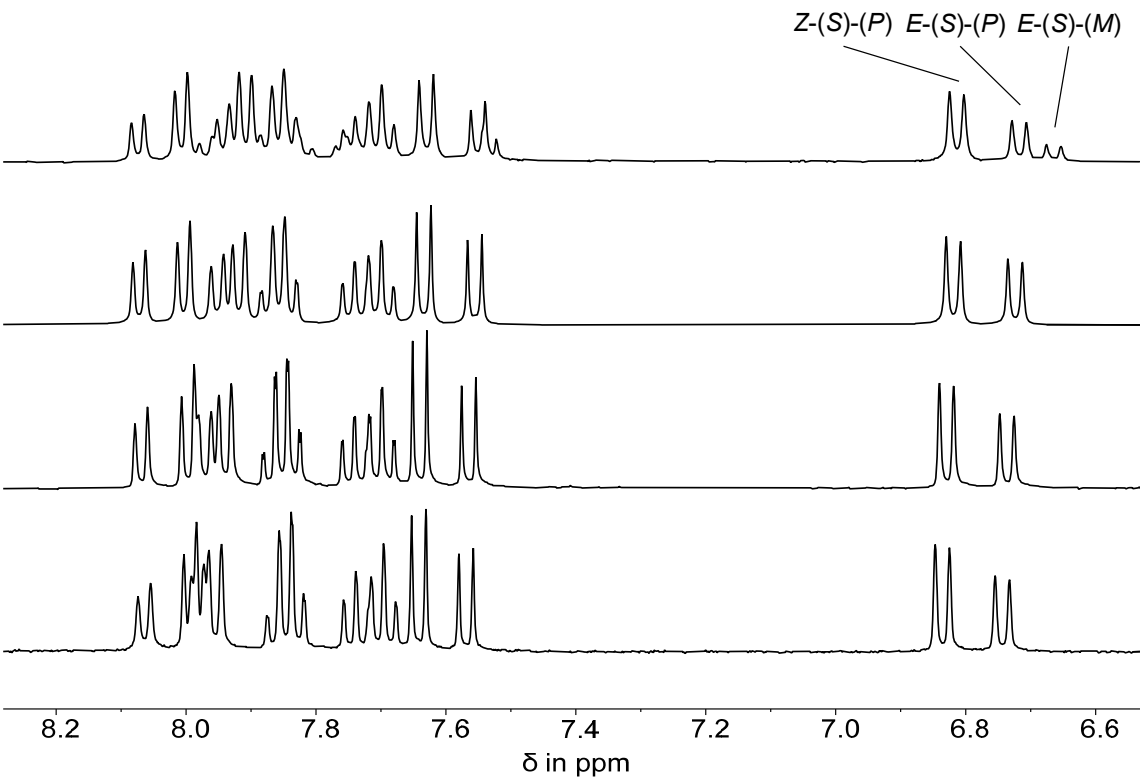

Figure 78 ^{1}H NMR spectra (400 MHz, CD_2Cl_2) measured during annealing of remaining **15c**-*E*-(*S*)-(*M*) after recording thermal isomerization kinetics. Spectra of racemic **15c**-*E*-(*S*)-(*M*), **15c**-*E*-(*S*)-(*P*) and **15c**-*Z*-(*S*)-(*P*) (12:30:57) mixture during thermal annealing from −90 °C (top) to −40 °C (second from the top), −20 °C (second from the bottom) and 25 °C (bottom) showing all **15c**-*E*-(*S*)-(*M*) has been converted to **15c**-*E*-(*S*)-(*P*).

5.6.4. Behavior of 15e

A solution containing a mixture of **15e**-*E* and **15e**-*Z* in CD_2Cl_2 solution was gradually cooled to −90 °C while ^{1}H NMR spectra were taken at 25 °C, −40 °C, −70 °C and −90 °C to track shifting of signals for each isomer shown in Figure 79a. Subsequently, spectra were recorded in irregular intervals before, during and after irradiation with a 470 nm LED at −90 °C until a maximum of **15e**-*E*-(*S*)-(*M*) = **15e**-**D** is accumulated, shown in Figure 79b ordered chronologically from top to bottom. No signals of intermediate **15e**-*Z*-(*S*)-(*M*) = **15e**-**B** are observed at this temperature which is in agreement with earlier studies on related HTI motors because the *Gibbs* energy of activation for thermal **15e**-**B** to **15e**-**C** conversion is usually smaller than 11.0 kcal mol^{-1}. Thermal isomerization barriers for **15e**-*E*-(*S*)-(*M*) → **15e**-*E*-(*S*)-(*P*) process were calculated at −80 °C from the changing isomer fractions using a first-order rate law without entering a thermal equilibrium since full conversion occurs shown in Figure 80. A linear regression fit translates to a *Gibbs* energy of activation $\Delta G^{\ddagger}$. Annealing and re-irradiation using 470 nm proved that the same PSS was reached and none of the shifting signals were mistaken for another isomer, as shown in Figure 81.

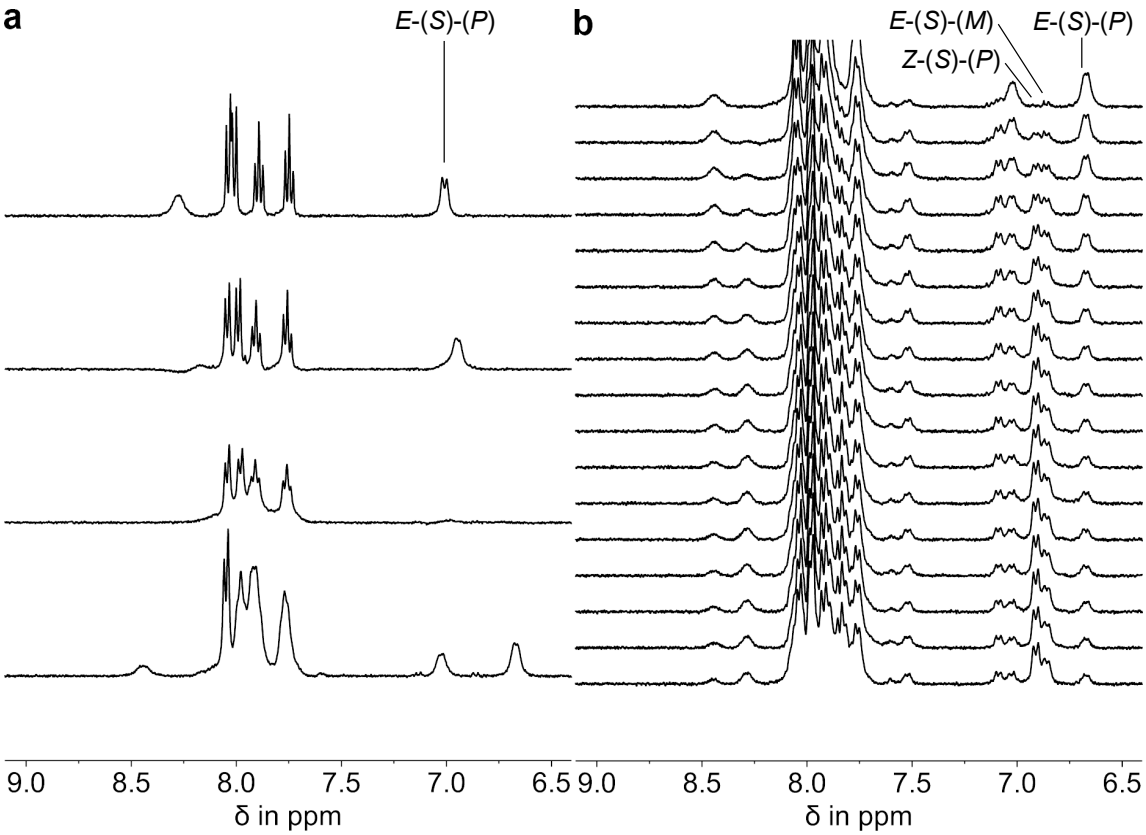

Figure 79 ^{1}H NMR spectra (400 MHz, CD_2Cl_2) of racemic **15e**-*Z* during cooling to −90 °C followed by irradiation with 470 nm light. **a** Stacked NMR spectra of pure **15e**-*E*-(*S*)-(*P*) at 25 °C, −40 °C, −70 °C and −90 °C from top to bottom. **b** Stacked NMR spectra before, during and after *in situ* irradiation using a 470 nm LED, starting from a pure **15e**-*E*-(*S*)-(*P*) solution at −90 °C (top). After 80 min a maximum of 16% **15e**-*E*-(*S*)-(*M*) is accumulated with spectra ordered chronologically from top to bottom.

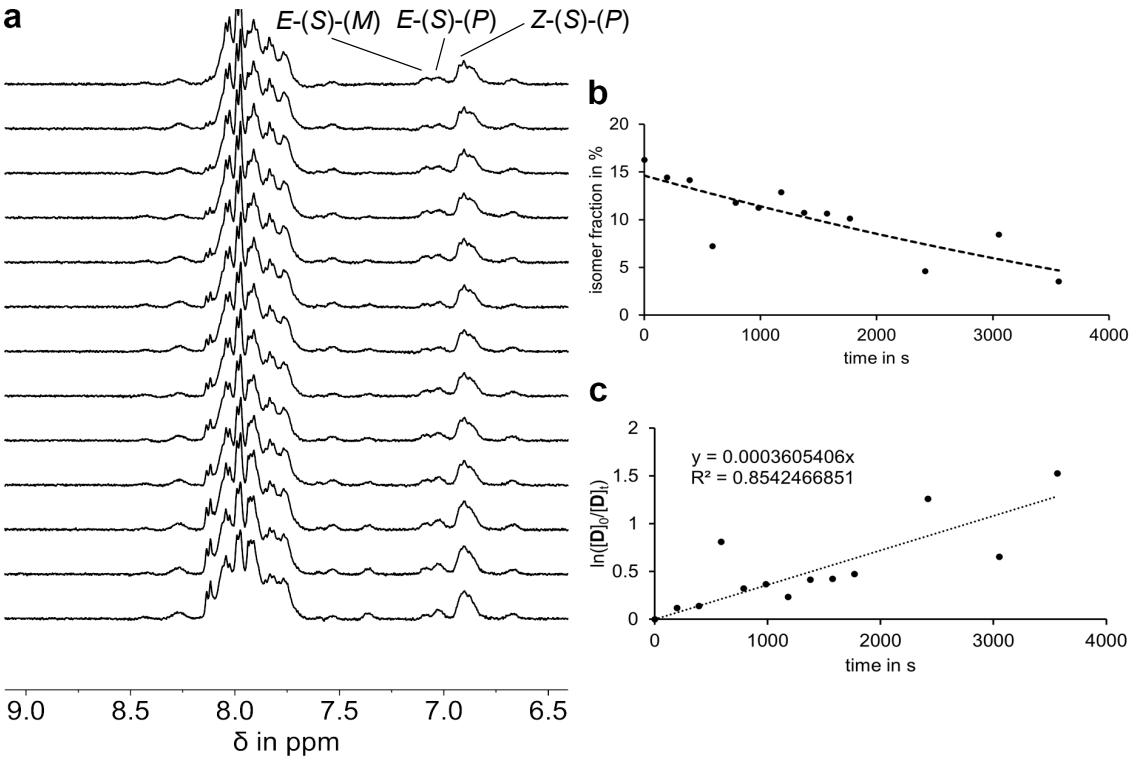

Figure 80 Kinetic analysis of thermal isomerization of racemic **15e**-*E*-(*S*)-(*M*) in CD_2Cl_2 at −80 °C. **a** ^{1}H NMR spectra (400 MHz, CD_2Cl_2, −80 °C) of racemic **15e**-*E*-(*S*)-(*M*), **15e**-*E*-(*S*)-(*P*) and **15e**-*Z*-*S*)-(*P*) during thermal isomerization of **15e**-*E*-(*S*)-(*M*) to **15e**-*E*-(*S*)-(*P*) starting from a mixture consisting of 16% **15e**-*E*-(*S*)-(*M*), 55% **15e**-*E*-(*S*)-(*P*) and 29% **15e**-*Z*-(*S*)-(*P*) (top spectrum). Spectra were recorded in intervals of 3 min and in irregular intervals after 30 min ordered chronologically from top to bottom. **b** Changing isomer fractions during thermal conversion starting from a **15e**-*E*-(*S*)-(*M*) enriched solution comprised of 16% **15e**-*E*-(*S*)-(*M*) (black dots), 55% **15e**-*E*-(*S*)-(*P*) and 29% **15e**-*Z*-(*S*)-(*P*). Data were simulated for visual guidance using a second-degree polynomial fit shown with a dashed line. **c** Kinetic evaluation using a first-order rate law without entering a thermal equilibrium since full conversion of **15e**-*E*-(*S*)-(*M*) to **15e**-*E*-(*S*)-(*P*) occurs, provides a linear correlation for the consumption of **15e**-*E*-(*S*)-(*M*). A simulation of the experimental data points using a linear regression fit (dotted black line) leads to a slope of $m = 0.0004989$, translating into a *Gibbs* energy of activation of $\Delta G^{\ddagger} = 14.0$ kcal mol^{-1}.

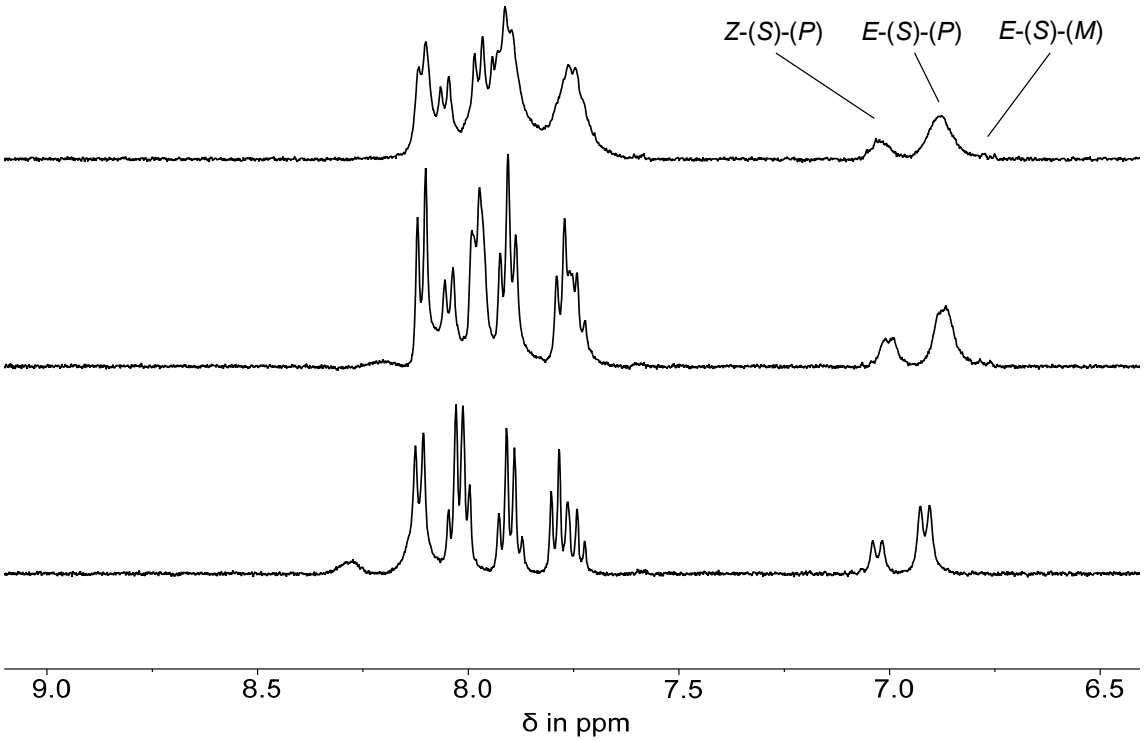

Figure 81 ^{1}H NMR spectra (400 MHz, CD_2Cl_2) measured during annealing of remaining **15e**-*E*-(*S*)-(*M*) after recording thermal isomerization kinetics. Spectra of racemic **15e**-*E*-(*S*)-(*M*), **15e**-*E*-(*S*)-(*P*) and **15e**-*Z*-(*S*)-(*P*) (4:67:29) mixture during thermal annealing from −80 °C (top) to −40 °C (middle) and 25 °C (bottom) showing all **15e**-*E*-(*S*)-(*M*) has been converted to **15e**-*E*-(*S*)-(*P*).

5.6.5. Behavior of 15e with TFA

A solution containing a mixture of **15e**-*E* and **15e**-*Z* in the presence of 2.0 equivalents TFA in CD_2Cl_2 solution was gradually cooled to −90 °C while ^{1}H NMR spectra were taken at 25 °C, −40 °C, −70 °C and −90 °C to track shifting of signals for each isomer shown in Figure 82a. Subsequently, spectra were recorded in irregular intervals before, during and after irradiation with a 470 nm LED at −90 °C until a maximum of **15e**-*E*-(*S*)-(*M*) = **15e**-**D** is accumulated, shown in Figure 82b ordered chronologically from top to bottom. No signals of intermediate **15e**-*Z*-(*S*)-(*M*) = **15e**-**B** are observed at this temperature which is in agreement with earlier studies on related HTI motors because the *Gibbs* energy of activation for thermal **15e**-**B** to **15e**-**C** conversion is usually smaller than 11.0 kcal mol^{-1}. Thermal isomerization barriers for **15e**-*E*-(*S*)-(*M*) → **15e**-*E*-(*S*)-(*P*) process were calculated at −80 °C from the changing isomer fractions using a first-order rate law without entering a thermal equilibrium since full conversion occurs shown in Figure 83. A linear regression fit translates to a *Gibbs* energy of activation $\Delta G^{\ddagger}$. Annealing and re-irradiation using 470 nm proved that the same PSS was reached and none of the shifting signals were mistaken for another isomer, as shown in Figure 84.

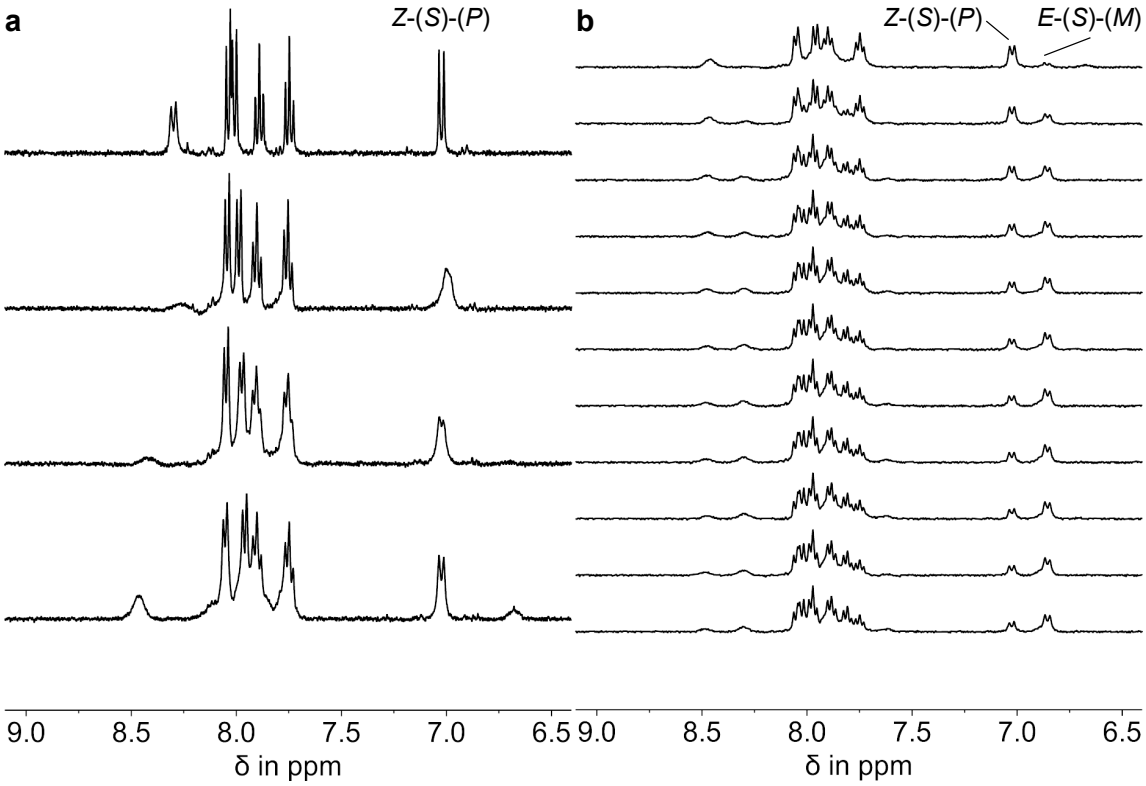

Figure 82 ^{1}H NMR spectra (400 MHz, CD_2Cl_2/TFA) of racemic **15e**-*Z* and 2.0 equivalents of trifluoroacetic acid (TFA) during cooling to −80 °C followed by irradiation with 470 nm light. **a** Stacked NMR spectra of **15e**-*E*-(*S*)-(*P*) at 25 °C, −40 °C, −70 °C and −80 °C from top to bottom. **b** Stacked NMR spectra before, during and after *in situ* irradiation using a 470 nm LED, starting from a **15e**-*E*-(*S*)-(*P*) solution at −90 °C (top). After 80 min a maximum of 66% **15e**-*E*-(*S*)-(*M*) is accumulated with spectra ordered chronologically from top to bottom.

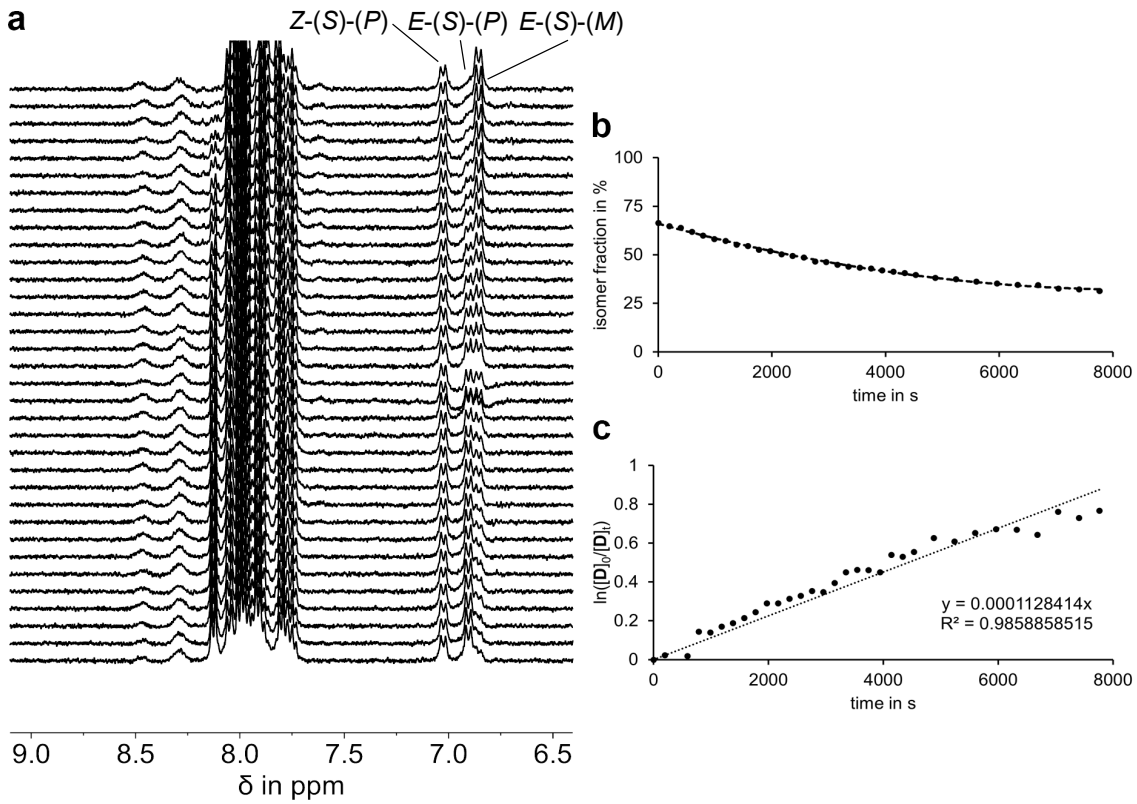

Figure 83 Kinetic analysis of thermal isomerization of racemic **15e**-*E*-(*S*)-(*M*) in CD_2Cl_2 at −80 °C in the presence of 2.0 equivalents TFA. **a** ^{1}H NMR spectra (400 MHz, CD_2Cl_2/TFA, −80 °C) of **15e**-*E*-(*S*)-(*M*), **15e**-*E*-(*S*)-(*P*) and **15e**-*Z*-*S*)-(*P*) during thermal isomerization of **15e**-*E*-(*S*)-(*M*) to **15e**-*E*-(*S*)-(*P*) starting from a mixture consisting of 66% **15e**-*E*-(*S*)-(*M*), 8% **15e**-*E*-(*S*)-(*P*) and 26% **15e**-*Z*-(*S*)-(*P*) (top spectrum). Spectra were recorded in intervals of 3 min and in irregular intervals after 75 min ordered chronologically from top to bottom. **b** Changing isomer fractions during thermal conversion starting from a **15e**-*E*-(*S*)-(*M*) enriched solution comprised of 66% **15e**-*E*-(*S*)-(*M*) (black dots), 8% **15e**-*E*-(*S*)-(*P*) and 26% **15e**-*Z*-(*S*)-(*P*). Data were simulated for visual guidance using a second-degree polynomial fit shown with a dashed line. **c** Kinetic evaluation using a first-order rate law without entering a thermal equilibrium since full conversion of **15e**-*E*-(*S*)-(*M*) to **15e**-*E*-(*S*)-(*P*) occurs, provides a linear correlation for the consumption of **15e**-*E*-(*S*)-(*M*). A simulation of the experimental data points using a linear regression fit (dotted black line) leads to a slope of m = 0.00011284, translating into a *Gibbs* energy of activation of $\Delta G^{\ddagger}$ = 14.7 kcal mol^{-1}.

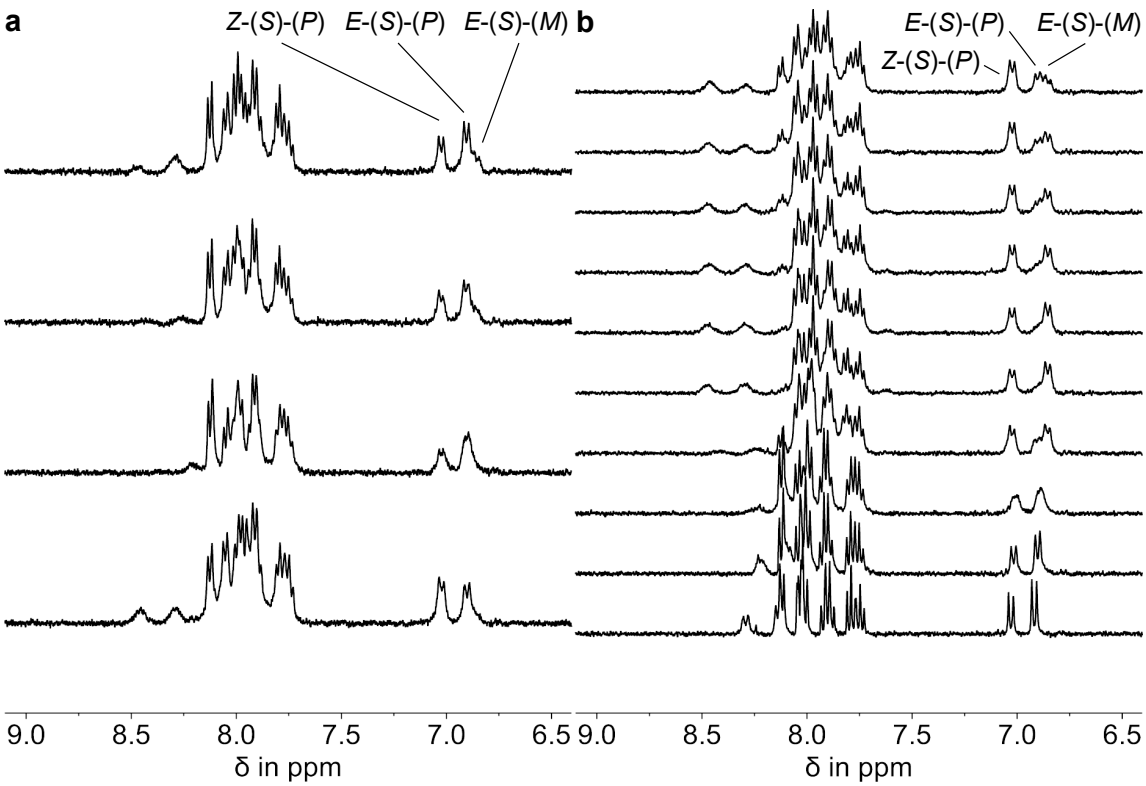

Figure 84 ^{1}H NMR spectra (400 MHz, CD_2Cl_2/TFA) measured during annealing of remaining **15e**-*E*-(*S*)-(*M*) after recording thermal isomerization kinetics in the presence of 2.0 equivalents TFA. **a** Spectra of racemic **15e**-*E*-(*S*)-(*M*), **15e**-*E*-(*S*)-(*P*) and **15e**-*Z*-(*S*)-(*P*) (31:43:26) mixture during thermal annealing from −80 °C (top) to −70 °C (second from the top) and −60 °C (second from the bottom). After thermal conversion was finished, the isomer mixture was cooled back to −90 °C ensuring only isomer **15e**-*E*-(*S*)-(*P*) formed from remaining **15e**-*E*-(*S*)-(*M*) (bottom). **b** Racemic mixture of **15e**-*E*-(*S*)-(*P*) and **15e**-*Z*-(*S*)-(*P*) (74:26) measured at −90 °C before (top), after repeated irradiation for 70 min with 470 nm LED. The second irradiation resulted in the same PSS of **15e**-*E*-(*S*)-(*M*), **15e**-*E*-(*S*)-(*P*) and **15e**-*Z*-(*S*)-(*P*) (66:8:26).

5.7. UV-Vis absorption spectra and molar extinction coefficients

Measuring PSS and QYs using a setup[231] from the *Riedle* group of motors **15a–15g** required molar extinction coefficients for all involved isomers which were measured in CH_2Cl_2 at 22 °C shown in Figure 85. Solutions with known concentrations of each isomer were used to calculate the molar extinctions given in Figure 86 based on the *Lambert-Beer* law. For more details on prospective molecular motor **15h**, see chapter 6 and for **15d** the corresponding literature.[154]

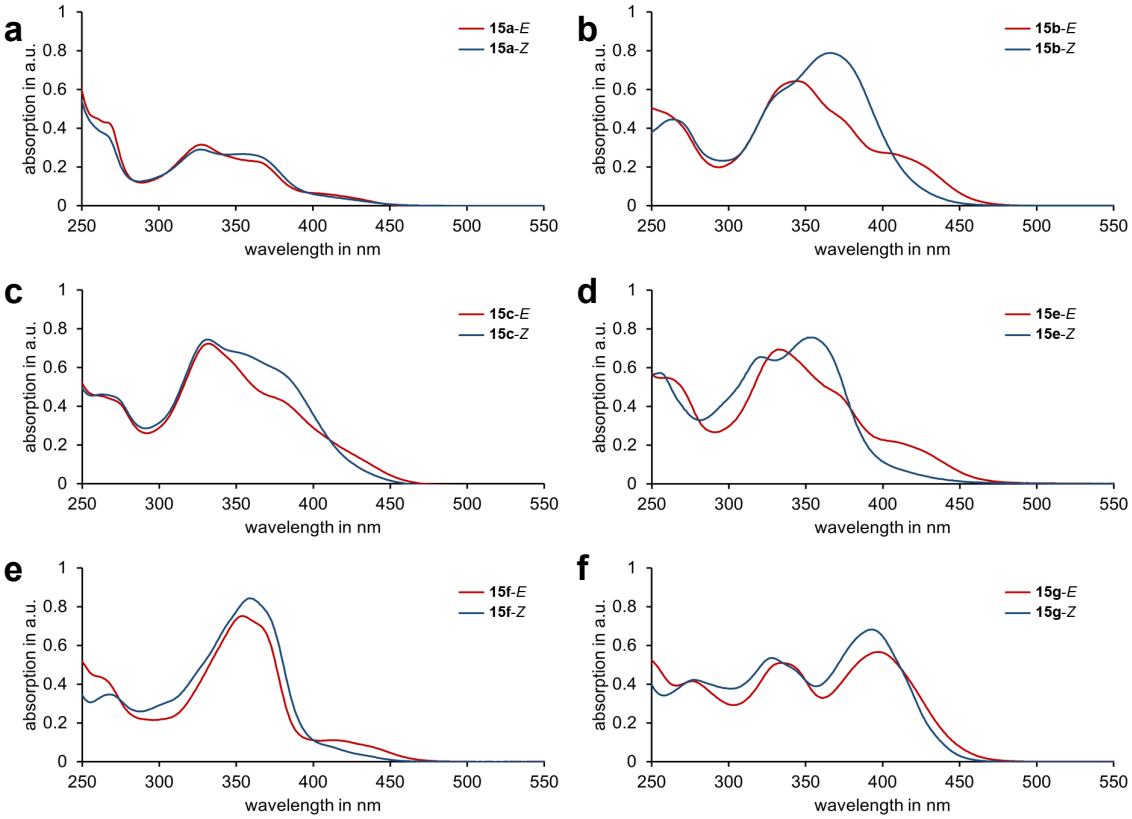

Figure 85 UV-Vis absorption spectra (CH_2Cl_2, 22 °C) of motors **15a–15g**. **a** Motor **15a** *Z*-isomer (blue, 18 µM) and *E*-isomer (red, scaled according to the isosbestic point at 404 nm). **b** Motor **15b** *Z*-isomer (blue, 49 µM) and *E*-isomer (red, scaled according to the isosbestic point at 404 nm). **c** Motor **15c** *Z*-isomer (blue, 51 µM) and *E*-isomer (red, scaled according to the isosbestic point at 404 nm). **d** Motor **15e** *Z*-isomer (blue, 34 µM) and *E*-isomer (red, scaled according to the isosbestic point at 400 nm). **e** Motor **15f** *Z*-isomer (blue, 46 µM) and *E*-isomer (red, scaled according to the isosbestic point at 400 nm). **f** Motor **15g** *Z*-isomer (blue, 54 µM) and *E*-isomer (red, scaled according to the isosbestic point at 410 nm).

Motor **15b** and **15e** display the strongest photochromicity with maxima differences of 26 and 32 nm at the highest extinction maxima and extinction strengths also increased for motors **15e**, **15f** and **15h**. It is noteworthy to mention that the initial design by *Guentner et al.* of the first HTI-based molecular motor **15d** exhibits the strongest redshifted lowest energy absorption maxima.[154]

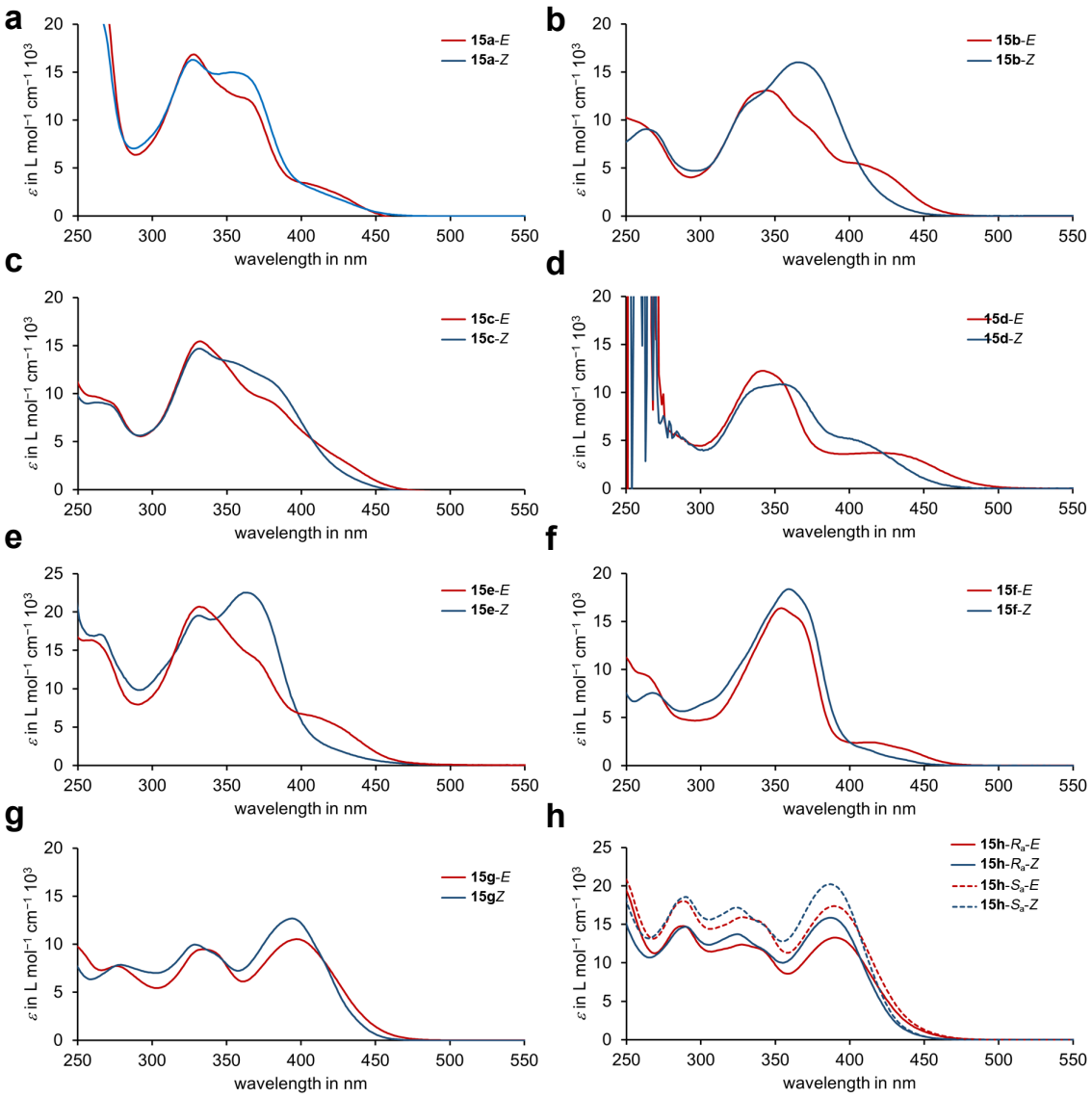

Figure 86 UV-Vis molar extinction coefficients (CH_2Cl_2, 22 °C) of motors **15a–15h**, *Z*-isomers are shown in blue and *E*-isomers in red. Graph (**a**) shows motor **15a**, (**b**) **15b**, (**c**) **15c**, (**d**) **15d**, (**e**) **15e**, (**f**) **15f**, (**g**) **15g**, and (**h**) **15h**. Prospective motor **15h**-R_a is shown with plain lines and **15h**-S_a with dashed lines (bottom right). For measured absorption data and further details, see chapter 6. Data for motor **15d** (top right) was obtained from *Nat. Commun.* **2015**, *6*, 8406 licensed under CC BY 4.0.[154]

5.8. Fluorescence spectra

Potential wavelength dependent fluorescence[244–246] was observed for dimethyl amine substituted indanone **16e** shown in Figure 87. However, when the indanone is incorporated in motor **15e** only limited remaining fluorescence can be observed as shown in Figure 88. For comparison fluorescence spectra of motor **15d**, **15f**, and **15a** were also measured shown in Figure 89, 90, and 91. Motor **15d** does still exhibit some fluorescence but for motors **15f** and **15a** no fluorescence signal could be observed. Despite significant fluorescence intensity loss in motor **15e** compared to parent indanone **16e**, this could still serve as an entry point for a fluorescent HTI-based molecular motor by further modifications introduced on the indanone.

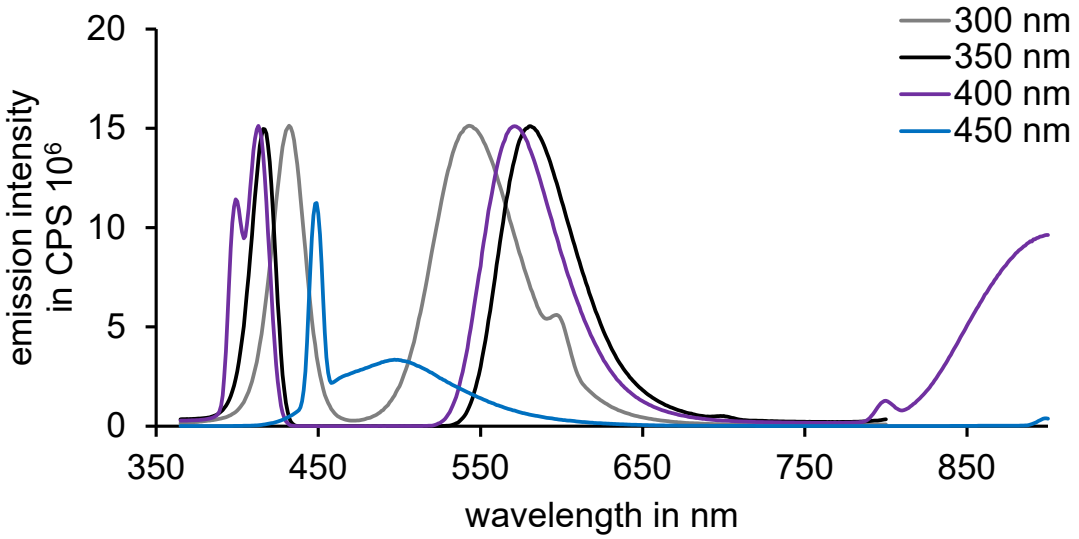

Figure 87 Fluorescence spectra (CH_2Cl_2, 22 °C) of pure indanone **16e** excited at 300 (grey), 350 (black), 400 (purple), and 450 nm (blue).

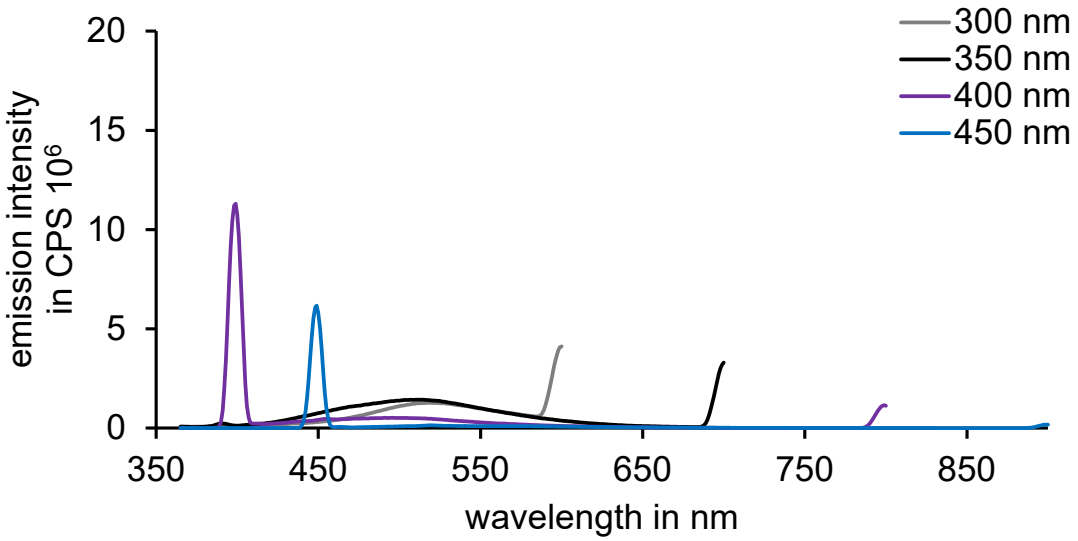

Figure 88 Fluorescence spectra (CH_2Cl_2, 22 °C) of motor **15e** excited at 300 (grey), 350 (black), 400 (purple), and 450 nm (blue).

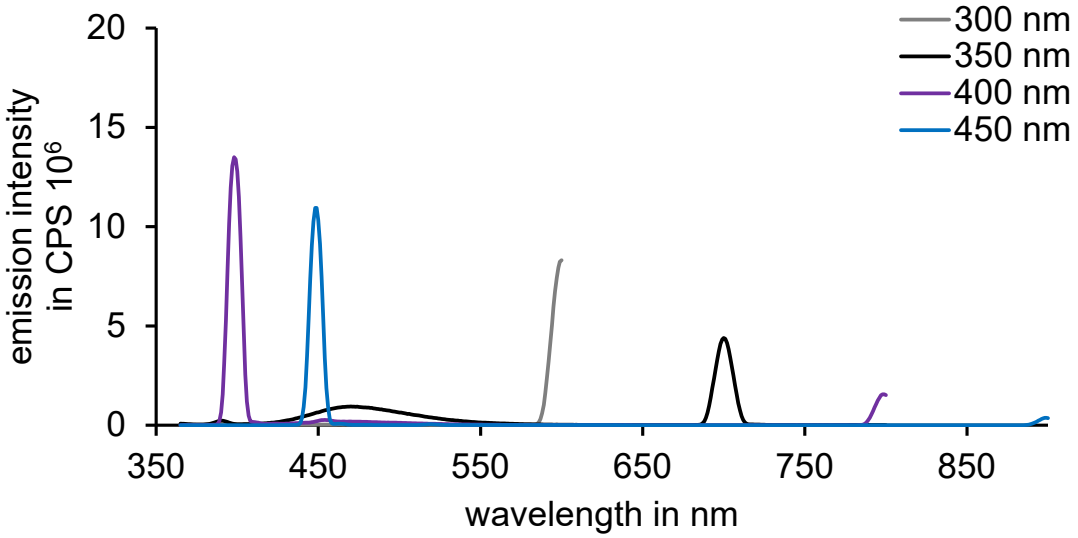

Figure 89 Fluorescence spectra (CH_2Cl_2, 22 °C) of motor **15d** excited at 300 (grey), 350 (black), 400 (purple), and 450 nm (blue).

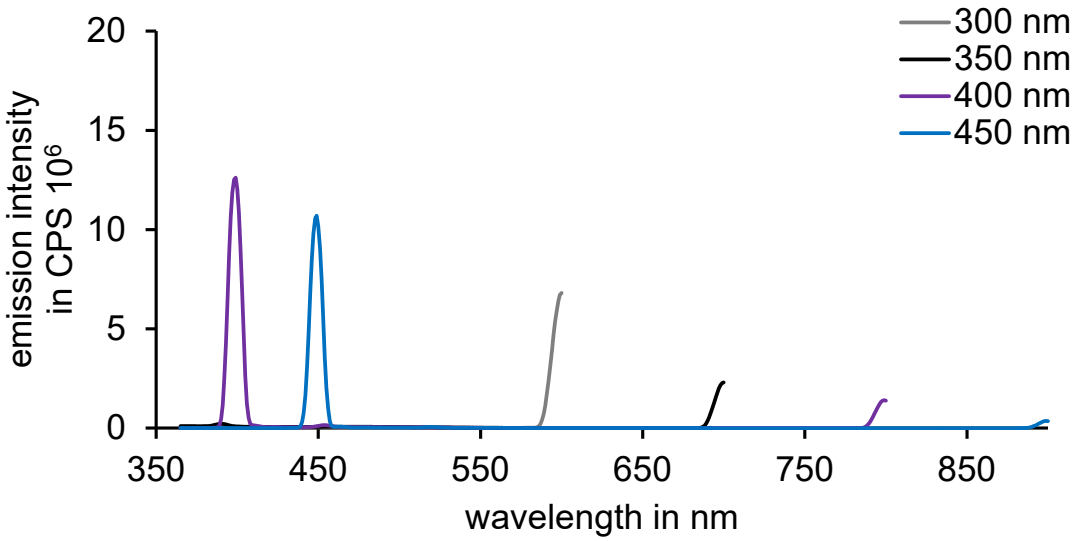

Figure 90 Fluorescence spectra (CH_2Cl_2, 22 °C) of motor **15f** excited at 300 (grey), 350 (black), 400 (purple), and 450 nm (blue).

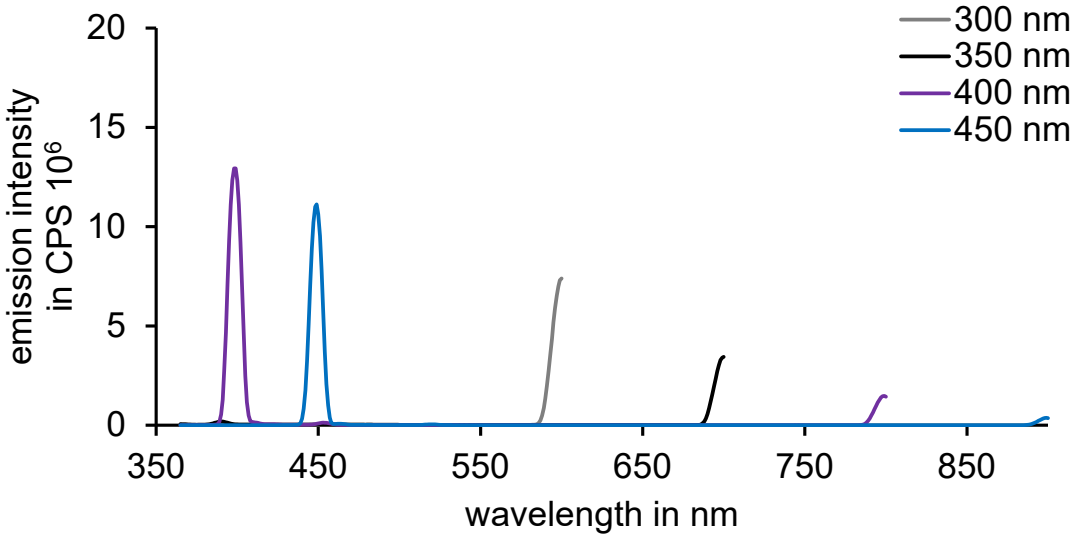

Figure 91 Fluorescence spectra (CH_2Cl_2, 22 °C) of motor **15a** excited at 300 (grey), 350 (black), 400 (purple), and 450 nm (blue).

5.9. Photostationary state determination

Determination of isomer ratios in the PSS at different wavelengths as given in Table 9–8 were carried out in CH_2Cl_2 at 22 °C using predetermined molar extinction coefficients of pure isomers given in chapter 5.7. Solutions containing mixtures of *E*- and *Z*-isomers were subjected to LED irradiation using various wavelengths between 340–530 nm corresponding to the respective absorption regions.

Table 7 Isomer composition in the PSS for molecular motor **15b** measured at 22 °C in CH_2Cl_2, ratios were obtained using UV-Vis spectroscopy.

wavelength in nm	**15b-*E*-(*S*)-(*P*) in %**	**15b-*Z*-(*S*)-(*P*) in %**
530	no isomerization	
505	no isomerization	
490	no isomerization	
470	19	81
450	26	74
430	39	61
415	50	50
405	61	39
395	71	29
385	72	28
365	70	30
340	59	41

Table 8 Isomer composition in the PSS for molecular motor **15d** measured at 22 °C in CH_2Cl_2, ratios were obtained using UV-Vis spectroscopy.

wavelength in nm	**15d-*E*-(*S*)-(*P*) in %**	**15d-*Z*-(*S*)-(*P*) in %**
530	no isomerization	
505	no isomerization	
490	21	79
470	37	63
450	61	39
430	79	21
415	87	13
405	88	12
395	90	10
385	95	5
365	94	6
340	79	21

Table 9 Isomer composition in the PSS for molecular motor **15f** measured at 22 °C in CH_2Cl_2, ratios were obtained using UV-Vis spectroscopy.

wavelength in nm	**15f-*E*-(*S*)-(*P*) in %**	**15f-*Z*-(*S*)-(*P*) in %**
530	no isomerization	
505	no isomerization	
490	no isomerization	
470	5	95
450	11	89
430	18	82
415	33	67
405	56	44
395	72	28
385	84	16
365	photodestruction	
340	photodestruction	

5.10. Quantum yield determination

All QYs Φ for motors **15a–15h** (except **15e**) were measured using an error-prone setup[231] and should therefore be remeasured to confirm the herein reported values using a revised setup.[247] However, the values reported here can be used as a rough estimation because it has been shown that these usually lie within a factor of two relative to the correct measured value. For experimental, mathematical, and operational details as well as an error analysis and comparison of values obtained with the initial and the revised setup see chapter 6.11 and 6.12. All values measured for motors **15a–15h** are summarized in Table 10. Detailed experimental data can be found in Figure 92–97 and for **15h** in chapter 6.11.1 and 6.11.2.

Table 10 Measured photoisomerization QYs Φ of molecular motors **15a–15h** (except **15e**). [a]Values were obtained using the revised QY measurement setup, see chapter 6.11.2 for more details.

isomer	Φ in %
15a-*E*	13.7
15a-*Z*	4.6
15b-*E*	0.2
15b-*Z*	8.2
15c-*E*	15.3
15c-*Z*	11.1
15d-*E*	9.4
15d-*Z*	18.9
15f-*E*	13.2
15f-*Z*	10.2
15g-*E*	7.9
15g-*Z*	5.6
15h-*E*-*S*-S_a	4.2[a]
15h-*Z*-*S*-S_a	3.5[a]
15h-*E*-*S*-R_a	4.6[a]
15h-*Z*-*S*-R_a	2.5[a]

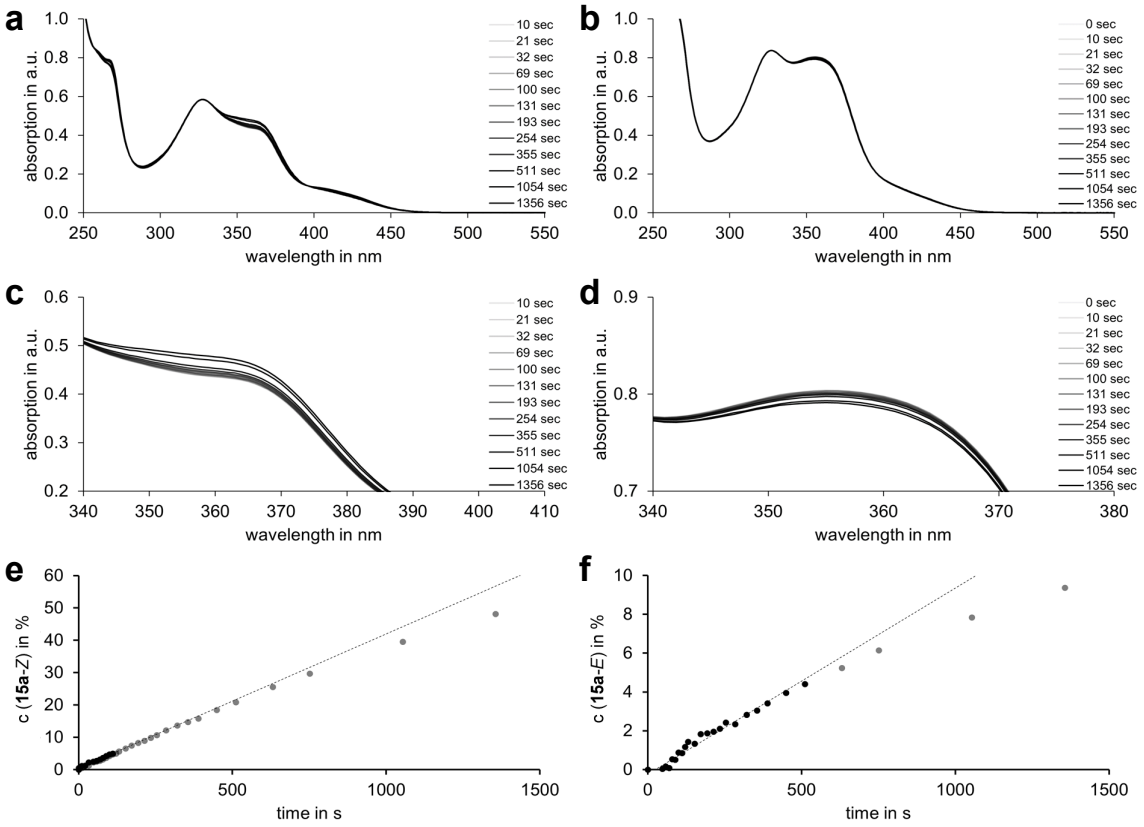

Figure 92 Photoisomerization QY determination of racemic **15a**-*E* and **15a**-*Z*. Irradiation was carried out with a 450 nm LED at 22 °C and changes in isomer ratios were monitored by UV-Vis spectroscopy (CH_2Cl_2, 22 °C) using molar extinction coefficients. For reasons of clarity only the first three spectra followed by every third measurement are shown. Linear regression analysis of initial slope is plotted excluding all grey colored dots beyond 5% concentration change. **a** Stacked UV-Vis absorption spectra of pure **15a**-*E* (35 μM) and corresponding mixtures of **15a**-*E* and **15a**-*Z* after indicated irradiation times. **b** Enlargement of the maximum absorption difference between *E*- and *Z*-spectra at 356 nm. **c** Accumulation of **15a**-*Z* during photoisomerization of **15a**-*E*. **d** Stacked UV-Vis absorption spectra of pure **15a**-*Z* (54 μM) and corresponding mixtures of **15a**-*Z* and **15a**-*E* after indicated irradiation times. **e** Enlargement of the maximum absorption difference between *E*- and *Z*-spectra at 356 nm. **f** Accumulation of **15a**-*E* during photoisomerization of **15a**-*Z*. QY determination using initial slope analysis (dotted black line) leads to an average of $\Phi_{E\rightarrow Z} = 13.7\%$ for the **15a**-*E* to **15a**-*Z* photoconversion as well as $\Phi_{Z\rightarrow E} = 4.6\%$ for the **15a**-*Z* to **15a**-*E* photoconversion, averaged over three measurements.

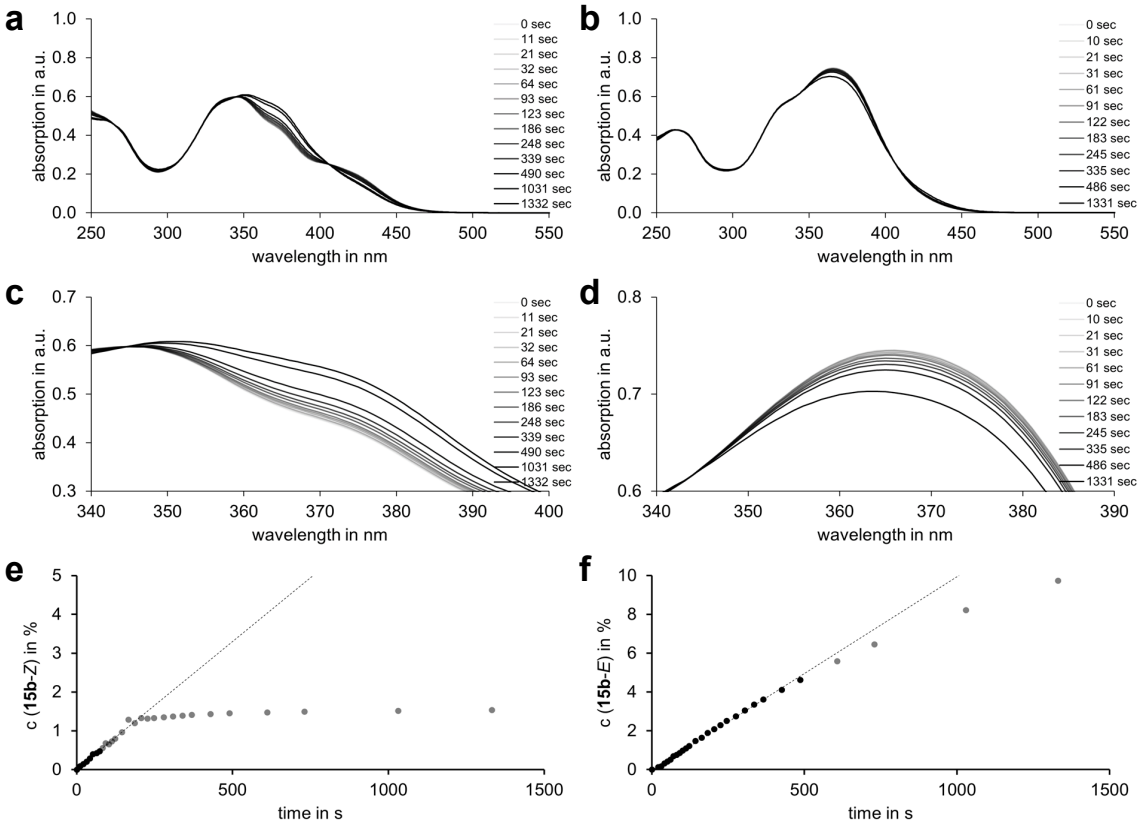

Figure 93 Photoisomerization QY determination of racemic **15b**-*E* and **15b**-*Z*. Irradiation was carried out with a 450 nm LED at 22 °C and changes in isomer ratios were monitored by UV-Vis spectroscopy (CH_2Cl_2, 22 °C) using molar extinction coefficients. For reasons of clarity only the first three spectra followed by every third measurement are shown. Linear regression analysis of initial slope is plotted excluding all grey colored dots beyond 5% concentration change. **a** Stacked UV-Vis absorption spectra of pure **15b**-*E* (39 μM) and corresponding mixtures of **15b**-*E* and **15b**-*Z* after indicated irradiation times. **b** Enlargement of the maximum absorption difference between *E*- and *Z*-spectra at 370 nm. **c** Accumulation of **15b**-*Z* during photoisomerization of **15b**-*E*. **d** Stacked UV-Vis absorption spectra of pure **15b**-*Z* (74 μM) and corresponding mixtures of **15b**-*Z* and **15b**-*E* after indicated irradiation times. **e** Enlargement of the maximum absorption difference between *E*- and *Z*-spectra at 370 nm. **f** Accumulation of **15b**-*E* during photoisomerization of **15b**-*Z*. QY determination using initial slope analysis (dotted black line) leads to an average of $\Phi_{E\rightarrow Z} = 0.2\%$ for the **15b**-*E* to **15b**-*Z* photoconversion as well as $\Phi_{Z\rightarrow E} = 8.2\%$ for the **15b**-*Z* to **15b**-*E* photoconversion, averaged over three measurements.

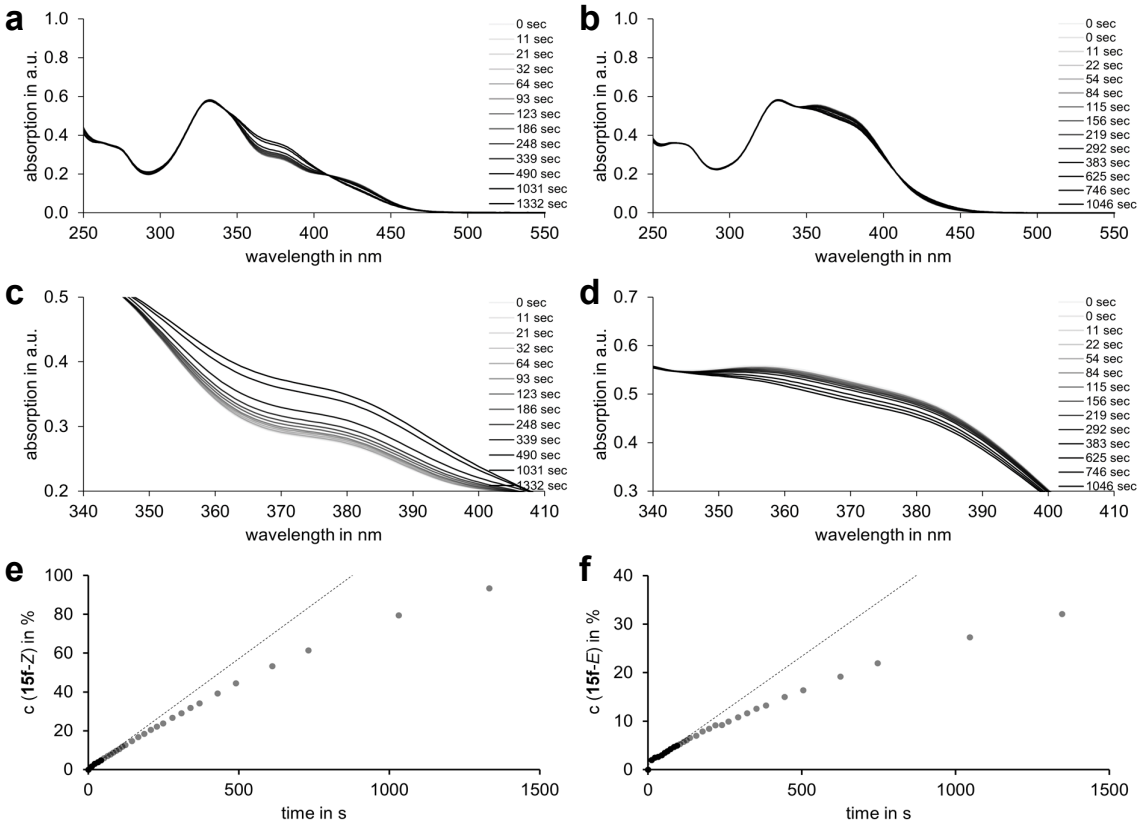

Figure 94 Photoisomerization QY determination of racemic **15c**-*E* and **15c**-*Z*. Irradiation was carried out with a 450 nm LED at 22 °C and changes in isomer ratios were monitored by UV-Vis spectroscopy (CH_2Cl_2, 22 °C) using molar extinction coefficients. For reasons of clarity only the first three spectra followed by every third measurement are shown. Linear regression analysis of initial slope is plotted excluding all grey colored dots beyond 5% concentration change. **a** Stacked UV-Vis absorption spectra of pure **15c**-*E* (49 μM) and corresponding mixtures of **15c**-*E* and **15c**-*Z* after indicated irradiation times. **b** Enlargement of the maximum absorption difference between *E*- and *Z*-spectra at 366 nm. **c** Accumulation of **15c**-*Z* during photoisomerization of **15c**-*E*. **d** Stacked UV-Vis absorption spectra of pure **15c**-*Z* (58 μM) and corresponding mixtures of **15c**-*Z* and **15c**-*E* after indicated irradiation times. **e** Enlargement of the maximum absorption difference between *E*- and *Z*-spectra at 366 nm. **f** Accumulation of **15c**-*E* during photoisomerization of **15c**-*Z*. QY determination using initial slope analysis (dotted black line) leads to an average of $\Phi_{E\rightarrow Z}$ = 15.3% for the **15c**-*E* to **15c**-*Z* photoconversion as well as $\Phi_{Z\rightarrow E}$ = 11.1% for the **15c**-*Z* to **15c**-*E* photoconversion, averaged over three measurements.

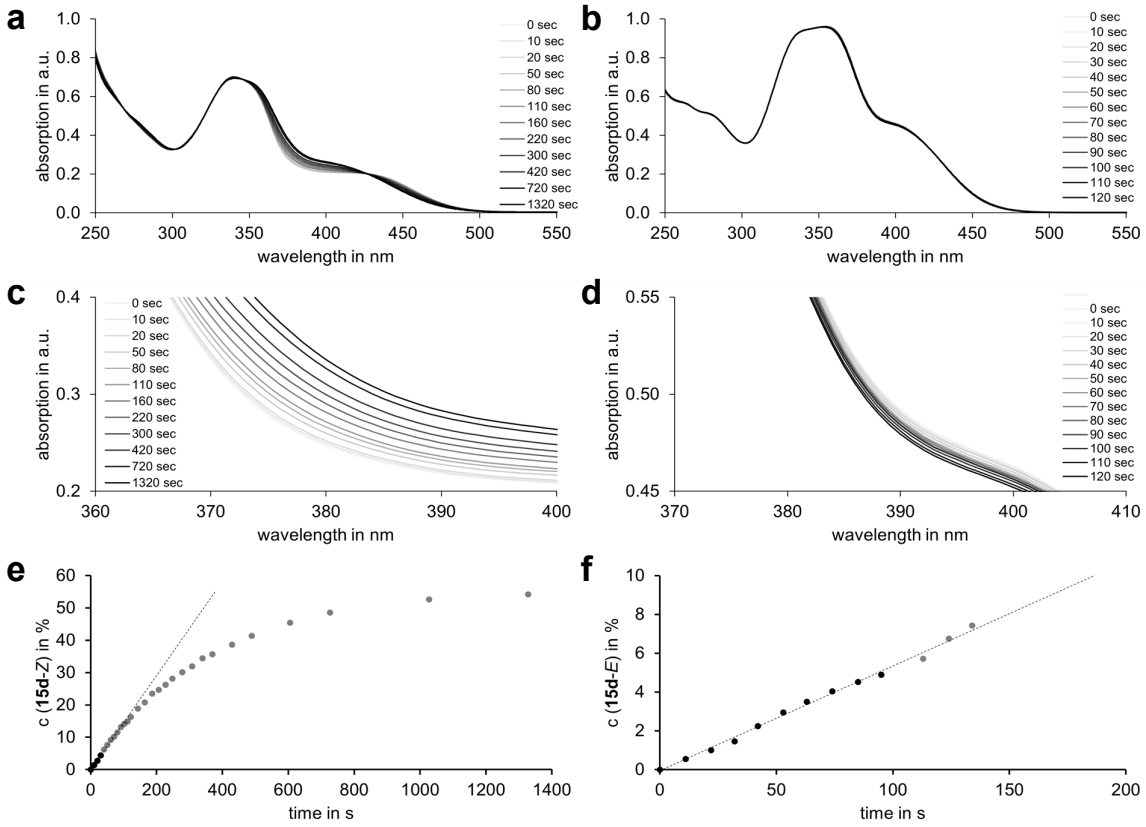

Figure 95 Photoisomerization QY determination of racemic **15d**-*E* and **15d**-*Z*. Irradiation was carried out with a 450 nm LED at 22 °C and changes in isomer ratios were monitored by UV-Vis spectroscopy (CH_2Cl_2, 22 °C) using molar extinction coefficients. For reasons of clarity only the first three spectra followed by every third measurement are shown. Linear regression analysis of initial slope is plotted excluding all grey colored dots beyond 5% concentration change. **a** Stacked UV-Vis absorption spectra of pure **15d**-*E* (62 µM) and corresponding mixtures of **15d**-*E* and **15d**-*Z* after indicated irradiation times. **b** Enlargement of the maximum absorption difference between *E*- and *Z*-spectra at 380 nm. **c** Accumulation of **15d**-*Z* during photoisomerization of **15d**-*E*. **d** Stacked UV-Vis absorption spectra of pure **15d**-*Z* (89 µM) and corresponding mixtures of **15d**-*Z* and **15d**-*E* after indicated irradiation times. **e** Enlargement of the maximum absorption difference between *E*- and *Z*-spectra at 390 nm. **f** Accumulation of **15d**-*E* during photoisomerization of **15d**-*Z*. QY determination using initial slope analysis (dotted black line) leads to an average of $\Phi_{E\rightarrow Z}$ = 9.4% for the **15d**-*E* to **15d**-*Z* photoconversion as well as $\Phi_{Z\rightarrow E}$ = 18.9% for the **15d**-*Z* to **15d**-*E* photoconversion, averaged over three measurements.

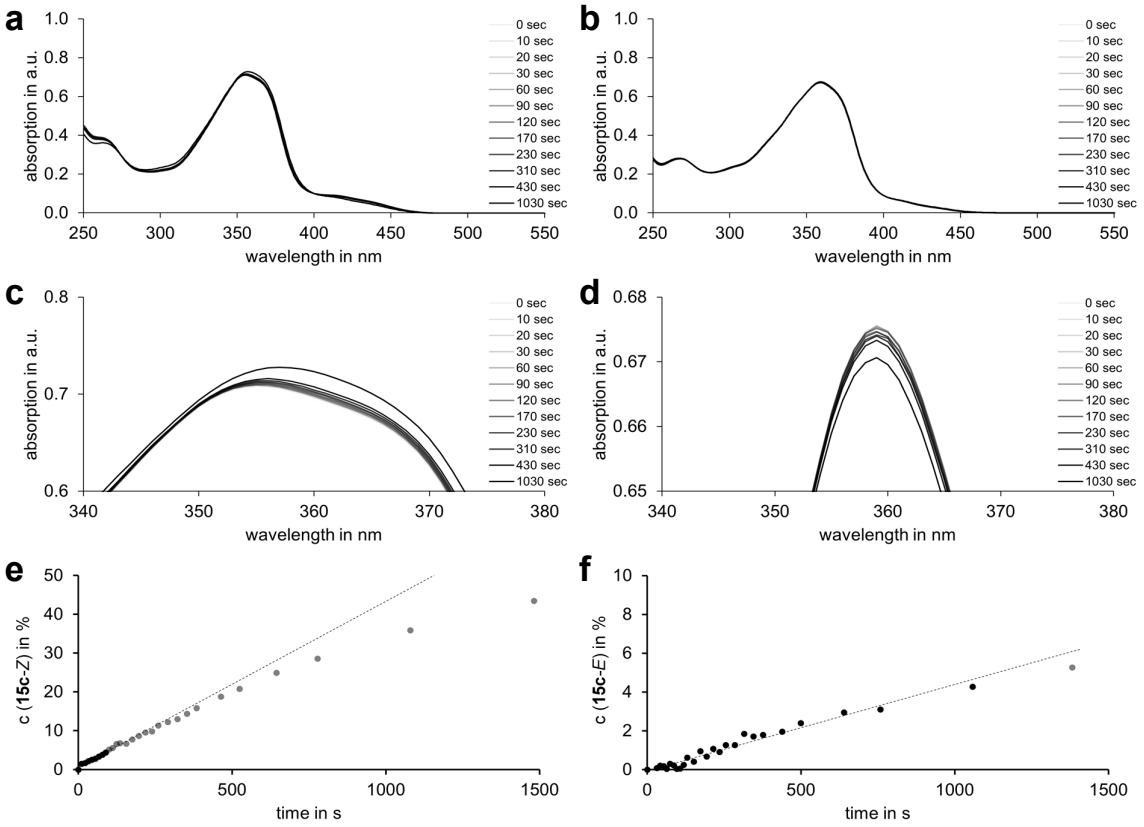

Figure 96 Photoisomerization QY determination of racemic **15f**-*E* and **15f**-*Z*. Irradiation was carried out with a 450 nm LED at 22 °C and changes in isomer ratios were monitored by UV-Vis spectroscopy (CH_2Cl_2, 22 °C) using molar extinction coefficients. For reasons of clarity only the first three spectra followed by every third measurement are shown. Linear regression analysis of initial slope is plotted excluding all grey colored dots beyond 5% concentration change. **a** Stacked UV-Vis absorption spectra of pure **15f**-*E* (35 μM) and corresponding mixtures of **15f**-*E* and **15f**-*Z* after indicated irradiation times. **b** Enlargement of the maximum absorption difference between *E*- and *Z*-spectra at 357 nm. **c** Accumulation of **15f**-*Z* during photoisomerization of **15f**-*E*. **d** Stacked UV-Vis absorption spectra of pure **15f**-*Z* (37 μM) and corresponding mixtures of **15f**-*Z* and **15f**-*E* after indicated irradiation times. **e** Enlargement of the maximum absorption difference between *E*- and *Z*-spectra at 357 nm. **f** Accumulation of **15f**-*E* during photoisomerization of **15f**-*Z*. QY determination using initial slope analysis (dotted black line) leads to an average of $\Phi_{E\rightarrow Z}$ = 13.2% for the **15f**-*E* to **15f**-*Z* photoconversion as well as $\Phi_{Z\rightarrow E}$ = 10.2% for the **15f**-*Z* to **15f**-*E* photoconversion, averaged over three measurements.

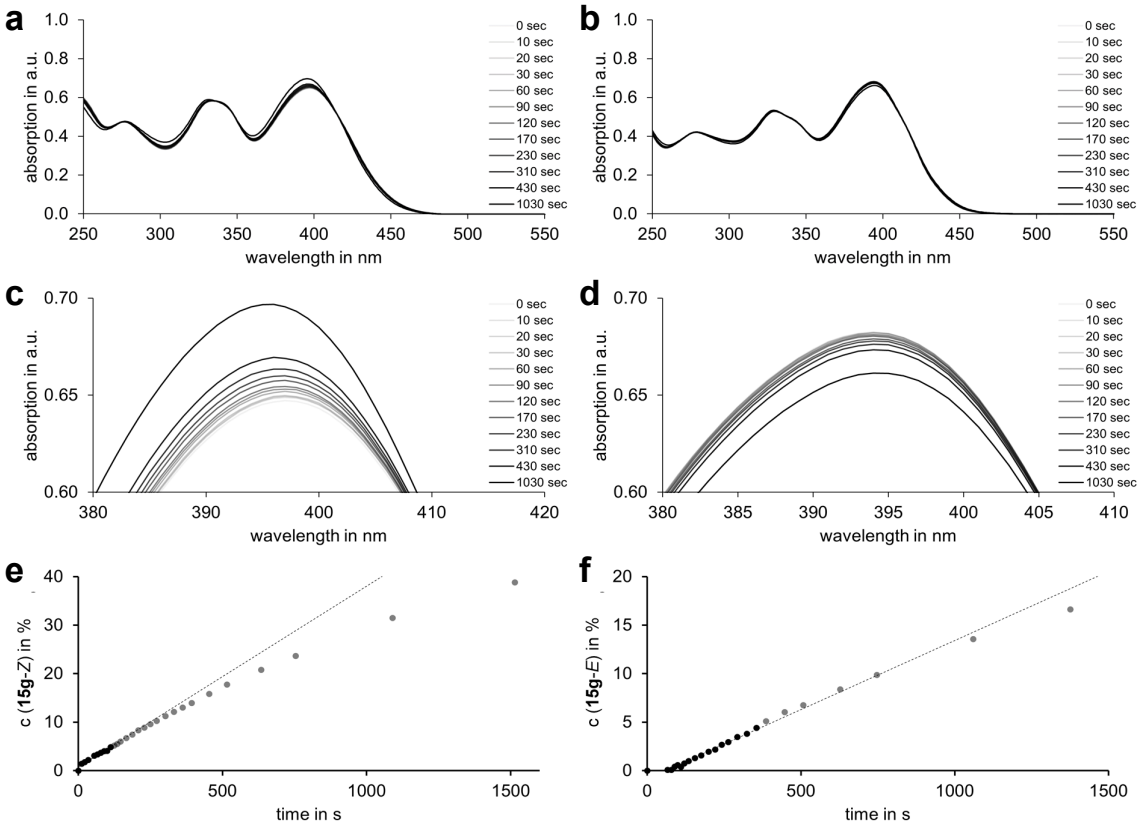

Figure 97 Photoisomerization QY determination of racemic **15g**-*E* and **15g**-*Z*. Irradiation was carried out with a 450 nm LED at 22 °C and changes in isomer ratios were monitored by UV-Vis spectroscopy (CH_2Cl_2, 22 °C) using molar extinction coefficients. For reasons of clarity only the first three spectra followed by every third measurement are shown. Linear regression analysis of initial slope is plotted excluding all grey colored dots beyond 5% concentration change. **a** Stacked UV-Vis absorption spectra of pure **15g**-*E* (61 μM) and corresponding mixtures of **15g**-*E* and **15g**-*Z* after indicated irradiation times. **b** Enlargement of the maximum absorption difference between *E*- and *Z*-spectra at 396 nm. **c** Accumulation of **15g**-*Z* during photoisomerization of **15g**-*E*. **d** Stacked UV-Vis absorption spectra of pure **15g**-*Z* (53 μM) and corresponding mixtures of **15g**-*Z* and **15g**-*E* after indicated irradiation times. **e** Enlargement of the maximum absorption difference between *E*- and *Z*-spectra at 396 nm. **f** Accumulation of **15g**-*E* during photoisomerization of **15g**-*Z*. QY determination using initial slope analysis (dotted black line) leads to an average of $\Phi_{E\rightarrow Z} = 7.9\%$ for the **15g**-*E* to **15g**-*Z* photoconversion as well as $\Phi_{Z\rightarrow E} = 5.6\%$ for the **15g**-*Z* to **15g**-*E* photoconversion, averaged over three measurements.

5.11. Conclusion and outlook

In summary, a series of HTI-based motors with substitution patterns allowing to investigate influences of EDG and EWG upon absorption behavior, rotation speed, QY and acid sensitivity of the motor rotation cycle was synthesized and analyzed. To this end, six HTI molecular motors were extensively investigated with respect to the electronic influences on the kinetics of the thermal ratcheting step, thermodynamic stability of isomers and photophysical properties. This enabled for the first time to directly gain detailed geometrical information about the *E*-configuration of metastable *E*-(*S*)-*M* intermediates using *in situ* low temperature irradiation 2D NMR spectroscopy. Additionally, a prospective acid sensitive functionalization has been introduced, for which the rotational cycle appears to be only slightly tunable *in situ* by addition of acid. Most importantly, it has been shown that the contribution from electronics to the THI is rather limited when compared to the influence originating from steric hindrance. Modulation of QYs does appear to be possible using this substitution approach leading to a deeper understanding of how to design HTI-based motors with respect to their desired properties depending on the application needs. Furthermore, substitution remote from the center of mechanical action enables introducing synthetic handles for *i.e*. implementation of acid or base sensitive functions which did in turn only allow for small *in situ* rotation speed modulation yet. Taken together, these results provide necessary information for designing novel optimized HTI-based motors which can find applications in future integrated molecular machinery with biological, medicinal, or material uses.

Since this is work in progress, further already planned experiments are necessary to complete this study, such as completing measurements at elevated temperatures, determination of PSSs, further examination of fluorescence signals, remeasuring of QYs using the new revised setup, and performing control experiments for the acid tunable rotation speed of motor **15e**. The latter involves, a control experiment testing the acid sensitivity of **15e** with respect to *e.g*. **15d** examining if it is an actual feature of the dimethylamine substitution pattern or a general feature of all HTI-based motor systems resembling the original system **15d**. Furthermore, remeasurement of accurate QYs for molecules **15f** and **15g** could potentially allow to determine their favored rotation directions according to chapter 6.

6. Evidencing fast directional molecular motions – A photochemical method

6.1. Aim

One standing challenge for light-driven synthetic molecular motor design is the acceleration of their rotation. To be more specific, it is known how to speed them up,[147,148,156,158,195,215,248–258] but proving unidirectionality becomes more challenging with increased rotation speed. Thus, directionalities for motors with the potential to move with THz frequency or faster are already challenging to be proven experimentally.[257,259–264] What is more, rotary cycles without any intermediates are almost impossible to evidence experimentally.[90,156,248,259] The only tools evidencing directionalities for these ultrafast motors are transient analytical experimental techniques such as *e.g.* transient UV-Vis absorption spectroscopy,[155,257,265–267] or theoretical predictions.[262–264] However, precise experimental geometric insights can usually not be obtained with UV-Vis methods. An overview of HTI-based motors **15d** and **21–26** is shown in Figure 98, sorted according to maximum possible rotation speed. Unsubstituted motor system **26** was predicted to be the fastest system of all synthesized motors based on the original HTI design **15d**.[154,156,259]

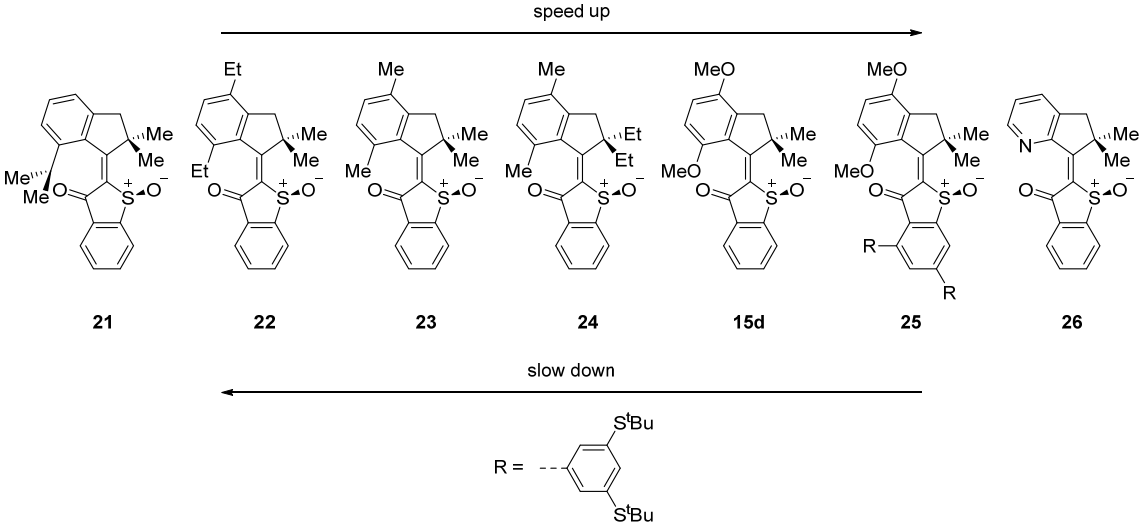

Figure 98 Speed comparison of molecular motors based on the slowest THI step, measured experimentally for **21**, **22**, **23**, **24**, **15d**, and **25** (from left to right). Additionally, speed was also predicted at the B3LYP/6-311G(d,p), B3LYP/6-311G(d,p) IEFPCM(CH_2Cl_2), and MPW1K/6-311G(d,p) levels of theory for **15d** and **26**. Order of reaction speed was established according to the average of measured values for the slowest helix inversion available or theoretical prediction thereof for **26**.[156,259]

There are many more literature-known prospective molecular motors such as **26**, shown in Figure 99 namely **27–32** for which unidirectionality has not yet been experimentally proven,[259–264] except **27** which has been examined with transient spectroscopy.[257]

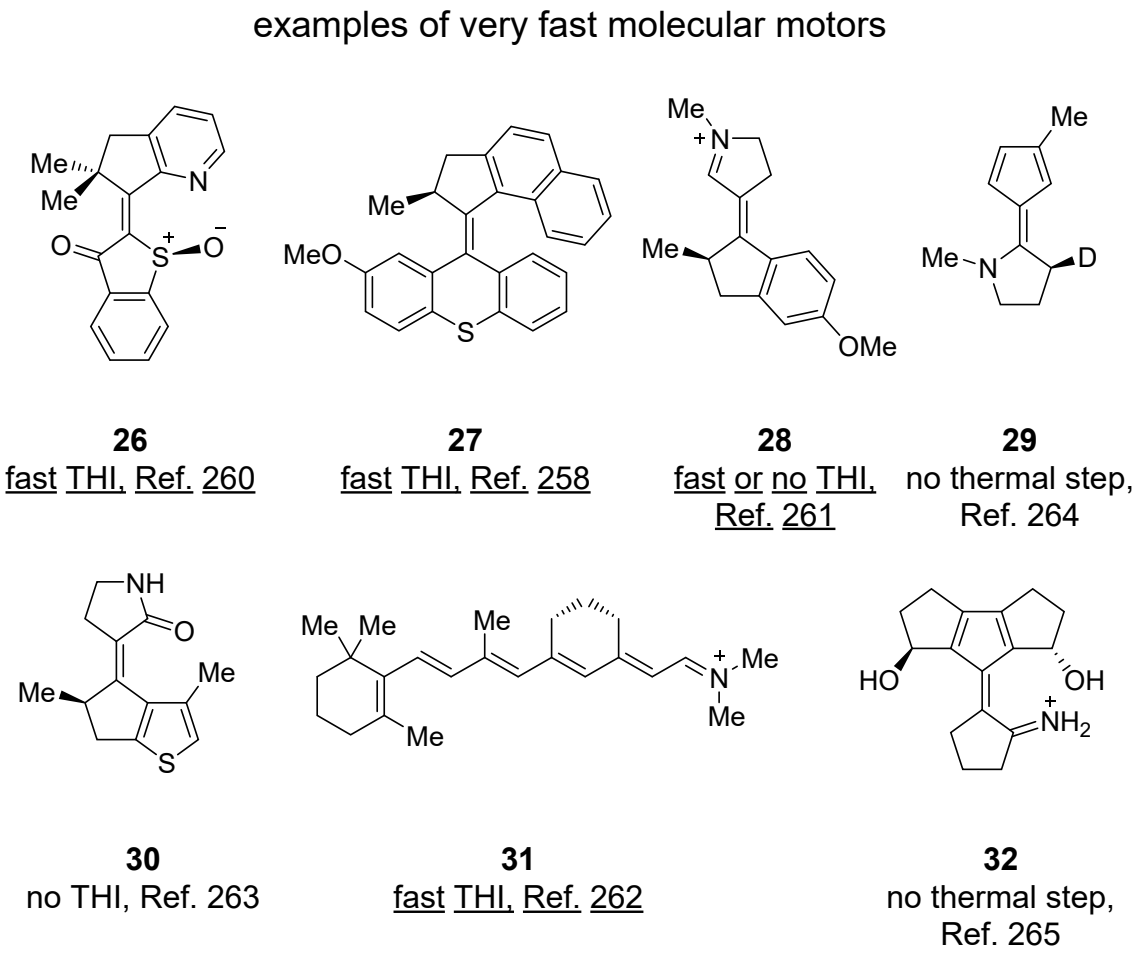

Figure 99 Various very fast molecular motors **26**, **27**, **28**, and **29** (top row left to right) as well as **30**, **31**, and **32** (bottom row left to right). All depicted examples share highly flexible helicities or non-existing thermal steps in the ground state. In the latter case evidencing directionality is challenging because of missing intermediates, necessary for directionality determination. Underlined examples were examined experimentally[257,259–261] as well as theoretically and non-underlined examples were scrutinized solely by theory.[262–264] However, unidirectionality has only been proven for **27** experimentally. Adapted with minor format modifications from *Nat. Commun.* **2023**, *14*, 4595 licensed under CC BY 4.0.[1]

Usually, HTI-based motors follow the rotary cycle shown in Figure 100. Evidencing their directionality relies on observation of at least three conformations. For these types of HTI-based motors, this means that one of the thermal steps must be observable to prove unidirectionality using conventional experimental techniques. If no thermal steps are present – as it is the case for some prospective motors

shown in Figure 99 – or barriers of these isomerizations are too low to be observed, experimental demonstration of directionality has not yet been accomplished.

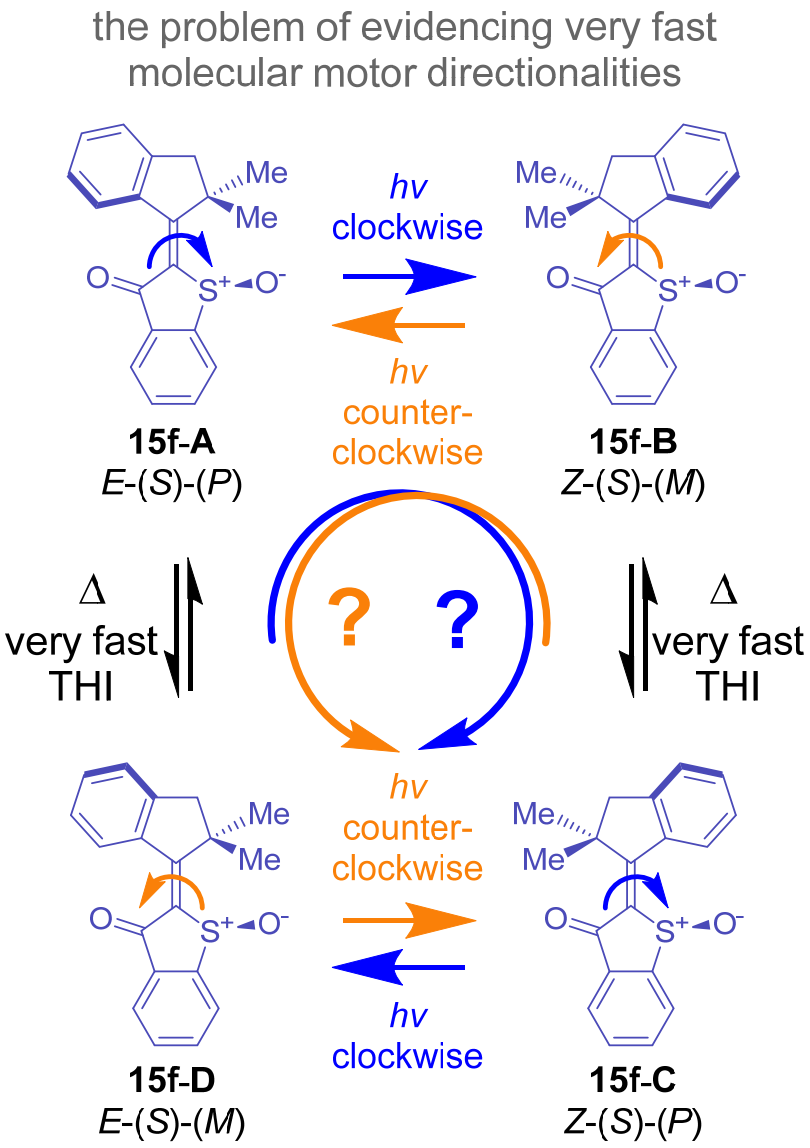

Figure 100 Determining directionality of very fast light-powered molecular motors *via* direct experimental evidence can be very challenging since it involves observation of short-lived intermediates. In the case of overcrowded alkene motors, such as the depicted HTI-based system **15f**, this requires tracing of thermal helix inversion (THI). Structural lability resulting from reduced steric interactions do enable different feasibly rotation directions, namely clockwise (cw) rotation illustrated with blue arrows, or counterclockwise (ccw) rotation illustrated with orange arrows. A preferred rotation direction according to the initial helical twist has been assumed but not yet demonstrated.[255] Adapted with minor format modifications from *Nat. Commun.* **2023**, *14*, 4595 licensed under CC BY 4.0.[1]

6.2. Design principles

The concept put forward by *Uhl et al.* in which the arbitrary assigned rotor and stator parts of a HTI-based motor are further functionalized with groups fulfilling a specific purpose for the functionality of the machine is picked up herein. Apart from the motor unit the original design did also consist of a biaryl reporter unit and a covalent linker, connecting the reporter and rotor unit shown in Figure 101. In this design setup, the reporter received the movement of the rotor and was used as a tracer following the rotation of the motor unit.

The underlying idea to trace molecular motions relied on this setup to dissect the HTI-based molecular motor function allowing a more in-depth analysis. To this end, the biaryl reporter unit was fixed in position by increasing steric hindrance around the biaryl axis and the covalent linker was elongated with one ethylene glycol unit to increase rotational freedom but still limit it to the respective 180° rotation half space. In other words, the locked atropisomer allowed to analyse the clockwise (cw) and counterclockwise (ccw) rotation within the same molecular framework dissecting the 360° rotation into two 180° rotation photo-equilibria at 22 °C. With this macrocyclization approach, a chromophore performing a molecular motion – a HTI-based molecular motor in this case – can be embedded to investigate its motion as shown in Figure 101 in a schematic depiction of **33**.

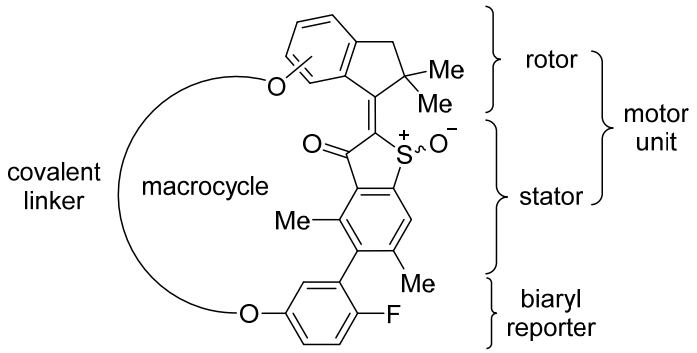

33
schematic representation

Figure 101 Schematic representation of molecular machine design and definition of its functional units exemplarily for **33**. The molecular motor unit consists of a rotor and a stator which are assigned arbitrarily as discussed in chapter 2.5, and used consistently to previously reported systems maximizing comparability. Motion is generated *via* integration of a visible-light-powered HTI-based prospective molecular motor. Transmission of motion is achieved through a covalent linker and reporter design realizes dissection of the 360° rotation space into 180° motion half spaces.

The principle of tracing the motor rotation using the biaryl atropisomer *via* ECD responses and biaryl plane tilts by observations made from NMR spectroscopy utilizing the nuclear *Overhauser* effect (NOE) in this case enabled determining rotational half-spaces of observed motions and conformational analysis

of structures. To this end, a macrocyclization approach was envisioned embedding the prospective ultrafast molecular motor **15f** and locking its rotation using a sterically hindered biaryl axis and a covalently attached linker connecting the biaryl axis on the one side of the motor with the rotating part on the other side. This leads to two separate 180° rotation-photoequilibria in **33** restricting the motion to one side of the dissected 360° rotation only. If steric strain around the biaryl axis is increased significant enough, the plane of the terminal aryl and the motor unit are almost orthogonal leading to equal distributed room for motions in each 180° rotation half space.

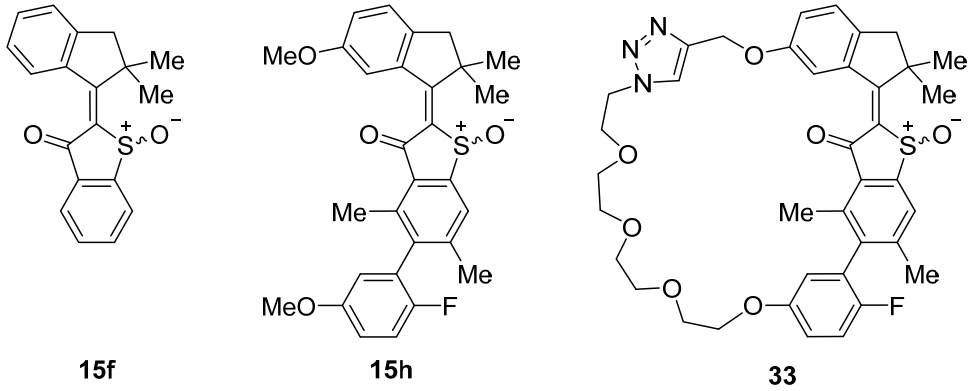

Figure 102 Macrocyclization approach in this work for experimental evidence of prospective molecular motor **15f**. Integration into the described setup requires two anchoring points for the covalent linker, capped with methoxy functions in molecule **15h**. Connection of rotor and stator elements lead to macrocycle **33**.

When considering a motor in this macrocyclization approach, the clockwise and counterclockwise 360° rotation can both be observed and subsequently compared to the unrestricted system **15h**. Elucidation of rotation directions can be made if QYs for all directions of the macrocyclic **33** and non-macrocyclic systems **15h** are known allocating each value measured in the unrestricted system with their respective match in the macrocyclic system. For the latter, there should be twice the amount of QYs observable because both directions can be measured in the macrocycle with respect to the unrestricted system for which only one direction can be measured, potentially observed as a mixture of both directions.

In case of a four-step motor (two thermal and two photochemical steps), this would mean that four photochemical steps are measurable in the macrocyclic embedding which can then be compared to what has been measured for the two observed photochemical steps in the unrestricted system. The closer match in QY values does then predict a preferred directionality. Having all configuration of isomers and thermal as well as photochemical interconversions precisely measured and defined, does then in combination with QY measurements enable to elucidate the motion sequence of an unrestricted prospective molecular motor.

6.3. Synthesis of fast molecular motor embedded macrocyclic HTI 33

Macrocyclic molecular machine **33** was synthesized from commercially available tetraethylene glycol **36**, 6-hydroxy indanone **49**, and 4-bromo-3,5-dimethylphenol **40**. Retrosynthetic analysis was done according to a modified literature procedure for integrated macrocyclic HTI-based molecular motors[158,240] leading to covalent linker building block **34**, indanone rotor part **35** and benzothiophenone stator **17** shown in Figure 103. Synthetic procedures towards all herein presented compounds are reported in the experimental chapter 8.5.1 starting from commercially available starting materials.

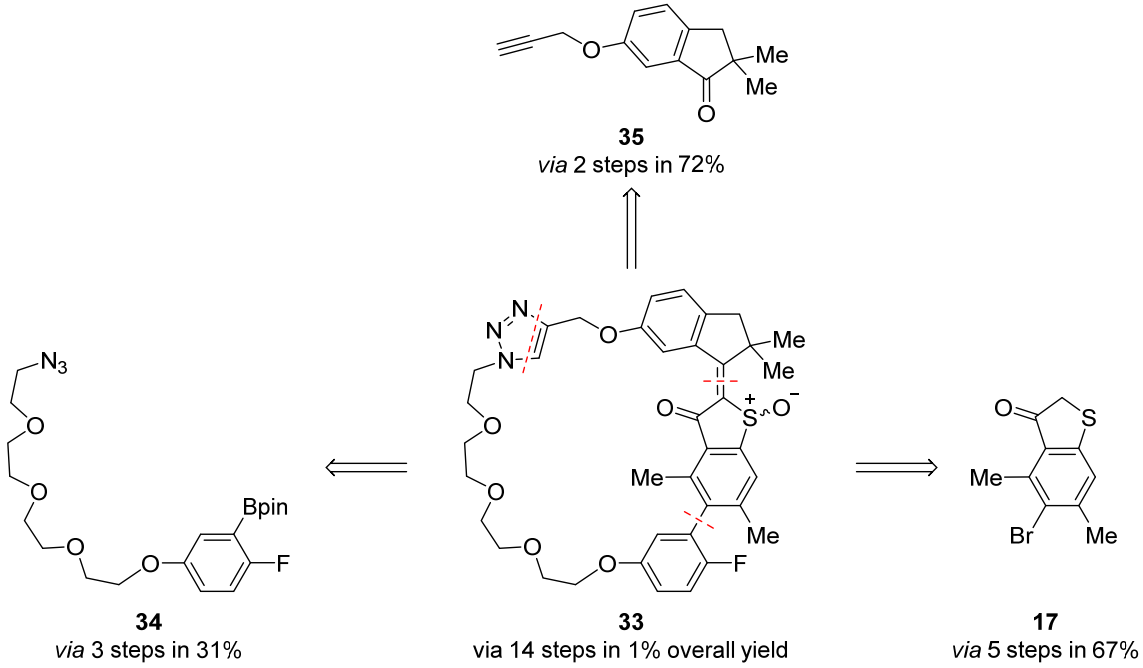

Figure 103 Retrosynthetic analysis of macrocyclic HTI-based molecular machine **33**. Cleavage along the central double bond, triazole moiety and the biaryl axis led to covalent linker building block **34**, indanone rotor part **35** and benzothiophenone stator **17**.

The covalent tetraethylene glycol linker **34** was synthesized from commercially available tetraethylene glycol **36** which was dibrominated *via* an *Appel* reaction with tetrabromomethane and triphenylphosphine in tetrahydrofuran to the corresponding 1,14-dibromotetraethylene glycol **37** in 70% yield.[156,268] Monosubstitution using sodium azide furnished the corresponding 1-azido-14-bromo tetraethylene glycol **38**[269] in 44% yield which was further transformed to the linker building block **34** through substitution of the bromide using the corresponding fluorinated aryl **39** shown in Figure 104.

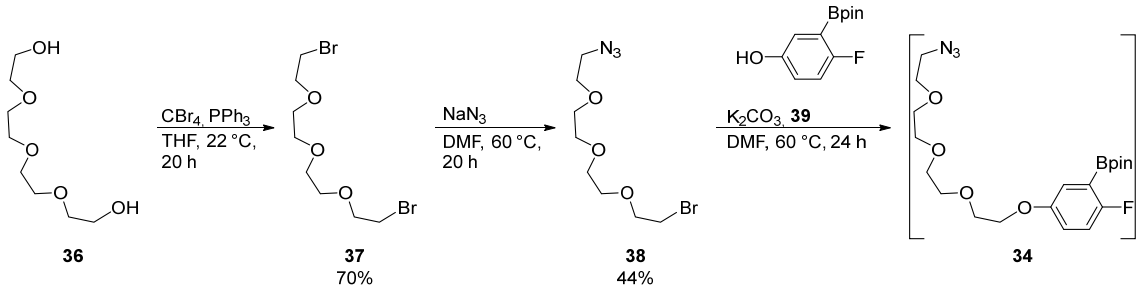

Figure 104 Synthesis of covalent linker fragment **34**. Commercially available tetraethylene glycol **36** was di-brominated in an *Appel* reaction giving compound **37** with tetrabromomethane and triphenylphosphine. Monosubstitution with sodium azide furnished bromine-azide di-functionalized **38**, which was further substituted with commercially available fluorinated aryl **39** yielding linker building block **34**.

Benzothiophenone **17** was synthesized starting from commercially available 4-bromo-3,5-dimethylphenol **40** which was esterified using dimethylcarbamoylchloride **41** quantitatively affording *O*-aryl thiocarbamate **42**. Upon sufficient thermal energy supplied the *S*-aryl thiocarbamate **43** is furnished in 90% yield through a *Newman-Kwart* rearrangement as a result of the energetically more favourable carbon oxygen double bond formed. The resulting thio-ester **43** can subsequently be cleaved using potassium methoxide leading to the corresponding thiol **44** in 85% yield. However, the disulfide dimer is always observed as a minor side product because of oxidative dimerization but does not interfere with the following step. Using bromoacetic acid **45**, the thiol **44** can then be converted to the corresponding acid **46** in 89% yield using potassium carbonate as base. Ring closing to benzothiophenone **17** was achieved using thionyl chloride followed by aluminum(III) chloride addition in an intramolecular *Friedel-Crafts* acylation in 98% yield as shown in Figure 105.[158]

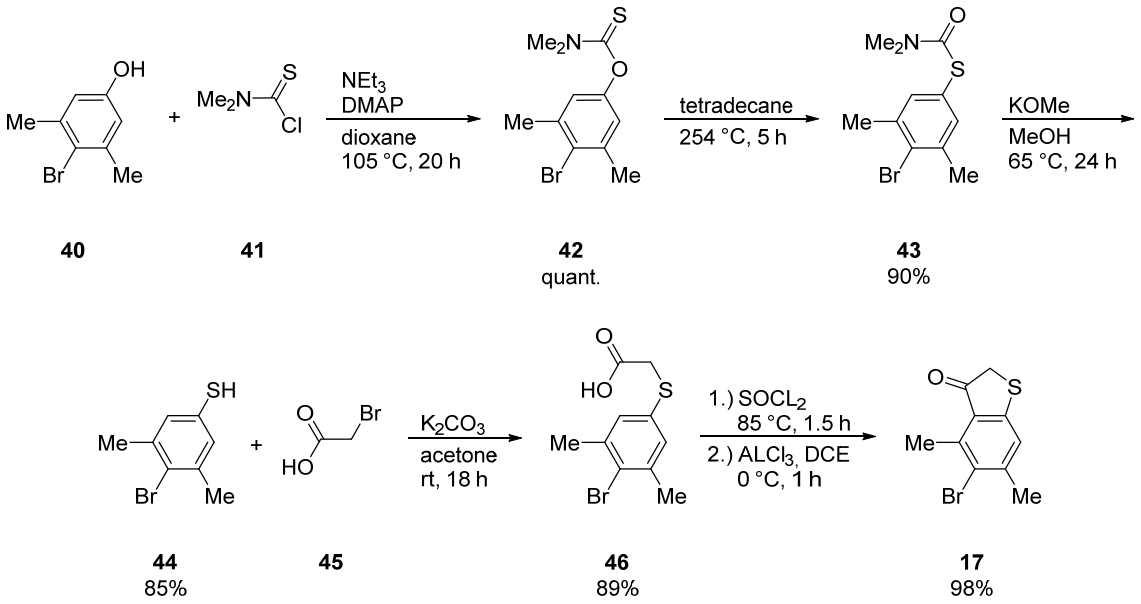

Figure 105 Synthesis of benzothiophenone building block **17**. Commercially available 4-bromo-3,5-dimethyl phenol **40** was reacted with dimethylthiocarbamoylchloride **41** giving *O*-aryl thiocarbamate **42**. *Newman-Kwart* rearrangement furnishes the corresponding thermodynamically more stable *S*-aryl thiocarbamate **43** followed by cleavage of the thioester with potassium methoxide giving thiol **44**. Substitution reaction of bromoacetic acid **45** with thiol **44** yields corresponding acid **46** which can be transformed into benzothiophenone **17** *via* the corresponding acid chloride. To this end the acid chloride was prepared with thionyl chloride followed by an *in situ* intramolecular *Friedel-Crafts* acylation with aluminum(III) chloride leading to **17**.

HTI core structure **49** bearing the poly ethylene glycol (PEG) chain attachment point for macrocyclization in the 6-position was synthesized *via* a modified previously established protocol shown in Figure 106.[158,159] Indanone fragment **35** was accessed starting from commercially available 6-hydroxy indanone **47** through a propargylation with quantitative conversion to **48** followed by methylation yielding 72% of indanone **35**. Benzothiophenone **17** was constructed using a *Friedel-Crafts* acylation from the corresponding acid **46** as mentioned above. Condensation of building blocks **35** and **17** using boron trichloride furnished HTI motor core **49** in high yield of 66% for this type of transformation. A mixture of *E*-and *Z*-isomers was obtained which was utilized for the next step as a mixture of isomers.

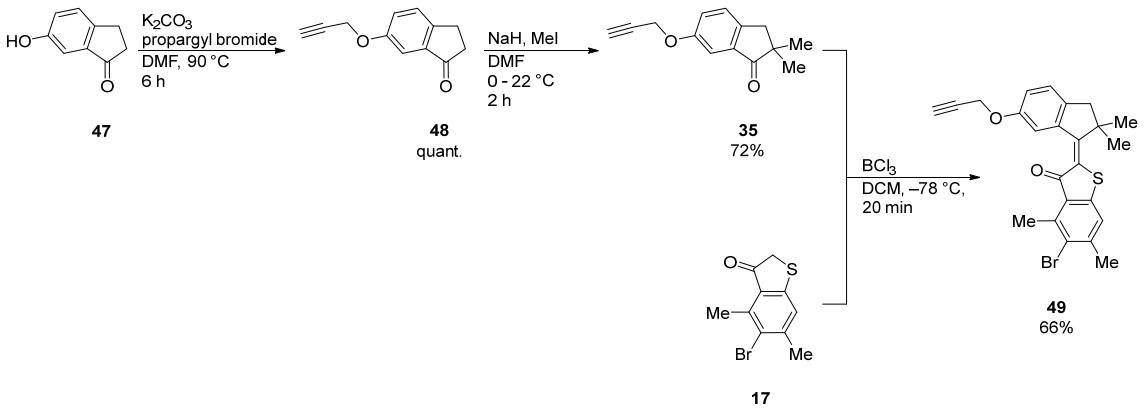

Figure 106 Synthesis of HTI core structure **49**. Indanone **35** was synthesized form the corresponding commercially available 6-hydroxy indanone **47** *via* propargylation with propargyl bromide yielding **48** followed by methylation using iodomethane furnishing **35**. Condensation of benzothiophenone **17** and indanone **35** with boron trichloride furnished HTI core **49** as a mixture of *E*- and *Z*-isomers.

The covalent linker **34** was attached to the motor fragment **49** using a 1,3-dipolar cycloaddition establishing a 1,2,3-triazol moiety as part of the linking chain in **50**. Ring closing of **51** was achieved using classical *Suzuki-Miyaura* cross coupling which worked best with sSPhos Pd G2, potassium phosphate in a toluene/ethanol/water mixture in 15% yield. As the final step the sulfide was oxidized to the corresponding sulfoxide using sodium perborate tetrahydrate yielding the final target **33** in 65% as a yellow solid shown in Figure 107. This oxidation agent is conventionally used for the oxidation of HTIs to their corresponding sulfoxides *via* formation of peracetic acid.[270] Increased oxidation strength through combination with acetic acid enables facile oxidation of the thioether if close monitoring of the reaction is done, avoiding overreaction to the respective sulfone.

Separation of diastereomers was accomplished through a combination of chromatographic techniques starting with flash chromatography on silica followed by HPLC separation using a *Macherey-Nagel Nucleosil* silica column in combination with a *Daicel* CHIRALPAK® IB-N or IC column. Only *E*-isomers were obtained from this isolation procedure and *Z*-isomers were received after irradiation of *E*-isomers and repeated purification using the same separation procedure.

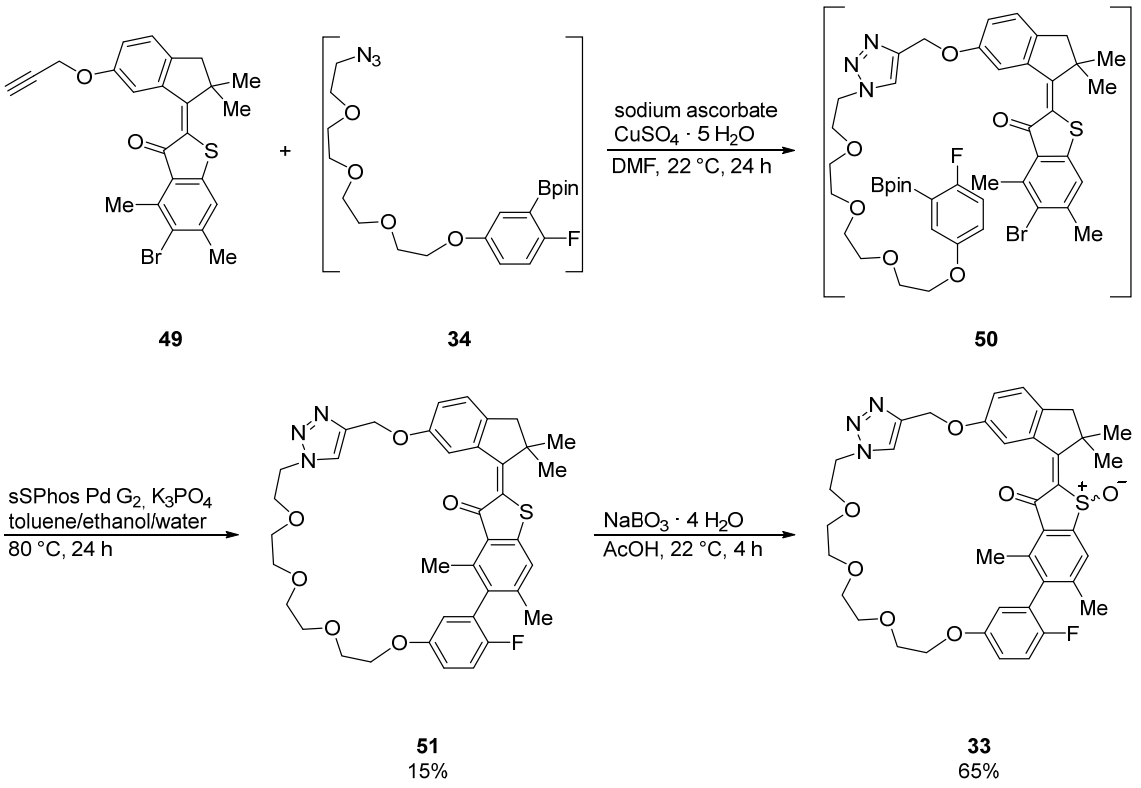

Figure 107 Final synthetic steps yielding macrocyclic molecular machine **33**. Attachement of covalent linker chain **34** onto HTI **49** was achieved using *Huisgen* azide-alkyne click chemistry through a 1,3-dipolar cycloaddition with copper(I) sulfate and sodium ascorbate. Cyclization of **50** was furnished through *Suzuki-Miyaura* cross coupling using sSPhos Pd G2 leading to macrocyclic **51**. Oxidation of the sulfide was established lastly using an excess of sodium perborate in acetic acid to generate the sulfoxide **33**. Structures in brackets were used in the next synthetic transformation without isolation.

Since overall yield of target compound **33** was severely limited by low yield during ring closing step *via Suzuki-Miyaura* cross coupling (similar to previous reports[158,159]), an optimization was attempted by exchanging catalyst ligand and solvent setup to a system successfully employed for more sterically hindered couplings.[77] Two different conditions were tested for this step with respect to limitations in starting material **50**. Exchanging the tetrakis(triphenylphosphine)palladium(0) conditions for a sSPhos Pd G2 system lead to improvement of reaction yields by up to 15% shown in Table 11.

Table 11 Tested reaction conditions for macrocyclization of **51**.

catalyst	base	solvent	temp in °C	time in h	yield in %
$Pd(PPh_3)_4$ (5 mol%)	K_2CO_3 (4.0 equiv.)	*N*,*N*-dimethylformamide (0.02 M)	80	23	<1
sSPhos Pd G2 (8 mol%)	K_3PO_4 (3.0 equiv.)	toluene/ethanol/water (3/3/1, 0.02 M)	80	18	15 (over 2 steps)

6.4. Synthesis of prospective fast HTI-based molecular motor 15h

Prospective HTI-based molecular motor **15h** was also synthesized from commercially available 6-hydroxy indanone **47** and 4-bromo-3,5-dimethylphenol **40** as well as hydroxy fluoroaryl **39**. Retrosynthetic analysis was done according to the macrocyclic analogue furnishing indanone rotor **52,** benzothiophenone stator **17** and aryl **53** respectively shown in Figure 108. Synthetic procedures towards all herein presented compounds are reported in the experimental chapter 8.5.2 starting from commercially available starting materials.

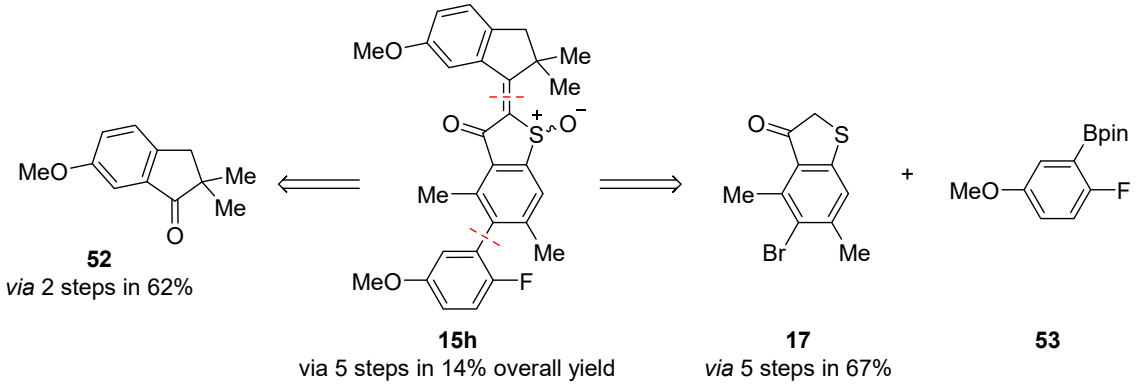

Figure 108 Retrosynthetic analysis of prospective HTI-based motor **15h**. Cleavage along the central double bond and the biaryl axis led to indanone rotor **52,** benzothiophenone stator **17** and aryl **53** as building blocks.

Indanone fragment **52** was accessed through selective methylation of the 6-hydroxy function using iodomethane followed by a double methylation procedure in α-position to the carbonyl with iodomethane as well, furnishing **52** in 62% over two steps *via* **54** from commercially available 6-hydroxy indanone **47** shown in Figure 109.

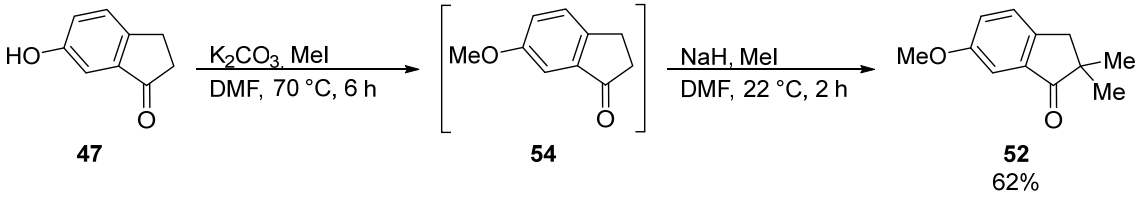

Figure 109 Synthesis of indanone building block **52** from the corresponding commercially available 6-hydroxy indanone **47** *via* methylation of the hydroxy position using iodomethane followed by double methylation in α-position to the carbonyl of **54** with iodomethane. Structures in brackets were used in the next synthetic transformation without isolation.

Benzothiophenone **17** was constructed starting from the corresponding commercially available 4-Bromo-3,5-dimethylphenol **40** as explained in chapter 6.3. Condensation of building blocks **52** and **17** using boron trichloride furnished HTI motor core **55** shown in Figure 110.

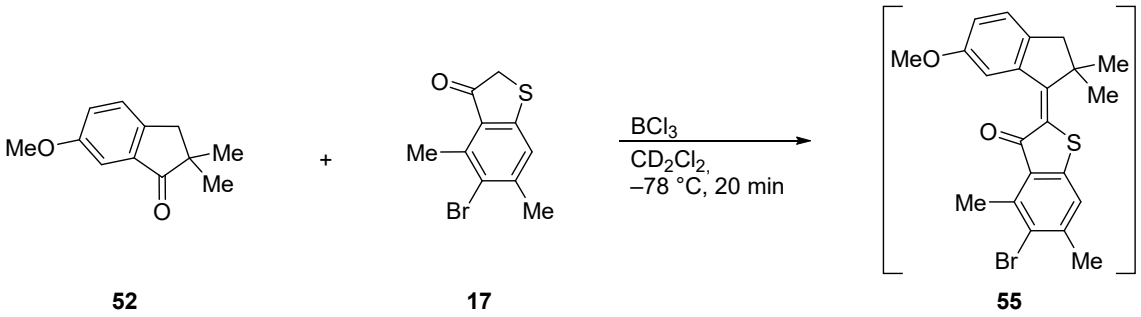

Figure 110 Condensation of benzothiophenone building block **17** (for synthesis see chapter 6.3) and indanone building block **52** with boron trichloride furnished HTI core **55**. Structures in brackets were used in the next synthetic transformation without isolation.

Aryl building block **53** was prepared from the commercially available hydroxy aryl **39**, which was methylated using iodomethane to furnish the corresponding methoxyaryl shown in Figure 111 and used in the next synthetic transformation without isolation.

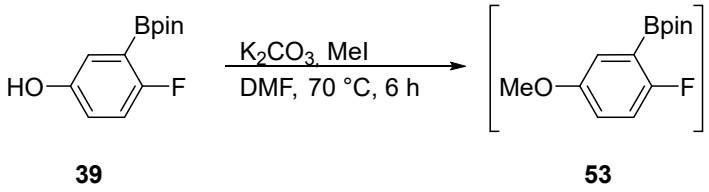

Figure 111 Preparation of methylated aryl building block **53**. Commercially available **39** was methylated to the corresponding methoxy aryl building block **53** using iodomethane. Structures in brackets were used in the next synthetic transformation without isolation.

Assembly of building blocks started with condensing indanone **52** and benzothiophenone **17** using boron trichloride in dichloromethane shown in Figure 110. The biaryl axis in **56** was then established using a *Suzuki-Miyaura* cross coupling with **53**, tetrakis(triphenylphosphine)palladium(0) and potassium carbonate in dimethylformamide in 40% yield. As the final step the sulfide in fully assembled **56** was oxidized to the corresponding sulfoxide using sodium perborate tetrahydrate in acetic acid, shown in Figure 112 providing the final prospective molecular motor **15h** in 55% yield as a yellow solid. Separation of diastereomers was accomplished through a combination of chromatographic techniques starting with flash chromatography on silica followed by HPLC separation using a *Daicel* CHIRALPAK® ID column.

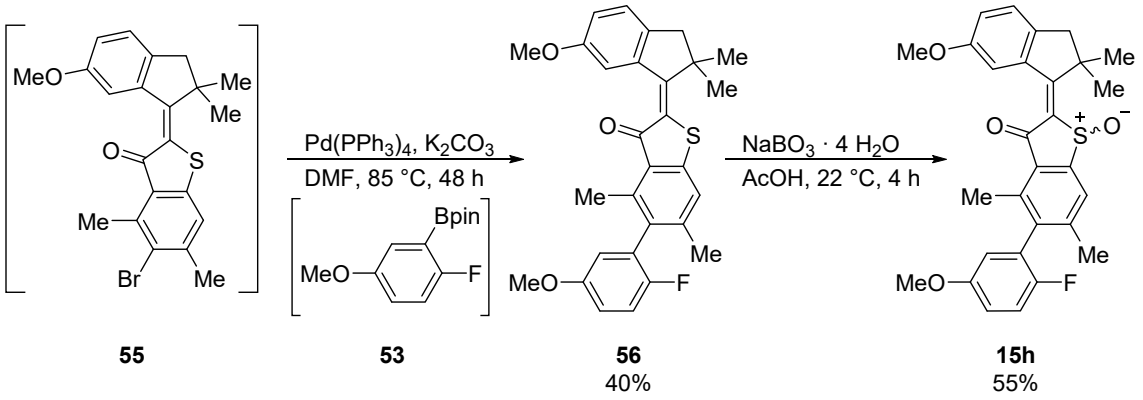

Figure 112 Final assembly of prospective molecular motor **15h**. Addition of aryl **53** onto HTI **55** was accomplished through *Suzuki-Miyaura* cross coupling using tetrakis(triphenylphosphine)palladium(0) furnishing HTI **56**. Oxidation of the thioether was established lastly using an excess of sodium perborate in acetic acid to generate the sulfoxide **15h**.

With the prospective molecular motor **15h** integrated into the corresponding macrocyclic framework necessary to elucidate directionality, macrocyclic machine **33** was subjected to extensive analysis of working mechanism including conformer analysis, thermal stabilities, kinetic barriers, photophysical properties, QY determination and theoretical description, see the next chapter and onwards.

6.5. Structural and conformational description

Molecular machine **33** can be divided into fragments also found in related systems.[158,159] These are the covalent linker establishing the macrocyclic connection, the indanone rotor part, benzothiophenone stator part and adjacent biaryl axis shown in Figure 113. The terms rotor and stator were used in accordance with previous usage, which is discussed in chapter 2. It is noteworthy, that for this system the biaryl axis does not work as a follower or reporter unit for the indanone rotation but does instead limit the rotation to one half side of the benzothiophenone plane. Enhanced sterically crowding of biaryl *ortho*-positions in combination with enlargement of the PEG linker prevents biaryl rotation during photoreaction which does in turn allow to observe QYs for clockwise and counterclockwise motions.

6.5.1. Overview of conformational states for macrocyclic HTI 33

All observable isomers at 22 °C of structure **33** shown in Figure 113 were elucidated in a combined approach using X-ray crystallographic data, 1D and 2D NMR experiments, UV-Vis and ECD spectroscopy and theoretical descriptions in comparison to experimental data. The helicity of motor core was omitted for all isomers since clear assignment was hampered because of the highly dynamic nature of this stereo element. For assignment of ^{1}H and ^{13}C signals and more analytical details, see chapter 8.5.1 or the corresponding literature.[1]

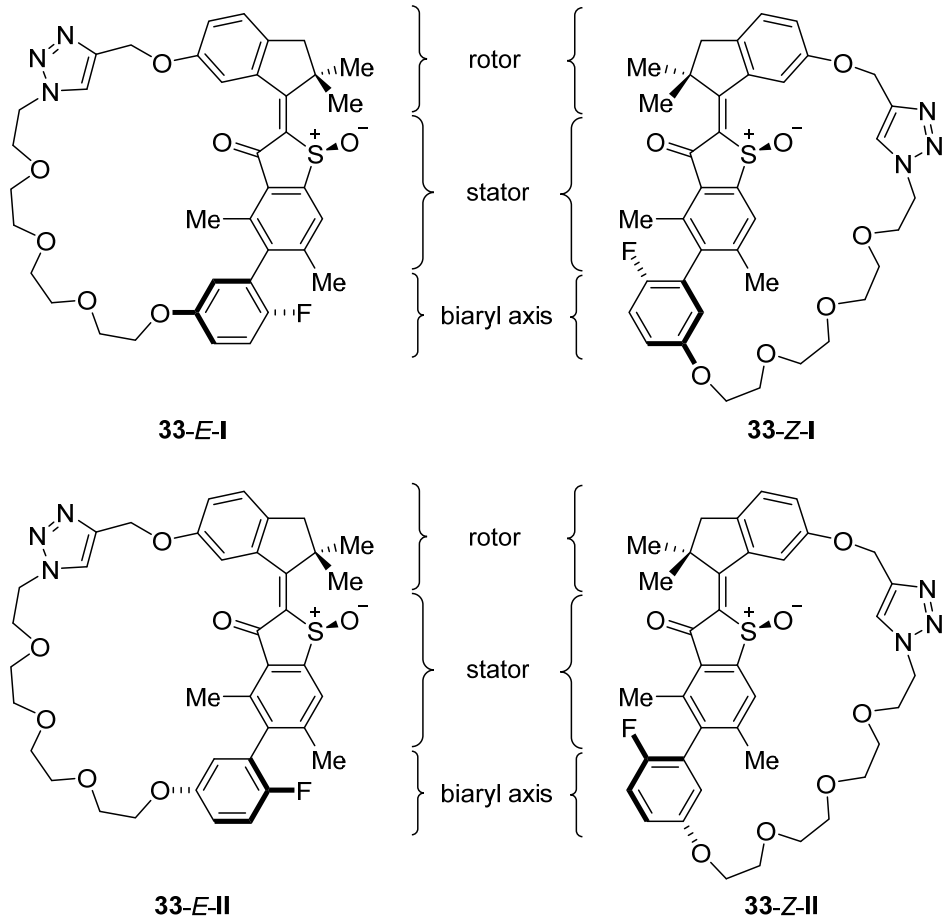

Figure 113 Overview of conformational states **33**-*E*-**I**, **33**-*Z*-**I**, **33**-*E*-**II**, and **33**-*Z*-**II**, of macrocyclic compound **33**, which are stable at 22 °C. For clarity only structures with *S*-configured sulfoxide are depicted. The set of isomers consists of two *E*- and two *Z*-configured isomers with either a R_a or S_a configured biaryl axis. The helicity of the rotor fragment is highly dynamic and can thus not be determined with certainty at ambient temperatures. Adapted with minor format modifications from *Nat. Commun.* **2023**, *14*, 4595 licensed under CC BY 4.0.[1]

6.5.2. Structure of macrocyclic HTI 33 in solution

Three-dimensional structure analysis in solution was started with an investigation of NMR spectra at 22 °C. Determination of double bond configuration was possible using NOESY or NOE experiments based on scalar dipole-dipole interactions transferred through space. Thus, spatial proximity of protons is revealed without the necessity for interactions through bonds between these protons. Proximity between specific parts of the rotor and the stator or the linker did then allow to assign *E*- or *Z*-configuration of the double bond. Furthermore, preferred biaryl tilts could be observed giving further evidence for double bond configurations through strain put upon the biaryl axis *via* the covalent linker. Therefore, all observed biaryl tilts do point with the biaryl linker attachment point towards the indanone linker attachment point. In other words, the linker anchoring points do always point towards the same direction. For *E*-isomers they point towards the carbonyl side and for *Z*-isomers towards the sulfoxide side of the benzothiophenone.

For isomers **33**-*E*-**II** and **33**-*Z*-**II** 1D NOE and 2D NOESY NMR experiments were made, both showing *E*- or *Z*-configuration of the respective double bond geometry indicating that these two experiments deliver the same information. For reasons of efficiency the faster NOE spectra were recorded for all other isomers.

6.5.2.1. Overview of all observed macrocyclic HTI 33 conformations in solution

A comparison of all isomers stable at 22 °C displaying distinct shifts of aromatic protons can be found in Figure 114. A distinct shift of the *ortho*-biaryl proton HC24 can be observed at approximately 6.70 ppm for *E*-isomers and 7.00–7.20 ppm for *Z*-isomers as well as recognizably shifted signals of protons HC8, HC17 and HC33. For detailed ^{1}H assignments, see chapter 8.5.1 or the corresponding literature.[1]

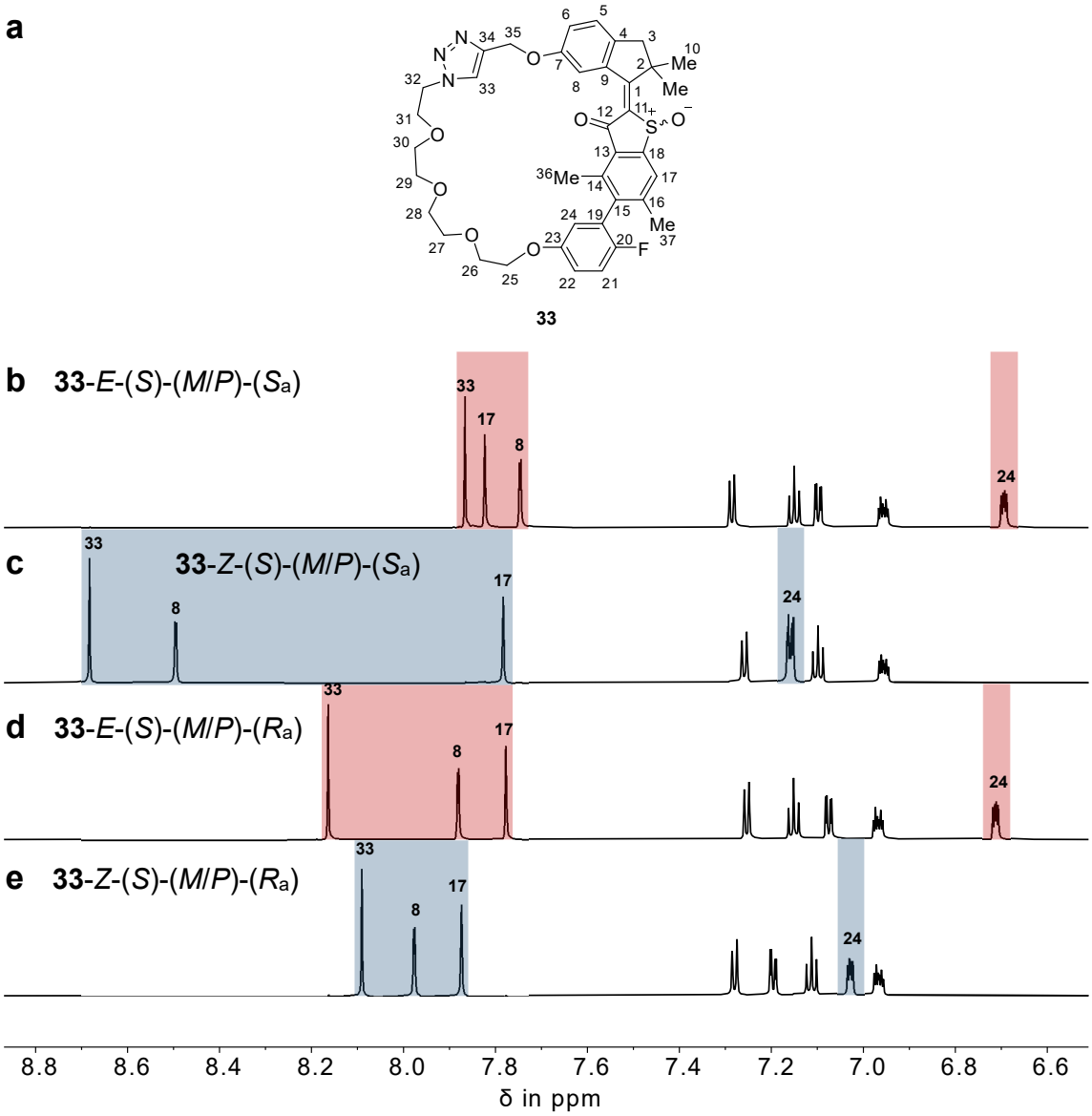

Figure 114 ^{1}H NMR spectra (801 MHz, CD_2Cl_2, 25 °C) overview of all macrocyclic HTI **33** isomers measured at 22 °C. **a** Structural representation of macrocyclic **33**. Aromatic region of isomers (**b**) **33**-*E*-(*S*)-(*M*/*P*)-(S_a), (**c**) **33**-*Z*-(*S*)-(*M*/*P*)-(S_a), (**d**) **33**-*E*-(*S*)-(*M*/*P*)-(R_a), and (**e**) **33**-*Z*-(*S*)-(*M*/*P*)-(R_a) from top to bottom. The distinct shift of protons HC8, HC17 and HC33 is highlighted in red for *E*-isomers and blue for *Z*-isomers.

6.5.2.2. 33-*E*-(*S*)-(S_a) = 33-*E*-I

Proximity of indanone proton HC8 and aromatic triazole proton HC33 to benzothiophenone methyl group H_3C36 revealed *E*-configuration of the central double bond in **33**-*E*-(*S*)-(S_a), shown in Figure 115.

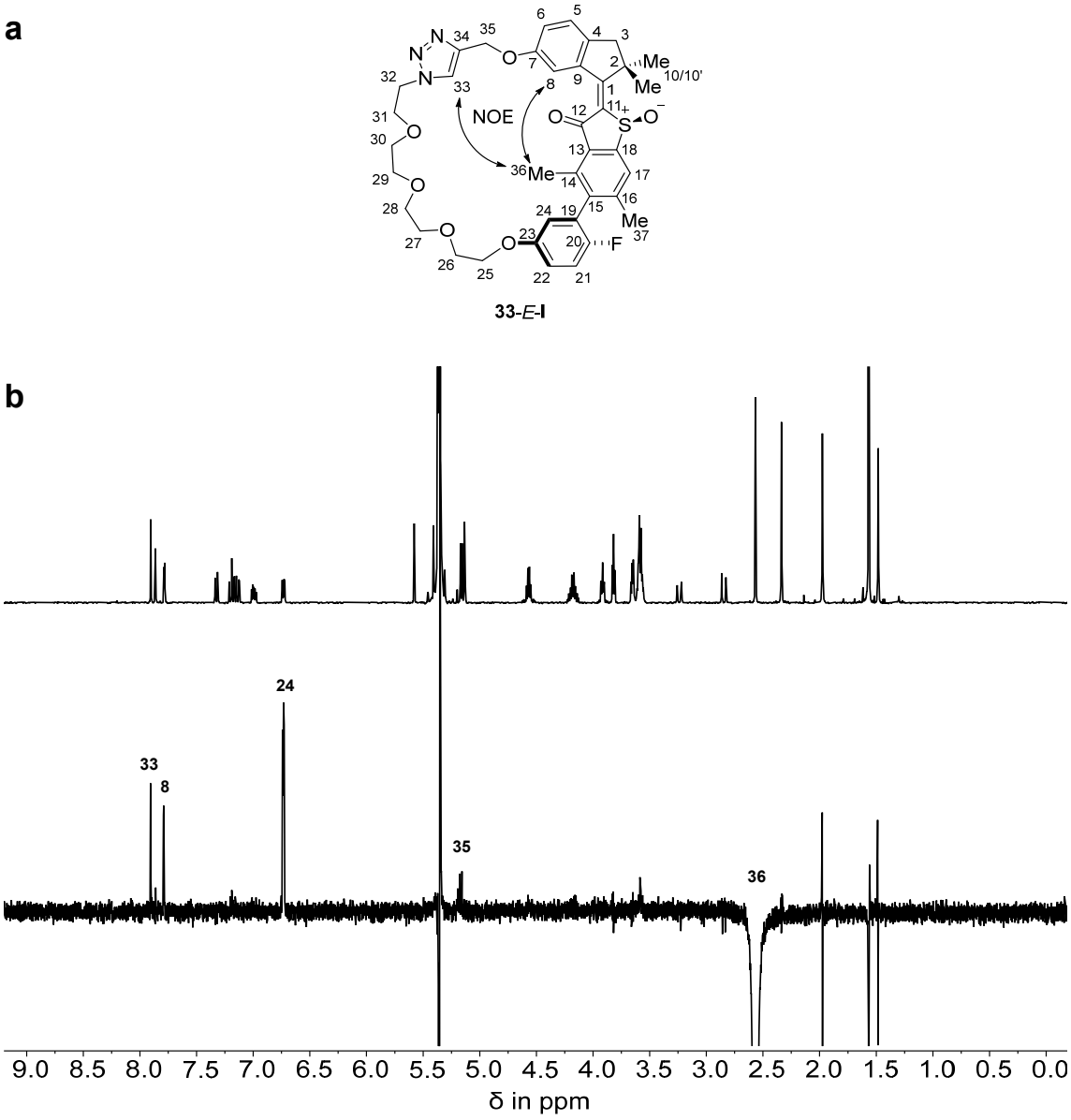

Figure 115 Double bond configuration analysis of isomer **33**-*E*-(*S*)-(S_a) measured in CD_2Cl_2 solution at 25 °C. **a** Structure of **33**-*E*-(*S*)-(S_a) including arrows depicting observed NOE signals. **b** ^{1}H (top) and NOE (bottom) NMR spectra (600 MHz, CD_2Cl_2, 25 °C) of **33**-*E*-(*S*)-(S_a) display proximity of HC8 and HC33 to H_3C36, revealing *E*-configuration of the double bond. Adapted with minor format modifications from *Nat. Commun.* **2023**, *14*, 4595 licensed under CC BY 4.0.[1]

Stronger signal intensity of aromatic *ortho*-biaryl proton HC24 to benzothiophenone methyl group H_3C36 revealed tilt of the covalent linker anchoring point on the biaryl towards the carbonyl side of the benzothiophenone fragment shown in Figure 116b. The tilt of the two biaryl planes is further illustrated in the *Newman* projection along the biaryl axis in Figure 116a.

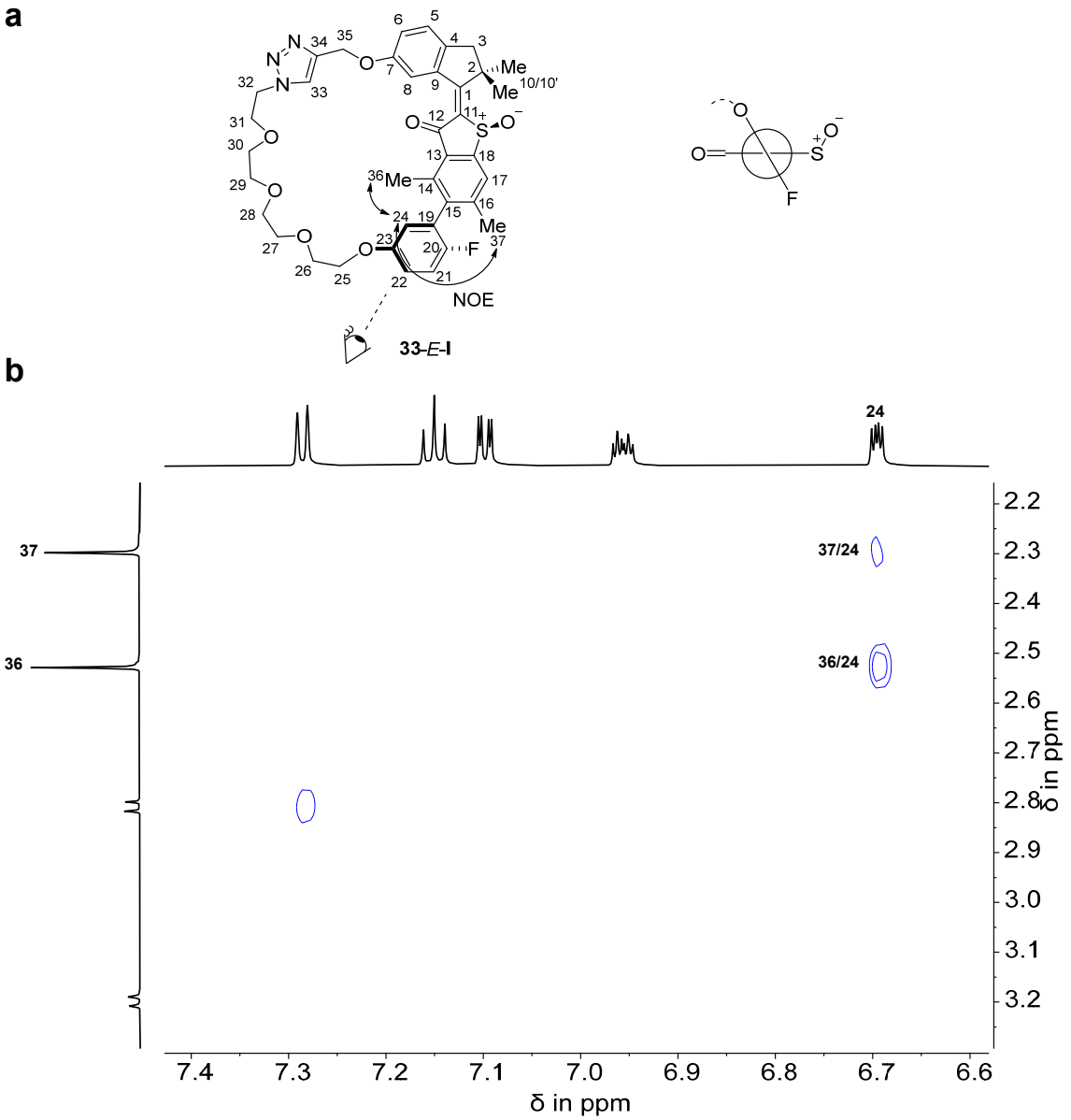

Figure 116 Biaryl axis tilt analysis of **33**-*E*-(*S*)-(S_a) measured in CD_2Cl_2 solution at 25 °C. **a** Structure of **33**-*E*-(*S*)-(S_a) including arrows depicting observed NOE signals (left). *Newman* projection of the biaryl axis showing the preferred tilt of the two biaryl planes (right). **b** NOESY NMR spectrum (CD_2Cl_2, 800 MHz, 25 °C) of **33**-*E*-(*S*)-(S_a) displaying cross signals of H_3C36 and H_3C37 to HC24. Intensity difference indicates non-orthogonality of the two biaryl planes and proximity between HC24 and H_3C36 is revealed because of increased signal strength. Therefore, a preferred tilt of the covalent linker anchoring point C23 towards H_3C36 and the poly ethylene glycol (PEG) chain is established. Adapted with minor format modifications from *Nat. Commun.* **2023**, *14*, 4595 licensed under CC BY 4.0.[1]

6.5.2.3. 33-*Z*-(*S*)-(S_a) = 33-*Z*-I

Proximity of benzothiophenone proton HC17 to aromatic triazole proton HC33 and indanone proton HC8 revealed *Z*-configuration of the central double bond in **33**-*Z*-(*S*)-(S_a), shown in Figure 117.

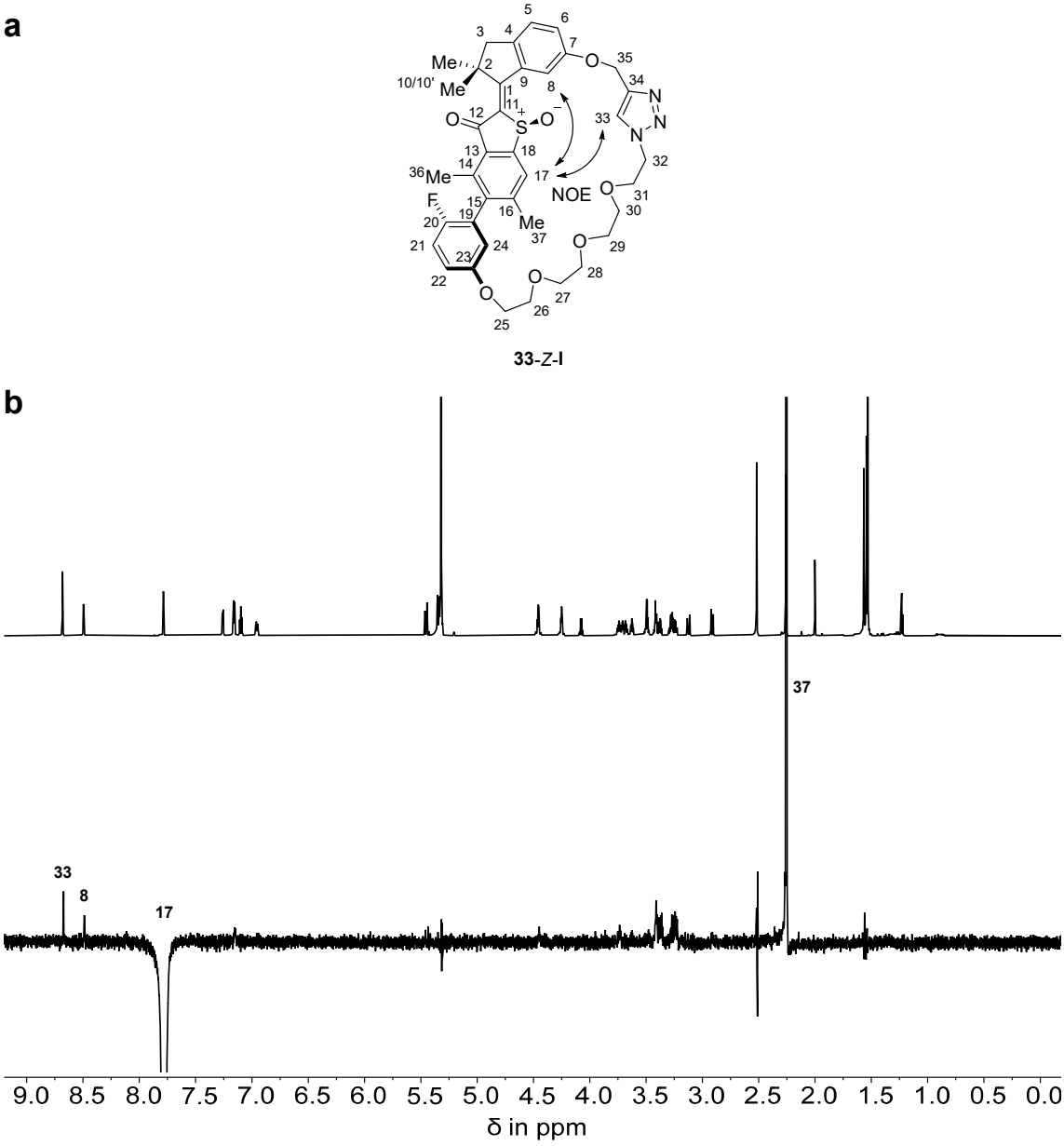

Figure 117 Double bond configuration analysis of isomer **33**-*Z*-(*S*)-(S_a) measured in CD_2Cl_2 solution at 25 °C. **a** Structure of **33**-*Z*-(*S*)-(S_a) including arrows depicting observed NOE signals. **b** ^{1}H (top) and NOE (bottom) NMR spectra (600 MHz, CD_2Cl_2, 25 °C) of **33**-*Z*-(*S*)-(S_a) display proximity of HC17 to HC33 and HC8, revealing *Z*-configuration of the double bond. Adapted with minor format modifications from *Nat. Commun.* **2023**, *14*, 4595 licensed under CC BY 4.0.[1]

Stronger signal intensity of aromatic *ortho*-biaryl proton HC24 to benzothiophenone methyl group H_3C37 revealed tilt of the covalent linker anchoring point on the biaryl towards the sulfoxide side of the benzothiophenone fragment shown in Figure 118b. The tilt of the two biaryl planes is further illustrated in the *Newman* projection along the biaryl axis in Figure 118a.

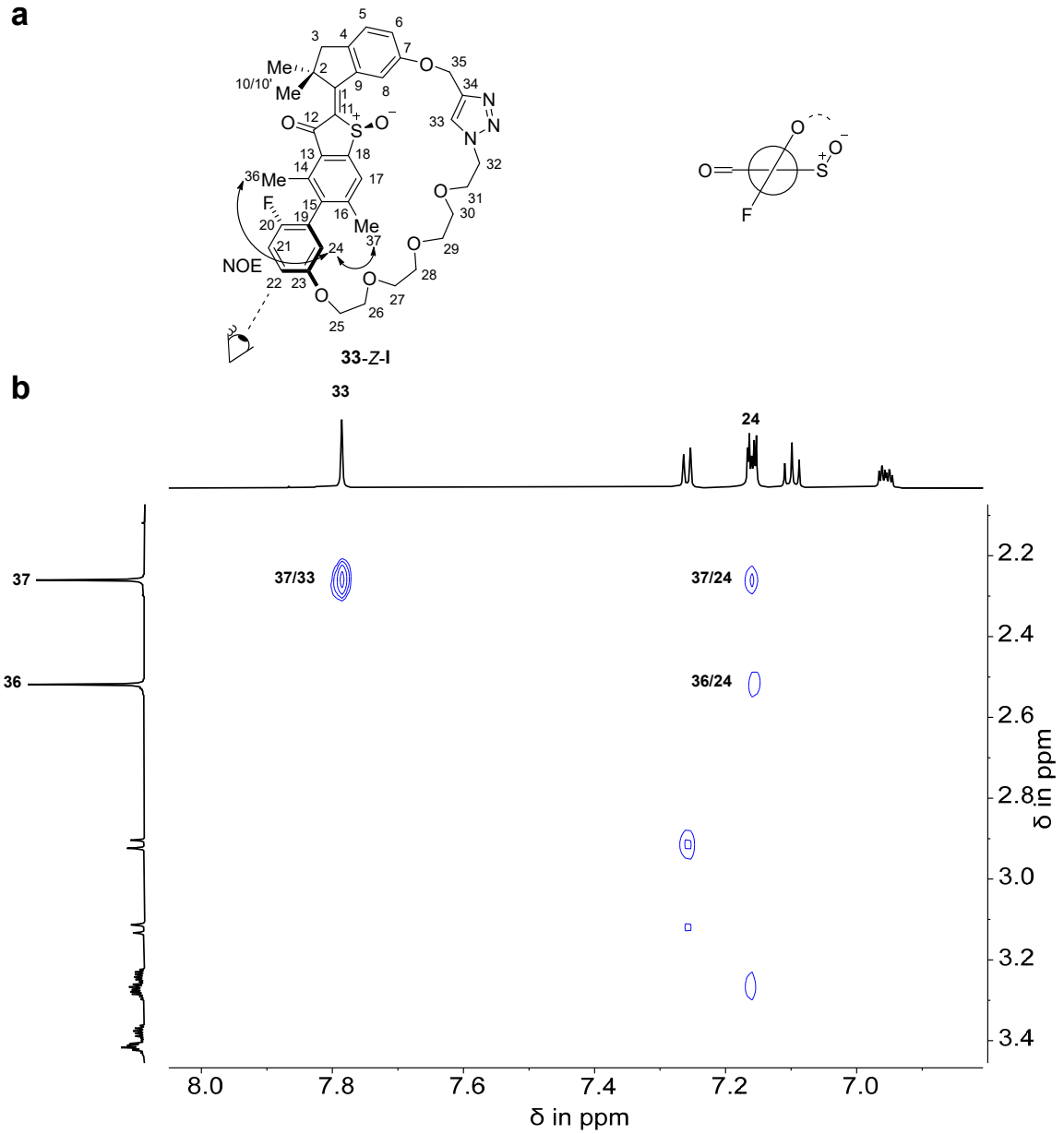

Figure 118 Biaryl axis tilt analysis of **33**-*Z*-(*S*)-(S_a) measured in CD_2Cl_2 solution at 25 °C. **a** Structure of **33**-*Z*-(*S*)-(S_a) including arrows depicting observed NOE signals (left). *Newman* projection of the biaryl axis showing the preferred tilt of the two biaryl planes (right). **b** NOESY NMR spectrum (CD_2Cl_2, 800 MHz, 25 °C) of **33**-*Z*-(*S*)-(S_a) displaying cross signals of H_3C36 and H_3C37 to HC24. Intensity difference indicates non-orthogonality of the two biaryl planes and proximity between HC24 and H_3C37 is revealed because of increased signal strength. Therefore, a preferred tilt of the covalent linker anchoring point C23 towards H_3C37 and the PEG chain is established. Adapted with minor format modifications from *Nat. Commun.* **2023**, *14*, 4595 licensed under CC BY 4.0.[1]

6.5.2.4. 33-*E*-(*S*)-(*R*$_a$) = 33-*E*-II

Proximity of indanone proton HC8 and aromatic triazole proton HC33 to benzothiophenone methyl group H_3C36 revealed *E*-configuration of the central double bond in **33**-*E*-(*S*)-(*S*$_a$), shown in Figure 119.

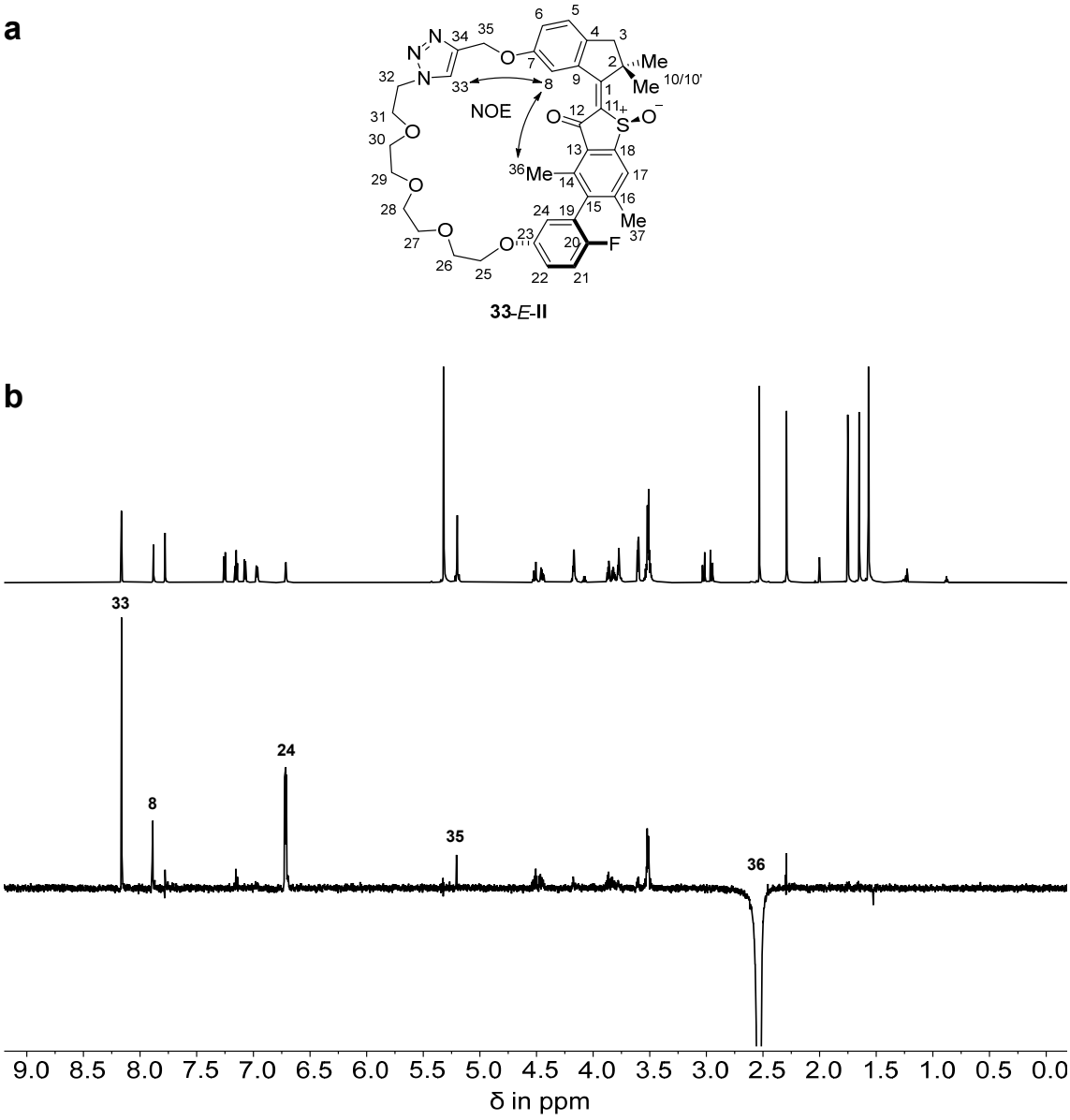

Figure 119 Double bond configuration analysis of isomer **33**-*E*-(*S*)-(*R*$_a$) measured in CD_2Cl_2 solution at 25 °C. **a** Structure of **33**-*E*-(*S*)-(*R*$_a$) including arrows depicting observed NOE signals. **b** ^{1}H (top) and NOE (bottom) NMR spectra (600 MHz, CD_2Cl_2, 25 °C) of **33**-*E*-(*S*)-(*R*$_a$) display proximity of HC8 and HC33 to H_3C36, revealing *E*-configuration of the double bond. Adapted with minor format modifications from *Nat. Commun.* **2023**, *14*, 4595 licensed under CC BY 4.0.[1]

Proximity of indanone proton HC8 and aromatic triazole proton HC33 to benzothiophenone methyl group H_3C36 revealed *E*-configuration of the central double bond in **33**-*E*-(*S*)-(*M*/*P*)-(S_a) observed in the 2D NOESY NMR experiment, shown in Figure 120.

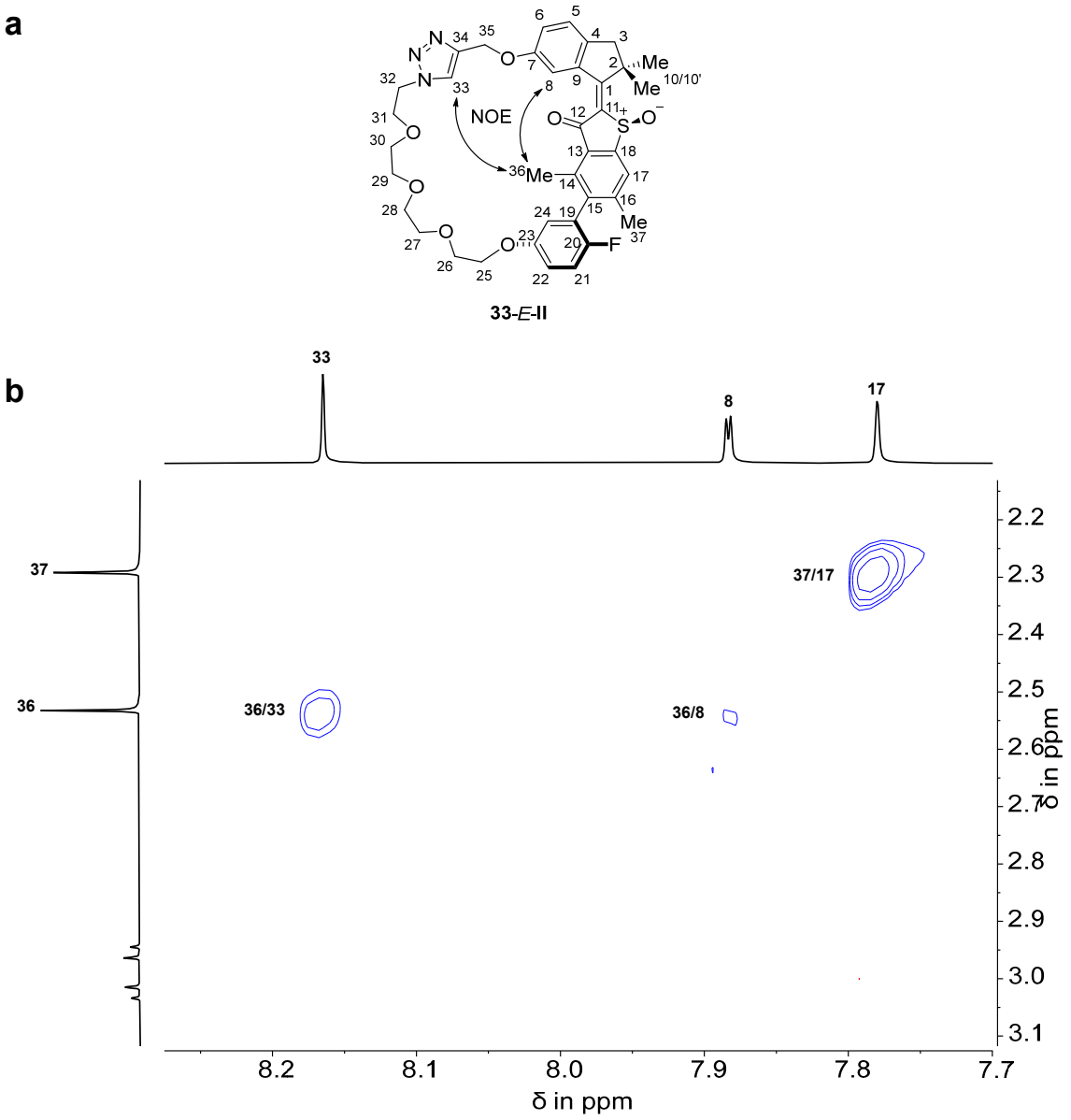

Figure 120 Double bond configuration analysis of **33**-*E*-(*S*)-(R_a) measured in CD_2Cl_2 solution at 25 °C. **a** Structure of **33**-*E*-(*S*)-(R_a) including arrows depicting observed NOE signals. **b** NOESY NMR spectrum (CD_2Cl_2, 800 MHz, 25 °C) of **33**-*E*-(*S*)-(R_a) reveals *E*-configuration of the double bond through a strong cross signal between H_3C36 and HC33 as well as HC8. Adapted with minor format modifications from *Nat. Commun.* **2023**, *14*, 4595 licensed under CC BY 4.0.[1]

Stronger signal intensity of aromatic *ortho*-biaryl proton HC24 to benzothiophenone methyl group H_3C36 revealed tilt of the covalent linker anchoring point on the biaryl towards the carbonyl side of the benzothiophenone fragment shown in Figure 121b. The tilt of the two biaryl planes is further illustrated in the *Newman* projection along the biaryl axis in Figure 121a.

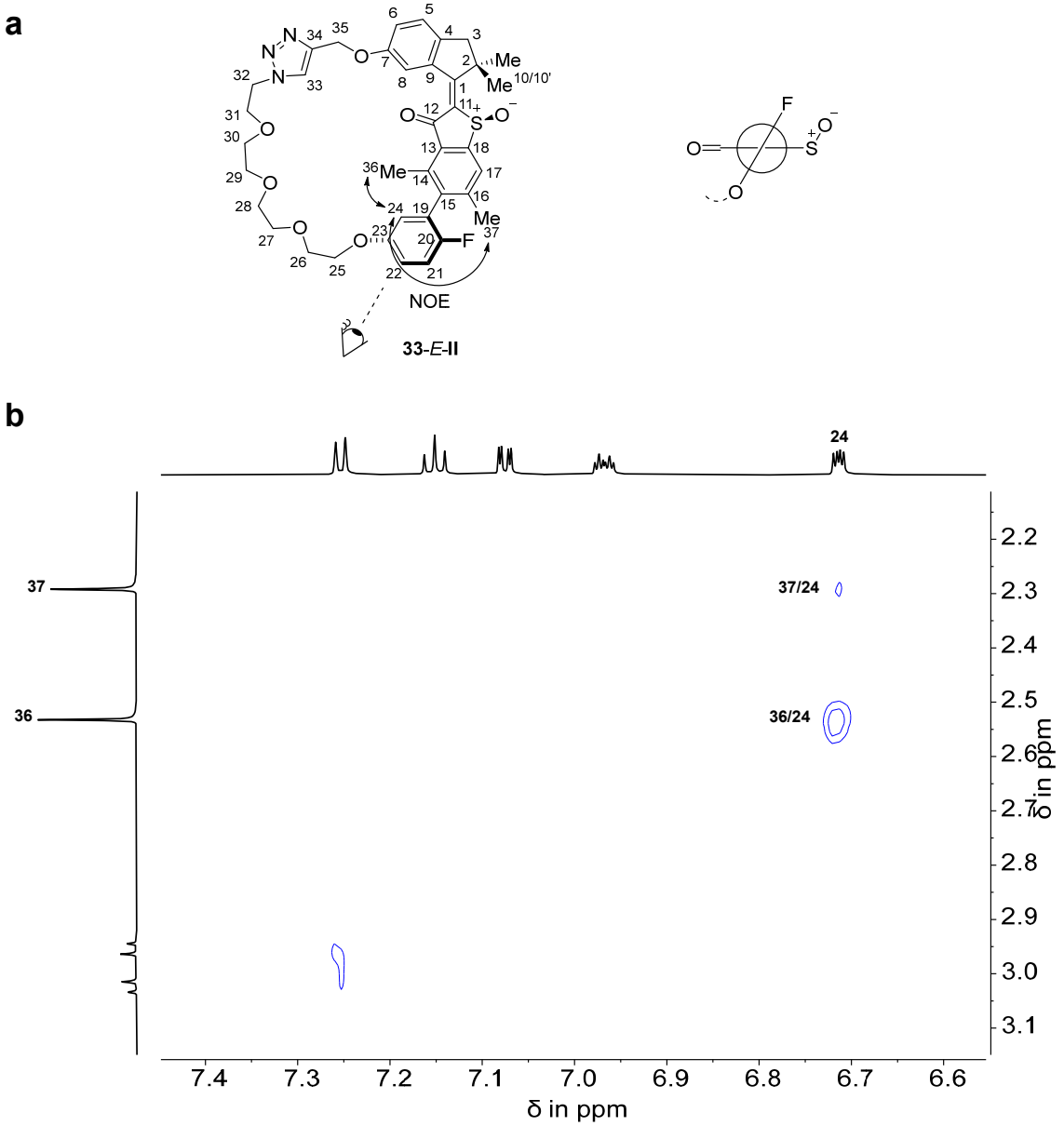

Figure 121 Biaryl axis tilt analysis of **33**-*E*-(*S*)-(R_a) measured in CD_2Cl_2 solution at 25 °C. **a** Structure of **33**-*E*-(*S*)-(R_a) including arrows depicting observed NOE signals (left). *Newman* projection of the biaryl axis showing the preferred tilt of the two biaryl planes (right). **b** NOESY NMR spectrum (CD_2Cl_2, 800 MHz, 25 °C) of **33**-*E*-(*S*)-(R_a) displaying cross signals of H_3C36 and H_3C37 to HC24. Intensity difference indicates non-orthogonality of the two biaryl planes and proximity between HC24 and H_3C36 is revealed because of increased signal strength. Therefore, a preferred tilt of the covalent linker anchoring point C23 towards H_3C36 and the PEG chain is established. Adapted with minor format modifications from *Nat. Commun.* **2023**, *14*, 4595 licensed under CC BY 4.0.[1]

6.5.2.5. 33-*Z*-(*S*)-(*R*$_a$) = 33-*Z*-II

Proximity of benzothiophenone proton HC17 to aromatic triazole proton HC8 and indanone proton HC8 revealed *Z*-configuration of the central double bond in **33**-*Z*-(*S*)-(*S*$_a$), shown in Figure 122.

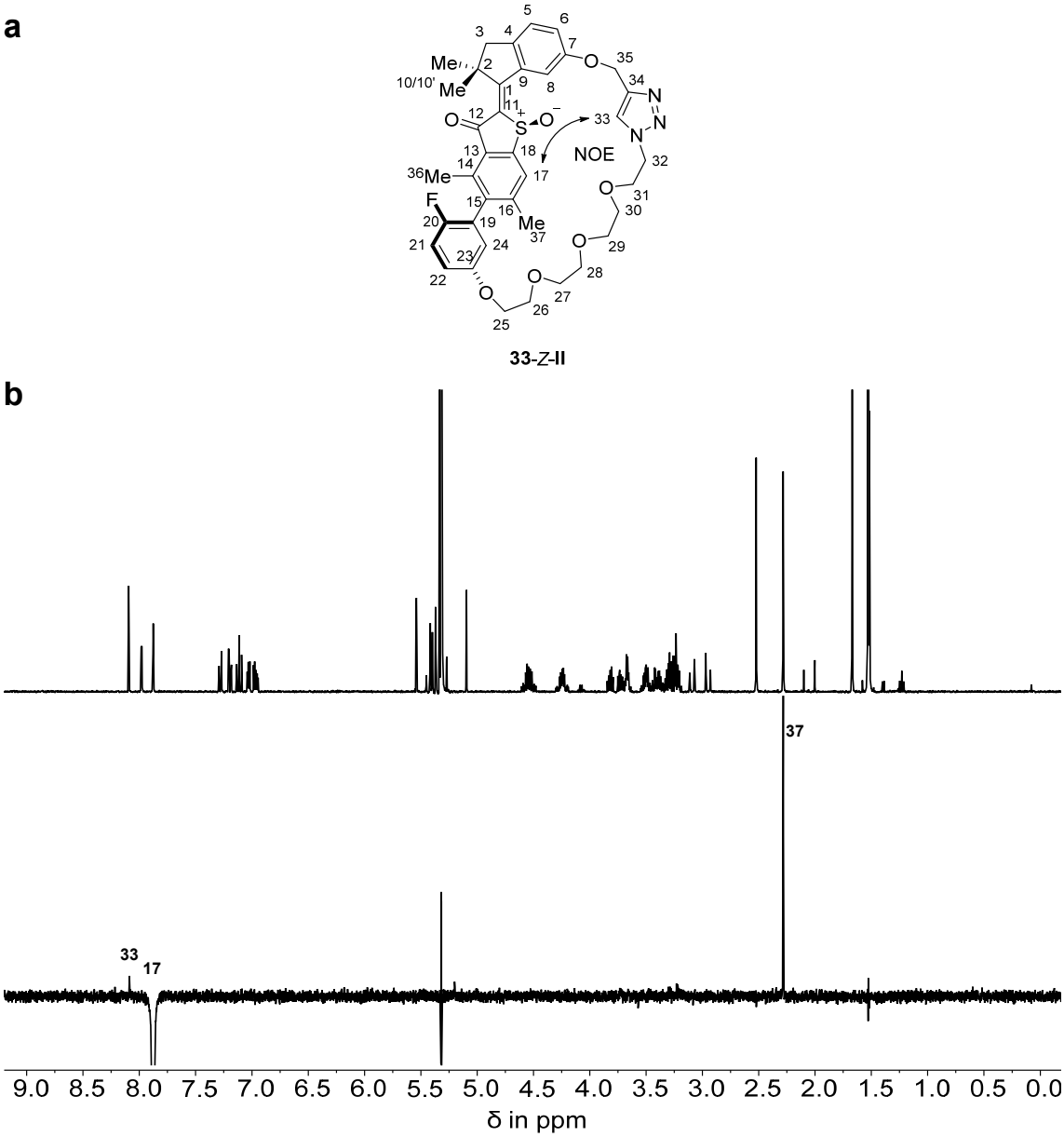

Figure 122 Double bond configuration analysis of isomer **33**-*Z*-(*S*)-(*R*$_a$) measured in CD_2Cl_2 solution at 25 °C. **a** Structure of **33**-*Z*-(*S*)-(*R*$_a$) including arrows depicting observed NOE signals. **b** ^{1}H (top) and NOE (bottom) NMR spectra (600 MHz, CD_2Cl_2, 25 °C) of **33**-*Z*-(*S*)-(*R*$_a$) display proximity of HC17 to HC33, revealing *Z*-configuration of the double bond. Adapted with minor format modifications from *Nat. Commun.* **2023**, *14*, 4595 licensed under CC BY 4.0.[1]

Proximity of aromatic benzothiophenone proton HC17 and covalent linker protons H_2C29, H_2C30, H_2C31 and H_2C32 revealed *Z*-configuration of the central double bond in **33**-*E*-(*S*)-(*M*/*P*)-(S_a) observed in the 2D NOESY NMR experiment, shown in Figure 123.

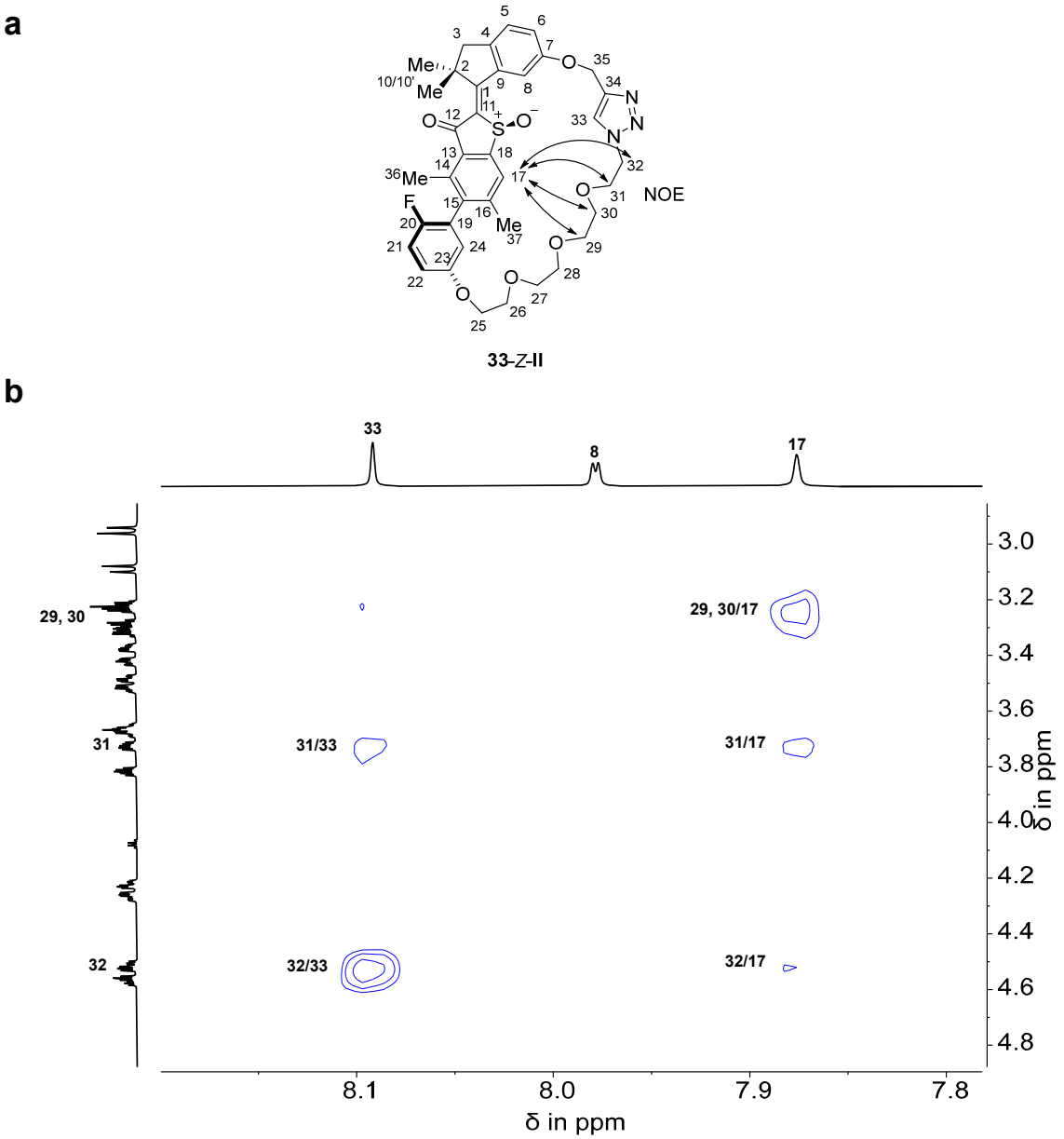

Figure 123 Double bond configuration analysis of **33**-*Z*-(*S*)-(R_a) measured in CD_2Cl_2 solution at 25 °C. **a** Structure of **33**-*Z*-(*S*)-(R_a) including arrows depicting observed NOE signals (left). **b** NOESY NMR spectrum (CD_2Cl_2, 800 MHz, 25 °C) of **33**-*Z*-(*S*)-(R_a) reveals *Z*-configuration of the double bond through cross signals between HC17 and H_2C29, H_2C30, H_2C31, and H_2C32 of the covalent linker chain. Adapted with minor format modifications from *Nat. Commun.* **2023**, *14*, 4595 licensed under CC BY 4.0.[1]

Stronger signal intensity of aromatic *ortho*-biaryl proton HC24 to benzothiophenone methyl group H_3C37 revealed tilt of the covalent linker anchoring point on the biaryl towards the sulfoxide side of the benzothiophenone fragment shown in Figure 124b. The tilt of the two biaryl planes is further illustrated in the *Newman* projection along the biaryl axis in Figure 124a.

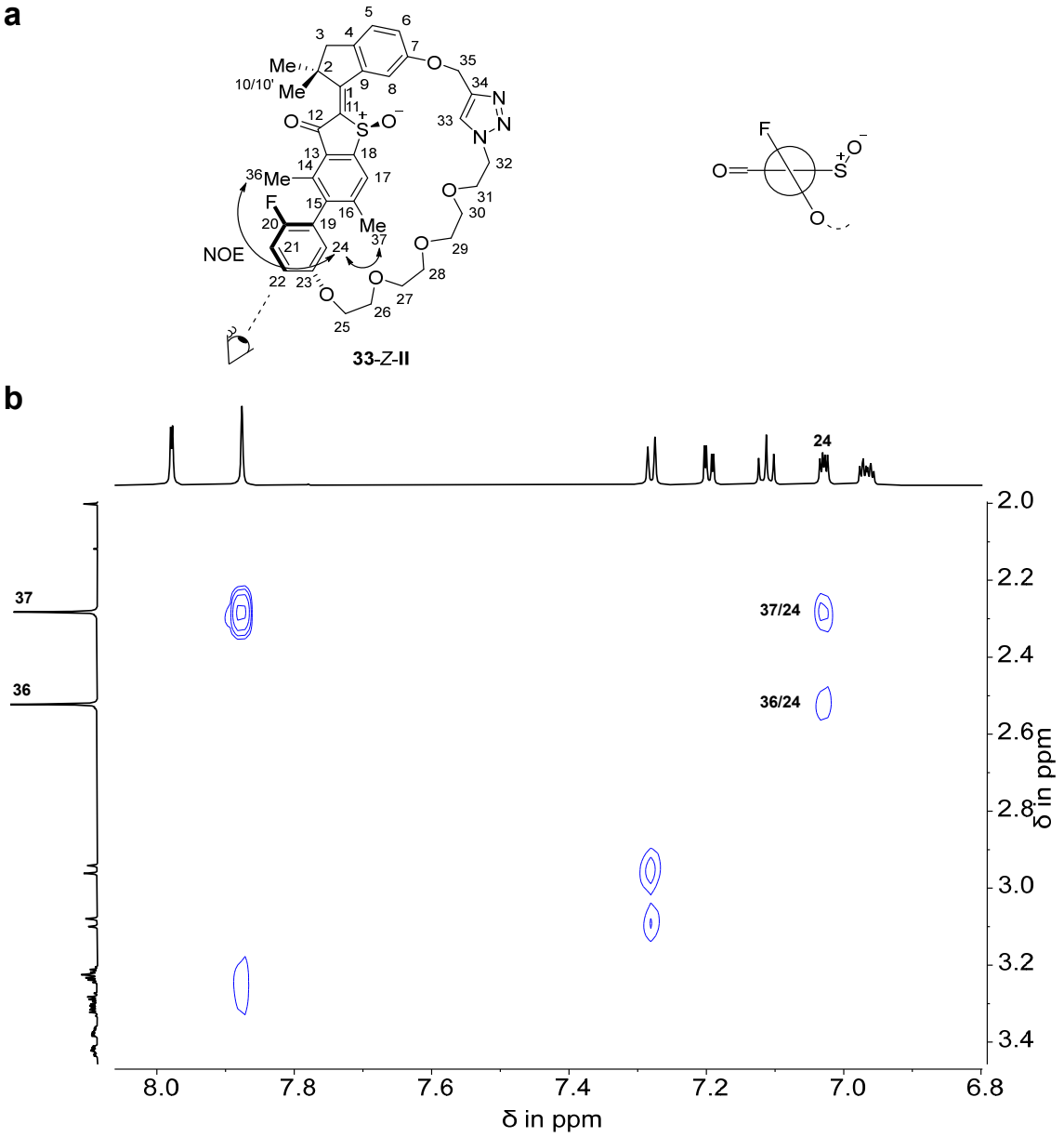

Figure 124 Biaryl axis tilt analysis of **33**-*Z*-(*S*)-(R_a) measured in CD_2Cl_2 solution at 25 °C. **a** Structure of **33**-*Z*-(*S*)-(R_a) including arrows depicting observed NOE signals (left). *Newman* projection of the biaryl axis showing the preferred tilt of the two biaryl planes (right). **b** NOESY NMR spectrum (CD_2Cl_2, 800 MHz, 25 °C) of **33**-*Z*-(*S*)-(R_a) displaying cross signals of H_3C36 and H_3C37 to HC24. Intensity difference indicates non-orthogonality of the two biaryl planes and proximity between HC24 and H_3C37 is revealed because of increased signal strength. Therefore, a preferred tilt of the covalent linker anchoring point C23 towards H_3C37 and the PEG chain is established. Adapted with minor format modifications from *Nat. Commun.* **2023**, *14*, 4595 licensed under CC BY 4.0.[1]

6.5.3. Overview of conformational states for HTI 15h

The same analytical methods which were employed for molecular machine **33** were also applied for conformer analysis of prospective fast molecular motor **15h**. An overview of stable states at 22 °C is given in Figure 125. The helicity of motor core was omitted for all isomers since clear assignment was hampered because of the highly dynamic nature of this stereo element. For assignment of ^{1}H and ^{13}C signals and more analytical details, see chapter 8.5.2 or the corresponding literature.[1]

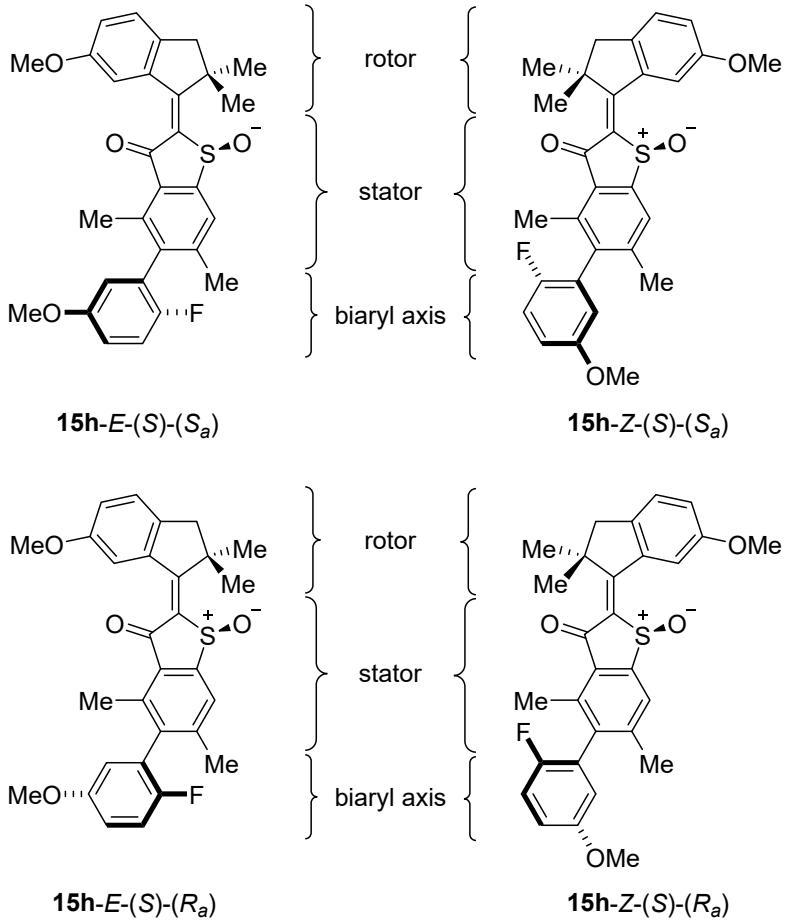

Figure 125 Overview of the isomeric states **15h**-*E*-(*S*)-(R_a), **15h**-*Z*-(*S*)-(R_a), **15h**-*E*-(*S*)-(S_a), and **15h**-*Z*-(*S*)-(S_a), which are stable at 22 °C. For clarity only structures with *S*-configured sulfoxide are depicted. The set of isomers consists of two *E*- and two *Z*-configured isomers with either a R_a- or S_a-configured atropisomer respectively. The helicity of the rotor fragment is highly dynamic and can thus not be determined with certainty at ambient temperatures. Adapted with minor format modifications from *Nat. Commun.* **2023**, *14*, 4595 licensed under CC BY 4.0.[1]

6.5.4. Structure of HTI 15h in solution

Three-dimensional structure analysis *via* NMR experiments was done according to the procedure described for macrocyclic machine **33** in chapter 6.5, investigating *E*- or *Z*-configuration of the central double bond. As a result of the highly dynamic nature of the motor core helicity, clear assignment was severely hampered and thus omitted for all isomers.

6.5.4.1. Overview of all observed HTI 15h conformations in solution

A comparison of all isomers stable at 22 °C showing distinct shifts of aromatic protons can be found in Figure 126. A distinct shift of the indanone protons HC6 can be observed with approximately 7.05 for *E*-isomers and 7.15 ppm for *Z*-isomers and HC8 with 8.10 for *E*-isomers and 7.85 ppm for *Z*-isomers. For assignment detailed ^{1}H assignments, see chapter 8.5.2 or the corresponding literature.[1]

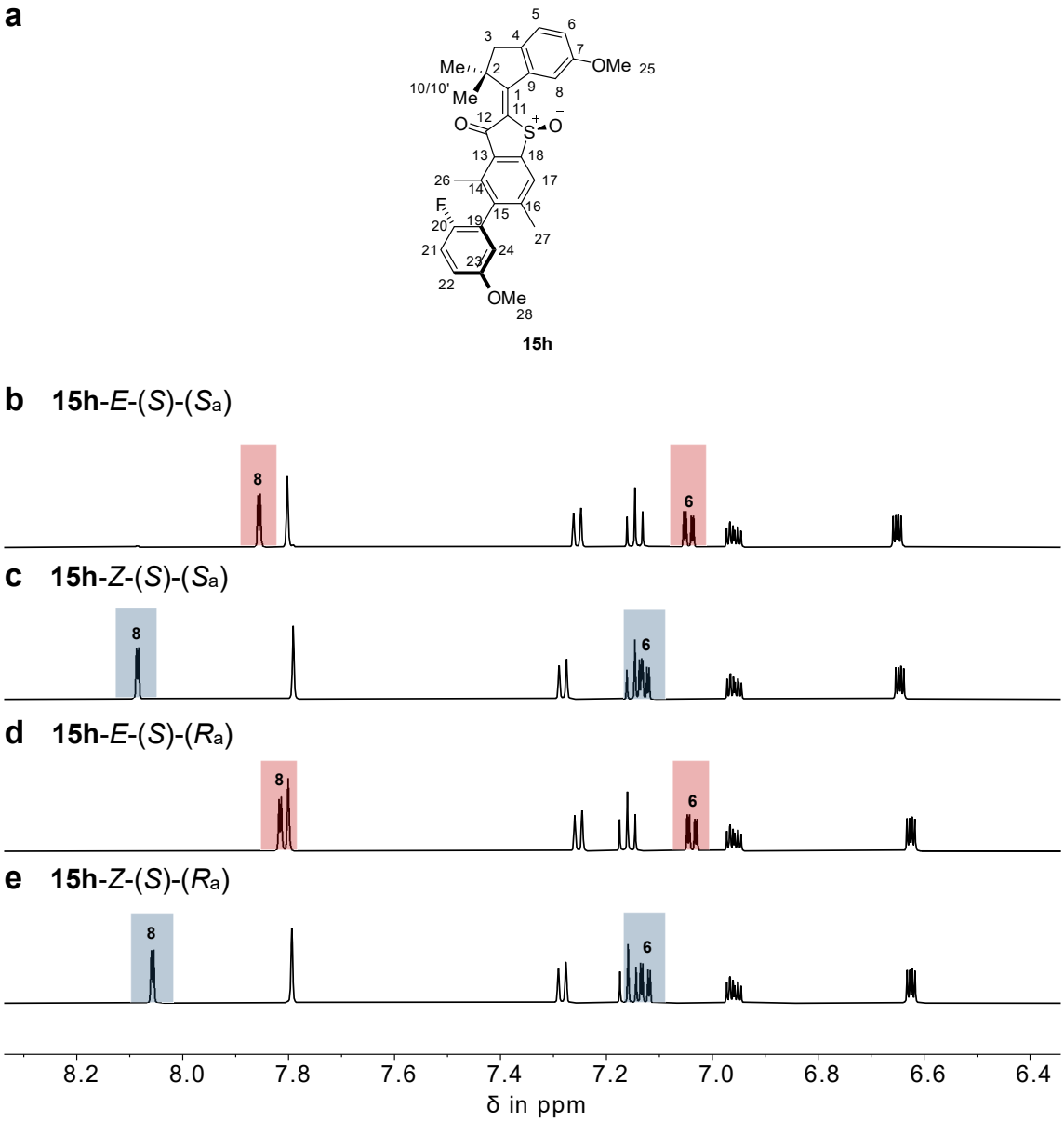

Figure 126 ^{1}H NMR spectra (601 MHz, CD_2Cl_2, 25 °C) overview of all HTI **15h** isomers measured at 22 °C. **a** Structural representation of non-cyclic **15h**. Aromatic region of isomers (**b**) **15h**-*E*-(*S*)-(S_a), (**c**) **15h**-*Z*-(*S*)-(S_a), (**d**) **15h**-*E*-(*S*)-(R_a), and (**e**) **15h**-*Z*-(*S*)-(R_a) from top to bottom. The distinct shift of indanone protons HC6 and HC8 with approximately 7.05 and 8.10 ppm respectively is highlighted in red for *E*-isomers as well as 7.15 and 7.85 ppm for *Z*-isomers in blue.

6.5.4.2. Isomer 15h-E-(S)-(Sa)

Proximity of aromatic benzothiophenone proton HC17 to aliphatic methyl groups H_3C10 and H_3C10' revealed *E*-configuration of the central double bond in **15h**-*E*-(*S*)-(S_a), shown in Figure 127.

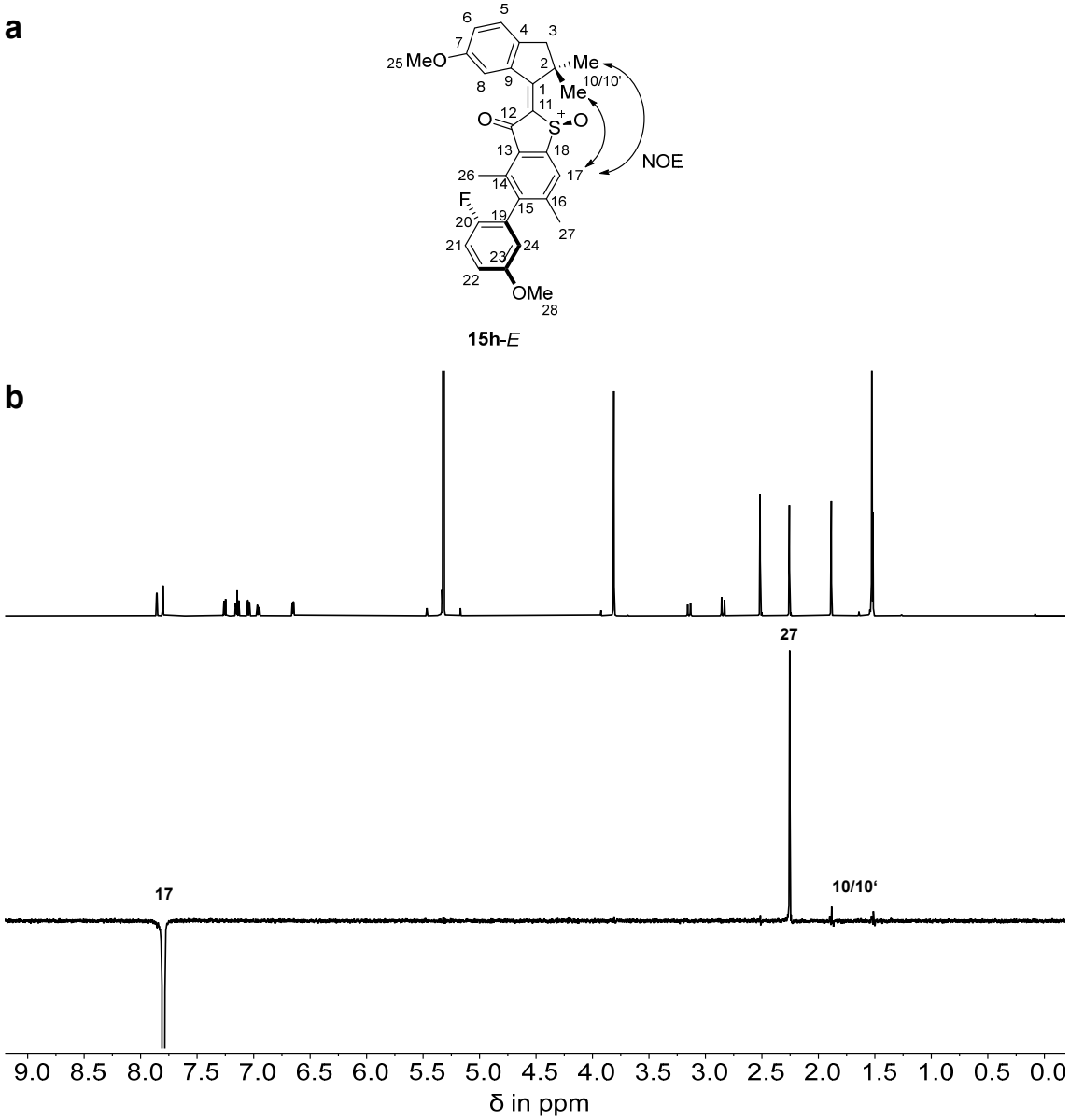

Figure 127 Double bond configuration analysis of isomer **15h**-*E*-(*S*)-(S_a) measured in CD_2Cl_2 solution at 25 °C. **a** Structure of **15h**-*E*-(*S*)-(S_a) including arrows depicting observed NOE signals. **b** ^{1}H (top) and NOE (bottom) NMR spectra (600 MHz, CD_2Cl_2, 25 °C) of **15h**-*E*-(*S*)-(S_a) display proximity of HC17 to H_3C10 and H_3C10', revealing *E*-configuration of the double bond. Adapted with minor format modifications from *Nat. Commun.* **2023**, *14*, 4595 licensed under CC BY 4.0.[1]

6.5.4.3. Isomer 15h-*Z*-(*S*)-(S_a)

Proximity of aromatic benzothiophenone proton HC17 to methoxy group H_3C25 revealed *Z*-configuration of the central double bond in **15h**-*Z*-(*S*)-(S_a), shown in Figure 128.

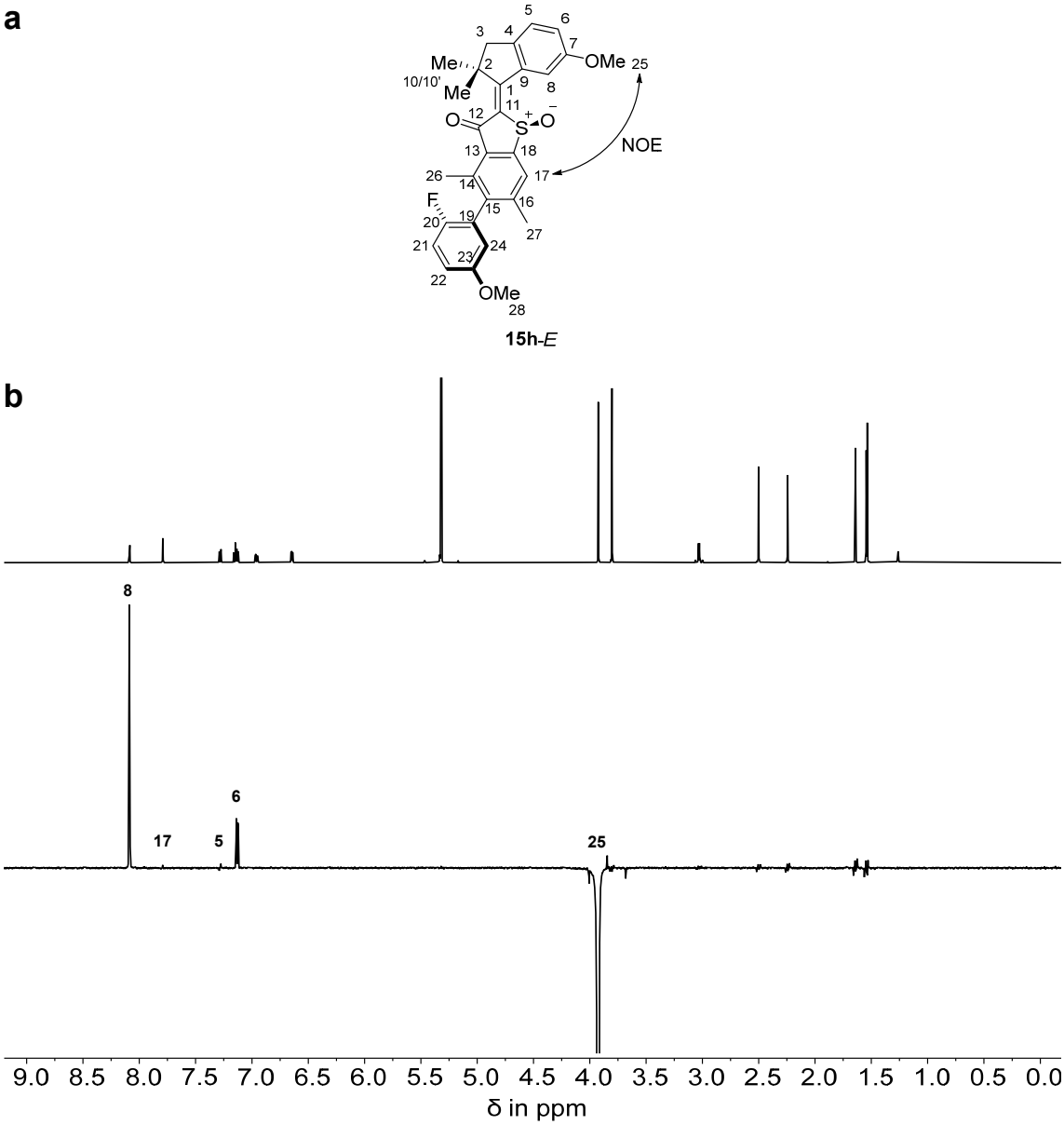

Figure 128 Double bond configuration analysis of isomer **15h**-*Z*-(*S*)-(S_a) measured in CD_2Cl_2 solution at 25 °C. **a** Structure of **15h**-*Z*-(*S*)-(S_a) including arrows depicting observed NOE signals. **b** ^1H (top) and NOE (bottom) NMR spectra (600 MHz, CD_2Cl_2, 25 °C) of **3**-*Z*-(*S*)-(S_a) display proximity of H_3C25 to HC17, revealing *Z*-configuration of the double bond. Adapted with minor format modifications from *Nat. Commun.* **2023**, *14*, 4595 licensed under CC BY 4.0.[1]

6.5.4.4. Isomer 15h-*E*-(*S*)-(*R*$_a$)

Proximity of aromatic benzothiophenone methyl group H_3C26 to methoxy group H_3C25 revealed *E*-configuration of the central double bond in **15h**-*E*-(*S*)-(*R*$_a$), shown in Figure 129.

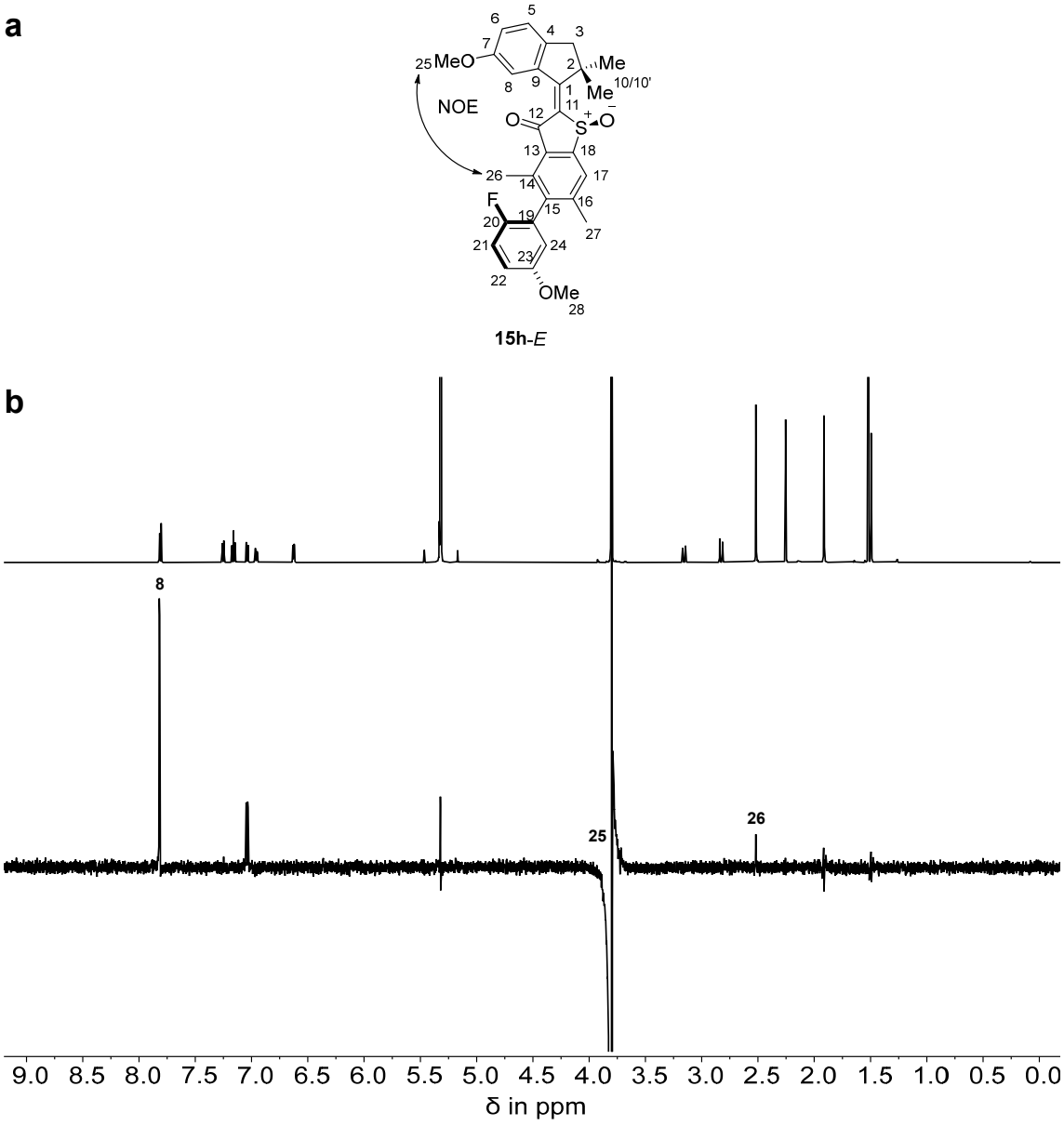

Figure 129 Double bond configuration analysis of isomer **15h**-*E*-(*S*)-(*R*$_a$) measured in CD_2Cl_2 solution at 25 °C. **a** Structure of **15h**-*E*-(*S*)-(*R*$_a$) including arrows depicting observed NOE signals. **b** ^{1}H (top) and NOE (bottom) NMR spectra (600 MHz, CD_2Cl_2, 25 °C) of **3**-*E*-(*S*)-(*R*$_a$) display proximity of H_3C25 to H_3C26 but not H_3C27, revealing *E*-configuration of the double bond. Adapted with minor format modifications from *Nat. Commun.* **2023**, *14*, 4595 licensed under CC BY 4.0.[1]

6.5.4.5. Isomer 15h-*Z*-(*S*)-(*R*$_a$)

Proximity of aromatic benzothiophenone methyl group H_3C26 to aliphatic methyl groups H_3C10 and H_3C10' revealed *Z*-configuration of the central double bond in **15h**-*Z*-(*S*)-(*R*$_a$), shown in Figure 130.

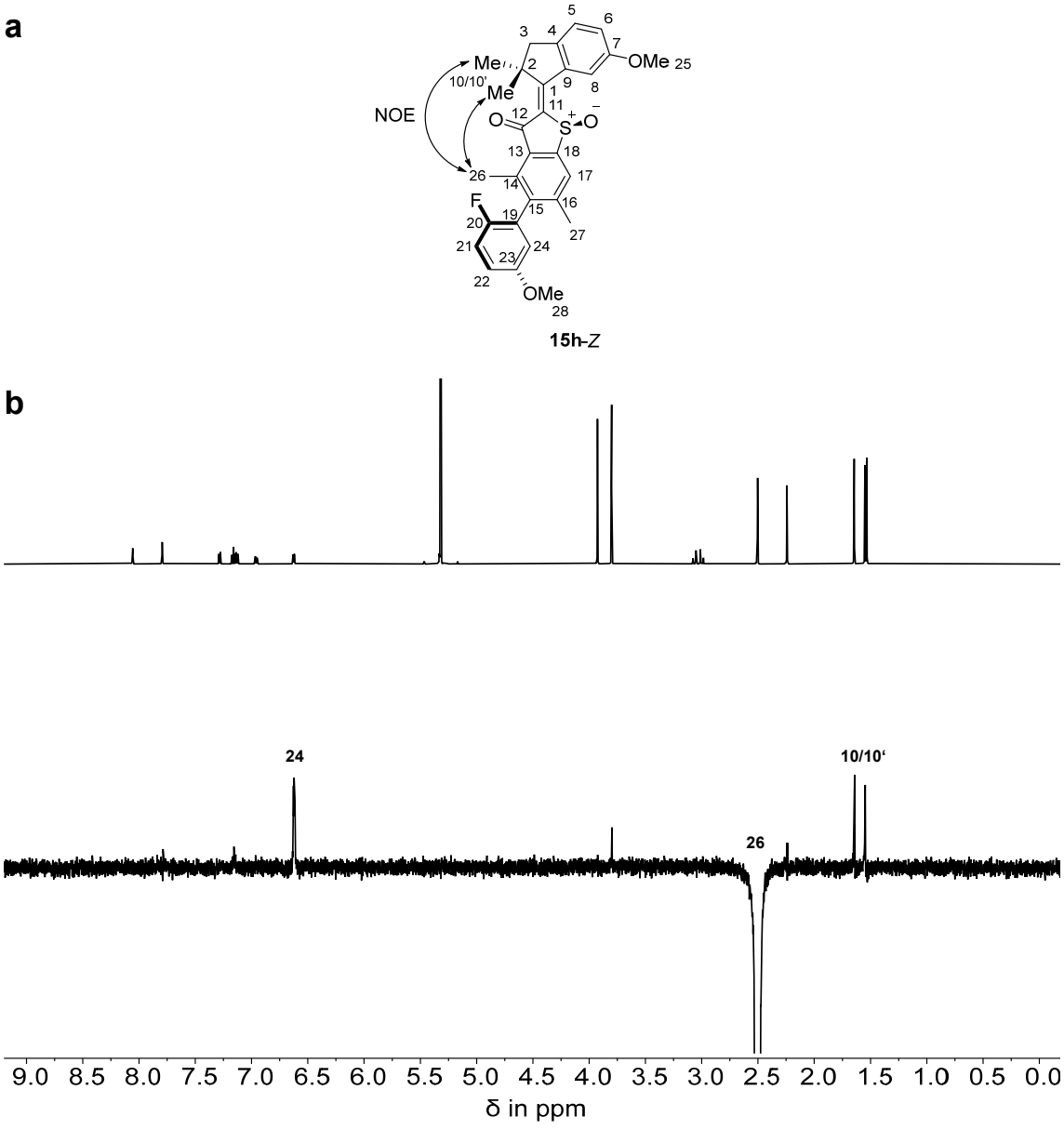

Figure 130 Double bond configuration analysis of isomer **15h**-*Z*-(*S*)-(*R*$_a$) measured in CD_2Cl_2 solution at 25 °C. **a** Structure of **15h**-*Z*-(*S*)-(*R*$_a$) including arrows depicting observed NOE signals. **b** ^{1}H (top) and NOE (bottom) NMR spectra (600 MHz, CD_2Cl_2, 25 °C) of **3**-*Z*-(*S*)-(*R*$_a$) display proximity of H_3C26 to H_3C10 and H_3C10', revealing *Z*-configuration of the double bond. Adapted with minor format modifications from *Nat. Commun.* **2023**, *14*, 4595 licensed under CC BY 4.0.[1]

6.6. Comparison of macrocyclic HTI 33 and unrestricted HTI 15h in solution

A comparison of signals from macrocyclic HTI-based machine **33** and prospective molecular motor **15h** showing distinct shifts of aromatic protons can be found in Figure 131. A distinct shift of the *ortho*-biaryl proton HC24 in **33** and in **15h** can be observed at approximately 6.70 and 7.05 ppm for *E*-isomers and 7.10 and 7.15 ppm for *Z*-isomers respectively.

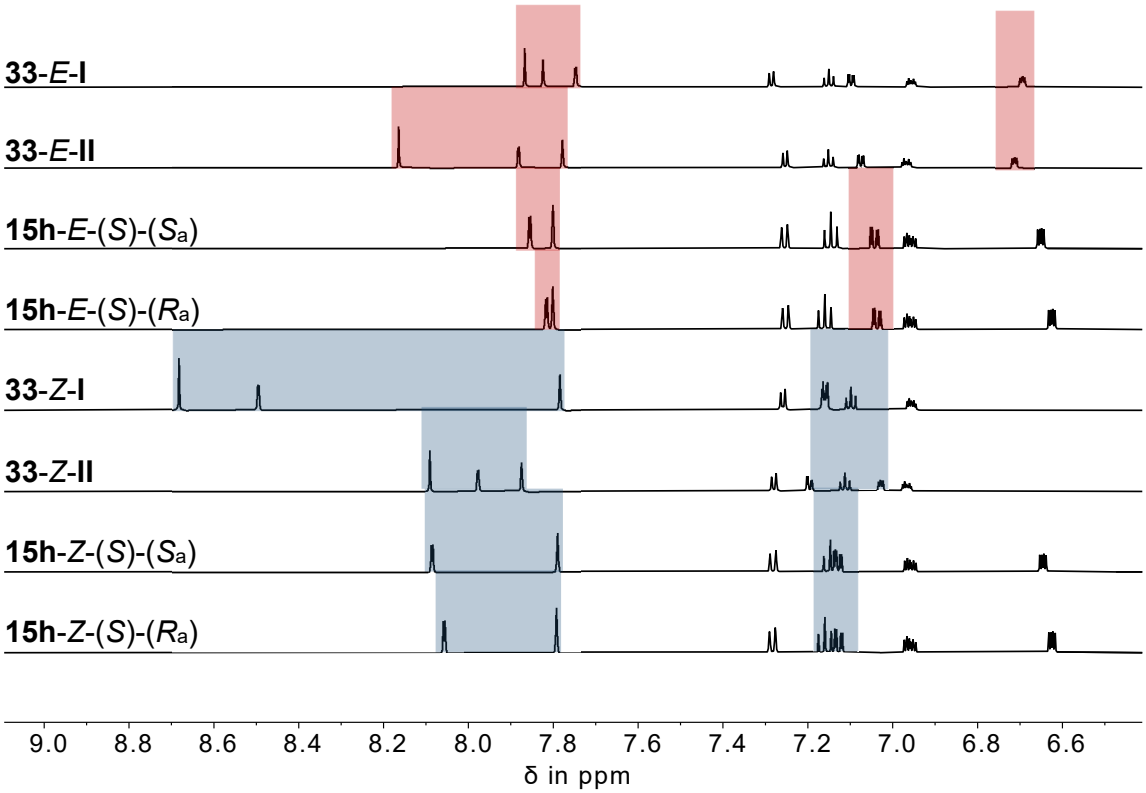

Figure 131 Comparison of aromatic spectral regions for HTIs **15h** and **33**. ^{1}H NMR spectra (400 MHz, CD_2Cl_2, 25 °C) of macrocyclic isomers **33**-*E*-**I**, **33**-*E*-**II**, **33**-*Z*-**I** and **33**-*Z*-**II** compared with non-cyclic isomers **15h**-*E*-(*S*)-(S_a), **15h**-*E*-(*S*)-(R_a), **15h**-*Z*-(*S*)-(S_a) and **15h**-*Z*-(*S*)-(R_a) highlighting the most distinctly shifted aromatic signals of *Z*- (blue) and *E*-isomers (red).

The same is possible when comparing ^{19}F NMR spectra, which allow determination of each isomer from **15h** and **33** within a few minutes only. A stack of all ^{19}F spectral signals is shown in Figure 132.

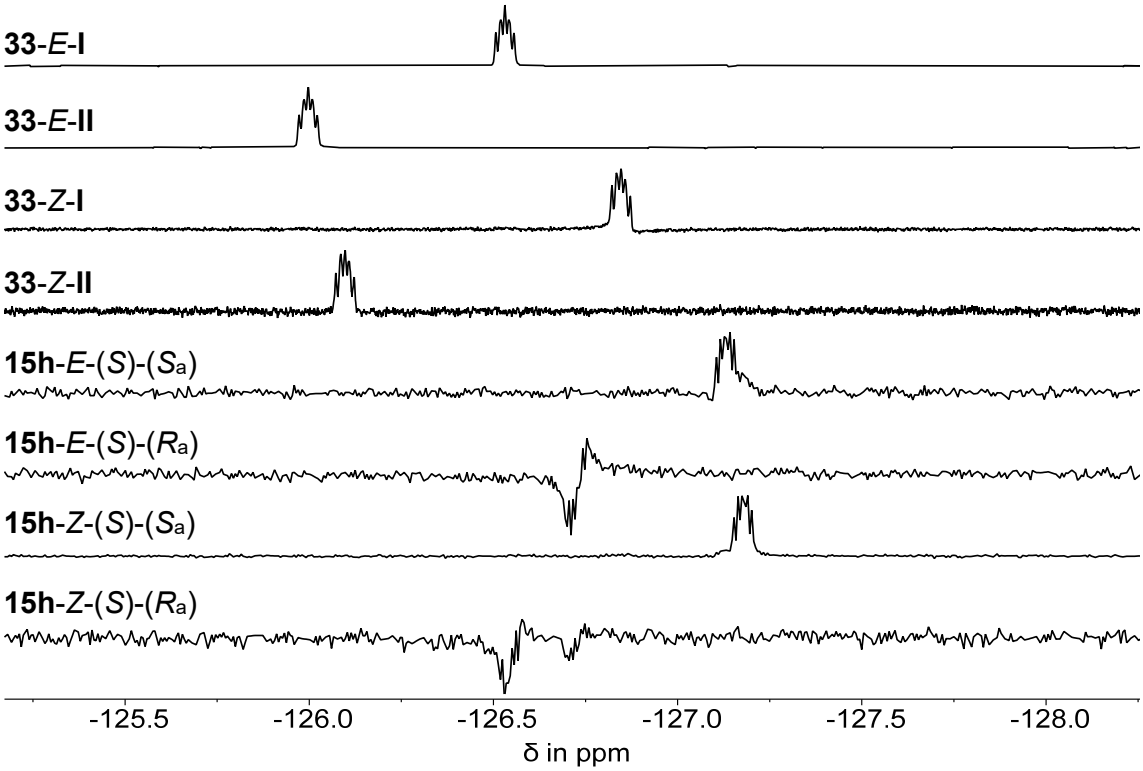

Figure 132 Comparison ^{19}F NMR signals of HTIs **15h** and **33**. ^{19}F NMR spectra (377 MHz, CD_2Cl_2, 25 °C) of macrocyclic isomers **33**-*E*-**I** (−126.53 ppm), **33**-*E*-**II** (−126.00 ppm), **33**-*Z*-**I** (−126.85 ppm) and **33**-*Z*-**II** (−126.10 ppm) with reference compound **15h**-*E*-(*S*)-(S_a) (−127.11 ppm), **15h**-*E*-(*S*)-(R_a) (−126.76 ppm), **15h**-*Z*-(*S*)-(S_a) (−127.17 ppm) and **15h**-*Z*-(*S*)-(R_a) (−126.53 ppm).

6.7. Structures in the crystalline state

Double bond and atropisomer configurations could be directly assigned to isomers **33**-*Z*-**I**, **33** *E*-**II**, **33**-*Z*-**II**, **51**-***E*** and **15h** from crystal structures shown in Figure 133–137. All crystal structures were determined by *Dr. Peter Mayer* (**33**-*Z*-**I**, **33**-*E*-**II**, **33**-*Z*-**II**, and **51**-***E***) and *Dr. Frank Hampel* (**15h**-*Z*).[VII,VIII]

6.7.1. Isomer 33-*Z*-I

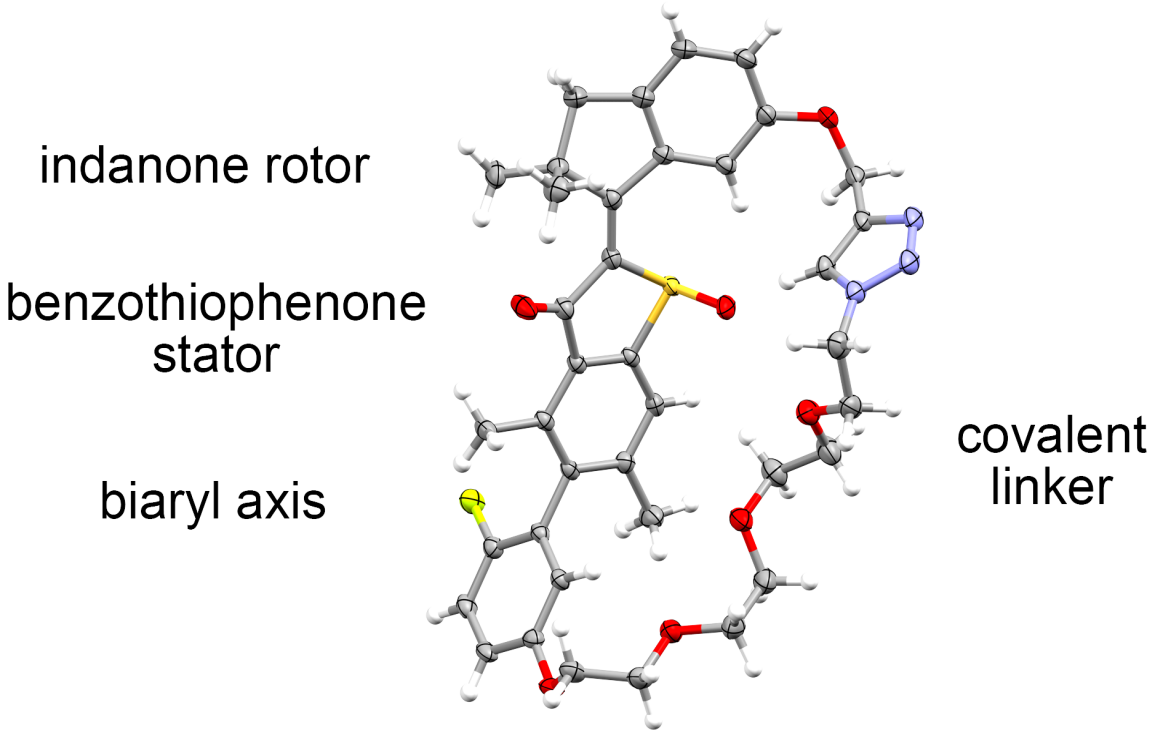

Figure 133 Structure of racemic isomer **33**-*Z*-**I** in the crystalline state clearly allowing the assignment of a *Z*-configured double bond of the motor unit, *S*-configured sulfoxide, as well as S_a-configured biaryl axis, which is tilted towards the attachment point of the linker on the rotor moiety. Taken together all stereo-elements macrocyclic **33**-*Z*-**I** adopts *Z*-(*S*)-(*M*)-(S_a) configuration in the solid state (the enantiomeric *Z*-(*R*)-(*P*)-(R_a) configuration is not shown for clarity). Adapted with minor format modifications from *Nat. Commun.* **2023**, *14*, 4595 licensed under CC BY 4.0.[1]

6.7.2. Isomer 33-*E*-II

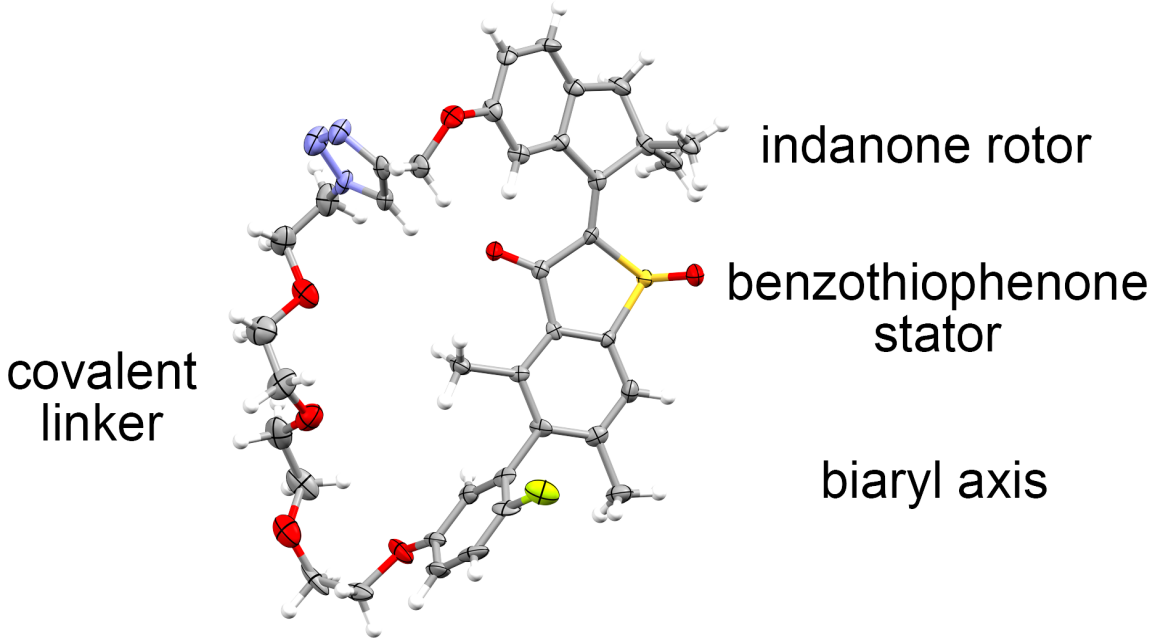

Figure 134 Structure of racemic isomer **33**-*E*-**II** in the crystalline state clearly allowing the assignment of an *E*-configured double bond of the motor unit, *S*-configured sulfoxide, as well as R_a-configured biaryl axis, which is tilted towards the attachment point of the linker on the rotor moiety. Taken together all stereo-elements macrocyclic **33**-*E*-**II** adopts *E*-(*S*)-(*P*)-(R_a) configuration in the solid state (the enantiomeric *E*-(*R*)-(*M*)-(S_a) configuration is not shown for clarity). Adapted with minor format modifications from *Nat. Commun.* **2023**, *14*, 4595 licensed under CC BY 4.0.[1]

6.7.3. Isomer 33-Z-II

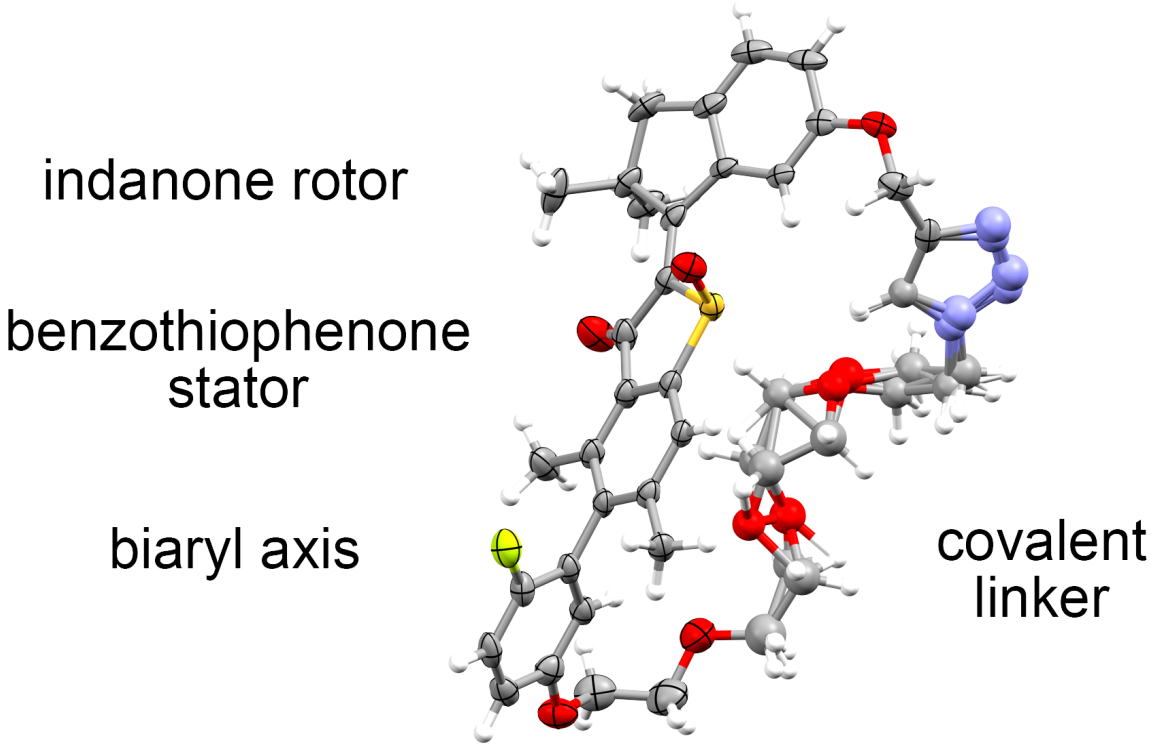

Figure 135 Structure of racemic isomer **33**-*Z*-**II** in the crystalline state clearly allowing the assignment of an *E*-configured double bond of the motor unit, *S*-configured sulfoxide, as well as R_a-configured biaryl axis, which is tilted towards the attachment point of the linker on the rotor moiety. Taken together all stereo-elements macrocyclic **33**-*E*-**II** adopts *Z*-(*S*)-(*P*)-(R_a) configuration in the solid state (the enantiomeric *Z*-(*R*)-(*M*)-(S_a) configuration is not shown for clarity). Adapted with minor format modifications from *Nat. Commun.* **2023**, *14*, 4595 licensed under CC BY 4.0.[1]

With the thermally highly stable biaryl axes and crystal structures for three isomers of **33**, relative configurations could be assigned to the corresponding isomers observed at 22 °C leaving only a single option for the last isomer. With this analysis all stereocenters of macromolecular machine **33** can be assigned solely from crystal structures. However, additional experimental evidence was used to support the findings from X-ray crystallographic analysis in the solid state.

6.7.4. Isomer 15h-*E*-(*R*)-(R_a)

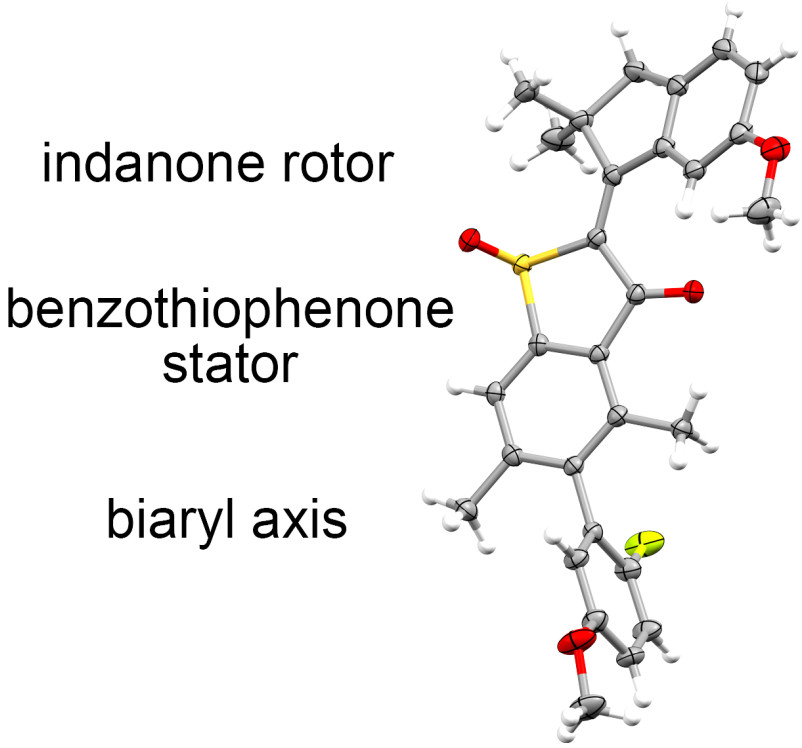

Figure 136 Structure of enantiomerically pure isomer **15h**-*E*-(*R*)-(R_a) in the crystalline state clearly allowing the assignment of an *E*-configured double bond of the motor unit, *R*-configured sulfoxide, as well as R_a-configured biaryl axis. Taken together all stereo-elements **15h**-*E*-(*R*)-(R_a) adopts *E*-(*R*)-(*M*)-(R_a) configuration in the solid state. Adapted with minor format modifications from *Nat. Commun.* **2023**, *14*, 4595 licensed under CC BY 4.0.[1]

6.7.5. Isomer 51-*Z*-(S_a/R_a)

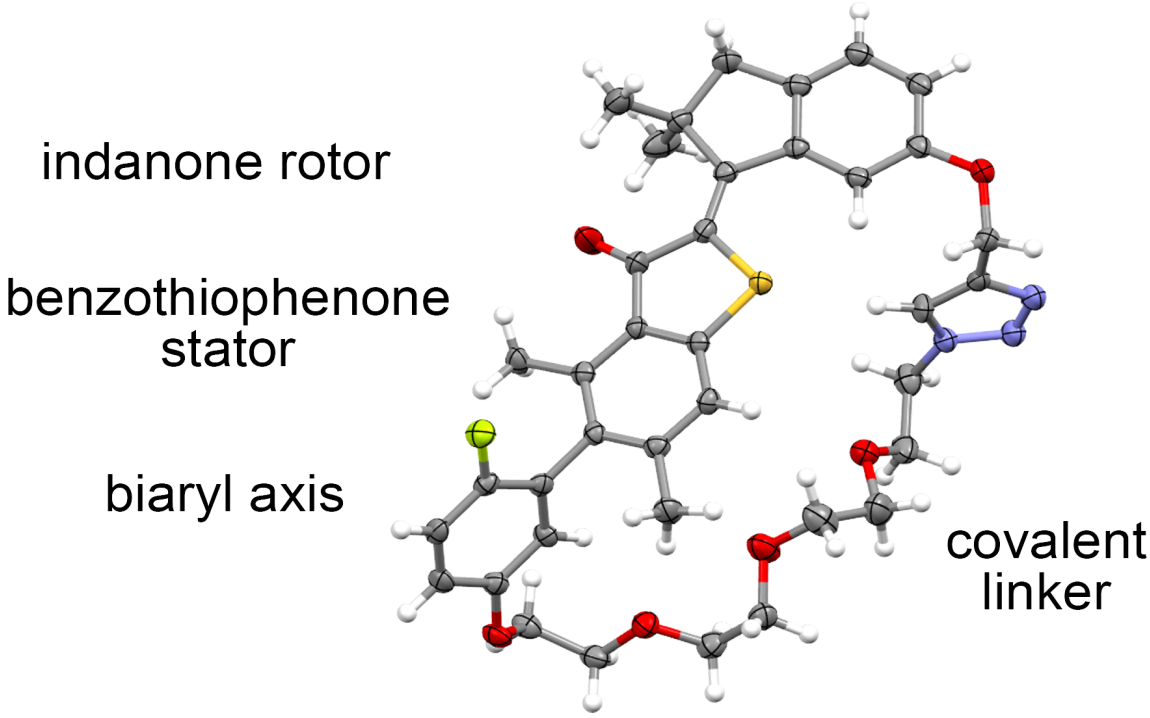

Figure 137 Structure of racemic isomer **51**-*Z*-(R_a) in the crystalline state clearly allowing the assignment of a *Z*-configured double bond of the motor unit as well as R_a-configured biaryl axis. Taken together all stereo-elements **51**-*Z*-(R_a) adopts *Z*-(R_a)-configuration in the solid state.

Taken together, based on the crystalline states obtained for HTI **15h** and **33** in combination with NMR and theoretical analysis see chapter 6.5.3 and 6.13, it seems impossible to deduce any trend for observed helicities. According to the theoretical description (see chapter 6.13), helix inversion in solution encounters a barrier of only a few kcal mol^{-1} and thus, assuming helicity in solution based on observations made in the solid state can be misleading. This can be illustratively shown for **33**-*Z*-**I**, which is pre-twisted against the observed direction of rotation. However, predicted diminished energy difference between *M*- and *P*-helicity of *Z*-isomers explain why a potentially less stable helicity could be observed in the solid state, as elaborated in more detail in chapters 6.10 and 6.13.

6.8. Thermal isomerization at elevated temperatures

Thermal conversions could be observed between **33**-*E*-**I** and **33**-*E*-**II**, **33**-*E*-**I** and **33**-*Z*-**I**, as well as **33**-*E*-**II** and **33**-*Z*-**II**. These isomerization processes continue until a stationary isomer distribution is reached allowing to classify them as first-order processes with entering a thermal equilibrium. Evaluation of corresponding kinetic and thermodynamic data is exemplarily described for the relationship between **33**-*E*-**I** and **33**-*Z*-**I**.

Solving the first-order rate law with entering a thermal equilibrium, shown in Equation 5, allows determination of the *Gibbs* energy of activation $\Delta G^{\ddagger}$ characterizing this process.

$$\ln\left[\frac{c_0(\mathbf{33}\text{-}E\text{-}\mathbf{I}) - c_{\mathrm{eq}}(\mathbf{33}\text{-}E\text{-}\mathbf{I})}{c_t(\mathbf{33}\text{-}E\text{-}\mathbf{I}) - c_{\mathrm{eq}}(\mathbf{33}\text{-}E\text{-}\mathbf{I})}\right] = \left[k_{(\mathbf{33}\text{-}E\text{-}\mathbf{I}\rightarrow\mathbf{33}\text{-}Z\text{-}\mathbf{I})} + k_{(\mathbf{33}\text{-}Z\text{-}\mathbf{I}\rightarrow\mathbf{33}\text{-}E\text{-}\mathbf{I})}\right] t \qquad \text{(Eq. 5)}$$

The observed conversion can be described by a combination of the rate constant for the **33**-*E*-**I** to **33**-*Z*-**I** process $k_{(\mathbf{33}\text{-}E\text{-}\mathbf{I}\rightarrow\mathbf{33}\text{-}Z\text{-}\mathbf{I})}$ and the reverse $k_{(\mathbf{33}\text{-}Z\text{-}\mathbf{I}\rightarrow\mathbf{33}\text{-}E\text{-}\mathbf{I})}$. Fitting this relationship with a linear regression analysis using the time t and known values for **33**-*E*-**I**, namely the initial concentration $c_0(\mathbf{33}\text{-}E\text{-}\mathbf{I})$, concentration in equilibrium $c_{\mathrm{eq}}(\mathbf{33}\text{-}E\text{-}\mathbf{I})$, and concentration after elapsed time $c_t(\mathbf{33}\text{-}E\text{-}\mathbf{I})$ enables determination of the slope m of the logarithmic plot. With the slope m at hand, rate constant $k_{(\mathbf{33}\text{-}E\text{-}\mathbf{I}\rightarrow\mathbf{33}\text{-}Z\text{-}\mathbf{I})}$ can be determined using Equation 6 and considering the law of mass action which is displayed in Equation 7.

$$\frac{c_{\mathrm{eq}}(\mathbf{33}\text{-}E\text{-}\mathbf{I})}{c_{\mathrm{eq}}(\mathbf{33}\text{-}Z\text{-}\mathbf{I})} = \frac{k_{(\mathbf{33}\text{-}Z\text{-}\mathbf{I}\rightarrow\mathbf{33}\text{-}E\text{-}\mathbf{I})}}{k_{(\mathbf{33}\text{-}E\text{-}\mathbf{I}\rightarrow\mathbf{33}\text{-}Z\text{-}\mathbf{I})}} \qquad \text{(Eq. 6)}$$

$$k_{(\mathbf{33}\text{-}E\text{-}\mathbf{I}\rightarrow\mathbf{33}\text{-}Z\text{-}\mathbf{I})} = \frac{m}{1 + \frac{c_{\mathrm{eq}}(\mathbf{33}\text{-}E\text{-}\mathbf{I})}{c_{\mathrm{eq}}(\mathbf{33}\text{-}Z\text{-}\mathbf{I})}} \qquad \text{(Eq. 7)}$$

Insertion of the rate constant $k_{(\mathbf{33}\text{-}E\text{-}\mathbf{I}\rightarrow\mathbf{33}\text{-}Z\text{-}\mathbf{I})}$ into the *Eyring* Equation 8, together with numerical values for the *Boltzmann* constant k_B, temperature T, *Planck* constant h, and the ideal gas constant R provides *Gibbs* energy of activation $\Delta G^{\ddagger}$, after rearrangement to Equation 9. The corresponding data used for evaluation can be found in Figures 138–141.

$$k_{(\mathbf{33}\text{-}E\text{-}\mathbf{I}\rightarrow\mathbf{33}\text{-}Z\text{-}\mathbf{I})} = \frac{k_B T}{h}\, \mathrm{e}^{\frac{-\Delta G^{\ddagger}}{RT}} \qquad \text{(Eq. 8)}$$

$$k_B = \text{ Boltzmann constant} = 1.381 \cdot 10^{-23}\ \mathrm{J \cdot K^{-1}}$$

$$T = \text{temperature in K}$$

$$h = \ Planck \text{ constant} = 6.626 \cdot 10^{-34}\ \mathrm{J \cdot s}$$

$$R = \ \text{ideal gas constant} = 8.314\ \mathrm{J \cdot K^{-1} \cdot mol^{-1}}$$

$$\Delta G^{\ddagger} = 8.314 \cdot T \cdot \left[23.760 + \ln\left(\frac{T}{k_{(\mathbf{33}\text{-}E\text{-}\mathbf{I}\rightarrow\mathbf{33}\text{-}Z\text{-}\mathbf{I})}}\right)\right] \qquad \text{(Eq. 9)}$$

The stationary equilibrium isomers composition enables determination of relative energy difference between **33**-*E*-**I** and **33**-*Z*-**I** by insertion of the equilibrium constant K into Equation 10. Energy differences between all isomers are summarized in Table 13.

$$\Delta G = R \cdot T \cdot \ln(K) = R \cdot T \cdot \ln\left(\frac{c_{\mathrm{eq}}(\mathbf{33}\text{-}E\text{-}\mathbf{I})}{c_{\mathrm{eq}}(\mathbf{33}\text{-}Z\text{-}\mathbf{I})}\right) \qquad \text{(Eq. 10)}$$

Standard deviation analysis allowed determination of lower and upper boundary conditions for the linear regression fit, displayed in Figures 138c–141c. Maximum upper and lower deviation within these boundaries allows an estimation of the upper and lower limits for the linear fit, giving a maximum possible deviation within a 95% confidence interval as shown in Table 12.

6.8.1. Isomers 33-*E*-I and 33-*Z*-I

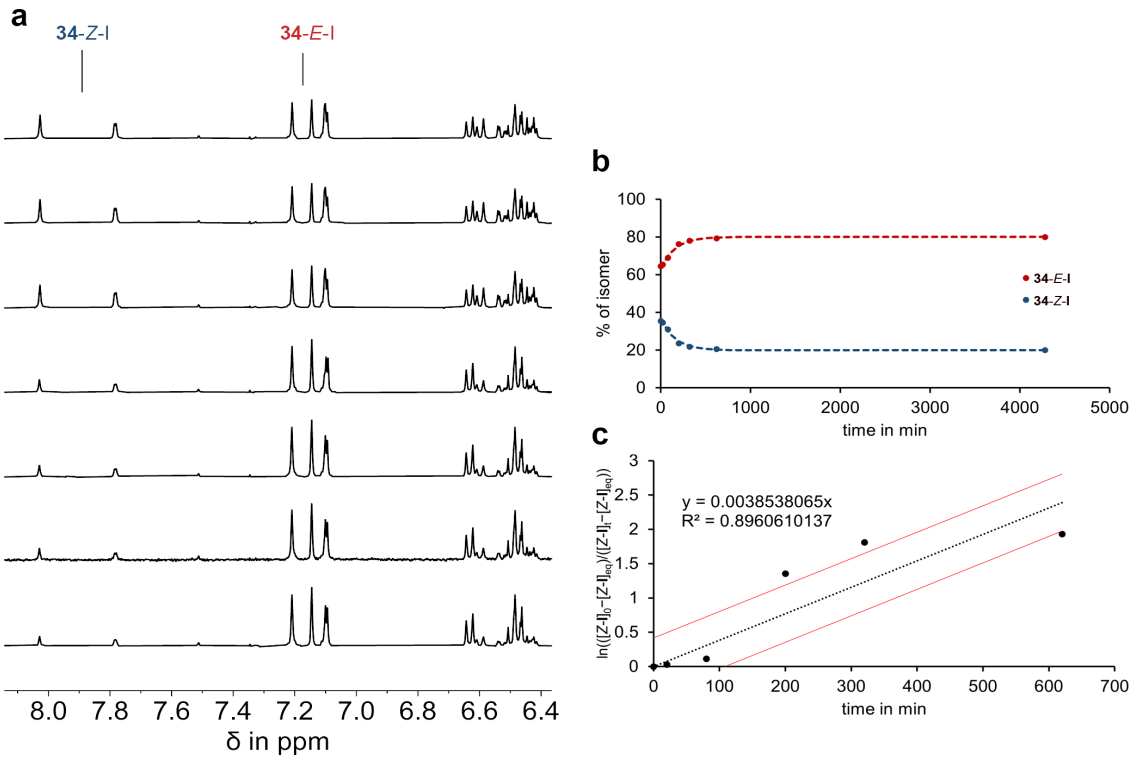

Figure 138 Kinetic analysis of thermal isomerization starting from an **33**-*E*-**I** enriched solution at 40 °C. **a** ^{1}H NMR spectra (400 MHz, $C_2D_2Cl_4$, 25 °C) of racemic **33**-*E*-**I** and **33**-*Z*-**I** during thermal isomerization of **33**-*Z*-**I** to **33**-*E*-**I** starting from an **33**-*E*-**I** enriched mixture consisting of 58% **33**-*E*-**I** and 42% **33**-*Z*-**I** (top spectrum). Spectra were recorded in irregular intervals ordered chronologically from top to bottom. **b** Changing isomer distribution during thermal conversion at 40 °C until a stable ratio of 84% **33**-*E*-**I** (red dots) and 16% **33**-*Z*-**I** (blue dots) is reached. Data were simulated for visual guidance using an exponential proportional rate growth or decrease fit shown with color-coded dashed lines. **c** Kinetic evaluation using a first-order rate law with entering a thermal equilibrium provides a linear correlation for the conversion of **33**-*Z*-**I**. A simulation of the experimental data points using a linear regression fit (dotted black line) leads to a slope of $m = 0.0038538 \pm 0.0013439$, translating into a *Gibbs* energy of activation of $\Delta G^{\ddagger} = 21.8 \pm 0.3$ kcal mol^{-1}. A standard deviation corridor was plotted for upper and lower boundaries (upper and lower red lines) according to the measured data.

6.8.2. Isomers 33-*E*-I and 33-*E*-II

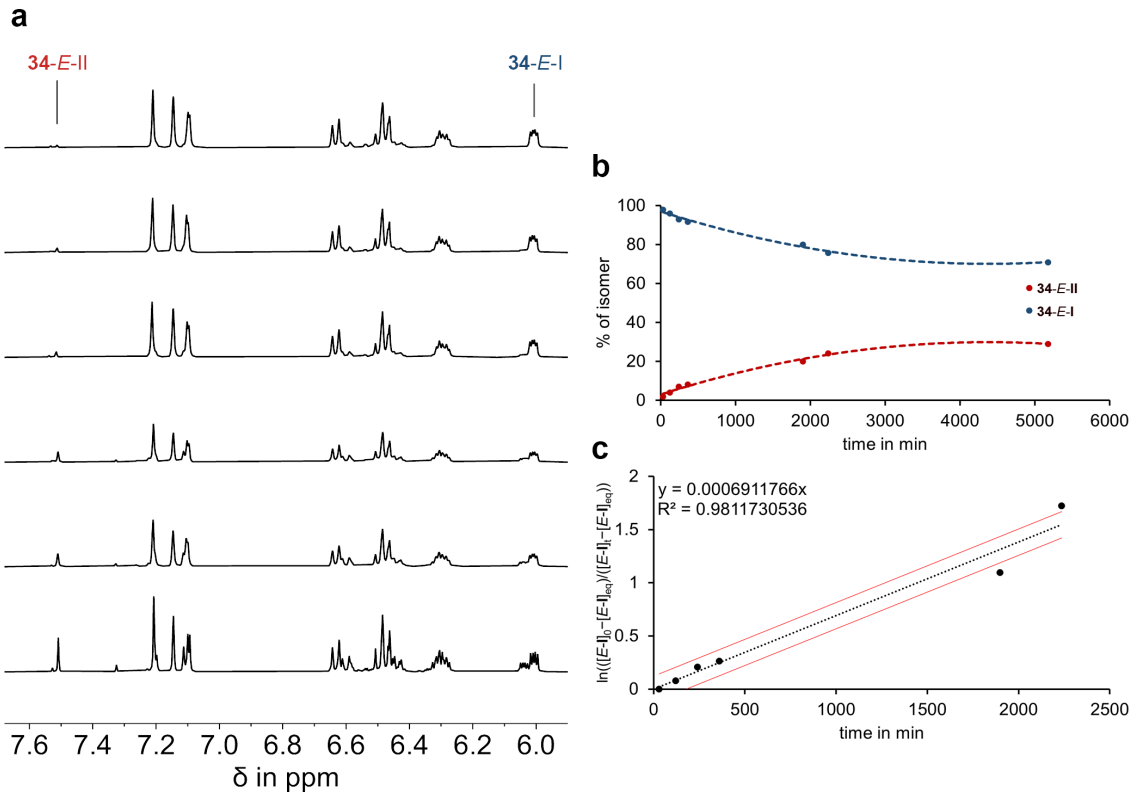

Figure 139 Kinetic analysis of thermal isomerization starting from an **33**-*E*-**I** enriched solution at 80 °C. **a** ^{1}H NMR spectra (400 MHz, $C_2D_2Cl_4$, 25 °C) of racemic **33**-*E*-**I** and **33**-*E*-**II** during thermal isomerization of **33**-*E*-**I** to **33**-*E*-**II** starting from an **33**-*E*-**I** enriched mixture consisting of 98% **33**-*E*-**I** and 2% **33**-*E*-**II** (top spectrum). Spectra were recorded in irregular intervals ordered chronologically from top to bottom. **b** Changing isomer distribution during thermal conversion at 80 °C until a stable ratio of 71% **33**-*E*-**I** (blue dots) and 29% **33**-*E*-**II** (red dots) reached. Data were simulated for visual guidance using a second-degree polynomial fit shown with color-coded dashed lines. **c** Kinetic evaluation using a first-order rate law with entering a thermal equilibrium provides a linear correlation for the conversion of **33**-*E*-**I**. A simulation of the experimental data points using a linear regression fit (dotted black line) leads to a slope of $m = 0.0006912 \pm 0.0001119$, translating into a *Gibbs* energy of activation of $\Delta G^{\ddagger} = 25.9 \pm 0.1$ kcal mol^{-1}. A standard deviation corridor was plotted for upper and lower boundaries (upper and lower red lines) according to the measured data.

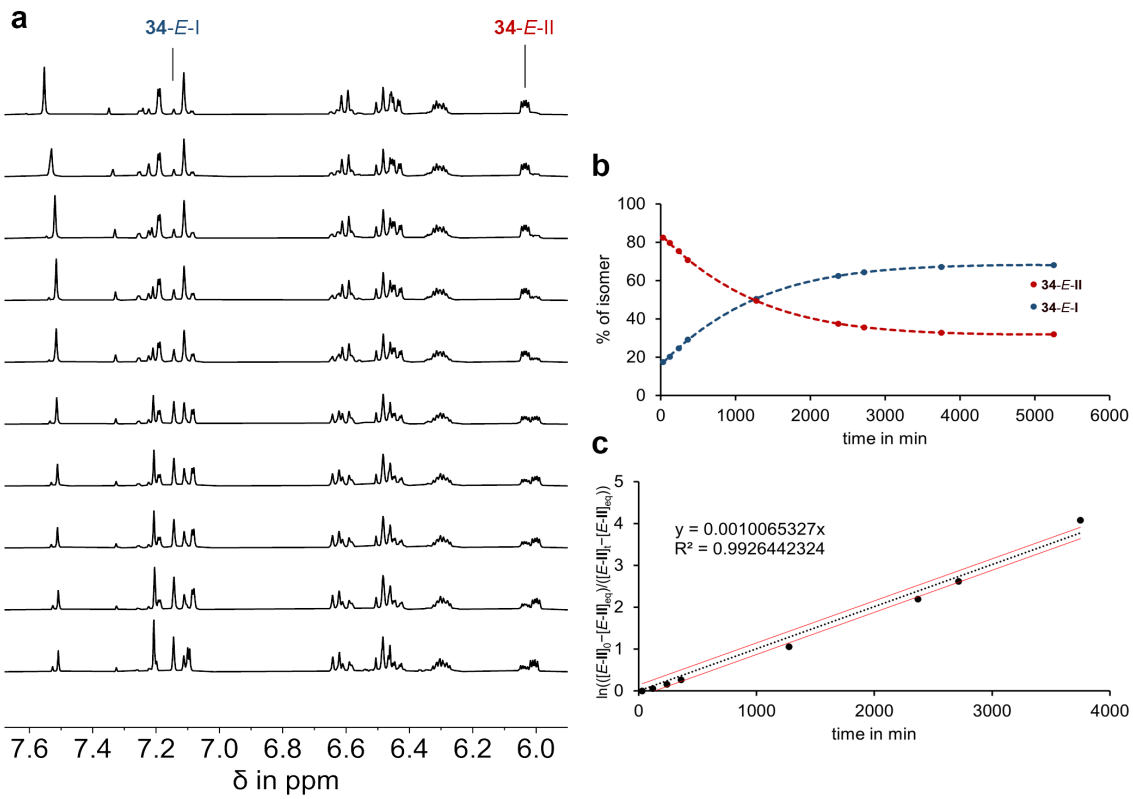

Figure 140 Kinetic analysis of thermal isomerization starting from an **33**-*E*-**II** enriched solution at 80 °C. **a** ^{1}H NMR spectra (400 MHz, $C_2D_2Cl_4$, 25 °C) of racemic **33**-*E*-**II** and **33**-*E*-**I** during thermal isomerization of **33**-*E*-**II** to **33**-*E*-**I** starting from an **33**-*E*-**II** enriched mixture consisting of 83% **33**-*E*-**II** and 17% **33**-*E*-**I** (top spectrum). Spectra were recorded in irregular intervals ordered chronologically from top to bottom. **b** Changing isomer distribution during thermal conversion at 80 °C until a stable ratio of 27% **33**-*E*-**II** (red dots) and 73% **33**-*E*-**I** (blue dots) is reached. Data were simulated for visual guidance using a fourth-degree polynomial fit shown with color-coded dashed lines. **c** Kinetic evaluation using a first-order rate law with entering a thermal equilibrium provides a linear correlation for the conversion of **33**-*E*-**II**. A simulation of the experimental data points using a linear regression fit (dotted black line) leads to a slope of $m = 0.0010065 \pm 0.0000746$, translating into a *Gibbs* energy of activation of $\Delta G^{\ddagger} = 25.6 \pm 0.1$ kcal mol^{-1}. A standard deviation corridor was plotted for upper and lower boundaries (upper and lower red lines) according to the measured data.

6.8.3. Isomers 33-*E*-II and 33-*Z*-II

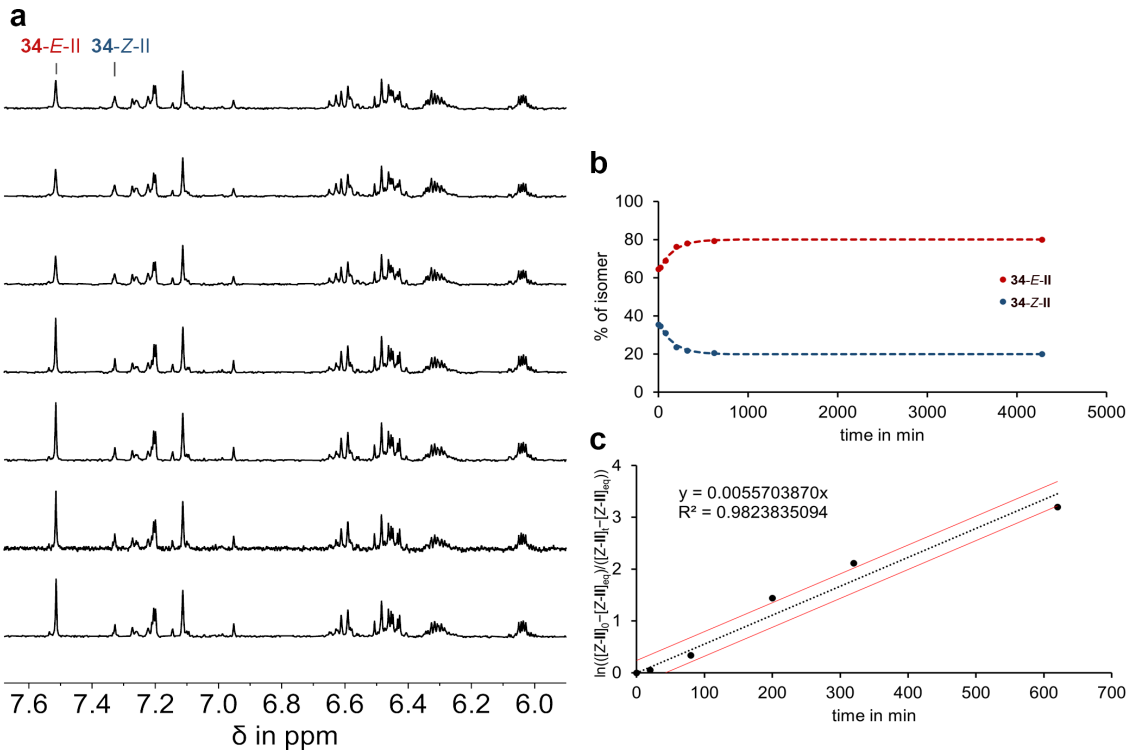

Figure 141 Kinetic analysis of thermal isomerization starting from an **33**-*E*-**II** enriched solution at 40 °C. **a** ^{1}H NMR spectra (400 MHz, $C_2D_2Cl_4$, 25 °C) of racemic **33**-*E*-**II** and **33**-*Z*-**II** during thermal isomerization of **33**-*Z*-**II** to **33**-*E*-**II** starting from an **33**-*E*-**II** enriched mixture consisting of 65% **33**-*E*-**II** and 35% **33**-*Z*-**II** (top spectrum). Spectra were recorded in irregular intervals ordered chronologically from top to bottom. **b** Changing isomer distribution during thermal conversion at 40 °C until a stable ratio of 80% **33**-*E*-**II** (red dots) and 20% **33**-*Z*-**II** (blue dots) is reached. Data were simulated for visual guidance using an exponential proportional rate growth or decrease fit shown with color-coded dashed lines. **c** Kinetic evaluation using a first-order rate law with entering a thermal equilibrium provides a linear correlation for the conversion of **33**-*Z*-**II**. A simulation of the experimental data points using a linear regression fit (dotted black line) leads to a slope of $m = 0.0055704 \pm 0.00076375$, translating into a *Gibbs* energy of activation of $\Delta G^{\ddagger} = 21.6 \pm 0.1$ kcal mol^{-1}. A standard deviation corridor was plotted for upper and lower boundaries (upper and lower red lines) according to the measured data.

It is noteworthy, that despite significant deviations observed in the recorded data for isomer **33**-*Z*-**I**, this does not result in unreasonably high deviations in *Gibbs* energies of activation with a maximum error of ± 0.3 kcal mol^{-1}. This is still accurate enough to conclude that barriers for conversion of **33**-*Z*-**I** and **33**-*Z*-**II** to **33**-*E*-**I** and **33**-*E*-**II** respectively are almost identical.

Table 12 Experimentally determined *Gibbs* energies of activation $\Delta G^{\ddagger}$ for macrocyclic HTI **33** given in kcal mol^{-1}. Configurations utilized as starting points are mentioned in the isomerization process column. Error margins were generated with standard deviations in a 95% confidence interval of the experimentally determined slope *m*, which was acquired in the linear regression analysis.

isomerization process	**linear regression slope *m***	**$\Delta G^{\ddagger}$ in kcal mol^{-1}**
33-*E*-**I** → **33**-*Z*-**I**	0.0038538 ± 0.0013439	21.8 ± 0.3
33-*E*-**II** → **33**-*Z*-**II**	0.0055704 ± 0.0007638	21.6 ± 0.1
33-*E*-**I** → **33**-*E*-**II**	0.0006912 ± 0.0001119	25.9 ± 0.1
33-*E*-**II** → **33**-*E*-**I**	0.0010065 ± 0.0000746	25.6 ± 0.1

Table 13 Measured ground state *Gibbs* energy differences ΔG for all *E*- and *Z*-isomers of macrocyclic HTI **33**. Error margins were generated assuming 5% accuracy in ^{1}H NMR spectra integration.

isomer	**ΔG in kcal mol^{-1}**
33-*E*-**I**	0.0
33-*E*-**II**	0.6 ± 0.2
33-*Z*-**I**	1.0 ± 0.3
33-*Z*-**II**	1.4 ± 0.3

6.9. UV-Vis absorption spectra and molar extinction coefficients

Molar extinction coefficients of macrocycle **33**, and HTI motor **15h**, unoxidized macrocycle **51** and unoxidized HTI motor **56** were measured from isomerically pure solutions in CH_2Cl_2 at 22 °C, as shown in Figure 142, 143 and 144 respectively. Solutions of each isomer with given concentrations were used to calculate the molar extinctions shwon in Figure 142c and d, 143c and d and 144c and d.

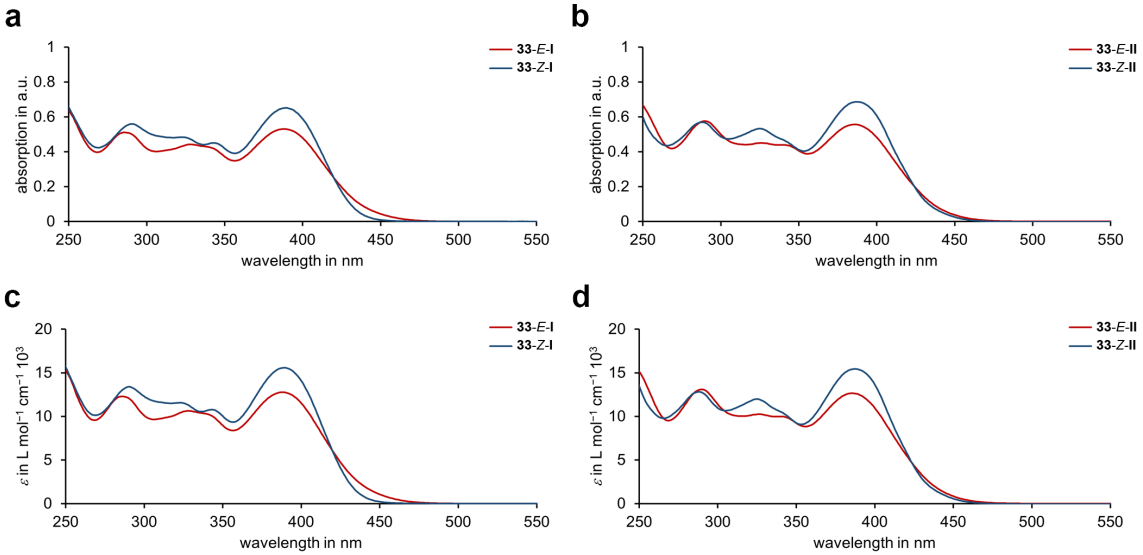

Figure 142 UV-Vis absorption spectra and molar extinction coefficients (CH_2Cl_2, 22 °C) of racemic HTI-based macrocyclic molecular machine **33**. **a** Isomer **33**-*E*-I (red, scaled according to the isosbestic point at 420 nm) and **33**-*Z*-I (blue, 42 μM). **b** Isomer **33**-*E*-II (red, scaled according to the isosbestic point at 424 nm) and **33**-*Z*-II (blue, 47 μM). **c** Molar extinction coefficients of isomer **33**-*E*-I (red) and **33**-*Z*-I (blue). **d** Molar extinction coefficients of isomer **33**-*E*-II (red) and **33**-*Z*-II (blue). Adapted with minor format modifications from *Nat. Commun.* **2023**, *14*, 4595 licensed under CC BY 4.0.[1]

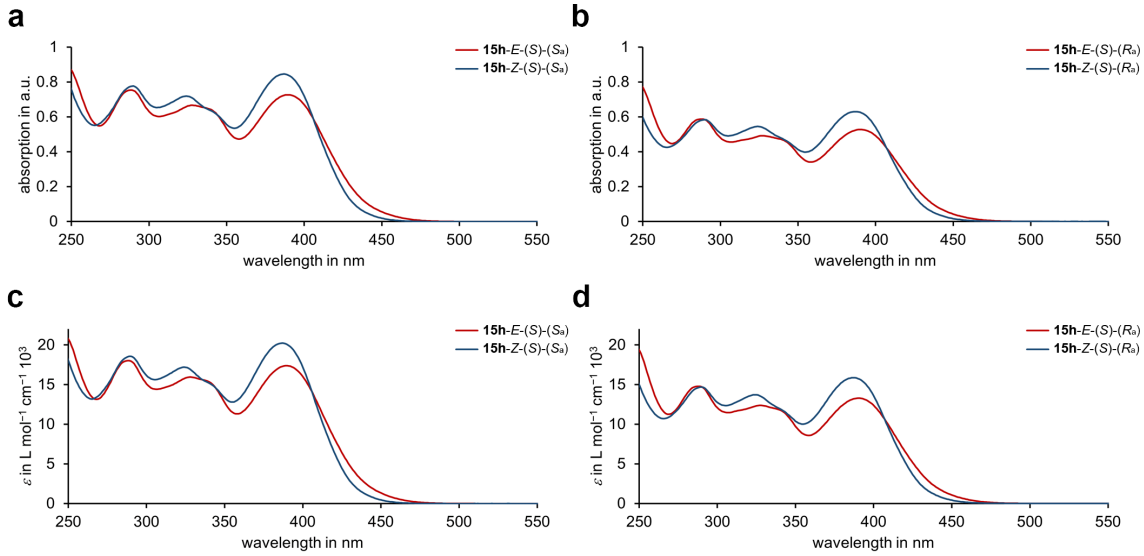

Figure 143 UV-Vis absorption spectra and molar extinction coefficients (CH_2Cl_2, 22 °C) of racemic HTI-based prospective molecular motor **15h**. **a** Isomer **15h**-*E*-(*S*)-(S_a) (red, scaled according to the isosbestic point at 407 nm) and **15h**-*Z*-(*S*)-(S_a) (blue, 42 μM). **b** Isomer **15h**-*E*-(*S*)-(R_a) (red, scaled according to the isosbestic point at 407 nm) and **15h**-*Z*-(*S*)-(R_a) (blue, 40 μM). **c** Molar extinction coefficients of isomer **15h**-*E*-(*S*)-(S_a) (red) and **15h**-*Z*-(*S*)-(S_a) (blue). **d** Molar extinction coefficients of isomer **15h**-*E*-(*S*)-(R_a) (red) and **15h**-*Z*-(*S*)-(R_a) (blue). Adapted with minor format modifications from *Nat. Commun.* **2023**, *14*, 4595 licensed under CC BY 4.0.[1]

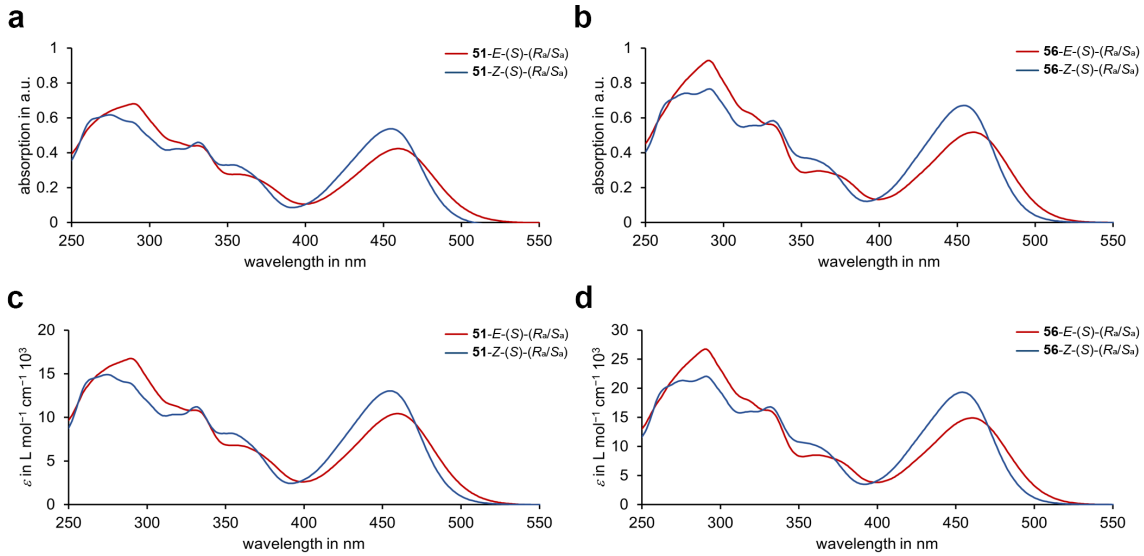

Figure 144 UV-Vis absorption spectra and molar extinction coefficients (CH_2Cl_2, 22 °C) of racemic unoxidized HTI-based non-macrocyclic **51** and macrocyclic **56**. **a** Isomer **51**-*E*-(R_a/S_a) (red, scaled according to the isosbestic point at 471 nm) and **51**-*Z*-(R_a/S_a) (blue, 31 μM). **b** Isomer **56**-*E*-(R_a/S_a) (red, scaled according to the isosbestic point at 470 nm) and **56**-*Z*-(R_a/S_a) (blue, 35 μM). **c** Molar extinction coefficients of isomer **51**-*E*-(R_a/S_a) (red) and **51**-*Z*-(R_a/S_a) (blue). **d** Molar extinction coefficients of isomer **56**-*E*-(R_a/S_a) (red) and **56**-*Z*-(R_a/S_a) (blue). Adapted with minor format modifications from *Nat. Commun.* **2023**, *14*, 4595 licensed under CC BY 4.0.[1]

It is noteworthy, that macrocyclic **51** and HTI motor **56** feature very similar absorption profiles which allows in combination with similar chromophores present in both systems to assume that their photochemical behaviour is comparable. This does strengthen the foundation for comparison of QYs between these molecules.

6.10. ECD data

Atropisomer assignments from crystal structures obtained for isomers **33**-*Z*-**I**, **33**-*E*-**II** and **33**-*Z*-**II** were attempted to be verified in solution. ECD spectra of all isomers were measured first, as shown in Figure 145. To this end an ECD spectrum of an enantiomerically pure sample obtained from chiral HPLC separation was recorded and then heated at 80 °C until a mixture of all four ground state isomers was obtained. This mixture was separated again using chiral HPLC and ECD spectra of the four obtained isomers were measured to record one diastereomeric set possessing only one sole sulfoxide configuration.

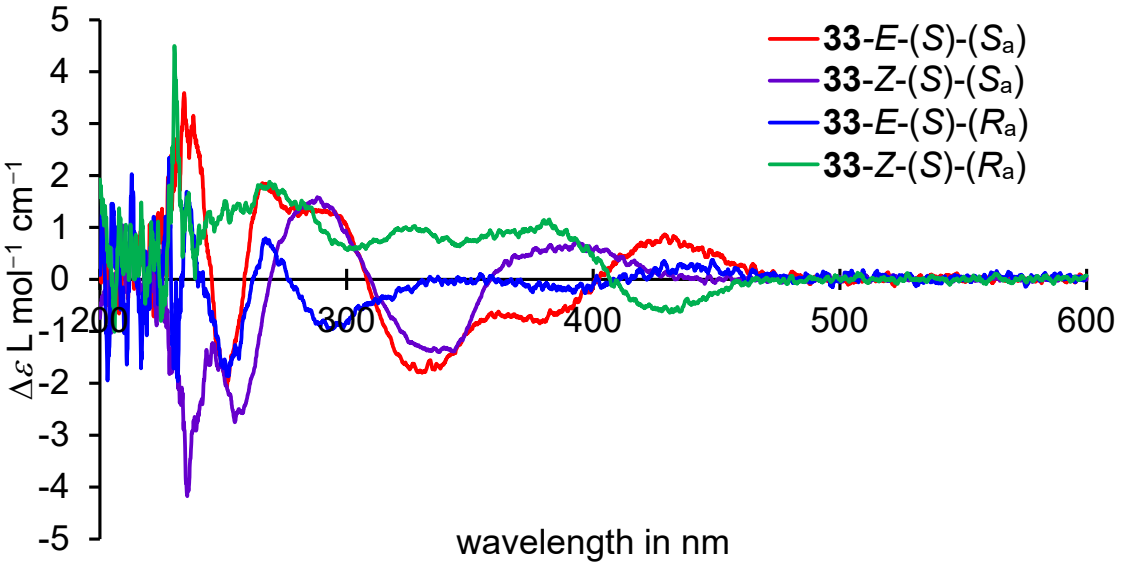

Figure 145 ECD spectra (CH_2Cl_2, 22 °C) of enantiomerically pure samples of all four stable conformational isomers of macrocyclic machine **33**. Two double bond configurations exist for each atropisomer, namely **33**-*E*-(*S*)-(S_a) (red) and **33**-*Z*-(*S*)-(S_a) (purple) for S_a- and **33**-*E*-(*S*)-(R_a) (blue) and **33**-*Z*-(*S*)-(R_a) (green) for R_a-configured atropisomers. Only *S*-configured sulfoxide isomers were measured.

6.10.1. ECD assignment using theoretical predicted macrocycle spectra

With ground state ECD spectra at hand, comparison to simulated spectra at the TD-B3LYP-GD3BJ/6-311+G(d,p) IEFPCM (CH_2Cl_2) level of theory could be made. It is noteworthy that helical flexibility resulting from a reduced barrier between *P*- and *M*-isomers might lead to presence of both helices at 22 °C in solution. To this end, comparison of *Boltzmann* averaged simulated spectra for *P*-, *M*- and a mixture of both helicities was performed separately as shown in Figure 146–153. For more experimental details see chapter 6.13. Only spectra within a range of 6.0 kcal mol^{-1} from the most stable conformer were considered for all presented ECD spectra predicted by theory.

Obtained structures for **33**-*E*-**I** predicted by theory did only possess *P*-helicity within a reasonable range of 6.0 kcal mol^{-1} between the most and least stable structures. Thus, it was only possible to compare the **33**-*E*-(*S*)-(*P*)-(S_a) with the experimentally obtained data, shown in Figure 146. However, these two spectra show some reasonable overlap between each other, indicating the majority of **33**-*E*-(*S*)-(S_a) adopts *P*-helicity according to theory.

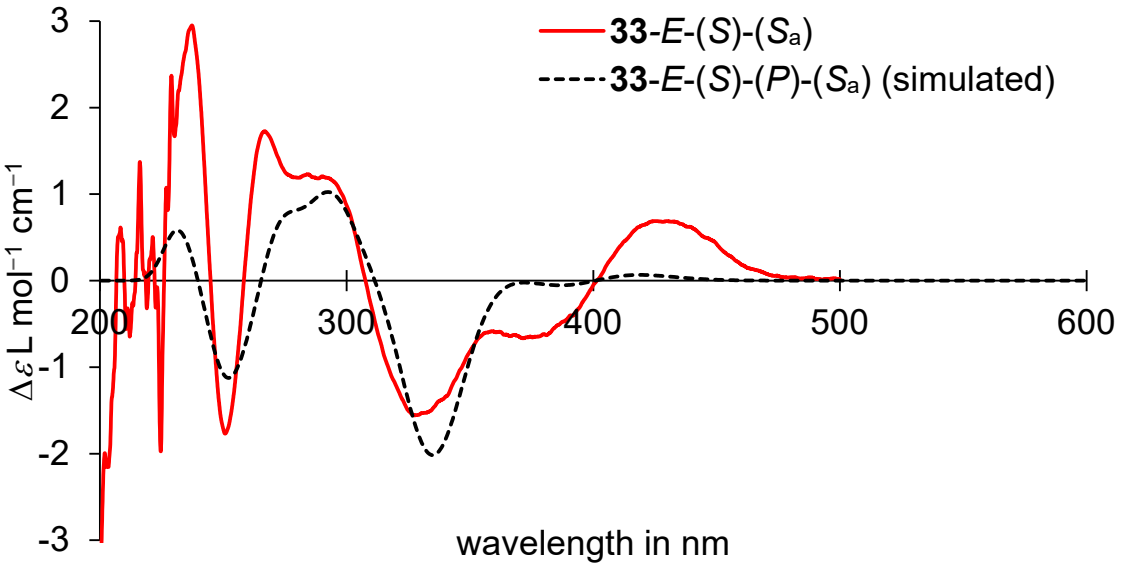

Figure 146 Comparison of ECD spectra (CH_2Cl_2, 22 °C) from an enantiomerically pure sample of **33**-*E*-(*S*)-(S_a) (red) and *Boltzmann* averaged simulated conformers of **33**-*E*-(*S*)-(*P*)-(S_a) (dashed black), bathochromically shifted by 12 nm. All structures predicted by theory adopt *P*-helicity.

This prediction of helicity is in good agreement with the attachment points of the covalent linker residing in the same 180° S_a rotational half-space **I**, see chapter 6.14 Figure 168.

For isomer **33**-*E*-(*S*)-(*P*)-(R_a) both *P*- and *M*-helicity were found within the 6.0 kcal mol^{-1} range, and corresponding ECD spectra are shown in Figure 147–148. However, obtained differences between the two simulated helicities were so small that a prediction of helicity in solution was not possible.

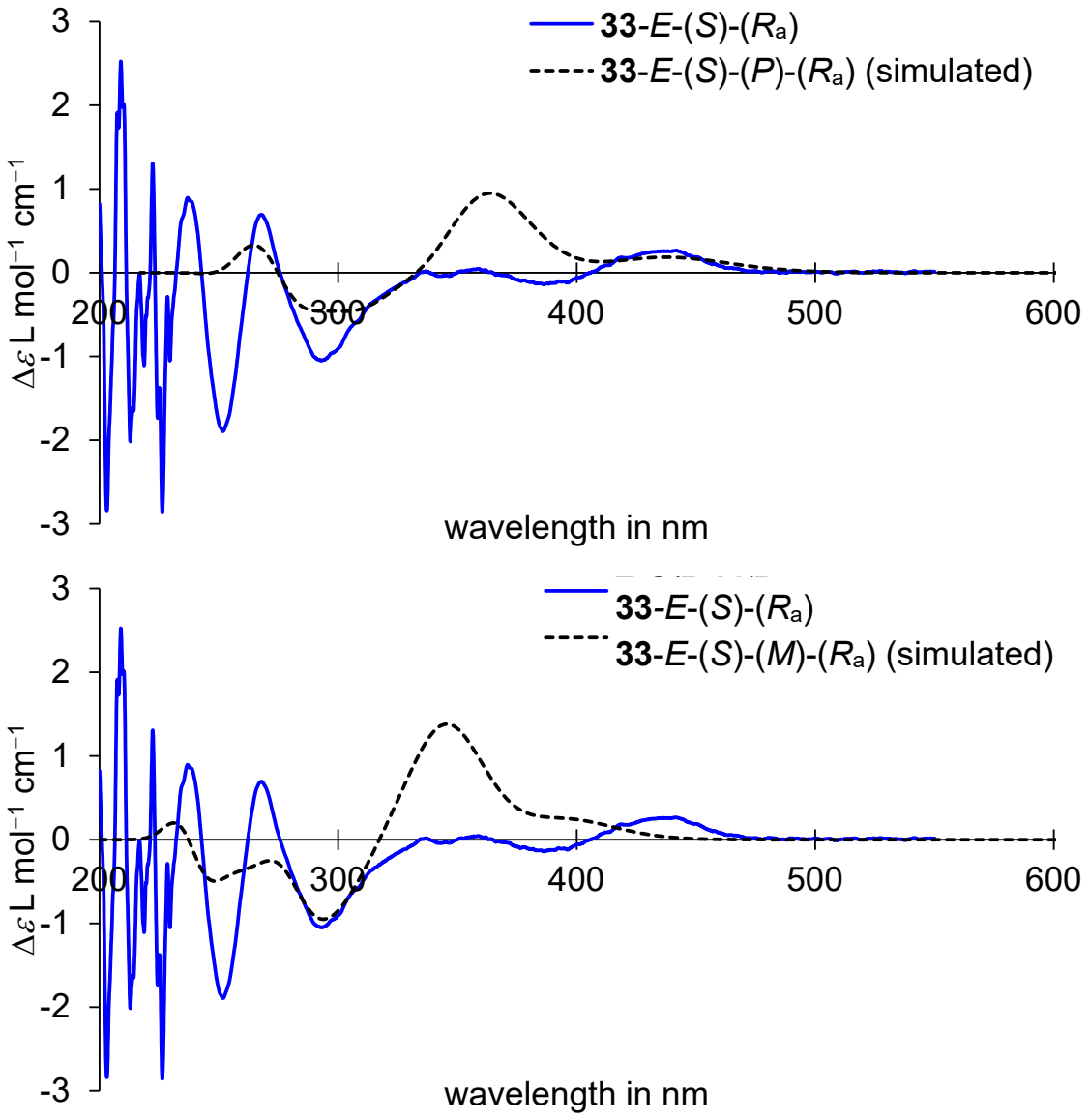

Figure 147 Comparison of ECD spectra (CH_2Cl_2, 22 °C) from an enantiomerically pure sample of **33**-*E*-(*S*)-(R_a) (blue) and *Boltzmann* averaged simulated conformers of **33**-*E*-(*S*)-(*P*)-(R_a) (dashed black top) and **33**-*E*-(*S*)-(*M*)-(R_a) (dashed black bottom), both bathochromically shifted by 10 nm.

With only minor differences between simulated *P*- and *M*-helicities, a prediction of **33**-*E*-(*S*)-(R_a) helicity in solution remained challenging. Mixing the *Boltzmann* averaged proportions of each helicity according to the obtained energies lead to the dashed black spectrum shown in Figure 148, which is dominated by the *M*-helical part of the spectra. This theoretical prediction of stability is not in agreement with the observation made in the crystalline state, which indicates that the stability of the *P*-helicity in the solid state potentially results from *e.g.* crystal packing effects. However, isomer **33**-*E*-(*S*)-(R_a) possessing *M*-helicity does point towards limitation of the rotor part to the 180° R_a rotation half space

II respectively. This is in good agreement with the covalent linker attachment points residing in the predicted rotational half space, see chapter 6.14 Figure 168.

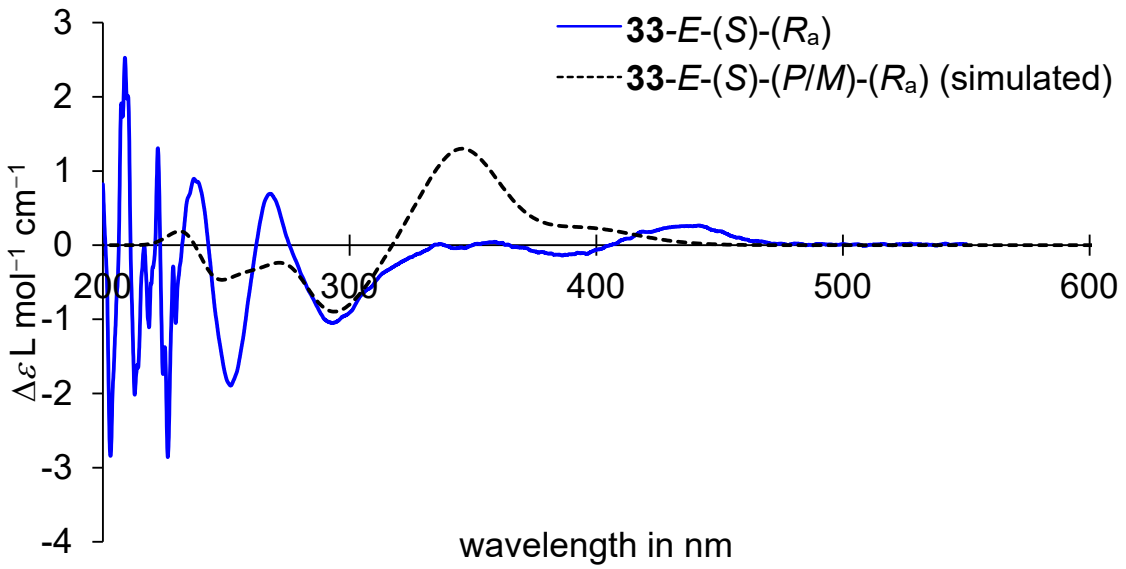

Figure 148 Comparison of ECD spectra (CH_2Cl_2, 22 °C) from an enantiomerically pure sample of **33**-*E*-(*S*)-(R_a) (blue) and *Boltzmann* averaged simulated conformers of **33**-*E*-(*S*)-(*P*/*M*)-(R_a) (dashed black), bathochromically shifted by 10 nm. The most stable structures predicted by theory adopt *M*-helicity.

Helicity of **33**-*Z*-(*S*)-(S_a) appears to be adopting *M*-conformation in solution according to predictions by DFT calculations at the B3LYP-GD3BJ/6-311G(d,p) IEFPCM (CH_2Cl_2) level of theory, for which corresponding ECD spectra are shown in Figure 149. This does match with the helicity observed in the solid state and the hypothesis that movement is limited to the corresponding 180° S_a rotational half-space **I** respectively.

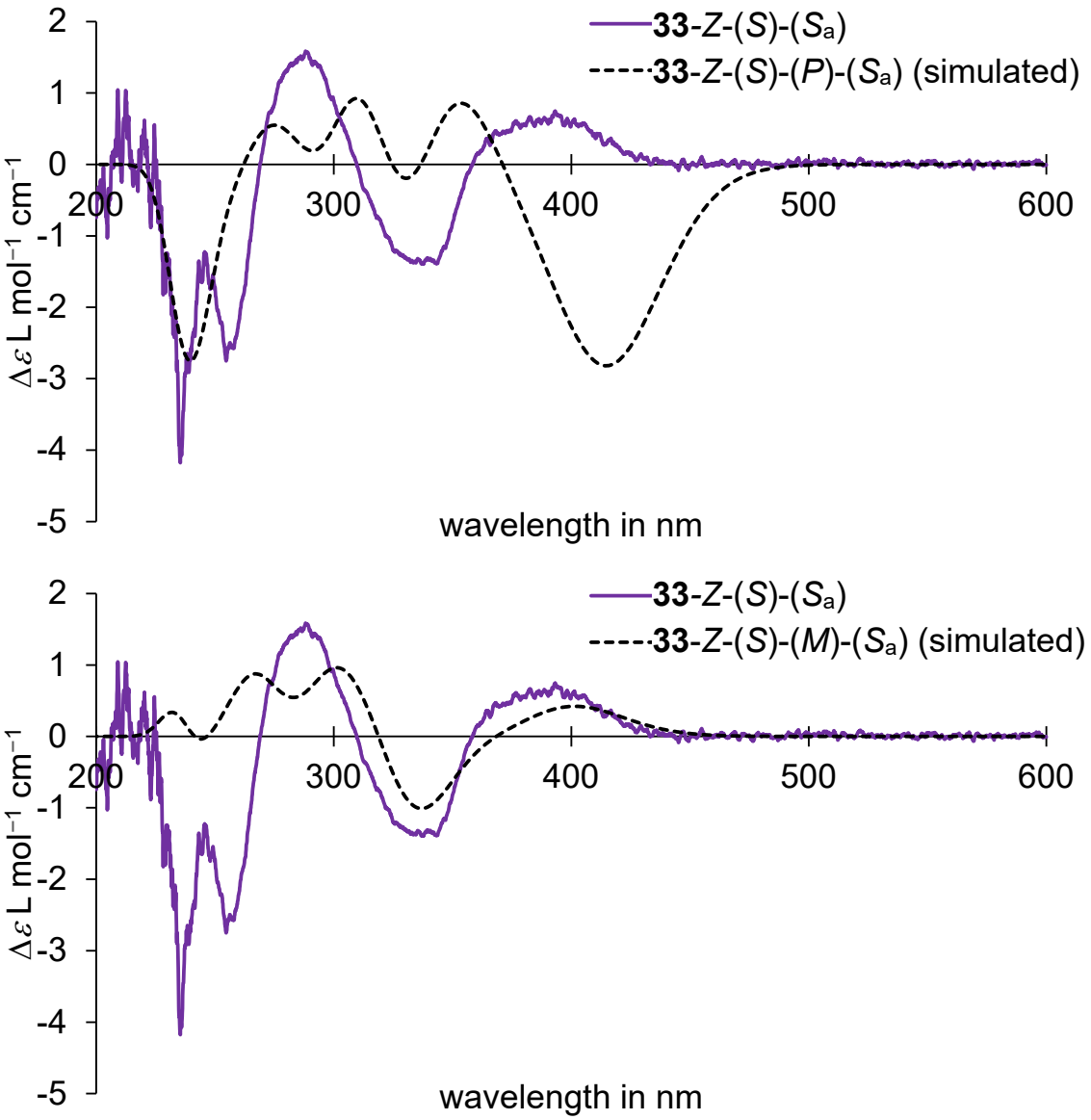

Figure 149 Comparison of ECD spectra (CH_2Cl_2, 22 °C) from an enantiomerically pure sample of **33**-*Z*-(*S*)-(S_a) (purple) and *Boltzmann* averaged simulated conformers of **33**-*Z*-(*S*)-(*P*)-(S_a) (dashed black top) and **33**-*Z*-(*S*)-(*M*)-(S_a) (dashed black bottom), both bathochromically shifted by 12 nm.

The combination of *Boltzmann* averaged predictions by theory of *P*- and *M*-helicities lead to a mixed spectrum dominated by *M*-helical conformers, which is shown in Figure 150. This prediction of stability is not in agreement with the observation made in the crystalline state, which indicates, that the stability of the *P*-helicity in the solid state might result from *e.g.* crystal packing effects. However, isomer **33**-*Z*-(*S*)-(S_a) possessing *P*-helicity does point towards limitation of the rotor part to the 180° S_a rotational half-space **I** respectively, see chapter 6.14 Figure 168.

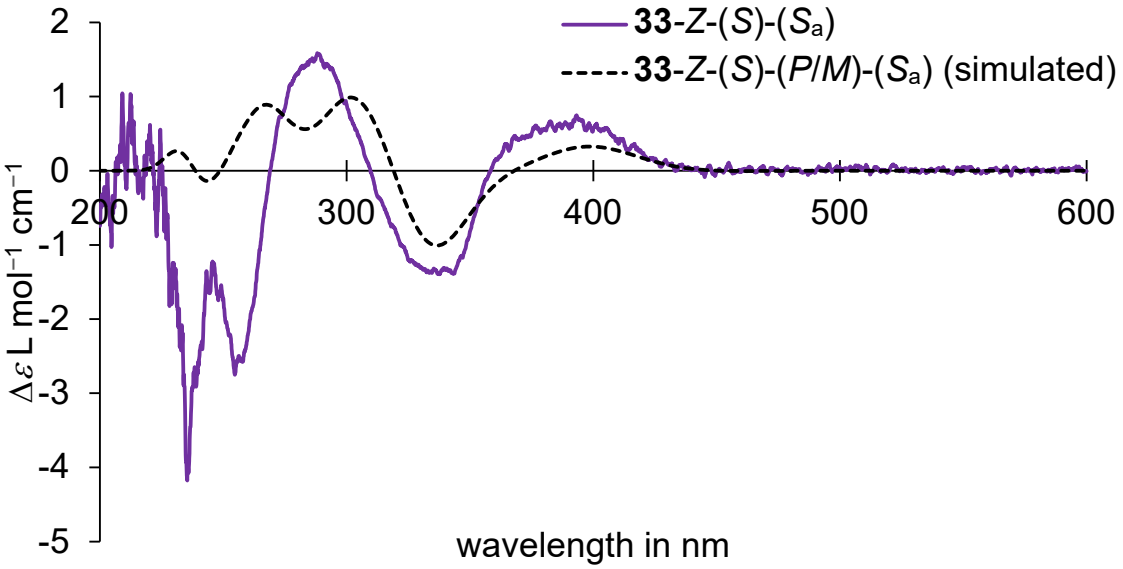

Figure 150 Comparison of ECD spectra (CH_2Cl_2, 22 °C) from an enantiomerically pure sample of **33**-*Z*-(*S*)-(S_a) (purple) and *Boltzmann* averaged simulated conformers of **33**-*Z*-(*S*)-(*P*/*M*)-(S_a) (dashed black), bathochromically shifted by 12 nm. The most stable structures predicted by theory adopt *M*-helicity.

Helicity prediction of **33**-*Z*-(*S*)-(R_a) in solution remains inconclusive according to simulations at the B3LYP-GD3BJ/6-311G(d,p) IEFPCM (CH_2Cl_2) level of theory, for which corresponding ECD spectra are shown in Figure 151.

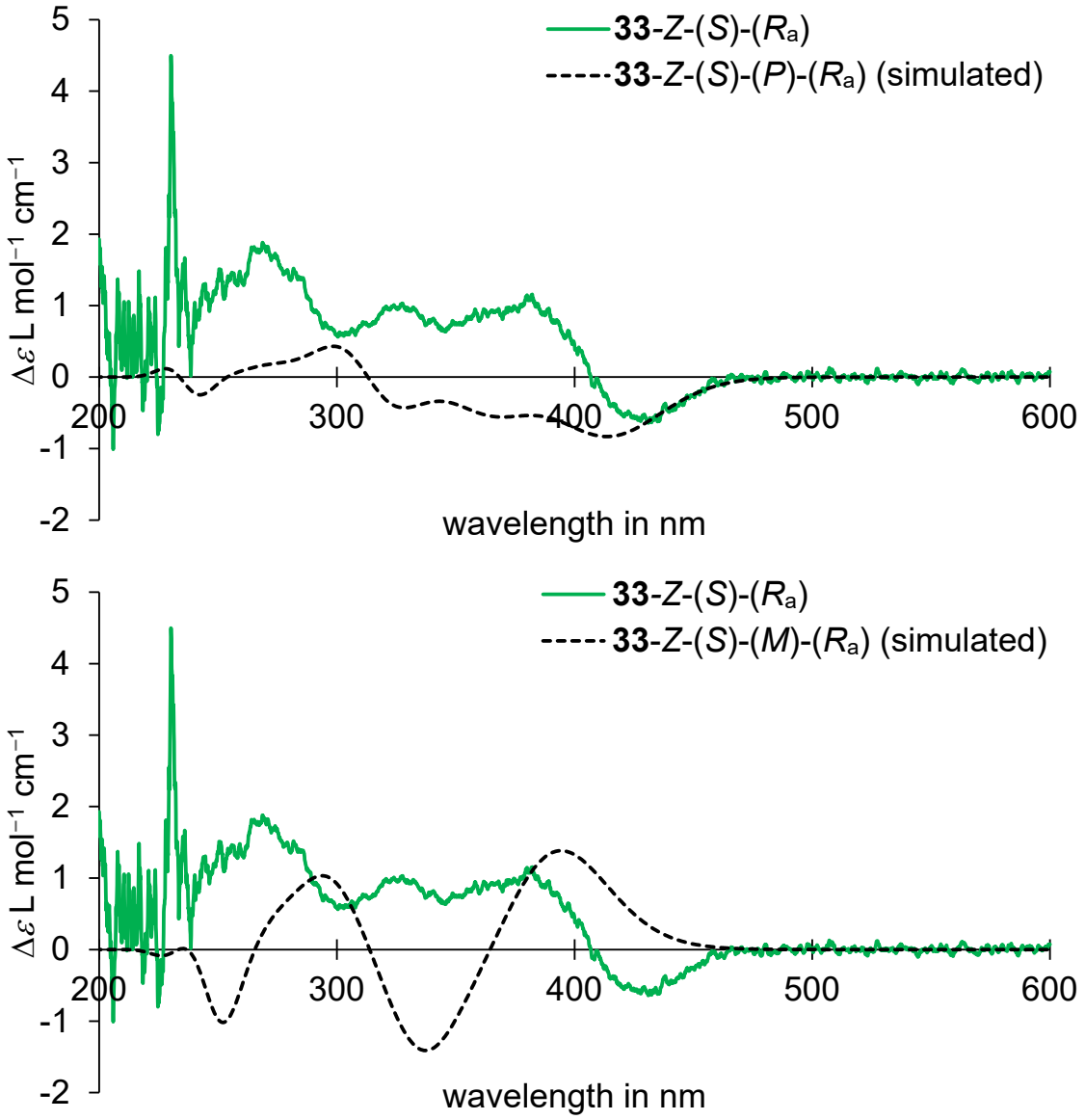

Figure 151 Comparison of ECD spectra (CH_2Cl_2, 22 °C) from an enantiomerically pure sample of **33**-*Z*-(*S*)-(R_a) (green) and *Boltzmann* averaged simulated conformers of **33**-*Z*-(*S*)-(*P*)-(R_a) (dashed black top) and **33**-*Z*-(*S*)-(*M*)-(R_a) (dashed black bottom), both bathochromically shifted by 12 nm.

Combining *Boltzmann* averaged predictions by theory for *P*- and *M*-helicities lead to a mixed spectrum dominated by *M*-helical conformers, which is shown in Figure 152. This prediction of stability is not in agreement with the observation made in the crystalline state. Isomer **33**-*Z*-(*S*)-(R_a) possessing *M*-helicity does furthermore not point towards limitation of the rotor part to the 180° R_a rotational half-space **II** respectively, see chapter 6.14 Figure 168.

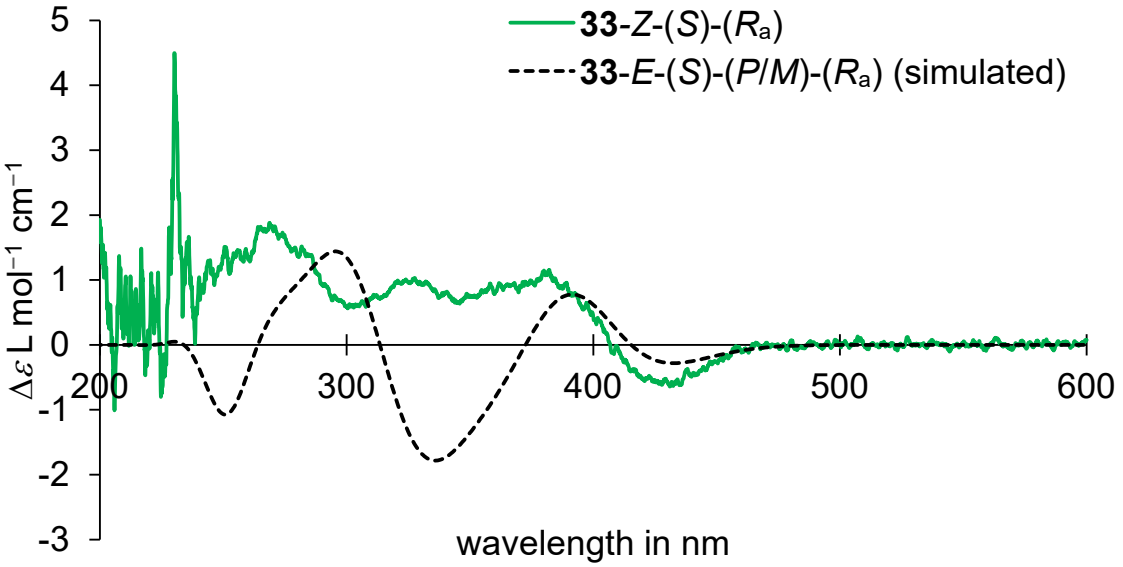

Figure 152 Comparison of ECD spectra (CH_2Cl_2, 22 °C) from an enantiomerically pure sample of **33**-*Z*-(*S*)-(R_a) (green) and *Boltzmann* averaged simulated conformers of **33**-*Z*-(*S*)-(*P*/*M*)-(R_a) (dashed black), bathocromically shifted by 12 nm. The most stable structures predicted by theory adopt *M*-helicity.

In summary, comparison of helicities observed in solution with predictions made at the B3LYP-GD3BJ/6-311G(d,p) IEFPCM (CH_2Cl_2) level of theory remains inconclusive. A summary of the most stable *Boltzmann* averaged simulated conformers in comparison to experimentally obtained spectra is shown in Figure 153. From this comparison it becomes apparent that neither helicity in solution, nor atropisomer configuration or double bond configuration can be determined or underpinned respectively from ECD data alone.

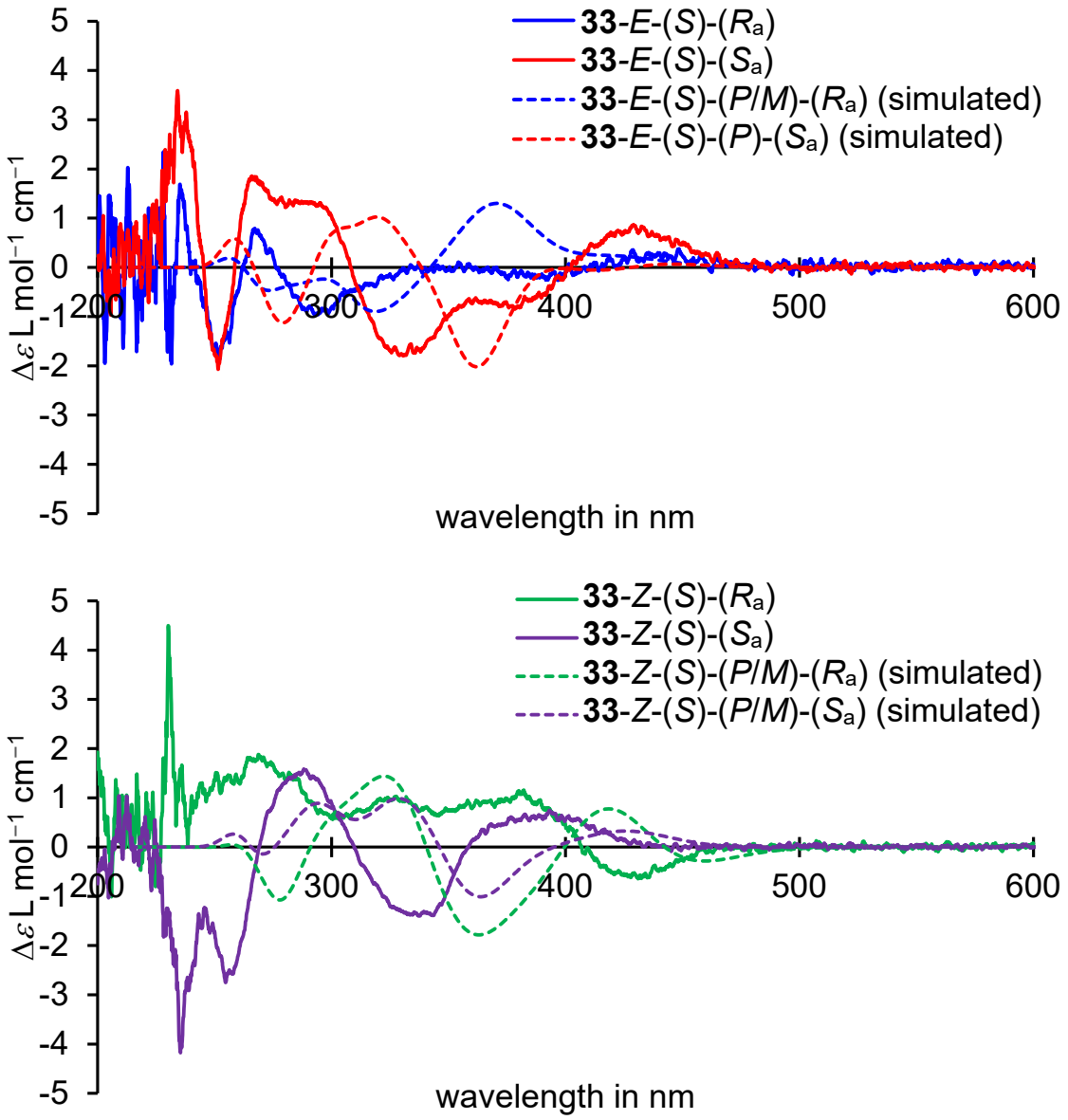

Figure 153 Comparison of ECD spectra (CH_2Cl_2, 22 °C) from enantiomerically pure samples of **33**-*E*-(*S*)-(S_a) (red), **33**-*E*-(*S*)-(R_a) (blue), **33**-*Z*-(*S*)-(S_a) (purple) and **33**-*Z*-(*S*)-(R_a) (green) with spectra of the respective *Boltzmann* averaged simulated conformers including both helicities (dashed). For **33**-*E*-(*S*)-(*P*)-(S_a) (red dashed) isomers with *P*-helicity, **33**-*E*-(*S*)-(*P*/*M*)-(S_a) (blue dashed) *M*-helicity, **33**-*Z*-(*S*)-(*P*/*M*)-(S_a) (purple dashed) *M*-helicity and **33**-*Z*-(*S*)-(*P*/*M*)-(R_a) (green dashed) also *M*-helicity dominated the *Boltzmann* averaged simulated spectra. All spectra predicted by theory were hypsochromically shifted 15 nm.

6.10.2. ECD assignment using reference system 15h

With theoretical predictions of macrocyclic structures compared to experiments being inconclusive, see also chapter 7.9, the strategy had to be changed. To this end, another approach was attempted, removing the covalent linker and capping the attachment points with methoxy functions as in **15h** is described in the following and shown in Figure 154 and 155.

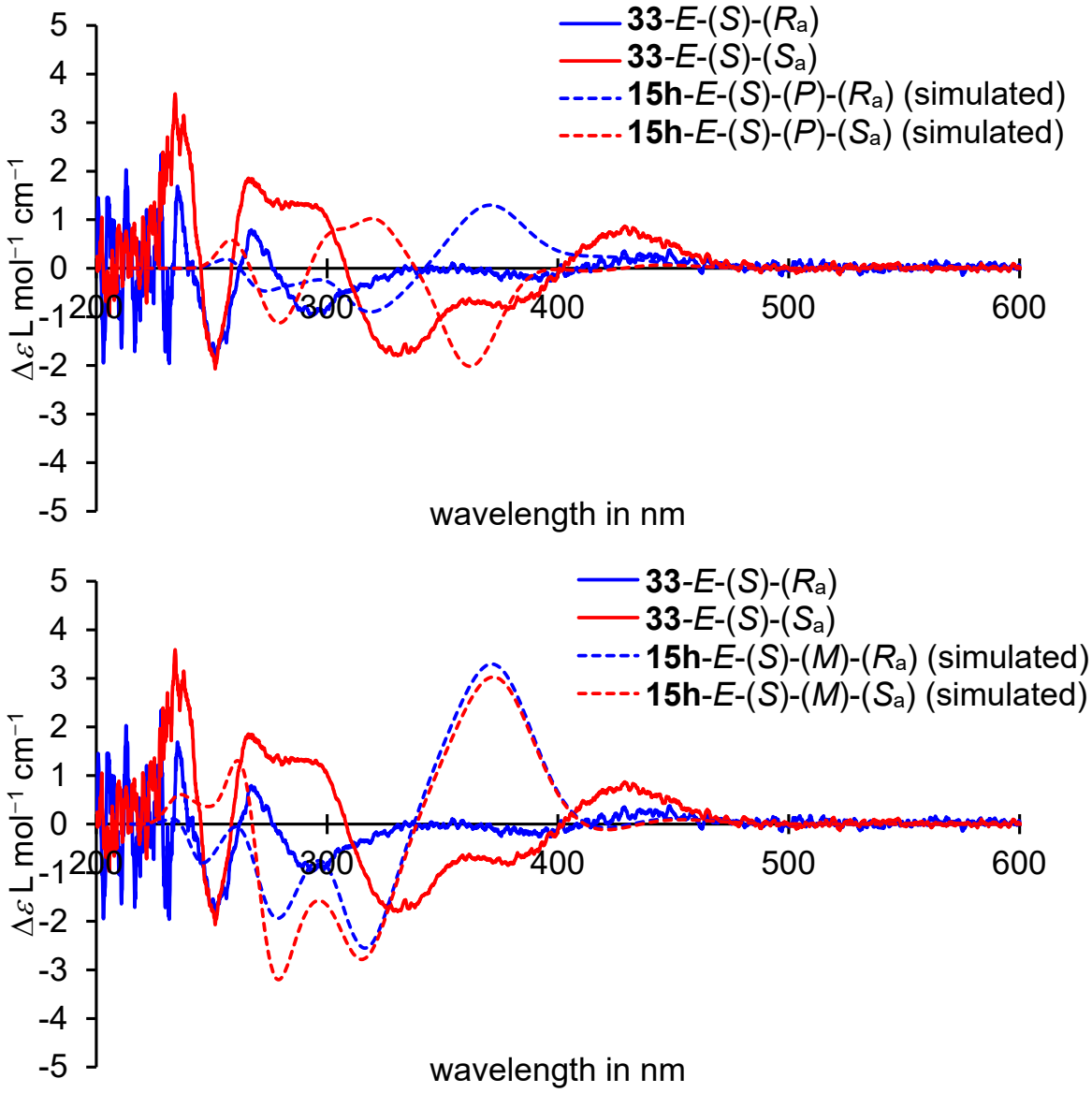

Figure 154 Comparison of ECD spectra (CH_2Cl_2, 22 °C) from enantiomerically pure samples of **33**-*E*-(*S*)-(S_a) (red) and **33**-*E*-(*S*)-(R_a) (blue) to the respective spectra predicted by theory for isomers with *P*-helicitiy (dashed top) and *M*-helicitiy (dashed bottom). Isomers consisting of **15h**-*E*-(*S*)-(S_a) *P*- and *M*-helicities are shown in dashed red and isomers with **15h**-*E*-(*S*)-(R_a) *P*- and *M*-helicities are shown in dashed blue, both hypsochromically shifted 15 nm.

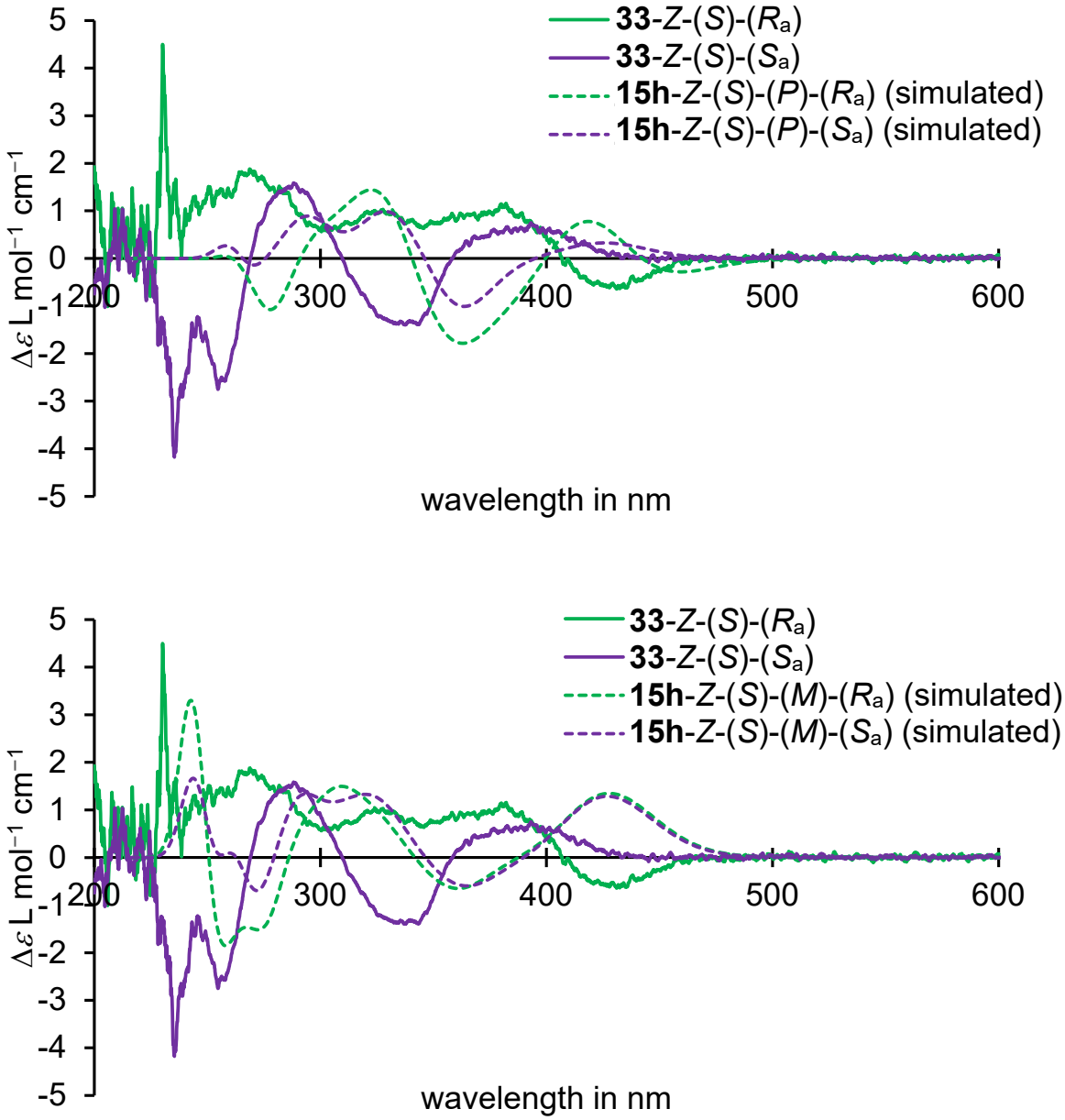

Figure 155 Comparison of ECD spectra (CH_2Cl_2, 22 °C) from enantiomerically pure samples of **33**-*Z*-(*S*)-(S_a) (purple) and **33**-*Z*-(*S*)-(R_a) (green) to the respective spectra predicted by theory for isomers with *P*-helicitiy (dashed top) and *M*-helicitiy (dashed bottom). Isomers consisting of **15h**-*Z*-(*S*)-(S_a) *P*- and *M*-helicities are shown in dashed purple and isomers with **15h**-*Z*-(*S*)-(R_a) *P*- and *M*-helicities are shown in dashed green, both hypsochromically shifted 15 nm.

However, predictions made at the B3LYP/6-311G(d,p) IEFPCM (CH_2Cl_2) level of theory for the prospective HTI-based molecular motor **15h** in comparison with macrocyclic conformers of **33** still remain inconclusive. Spectral similarities between R_a- and S_a-conformations of the same helicity were so large that no assignment to one or the other atropisomer was possible. The same was true for helicities which showed rather distinctly different spectra for *M*- and *P*-conformations but none of these were

unambiguously assignable to any of the experimentally obtained spectra. This does indicate that the helicity in macrocyclic machine **33** is actually highly dynamic and unfortunately not assignable with certainty. For atropisomer and double bond configuration, determination through three out of four crystal structures had to be relied on which is reasonable for barriers above 22.0 kcal mol^{-1}. Furthermore, assignments of double bond configurations were also made *via* 2D NMR spectroscopy, see chapter 6.5. Only helicities in solution could not be assigned, which is fortunately not necessary for the predictions made in the following using QY values.

6.11. Quantum yield determination

The photochemical QYs Φ of macrocyclic HTI **33**, prospective molecular motor **15h** and their unoxidized equivalents **51** and **56** respectively were initially measured in solution using UV-Vis spectroscopy using a setup for QY determination from the *Riedle* group published in 2010.[231] However, this experimental setup did not allow unambiguous determination of QYs for values which are close together in absolute numbers. Thus, correlation between the cyclic and the non-cyclic structures could not be made with the necessary certainty. Therefore, a new improved setup with a significantly reduced measurement error – developed in 2019 in the same group – was employed to remeasure the QYs for **33**, **15h**, **51** and **56**.[247]

These two above-mentioned methods for QY determination are described in the following and values obtained from both setups are compared with each other. The standard deviation for repeated measurements was significantly reduced using the advanced setup, which allowed for a much more precise matching of recorded values as discussed in chapter 6.12.

6.11.1. Quantum yield measurements

Photoisomerization QYs Φ can be calculated from the ratio between the number of isomerized molecules n per number of absorbed photons n as displayed in Equation 11.

$$\Phi = \frac{n\,(\text{photoisomerized molecules})}{n\,(\text{absorbed photons})} \qquad \text{(Eq. 11)}$$

To this end, the number of photoisomerized molecules and photons must be recorded during QY measurement. This was achieved using a cuvette with a path length of 1 cm, which was filled with a defined volume of pure isomer solutions of macrocyclic **33**, motor **15h** or unoxidized equivalents **51** and **56** in CH_2Cl_2. Irradiation of isomers was conducted at 22 °C with a 450 nm LED in an instrumental setup designated for QY measurements by the *Riedle* group.[231]

Photoisomerized molecules were counted by UV-Vis absorption spectra recorded at 22 °C prior to and after each irradiation interval. Thereby, isomer composition of the solution can be monitored *via* predetermined molar extinction coefficients, which allows to calculate the number of photoisomerization processes. Reverse photoisomerizations during irradiation were considered through the initial slope method. Thus, only 5% initial change in concentration was utilized for QY calculations, neglecting the backwards photoisomerization process because the starting isomer is in large excess. However, measurements were performed until a PSS was discernible but data beyond 5% change was excluded for QY calculations, depicted as grey dots in the corresponding Figures 156–161.

The number of photons can be measured directly with a thermal photometer considering the respective irradiation intervals according to Equation 12.

$$n\,(\text{absorbed photons}) = \frac{\Delta P \cdot \lambda_{ex} \cdot t}{c \cdot h} \qquad \text{(Eq. 12)}$$

$$\Delta P = \text{ power readout in } \mathrm{J \cdot s^{-1}}$$

$$\lambda_{ex} = 4.5 \cdot 10^{-7}\ \mathrm{m}$$

$$t = \text{time in s}$$

$$c = \text{speed of light} = 2.998 \cdot 10^{-7}\ \mathrm{m \cdot s^{-1}}$$

$$h = \textit{Planck}\ \text{constant} = 6.626 \cdot 10^{-34}\ \mathrm{J \cdot s}$$

The number of absorbed photons was determined by insertion of the constant numerical values for the speed of light c, the *Planck* constant h and the excitation wavelength from the irradiation source λ_{ex} into Equation 12. Additionally, the varying time t and difference in power readout ΔP was inserted for each irradiation interval. The power readout ΔP was obtained by subtraction of the photometer value of a predetermined blank sample P_0 (the same cuvette filled with solvent only) from the value measured during the corresponding irradiation interval P_t as displayed in Equation 13.

$$\Delta P = P_t - P_0 \qquad \text{(Eq. 13)}$$

The power readouts were plotted over irradiation intervals and extrapolated to t_0 taking photometer drift (resulting from temperature rise with increasing irradiation time intervals) into account similar to a previous report.[271,272]

Photoisomerization QYs for **33** and **15h** were averaged over three and **51** and **56** over two measurements from which only the first stacked UV-Vis absorption spectra are shown in the following for reasons of clarity. QYs for each individual measurement can be found in Tables 14–16, whereas the corresponding UV-Vis spectra and linear regression simulations can be found in Figures 156–161.

Table 14 Experimentally determined QYs Φ of macrocycle **33** in CH_2Cl_2 at 25 °C irradiated with a 450 nm LED.

isomer	measurement #	Φ in %	$\Phi_{aver.}$ in %
33-*E*-**I**	1	3.85	3.50
	2	3.14	
	3	3.52	
33-*Z*-**I**	1	15.22	12.08
	2	12.99	
	3	8.03	
33-*E*-**II**	1	5.50	4.40
	2	2.91	
	3	4.79	
33-*Z*-**II**	1	5.79	4.60
	2	4.29	
	3	3.71	

Table 15 Experimentally determined QYs Φ of prospective non-macrocyclic motor **15h** in CH_2Cl_2 at 25 °C irradiated with a 450 nm LED.

isomer	measurement #	Φ in %	$\Phi_{aver.}$ in %
15h-*E*-(*S*)-(S_a)	1	3.27	4.18
	2	4.52	
	3	4.75	
15h-*Z*-(*S*)-(S_a)	1	2.89	3.52
	2	4.37	
	3	3.31	
15h-*E*-(*S*)-(R_a)	1	4.55	4.61
	2	4.81	
	3	4.46	
15h-*Z*-(*S*)-(R_a)	1	2.15	2.47
	2	2.26	
	3	3.01	

Table 16 Experimentally determined QYs Φ of unoxidized macrocycle **51** and unoxidized non-macrocyclic HTI **56** in CH_2Cl_2 at 25 °C irradiated with a 450 nm LED.

isomer	measurement #	Φ in %	$\Phi_{aver.}$ in %
51-*E*-*(R*$_a$/*S*$_a$*)*	1	2.43	2.12
	2	1.81	
51-*Z*-*(R*$_a$/*S*$_a$*)*	1	3.79	3.51
	2	3.23	
56-*E*-*(R*$_a$/*S*$_a$*)*	1	4.04	3.49
	2	2.94	
56-*Z*-*(R*$_a$/*S*$_a$*)*	1	2.88	3.36
	2	3.84	

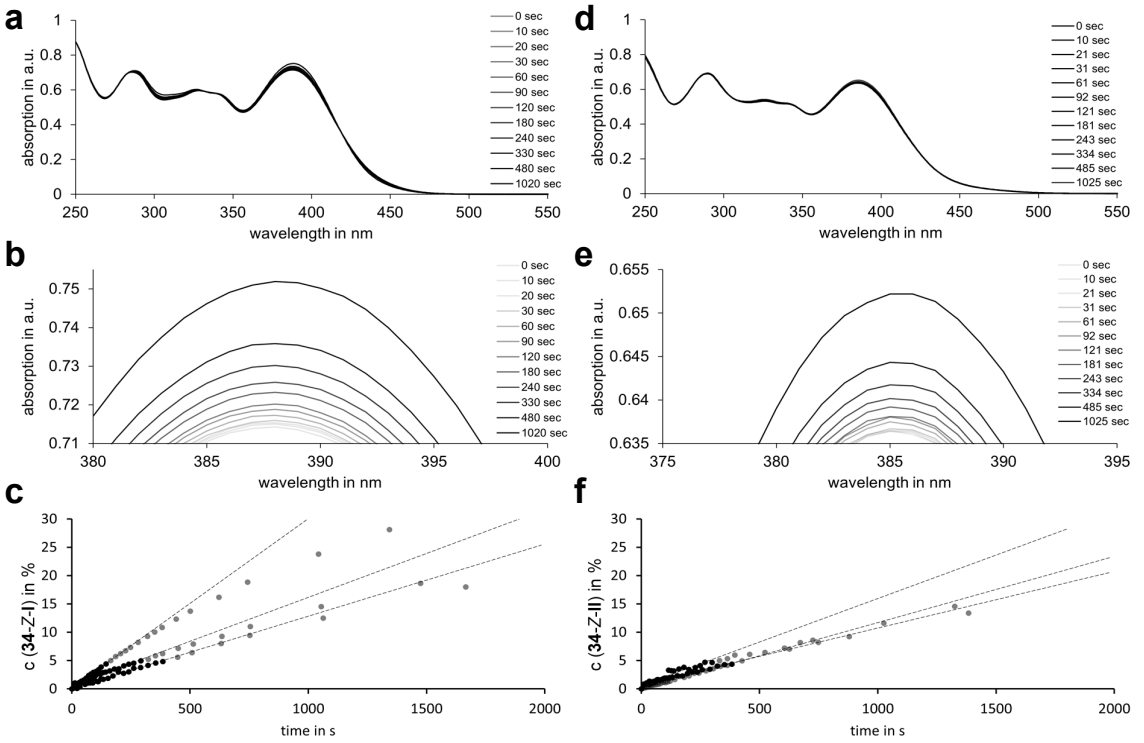

Figure 156 Photoisomerization QY determination of racemic **33**-*E*-**I** and **33**-*E*-**II**. Irradiation of pure solutions was carried out with a 450 nm LED at 22 °C and changes in isomer ratios were monitored by UV-Vis spectroscopy (CH_2Cl_2, 22 °C) using molar extinction coefficients. For reasons of clarity only the first three spectra followed by every third measurement are shown. Linear regression analysis of initial slope is plotted excluding all grey colored dots beyond 5% concentration change. **a** Stacked UV-Vis absorption spectra of **33**-*E*-**I** (56 μM) and corresponding mixtures of **33**-*E*-**I** and **33**-*Z*-**I** after indicated irradiation times. **b** Enlargement of the absorption maxima at 389 nm. **c** Accumulation of **33**-*Z*-**I** during photoisomerization of **33**-*E*-**I**. **d** Stacked UV-Vis absorption spectra of **33**-*E*-**II** (42 μM) and corresponding mixtures of **33**-*E*-**II** and **33**-*Z*-**II** after indicated irradiation times. **e** Enlargement of the absorption maxima at 386 nm. **f** Accumulation of **33**-*Z*-**II** during photoisomerization of **33**-*E*-**II**. QY determination using initial slope analysis (dotted black lines) leads to an average of $\Phi_{E\rightarrow Z} = 3.5\%$ for the **33**-*E*-**I** to **33**-*Z*-**I** photoconversion as well as $\Phi_{E\rightarrow Z} = 4.4\%$ for the **33**-*E*-**II** to **33**-*Z*-**II** photoconversion, averaged over three measurements. Adapted with minor format modifications from *ChemRxiv* **2022**, doi:10.26434/chemrxiv-2022-4th46 licensed under CC BY NC ND 4.0.[1]

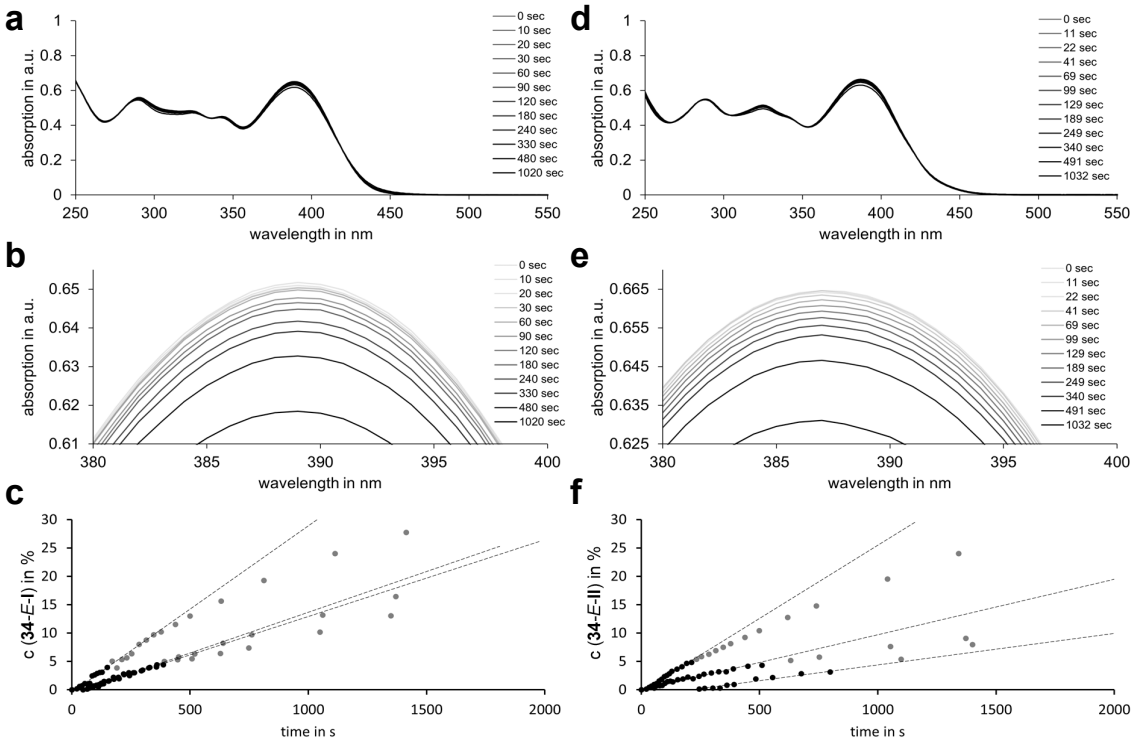

Figure 157 Photoisomerization QY determination of racemic **33**-*Z*-**I** and **33**-*Z*-**II**. Irradiation of pure solutions was carried out with a 450 nm LED at 22 °C and changes in isomer ratios were monitored by UV-Vis spectroscopy (CH_2Cl_2, 22 °C) using molar extinction coefficients. For reasons of clarity only the first three spectra followed by every third measurement are shown. Linear regression analysis of initial slope is plotted excluding all grey colored dots beyond 5% concentration change. **a** Stacked UV-Vis absorption spectra of **33**-*Z*-**I** (42 μM) and corresponding mixtures of **33**-*Z*-**I** and **33**-*E*-**I** after indicated irradiation times. **b** Enlargement of the absorption maxima at 389 nm. **c** Accumulation of **33**-*E*-**I** during photoisomerization of **33**-*Z*-**I**. **d** Stacked UV-Vis absorption spectra of **33**-*Z*-**II** (35 μM) and corresponding mixtures of **33**-*Z*-**II** and **33**-*E*-**II** after indicated irradiation times. **e** Enlargement of the absorption maxima at 386 nm. **f** Accumulation of **33**-*E*-**II** during photoisomerization of **33**-*Z*-**II**. QY determination using initial slope analysis (dotted black lines) leads to an average of $\Phi_{Z\rightarrow E} = 12.1\%$ for the **33**-*Z*-**I** to **33**-*E*-**I** photoconversion as well as $\Phi_{Z\rightarrow E} = 4.6\%$ for the **33**-*Z*-**II** to **33**-*E*-**II** photoconversion, averaged over three measurements. Adapted with minor format modifications from *ChemRxiv* **2022**, doi:10.26434/chemrxiv-2022-4th46 licensed under CC BY NC ND 4.0.[1]

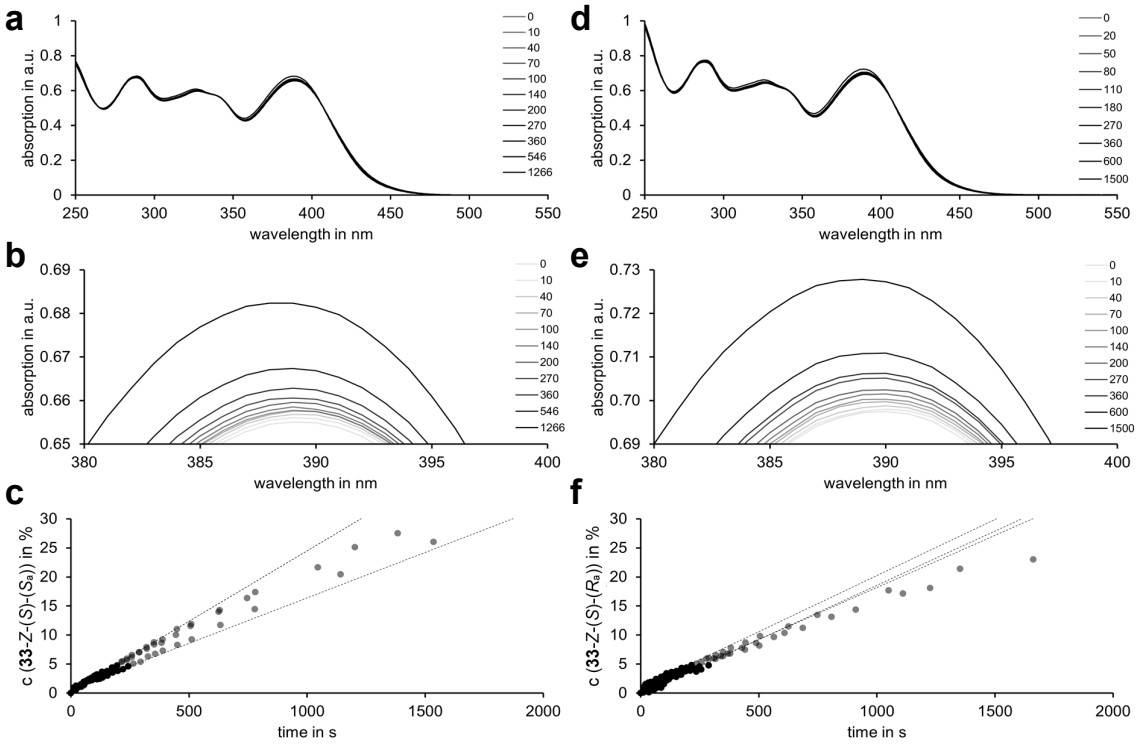

Figure 158 Photoisomerization QY determination of racemic **15h**-*E*-(*S*)-(S_a) and **15h**-*E*-(*S*)-(R_a). Irradiation of pure solutions was carried out with a 450 nm LED at 22 °C and changes in isomer ratios were monitored by UV-Vis spectroscopy (CH_2Cl_2, 22 °C) using molar extinction coefficients. For reasons of clarity only the first three spectra followed by every third measurement are shown. Linear regression analysis of initial slope is plotted excluding all grey colored dots beyond 5% concentration change. **a** Stacked UV-Vis absorption spectra of **15h**-*E*-(*S*)-(S_a) (37 μM) and corresponding mixtures of **15h**-*E*-(*S*)-(S_a) and **15h**-*Z*-(*S*)-(S_a) after indicated irradiation times. **b** Enlargement of the absorption maxima at 388 nm. **c** Accumulation of **15h**-*Z*-(*S*)-(S_a) during photoisomerization of **15h**-*E*-(*S*)-(S_a). **d** Stacked UV-Vis absorption spectra of **15h**-*E*-(*S*)-(R_a) (51 μM) and corresponding mixtures of **15h**-*E*-(*S*)-(R_a) and **15h**-*Z*-(*S*)-(R_a) after indicated irradiation times. **e** Enlargement of the absorption maxima at 388 nm. **f** Accumulation of **15h**-*Z*-(*S*)-(R_a) during photoisomerization of **15h**-*E*-(*S*)-(R_a). QY determination using initial slope analysis (dotted black lines) leads to an average of $\Phi_{E\rightarrow Z}$ = 4.2% for the **15h**-*E*-(*S*)-(S_a) to **15h**-*Z*-(*S*)-(S_a) photoconversion as well as $\Phi_{E\rightarrow Z}$ = 4.6% for the **15h**-*E*-(*S*)-(R_a) to **15h**-*Z*-(*S*)-(R_a) photoconversion, averaged over three measurements. Adapted with minor format modifications from *ChemRxiv* **2022**, doi:10.26434/chemrxiv-2022-4th46 licensed under CC BY NC ND 4.0.[1]

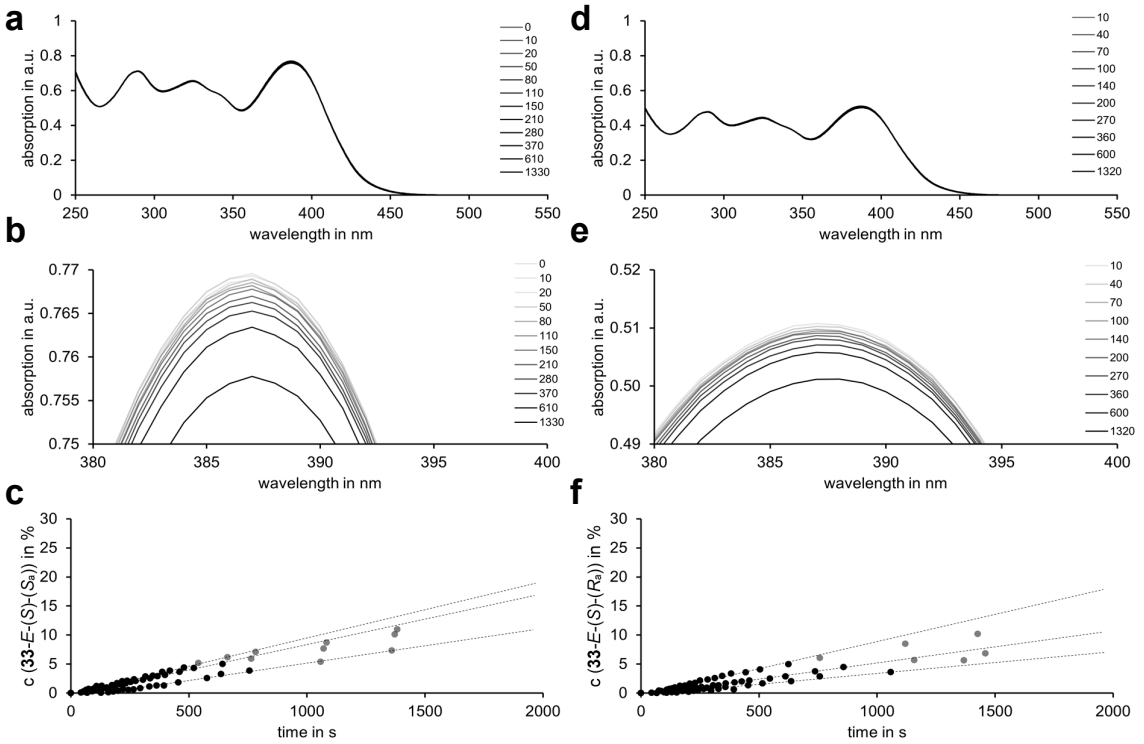

Figure 159 Photoisomerization QY determination of racemic **15h**-*Z*-(*S*)-(S_a) and **15h**-*Z*-(*S*)-(R_a). Irradiation of pure solutions was carried out with a 450 nm LED at 22 °C and changes in isomer ratios were monitored by UV-Vis spectroscopy (CH_2Cl_2, 22 °C) using molar extinction coefficients. For reasons of clarity only the first three spectra followed by every third measurement are shown. Linear regression analysis of initial slope is plotted excluding all grey colored dots beyond 5% concentration change. **a** Stacked UV-Vis absorption spectra of **15h**-*Z*-(*S*)-(S_a) (38 μM) and corresponding mixtures of **15h**-*Z*-(*S*)-(S_a) and **15h**-*E*-(*S*)-(S_a) after indicated irradiation times. **b** Enlargement of the absorption maxima at 388 nm. **c** Accumulation of **15h**-*E*-(*S*)-(S_a) during photoisomerization of **15h**-*Z*-(*S*)-(S_a). **d** Stacked UV-Vis absorption spectra of **15h**-*Z*-(*S*)-(R_a) (32 μM) and corresponding mixtures of **15h**-*Z*-(*S*)-(R_a) and **15h**-*E*-(*S*)-(R_a) after indicated irradiation times. **e** Enlargement of the absorption maxima at 388 nm. **f** Accumulation of **15h**-*E*-(*S*)-(R_a) during photoisomerization of **15h**-*Z*-(*S*)-(R_a). QY determination using initial slope analysis (dotted black lines) leads to an average of $\Phi_{Z\rightarrow E}$ = 3.5% for the **15h**-*Z*-(*S*)-(S_a) to **15h**-*E*-(*S*)-(S_a) photoconversion as well as $\Phi_{Z\rightarrow E}$ = 2.5% for the **15h**-*Z*-(*S*)-(R_a) to **15h**-*E*-(*S*)-(R_a) photoconversion, averaged over three measurements. Adapted with minor format modifications from *ChemRxiv* **2022**, doi:10.26434/chemrxiv-2022-4th46 licensed under CC BY NC ND 4.0.[1]

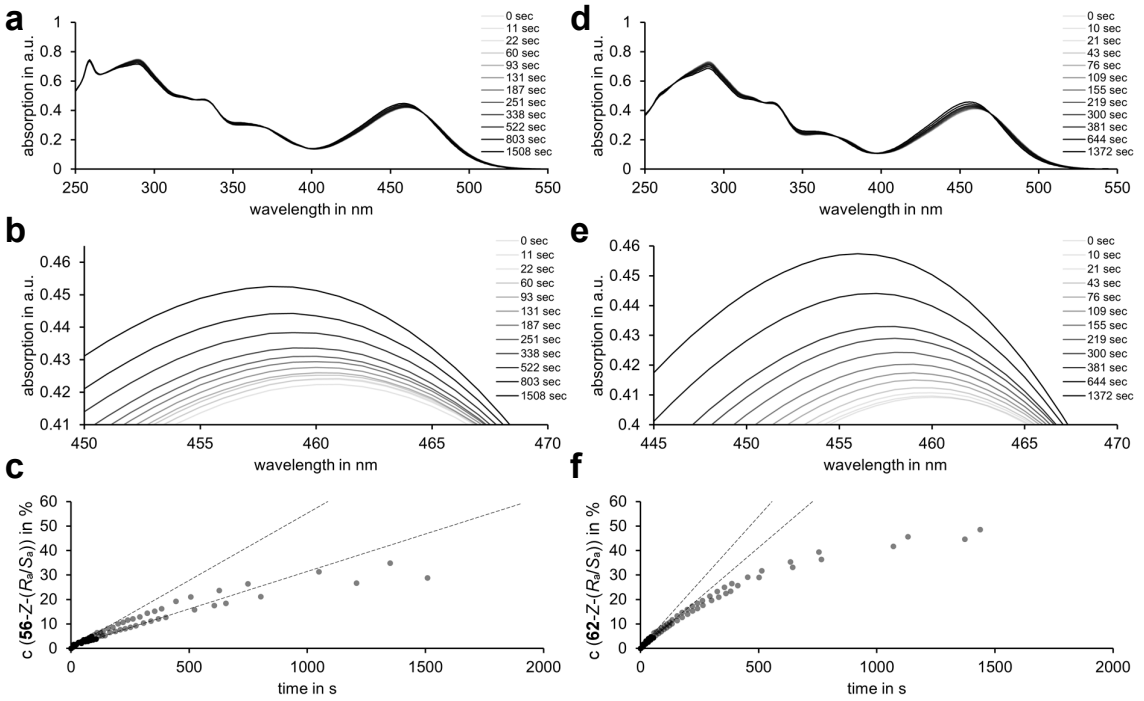

Figure 160 Photoisomerization QY determination of racemic **51**-*E*-(R_a/S_a) and **56**-*E*-(R_a/S_a). Irradiation of pure solutions was carried out with a 450 nm LED at 22 °C and changes in isomer ratios were monitored by UV-Vis spectroscopy (CH_2Cl_2, 22 °C) using molar extinction coefficients. For reasons of clarity only the first three spectra followed by every third measurement are shown. Linear regression analysis of initial slope is plotted excluding all grey colored dots beyond 5% concentration change. **a** Stacked UV-Vis absorption spectra of **51**-*E*-(R_a/S_a) (37 μM) and corresponding mixtures of **51**-*E*-(R_a/S_a) and **51**-*Z*-(R_a/S_a) after indicated irradiation times. **b** Enlargement of the absorption maxima at 458 nm. **c** Accumulation of **51**-*Z*-(R_a/S_a) during photoisomerization of **51**-*E*-(R_a/S_a). **d** Stacked UV-Vis absorption spectra of **56**-*E*-(R_a/S_a) (27 μM) and corresponding mixtures of **56**-*E*-(R_a/S_a) and **56**-*Z*-(R_a/S_a) after indicated irradiation times. **e** Enlargement of the absorption maxima at 457 nm. **f** Accumulation of **56**-*Z*-(R_a/S_a) during photoisomerization of **56**-*E*-(R_a/S_a). QY determination using initial slope analysis (dotted black lines) leads to an average of $\Phi_{E\rightarrow Z}$ = 2.1% for the **51**-*E*-(R_a/S_a) to **51**-*Z*-(R_a/S_a) photoconversion as well as $\Phi_{E\rightarrow Z}$ = 3.5% for the **56**-*E*-(R_a/S_a) to **56**-*Z*-(R_a/S_a) photoconversion, averaged over three measurements. Adapted with minor format modifications from *ChemRxiv* **2022**, doi:10.26434/chemrxiv-2022-4th46 licensed under CC BY NC ND 4.0.[1]

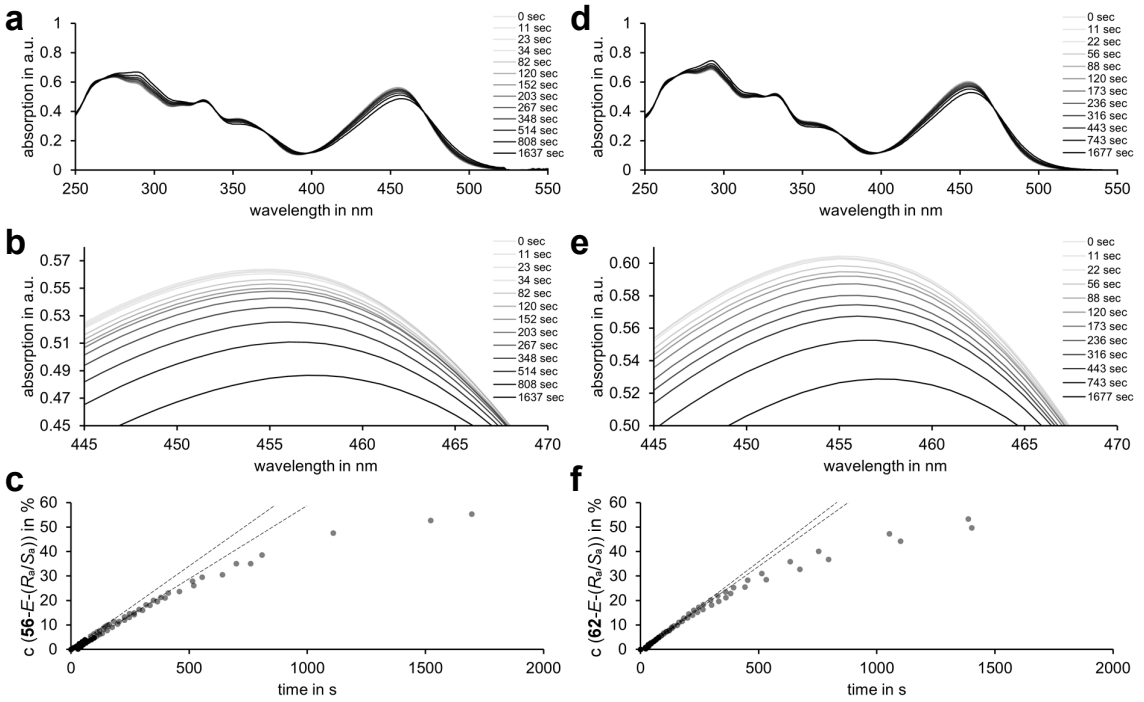

Figure 161 Photoisomerization QY determination of racemic **51**-*Z*-(R_a/S_a) and **56**-*Z*-(R_a/S_a). Irradiation of pure solutions was carried out with a 450 nm LED at 22 °C and changes in isomer ratios were monitored by UV-Vis spectroscopy (CH_2Cl_2, 22 °C) using molar extinction coefficients. For reasons of clarity only the first three spectra followed by every third measurement are shown. Linear regression analysis of initial slope is plotted excluding all grey colored dots beyond 5% concentration change. **a** Stacked UV-Vis absorption spectra of **51**-*Z*-(R_a/S_a) (41 μM) and corresponding mixtures of **51**-*Z*-(R_a/S_a) and **51**-*E*-(R_a/S_a) after indicated irradiation times. **b** Enlargement of the absorption maxima at 458 nm. **c** Accumulation of **51**-*E*-(R_a/S_a) during photoisomerization of **51**-*Z*-(R_a/S_a). **d** Stacked UV-Vis absorption spectra of **56**-*Z*-(R_a/S_a) (32 μM) and corresponding mixtures of **56**-*Z*-(R_a/S_a) and **56**-*E*-(R_a/S_a) after indicated irradiation times. **e** Enlargement of the absorption maxima at 457 nm. **f** Accumulation of **56**-*E*-(R_a/S_a) during photoisomerization of **56**-*Z*-(R_a/S_a). QY determination using initial slope analysis (dotted black lines) leads to an average of $\Phi_{Z\rightarrow E}$ = 3.5% for the **51**-*Z*-(R_a/S_a) to **51**-*E*-(R_a/S_a) photoconversion as well as $\Phi_{Z\rightarrow E}$ = 3.4% for the **56**-*Z*-(R_a/S_a) to **56**-*E*-(R_a/S_a) photoconversion, averaged over three measurements. Adapted with minor format modifications from *ChemRxiv* **2022**, doi:10.26434/chemrxiv-2022-4th46 licensed under CC BY NC ND 4.0.[1]

6.11.2. Revised quantum yield measurements

All QY measurements were repeated for verification by *Dr. Ani Özcelik*[V] using the improved instrumental setup from the *Riedle* group[247] which was operated as described in the following. The revised setup records entire photoisomerization kinetics of a given system from start until a stable PSS is reached, thus forwards and backwards QYs of a two-state photoswitching system can be obtained directly from a single measurement. To this end, a quartz cuvette of 1 cm path length was filled with 2.00 mL of CH_2Cl_2 which was used to measure the initial illumination power P_{ill}. Another identical cuvette was filled with 2.00 mL of a CH_2Cl_2 solution containing the pure or enriched photoswitching system of interest adjusted to an absorption of 0.6–1.7 a.u. at the irradiation wavelength. The sample was illuminated with a 400 nm or 450 nm LED in predefined time intervals, irradiation power recorded using a solar cell detector, and a UV-Vis absorption spectrum measured after each irradiation step. Thus, isomer composition of the solution can be monitored *via* predetermined molar extinction coefficients, which allows to calculate the number of photoisomerization processes after each interval.

The number of photoisomerized molecules n_Z or n_E over a given time interval t can be described with Equations 14 and 15.[247]

$$\frac{dn_Z(t)}{dt} = -\Phi_{Z\rightarrow E}\int \frac{c_Z(t)\cdot\varepsilon_Z(\lambda)}{c_Z(t)\cdot\varepsilon_Z(\lambda)+c_E(t)\cdot\varepsilon_E(\lambda)}\cdot\frac{P_{\text{ill}}\cdot f(\lambda)\cdot\lambda}{h\cdot c}\cdot A(t,\lambda)d\lambda + \Phi_{E\rightarrow Z}\int \frac{c_E(t)\cdot\varepsilon_E(\lambda)}{c_Z(t)\cdot\varepsilon_Z(\lambda)+c_E(t)\cdot\varepsilon_E(\lambda)}\cdot\frac{P_{\text{ill}}\cdot f(\lambda)\cdot\lambda}{h\cdot c}\cdot A(t,\lambda)d\lambda \quad \text{(Eq. 14)}$$

$$\frac{dn_E(t)}{dt} = -\Phi_{E\rightarrow Z}\int \frac{c_E(t)\cdot\varepsilon_E(\lambda)}{c_Z(t)\cdot\varepsilon_Z(\lambda)+c_E(t)\cdot\varepsilon_E(\lambda)}\cdot\frac{P_{\text{ill}}\cdot f(\lambda)\cdot\lambda}{h\cdot c}\cdot A(t,\lambda)d\lambda + \Phi_{Z\rightarrow E}\int \frac{c_Z(t)\cdot\varepsilon_Z(\lambda)}{c_Z(t)\cdot\varepsilon_Z(\lambda)+c_E(t)\cdot\varepsilon_E(\lambda)}\cdot\frac{P_{\text{ill}}\cdot f(\lambda)\cdot\lambda}{h\cdot c}\cdot A(t,\lambda)d\lambda \quad \text{(Eq. 15)}$$

The change in number of molecules with *Z*- or *E*-configuration n_Z or n_E over time t can be described with the QY from *E*- to *Z*-configuration $\Phi_{E\rightarrow Z}$ and *Z*- to *E*-configuration $\Phi_{Z\rightarrow E}$, concentration of the *E*-isomer $c_E(t)$ and *Z*-isomer $c_Z(t)$ at time *t* and molar extinction coefficient of the *E*-isomer $\varepsilon_E(\lambda)$ and *Z*-isomer $\varepsilon_Z(\lambda)$ at wavelength λ. Furthermore, the illumination power P_{ill}, spectral distribution of the LED light $f(\lambda)$, *Planck* constant h, speed of light c, and absorbance A at time t and wavelength λ are necessary to solve this system of differential equations.

$$P_{\text{ill}} = \text{ illumination power in } \text{J}\cdot\text{s}^{-1}$$

$$h = \ Planck \text{ constant} = 6.626 \cdot 10^{-34}\ \mathrm{J \cdot s}$$

$$c = 2.998 \cdot 10^{-7}\ \mathrm{m \cdot s^{-1}}$$

Numerical values for physical constant are given in chapter 6.11.1 and predetermined values for spectral distribution of LEDs, acquired as part of the setup were used. The absorbance can be determined from the cuvette thickness d and values for concentration as well as extinction of *E*- and *Z*-isomers according to Equation 16.

$$A(t,\lambda) = 1 - 10^{-d(c_Z(t)\cdot\varepsilon_Z(\lambda)+c_E(t)\cdot\varepsilon_E(\lambda))} \qquad \text{(Eq. 16)}$$

As already stated above, the forwards and backwards QYs $\Phi_{E\rightarrow Z}$ and $\Phi_{Z\rightarrow E}$ can be obtained by fitting the photoconversions in this two-component system. This method does therefore allow determination of two photoisomerization QYs in one sole measurement, reducing the number of experiments by 50% while increasing accuracy (see chapter 6.12). Hence, only pure and/or enriched solutions of macrocyclic molecular machine **33**-*E*-**I** and **33**-*E*-**II**, prospective molecular motor **15h**-*E*-(*S*)-(R_a), **15h**-*E*-(*S*)-(S_a) and **15h**-*Z*-(*S*)-(R_a), unoxidized macrocyclic **51**-*Z*-(R_a/S_a), and unoxidized non-cyclic **56**-*E*-(R_a/S_a) and **56**-*Z*-(R_a/S_a) were measured delivering QYs for all isomerization directions. Macrocyclic machine **33** and prospective motor **15h** were irradiated with a 400 nm LED, whereas for unoxidized macrocyclic **51** and unoxidized non-cyclic **56** a 450 nm LED was used.

Evaluation of QYs is shown exemplarily for one measurement of each isomer in Figures 162–164 and all measured values are summarized in Tables 17–19. For **15h**-*E*-(*S*)-(S_a) and **15h**-*E*-(*S*)-(R_a) one measurement each was performed to verify QY determination for the forwards and backwards photoisomerization from one sole experiment are sufficiently accurate, which was proven to be the case as shown in Table 18.

Table 17 Experimentally determined QYs Φ of macrocycle **33** in CH_2Cl_2 at 25 °C irradiated with a 400 nm LED. Error margins were generated with standard deviations in a 95% confidence interval assuming normally distributed data. [a]Values were acquired from experimental data for the reverse reaction as explained in the revised QY determination chapter 6.11.2.

isomer	measurement #	Φ in %	$\Phi_{aver.}$ in %	population standard deviation (σ)	standard error (σ_M)	confidence interval (CI)
33-*E*-**I**	1 2	3.38 3.51	3.45	0.06	0.06	3.45 ± 0.09
33-*Z*-**I**	1[a] 2[a]	16.18 16.07	16.13	0.05	0.05	16.13 ± 0.08
33-*E*-**II**	1 2	4.26 4.47	4.37	0.11	0.11	4.37 ± 0.15
33-*Z*-**II**	1[a] 2[a]	9.06 9.46	9.26	0.20	0.20	9.26 ± 0.28

Table 18 Experimentally determined QYs Φ of prospective non-macrocyclic motor **15h** in CH_2Cl_2 at 25 °C irradiated with a 400 nm LED. Error margins were generated with standard deviations in a 95% confidence interval assuming normally distributed data. [a]Values were acquired from experimental data for the reverse reaction as explained in the revised QY determination chapter 6.11.2.

isomer	measurement #	Φ in %	$\Phi_{aver.}$ in %	population standard deviation (σ)	standard error (σ_M)	confidence interval (CI)
15h-*E*-(*S*)-(S_a)	1 2	4.15 3.83	3.99	0.16	0.16	3.99 ± 0.22
15h-*Z*-(*S*)-(S_a)	1[a] 2[a]	6.95 7.03	6.99	0.04	0.04	6.99 ± 0.06
15h-*E*-(*S*)-(R_a)	1 2	4.88 4.65	4.77	0.16	0.12	4.86 ± 0.19
	3[a]	5.05	4.86[b]			
15h-*Z*-(*S*)-(R_a)	1[a] 2[a]	7.89 7.75	7.82	0.06	0.04	7.81 ± 0.07
	3	7.79	7.81[b]			

Table 19 Experimentally determined QYs Φ of unoxidized macrocycle **51** and unoxidized non-macrocyclic **56** in CH_2Cl_2 at 25 °C irradiated with a 400 nm LED. Error margins were generated with standard deviations in a 95% confidence interval assuming normally distributed data. [a]Values were acquired from experimental data for the reverse reaction as explained in the revised QY determination chapter 6.11.2.

isomer	measurement #	Φ in %	$\Phi_{aver.}$ in %	population standard deviation (σ)	standard error (σ_M)	confidence interval (CI)
51-*E*-(R_a/S_a)	1	1.41	1.41	0.02	0.02	1.41 ± 0.02
	2	1.42				
51-*Z*-(R_a/S_a)	1[a]	4.26	4.37	0.10	0.10	4.37 ± 0.14
	2[a]	4.47				
56-*E*-(R_a/S_a)	1	3.64	3.74	0.07	0.05	3.73 ± 0.08
	2	3.83				
	3[a]	3.65	3.73[b]			
56-*Z*-(R_a/S_a)	1[a]	2.58	2.71	0.18	0.13	2.60 ± 0.20
	2[a]	2.83				
	3	2.45	2.60[b]			

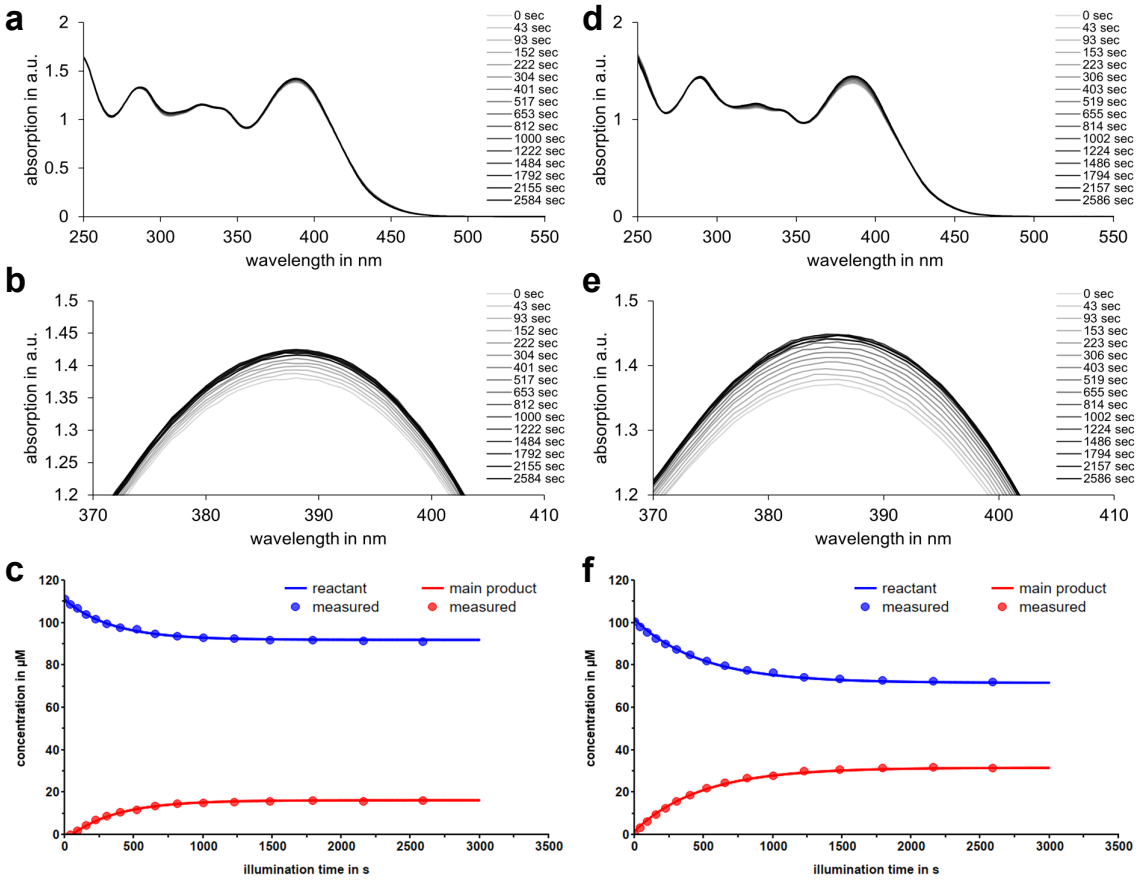

Figure 162 Photoisomerization QY determination for racemic **33**-*E*-**I**, **33**-*Z*-**I**, **33**-*E*-**II**, and **33**-*Z*-**II**. Irradiation was carried out with a 400 nm LED at 22 °C and changes in isomer ratios were monitored by UV-Vis spectroscopy (CH_2Cl_2, 22 °C) using molar extinction coefficients. **a** Stacked UV-Vis absorption spectra of pure **33**-*E*-**I** (116 µM) and corresponding mixtures of **33**-*E*-**I** and **33**-*Z*-**I** after indicated irradiation times. **b** Enlargement of the absorption maxima at 389 nm. **c** Changing concentrations of **33**-*E*-**I** (blue) and **33**-*Z*-**I** (red) during photoisomerization. **d** Stacked UV-Vis absorption spectra of pure **33**-*E*-**II** (111 µM) and corresponding mixtures of **33**-*E*-**II** and **33**-*Z*-**II** after indicated irradiation times. **e** Enlargement of the absorption maxima at 386 nm. **f** Changing concentrations of **33**-*E*-**II** (blue) and **33**-*Z*-**II** (red) during photoisomerization. QY determination *via* fitting of the differential equation system leads to $\Phi_{E\rightarrow Z} = 3.5\%$ for the **33**-*E*-**I** to **33**-*Z*-**I** photoconversion and $\Phi_{Z\rightarrow E} = 16.1\%$ for the reverse reaction as well as $\Phi_{E\rightarrow Z} = 4.4\%$ for the **33**-*E*-**II** to **33**-*Z*-**II** photoconversion and $\Phi_{Z\rightarrow E} = 9.3\%$ for the reverse reaction, averaged over two measurements.

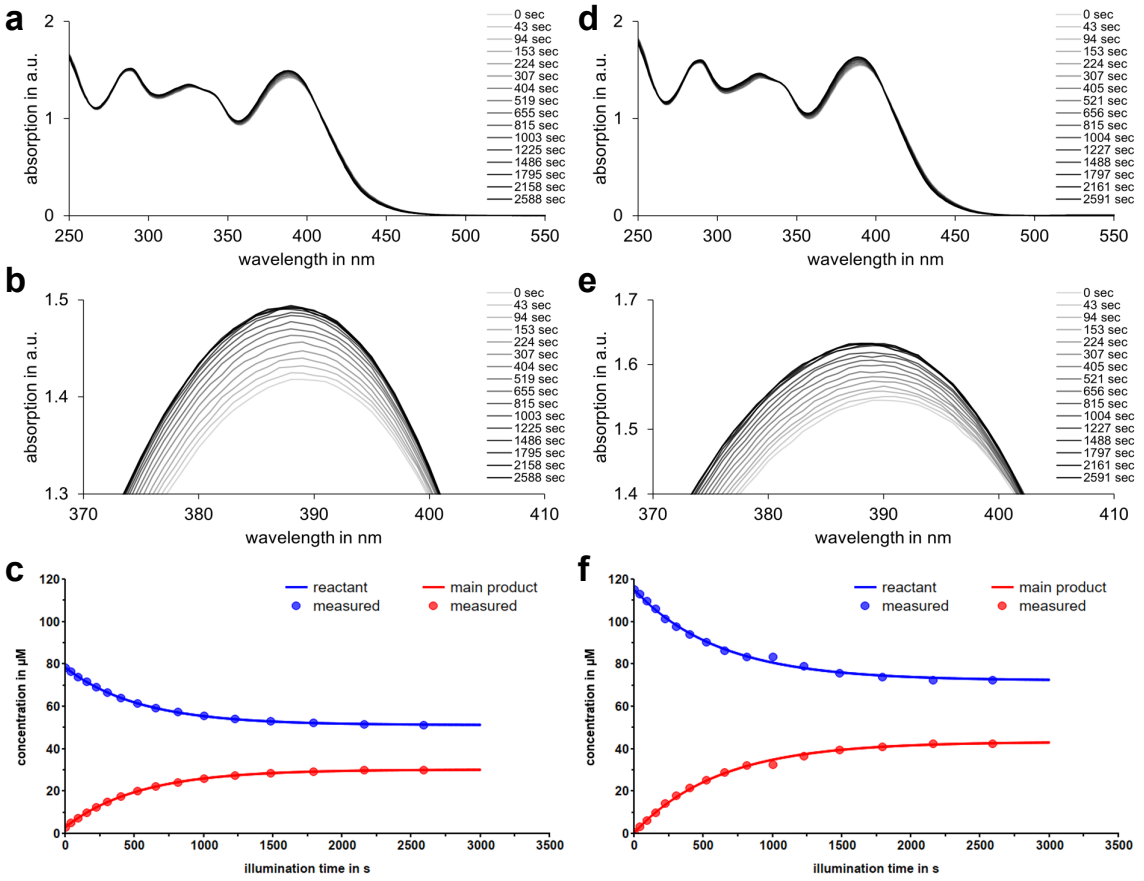

Figure 163 Photoisomerization QY determination for racemic **15h**-*E*-(*S*)-(S_a), **15h**-*Z*-(*S*)-(S_a), **15h**-*E*-(*S*)-(R_a), and **15h**-*Z*-(*S*)-(R_a). Irradiation was carried out with a 400 nm LED at 22 °C and changes in isomer ratios were monitored by UV-Vis spectroscopy (CH_2Cl_2, 22 °C) using molar extinction coefficients. **a** Stacked UV-Vis absorption spectra of pure **15h**-*E*-(*S*)-(S_a) (78 µM) and corresponding mixtures of **15h**-*E*-(*S*)-(S_a) and **15h**-*Z*-(*S*)-(S_a) after indicated irradiation times. **b** Enlargement of the absorption maxima at 389 nm. **c** Changing concentrations of **15h**-*E*-(*S*)-(S_a) (blue) and **15h**-*Z*-(*S*)-(S_a) (red) during photoisomerization. **d** Stacked UV-Vis absorption spectra of pure **15h**-*E*-(*S*)-(R_a) (118 µM) and corresponding mixtures of **15h**-*E*-(*S*)-(R_a) and **15h**-*Z*-(*S*)-(R_a) after indicated irradiation times. **e** Enlargement of the absorption maxima at 390 nm. **f** Changing concentrations of **15h**-*E*-(*S*)-(R_a) (blue) and **15h**-*Z*-(*S*)-(R_a) (red) during photoisomerization. QY determination *via* fitting of the differential equation system leads to $\Phi_{E\rightarrow Z} = 4.0\%$ for the **15h**-*E*-(*S*)-(S_a) to **15h**-*Z*-(*S*)-(S_a) photoconversion and $\Phi_{Z\rightarrow E} = 7.0\%$ for the reverse reaction as well as $\Phi_{E\rightarrow Z} = 4.9\%$ for the **15h**-*E*-(*S*)-(R_a) to **15h**-*Z*-(*S*)-(R_a) photoconversion and $\Phi_{Z\rightarrow E} = 7.8\%$ for the reverse reaction, averaged over two measurements.

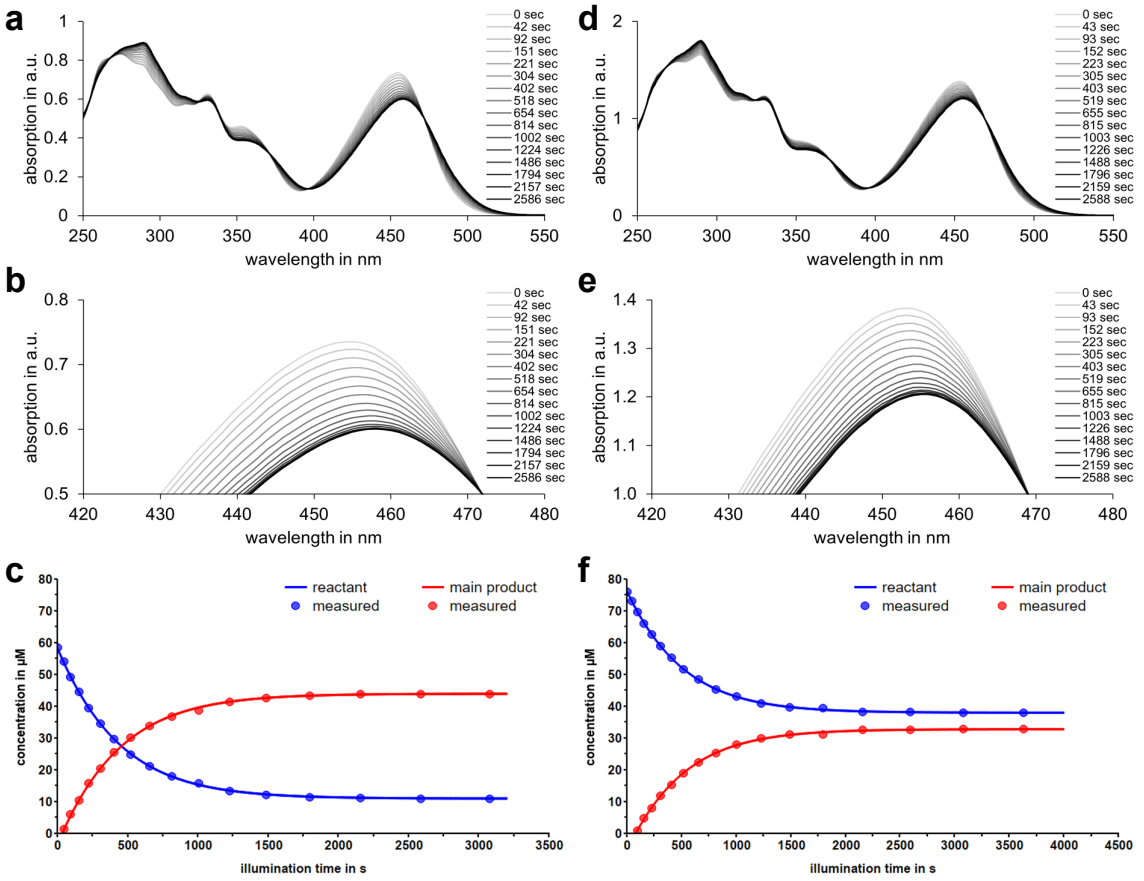

Figure 164 Photoisomerization QY determination for racemic **51**-*Z*-(R_a/S_a), **51**-*E*-(R_a/S_a), **56**-*Z*-(R_a/S_a), and **56**-*E*-(R_a/S_a). Irradiation was carried out with a 400 nm LED at 22 °C and changes in isomer ratios were monitored by UV-Vis spectroscopy (CH_2Cl_2, 22 °C) using molar extinction coefficients. **a** Stacked UV-Vis absorption spectra of pure **51**-*Z*-(R_a/S_a) (59 µM) and corresponding mixtures of **51**-*Z*-(R_a/S_a) and **51**-*E*-(R_a/S_a) after indicated irradiation times. **b** Enlargement of the absorption maxima at 456 nm. **c** Changing concentrations of **51**-*Z*-(R_a/S_a) (blue) and **51**-*E*-(R_a/S_a) (red) during photoisomerization. **d** Stacked UV-Vis absorption spectra of pure **56**-*Z*-(R_a/S_a) (76 µM) and corresponding mixtures of **56**-*Z*-(R_a/S_a) and **56**-*E*-(R_a/S_a) after indicated irradiation times. **e** Enlargement of the absorption maxima at 455 nm. **f** Changing concentrations of **56**-*Z*-(R_a/S_a) (blue) and **56**-*E*-(R_a/S_a) (red) during photoisomerization. QY determination *via* fitting of the differential equation system leads to $\Phi_{E\rightarrow Z}$ = 1.4% for the **51**-*E*-(R_a/S_a) to **51**-*Z*-(R_a/S_a) photoconversion and $\Phi_{Z\rightarrow E}$ = 4.4% for the reverse reaction as well as $\Phi_{E\rightarrow Z}$ = 3.7% for the **56**-*E*-(R_a/S_a) to **56**-*Z*-(R_a/S_a) photoconversion and $\Phi_{Z\rightarrow E}$ = 2.6% for the reverse reaction, averaged over two measurements.

6.12. Quantum yield error margin estimation

Measurements of all QYs for macrocycle **15h**, non-macrocyclic **33**, unoxidized macrocycle **51** and unoxidized non-macrocyclic **56** with the initial and the revised setup are compared in Table 20. From these values it becomes apparent that the precision delivered from the new setup is superior to the initial method, which is necessary for the photochemical method put forward within this work.

Table 20 Comparison of average QYs $\Phi_{aver.}$ measured for macrocycle **33**, non-macrocyclic **15h**, unoxidized macrocycle **51** and unoxidized non-macrocyclic **56** with the initial and the revised setup described in chapter 6.11.1 and 6.11.2 respectively. Errors for the revised setup are given with each sample considered normally distributed, where average QYs $\Phi_{aver.}$ are presented with 95% confidence intervals.

isomer	initial $\Phi_{aver.}$ in %	revised $\Phi_{aver.}$ in %
33-*E*-**I**	3.50	3.45 ± 0.09
33-Z-**I**	12.08	16.13 ± 0.08
33-*E*-**II**	4.40	4.37 ± 0.15
33-Z-**II**	4.60	9.26 ± 0.28
15h-*E*-(*S*)-(S_a)	4.18	3.99 ± 0.22
15h-*Z*-(*S*)-(S_a)	3.52	6.99 ± 0.06
15h-*E*-(*S*)-(R_a)	4.61	4.86 ± 0.19
15h-*Z*-(*S*)-(R_a)	2.47	7.81 ± 0.07
51-*E*-*(R_a/S_a)*	2.12	1.41 ± 0.02
51-*Z*-*(R_a/S_a)*	3.51	4.37 ± 0.14
56-*E*-*(R_a/S_a)*	3.49	3.73 ± 0.08
56-*Z*-*(R_a/S_a)*	3.36	2.60 ± 0.20

In addition to variations from repeated QY measurements, deviations resulting from experimental determination of molar extinction coefficients were also considered for an error assessment of QYs. Given the necessity to differentiate and match QYs within a 1% range, the intrinsic error of these measurements plays a crucial role for the presented photochemical method. Without absolute error assessment available while using a setup for which accuracy is predicted to be in the lower percentage range, an estimation of errors within the recorded QY data was necessary.

To this end, the error introduced from deviations in the initial molar extinction coefficients was determined as shown in Figures 165 and 166. Then QYs were measured repetitively starting from *E*- and *Z*-isomers presented in Table 21 and 22. Upper and lower limits were defined *via* lowest and highest individual molar extinction coefficients which led to the most extreme QYs possible for the recorded

data set. These deviations are within a 1% range, which is even more precise than the error of ~3% given as a rough estimation of the developer.

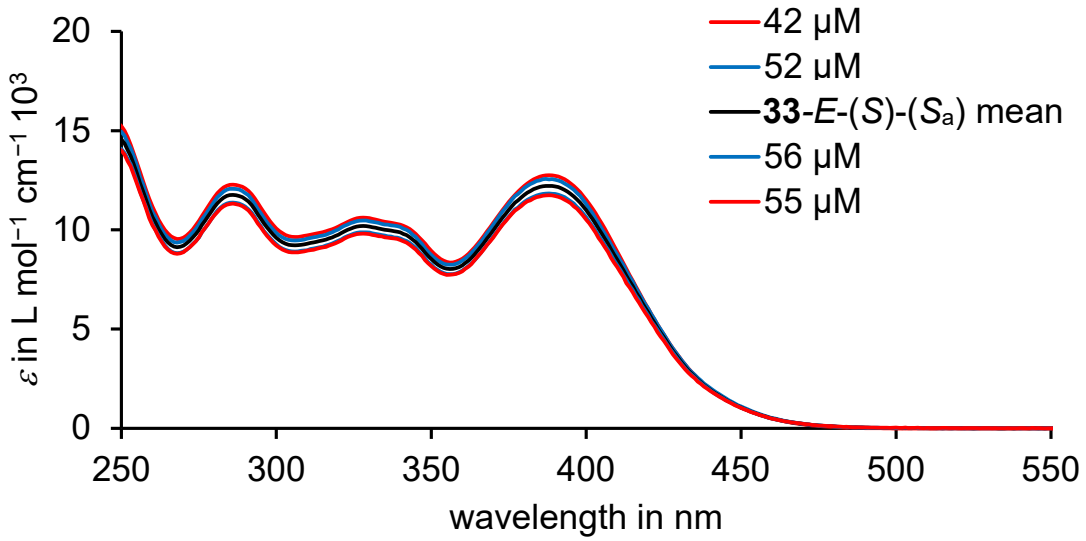

Figure 165 Error margins from four different molar extinction coefficient (CH_2Cl_2, 22 °C) measurements of macrocycle **33**-*E*-**I** at concentrations of 42, 52, 56 and 55 μM, respectively.

Table 21 Influence of experimental error in molar extinction coefficient measurements on QY Φ of macrocycle **33**. Extinction coefficients were repeatedly measured four times and utilized in two QY measurements for **33**-*E*-**I** and **33**-*Z*-**I** each. Error margins were generated with standard deviations in a 95% confidence interval assuming normally distributed data.

isomer	measurement of ε #	measurement of Φ #	Φ in %	$\Phi_{aver.}$ in %	population standard deviation (σ)	standard error (σ_M)	confidence interval (CI)
33-*E*-**I**	1	1	3.38	4.04	0.39	0.22	4.04 ± 0.38
	2		4.37				
	3		4.17				
	4		4.22				
33-*E*-**I**	1	2	3.51	4.17	0.39	0.22	4.17 ± 0.38
	2		4.50				
	3		4.29				
	4		4.36				
33-*Z*-**I**	1	1	16.18	15.73	0.27	0.15	15.73 ± 0.26
	2		15.53				
	3		15.55				
	4		15.65				
33-*Z*-**I**	1	2	16.07	15.61	0.27	0.16	15.61 ± 0.27
	2		15.41				
	3		15.42				
	4		15.54				

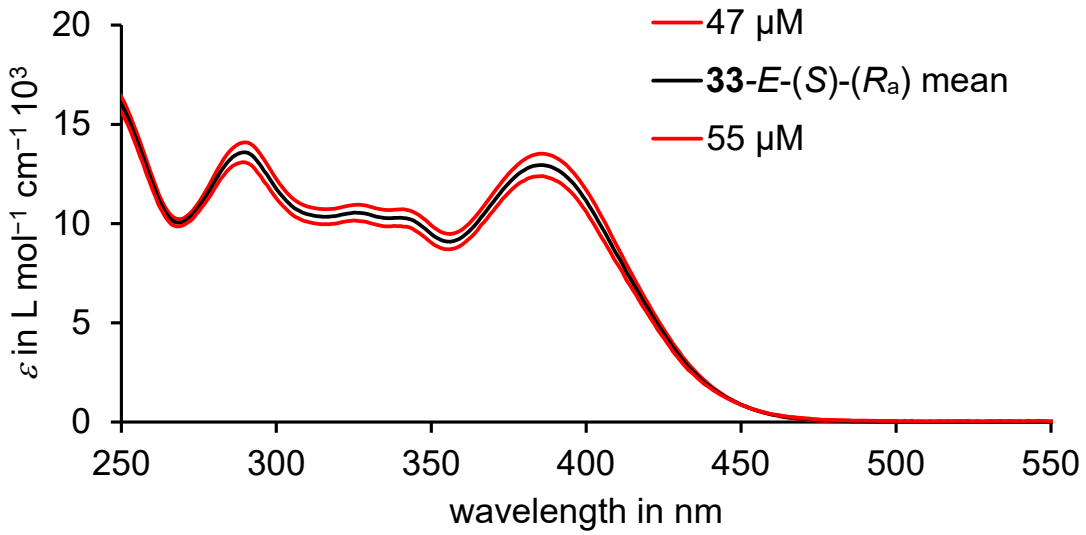

Figure 166 Error margins from two different molar extinction coefficient (CH_2Cl_2, 22 °C) measurements of macrocycle **33**-*E*-**II** at concentrations of 47 and 55 μM respectively.

Table 22 Influence of experimental error in molar extinction coefficient measurements on QY Φ of macrocycle **33**. Extinction coefficients were repeatedly measured two times and utilized in two QY measurements for **33**-*E*-**II** and **33**-*Z*-**II** each. Error margins were generated with standard deviations in a 95% confidence interval assuming normally distributed data.

isomer	measurement of ε #	measurement of Φ #	Φ in %	$\Phi_{aver.}$ in %	population standard deviation (σ)	standard error (σ_M)	confidence interval (CI)
33-*E*-**II**	1 2	1	4.26 4.47	4.37	0.11	0.11	4.37 ± 0.15
33-*E*-**II**	1 2	2	4.69 5.84	5.27	0.57	0.57	5.27 ± 0.80
33-*Z*-**II**	1 2	1	9.06 9.46	9.26	0.20	0.20	9.26 ± 0.28
33-*Z*-**II**	1 2	2	8.92 10.17	9.55	0.63	0.63	9.55 ± 0.87

6.13. Theoretical description

All theoretical descriptions of macrocycle **33** and prospective molecular motors **15f**, **15h**-(R_a) and **15h**-(S_a) were obtained through *ab initio* simulations as explained in detail in chapter 7.11. Theoretical descriptions were conducted with the support from *Dr. Stefan Thumser*.[VI]

6.13.1. Theoretical description of macrocyclic molecular machine 33

For isomers **A**, **B** and **D** crystal structures were utilized as starting points to obtain the optimized ground state geometries in solution. Molecular dynamics simulations using the MMFFs force field with the MacroModel software package from Schrödinger Software were carried out using a mixed torsional/low-mode sampling with a threshold of 6.0 kcal mol^{-1} starting from the crystal geometry of isomer **A** as a seeding structure. Within the distribution of conformers, a structure with opposite atropisomer configuration was used to obtain the optimized ground state geometry of **C** and to perform the above-mentioned molecular dynamics using this seeding structure. From these structures of **A** and **C** the 100 most stable conformers were then optimized at the B3LYP-GD3BJ/6-311G(d,p) IEFPCM (CH_2Cl_2) level of theory to account for the degrees of freedom present in this macrocycle. The following frequency analysis revealed no imaginary frequencies for these structures, indicating only minima were found. Energetically- and geometrically redundant structures were subsequently eliminated and TD-B3LYP-GD3BJ/6-311+G(d,p) IEFPCM (CH_2Cl_2) simulations provided predicted electronic circular dichroism (ECD) excitation spectra. The conformers were then sorted according to their free energies and only spectra from conformations with less than 6.0 kcal mol^{-1} deviation from the most stable structure were considered for the *Boltzmann*-weighted ECD spectra. All plotted spectra can be found in Figures 146–153.

6.13.2. Theoretical description of unrestricted motor systems 15f and 15h

All four or eight isomeric ground state geometriess as well as two or four transition states were optimized at the B3LYP/6-311G(d,p) IEFPCM (CH_2Cl_2) level of theory for reference compounds **15f**, **15h**-(R_a) and **15h**-(S_a) respectively. For clarity, only one sulfoxide configuration was considered, and all obtained minima ground state structures revealed no- and all transition states one imaginary frequency, confirming that they represent either minima or for the ladder saddle points on the potential energy surface. The obtained results can be found in Tables 23 and 24.

Directionalities of molecular motors **15f**, **15h**-(R_a) and **15h**-(S_a) were predicted at the B3LYP/6-311G(d,p) IEFPCM (CH_2Cl_2) level of theory shown in Figure 167. To this end, ground state energies of all stable and metastable isomers **A**-**D** were simulated including transition states for both THI steps revealing very small barriers of about 2.5–4.0 kcal mol^{-1}.

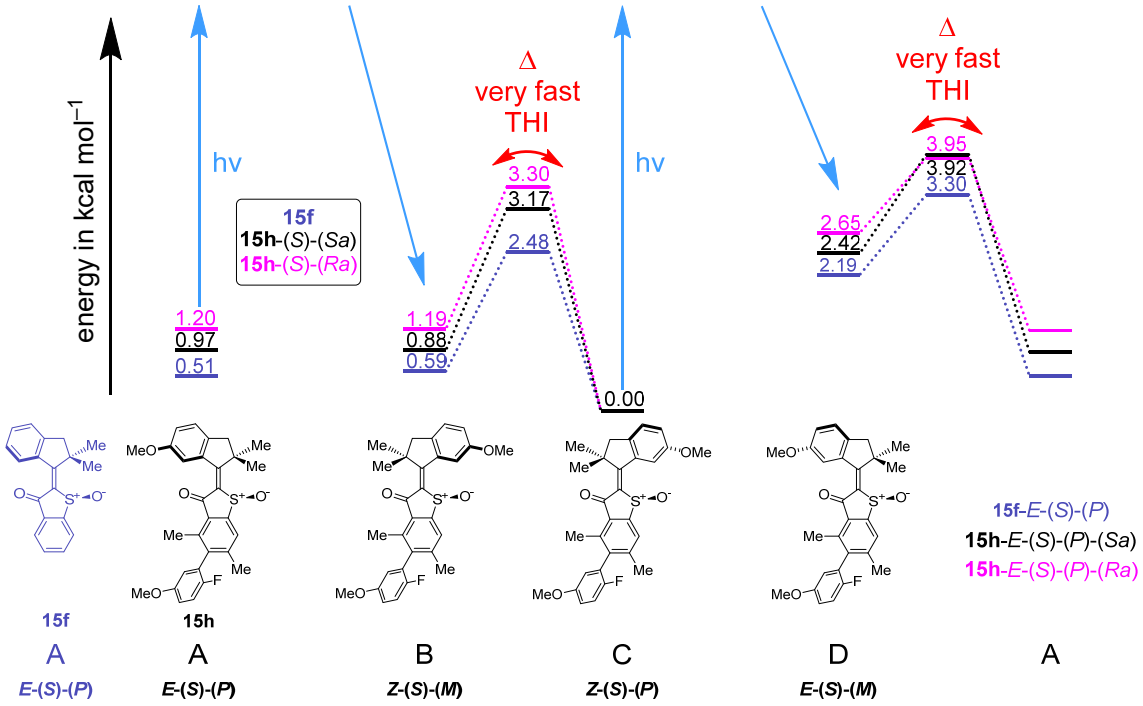

Figure 167 Simulated potential energy profile of HTI-based prospective molecular motors **15f** (purple), **15h**-(R_a) (pink) and **15h**-(S_a) (black). The energies were determined at the B3LYP/6-311G(d,p) IEFPCM (CH_2Cl_2) level of theory. Red arrows indicate very fast THI (Δ) steps. For simplicity only structures with *S*-configured sulfoxide are shown. Adapted with minor format modifications from *Nat. Commun.* **2023**, *14*, 4595 licensed under CC BY 4.0.[1]

Theoretical predictions of directionalities for prospective molecular motors **15f**, **15h**-(R_a) and **15h**-(S_a) revealed very similar pictures for these fast rotating machines with respect to the original motor system for which all intermediate steps are fully verified.[154,155] The pictures drawn from these predictions show that with reduction of steric bulk in the fjord region general trends for HTI-based motors are not

universally true. The barrier for *Z*-(*S*)-(*M*) → *Z*-(*S*)-(*P*) THI step is now higher than the corresponding *E*-(*S*)-(*M*) → *E*-(*S*)-(*P*) conversion but the gap between these barriers in absolute and relative terms is reduced leading to comparable orders of magnitude for these barriers within the range of +1.1–+2.3 kcal mol^{-1}. This shows that the influence of reducing steric strain primarily lowers the *E*-(*S*)-(*M*) → *E*-(*S*)-(*P*) barrier and impact on the *Z*-(*S*)-(*M*) → *Z*-(*S*)-(*P*) barrier becomes smaller. Additionally, the most stable isomer still possesses *Z*-(*S*)-(*P*) configuration which is usually a general trend for HTI-based molecular motors[154,157,161,211] except for increased steric bulk at the rotor part[156] or some of their macrocyclic embedded counterparts.[158,159] It is noticeable that absolute stabilities of *E*-(*S*)-(*P*) and *Z*-(*S*)-(*M*) seem to be almost identical while for previously reported related HTI systems the *E*-(*S*)-(*P*) configuration is usually the more stable one if compared to *Z*-(*S*)-(*M*).[154,156,161,211] This is also reflected in the crystal structures for which **33**-*Z*-**II** is the only isomer possessing *M*-helicity despite *P*-helicity being slightly more stable pointing towards a diminished energy difference between *Z*-(*S*)-(*M*) and *Z*-(*S*)-(*P*). This might be caused by increased stability of *Z*-(*S*)-(*M*) because of reduced steric interactions between the sulfoxide and the aromatic part of the indanone moiety in this configuration compared to *E*-(*S*)-(*M*) for which the interactions with the sulfoxide are not changed significantly. Alternatively, this might be caused by enhanced hydrogen bonding with the sulfoxide. However, this does not hamper overall unidirectionality since *E*-(*S*)-(*P*) is still thermodynamically more stable than *E*-(*S*)-(*M*) and *E*-(*S*)-(*P*) does not isomerize thermally to *Z*-(*S*)-(*M*) at 22 °C. Despite the differences with respect to what has been observed previously for HTI-based molecular motors, overall unidirectionality might be reduced in relative terms, but according to predictions at the B3LYP/6-311G(d,p) IEFPCM (CH_2Cl_2) level of theory, systems **15f**, **15h**-(R_a) and **15h**-(S_a) with significant reduced strain in the fjord region are still unidirectional rotating molecular motors. This finding does also match with previous predictions by theory made for molecule **26**.[259] All predicted values for **15f** and **15h** can be found in Tables 23–24.

Table 23 Theoretical obtained minima and transition state energies of non-macrocyclic **15f** simulated at the B3LYP/6-311G(d,p) IEFPCM (CH_2Cl_2) level of theory.

isomer	G_0 in Hartree	ΔG in Hartree	ΔG in kcal mol^{-1}
15f-*Z*-(*S*)-(*P*)	-1282.2405	0.0	0.0
15f-*Z*-(*S*)-(*M*)	-1282.2395	0.000941	0.6
15f-*E*-(*S*)-(*P*)	-1282.2397	0.000817	0.5
15f-*E*-(*S*)-(*M*)	-1282.2370	0.003496	2.2
TS-**15f**-*E*-(*S*)-(*M*/*P*)	-1282.2352	0.005271	3.3
TS-**15f**-*Z*-(*S*)-(*M*/*P*)	-1282.2365	0.003956	2.5

Table 24 Theoretical obtained minima and transition state energies of non-macrocyclic molecular motors **15h**-(*S*)-(S_a) and **15h**-(*S*)-(R_a) simulated at the B3LYP/6-311G(d,p) IEFPCM (CH_2Cl_2) level of theory.

isomer	G_0 in Hartree	ΔG In Hartree	ΔG in kcal mol^{-1}
15h-*Z*-(*S*)-(*P*)-(S_a)	-1920.1997	0.0	0.0
15h-*Z*-(*S*)-(*M*)-(S_a)	-1920.1983	0.001405	0.9
15h-*E*-(*S*)-(*P*)-(S_a)	-1920.1978	0.001918	1.2
15h-*E*-(*S*)-(*M*)-(S_a)	-1920.1955	0.004228	2.7
TS-**15h**-*E*-(*S*)-(*M*/*P*)-(S_a)	-1920.1934	0.006328	3.9
TS-**15h**-*Z*-(*S*)-(*M*/*P*)-(S_a)	-1920.1944	0.005329	3.3
15h-*Z*-(*S*)-(*P*)-(R_a)	-1920.1997	0.0	0.0
15h-*Z*-(*S*)-(*M*)-(R_a)	-1920.1978	0.001902	1.2
15h-*E*-(*S*)-(*P*)-(R_a)	-1920.1981	0.001544	1.0
15h-*E*-(*S*)-(*M*)-(R_a)	-1920.1958	0.003858	2.4
TS-**15h**-*E*-(*S*)-(*M*/*P*)-(R_a)	-1920.1934	0.006307	4.0
TS-**15h**-*Z*-(*S*)-(*M*/*P*)-(R_a)	-1920.1946	0.005060	3.2

In summary, the predictions by theory confirm what has been proposed previously, that a small initial helical preference can be enough to enable full unidirectionality in a molecular motor setup.[273,274]

6.14. Motion sequence of macrocyclic molecular machine 33

After establishing all configurations of macrocyclic HTI **33** and unrestricted HTI **15h** as well as determination of visible-light-induced isomerizations, and their corresponding QYs a prediction of the rotation direction for the unrestricted system can be made. The approach for this prediction is shown in Figure 168. Measured QY values of **33**-*E*-**I** and **33**-*E*-**II**-isomers were matched with the corresponding closer value of the two **15h**-*E*-isomers. This allows to predict the preferred observed directionality for **15h**-*E* to be clockwise (cw) or counterclockwise (ccw). In a similar approach the **33**-*Z*-**I** and **33**-*Z*-**II** values can be compared to the two **15h**-*Z* isomers. When experimentally observed directionalities and predictions by theory match, an unambiguous elucidation could be made. If there is a mismatch, an analysis of the exact differences can still allow establishment of overall unidirectionality.

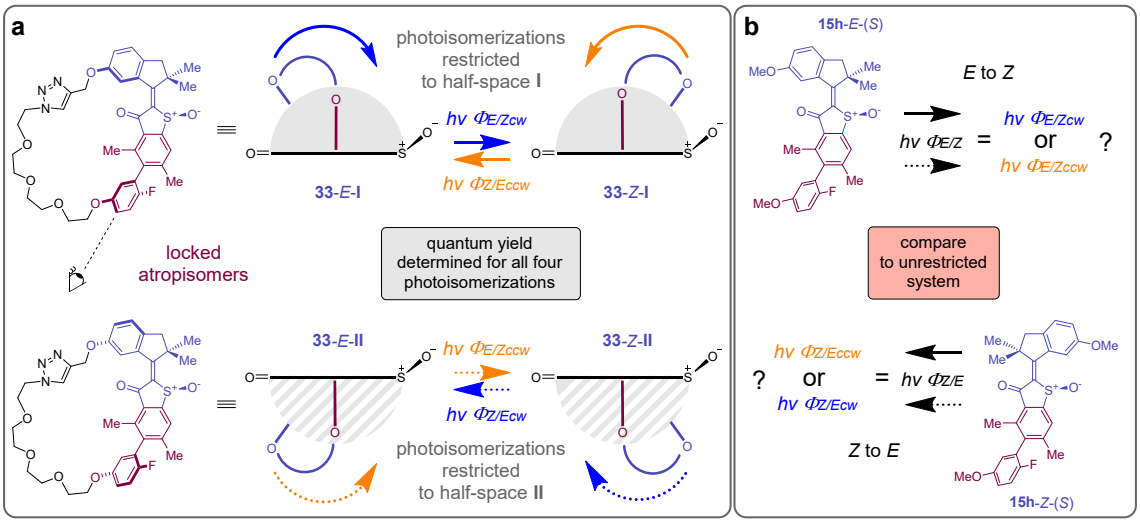

Figure 168 Determining of very fast molecular motor directionalities. **a** Setup for macrocyclic embedding **33** of very fast molecular motions including the motor of interest (blue), a biaryl moiety (purple), and a linking chain (black). Motions are restricted to either half-space **I** (grey, solid arrows) or **II** (dashed grey, dotted arrows) with respect to the sulfoxide oxygen by locked atropisomers. Individual measurement of QYs Φ for all four possible photoisomerization directions allows to determine QYs for the cw rotation (blue arrows) and ccw (orange arrows). **b** These QYs can then be assigned to their respective counterparts in the unrestricted non-macrocyclic system **15h** (black arrows) allowing to predict its motion direction. Adapted with minor format modifications from *Nat. Commun.* **2023**, *14*, 4595 licensed under CC BY 4.0.[1]

Before this prediction can be finally made it must be noted that macrocyclization might have a substantial influence on the observed QYs, leading to potential false prediction of directionality. To account for this bias, the most accurate correction is obtained from comparing values of the macrocyclic, restricted, and unoxidized non-motor HTI systems with its non-cyclic unrestricted and unoxidized counterparts shown in Figure 169. Isomers containing the same degree of pre-twist and maximized chromophore similarities have the same rotation direction possibilities for each pair of isomers. In other words, no directionality bias exists in unoxidized systems thus cw and ccw QYs have the same value. Furthermore, similarity between the isomers from which the macrocycle effect is obtained and the ones which it should be applied to should also be as large as possible. These requirements are fulfilled best for **51**-*E* and **56**-*E* as well as **51**-*Z* and **56**-*Z* without the chiral center at the sulfoxide removing the helical pre-twisted bias towards one rotation direction commonly encountered for these types of systems.[255] Macrocyclization effect factors were determined from the ratios between the cyclic and non-cyclic system as shown in Figure 169.

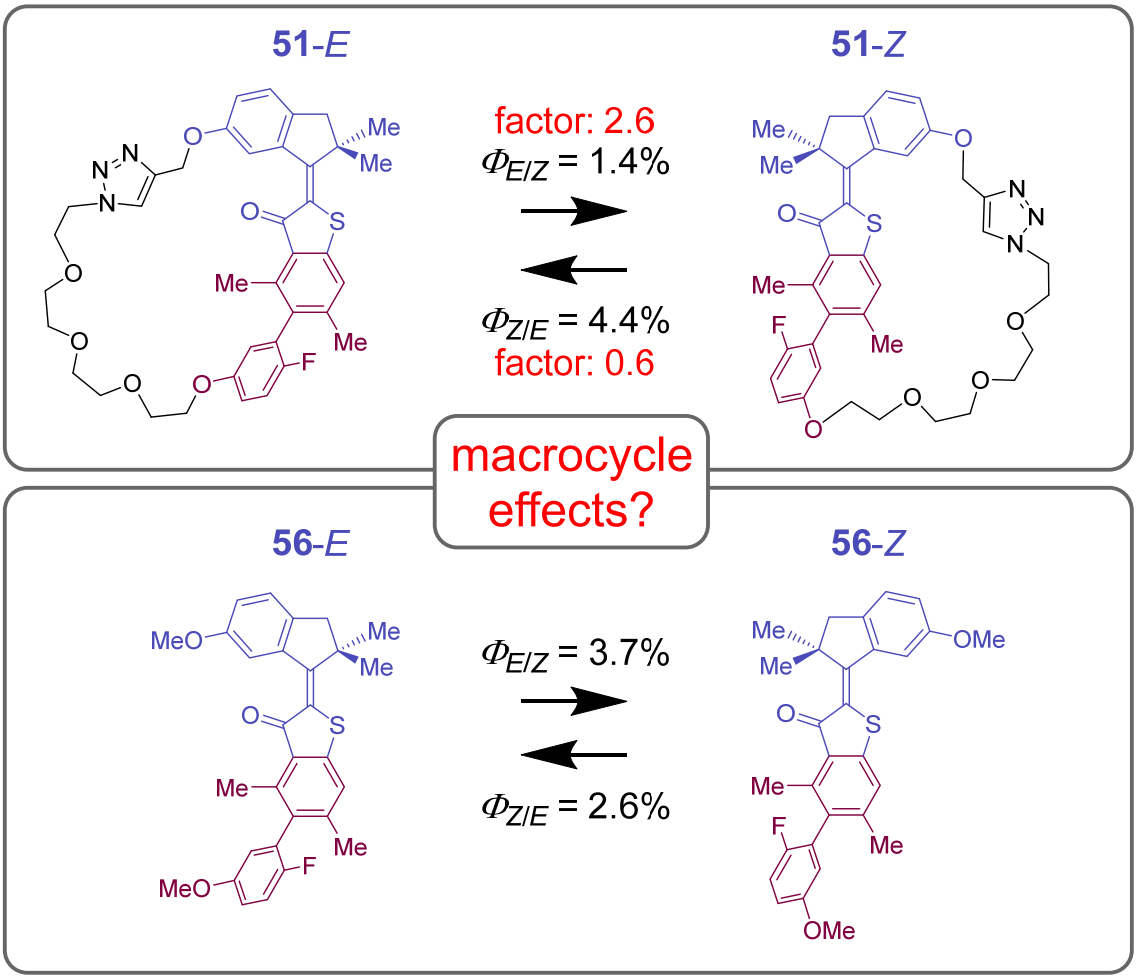

Figure 169 Determination of macrocyclization effect on photoisomerization QYs. Differences in QYs between unoxidized macrocycle **51** and unoxidized unrestricted **56** result in a factor which can be used to correct QYs for macrocyclization effects. Adapted with minor format modifications from *Nat. Commun.* **2023**, *14*, 4595 licensed under CC BY 4.0.[1]

Macrocyclization effect factor of 0.6 for the ratio between values of **51**-*E* and **56**-*E* indicates an increased QY upon macrocyclization for the *E*-isomers. The opposite is true with a factor of 2.6 for **51**-*Z* and **56**-*Z* indicating a reduced QY for the *Z*-isomers. With these factors at hand, a more meaningful prediction of directionality *via* comparison of QYs can be made. To this end, the motor macrocycle QY values were corrected according to their corresponding macrocyclization factors affording the final values used for all predictions made with this method. All measured data, calculated factors and corrected values are illustrated in Table 25.

Table 25 Experimentally determined average QYs $\Phi_{aver.}$ of macrocycle **33**, non-macrocyclic **15h**, unoxidized macrocycle **51** and unoxidized non-macrocyclic **56** in CH_2Cl_2 at 25 °C. Irradiation of **33** and **15h** was conducted using a 400 nm LED whereas a 450 nm light was used for **51** and **56**. Error margins were generated with standard deviations in a 95% confidence interval assuming normally distributed data and contain maximum errors of molar extinction coefficient and QY measurements. For individual error determination see chapter 6.12.

isomer	$\Phi_{aver.}$ in %	confidence interval (CI)
33-*E*-**I**	3.45	3.45 ± 0.87
33-*Z*-**I**	16.13	16.13 ± 0.87
33-*E*-**II**	4.37	4.37 ± 0.87
33-*Z*-**II**	9.26	9.26 ± 0.87
15h-*E*-(*S*)-(S_a)	3.99	3.99 ± 0.87
15h-*Z*-(*S*)-(S_a)	6.99	6.99 ± 0.87
15h-*E*-(*S*)-(R_a)	4.86	4.86 ± 0.87
15h-*Z*-(*S*)-(R_a)	7.81	7.81 ± 0.87
51-*E*-*(Ra/Sa)*	1.41	1.41 ± 0.87
51-*Z*-*(Ra/Sa)*	4.37	4.37 ± 0.87
56-*E*-*(Ra/Sa)*	3.73	3.73 ± 0.87
56-*Z*-*(Ra/Sa)*	2.60	2.60 ± 0.87
macrocycle effect *E*		2.64
macrocycle effect *Z*		0.59
macrocyc. corr. 33-*E*-**I**		8.97
macrocyc. corr. 33-Z-**I**		9.68
macrocyc. corr. 33-*E*-**II**		11.36
macrocyc. corr. 33-*Z*-**II**		5.56

Conclusions drawn from measured QY values and predictions for prospective fast molecular motor **15h** are summarized in Figure 170.

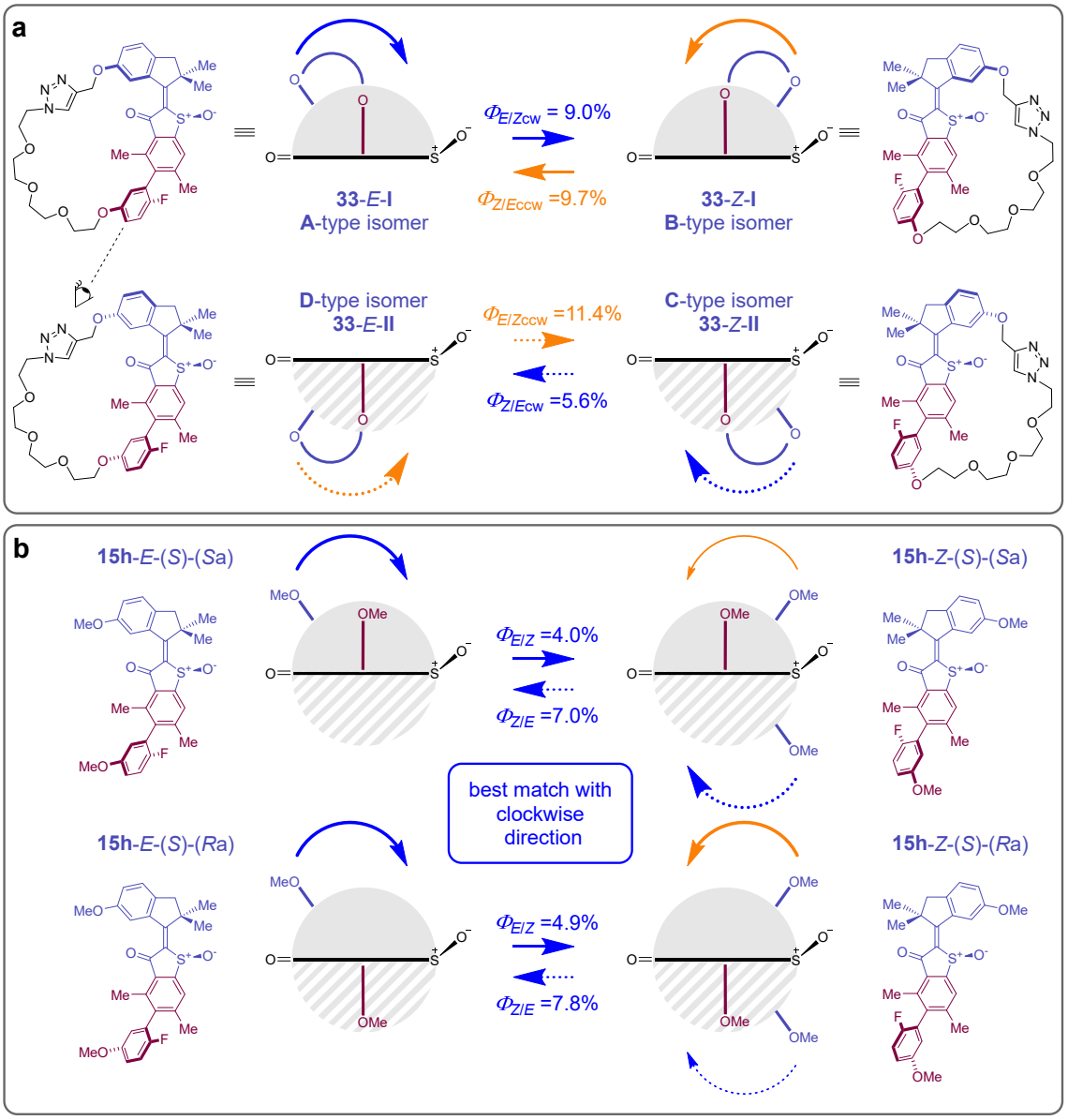

Figure 170 Directionality prediction of HTI-based prospective molecular motor **15h** *via* quantitative comparison of photoisomerization QYs with macrocyclic **33**. Rotation directions and corresponding QYs are depicted in blue for cw and orange for ccw rotation directions. **a** Visible-light-induced motions are restricted to either half space **I** (solid grey half circle and solid arrows) or **II** (dashed grey half circle and dotted arrows) in macrocycle **33**. QY values of **33** shown here are corrected for the macrocyclization effect illustrated in Figure 169. **b** QYs measured for photoisomerization of **15h**-(*S*)-(S_a) (top) and **15h**-(*S*)-(R_a) (bottom). Comparison of QYs between macrocycle **33** and unrestricted prospective motors **15h**-(*S*)-(S_a) and **15h**-(*S*)-(R_a) reveal an overall unidirectional rotation in cw (blue) direction for both systems. However, a larger degree of unidirectionality is detected for **15h**-(*S*)-(S_a) with respect to **15h**-(*S*)-(R_a), for which a higher degree of backwards rotation is observed for the *Z*- to *E*-isomerization (compare right side top and bottom). Adapted with minor format modifications from *Nat. Commun.* **2023**, *14*, 4595 licensed under CC BY 4.0.[1]

6.15. Conclusion

In summary, a photochemical method was developed, enabling to evidence fast light-induced molecular motions experimentally using a synthetic approach. Commonly, ultrafast motions for molecules for which intermediates are either not observable using standard analytical methods – or not even present – are attempted to be resolved by ultrafast transient techniques such as transient absorption spectroscopy, or predictions by theory. This is one reason why fast molecular motors are scarce. However, these methods do rarely deliver detailed experimental geometrical information about configuration of intermediates or fail completely in cases where no observable high-energy intermediates are present. To this end, a synthetic/photochemical-based approach is presented embedding the molecular structure of interest into a macrocyclic framework. Through connecting the rotating part with a sterically locked biaryl axis which is linked to the other end of the molecule with a covalently attached flexible linker all possible motions, clockwise and counterclockwise can be observed. The plane of the terminal aryl should be as perpendicular to the system of interest as possible leading to a restriction of rotation within one molecular half-space. This was achieved through increasing steric bulk in *ortho*-positions of the biaryl axis. Consequently, the light-induced 360° rotation in the unrestricted system is now limited to two separate ~180° rotation-photoequilibria in the restricted macrocyclic system. This allows to measure QYs for the clockwise and counterclockwise rotation in case of *e.g.* a molecular motor leading to values attributable to both directions. In other words, a thorough quantification of all possible involved rotational movements induced by light was feasible. After taking the macrocyclization effect into account, comparison of QYs to the corresponding unrestricted system delivered a direct prediction of unidirectionality according to best matching values.

This method does offer the possibility to make the distinction between a motor and a switch determining a preferred directionality if differences in QY for the respective directions are small. However, if QY differences of clockwise and counterclockwise motions are large enough, it is possible to determine a semi-quantitative high or low degree of unidirectionality.

What is more, this methodology can also be extended to fast molecular motions without any high energy intermediates present since it does not rely on the observation of intermediate states but can instead trace back a motion to its starting state.

7. Structural reconfiguration of macrocyclic molecular motors – Defining unidirectional motions

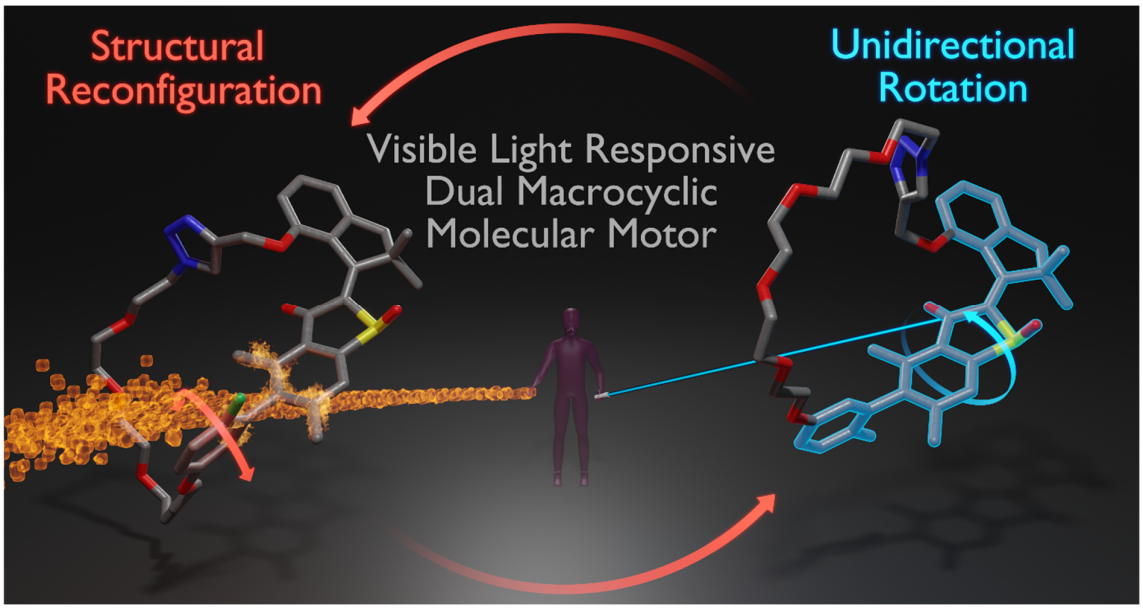

Figure 171 Table of contents image, adapted from *J. Am. Chem. Soc.* **2023**, *145*, 13081–13088 licensed under CC BY-NC-ND 4.0. Copyright © 2023 The Authors. Published by American Chemical Society.[2]

7.1. Aim

Molecular machine research took great inspiration from nanomachinery found in nature, such as the linear movement of kinesin along microtubule, rotating ATP synthase[8,9] or interactions inside the ribosome.[275] When comparing this level of control found in nature to systems developed artificially such as the thermally-activated molecular rotors,[276,277] brakes,[98,172] and gears[175–184] or the actively-powered systems such as pumps,[122,123,174] motors,[14,174,236,255,278,279] and the more recently developed photogears,[85,185–189] it becomes evident that it is apparently still a long way to come anywhere near the sophisticated precision found in nature's elaborated nanomachinery.

Controlling and transmitting molecular motions with utmost precision is therefore key for the development of sophisticated integrated molecular machines. One compound class of such machinery for which various concepts of motions have been examined are molecular motors and especially the well examined light-driven overcrowded alkene[22,280–285] **57** or visible-light-driven HTI-based motors[141,142,154,156–161,259] **15d** shown in Figure 172 amongst others,[137,117,140,286] such as imine motors.[138] The movement trajectories of molecular motors do occur in a unidirectional fashion, which makes them ideal building blocks for actively-powered functional nanomachinery. What is more, the molecular design of such HTI-based units has been studied intensively in the past regarding control of speed,[156] operational wavelengths, temperature dependencies,[141] trajectories of motions,[142] and supramolecular interactions[161] to name only a few aspects of molecular motor manipulation. The next logical step is therefore to harness the unidirectional motion generated by the motor rotation to actively power a remote entity.

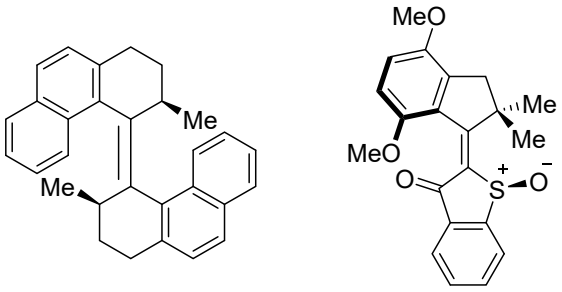

Figure 172 The original overcrowded alkene **57** (left) and HTI **15d** (right) based motors.

One persuasive strategy to make use of molecular motions represents macrocyclization.[286–291] For molecular motors there are two options for incorporating into macrocycles. Either solely rotor or stator[145,292] can be embedded or both fragments can be interconnected.[2,158,159,190–194,196] To this end, the unidirectional rotating motor unit needs to be part of a larger functional setup allowing the movement to be transmitted. Integrating molecular motors into macrocycles is one especially powerful approach

for harnessing their light-fueled directional motion for the execution of functions in a remote position.[158,159,192] This is illustrated for a few selected examples in Figure 173 among which are self-locked **58**,[145] molecular winding **59** and **63**,[190,191,193,196] metallacycles **60**,[292] cation binding **61**,[192] and strain modulated macrocyclic molecular motors **62**.[194]

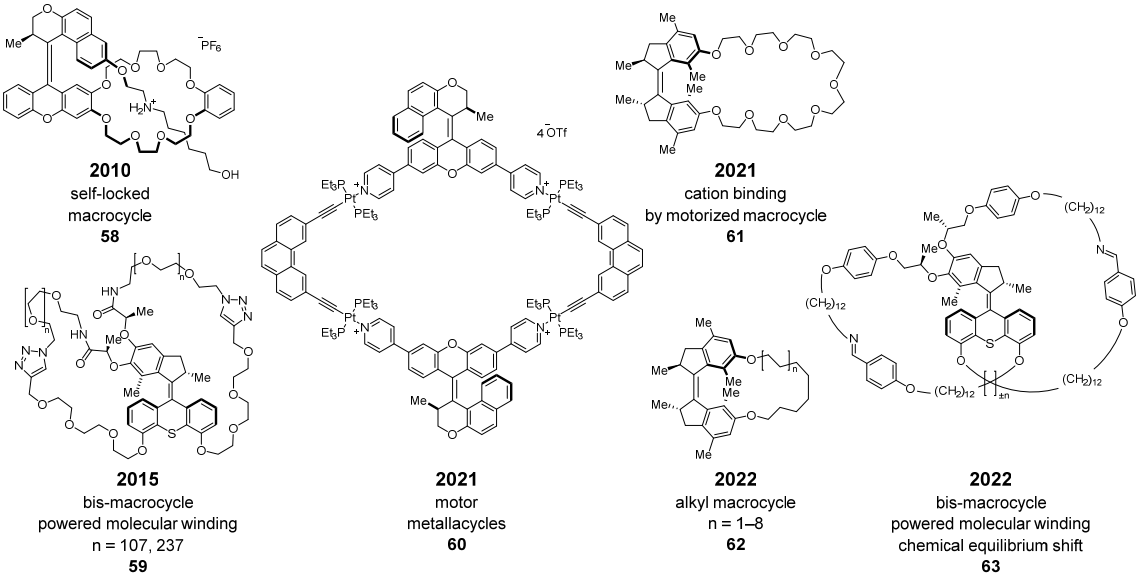

Figure 173 Molecular motor-based macrocyclic machines providing advanced functionality. Several macrocyclic examples are displayed, including self-locked **58**, molecular winding **59** and **63**, metallacycles **60**, cation binding **61** and strain modulated **62** molecular motors. Adapted with minor format modifications from *J. Am. Chem. Soc.* **2023**, 145, 13081–13088 licensed under CC BY-NC-ND 4.0. Copyright © 2023 The Authors. Published by American Chemical Society.[2]

The macrocyclization of a HTI-based motor has been achieved for the first time in 2018 by *Uhl et al.* transmitting unidirectional rotation onto a passive remote biaryl axis, which does synchronously follow the motor movement.[159] In a subsequent investigation, the motor rotation enabled the active acceleration of a biaryl axis rotation by several orders of magnitude.[158] The newest work using macrocyclic HTIs from *Bach et al.* comprised of the first active mechanical threading process powered by the same visible-light-driven molecular motor.[157] All these macrocyclic embeddings are shown in Figure 174 and make use of precisely defining the revolving door fragment in order to achieve the desired functionality (orange fragment show in Figure 174). The revolving door core structure is in each case made of an aromatic ring fused with a non-aromatic five membered ring substituted with various functional groups, rendering this segment rather rigid without many possibilities for conformational changes.

Extending the revolving door through a thermally locked biaryl axis would not only enlarge the revolving door section, but would also allow reversible conformational changes within the revolving door leading to a level of motion control unprecedented for macrocyclic molecular motors to date.

However, apart from thermally locking the biaryl barrier another necessity was to elongate the covalent linker connecting the indanone rotor unit and the biaryl attached to the benzothiophenone stator unit. Without the enlarged macrocycle the motor rotation would be hampered by the enlarged revolving door not having enough space for the unidirectional 360° rotation.

7.2. Design principles

Integrating molecular motors into more complex functional nanomachinery enabled a series of advances. After the development of a first functional HTI-based molecular motor by *Guentner et al.* in 2015,[154] *Huber et al.* enabled the prove of all involved motions in 2017,[293] proceeded by *Wilcken et al.* in 2018[155] drawing an even more complete picture involving all excited states. In the same year *Uhl et al.* analyzed the first HTI-based macrocyclic molecular motor **64** able to transfer unidirectional motion onto a passive biaryl receiver[159] which was further accelerated in **65** by *Uhl et al.* in 2020.[158] A related concept was put forward by *Bach et al.* in 2022 by developing a first setup paving the way for mechanical threading using a molecular motor **66**.[157] Additionally, a related setup **67** was put forward by *Reißenweber et al.* in 2024 shifting the biaryl axis by 120°, leading to directionality reversal of the rotation.[160]

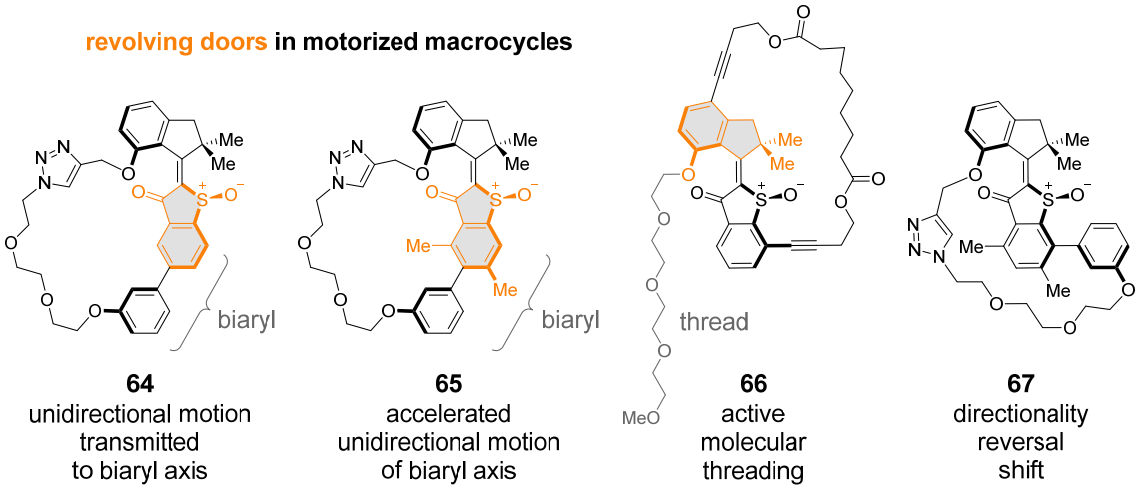

Figure 174 HTI-based macrocyclic molecular motors **64**, **65**, and **66** with defined revolving doors as well as **67** with a 120° shifted biaryl axis developed in the Dube group between 2018–2024. The revolving door units are highlighted in orange. Systems **64** and **65** developed by *Uhl et al.* in 2018 and 2020, enable the transmission of unidirectional rotation onto a passive receiver unit and their respective acceleration[158,159] and system **66** reported by *Bach et al.* in 2022 showing the first actively-powered molecular threading event at the nanoscale.[157] Most recently, a 120° shifted biaryl axis was incorporated into **67** inducing directionality reversal of the motor rotation.[160] Adapted with minor format modifications from *J. Am. Chem. Soc.* **2023**, 145, 13081–13088 licensed under CC BY-NC-ND 4.0. Copyright © 2023 The Authors. Published by American Chemical Society.[2]

Increasing the level of motion control can be achieved by incorporating an isomerizable unit, that is stable during unidirectional rotation fueled by visible light irradiation, but able to change conformation upon an additional orthogonal stimulus. In this case the additional orthogonal stimulus would be thermal energy resulting in atropisomerization. The most straightforward approach to do this is to take an already present element in one of the macrocycles shown in Figure 174 and modify it to be independently isomerizable. The only unit left connected in a rigid fashion without serving a direct purpose for

macrocyclic motor rotation in this regard is the biaryl axis. Modifying this axis by *e.g.* increasing the barrier for rotation in combination with an increased macrocycle ring size would allow a larger revolving door element, which includes the biaryl unit, to rotate unidirectionally through the macrocycle.

In order to lock the biaryl axis during visible-light-driven motor rotation at 22 °C, it was necessary to sufficiently raise the respective energy barrier as found in **64** and **65** (approximately <13.0 and 18.0 kcal mol^{-1}) to a significantly higher value of about 27.0 kcal mol^{-1}. This would result in a thermal half-life of days at ambient temperatures for such hindered biaryl rotation, rendering routine spectroscopic analysis possible avoiding additional expenditure. The smallest conceivable change would consist of exchanging one of the hydrogens in *ortho*-position for a fluorine (as done in **33** and **68**) since raising the barrier for thermal atropisomerization far beyond the one for thermal double bond isomerization would disturb overall motor directionality during thermal biaryl rotation shown in Figure 175.

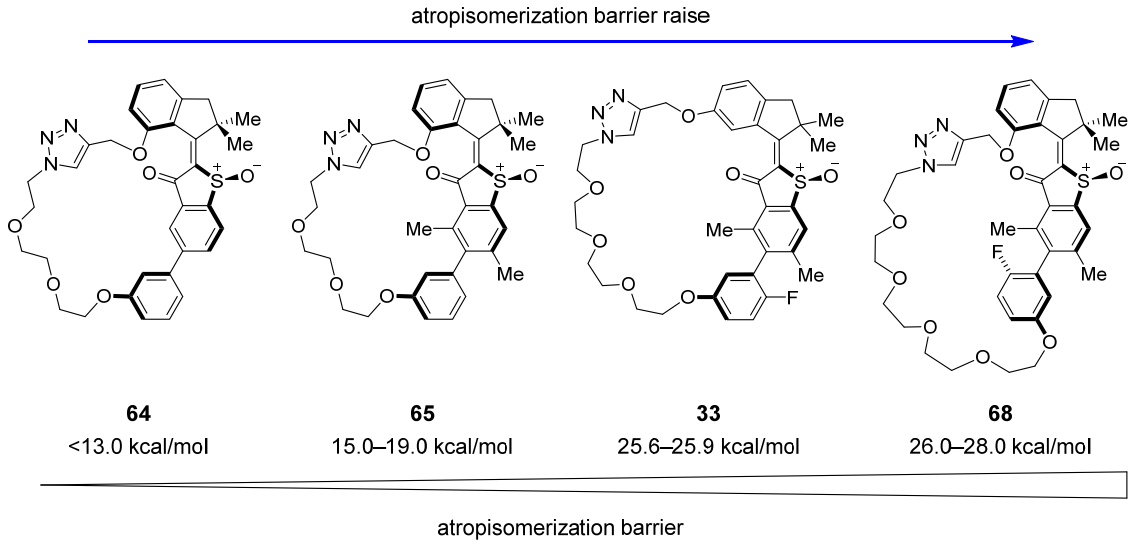

Figure 175 Atropisomerisation barrier raise from below 13.0 kcal mol^{-1} for macrocycle **64** to 15.0–19.0 kcal mol^{-1} for **65**. The corresponding non-cyclic counterpart of **65** possesses a barrier of around 21.0 kcal mol^{-1} leading to an atropisomerisation rate acceleration of up to 6.0 kcal mol^{-1}. Barriers were raised further to 25.6–25.9 kcal mol^{-1} for **33** and 26.0–28.0 kcal mol^{-1} for **68** in this work.

Increasing steric bulk on the revolving door allowed to raise the biaryl rotation barrier from below approximately 13.0 kcal mol^{-1} in **64** to 15.0–19.0 kcal mol^{-1} in **65** actively accelerating the atropisomerization process from a barrier of about 21.0 kcal mol^{-1} in the corresponding non-cyclic system of **65**. For both latter systems containing a biaryl axis, unidirectional motor rotation and atropisomerization are always co-dependent. This means that with an atropisomerization process as part of the rotational cycle both systems **64** and **65** cannot continuously rotate with a halted biaryl rotation. This could be changed with a conscious design of the revolving door and macrocycle ring size leading to a molecular motor, which could rotate independently from its atropisomer conformation.

Furthermore, elongating the ethylene glycol linker should further facilitate raising the atropisomerization barrier by releasing some of the up to approximately 6.0 kcal mol^{-1} strain present in system **65**.[158] To this end, system **68** was conceptualized bearing a linker elongated by two ethylene glycol units and a biaryl axis containing a fluorine in *otho*-position instead of a hydrogen as shown in Figure 176. Macrocyclic system **65** containing a raised biaryl barrier prevents synchronous coupled unidirectional motor and biaryl rotation. An elongated covalent linker allows for the tether to rotate around the revolving door despite fixed biaryl configuration. This design allows for two different unidirectional motor cycles to take place – one for R_a and one for the S_a atropisomer configuration of the revolving door – within one macrocyclic motor embedding. In both unidirectional cycles unidirectionality of the revolving door rotation is the same, however the different photochemical and THI steps occur in different macrocycle configurations shown in Figure 176.

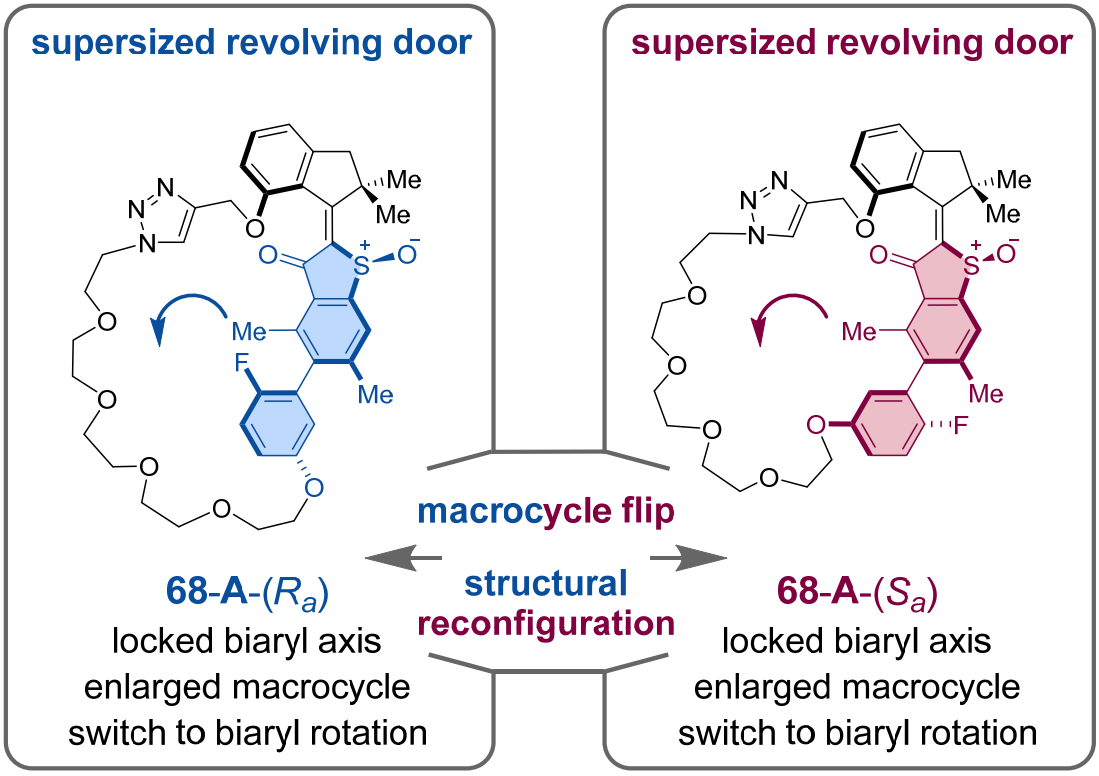

Figure 176 Overview of macrocyclic molecular motor design **68** presented in this work, containing an enlarged redefined revolving door. Two diastereomeric macrocycles **68**-(R_a) and **68**-(S_a) can independently rotate unidirectional in the same direction. Interconversion between the two rotation cycles is possible by atropisomerization at elevated temperatures through an unprecedentedly selective structural reconfiguration step. Adapted with minor format modifications from *J. Am. Chem. Soc.* **2023**, 145, 13081–13088 licensed under CC BY-NC-ND 4.0. Copyright © 2023 The Authors. Published by American Chemical Society.[2]

The already described approach for macrocyclization put forward by *Uhl et al.*, see chapter 1 was once more modified to achieve a new type of dual-motor macrocyclic molecular machine. To this end, the immobilization at ambient temperature (described in chapter 6) was retained in system **68**, the covalent linker elongated with one additional ethylene glycol unit and a molecular HTI motor based on the original fully unidirectional system[154] was utilized. For the latter, a motor possessing sufficient steric strain in the fjord region to achieve 100% unidirectionality at 22 °C was used. The full synthetic target design is shown in Figure 177.

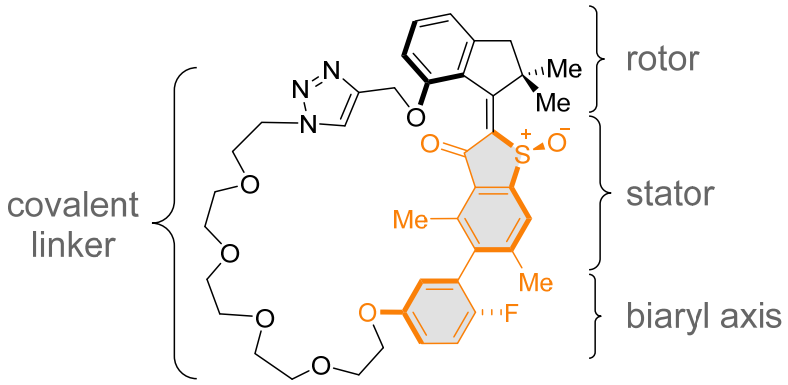

68

Figure 177 Representation of molecular machine design and definition of functional units in macrocyclic **68**. The molecular motor unit consists of a rotor and a stator which are assigned arbitrarily as discussed in chapter 2, and used consistently to previously reported systems maximizing comparability. The supersized revolving door is shown in orange. Unidirectional rotation is generated *via* integration of a modified visible-light-powered HTI motor based on the original design.[154] Full 360° rotation is realized in both atropisomer configurations through an elongated covalent linker. Biaryl design enables two separate 360° rotations within the macrocycle and their reversible interconversions *via* structural reconfiguration respectively.

In this case the biaryl tracer unit was utilized *via* ECD responses for reporting of current operational molecular motor configuration. Furthermore, isomers possessing maximum biaryl tilt are also isomers with highest selectivity upon structural reconfiguration (see chapters 7.4.2 and 7.9).

7.3. Synthesis of enlarged revolving door HTI 68

Macrocyclic molecular motor **68** was synthesized from commercially available 7-hydroxy indanone **74**, pentaethylene glycol **71**, and 4-bromo-3,5-dimethylphenol **40** (for synthesis see chapter 6.3). Retrosynthetic analysis was done according to a modified literature procedure for integrated macrocyclic HTI-based molecular motors[158,240] leading to linker building block **69**, indanone rotor part **70** and benzothiophenone stator **17** shown in Figure 178. The highly modular design of macrocyclic HTI-based molecular motors was used to incorporate the functional units mentioned in chapter 7.2.[158,159,240] Details for the synthesis of benzothiophenone building block **17** can be found in chapter 6.3. For more experimental details see chapter 8.2 or the corresponding literature.[2] Synthetic procedures for all herein presented compounds are reported in the experimental chapter 8.6 starting from commercially available starting materials.

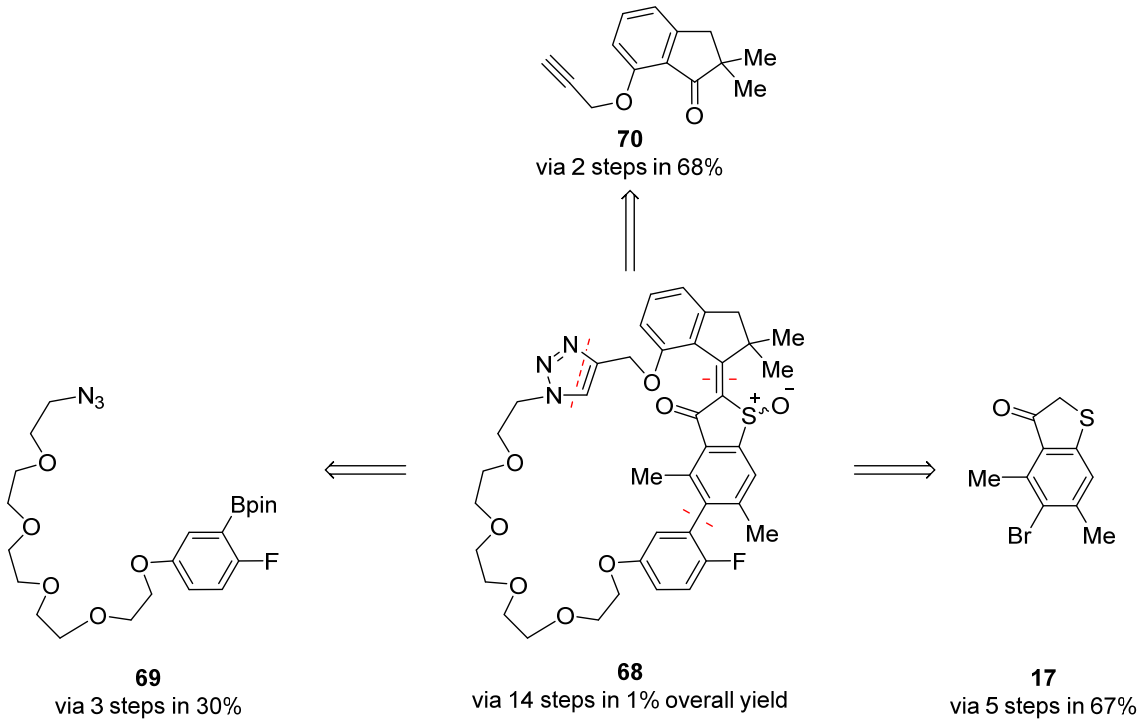

Figure 178 Retrosynthetic analysis of macrocyclic HTI-based molecular motor **68**. Cleavage along the central double bond, triazole moiety and the biaryl axis lead to covalent linker building block **69**, indanone rotor part **70** and benzothiophenone stator **17**.

The covalent pentaethylene glycol linker was synthesized from commercially available pentaethylene glycol **71**, which was dibrominated through an *Appel* reaction to the corresponding 1,14-dibromopentaethylene glycol **72** in 88% yield. Monosubstitution using sodium azide furnished the corresponding 1-azido-14-bromo pentaethylene glycol **73** in 34% yield, which was further transformed to the linker building block **69** through substitution of the bromide using the corresponding fluorinated

aryl **39** shown in Figure 179. Because of decomposition of the boronic acid pinacol ester in **69** on silica columns, this building block was utilized as crude product after extraction without further purification for the next synthetic transformation.

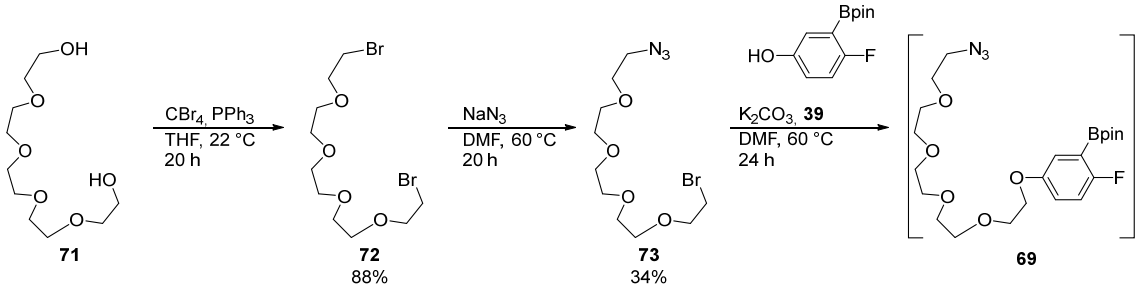

Figure 179 Synthesis of covalent linker fragment **69**. Commercially available pentaethylene glycol **71** was di-brominated in an *Appel* reaction giving compound **72**. Monosubstitution with sodium azide furnished bromine-azide di-functionalized **73**, which was further substituted with commercially available fluorinated aryl **39** yielded linker building block **69**. Structures in brackets were used without full purification.

Indanone fragment **70** was accessed through a propargylation followed by a double methylation procedure in 86% for **75** and 79% yield for **70**, respectively starting from commercially available 7-hydroxy indanone **74**. Benzothiophenone **17** was constructed starting from the corresponding commercially available 4-bromo-3,5-dimethylphenol **40** as explained in chapter 6.3. Condensation of building blocks **70** and **17** using boron trichloride furnished HTI motor core **76** in high yield of 71% as shown in Figure 180.

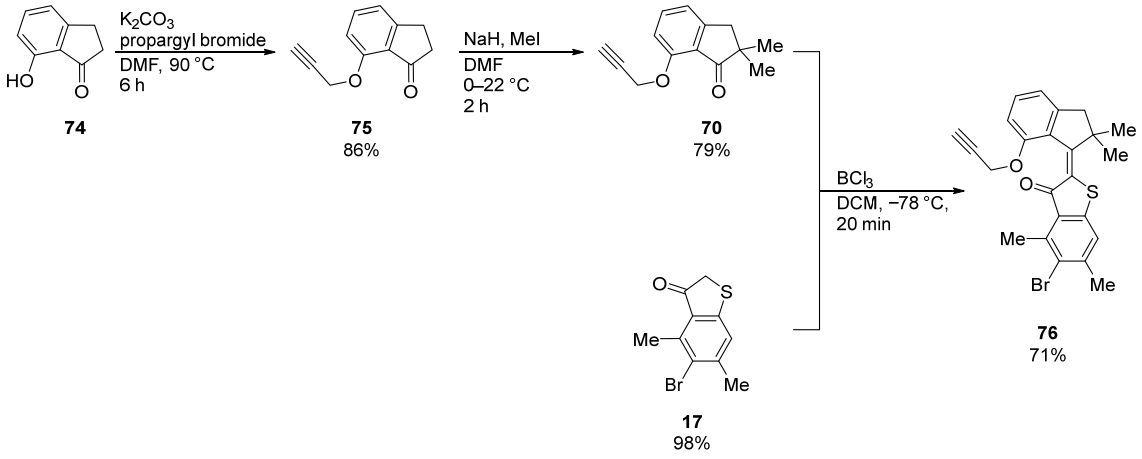

Figure 180 Synthesis of macrocyclic HTI-based core structure **76**. Indanone building block **70** was synthesized form the corresponding commercially available 7-hydroxy indanone **74** *via* propargylation with propargyl bromide followed by methylation of **75** using iodomethane. Condensation of indanone building block **70** and benzothiophenone building block **17** (for synthesis see chapter 6.3) with boron trichloride furnished HTI core **76**.

The covalent linker **69** was attached to the HTI motor fragment **76** using *Huisgen* azide-alkyne chemistry through a 1,3-dipolar cycloaddition. The 1,2,3-triazol moiety as part of the linking chain was established with sodium ascorbate and copper(II) sulfate pentahydrate in *N*,*N*-dimethyl formamide furnishing **77** with all building blocks in place. Macrocyclic ring closing was achieved using classical *Suzuki-Miyaura* cross coupling, which worked best with sSPhos Pd G2 and potassium phosphate in a toluene/ethanol/water mixture. Separation of enlarged cyclic HTI **77** from sideproducts proved to be significantly more challenging compared to smaller analogs **64**,[159] **65**,[158] and **33**,[1] which is why the crude mixture was utilized for the final synthetic transformation. As the final step the sulfide in fully assembled **78** was oxidized to the corresponding sulfoxide using sodium perborate tetrahydrate in acetic acid, shown in Figure 181 providing the final macrocyclic molecular motor target **68** in 71% over three steps as a yellow solid. Separation of diastereomeres was accomplished through a series of chromatographic techniques starting with flash chromatography on silica followed by HPLC separation using a *Macherey-Nagel Nucleosil* silica column in combination with a *Daicel* CHIRALPAK® IB-N or IC column.

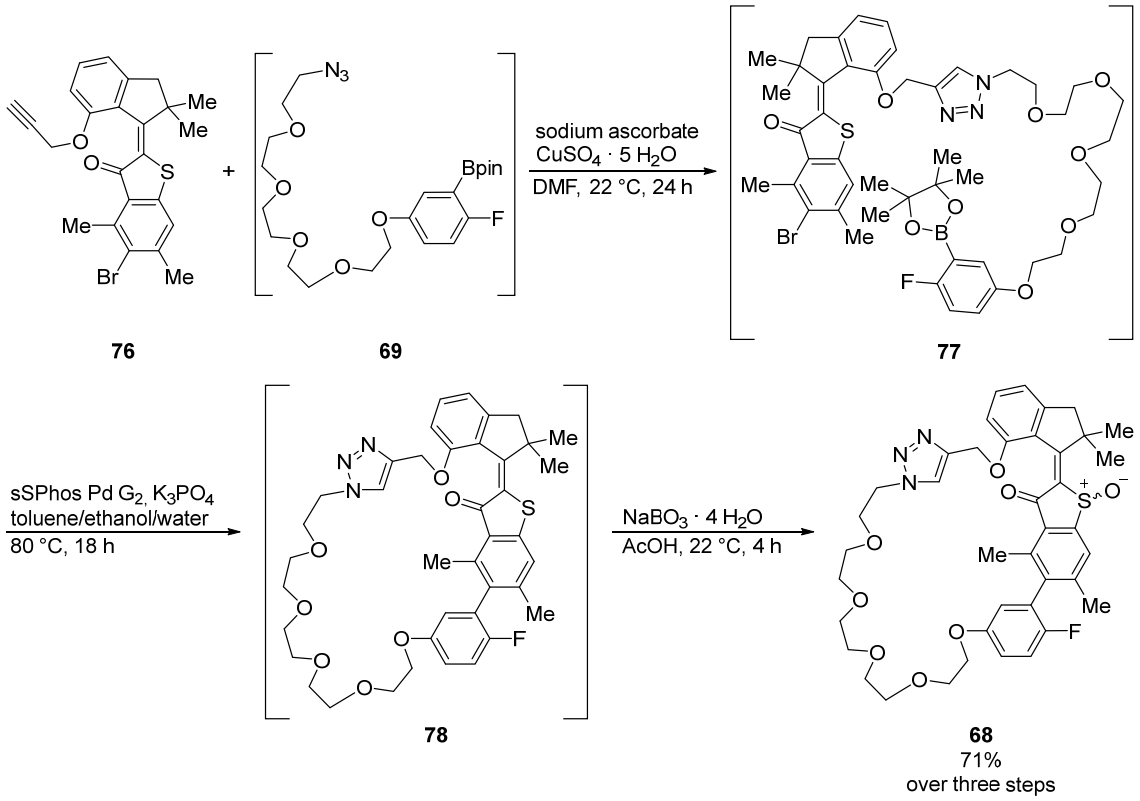

Figure 181 Final synthetic steps of macrocyclic molecular motor **68**. Addition of covalent linker chain **69** onto HTI **76** was achieved using *Huisgen* azide-alkyne chemistry through a 1,3-dipolar cycloaddition with copper(II) sulfate and sodium ascorbate. Cyclization of **77** was furnished through *Suzuki-Miyaura* cross coupling using sSPhos Pd G2 leading to macrocyclic **79**. Oxidation of the sulfide was established lastly using an excess of sodium perborate in acetic acid to generate the sulfoxide **68**. Only the target compound was isolated as a result of isolation difficulties originating from the elongated polyethylene glycol linker. Structures in brackets were not isolated.

Since the low 1% overall yield of target compound **68** was caused mainly by the low yielding ring closing step *via Suzuki-Miyaura* cross coupling similar to previous reports,[158,159] an attempt to exchange catalyst ligand and solvents to a system successfully employed for more sterically hindered couplings was carried out.[77] Two different conditions were used for this step with respect to limitations in starting material **77** using the observations made from synthesis of HTI **33** (see chapter 6.3). Exchange of tetrakis(triphenylphosphine)palladium(0) conditions for the already mentioned sSPhos Pd G2 system did also lead to improvement of reaction yield for the synthesis of **68** by up to 71% over 3 steps shown in Table 26.

Table 26 Tested reaction conditions for macrocyclization of **68**. For the entry utilizing tetrakis(triphenylphosphine)palladium(0), only protodeboronation has been observed.

catalyst	**base**	**solvent**	**temp in °C**	**time in h**	**yield in %**
$Pd(PPh_3)_4$ (5 mol%)	K_2CO_3 (4.0 equiv.)	*N*,*N*-dimethylformamide (5.0 μM)	80	23	–
sSPhos Pd G2 (8 mol%)	K_3PO_4 (3.0 equiv.)	toluene/ethanol/water (3/3/1, 0.020 M)	80	18	71 (over 3 steps)

7.4. Structural and conformational description

In principle, 16 different stereoisomers of macrocyclic HTI **68** can be obtained from synthesis possessing an *E*- or *Z*-configured double bond, *S*- or *R*-configured sulfoxide, *P*- or *M*-configured helicity, and R_a- or S_a-configured biaryl axis. However, due to isomerization kinetics and stability differences only one of the two *P*- or *M*-helicities is observed at 22 °C. For the *S*-sulfoxide configuration only *P*-helicity and for the *R*-sulfoxide configuration only *M*-helicity can be observed at 22 °C respectively, reducing the number of stereoisomers to eight. This makes up for four sets of enantiomers possessing sets of entirely opposed stereocenters, and multiple variations of four diastereomere sets with *e.g.* one being the *S*- or *R*-configured sulfoxide and all possible combinations of the other stereo-elements stable at 22 °C shown in Figure 182. Only *S*-configured sulfoxide diastereomeres were considered for all following descriptions for reason of simplicity, with the ones stable at 22 °C shown in Figure 182. Furthermore, if not stated otherwise racemates were obtained from synthesis and utilized as such in experiments.

7.4.1. Overview of conformational states

All observable isomers at 22 °C of structure **68** shown in Figure 182 were elucidated in a combined approach using, 1D and 2D NMR experiments, UV-Vis and ECD spectroscopy and theoretical descriptions in comparison to experimental data. For assignment of ^{1}H and ^{13}C signals and more analytical details, see chapter 8.6 or the corresponding literature.[1]

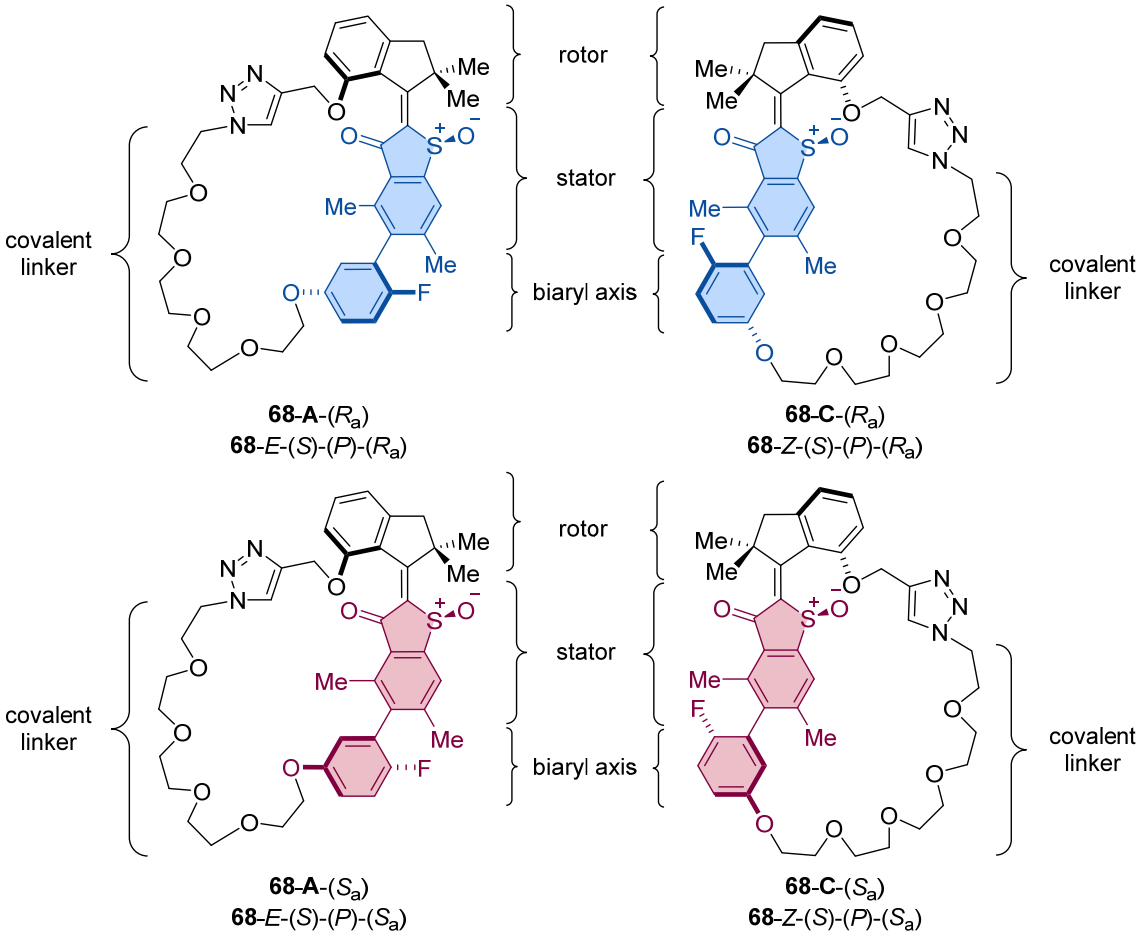

Figure 182 Overview of all four macrocyclic HTI **68** diastereomeres stable at 22 °C, namely **68**-*E*-(*S*)-(*P*)-(R_a) = **A**-(R_a), **68**-*Z*-(*S*)-(*P*)-(R_a) = **C**-(R_a), **68**-*E*-(*S*)-(*P*)-(S_a) = **A**-(S_a), and **68**-*Z*-(*S*)-(*P*)-(S_a) = **C**-(S_a). Stable structures at 22 °C of the R_a motor cycle are colored blue and the S_a motor cycle red. Only *S*-configured sulfoxides are shown for reason of simplicity. For *S*-configured sulfoxides the sole helix configuration stable at 22 °C is *P*-helicity.

7.4.2. Structures of macrocyclic HTI 68 in solution

Conformations of macrocyclic **68** were characterized first in solution after separation of all isomers stable at 22 °C. Pure solutions of each isomer in CD_2Cl_2 were extensively examined using 1D, 2D and VT NMR spectroscopy. For a detailed ^{1}H and ^{13}C spectroscopic analysis of each isomer see chapter 8.6 or the corresponding literature.[2]

7.4.2.1. Overview of all observed macrocyclic HTI 68 conformations in solution

First ^{1}H NMR spectra of each isomer was recorded shown in Figure 183 followed by an in-depth analysis including ^{13}C, COSY, HSQC, HMBC, ^{19}F and NOE or ROE spectra. ^{1}H NMR spectra were also recorded for accumulated metastable isomers at −90 °C shown in Figure 183c and f.

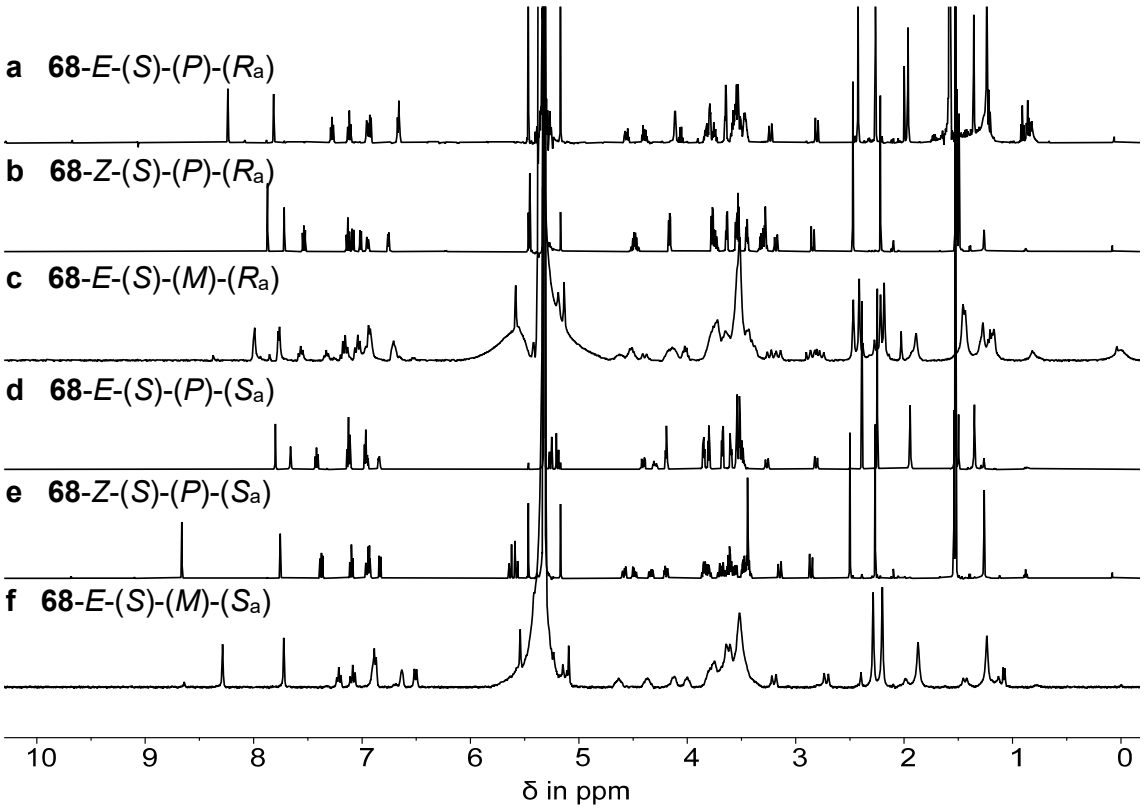

Figure 183 ^{1}H NMR spectra (CD_2Cl_2) overview of racemic macrocyclic HTI **68** isomer solutions measured as low as −90 °C. Starting with isomer (a) **68**-*E*-(*S*)-(*P*)-(R_a) (601 MHz, 25 °C), (b) **68**-*Z*-(*S*)-(*P*)-(R_a) (601 MHz, 25 °C), (c) **68**-*E*-(*S*)-(*M*)-(R_a) (401 MHz, −90 °C), (d) **68**-*E*-(*S*)-(*P*)-(S_a) (601 MHz, 0 °C), (e) **68**-*Z*-(*S*)-(*P*)-(S_a) (601 MHz, 25 °C), and (f) **68**-*E*-(*S*)-(*M*)-(S_a) (401 MHz, −90 °C) from top to bottom.

Furthermore, measurement of ^{19}F NMR spectra for all ground state isomers – depicted in Figure 182 – prove that indeed four different conformers of isomer **68** are stable at 22 °C, which can be observed by distinct chemical shifts shown in Figure 184.

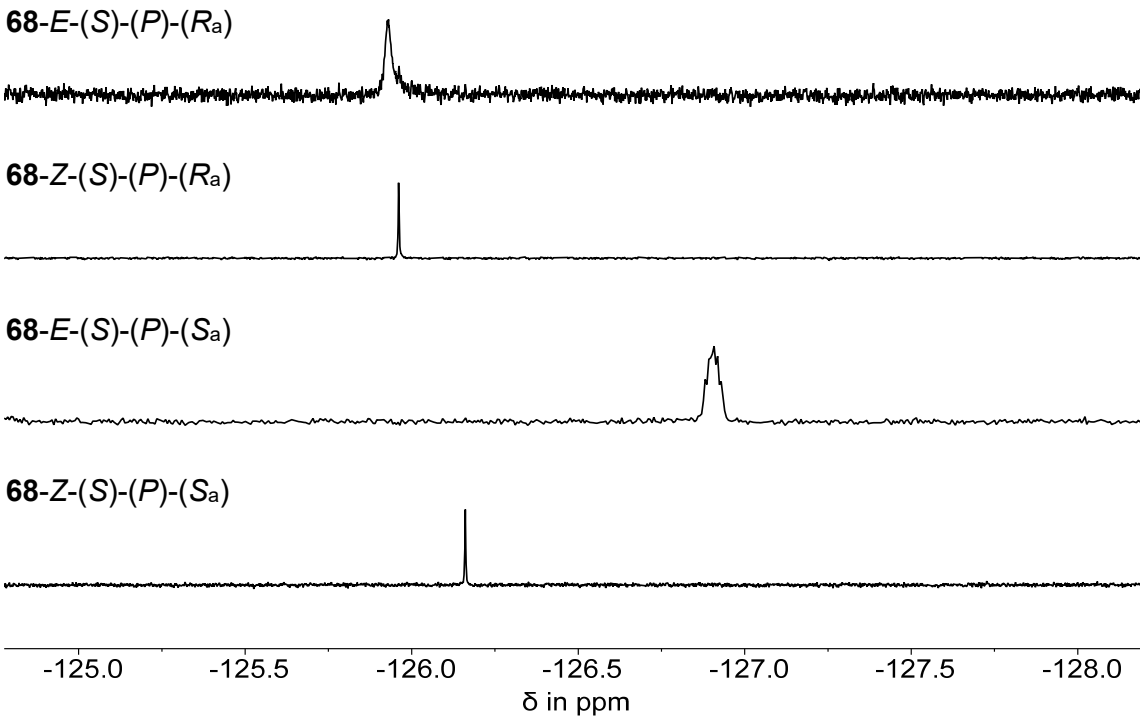

Figure 184 ^{19}F NMR spectra (377 MHz, CD_2Cl_2, 25 °C) overview of all macrocyclic HTI **68** isomers stable at 25 °C. Starting with isomer **68**-*E*-(*S*)-(*P*)-(R_a) (−125.93 ppm), **68**-*Z*-(*S*)-(*P*)-(R_a) (−125.96 ppm), **68**-*E*-(*S*)-(*P*)-(S_a) (−126.90 ppm) and **68**-*Z*-(*S*)-(*P*)-(S_a) (−126.16 ppm) from top to bottom.

Similarly, all ground state isomers of **68** were measured in toluene-d_8 solution shown in Figure 185 to investigate elevated temperature behavior of each individual isomer. A detailed analysis can be found in chapter 7.5.

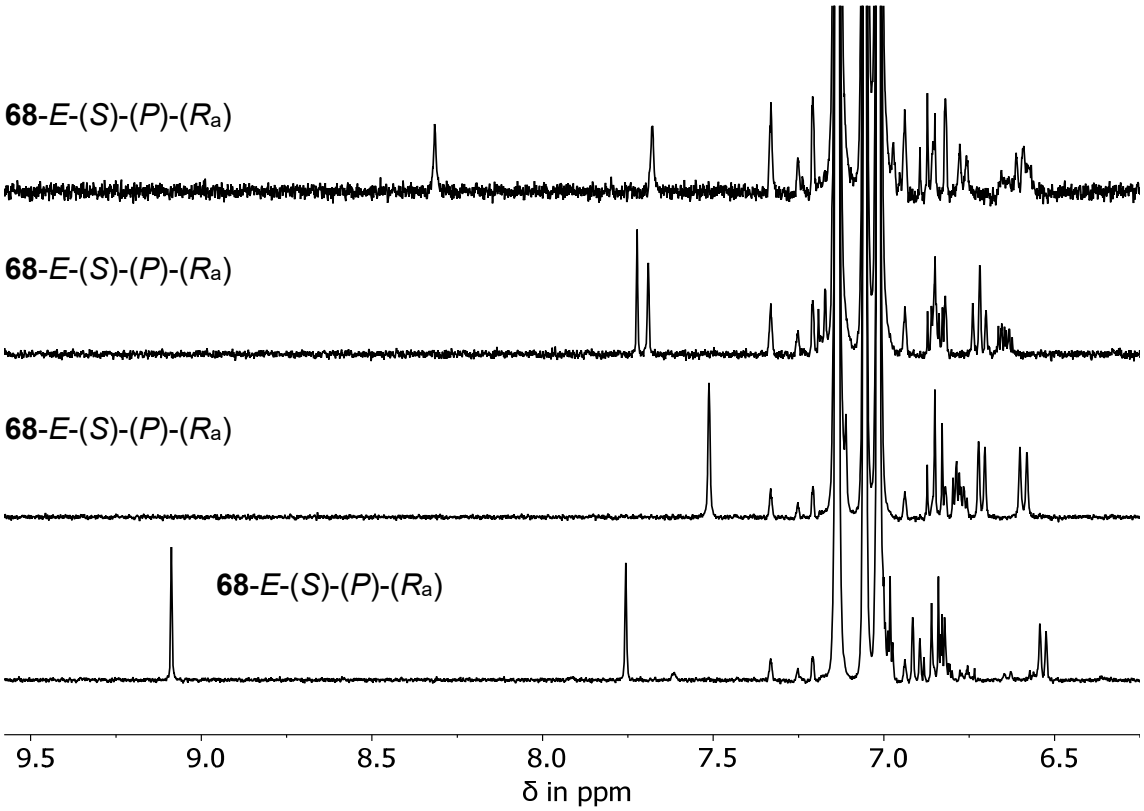

Figure 185 ^{1}H NMR spectra (toluene-d_8, 400 MHz, 25 °C) overview of all macrocyclic HTI **68** isomers stable at 25 °C. Starting with isomer **68**-*E*-(*S*)-(*P*)-(R_a), **68**-*Z*-(*S*)-(*P*)-(R_a), **68**-*E*-(*S*)-(*P*)-(S_a) and **68**-*Z*-(*S*)-(*P*)-(S_a) from top to bottom.

The nuclear *Overhauser* effect (NOE) proved to be a powerful tool in examining *E*- or *Z*-configurations of HTI isomers in solution.[154,156–159,185,211] Population transfer of spin polarization from one NMR active nucleus to another through space over a distance of up to 5–6 Å fits perfectly for conformation elucidation of macrocycles with a size of up to 15–16 Å according to crystal structures of similar molecules (see chapter 6.7) and theoretical descriptions. Double bond configuration of the central motor core unit in **68** was therefore unveiled using NOE or ROE NMR spectroscopy *via* observable proximity between H_3C38, HC35, H_2C37, HC35, HC17, and H_3C39 as shown in Figures 187, 189, 191, and 193. For illustration of atom numbering see Figure 186. Furthermore, biaryl tilt towards the sulfoxide or the carbonyl part of the benzothiophenone was probed through signal intensity differences from HC24 to H_3C38 or H_3C39 as shown in Figure 186.

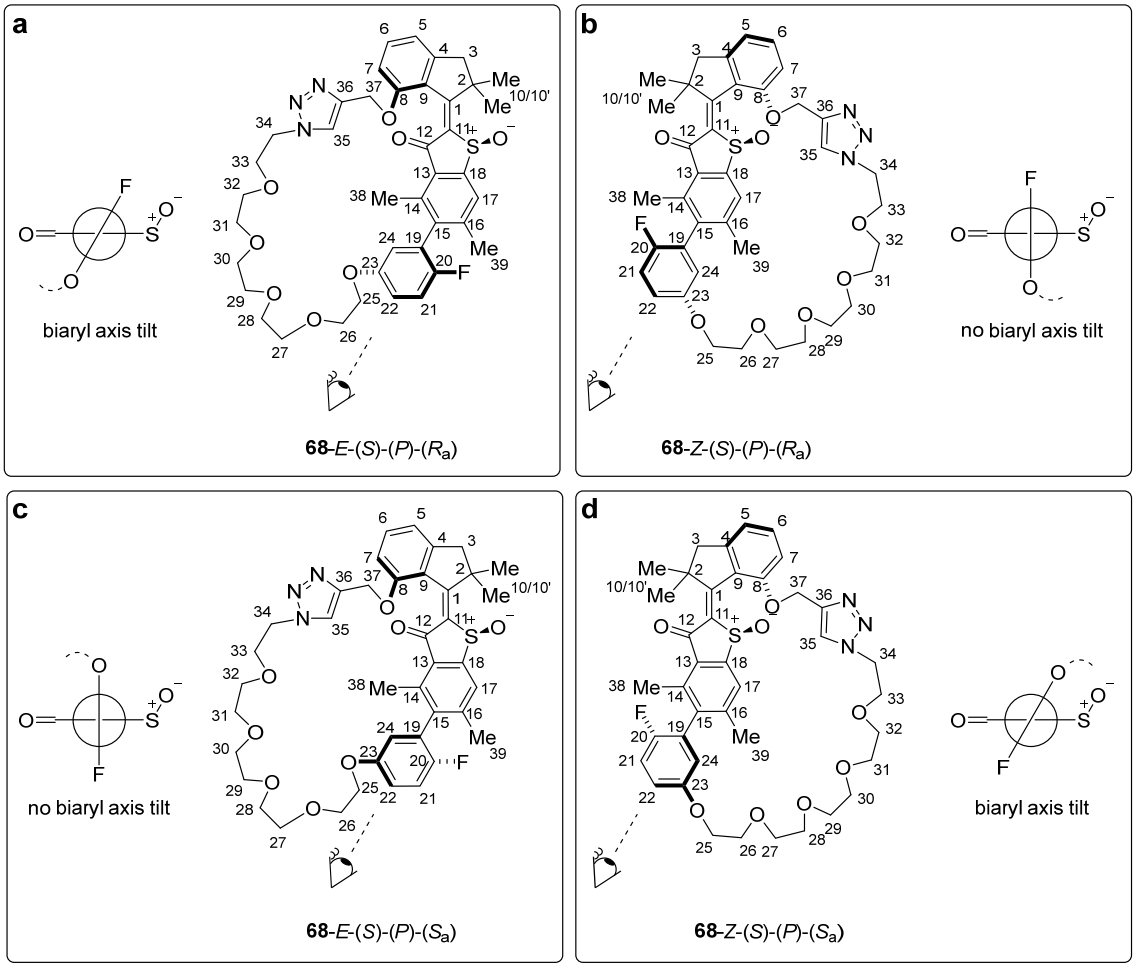

Figure 186 Depiction of biaryl axis tilt in (**a**) **68**-*E*-(*S*)-(*P*)-(R_a) and (**d**) **68**-*Z*-(*S*)-(*P*)-(S_a) as well as biaryl axis orthogonality in (**b**) **68**-*Z*-(*S*)-(*P*)-(R_a) and (**c**) **68**-*E*-(*S*)-(*P*)-(S_a). The corresponding *Newman* projections illustrate tilt angle of biaryl planes according to indicated angles of view. Plane angles can be examined by relative NOE signal strength between aromatic proton H-C24 and aromatic methyl groups H_3C38 and H_3C39.

Biaryl tilts of **68**-*E*-(*S*)-(*P*)-(R_a) and **68**-*Z*-(*S*)-(*P*)-(S_a) were both in agreement with observed double bond configurations of the motor core, which were both tilted with their covalent linker anchoring points on the biaryl towards the respective anchoring points on the indanone as illustrated in Figure 186. This can be explained through the attachment point of the PEG linker residing on different sides of the motor plane requiring the chain to be wind around the revolving door. As a result, the covalent linker has less degrees of freedom for wiggling, which subsequently applies strain upon the two biaryl planes. This force is released to some extent through an observable tilt in the biaryl axis. Axis tilts of **68**-*Z*-(*S*)-(*P*)-(R_a) and **68**-*E*-(*S*)-(*P*)-(S_a) are not observable, which is in good agreement with both attachment points of the PEG linker being on the same side resulting in no residual strain upon the two biaryl planes or the PEG linker chain. This explanation is further strengthened by structural

configurations observed in theoretical descriptions of the macrocycle at the B3LYP-GD3BJ/6-311G(d,p) IEFPCM (CH_2Cl_2) level of theory discussed in chapter 7.11.

7.4.2.2. 68-*E*-(*S*)-(*P*)-(R_a) = A-(R_a)

Proximity of H_3C38 to triazole HC35 revealed *E*-configuration of the central double bond in **68**-*E*-(*S*)-(*P*)-(R_a), shown in Figure 187.

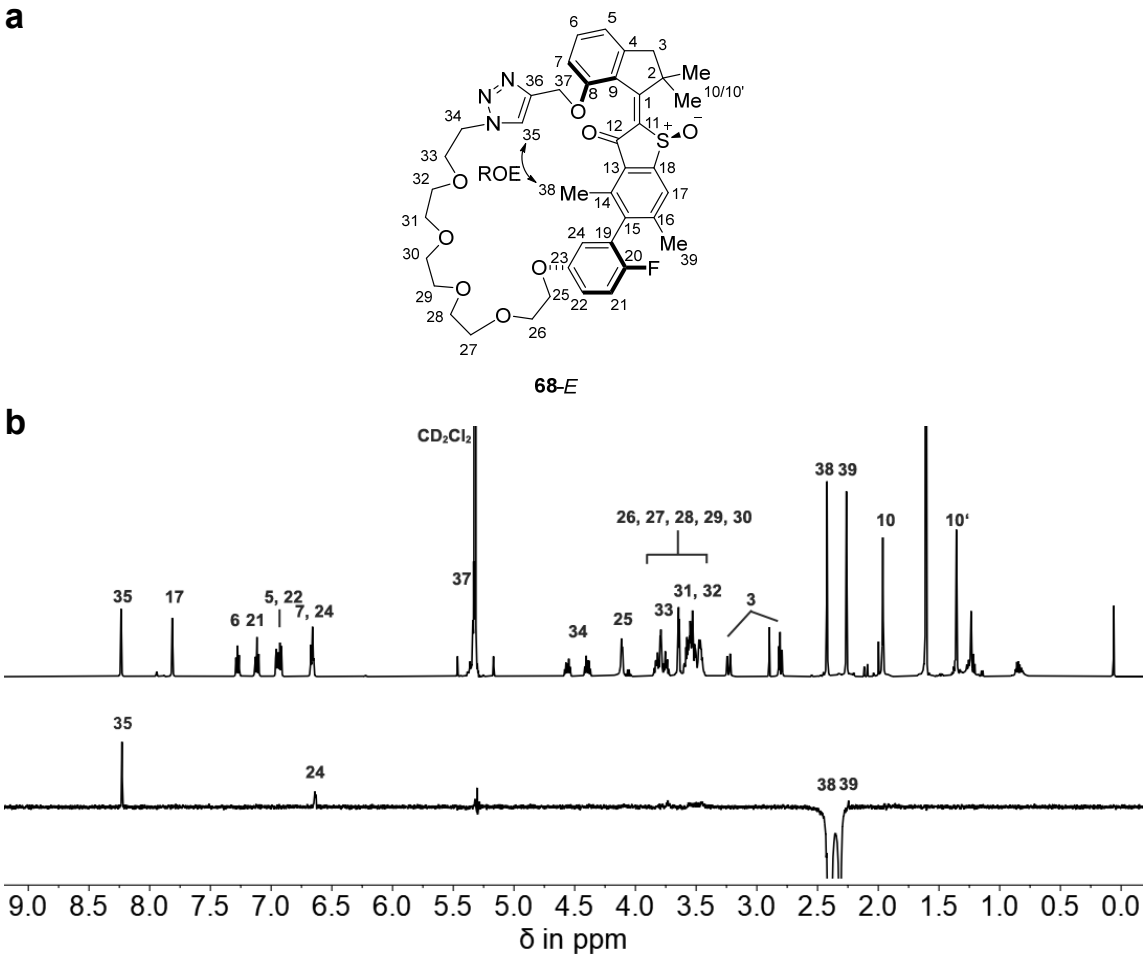

Figure 187 Double bond configuration analysis of isomer **68**-*E*-(*S*)-(*P*)-(R_a) measured in CD_2Cl_2 solution at 25 °C. **a** Structure of **68**-*E*-(*S*)-(*P*)-(R_a) including arrows depicting observed ROE signals. **b** ^{1}H (top) and ROE (bottom) NMR spectra (600 MHz, CD_2Cl_2, 25 °C) of **68**-*E*-(*S*)-(*P*)-(R_a) display proximity of HC35 and HC24 to H_3C38, revealing *E*-configuration of the integrated motor. Adapted with minor format modifications from *J. Am. Chem. Soc.* **2023**, *145*, 13081–13088 licensed under CC BY-NC-ND 4.0. Copyright © 2023 The Authors. Published by American Chemical Society.[2]

Stronger signal intensity of HC24 to H_3C38 compared to H_3C39 revealed tilt of the covalent linker anchoring point on the biaryl towards the carbonyl side of the benzothiophenone fragment shown in Figure 188b. The tilt of the two biaryl planes is further illustrated in the *Newman* projection along the biaryl axis in Figure 188a.

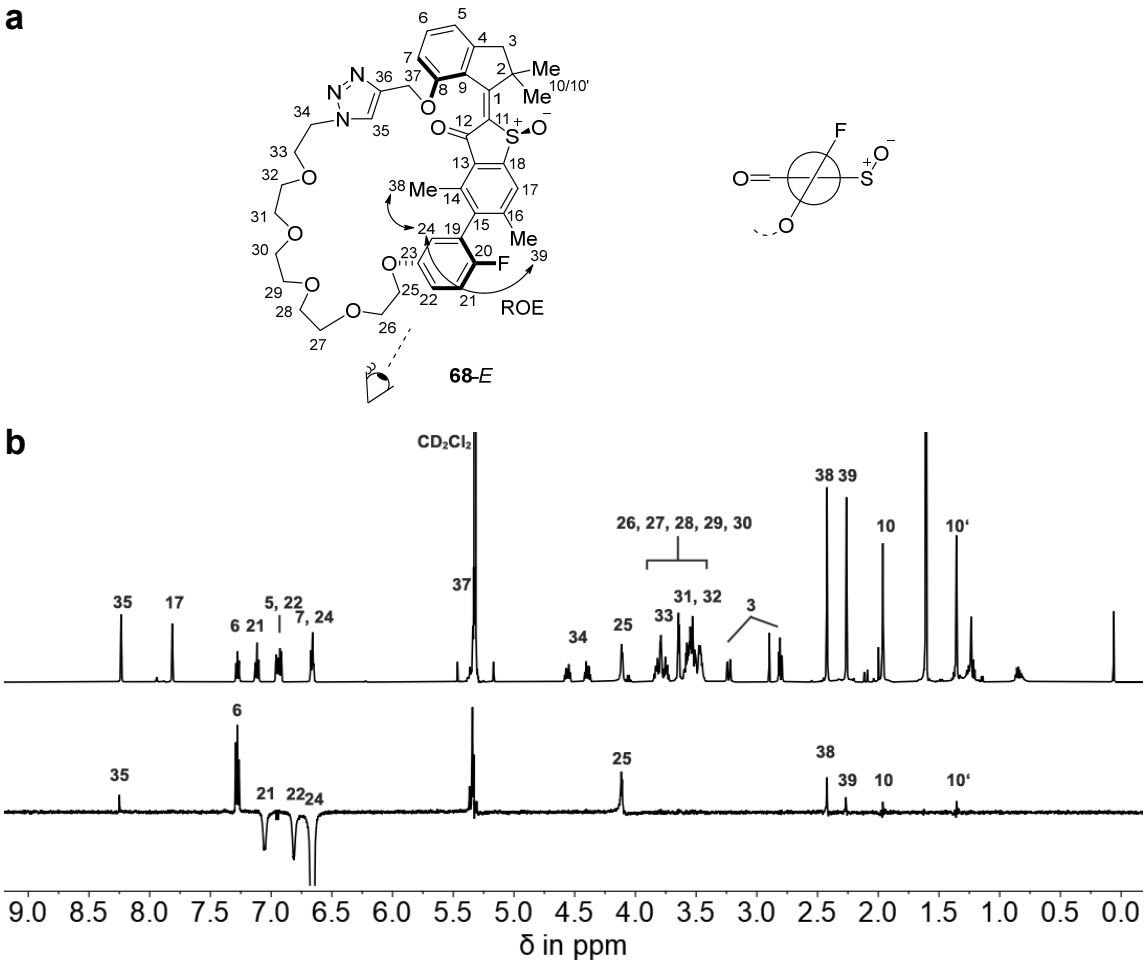

Figure 188 Biaryl axis tilt analysis of **68**-*E*-(*S*)-(*P*)-(R_a) measured in CD_2Cl_2 solution at 25 °C. **a** Structure of **68**-*E*-(*S*)-(*P*)-(R_a) including arrows depicting observed ROE signals (left). *Newman* projection of the biaryl axis illustrating the preferred tilt of the two biaryl planes (right). **b** ^{1}H (top) and ROE (bottom) NMR spectra (600 MHz, CD_2Cl_2, 25 °C) of **68**-*E*-(*S*)-(*P*)-(R_a) display signal intensity differences between H_3C38 and H_3C39 to HC24. Increased spatial proximity of H_3C38 and HC24 indicates biaryl tilt of the covalent linker anchoring point towards the carbonyl side of the benzothiophenone part. Adapted with minor format modifications from *J. Am. Chem. Soc.* **2023**, *145*, 13081–13088 licensed under CC BY-NC-ND 4.0. Copyright © 2023 The Authors. Published by American Chemical Society.[2]

The inclination of the biaryl anchoring point towards H_3C38 indicates the two chain attachment points are located on opposite sides of the benzothiophenone plane since the opposite would probably result in no observable tilt angle as a result of the relaxed covalent PEG linker. It is to be noticed that this is a

first clue about the biaryl axis having a R_a configuration with respect to correct assignment of all other stereodescriptors and the corresponding **68**-*E*-(*S*)-(*P*)-(S_a) isomer.

7.4.2.3. 68-*Z*-(*S*)-(*P*)-(R_a) = C-(R_a)

Proximity of H_3C39 and HC17 to triazole HC35 revealed *Z*-configuration of the central double bond in **68**-*Z*-(*S*)-(*P*)-(R_a), shown in Figure 189.

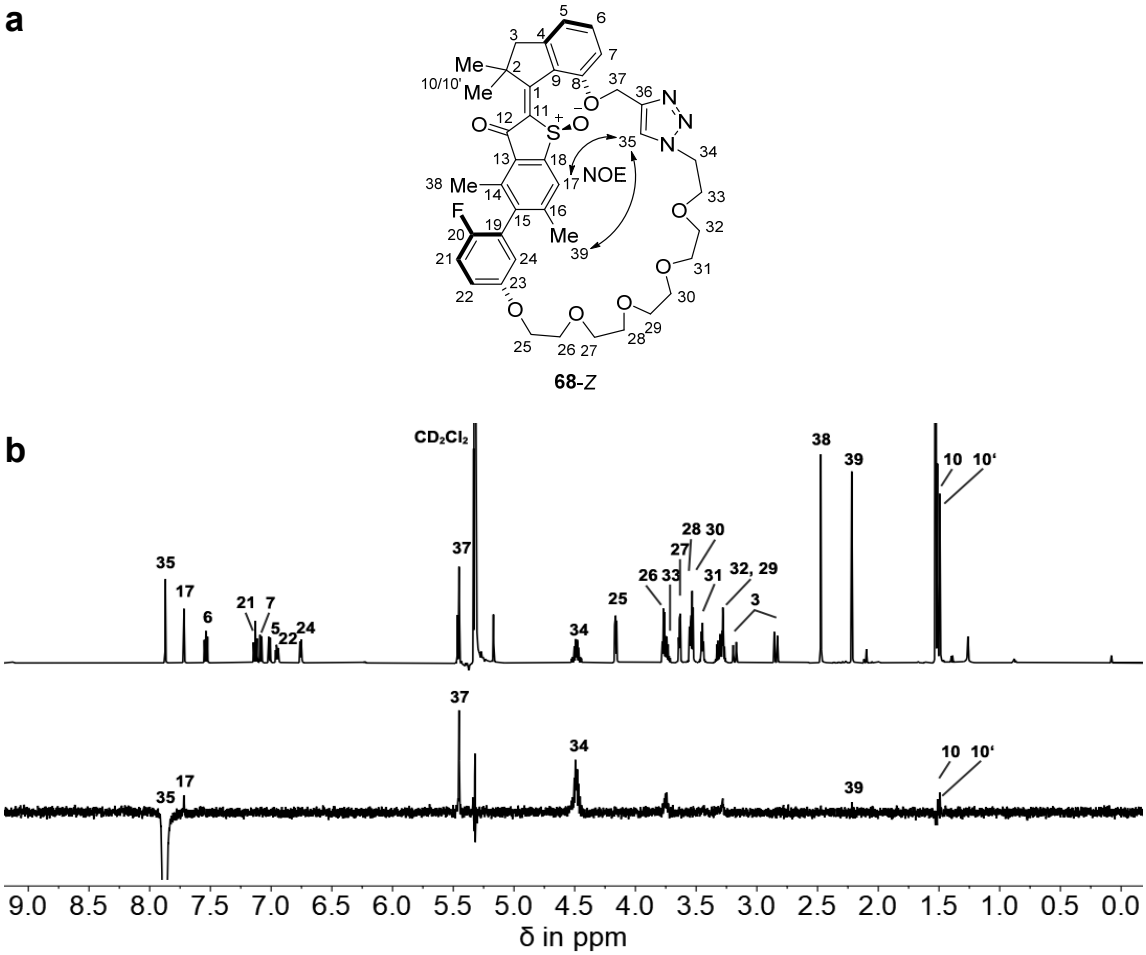

Figure 189 Double bond configuration analysis of isomer **68**-*Z*-(*S*)-(*P*)-(R_a) measured in CD_2Cl_2 solution at 25 °C. **a** Structure of **68**-*Z*-(*S*)-(*P*)-(R_a) including arrows depicting observed NOE signals. **b** ^1H (top) and NOE (bottom) NMR spectra (600 MHz, CD_2Cl_2, 25 °C) of **68**-*Z*-(*S*)-(*P*)-(R_a) display proximity of HC17 and H_3C39 to HC35, revealing *Z*-configuration of the integrated motor. Adapted with minor format modifications from *J. Am. Chem. Soc.* **2023**, *145*, 13081–13088 licensed under CC BY-NC-ND 4.0. Copyright © 2023 The Authors. Published by American Chemical Society.[2]

Equal signal intensities of HC24 to H_3C38 and H_3C39 revealed the two biaryl planes are orthogonal, shown in Figure 190b and further illustrated in the *Newman* projection along the biaryl axis in Figure 190a.

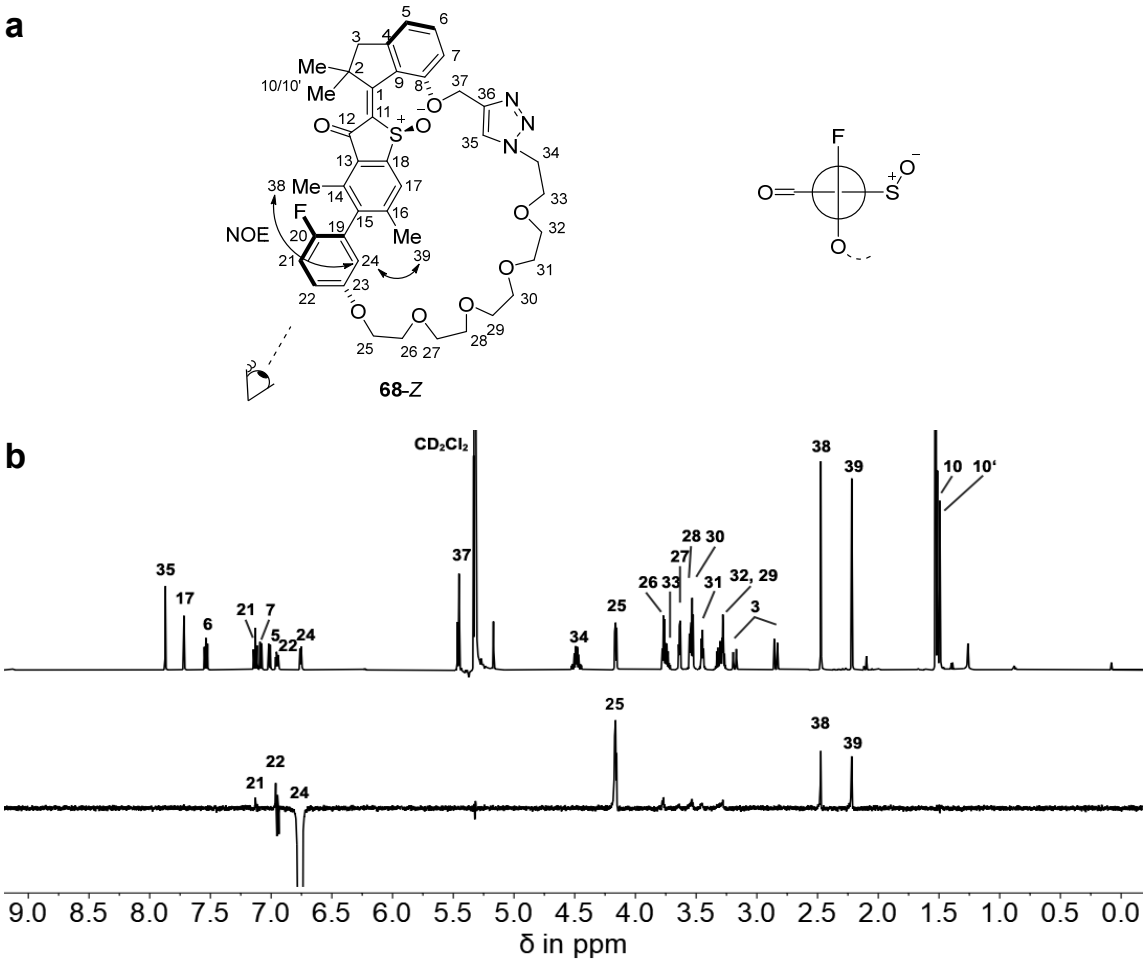

Figure 190 Biaryl axis tilt analysis of **68**-*Z*-(*S*)-(*P*)-(R_a) measured in CD_2Cl_2 solution at 25 °C. **a** Structure of **68**-*Z*-(*S*)-(*P*)-(R_a) including arrows depicting observed NOE signals (left). *Newman* projection of the biaryl axis illustrating no preferred tilt of the two biaryl planes (right). **b** ^{1}H (top) and NOE (bottom) NMR spectra (600 MHz, CD_2Cl_2, 25 °C) of **68**-*Z*-(*S*)-(*P*)-(R_a) display similar signal intensities of H_3C38 and H_3C39 indicating the two biaryl planes are orthogonal. Adapted with minor format modifications from *J. Am. Chem. Soc.* **2023**, *145*, 13081–13088 licensed under CC BY-NC-ND 4.0. Copyright © 2023 The Authors. Published by American Chemical Society.[2]

No observable inclination of the biaryl plane indicates the two chain attachment point are located on the same side of the benzothiophenone plane since the opposite would probably result in an observable tilt angle as a result of the strained covalent linker. Hence, this gives a first clue about the biaryl axis having a R_a-configuration in this isomer with respect to correct assignment of all other stereodescriptors and the corresponding **68**-*Z*-(*S*)-(*P*)-(S_a) isomer.

7.4.2.4. 68-*E*-(*S*)-(*P*)-(S_a) = A-(S_a)

Proximity of H_3C38 to triazole HC35 and H_2C37 revealed *E*-configuration of the central double bond in **68**-*E*-(*S*)-(*P*)-(S_a), shown in Figure 191.

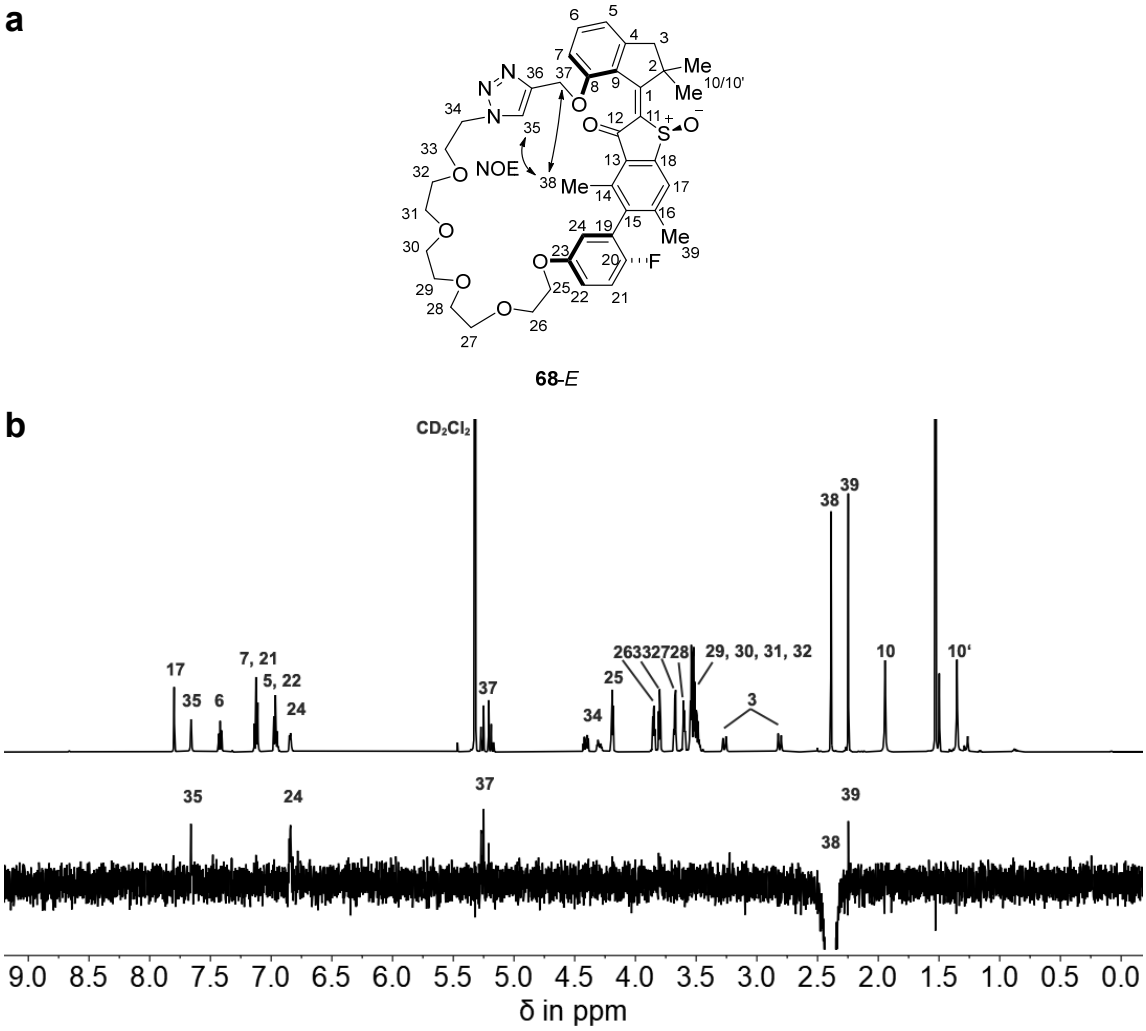

Figure 191 Double bond configuration analysis of isomer **68**-*Z*-(*S*)-(*P*)-(S_a) measured in CD_2Cl_2 solution at 25 °C. **a** Structure of **68**-*Z*-(*S*)-(*P*)-(S_a) including arrows depicting observed NOE signals. **b** ^1H (top) and NOE (bottom) NMR spectra (600 MHz, CD_2Cl_2, 25 °C) of **68**-*Z*-(*S*)-(*P*)-(S_a) display proximity of HC35 and H_2C37 to HC38, revealing *Z*-configuration of the integrated motor. Adapted with minor format modifications from *J. Am. Chem. Soc.* **2023**, *145*, 13081–13088 licensed under CC BY-NC-ND 4.0. Copyright © 2023 The Authors. Published by American Chemical Society.[2]

Equal signal intensities of HC24 to H_3C38 and H_3C39 revealed the two biaryl planes are orthogonal, shown in Figure 192b and further illustrated in the *Newman* projection along the biaryl axis in Figure 192a.

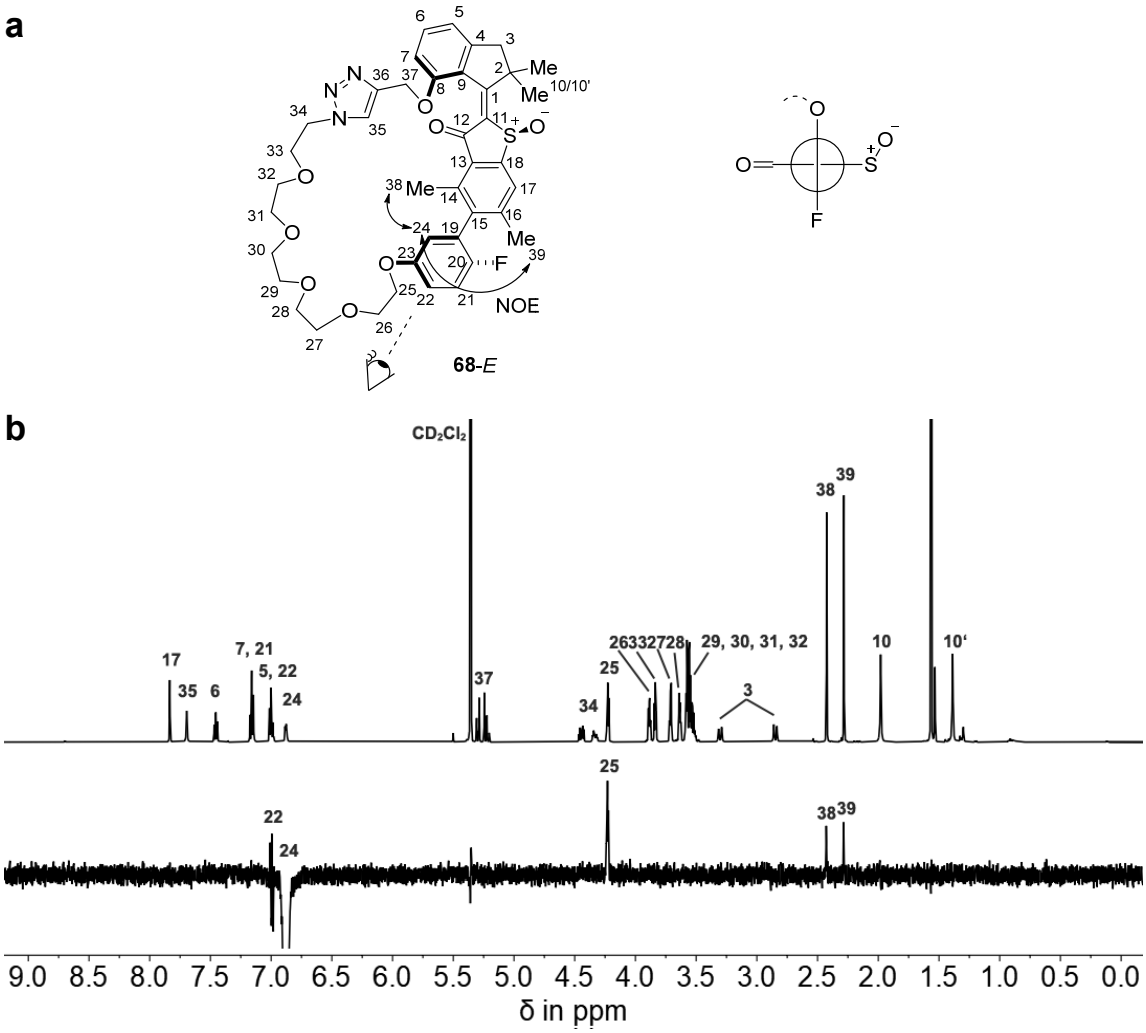

Figure 192 Biaryl axis tilt analysis of **68**-*E*-(*S*)-(*P*)-(S_a) measured in CD_2Cl_2 solution at 25 °C. **a** Structure of **68**-*E*-(*S*)-(*P*)-(S_a) including arrows depicting observed NOE signals (left). *Newman* projection of the biaryl axis illustrating no preferred tilt of the two biaryl planes (right). **b** ^{1}H (top) and NOE (bottom) NMR spectra (600 MHz, CD_2Cl_2, 25 °C) of **68**-*E*-(*S*)-(*P*)-(S_a) display similar signal intensities of H_3C38 and H_3C39 indicating the two biaryl planes are orthogonal. Adapted with minor format modifications from *J. Am. Chem. Soc.* **2023**, *145*, 13081–13088 licensed under CC BY-NC-ND 4.0. Copyright © 2023 The Authors. Published by American Chemical Society.[2]

No observable inclination of the biaryl plane indicates the two chain attachment point are located on the same side of the benzothiophenone plane since the opposite would probably result in an observable tilt angle. Hence, this gives a another clue about the biaryl axis having S_a configuration with respect to correct assignment of all other stereodescriptors and the corresponding **68**-*E*-(*S*)-(*P*)-(R_a) isomer.

7.4.2.5. 68-*Z*-(*S*)-(*P*)-(S_a) = C-(S_a)

Proximity of HC17 to triazole HC35 revealed *Z*-configuration of the central double bond in **68**-*Z*-(*S*)-(*P*)-(S_a), shown in Figure 193.

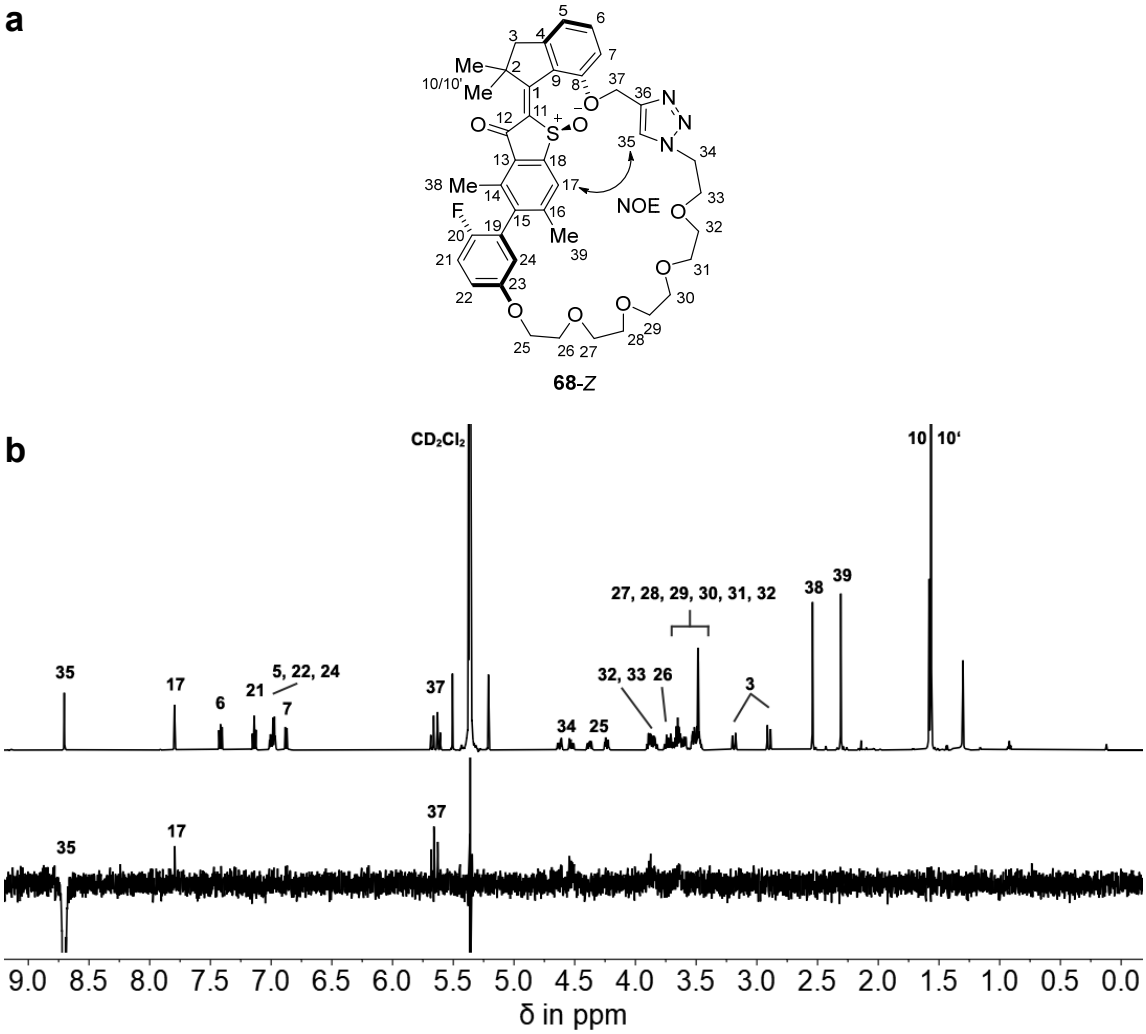

Figure 193 Double bond configuration analysis of isomer **68**-*Z*-(*S*)-(*P*)-(S_a) measured in CD_2Cl_2 solution at 25 °C. **a** Structure of **68**-*Z*-(*S*)-(*P*)-(S_a) including arrows depicting observed NOE signals. **b** ^{1}H (top) and NOE (bottom) NMR spectra (600 MHz, CD_2Cl_2, 25 °C) of **68**-*Z*-(*S*)-(*P*)-(S_a) display proximity of HC17 to HC35, revealing *Z*-configuration of the integrated motor. Adapted with minor format modifications from *J. Am. Chem. Soc.* **2023**, *145*, 13081–13088 licensed under CC BY-NC-ND 4.0. Copyright © 2023 The Authors. Published by American Chemical Society.[2]

Stronger signal intensity of HC24 to H_3C39 compared to H_3C38 revealed tilt of the covalent linker anchoring point on the biaryl towards the carbonyl side of the benzothiophenone fragment shown in Figure 194b. The tilt of the two biaryl planes is further illustrated in the *Newman* projection along the biaryl axis in Figure 194a.

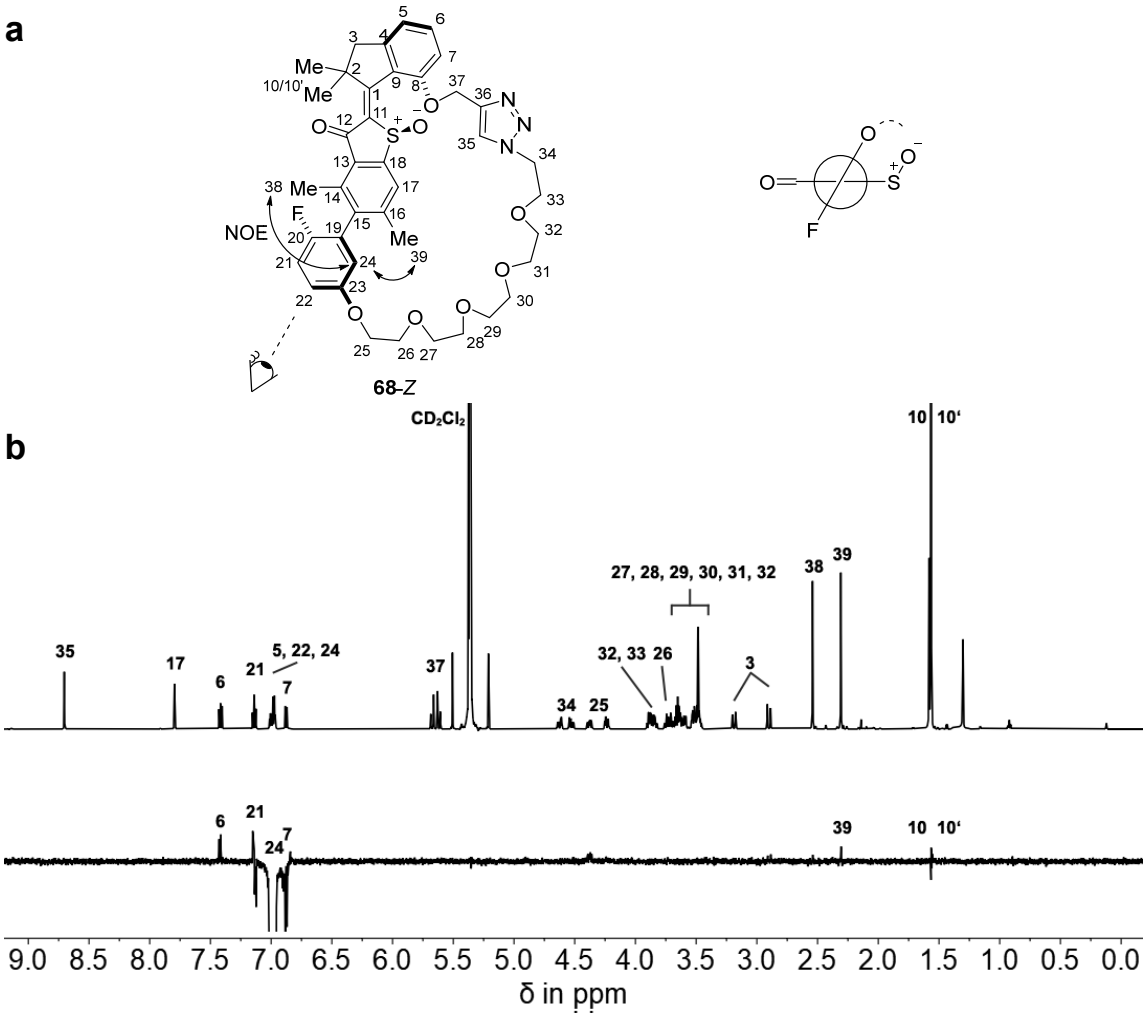

Figure 194 Biaryl axis tilt analysis of **68**-*Z*-(*S*)-(*P*)-(S_a) measured in CD_2Cl_2 solution at 25 °C. **a** Structure of **68**-*Z*-(*S*)-(*P*)-(S_a) including arrows depicting observed ROE signals (left). *Newman* projection of the biaryl axis illustrating the preferred tilt of the two biaryl planes (right). **b** ^{1}H (top) and NOE (bottom) NMR spectra (600 MHz, CD_2Cl_2, 25 °C) of **68**-*Z*-(*S*)-(*P*)-(S_a) display signal intensity differences between H_3C38 and H_3C39 to HC24. Increased spatial proximity of H_3C39 and HC24 indicates biaryl tilt of the covalent linker anchoring point towards the carbonyl side of the benzothiophenone part. Adapted with minor format modifications from *J. Am. Chem. Soc.* **2023**, *145*, 13081–13088 licensed under CC BY-NC-ND 4.0. Copyright © 2023 The Authors. Published by American Chemical Society.[2]

Again, the inclination of the biaryl anchoring point towards H_3C39 indicates the two chain attachment point are located on opposite sides of the benzothiophenone plane since the opposite would probably result in no observable tilt angle. This does therefore complete the previously drawn conclusions for the

other isomers indicating this biaryl axis having a S_a configuration with respect to correct assignment of all other stereodescriptors and the corresponding **68**-*Z*-(*S*)-(*P*)-(R_a) isomer.

7.5. Thermal isomerization at elevated temperatures

To obtain information about isomer interconversions at elevated temperatures and absolute thermodynamic stabilities of individual isomers, pure racemic solutions of **68**-*E*-(*S*)-(*P*)-(R_a), **68**-*Z*-(*S*)-(*P*)-(R_a), **68**-*E*-(*S*)-(*P*)-(S_a), and **68**-*Z*-(*S*)-(*P*)-(S_a) were heated at 80 °C in toluene-d_8 while isomer composition was monitored by ^{1}H NMR spectroscopy as shown in Figure 195.

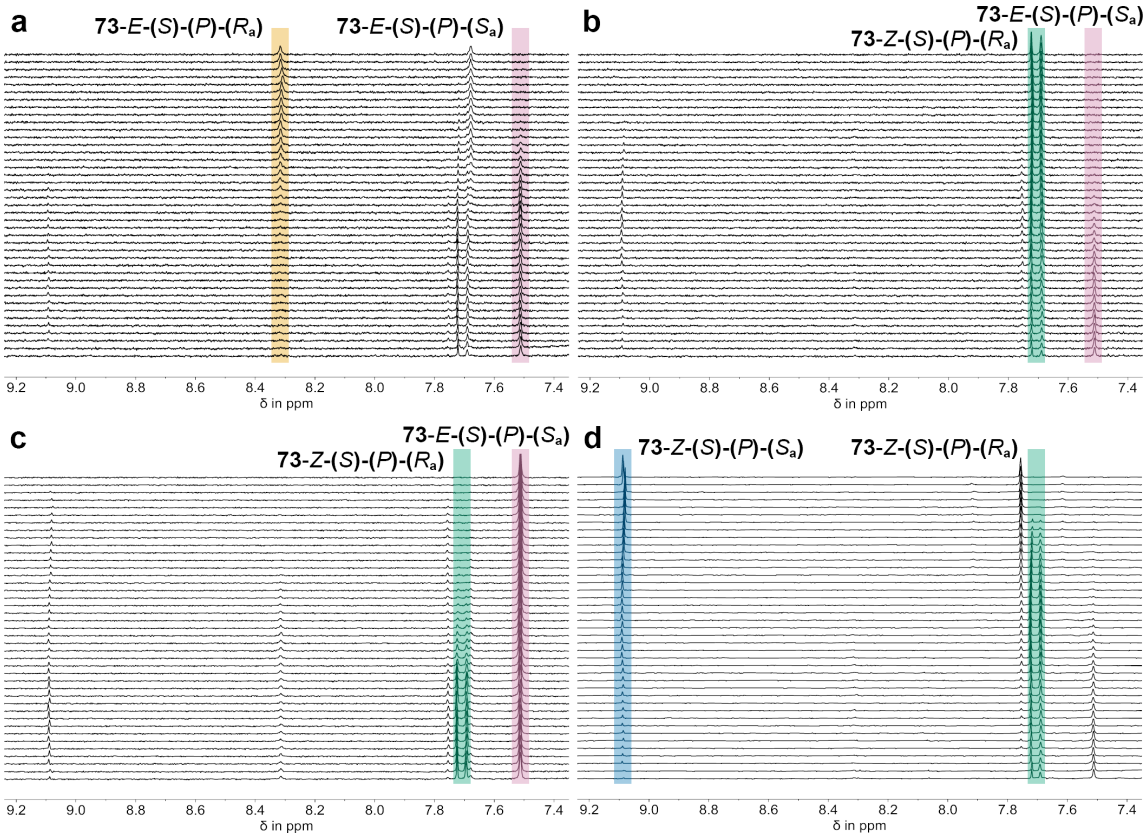

Figure 195 ^{1}H NMR spectra (400 MHz, toluene-d_8, 25 °C) of pure racemic (**a**) **68**-*E*-(*S*)-(*P*)-(R_a) (yellow), (**b**) **68**-*Z*-(*S*)-(*P*)-(R_a) (green), (**c**) **68**-*E*-(*S*)-(*P*)-(S_a) (pink) and (**d**) **68**-*Z*-(*S*)-(*P*)-(S_a) (blue) during thermal isomerization at 80 °C. Only main emerging isomers are highlighted for clarity. Spectra were recorded in irregular intervals starting from pure solutions of the corresponding isomer ordered chronologically from top to bottom. After 89,417 min the temperature was increased to 100 °C to reduce the remaining time for reaching thermal equilibrium.

The recorded spectra allowed calculations of isomer distribution at each measurement point for all four individual experiments. After 62 days of heating the temperature was increased to 100 °C, reducing the remaining time to reach thermal equilibrium. Therefore, values for thermal equilibrium are given at 100 °C. Changing isomer ratios of all data points were plotted over time as shown in Figure 196 to obtain kinetic data as well as relative stabilities for each isomer in thermal equilibrium.

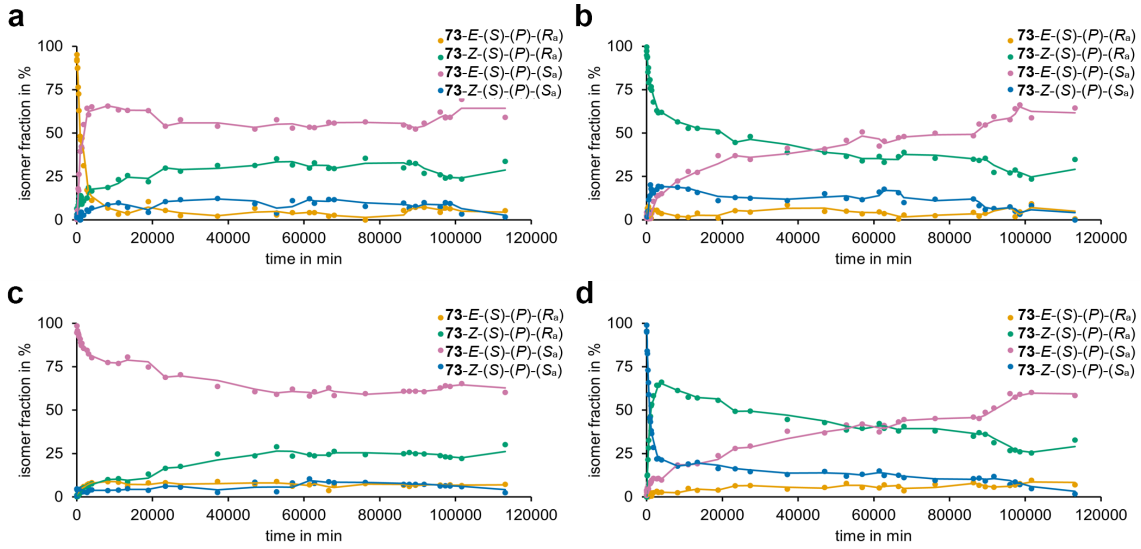

Figure 196 Changing isomer fractions (colored dots) of **68** recorded using ^{1}H NMR spectroscopy (400 MHz, toluene-d_8, 25 °C) during thermal isomerization at 80 °C. Experiments were started from pure racemic solutions of each isomer, namely (**a**) **68**-*E*-(*S*)-(*P*)-(R_a) (yellow dots), (**b**) **68**-*Z*-(*S*)-(*P*)-(R_a) (green dots), (**c**) **68**-*E*-(*S*)-(*P*)-(S_a) (pink dots) and (**d**) **68**-*Z*-(*S*)-(*P*)-(S_a) (blue dots). Plain lines indicate moving averages of the corresponding color-coded measurement. Temperature was increased to 100 °C after 89,417 min, reducing the remaining time to reach thermal equilibrium. Adapted with minor format modifications from *J. Am. Chem. Soc.* **2023**, 145, 13081–13088 licensed under CC BY-NC-ND 4.0. Copyright © 2023 The Authors. Published by American Chemical Society.[2]

The equilibrium isomer distribution was established by averaging the data of the last three measurements of each experiment concluding the most stable isomer is **68**-*E*-(*S*)-(*P*)-(S_a) (62% in thermal equilibrium) followed by **68**-*Z*-(*S*)-(*P*)-(R_a) (27%), **68**-*Z*-(*S*)-(*P*)-(S_a) (6%) and **68**-*E*-(*S*)-(*P*)-(R_a) (5%) at 100 °C in toluene-d_8 solution taken as the mean from all four experiments. All experimental values are shown in Table 27.

Table 27 Experimentally determined isomer distribution of motor **68** given in % after entering thermal equilibrium at 100 °C, starting from pure solutions in toluene-d_8 of **68**-*E*-(*S*)-(*P*)-(R_a) (Measurement 1), **68**-*Z*-(*S*)-(*P*)-(R_a) (Measurement 2), **68**-*E*-(*S*)-(*P*)-(S_a) (Measurement 3), and **68**-*Z*-(*S*)-(*P*)-(S_a) (Measurement 4)

isomer	1	2	3	4	average
68-*E*-(*S*)-(*P*)-(S_a)	63	63	63	59	62
68-*Z*-(*S*)-(*P*)-(R_a)	27	28	25	28	27
68-*Z*-(*S*)-(*P*)-(S_a)	5	5	7	8	6
68-*E*-(*S*)-(*P*)-(R_a)	5	4	5	5	5

Relative *Gibbs* energy differences between individual isomers were calculated using Equation 17 according to their ratios *K* in thermal equilibrium (*via* Equation 18) obtained from Table 27.

$$\Delta G = -R \cdot T \cdot \ln(K) \quad \text{(Eq. 17)}$$

$$R = \text{ ideal gas constant} = 8.314\ \text{J} \cdot \text{K}^{-1} \cdot \text{mol}^{-1}$$

$$T = \text{temperature in K}$$

$$K = \text{equilibrium constant} = \frac{[\text{isomer } \mathbf{X}]}{[\text{isomer } \mathbf{Y}]} \quad \text{(Eq. 18)}$$

With the energy of the most stable isomer **68**-*E*-(*S*)-(*P*)-(S_a) set to 0.0 kcal mol^{-1} the relative difference to the second most stable isomer **68**-*Z*-(*S*)-(*P*)-(R_a) is 0.6 kcal mol^{-1} followed by **68**-*Z*-(*S*)-(*P*)-(S_a) and **68**-*E*-(*S*)-(*P*)-(R_a) with an energy difference of 1.6 kcal mol^{-1} relative to **68**-*E*-(*S*)-(*P*)-(S_a) as shown in Table 28.

Table 28 Experimentally determined ground state *Gibbs* energy differences Δ*G* for all *E*- and *Z*-isomers of macrocyclic motor **68** at 100 °C, starting from pure solutions in toluene-d_8 averaged over four measurements.

isomer	**Δ*G* in kcal mol^{-1}**
68-*E*-(*S*)-(*P*)-(S_a)	0.0
68-*Z*-(*S*)-(*P*)-(R_a)	0.6
68-*Z*-(*S*)-(*P*)-(S_a)	1.6
68-*E*-(*S*)-(*P*)-(R_a)	1.6

Furthermore, isomerization kinetics were simulated to fit the experimentally obtained data since some isomerization processes are inseparable from each other, rendering an exact analytical solution impossible. Therefore COPASI 4.36 (BUILD 260)[294] was used to fit the experimentally obtained data similar to a previous report,[157] using the Genetic Algorithm method with the number of generations set to 200,000 and the population size set to 20. All four observable species namely **68**-*E*-(*S*)-(*P*)-(R_a), **68**-*Z*-(*S*)-(*P*)-(R_a), **68**-*E*-(*S*)-(*P*)-(S_a) and **68**-*Z*-(*S*)-(*P*)-(S_a) with their respective distributions and the rate constants for their interconversions were defined as variables starting from initially pure solutions for the respective experiment. Iterations simulating the experimental data were continued until input and generated data were identical shown for the last iteration in Figure 197.

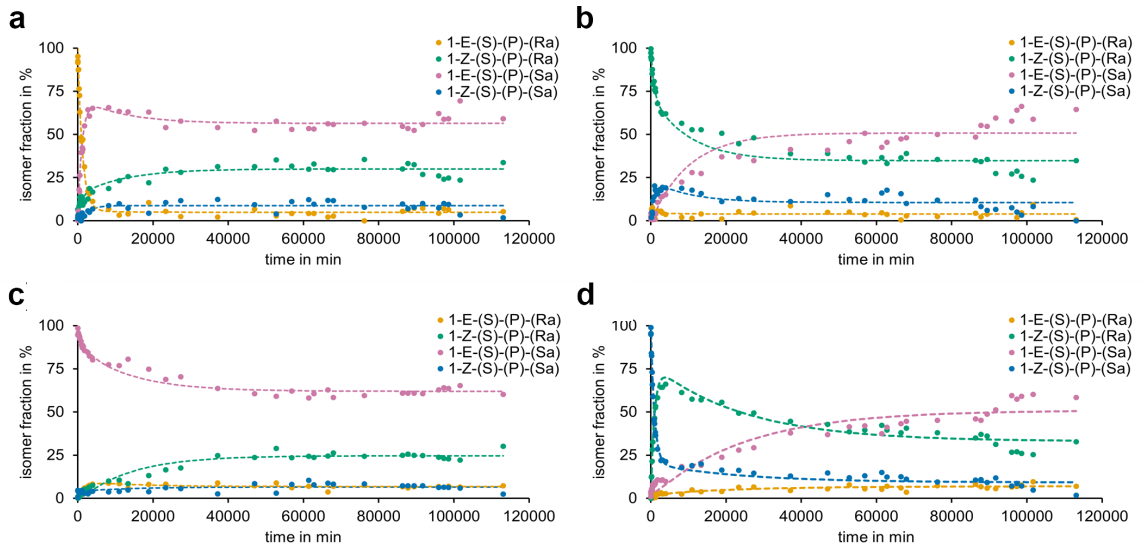

Figure 197 Simulated kinetics (dashed lines) of recorded ^{1}H NMR spectroscopic data (colored dots, 400 MHz, toluene-d_8, 25 °C) acquired during thermal isomerization of **68** at 80 °C. Experiments were started from pure racemic solutions of each isomer, namely (**a**) **68**-*E*-(*S*)-(*P*)-(R_a) (yellow dots), (**b**) **68**-*Z*-(*S*)-(*P*)-(R_a) (green dots), (**c**) **68**-*E*-(*S*)-(*P*)-(S_a) (pink dots) and (**d**) **68**-*Z*-(*S*)-(*P*)-(S_a) (blue dots). Dashed lines indicate fitted kinetics of the corresponding color-coded measurement. The temperature was increased to 100 °C after 89,417 min, reducing the remaining time to reach thermal equilibrium. Adapted with minor format modifications from *J. Am. Chem. Soc.* **2023**, 145, 13081–13088 licensed under CC BY-NC-ND 4.0. Copyright © 2023 The Authors. Published by American Chemical Society.[2]

With multiple processes on different timescales an analytical mathematical solution of such a complex system of differential Equations requiring knowledge of all involved processes would call for an extensive study of this four-component system. Thereby a much faster approach would be simulating the underlying kinetic reactions using a *Markov* matrice containing all relevant transformations as performed previously in literature.[84,85,142,157,185,295] The following isomerization processes are conceivable, shown in Equation 19–24.

atropisomerizations

68-*E*-(*S*)-(*P*)-(R_a) ⇌ **68**-*E*-(*S*)-(*P*)-(S_a) mass action (reversible) (Eq. 19)

68-*Z*-(*S*)-(*P*)-(R_a) ⇌ **68**-*Z*-(*S*)-(*P*)-(S_a) mass action (reversible) (Eq. 20)

TDBI

68-*E*-(*S*)-(*P*)-(R_a) ⇌ **68**-*Z*-(*S*)-(*P*)-(R_a) mass action (reversible) (Eq. 21)

68-*E*-(*S*)-(*P*)-(S_a) ⇌ **68**-*Z*-(*S*)-(*P*)-(S_a) mass action (reversible) (Eq. 22)

synchronous atropisomerization/TDBI

68-*E*-(*S*)-(*P*)-(R_a) ⇌ **68**-*Z*-(*S*)-(*P*)-(S_a) mass action (reversible) (Eq. 23)

68-*E*-(*S*)-(*P*)-(S_a) ⇌ **68**-*Z*-(*S*)-(*P*)-(S_a) mass action (reversible) (Eq. 24)

Atropisomerizations **68**-*E*-(*S*)-(*P*)-(R_a) → **68**-*E*-(*S*)-(*P*)-(S_a) and **68**-*Z*-(*S*)-(*P*)-(S_a) → **68**-*Z*-*S*)-(*P*)-(R_a) were experimentally determined (see chapter 7.10) and thermal double bond isomerizations (TDBIs) were assumed to occur reversibly for both atropisomers. Simulation of experimental data using Equations 19–22 rendered the synchronous atropisomerization/TDBI process negligible for this system. Solving this four-component system using Equations 19–22 resulted in four rate constant estimations for each process involved, which are displayed in Table 29.

Table 29 Estimated rate constants for each process involved in the four-component system derived from simulation of experimental data starting from pure racemic toluene-d_8 solutions of **68**-*E*-(*S*)-(*P*)-(R_a) (Measurement 1), **68**-*Z*-(*S*)-(*P*)-(R_a) (Measurement 2), **68**-*E*-(*S*)-(*P*)-(S_a) (Measurement 3), and **68**-*Z*-(*S*)-(*P*)-(S_a) (Measurement 4). Numerical values were obtained from simulating experimental kinetic data using COPASI.[294]

isomerization process	1	2	3	4
68-*E*-(*S*)-(*P*)-(S_a) → **68**-*E*-(*S*)-(*P*)-(R_a)	$5.4\cdot10^{-5}$	$5.6\cdot10^{-5}$	$2.4\cdot10^{-5}$	$8.6\cdot10^{-5}$
68-*E*-(*S*)-(*P*)-(S_a) ← **68**-*E*-(*S*)-(*P*)-(R_a)	$4.9\cdot10^{-4}$	$6.2\cdot10^{-4}$	$1.3\cdot10^{-4}$	$1.1\cdot10^{-3}$
68-*Z*-(*S*)-(*P*)-(S_a) → **68**-*Z*-(*S*)-(*P*)-(R_a)	$4.5\cdot10^{-4}$	$1.8\cdot10^{-4}$	$9.0\cdot10^{-4}$	$8.7\cdot10^{-4}$
68-*Z*-(*S*)-(*P*)-(S_a) ← **68**-*Z*-(*S*)-(*P*)-(R_a)	$1.2\cdot10^{-4}$	$5.8\cdot10^{-5}$	$2.7\cdot10^{-4}$	$2.6\cdot10^{-4}$
68-*E*-(*S*)-(*P*)-(R_a) → **68**-*Z*-(*S*)-(*P*)-(R_a)	$8.5\cdot10^{-8}$	$1.5\cdot10^{-4}$	$1.2\cdot10^{-4}$	$1.4\cdot10^{-3}$
68-*E*-(*S*)-(*P*)-(R_a) ← **68**-*Z*-(*S*)-(*P*)-(R_a)	$1.4\cdot10^{-7}$	$2.1\cdot10^{-5}$	$1.3\cdot10^{-5}$	$1.6\cdot10^{-4}$
68-*E*-(*S*)-(*P*)-(S_a) → **68**-*Z*-(*S*)-(*P*)-(S_a)	$4.1\cdot10^{-5}$	$5.7\cdot10^{-5}$	$8.9\cdot10^{-8}$	$1.8\cdot10^{-8}$
68-*E*-(*S*)-(*P*)-(S_a) ← **68**-*Z*-(*S*)-(*P*)-(S_a)	$3.9\cdot10^{-4}$	$3.8\cdot10^{-4}$	$5.6\cdot10^{-5}$	$1.0\cdot10^{-4}$

Gibbs energies of activation $\Delta G^{\ddagger}$ for each reaction involved in the simulation of the experimental data at 80 °C can be directly calculated using the *Eyring* Equation shown exemplarily in Equation 25 for the rate constant of **68**-*E*-(*S*)-(*P*)-(S_a) → **68**-*E*-(*S*)-(*P*)-(R_a).

$$k_{(\mathbf{68}\text{-}E\text{-}(S)\text{-}(P)\text{-}(S_a)\rightarrow\mathbf{68}\text{-}E\text{-}(S)\text{-}(P)\text{-}(R_a))} = \frac{k_B T}{h} e^{\frac{-\Delta G^{\ddagger}}{RT}} \quad \text{(Eq. 25)}$$

$$k_B = \textit{Boltzmann}\ \text{constant} = 1.381\ \text{J}\cdot\text{K}^{-1}$$

$$T = \text{temperature in K}$$

$$h = \textit{Planck}\ \text{constant} = 6.626\cdot10^{-34}\ \text{J}\cdot\text{s}$$

$$R = \text{ ideal gas constant} = 8.314\ \text{J} \cdot \text{K}^{-1} \cdot \text{mol}^{-1}$$

Inserting physical constants and rearranging Equation 25, the *Gibbs* energies of activation $\Delta G^{\ddagger}$ can be directly obtained from Equation 26.

$$\Delta G^{\ddagger} = 8.314 \cdot T \cdot \left[23.760 + \ln\left(\frac{T}{k_{(\mathbf{X}\text{-}E\text{-}(S)\text{-}(P)\text{-}(S_a)\rightarrow\mathbf{X}\text{-}E\text{-}(S)\text{-}(P)\text{-}(R_a))}}\right)\right] \qquad \text{(Eq. 26)}$$

Values of $\Delta G^{\ddagger}$ obtained from the simulation of the experimental data are summarized in Table 30 given in kcal mol^{-1}. Noticeable from the obtained $\Delta G^{\ddagger}$ values is that the two lowest values of $\Delta G^{\ddagger}$ for the **68**-*E*-(*S*)-(*P*)-(R_a) → **68**-*E*-(*S*)-(*P*)-(S_a) process with 26.2 kcal mol^{-1} and for the **68**-*Z*-(*S*)-(*P*)-(S_a) → **68**-*Z*-(*S*)-(*P*)-(R_a) process with 26.1 kcal mol^{-1} match well with the first processes observed in experiments shown in Figure 196a and d and magnified in Figure 198. If these experiments are treated as first-order processes with entering a thermal equilibrium (see chapter 6.8), neglecting all side reactions, approximate values of 25.7 kcal mol^{-1} and 25.4 kcal mol^{-1} are obtained for these processes respectively, shown in Figure 199 and 200. This approximation appears valid as within the first 5,000 min, these two processes are dominant allowing to neglect all other processes on this timescale. The similarity between the simulation and the approximation indicates that taking the above-mentioned model as a basis for reproducing the experimental values appears to be a reasonable approach.

Table 30 Experimentally estimated *Gibbs* energies of activation $\Delta G^{\ddagger}$ for macrocyclic molecular motor **68** given in kcal mol^{-1}. Energies for each possible interconversion in the four-component system were derived by simulation of measured data. Pure racemic solutions of **68**-*E*-(*S*)-(*P*)-(R_a) (Measurement 1), **68**-*Z*-(*S*)-(*P*)-(R_a) (Measurement 2), **68**-*E*-(*S*)-(*P*)-(S_a) (Measurement 3), and **68**-*Z*-(*S*)-(*P*)-(S_a) (Measurement 4) in toluene-d_8 were utilized as starting points. All processes were simulated using COPASI[294] fitting the experimentally observed kinetic data.

isomerization process	1 in kcal mol^{-1}	2 in kcal mol^{-1}	3 in kcal mol^{-1}	4 in kcal mol^{-1}	average in kcal mol^{-1}
68-*E*-(*S*)-(*P*)-(S_a) → **68**-*E*-(*S*)-(*P*)-(R_a)	27.7	27.6	28.2	27.3	27.7
68-*E*-(*S*)-(*P*)-(S_a) ← **68**-*E*-(*S*)-(*P*)-(R_a)	26.1	26.0	27.1	25.5	26.2
68-*Z*-(*S*)-(*P*)-(S_a) → **68**-*Z*-(*S*)-(*P*)-(R_a)	26.2	26.8	25.7	25.7	26.1
68-*Z*-(*S*)-(*P*)-(S_a) ← **68**-*Z*-(*S*)-(*P*)-(R_a)	27.1	27.6	26.5	26.6	27.0
68-*E*-(*S*)-(*P*)-(R_a) → **68**-*Z*-(*S*)-(*P*)-(R_a)	32.2	26.9	27.1	25.4	27.9
68-*E*-(*S*)-(*P*)-(R_a) ← **68**-*Z*-(*S*)-(*P*)-(R_a)	31.8	28.4	28.6	26.9	28.9
68-*E*-(*S*)-(*P*)-(S_a) → **68**-*Z*-(*S*)-(*P*)-(S_a)	27.9	27.6	32.2	33.3	30.2
68-*E*-(*S*)-(*P*)-(S_a) ← **68**-*Z*-(*S*)-(*P*)-(S_a)	26.3	26.3	27.6	36.9	29.3

These two processes describing structural reconfiguration steps as shown in Figure 198, which occur as the main isomerizations before any other process leads to a significant amount of sideproduct are the key steps for the operation of molecular machine **68**. Both reactions **68**-*E*-(*S*)-(*P*)-(R_a) → **68**-*E*-(*S*)-(*P*)-(S_a) and **68**-*Z*-(*S*)-(*P*)-(S_a) → **68**-*Z*-(*S*)-(*P*)-(R_a) allowed for conversion of 66% starting material to the corresponding opposing atropisomer in each case.

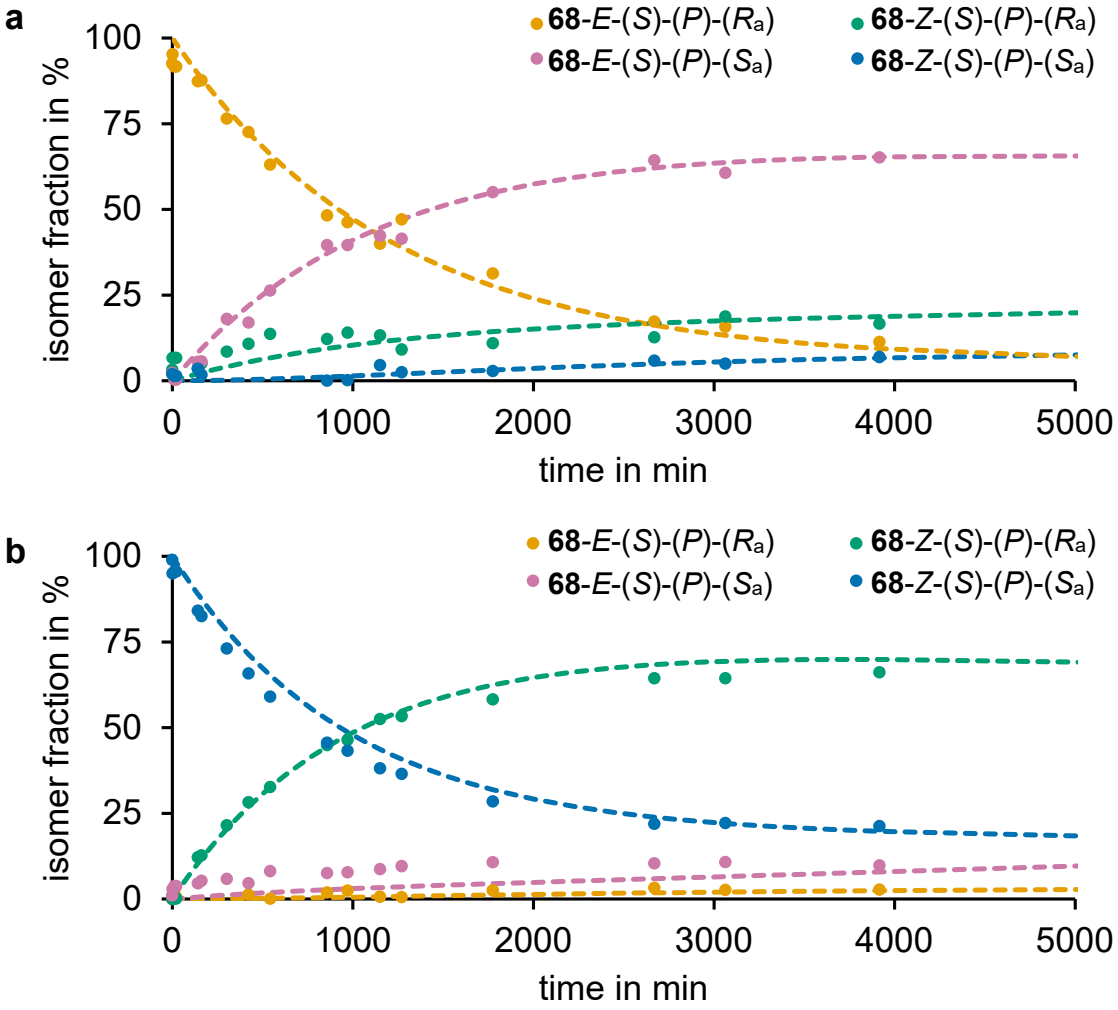

Figure 198 Magnification of the simulated kinetics (dashed lines) based on ^{1}H NMR data (colored dots, 400 MHz, toluene-d_8) acquired at 25 °C during thermal isomerization at 80 °C. Experiments were started from pure solutions of each isomer, namely (**a**) **68**-*E*-(*S*)-(*P*)-(R_a) (yellow dots), and (**b**) **68**-*Z*-(*S*)-(*P*)-(S_a) (blue dots). Dashed lines indicate fitted kinetics of the corresponding color-coded measurement showing that atropisomerizations are the dominant reactions in the beginning of thermal isomerizations starting from **68**-*E*-(*S*)-(*P*)-(R_a) and **68**-*Z*-(*S*)-(*P*)-(S_a).

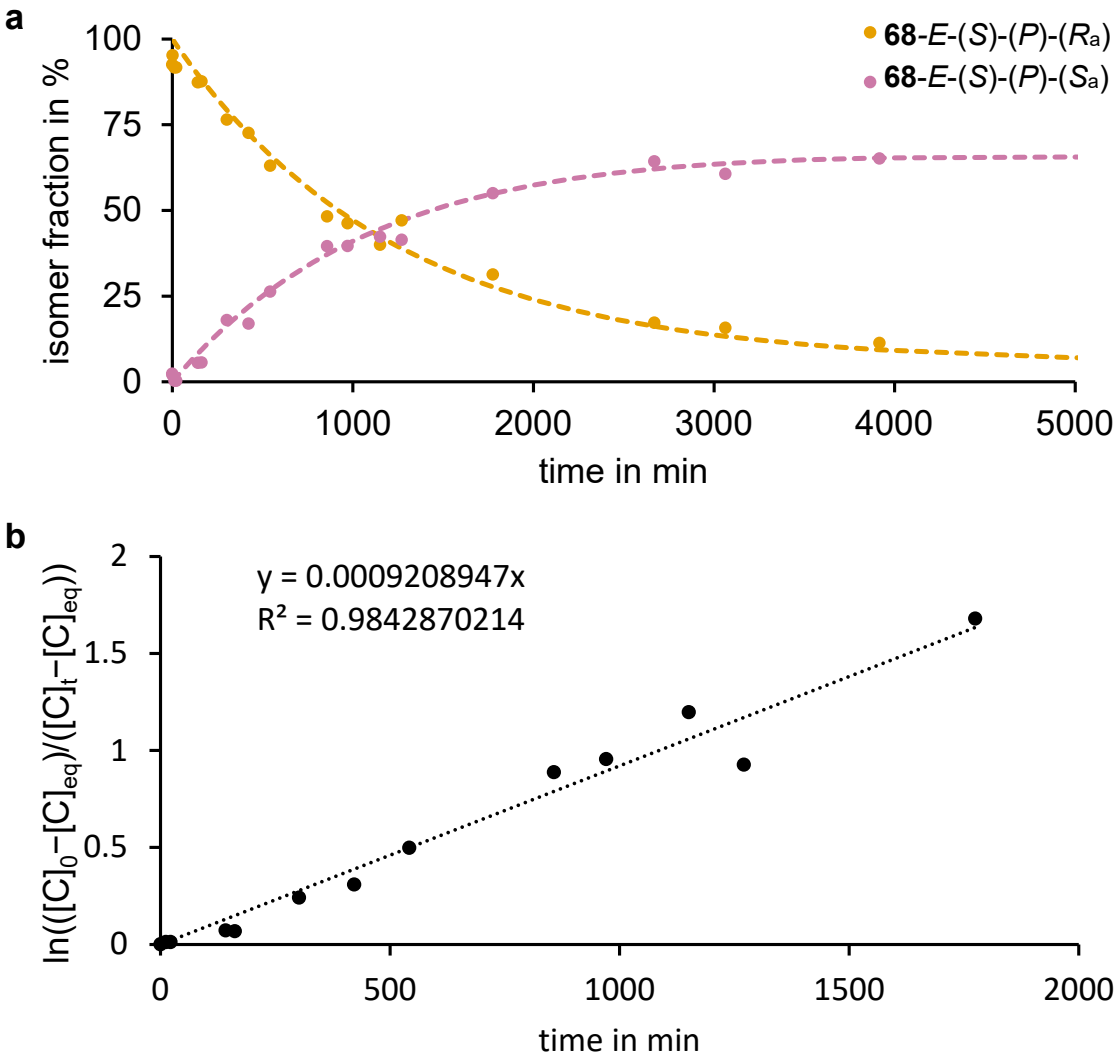

Figure 199 Approximation for the rate constant value obtained from simulation of the **68**-*E*-(*S*)-(*P*)-(R_a) → **68**-*E*-(*S*)-(*P*)-(S_a) process given in Table 30. (**a**) Simulated kinetics based on ^{1}H NMR data (colored dots, 400 MHz, toluene-d_8) are shown with color-coded dashed lines. (**b**) Approximated experimental data utilizing a linear regression fit (dotted black line) treating the isomerization as a first-order processes with entering a thermal equilibrium (see chapter 6.8). The obtained $\Delta G^{\ddagger}$ value of 26.2 kcal mol^{-1} neglecting all side reactions, does match well with the estimated $\Delta G^{\ddagger}$ value of 25.7 kcal mol^{-1} obtained from simulated kinetics.

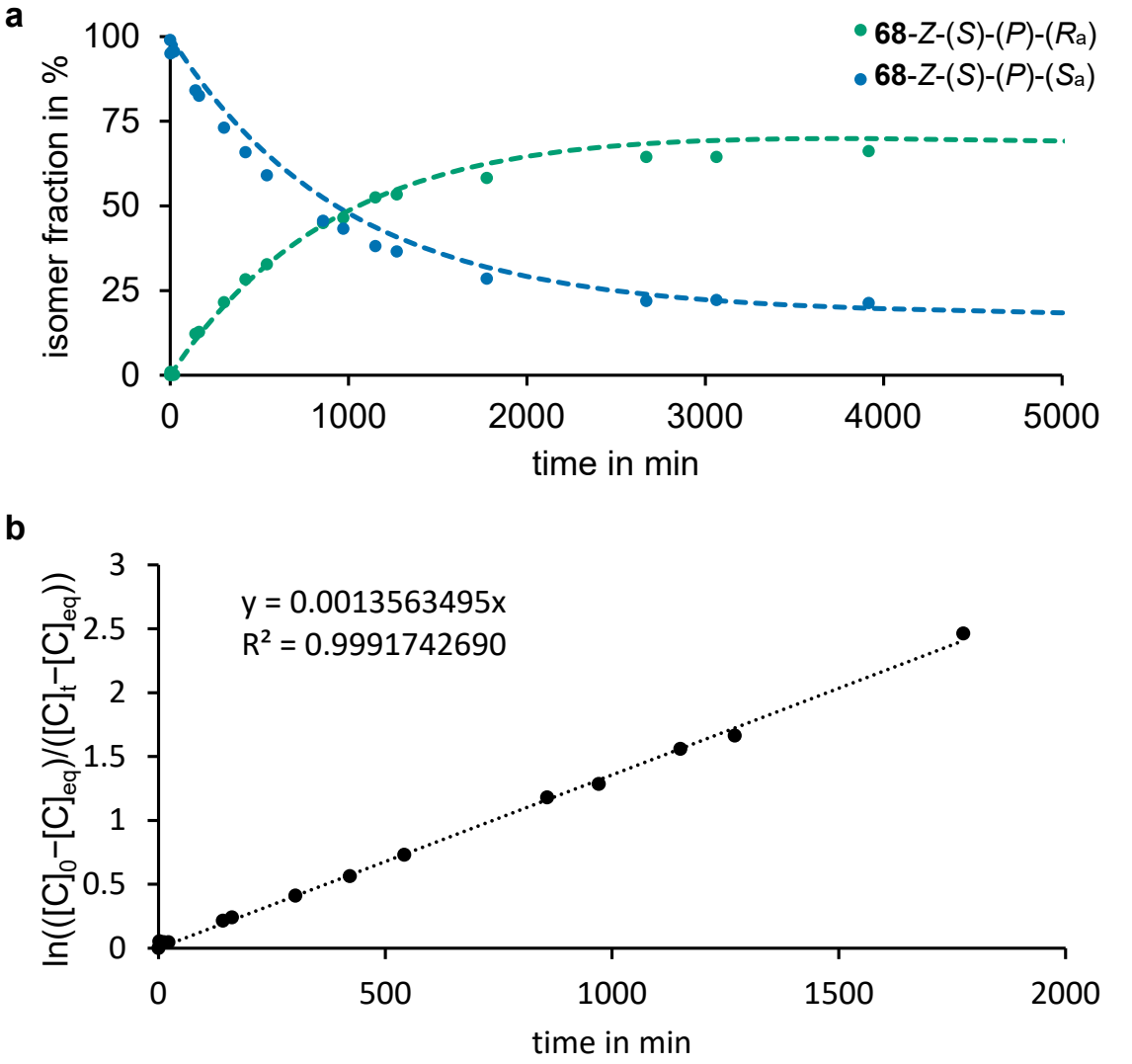

Figure 200 Approximation for the rate constant value obtained from simulation of the **68**-*Z*-(*S*)-(*P*)-(S_a) → **68**-*Z*-(*S*)-(*P*)-(R_a) process given in Table 30. (**a**) Simulated kinetics based on ^{1}H NMR data (colored dots, 400 MHz, toluene-d_8) are shown with color-coded dashed lines. (**b**) Approximated experimental data utilizing a linear regression fit (dotted black line) treating the isomerization as a first-order processes with entering a thermal equilibrium (see chapter 6.8). The obtained $\Delta G^{\ddagger}$ value of 26.1 kcal mol^{-1} neglecting all side reactions, does match well with the estimated $\Delta G^{\ddagger}$ value of 25.4 kcal mol^{-1} obtained from simulated kinetics.

Isomerizations **68**-*E*-(*S*)-(*P*)-(R_a) → **68**-*E*-(*S*)-(*P*)-(S_a) and **68**-*Z*-(*S*)-(*P*)-(S_a) → **68**-*Z*-(*S*)-(*P*)-(R_a) were termed structural reconfiguration. These are the two processes allowing for efficient interconversion between the individual revolving door configurations in 66% for the R_a → S_a and 66% for the S_a → R_a configuration respectively. With these barriers being the lowest overall, structural reconfiguration is enabled before any other process, allowing for distinct selective switching between individual R_a and S_a unidirectional motor cycles and *vice versa*.

7.6. Motion sequence elucidation of molecular motor 68

Conformer analysis using VT ^{1}H NMR and low temperature ECD spectroscopy in combination with *in situ* irradiation allowed elucidating the motion sequence of molecular motor **68**. With isomer interconversion barriers at 80 °C and ground state energy distribution of molecular motor **68** at 100 °C at hand, low temperature experiments were conducted. Especially ^{1}H NMR and ECD spectroscopy (see chapter 7.9.2) at low temperatures (−90 °C) helped gaining information about reaction barriers from elusive *E*-(*S*)-(*M*) and *Z*-(*S*)-(*M*) isomers towards stable *E*-(*S*)-(*P*) and *Z*-(*S*)-(*P*) isomers respectively. A detailed description of the procedure can be found in chapter 5.6.

7.6.1. Low temperature ^{1}H NMR measurements

Motor isomers **A**, **B**, **C** and **D** shown in Figure 201 present in the original HTI motor[154] – as well as in most derivatives of this system – can also be found in the embedded cyclic structure since these key characteristics were not affected from macrocyclization. Thermodynamic stable isomers at 22 °C, namely isomer **A** with *E*-(*S*)-(*P*)-(R_a) and *E*-(*S*)-(*P*)-(S_a) as well as **C** with *Z*-(*S*)-(*P*)-(R_a) and *Z*-(*S*)-(*P*)-(S_a) conformation were already described in chapters 2 and 5. Conformers **B** with *Z*-(*S*)-(*M*)-(R_a) and *Z*-(*S*)-(*M*)-(S_a) as well as **D** with *E*-(*S*)-(*M*)-(R_a) and *E*-(*S*)-(*M*)-(S_a) conformation were attempted to be observed using low temperature ^{1}H NMR spectroscopy in combination with *in situ* irradiation using a 470 nm LED. All low temperature experiments were conducted together with *Christian Placht*.[IX]

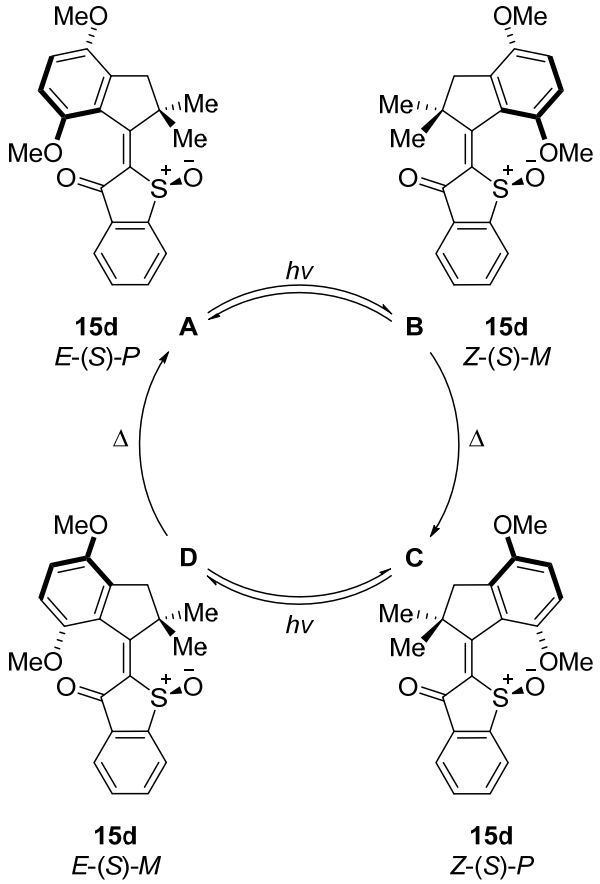

Figure 201 Four-step unidirectional rotation of first HTI-based original molecular motor **15d**. Irradiation of *E*-(*S*)-(*P*) = **A** leads to double bond inversion (DBI) and thus population of metastable *Z*-(*S*)-(*M*) = **B**, which subsequently isomerizes quickly *via* THI to *Z*-(*S*)-(*P*) = **C** at 22 °C finishing the first 180° rotation. Stable isomer *Z*-(*S*)-(*P*) = **C** photoisomerizes to metastable *E*-(*S*)-(*M*) = **D** through DBI followed by fast THI to regenerate starting isomer *E*-(*S*)-(*P*) = **A** finishing the unidirectional 360° rotation, as already described in chapter 5.4.

Comparing system **68** to the original system **15d**, identical behavior was observed with isomer **B** remaining elusive even at −90 °C. No additional set of isomer signals attributable to a photoproduct of **A** for both atropisomers S_a and R_a could be observed at this temperature. In combination with the comparable barriers for thermal decay of **D**, which are +13.6 kcal mol^{-1} for **68**-S_a and **68**-R_a with respect to 13.1 kcal mol^{-1} in the original system, this allows to conclude that macrocyclization with an elongated chain does not affect the rate determining THI barrier for motor rotation substantially enough to be measurable with certainty. This is in stark contrast to smaller motorized macrocycles where significant strain leads to strong effects on the THI barriers, e.g. in partially strained system **64** (+13.9 kcal mol^{-1}),[158] sterically non-restricted biaryl system **65** (+14.5 kcal mol^{-1})[159] or initial motor system **15d** (+13.1 kcal mol^{-1}).[154]

7.6.1.1. R_a atropisomer motor function analysis

A solution containing a mixture of **68**-*E*-(*S*)-(*P*)-(R_a) and **68**-*Z*-(*S*)-(*P*)-(R_a) (96:4) in CD_2Cl_2 solution was gradually cooled to −90 °C while ^{1}H NMR spectra were taken at 25 °C, −20 °C, −40 °C, −70 °C and −90 °C to track shifting of signals for each isomer as shown in Figure 202a. Subsequently, spectra were recorded in irregular intervals before, during and after irradiation with a 470 nm LED at −90 °C until a maximum of 39% **68**-*E*-(*S*)-(*M*)-(R_a) = **68**-**D**-(R_a) is accumulated after 30 min, ordered chronologically from top to bottom. No signals of intermediate **68**-*Z*-(*S*)-(*M*)-(R_a) = **68**-**B**-(R_a) are observed at this temperature which is in agreement with earlier studies on related HTI motors because the *Gibbs* energy of activation for thermal **68**-**B**-(R_a) to **68**-**C**-(R_a) conversion is smaller than 11.0 kcal mol^{-1}. Thermal isomerization barriers for **68**-*E*-(*S*)-(*M*)-(R_a) → **68**-*E*-(*S*)-(*P*)-(R_a) process were determined at −90 and −80 °C from the changing isomer fractions using a first-order rate law not entering a thermal equilibrium since full conversion occurs. A linear regression fit translates to a *Gibbs* energy of activation $\Delta G^{\ddagger}$ of 13.5 and 13.7 kcal mol^{-1} respectively, as shown in Figure 203 and 204. Annealing and re-irradiation using 470 nm proved that the same PSS was reached and none of the shifting signals were mistaken for another isomer, as shown in Figure 205.

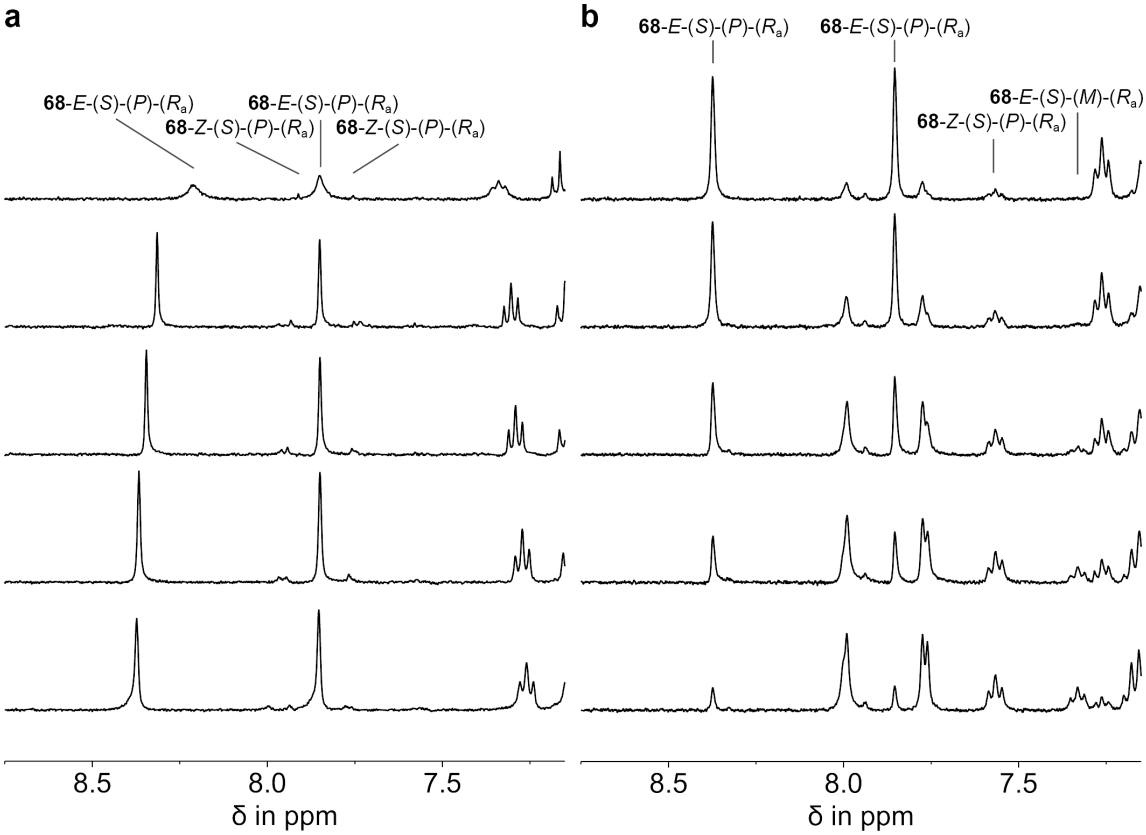

Figure 202 ^{1}H NMR spectra (400 MHz, CD_2Cl_2) of racemic **68**-(R_a) recorded during cooling to −90 °C followed by irradiation with 470 nm light. **a** Stacked NMR spectra of **68**-*E*-(*S*)-(*P*)-(R_a) and **68**-*Z*-(*S*)-(*P*)-(R_a) (96:4) at 25 °C, −20 °C, −40 °C, −70 °C and −90 °C from top to bottom. **b** Stacked NMR spectra before, during and after *in situ* irradiation using a 470 nm LED, starting from a mixture of **68**-*E*-(*S*)-(*P*)-(R_a) and **68**-*Z*-(*S*)-(*P*)-(R_a) (96:4) at −90 °C (top). After 90 min a maximum of 39% **68**-*E*-(*S*)-(*M*)-(R_a) is accumulated with spectra ordered chronologically from top to bottom. At first **68**-*Z*-(*S*)-(*P*)-(R_a) is accumulated followed by **68**-*E*-(*S*)-(*M*)-(R_a) buildup, revealing the order of interconversions starting with **68**-*E*-(*S*)-(*P*)-(R_a) (**A**-(R_a)) to **68**-*Z*-(*S*)-(*M*)-(R_a) (**B**-(R_a)) – not observed because of low thermal stability at −90 °C – which is directly converted to **68**-*Z*-(*S*)-(*P*)-(R_a) (**C**-(R_a)), and closing the unidirectional cycle with **68**-*E*-(*S*)-(*M*)-(R_a) (**D**-(R_a)) respectively.

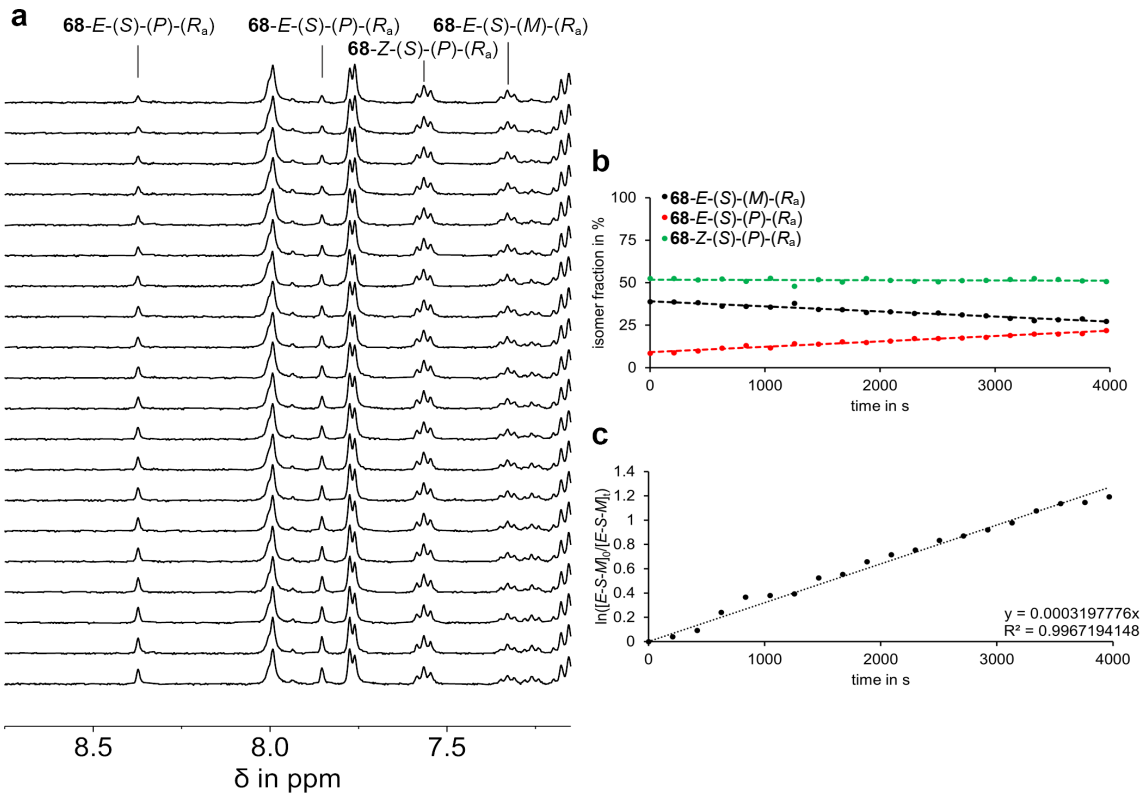

Figure 203 Kinetic analysis of thermal isomerization of racemic **68**-*E*-(*S*)-(*M*)-(R_a) in CD_2Cl_2 at −90 °C. **a** ^{1}H NMR spectra (400 MHz, CD_2Cl_2, −90 °C) of **68**-*E*-(*S*)-(*M*)-(R_a), **68**-*E*-(*S*)-(*P*)-(R_a) and **68**-*Z*-(*S*)-(*P*)-(R_a) during thermal isomerization of **68**-*E*-(*S*)-(*M*)-(R_a) to **68**-*E*-(*S*)-(*P*)-(R_a) starting from a mixture consisting of 39% **68**-*E*-(*S*)-(*M*)-(R_a), 9% **68**-*E*-(*S*)-(*P*)-(R_a) and 52% **68**-*Z*-(*S*)-(*P*)-(R_a) (top spectrum). Spectra were recorded in intervals of 3 min ordered chronologically from top to bottom. **b** Changing isomer fractions during thermal conversion starting from a **68**-*E*-(*S*)-(*M*)-(R_a) enriched solution comprised of 39% **68**-*E*-(*S*)-(*M*)-(R_a) (black dots), 9% **68**-*E*-(*S*)-(*P*)-(R_a) (red dots) and 52% **68**-*Z*-(*S*)-(*P*)-(R_a) (green dots). Data were simulated for visual guidance using a linear fit shown with color-coded dashed lines. **c** Kinetic evaluation using a first-order rate law without entering a thermal equilibrium since full conversion of **68**-*E*-(*S*)-(*M*)-(R_a) to **68**-*E*-(*S*)-(*P*)-(R_a) occurs, provides a linear correlation for the consumption of **68**-*E*-(*S*)-(*M*)-(R_a). A simulation of the experimental data points using a linear regression fit (dotted black line) leads to a slope of m = 0.0003198, translating into a *Gibbs* energy of activation of $\Delta G^{\ddagger}$ = 13.5 kcal mol^{-1}.

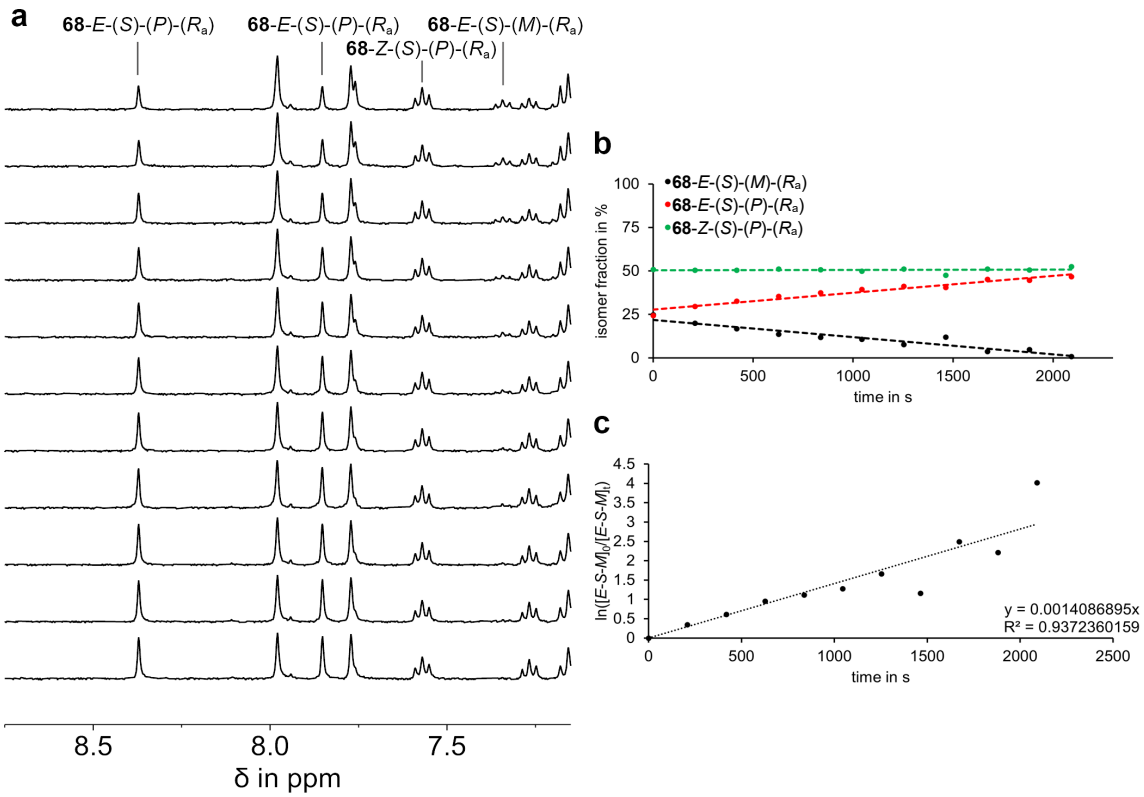

Figure 204 Second kinetic analysis of accelerated thermal isomerization of racemic **68**-*E*-(*S*)-(*M*)-(R_a) in CD_2Cl_2 at −80 °C. **a** ^{1}H NMR spectra (400 MHz, CD_2Cl_2, −80 °C) of **68**-*E*-(*S*)-(*M*)-(R_a), **68**-*E*-(*S*)-(*P*)-(R_a) and **68**-*Z*-(*S*)-(*P*)-(R_a) during thermal isomerization of **68**-*E*-(*S*)-(*M*)-(R_a) to **68**-*E*-(*S*)-(*P*)-(R_a) starting from a mixture consisting of 25% **68**-*E*-(*S*)-(*M*)-(R_a), 24% **68**-*E*-(*S*)-(*P*)-(R_a) and 51% **68**-*Z*-(*S*)-(*P*)-(R_a) (top spectrum). Spectra were recorded in intervals of 3.5 min ordered chronologically from top to bottom. **b** Changing isomer fractions during thermal conversion starting from a **68**-*E*-(*S*)-(*M*)-(R_a) enriched solution comprised of 25% **68**-*E*-(*S*)-(*M*)-(R_a) (black dots), 24% **68**-*E*-(*S*)-(*P*)-(R_a) (red dots) and 51% **68**-*Z*-(*S*)-(*P*)-(R_a) (green dots). Data were simulated for visual guidance using a linear fit shown with color-coded dashed lines. **c** Kinetic evaluation using a first-order rate law without entering a thermal equilibrium since full conversion of **68**-*E*-(*S*)-(*M*)-(R_a) to **68**-*E*-(*S*)-(*P*)-(R_a) occurs, provides a linear correlation for the consumption of **68**-*E*-(*S*)-(*M*)-(R_a). A simulation of the experimental data points using a linear regression fit (dotted black line) leads to a slope of m = 0.001409, translating into a *Gibbs* energy of activation of $\Delta G^{\ddagger}$ = 13.7 kcal mol^{-1}.

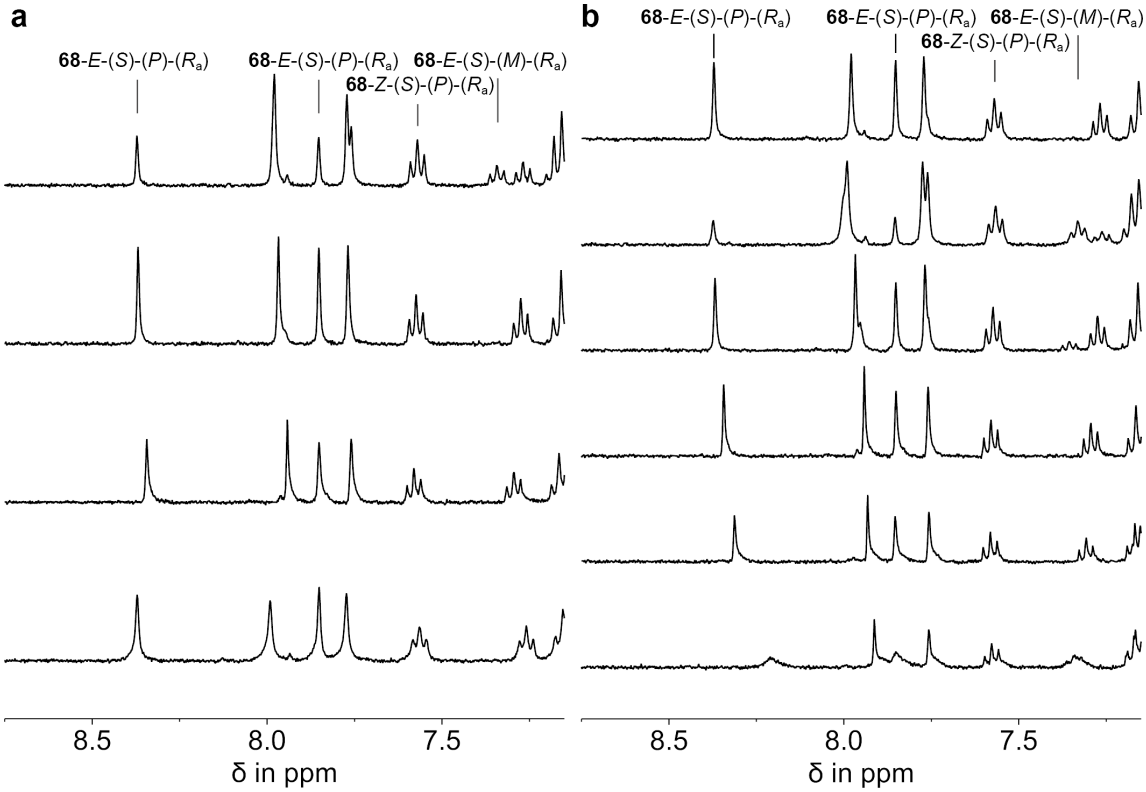

Figure 205 ^{1}H NMR spectra (400 MHz, CD_2Cl_2) obtained during thermal annealing and re-irradiation of remaining **68**-*E*-(*S*)-(*M*)-(R_a) after recording thermal isomerization kinetics. **a** Racemic mixture consisting of **68**-*E*-(*S*)-(*M*)-(R_a), **68**-*E*-(*S*)-(*P*)-(R_a) and **68**-*Z*-(*S*)-(*P*)-(R_a) (25:24:51), during thermal annealing from −80 °C (top) to −70 °C (second from the top) and −40 °C (third from the top). After completed conversion, the isomer mixture was cooled back to −90 °C ensuring exclusive **68**-*E*-(*S*)-(*P*)-(R_a) formation from remaining **68**-*E*-(*S*)-(*M*)-(R_a) (bottom). **b** Mixture of racemic **68**-*E*-(*S*)-(*P*)-(R_a) and **68**-*Z*-(*S*)-(*P*)-(R_a) (48:52) measured at −90 °C before (top) and after repeated irradiation for 30 min with a 470 nm LED (second from the top). The second irradiation resulted in the same PSS of **68**-*E*-*S*)-(*M*)-(R_a), **68**-*E*-(*S*)-(*P*)-(R_a) and **68**-*Z*-(*S*)-(*P*)-(R_a) (39:8:52) as if starting from a mixture consisting of **68**-*E*-(*S*)-(*P*)-(R_a) and **68**-*Z*-(*S*)-(*P*)-(R_a) (96:4, first irradiation). The solution was further annealed to −70 °C (third from the top), −40 °C (fourth from the top), −20 °C (fifth from the top), and 25 °C (bottom) ensuring only isomers **68**-*E*-(*S*)-(*P*)-(R_a) and **68**-*Z*-(*S*)-(*P*)-(R_a) are present after two irradiation cycles.

7.6.1.2. S_a atropisomer motor function analysis

A solution containing a mixture of **68**-*E*-(*S*)-(*P*)-(S_a) and **68**-*Z*-(*S*)-(*P*)-(S_a) (35:65) in CD_2Cl_2 solution was cooled to −90 °C while ^{1}H NMR spectra were taken at 25 °C, −20 °C, −40 °C, −70 °C and −90 °C to keep track of shifting signals for each isomer shown in Figure 206a. Next, spectra were recorded in irregular intervals before, during and after irradiation with a 470 nm LED until a maximum of 89% **68**-*E*-(*S*)-(*M*)-(S_a) = **68**-**D**-(S_a) is accumulated after 30 min, shown in Figure 206b ordered chronologically from top to bottom. No signals of intermediate **68**-*Z*-(*S*)-(*M*)-(S_a) = **68**-**B**-(S_a) are observed at this temperature, which is in agreement with earlier studies on related HTI motors because the *Gibbs* energy of activation for thermal **68**-**B**-(S_a) to **68**-**C**-(S_a) conversion is smaller than 11.0 kcal mol^{-1}. Thermal isomerization barriers for **68**-*E*-(*S*)-(*M*)-(S_a) → **68**-*E*-(*S*)-(*P*)-(S_a) process were determined at −90 and −80 °C from the changing isomer fractions using a first-order rate law without entering a thermal equilibrium since full conversion occurs. A linear regression fit translates to a *Gibbs* energy of activation $\Delta G^{\ddagger}$ of 13.6 and 13.6 kcal mol^{-1} respectively, as shown in Figure 207 and 208. Annealing and re-irradiation using 470 nm proved that the same PSS was reached and none of the shifting signals were mistaken for another isomer, as shown in Figure 209.

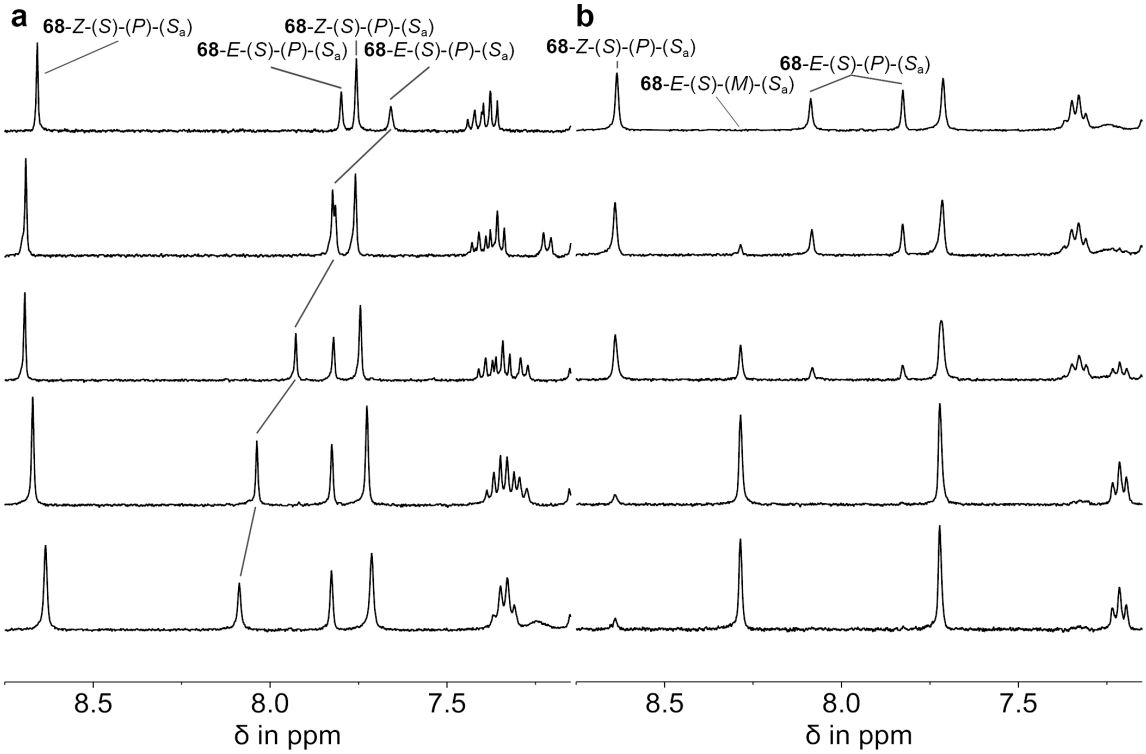

Figure 206 ^{1}H NMR spectra (400 MHz, CD_2Cl_2) of racemic **68**-(S_a) recorded during cooling to −90 °C followed by irradiation with 470 nm light. **a** Stacked NMR spectra of **68**-*E*-(*S*)-(*P*)-(S_a) and **68**-*Z*-(*S*)-(*P*)-(S_a) (35:65) at 25 °C, −20 °C, −40 °C, −70 °C and −90 °C from top to bottom. **b** Stacked NMR spectra before, during and after *in situ* irradiation using a 470 nm LED, starting from a mixture of **68**-*E*-(*S*)-(*P*)-(S_a) and **68**-*Z*-(*S*)-(*P*)-(S_a) (35:65) at −90 °C (top). After 30 min a maximum of 89% **68**-*E*-(*S*)-(*M*)-(S_a) is accumulated with spectra ordered chronologically from top to bottom. At first **68**-*Z*-(*S*)-(*P*)-(S_a) is converted to **68**-*E*-(*S*)-(*M*)-(S_a) which is accumulated, while **68**-*E*-(*S*)-(*P*)-(S_a) (**A**-(S_a)) isomerizes to **68**-*Z*-(*S*)-(*M*)-(S_a) (**B**-(S_a)) – not observed because of low thermal stability at −90 °C – which is directly converted to **68**-*Z*-(*S*)-(*P*)-(S_a) (**C**-(S_a)) – which does therefore not change much initially – and closing the unidirectional cycle with **68**-*E*-(*S*)-(*M*)-(S_a) (**D**-(S_a)) respectively.

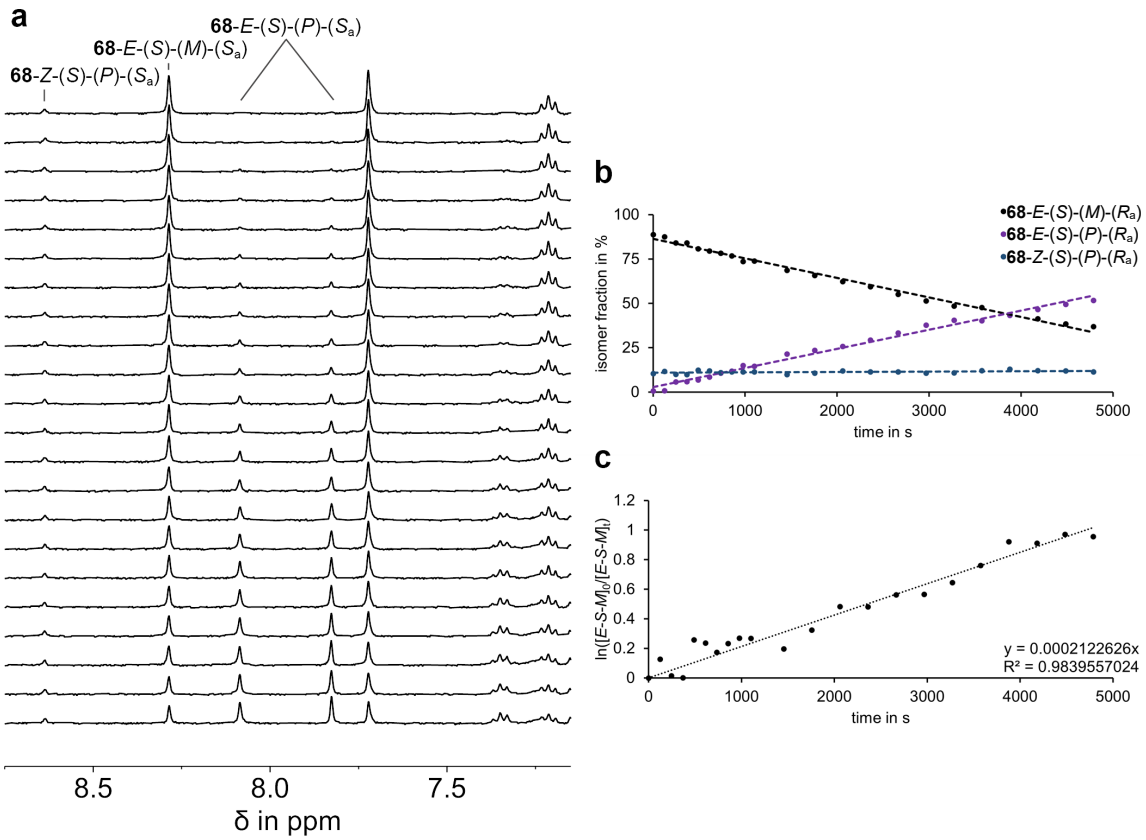

Figure 207 Kinetic analysis of thermal isomerization of racemic **68**-*E*-(*S*)-(*M*)-(S_a) in CD_2Cl_2 at −90 °C. **a** ^{1}H NMR spectra (400 MHz, CD_2Cl_2, −90 °C) of **68**-*E*-(*S*)-(*M*)-(S_a), **68**-*E*-(*S*)-(*P*)-(S_a) and **68**-*Z*-(*S*)-(*P*)-(S_a) during thermal isomerization of **68**-*E*-(*S*)-(*M*)-(S_a) to **68**-*E*-(*S*)-(*P*)-(S_a) starting from a mixture consisting of 89% **68**-*E*-(*S*)-(*M*)-(S_a), 1% **68**-*E*-(*S*)-(*P*)-(S_a) and 10% **68**-*Z*-(*S*)-(*P*)-(S_a) (top spectrum). Spectra were recorded in intervals of 3 min ordered chronologically from top to bottom. **b** Changing isomer fractions during thermal conversion starting from a **68**-*E*-(*S*)-(*M*)-(R_a) enriched solution comprised of 89% **68**-*E*-(*S*)-(*M*)-(S_a) (black dots), 1% **68**-*E*-(*S*)-(*P*)-(S_a) (purple dots) and 10% **68**-*Z*-*S*)-(*P*)-(S_a) (blue dots). Data were simulated for visual guidance using a linear fit shown with color-coded dashed lines. **c** Kinetic evaluation using a first-order rate law without entering a thermal equilibrium since full conversion of **68**-*E*-(*S*)-(*M*)-(S_a) to **68**-*E*-(*S*)-(*P*)-(S_a) occurs, provides a linear correlation for the consumption of **68**-*E*-(*S*)-(*M*)-(S_a). A simulation of the experimental data points using a linear regression fit (dotted black line) leads to a slope of m = 0.0002123, translating into a *Gibbs* energy of activation of $\Delta G^{\ddagger}$ = 13.6 kcal mol^{-1}.

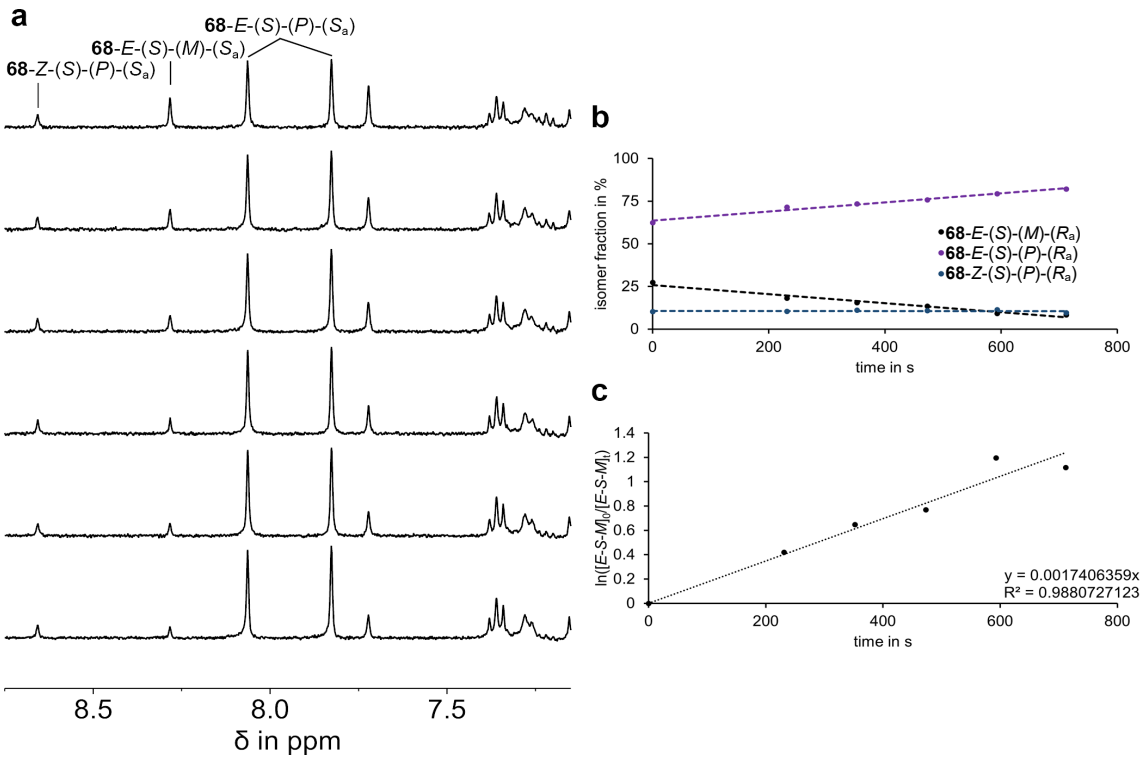

Figure 208 Second kinetic analysis of accelerated thermal isomerization of racemic **68**-*E*-(*S*)-(*M*)-(S_a) in CD_2Cl_2 at −80 °C. **a** ^{1}H NMR spectra (400 MHz, CD_2Cl_2, −80 °C) of **68**-*E*-(*S*)-(*M*)-(S_a), **68**-*E*-(*S*)-(*P*)-(S_a) and **68**-*Z*-(*S*)-(*P*)-(S_a) during thermal isomerization of **68**-*E*-(*S*)-(*M*)-(S_a) to **68**-*E*-(*S*)-(*P*)-(S_a) starting from a mixture consisting of 28% **68**-*E*-(*S*)-(*M*)-(S_a), 62% **68**-*E*-(*S*)-(*P*)-(S_a) and 10% **68**-*Z*-(*S*)-(*P*)-(S_a) (top spectrum). Spectra were recorded in intervals of 2 min ordered chronologically from top to bottom. **b** Changing isomer fractions during thermal conversion starting from a **68**-*E*-(*S*)-(*M*)-(S_a) enriched solution comprised of 28% **68**-*E*-(*S*)-(*M*)-(S_a) (black dots), 62% **68**-*E*-(*S*)-(*P*)-(S_a) (purple dots) and 10% **68**-*Z*-(*S*)-(*P*)-(S_a) (blue dots). Data were simulated for visual guidance using a linear fit shown with color-coded dashed lines. **c** Kinetic evaluation using a first-order rate law without entering a thermal equilibrium since full conversion of **68**-*E*-(*S*)-(*M*)-(S_a) to **68**-*E*-(*S*)-(*P*)-(S_a) occurs, provides a linear correlation for the consumption of **68**-*E*-(*S*)-(*M*)-(S_a). A simulation of the experimental data points using a linear regression fit (dotted black line) leads to a slope of m = 0.001741, translating into a *Gibbs* energy of activation of $\Delta G^{\ddagger}$ = 13.6 kcal mol^{-1}.

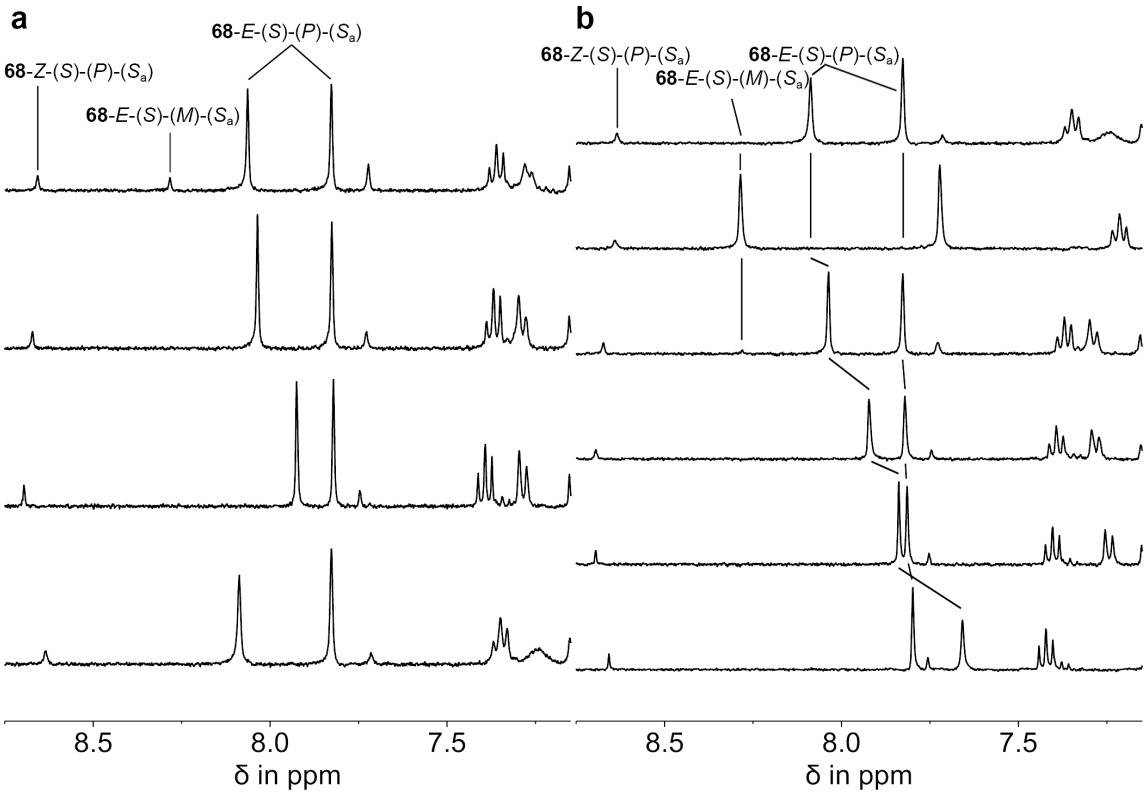

Figure 209 ^{1}H NMR spectra (400 MHz, CD_2Cl_2) obtained during thermal annealing and re-irradiation of remaining **68**-*E*-(*S*)-(*M*)-(S_a) after recording thermal isomerization kinetics. **a** Racemic mixture consisting of **68**-*E*-(*S*)-(*M*)-(S_a), **68**-*E*-(*S*)-(*P*)-(S_a) and **68**-*Z*-(*S*)-(*P*)-(S_a) (28:62:10), during thermal annealing from −80 °C (top) to −70 °C (second from the top) and −40 °C (third from the top). After completed conversion, the isomer mixture was cooled back to −90 °C ensuring exclusive **68**-*E*-(*S*)-(*P*)-(S_a) formation from remaining **68**-*E*-*S*)-(*M*)-(S_a) (bottom). **b** Mixture of racemic **68**-*E*-(*S*)-(*P*)-(S_a) and **68**-*Z*-(*S*)-(*P*)-(S_a) (90:10) measured at −90 °C before (top) and after repeated irradiation for 30 min with a 470 nm LED (second from the top). The second irradiation resulted in the same PSS of **68**-*E*-(*S*)-(*M*)-(S_a), **68**-*E*-(*S*)-(*P*)-(S_a) and **68**-*Z*-(*S*)-(*P*)-(S_a) (89:1:10) as if starting from a mixture consisting of **68**-*E*-(*S*)-(*P*)-(S_a) and **68**-*Z*-(*S*)-(*P*)-(S_a) (35:65, first irradiation). The solution was further annealed to −70 °C (third from the top), −40 °C (fourth from the top), −20 °C (fifth from the top), and 25 °C (bottom) ensuring only isomers **68**-*E*-(*S*)-(*P*)-(S_a) and **68**-*Z*-(*S*)-(*P*)-(S_a) are present after two irradiation cycles.

All experimentally obtained isomerization barriers towards the more stable product are summarized in Table 31. The structural reconfiguration steps display *Gibbs* energies of activation $\Delta G^{\ddagger}$ of 26.1 and 26.2 kcal mol^{-1} as highlighted in grey. The displayed data were used for the experimental energy scheme shown in Figure 210, see also chapter 7.12.

Table 31 Experimentally obtained *Gibbs* energies of activation $\Delta G^{\ddagger}$ given in kcal mol^{-1} for each process towards the more stable product, summarized for each THI, atropisomerisation and thermal double bond inversion (TDBI) for the respective R_a and S_a atropisomer configurations in this order (from low to high). Structural reconfiguration steps are highlighted in grey. Configurations utilized as starting points are mentioned in the isomerization process column. [a]Data were obtained from CD_2Cl_2 solutions at −90 °C. [b]Data were obtained from toluene-d_8 solutions at 80–100 °C.

isomerization process	**$\Delta G^{\ddagger}$ in kcal mol^{-1}**
68-*E*-(*S*)-(*M*)-(R_a) → **68**-*E*-(*S*)-(*P*)-(R_a)	13.6[a]
68-*E*-(*S*)-(*M*)-(S_a) → **68**-*E*-(*S*)-(*P*)-(S_a)	13.6[a]
68-*Z*-(*S*)-(*P*)-(S_a) → **68**-*Z*-(*S*)-(*P*)-(R_a)	26.1[b]
68-*E*-(*S*)-(*P*)-(R_a) → **68**-*E*-(*S*)-(*P*)-(S_a)	26.2[b]
68-*E*-(*S*)-(*P*)-(R_a) → **68**-*Z*-(*S*)-(*P*)-(R_a)	27.9[b]
68-*Z*-(*S*)-(*P*)-(S_a) → **68**-*E*-(*S*)-(*P*)-(S_a)	29.3[b]

7.6.2. Experimental potential energy landscape of macrocyclic motor 68

Combining values from Table 28, 30 and 31 allows to draw a comprehensive energy scheme for the unidirectional 360° rotation cycles for **68**-(R_a) and **68**-(S_a), shown in Figure 210.

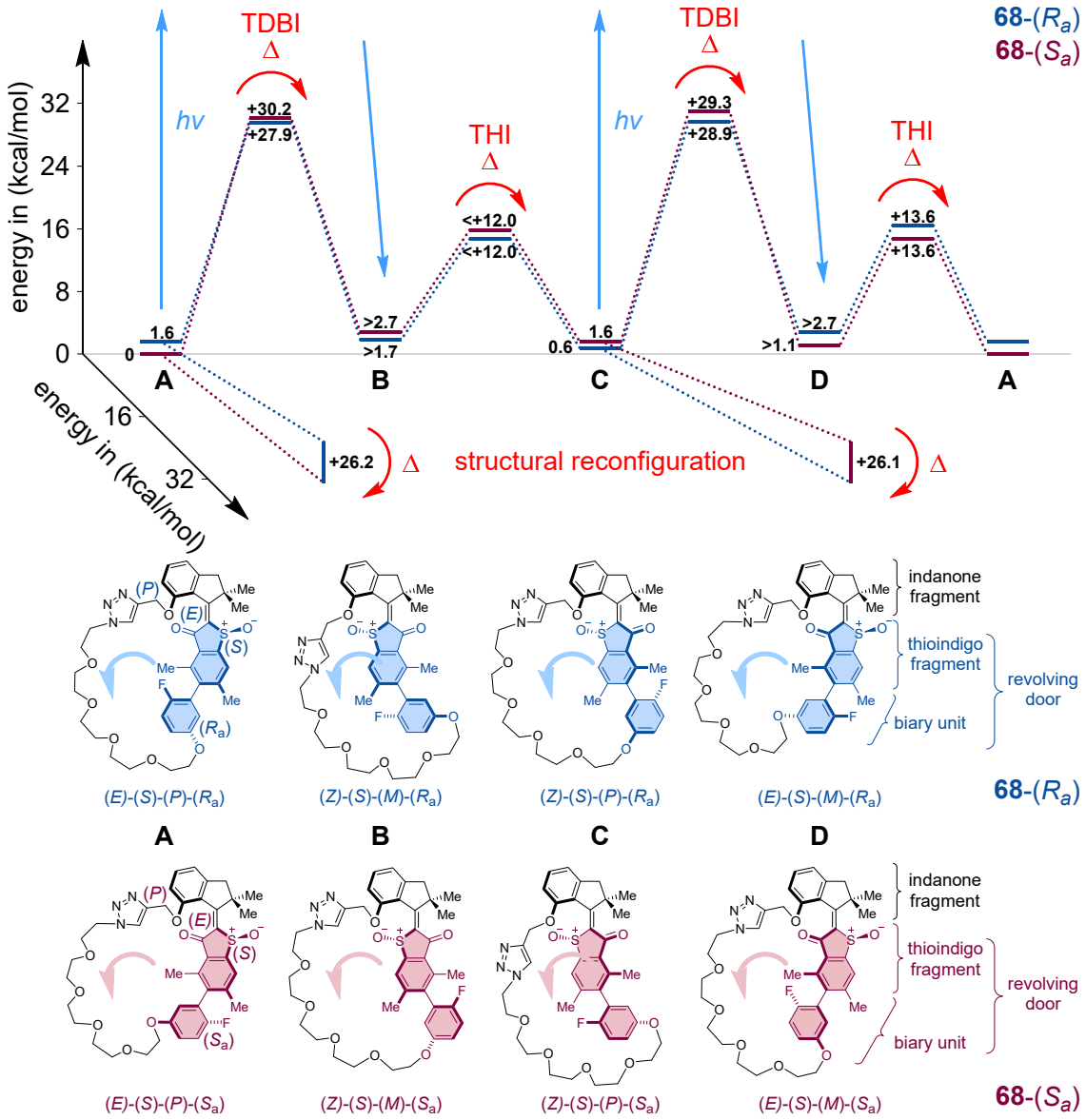

Figure 210 Experimentally determined quantitative potential energy profile of macrocyclic HTI-based molecular motors **68**-(R_a) and **68**-(S_a). All numeric values displayed were obtained from experiments. Ground state energies, THI and TDBI are depicted on the vertical axis and atropisomer rotation barriers namely structural reconfiguration on the diagonal axis. Values of THI and associated relative minimum energies of corresponding metastable states were acquired at –90 °C, TDBI and structural reconfiguration at 80 °C and ground state energies of stable isomers at 100 °C. For simplicity only structures with *S*-configured sulfoxide are shown. Adapted with minor format modifications from *J. Am. Chem. Soc.* **2023**, 145, 13081–13088 licensed under CC BY-NC-ND 4.0. Copyright © 2023 The Authors. Published by American Chemical Society.[2]

According to the quantitative potential energy landscape of **68** shown in Figure 210, a unique motor operation mechanism was elucidated – with respect to previously reported systems[154–156,158,159,293] – which is shown in Figure 211. Full further experimental and theoretical evidence for this model can be found in chapter 7.7–7.12.

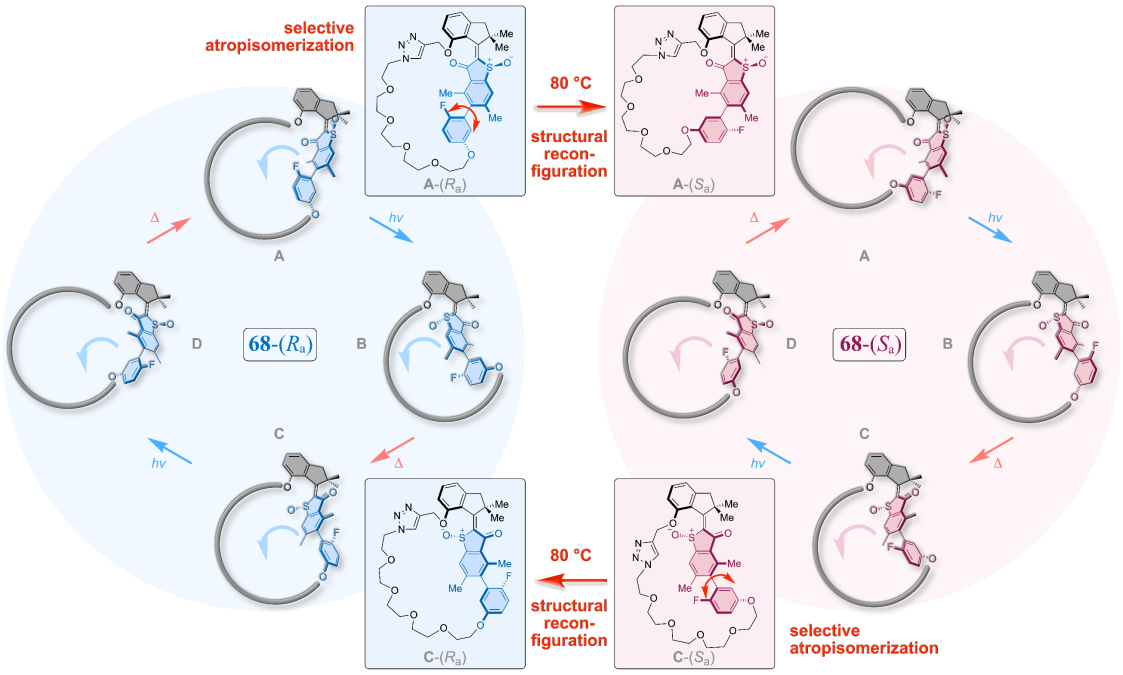

Figure 211 Structural reconfiguration combines macrocyclic molecular motor cycle of **68**-(R_a) with **68**-(S_a). Independent rotation of enlarged revolving doors (blue and red highlighted structures) with identical directionality is achieved in **68**-(R_a) (blue) and **68**-(S_a) (red) within the same macrocyclic framework under illumination with visible light at ambient temperatures. The macrocyclic environment of the embedded molecular motor can be switched from **A**-(R_a) to **A**-(S_a) and from **C**-(S_a) to **C**-(R_a) at elevated temperatures *via* selective atropisomerization, namely structural reconfiguration. Adapted with minor format modifications from *J. Am. Chem. Soc.* **2023**, 145, 13081–13088 licensed under CC BY-NC-ND 4.0. Copyright © 2023 The Authors. Published by American Chemical Society.[2]

7.7. UV-Vis absorption spectra and molar extinction coefficients

Measuring PSS of macrocyclic **68** at various wavelengths required molar extinction coefficients for all involved isomers of **68** which were measured in CH_2Cl_2 at 22 °C shown in Figure 212. Solutions with known concentrations of each isomer were used to calculate the molar extinctions given in Figure 212c and d.

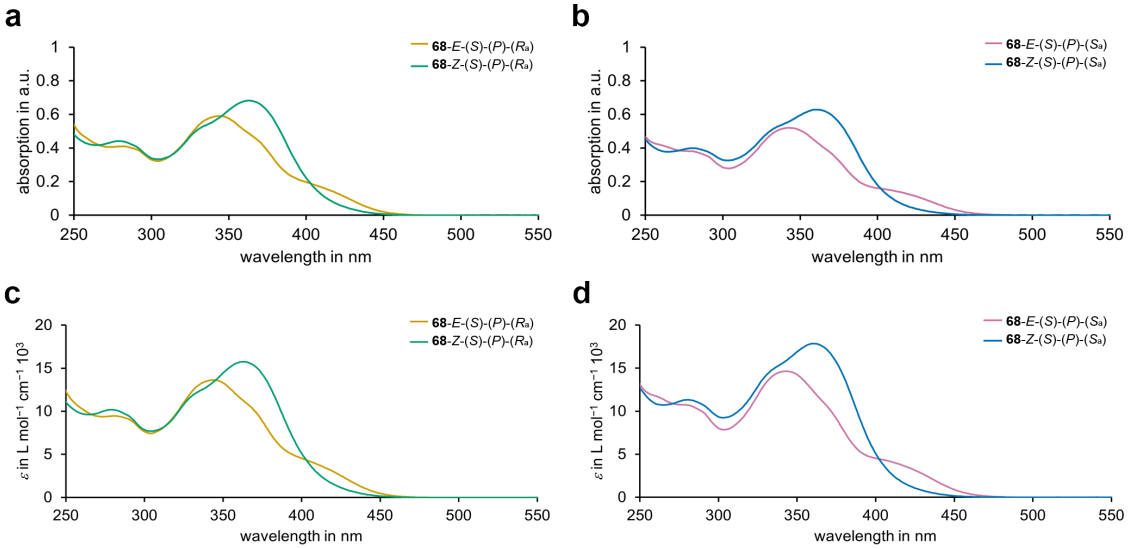

Figure 212 UV-Vis absorption spectra (CH_2Cl_2, 22 °C) of racemic macrocyclic molecular motor **68** isomers. **a** Isomer **68**-*E*-(*S*)-(*P*)-(R_a) (yellow, scaled according to the isosbestic point at 404 nm) and **68**-*Z*-(*S*)-(*P*)-(R_a) (green, 43 µM). **b** Isomer **68**-*E*-(*S*)-(*P*)-(S_a) (pink, scaled according to the isosbestic point at 402 nm) and **68**-*Z*-(*S*)-(*P*)-(S_a) (blue, 51 µM). **c** Molar extinction coefficients of **68**-*E*-(*S*)-(*P*)-(R_a) (yellow) and **68**-*Z*-(*S*)-(*P*)-(R_a) (green) isomers. **d** Molar extinction coefficients of **68**-*E*-(*S*)-(*P*)-(S_a) (pink) and **68**-*Z*-(*S*)-(*P*)-(S_a) (blue) isomers. Adapted with minor format modifications from *J. Am. Chem. Soc.* **2023**, 145, 13081–13088 licensed under CC BY-NC-ND 4.0. Copyright © 2023 The Authors. Published by American Chemical Society.[2]

7.8. Photostationary state determination

Determination of PSS ratios were carried out in CH_2Cl_2 at 22 °C using predetermined molar extinction coefficients of pure isomers as shown in Figure 212c and d as references. Then solutions containing mixtures of *E*- and *Z*-isomers of one atropisomer only were subjected to LED irradiation using various wavelengths corresponding to the absorption region (250–500 nm) of **68** as shown in Table 32. No wavelengths below 365 nm are reported since photodestruction hampered PSS determination. Spectra of mixtures after irradiation with wavelengths leading to the highest *E*-isomer enrichment with 70:30 for **68**-*E*-(*S*)-(*P*)-(R_a):**68**-*Z*-(*S*)-(*P*)-(R_a) and 84:16 for **68**-*E*-(*S*)-(*P*)-(S_a):**68**-*Z*-(*S*)-(*P*)-(S_a) using 385 nm UV-light and 54:46 for **68**-*E*-(*S*)-(*P*)-(R_a):**68**-*Z*-(*S*)-(*P*)-(R_a) and 61:39 for **68**-*E*-(*S*)-(*P*)-(S_a):**68**-*Z*-(*S*)-(*P*)-(S_a) using 405 nm visible light as well as *Z*-isomer enrichment with 34:66 for **68**-*E*-(*S*)-(*P*)-(R_a):**68**-*Z*-(*S*)-(*P*)-(R_a) and 31:69 for **68**-*E*-(*S*)-(*P*)-(S_a):**68**-*Z*-(*S*)-(*P*)-(S_a) with 490 nm visible light are shown in Figure 213a and b for R_a and S_a, respectively.

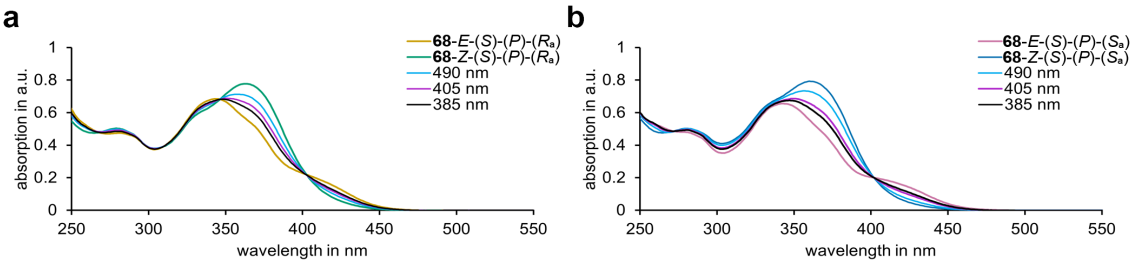

Figure 213 UV-Vis absorption spectra (CH_2Cl_2, 22 °C) of racemic macrocyclic molecular motor **68** isomers obtained after irradiation to the respective PSS. **a** Pure isomers **68**-*E*-(*S*)-(*P*)-(R_a) (yellow) and **1**-*Z*-(*S*)-(*P*)-(R_a) (green), as well as PSS recorded after 490 (cyan), 405 (purple), and 385 nm (black) irradiation. Isomer compositions in the PSS given in Table 32 were determined *via* absorption change at 364 nm. **b** Pure isomers **68**-*E*-(*S*)-(*P*)-(S_a) (pink), **68**-*Z*-(*S*)-(*P*)-(S_a) (blue), as well as PSS of 490 (cyan), 405 (purple), and 385 nm (black). Isomer compositions in the PSS given in Table 32 were determined *via* absorption change at 362 nm. Adapted with minor format modifications from *J. Am. Chem. Soc.* **2023**, 145, 13081–13088 licensed under CC BY-NC-ND 4.0. Copyright © 2023 The Authors. Published by American Chemical Society.[2]

Explicit isomer composition and approximate irradiation time of **68**-*E*-(*S*)-(*P*)-(R_a) and **68**-*Z*-(*S*)-(*P*)-(R_a) as well as **68**-*E*-(*S*)-(*P*)-(S_a) and **68**-*Z*-(*S*)-(*P*)-(S_a) mixtures for each irradiation wavelength in the PSS are given in Table 32.

Table 32 Isomer ratios in the PSS determined for **68**-*E*-(*S*)-(*P*)-(R_a):**68**-*Z*-(*S*)-(*P*)-(R_a) and **68**-*E*-(*S*)-(*P*)-(S_a):**68**-*Z*-(*S*)-(*P*)-(S_a) after irradiation with LED light of given wavelengths. Isomer ratios were determined at 364 and 362 nm respectively *via* UV-Vis absorption spectroscopy at 22 °C in CH_2Cl_2 solution. Irradiation was stopped after stable PSS ratios were reached.

wavelength in nm	irradiation time in min	**68**-***E*-(*S*)-(*P*)-(R_a)**: **73**-***Z*-(*S*)-(*P*)-(R_a)** in %	irradiation time in min	**68**-***E*-(*S*)-(*P*)-(S_a)**: **73**-***Z*-(*S*)-(*P*)-(S_a)** in %
530	1	34:66	1	31:69
505	2	34:66	2	31:69
490	1	34:66	1	31:69
470	3	34:66	1	32:68
450	10	34:66	9	33:67
430	4	40:60	8	44:56
415	9	48:52	4	55:45
405	2	54:46	2	61:39
395	4	66:34	3	79:21
385	1	70:30	1	84:16
365	1	68:32	1	84:16

After determining the most efficient directions of structural reconfiguration steps and ideal wavelengths for accumulation of *E*- or Z-isomers respectively, it was possible to design a cycling experiment passing through each state of macrocyclic molecular motor **68**. To this end, the thermal processes with the highest structural reconfiguration efficiency (**68**-*Z*-(*S*)-(*P*)-(S_a) → **68**-*Z*-(*S*)-(*P*)-(R_a) and **68**-*E*-(*S*)-(*P*)-(R_a) → **68**-*E*-(*S*)-(*P*)-(S_a)) were combined with the wavelengths of irradiation achieving the highest PSS ratios for the **68**-*E*-(*S*)-(*P*)-(R_a) → **68**-*Z*-(*S*)-(*P*)-(R_a) (490 nm) and **68**-*Z*-(*S*)-(*P*)-(S_a) → **68**-*E*-(*S*)-(*P*)-(S_a) (405 nm) processes. The resulting experimental data for this cycle – passing through all conformational states of **68** starting from **68**-*E*-(*S*)-(*P*)-(R_a) – after which 54% of the initial isomer is regenerated can be found in Figure 220 in chapter 7.10.

7.9. Atropisomer assignment

Since precise atropisomer configuration assignment of macrocyclic **68** is crucial for a conclusive picture of the molecular motor operation cycle, ECD spectra of all isomers stable at 22 °C as well as low temperature ECD spectra at −90 °C were measured and compared with simulated spectral data. Only spectra within a range of 6.0 kcal mol^{-1} from the most stable conformer were considered for all presented ECD spectra predicted by theory.

7.9.1. ECD spectra assignment at 22 °C

First ECD spectra of all enantiomerically pure ground state configurations were measured at 22 °C in CH_2Cl_2 shown in Figure 214.

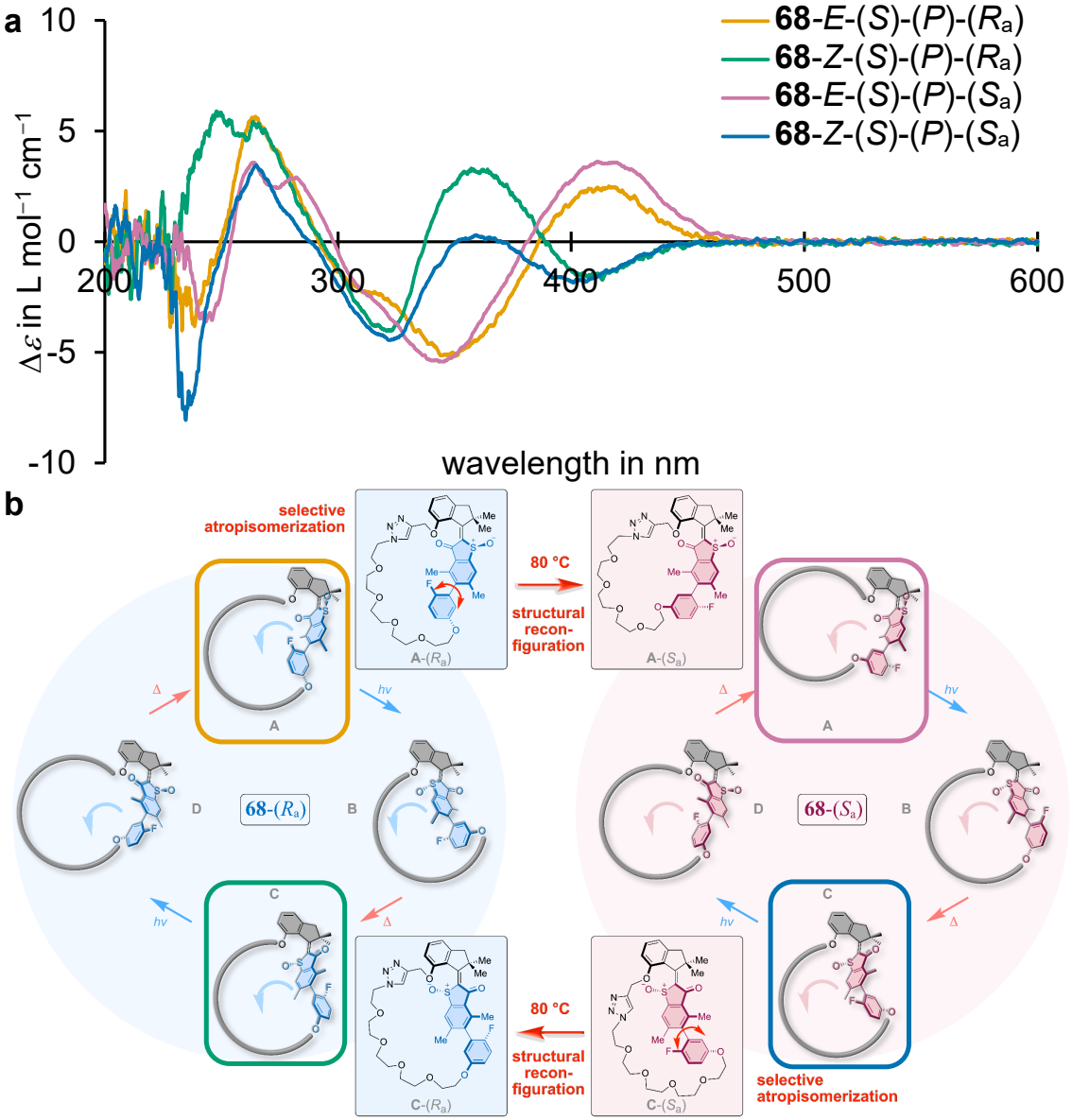

Figure 214 Experimentally acquired ECD spectra (CH_2Cl_2, 22 °C) of enantiomerically pure samples of all four stable conformational isomers of **68** and the corresponding unidirectional macrocyclic molecular motor cycle. **a** Two motor core double bond configurations exist for each atropisomer, namely **68**-*E*-(*S*)-(*P*)-(R_a) (**A**-(R_a)) (yellow) and **68**-*Z*-(*S*)-(*P*)-(R_a) (**C**-(R_a)) (green) for R_a- and **68**-*E*-(*S*)-(*P*)-(S_a) (**A**-(S_a)) (pink) and **68**-*Z*-(*S*)-(*P*)-(S_a) (**C**-(S_a)) (blue) for S_a-configured atropisomers. All *S*-configured sulfoxide isomers possess *P*-helicity at 22 °C. **b** Visualization of both structural reconfiguration cycles of macrocyclic motors **68**-(R_a) and **68**-(S_a). Adapted with minor format modifications from *J. Am. Chem. Soc.* **2023**, 145, 13081–13088 licensed under CC BY-NC-ND 4.0. Copyright © 2023 The Authors. Published by American Chemical Society.[2]

With ground state ECD spectra at hand, comparison to simulated spectra at the TD-B3LYP-GD3BJ/6-311+G(d,p) IEFPCM (CH_2Cl_2) level of theory could be made as shown in Figure 215.

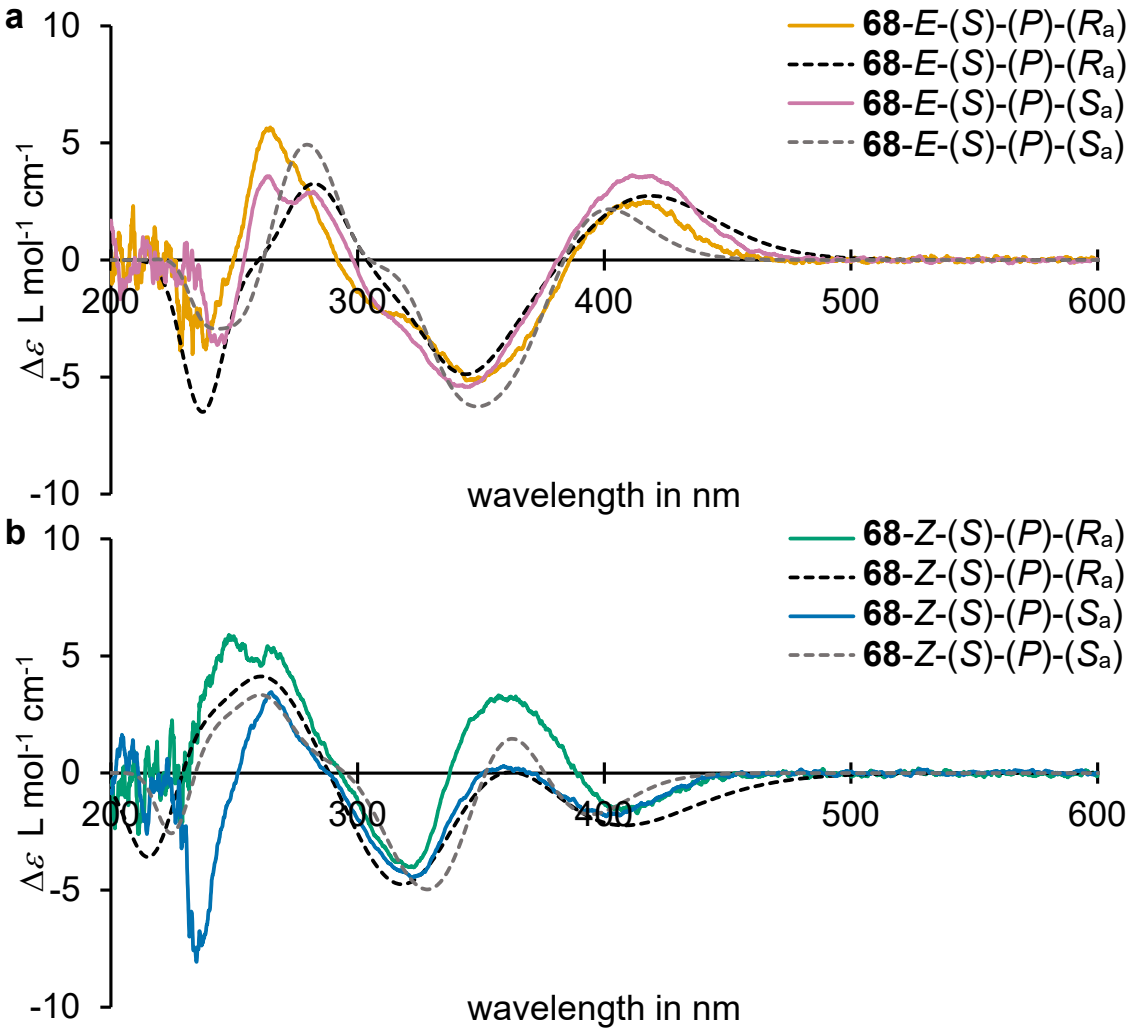

Figure 215 Experimental ECD spectra (colored, CH_2Cl_2, 22 °C) in comparison with simulated (dashed, TD-B3LYP-GD3BJ/6-311+G(d,p) IEFPCM (CH_2Cl_2) level of theory) spectra which are bathochromically shifted by 12 nm. **a** Experimental **68**-*E*-(*S*)-(*P*)-(R_a) spectra displayed in green and simulated in dashed black and **68**-*E*-(*S*)-(*P*)-(S_a) in blue and dashed grey respectively. **b** Experimental **68**-*Z*-(*S*)-(*P*)-(R_a) spectra displayed in green and simulated in dashed black and **68**-*Z*-(*S*)-(*P*)-(S_a) in blue and dashed grey, respectively.

While *E*- and *Z*-isomers were unambiguously identifiable from the comparison of experimental and simulated ECD spectra, the assignment of R_a- or S_a-configured atropisomers was inconclusive. Despite distinct features being present for the experimental and the simulated sets of **A**-R_a/S_a and **C**-R_a/S_a, which

are necessary to predict absolute stereoconfiguration based on theoretical descriptions, the quality of experimental data and the distinctiveness of the simulated spectra was unfortunately insufficient.

Furthermore, another attempt was made simulating the experimental ECD spectra using the motor core fragments only for the generation of the absorption signal at the TD-B3LYP-GD3BJ/6-311+G(d,p) IEFPCM (CH_2Cl_2) level of theory. To this end, the covalent linker was removed, and the attachment points were capped with methoxy groups in the now non-cyclic fragment shown in Figure 216. This was attempted since sampling of the macrocyclic molecular motor **68** for minima with respect to the degrees of freedom present gave a rather inconclusive picture. The sampled structures resulted in configurations with rather similar core structures of the rigid structure elements around the stereocenters and many different configurations of the surrounding PEG linker chain in space. Energies obtained from these minima structures varied greatly and only a few structures ended up as the main contributors to the resulting simulated ECD signal at 22 °C. The insufficient overlap between simulated and experimental data were therefore suspected to originate from the poor sampling of macrocyclic structures, for a more detailed description of the analysis see chapter 7.11. It turned out that the poor sampling of the covalent linker was presumably not the reason for the inconclusive assignment since the match between the fragments without the linker **80** and the experimental data did also not give a convincing prediction of the atropisomer configuration shown in Figure 217.

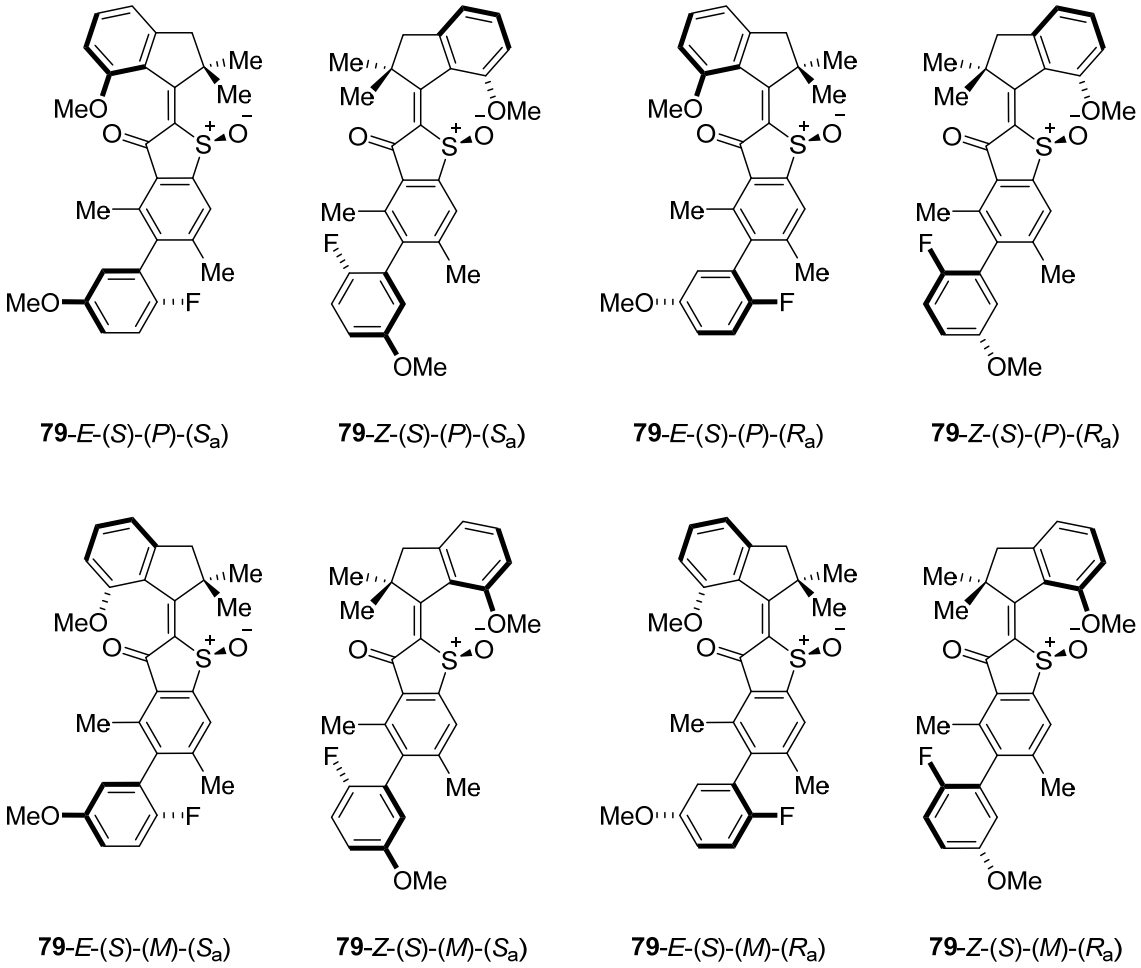

Figure 216 Overview of molecular motor core fragments **80**, representing all conformations involved in the dual motor macrocycle motion of **68** shown in Figure 211.

However, predicted energies of these fragments by theory did allow to draw a much more convincing picture of the energetical distribution of states representing the experimentally obtained values much more accurately as discussed in chapter 7.12.

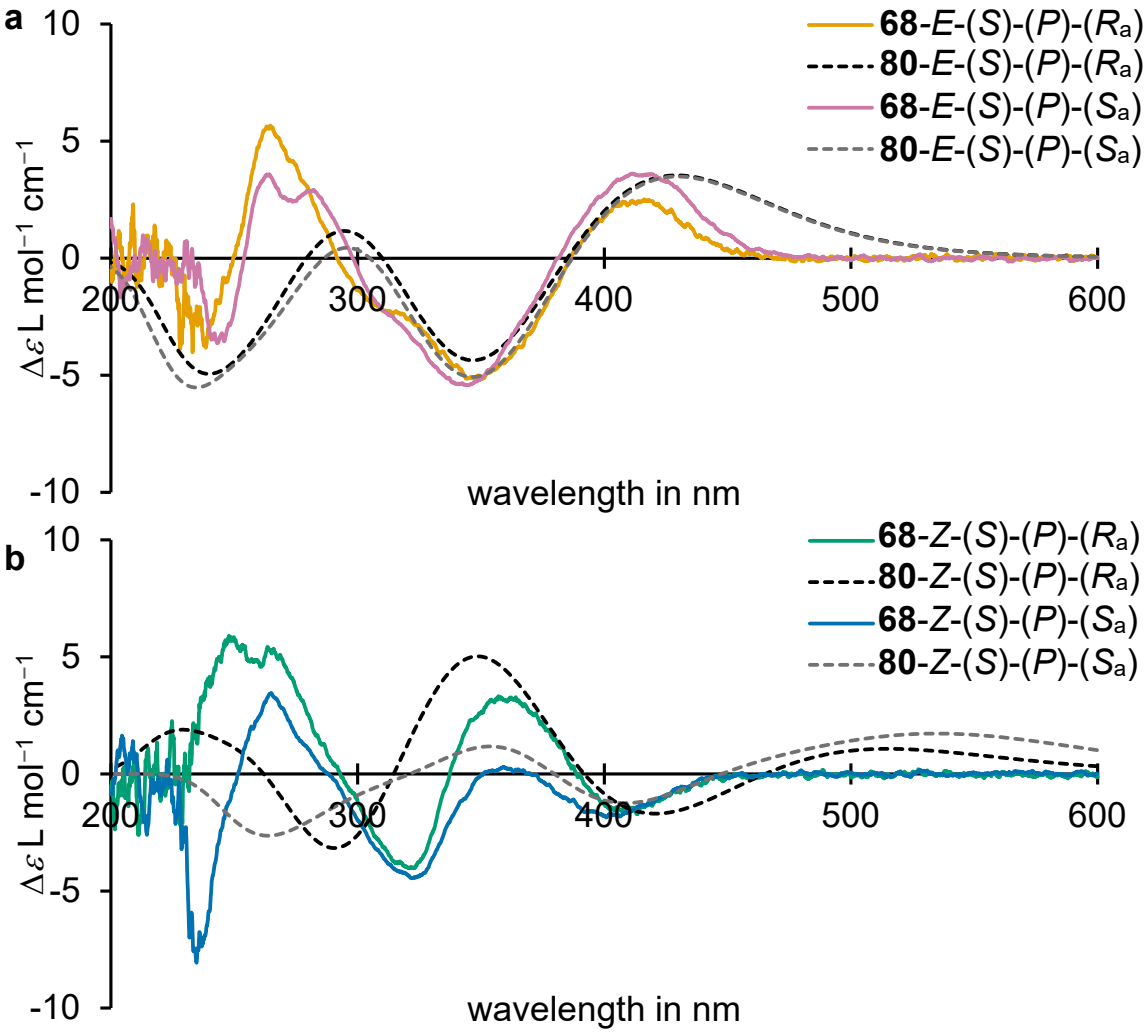

Figure 217 Experimental ECD spectra (colored, CH_2Cl_2, 22 °C) in comparison with simulated (dashed, TD-B3LYP-GD3BJ/6-311+G(d,p) IEFPCM (CH_2Cl_2) level of theory) spectra of motor core fragment **80**. **a** Experimental **68**-*E*-(*S*)-(*P*)-(R_a) spectra displayed in green and corresponding simulated fragment **80** in dashed black as well as **68**-*E*-(*S*)-(*P*)-(S_a) in blue and corresponding simulated fragment **80** in dashed grey. **b** Experimental **68**-*Z*-(*S*)-(*P*)-(R_a) spectra displayed in green and corresponding simulated fragment **80** in dashed black as well as **68**-*Z*-(*S*)-(*P*)-(S_a) in blue and corresponding simulated fragment **80** in dashed grey.

A comparison of simulated and experimentally obtained ECD spectra was also attempted using the SpecDis[296,297] software to prevent any bias from comparing with the naked eye. However, the mathematically derived similarity factors for deviations between individual spectra did also result in inconclusive assignments of theory and experiment. Thus, comparison of experimental and simulated ECD data at 22 °C did only allow to confirm already assigned *E*- and *Z*-configuration of the central motor double bond. However, a convincing atropisomer assignment could also be made via the comprehensive NMR analysis described in chapter 7.4.2, when taking into account biaryl tilts and NOE effects.

7.9.2. ECD spectra assignment at −90 °C

With the atropisomer assignment *via* comparison of ECD spectra at 22 °C being inconclusive another potential prediction could be made from the same approach attempting to match the elusive **68**-*E*-(*S*)-(*M*)-(R_a) or **68**-*E*-(*S*)-(*M*)-(S_a) states observed at −90 °C from low temperature NMR experiments (see chapter 7.6.1) with predictions by theory.

For measuring low temperature ECD spectra, enantiomerically pure samples of **68**-*Z*-(*S*)-(*P*)-(R_a) and **68**-*Z*-(*S*)-(*P*)-(S_a) were subjected to *in situ* irradiation at −90 °C using a 490 nm LED with ECD spectra being recorded before, during and after irradiation and annealing as shown in Figure 218 and 219. Spectra of pure **68**-*E*-(*S*)-(*M*)-(R_a) and **68**-*E*-(*S*)-(*M*)-(S_a) can be obtained by simple subtraction of remaining **68**-*Z*-(*S*)-(*P*)-(R_a) or **68**-*Z*-(*S*)-(*P*)-(S_a) respectively, from the accumulated **68**-*Z*-(*S*)-(*P*) and **68**-*E*-(*S*)-(*M*) mixture spectra recorded after irradiation of pure *Z*-samples at −90 °C. To know the fraction of **68**-*E*-(*S*)-(*M*) being present in the mixture at −90 °C, annealing of the mixture to 22 °C lead to exclusively conversion of the **68**-*E*-(*S*)-(*M*)-(R_a) or **68**-*E*-(*S*)-(*M*)-(S_a) fraction to **68**-*E*-(*S*)-(*P*)-(R_a) or **68**-*E*-(*S*)-(*P*)-(S_a) respectively for a more detailed description see chapter 7.6.1.1 and 7.6.1.2. The resulting spectra of the elusive states and an illustrative explanation can be found in Figure 218, 219 and in the corresponding caption.

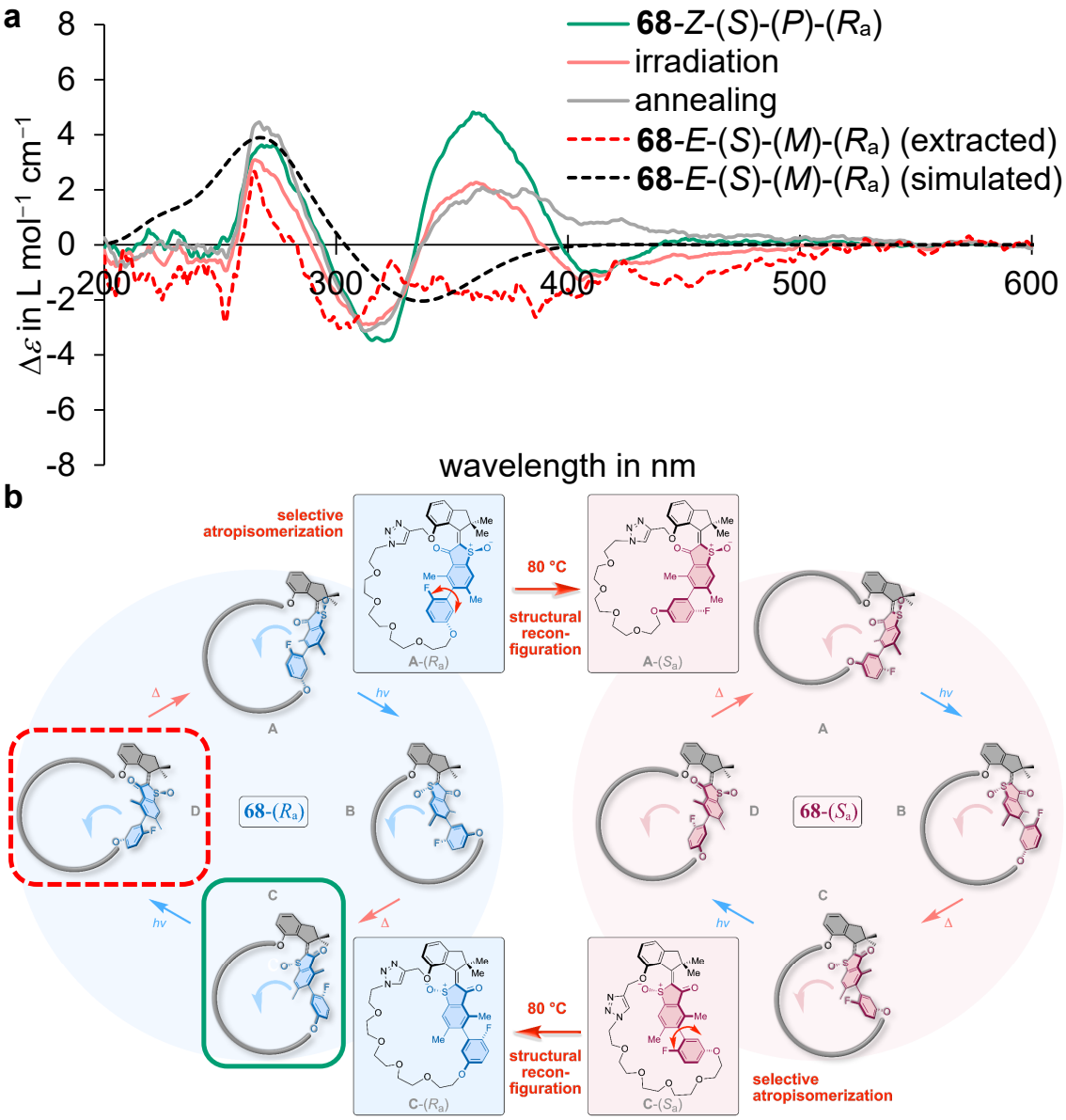

Figure 218 Experimental low temperature ECD spectra (colored, CH_2Cl_2, −90 °C) compared with simulated **68**-*E*-(*S*)-(*M*)-(R_a) spectrum (dashed black, TD-B3LYP-GD3BJ/6-311+G(d,p) IEFPCM (CH_2Cl_2) level of theory) and full motor cycle shown as reference. **a** ECD spectra of pure **68**-*Z*-(*S*)-(*P*)-(R_a) before (green), after accumulating 39% **68**-*E*-(*S*)-(*M*)-(R_a) (red) by *in situ* irradiation with 490 nm and after annealing to 22 °C (grey). Pure **68**-*E*-(*S*)-(*M*)-(R_a) spectrum (dashed red) was obtained *via* subtracting the remaining amount of 61% **68**-*Z*-(*S*)-(*P*)-(R_a) from the red spectrum after irradiation. The simulated (TD-B3LYP-GD3BJ/6-311+G(d,p) IEFPCM (CH_2Cl_2) level of theory) ECD spectrum of **68**-*E*-(*S*)-(*M*)-(R_a) (dashed black) is shown for comparison. **b** Visualization of both structural reconfiguration cycles of macrocyclic motors **68**-(R_a) and **68**-(S_a). Adapted with minor format modifications from *J. Am. Chem. Soc.* **2023**, 145, 13081–13088 licensed under CC BY-NC-ND 4.0. Copyright © 2023 The Authors. Published by American Chemical Society.[2]

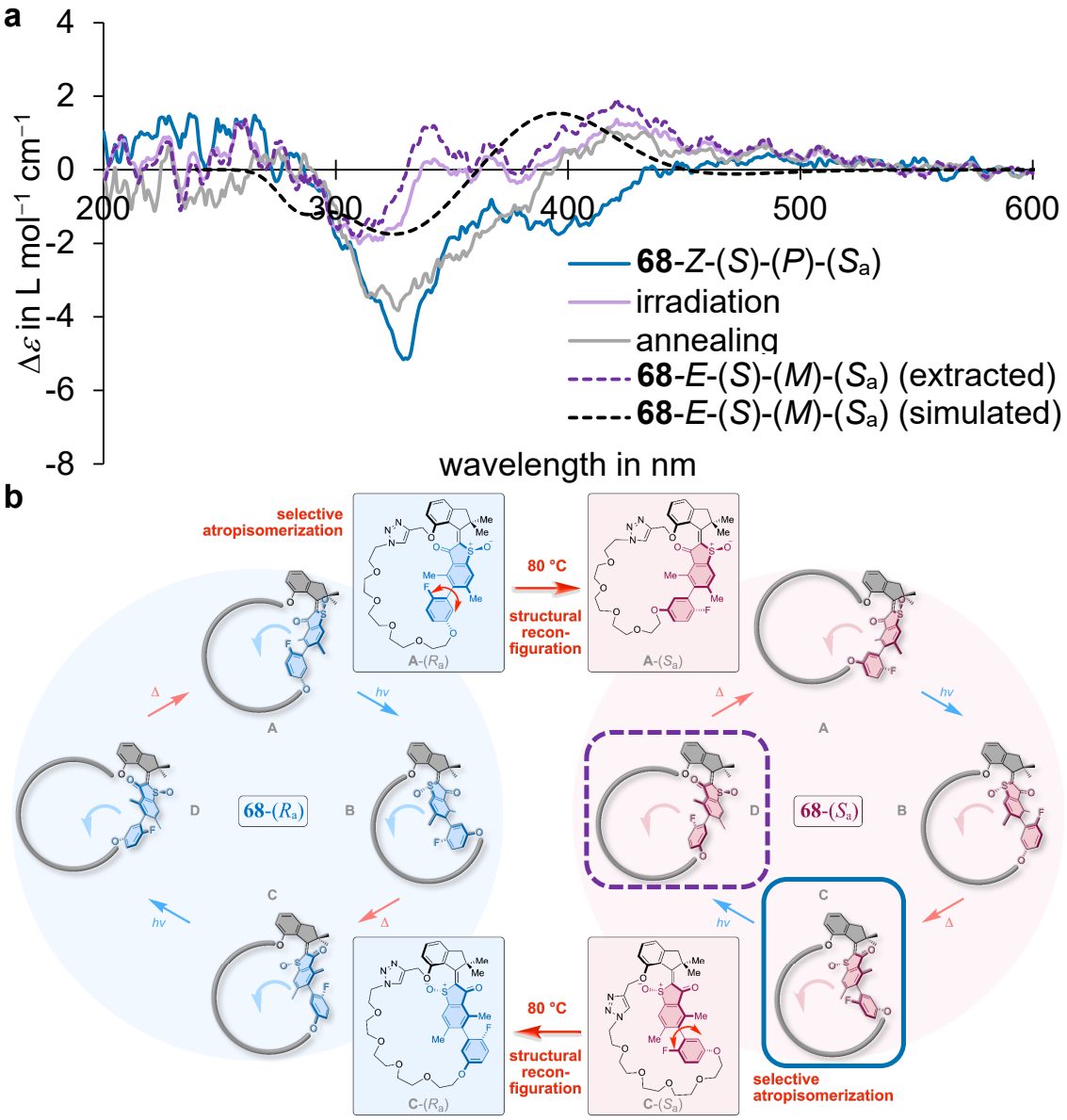

Figure 219 Experimental low temperature ECD spectra (colored, CH_2Cl_2, −90 °C) compared with simulated **68**-*E*-(*S*)-(*M*)-(S_a) spectrum (dashed black, TD-B3LYP-GD3BJ/6-311+G(d,p) IEFPCM (CH_2Cl_2) level of theory) and full motor cycle shown as reference. **a** ECD spectra of pure **68**-*Z*-(*S*)-(*P*)-(S_a) before (blue), after accumulating 89% **68**-*E*-(*S*)-(*M*)-(S_a) (violet) by *in situ* irradiation with 490 nm and after annealing to 22 °C (grey). Pure **68**-*E*-(*S*)-(*M*)-(S_a) spectrum (dashed purple) was obtained *via* subtracting the remaining amount of 11% **68**-*Z*-*S*)-(*P*)-(S_a) from the violet spectrum after irradiation. The simulated (TD-B3LYP-GD3BJ/6-311+G(d,p) IEFPCM (CH_2Cl_2) level of theory) ECD spectrum of **68**-*E*-(*S*)-(*M*)-(S_a) (dashed black) is shown for comparison. **b** Visualization of both structural reconfiguration cycles of macrocyclic motors **68**-(R_a) and **68**-(S_a). Adapted with minor format modifications from *J. Am. Chem. Soc.* **2023**, 145, 13081–13088 licensed under CC BY-NC-ND 4.0. Copyright © 2023 The Authors. Published by American Chemical Society.[2]

Comparison of experimental with simulated **68**-*E*-(*S*)-(*M*)-(R_a) and **68**-*E*-(*S*)-(*M*)-(S_a) spectra did indeed allow to assign absolute stereoconfiguration of atropisomers to the metastable states allowing to separate R_a- from S_a-rotation cycles. The two spectra of isomers possessing *M*-helicity shown in dashed red and purple respectively in Figure 218a and 219a do match the predictions by theory shown in dashed black and do not match with the opposite diastereomeres which have opposite phases below 250 and above 300 nm. Therefore, association of atropisomers made previously from *i.e.* rational prediction of strain being present from biaryl tilts as discussed in chapter 7.4.2 were validated with these experiments.

7.10. Executing R_a and S_a atropisomers enriched cycles in a one pot mixture

With all stereodescriptors assigned for all observable configurations between −90–100 °C an operation of both unidirectional motor cycles and their respective interconversion can be performed in consecutive reactions during one single experiment shown in Figure 220. This shows that each state can be passed through being a majority in the mixture, consecutively leading to a final composition containing the starting isomer as the main fraction again.

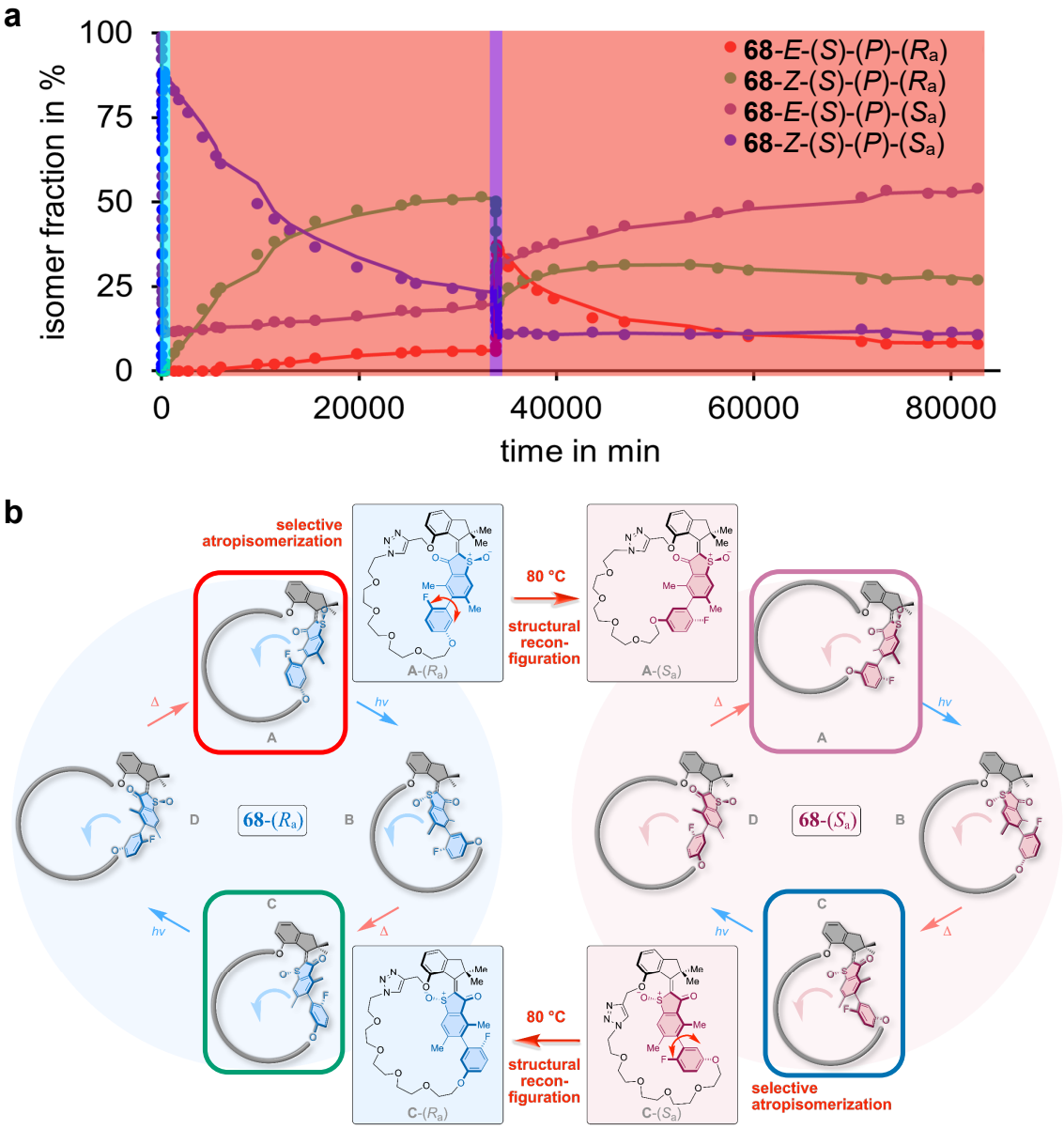

Figure 220 Cycling experiment depicting execution of both motor cycles of **68**-(R_a) and **68**-(S_a) in a one pot experiment. **a** Starting from a pure **68**-*E*-(*S*)-(*P*)-(S_a) solution in toluene-d_8, the turquoise colored range depicts **68**-*Z*-(*S*)-(*P*)-(S_a) enrichment to 89% *via* 490 nm irradiation followed by red the colored range depicting **68**-*Z*-(*S*)-(*P*)-(R_a) accumulation to 52% through structural reconfiguration. The purple-colored range depicts **68**-*E*-(*S*)-(*P*)-(R_a) enrichment to 37% *via* 405 nm irradiation followed by the red colored range depicting structural reconfiguration to **68**-*E*-(*S*)-(*P*)-(S_a) in 54%. The whole data series was measured in toluene-d_8 during one experiment. **b** Visualization of both structural reconfiguration cycles of macrocyclic motors **68**-(R_a) and **68**-(S_a). Adapted with minor format modifications from *J. Am. Chem. Soc.* **2023**, 145, 13081–13088 licensed under CC BY-NC-ND 4.0. Copyright © 2023 The Authors. Published by American Chemical Society.[2]

Starting with irradiation of thermodynamically most stable **68**-*E*-(*S*)-(*P*)-(S_a) = **A**-(S_a) in toluene-d_8 using 490 nm light leads to a mixture enriched in 89% **68**-*Z*-(*S*)-(*P*)-(S_a) = **C**-(S_a) which can in turn be

converted from an S_a enriched solution to a R_a-enriched one *via* structural reconfiguration at 60 °C to a mixture consisting of 52% **68**-*Z*-(*S*)-(*P*)-(R_a) = **C**-(R_a) as the main component. After enrichment of the R_a-atropisomer the unidirectional motor cycle can be operated again enriching 37% **68**-*E*-(*S*)-(*P*)-(R_a) = **A**-(R_a) as the dominant isomer in solution using 405 nm light. From this point the atropisomer configuration can be flipped again *via* structural reconfiguration at 60 °C enriching the solution in starting isomer configuration **68**-*E*-(*S*)-(*P*)-(S_a) = **A**-(S_a) which can finally be accumulated in 54%.

7.11. Theoretical description

All theoretical DFT descriptions of macrocycle **68** and **80** were obtained through *ab initio* simulations carried out using Gaussian16 Revision B.01 or C.01 software.[298] Molecular dynamic simulations were performed to account for the many degrees of freedom in **68**. Sets of up to 100 local minima were generated using the MacroModel[299] software suite from Maestro[300] using a MMFFs force field (based on OPLS3e[301]), followed by an optimization at the B3LYP-GD3BJ/6-311G(d,p) IEFPCM (CH_2Cl_2) level of theory at 25 °C using Gaussian. Only geometries with no imaginary frequencies for minima or only one for transition states found in frequency calculations at 25 °C were considered any further, otherwise optimization was continued.

7.11.1. Theoretical prediction of energies

Ground state energies were obtained at the B3LYP-GD3BJ/6-311G(d,p) IEFPCM (CH_2Cl_2) level of theory following the above-mentioned procedure for all isomers stable at 22 °C shown in Figure 182, namely **68**-*E*-(*S*)-(*P*)-(R_a), **68**-*Z*-(*S*)-(*P*)-(R_a), **68**-*E*-(*S*)-(*P*)-(S_a), and **68**-*Z*-(*S*)-(*P*)-(S_a). Furthermore, energies for isomers **68**-*E*-(*S*)-(*M*)-(R_a) and **68**-*E*-(*S*)-(*M*)-(S_a) were also predicted by theory for assignment of ECD spectra at −90 °C, see chapter 7.9.2.

Since sampling of isomers using molecular dynamics on the force field level led to inaccurate energetic descriptions of states compared to experimentally obtained values after optimization on DFT level, an approach using only a fragment shown in Figure 221 of the macrocyclic structure was utilized giving significantly more accurate results. The limitation of the above-mentioned approach can be clearly seen by comparing energies predicted by theory of both methods with experimental values. The shortcoming when simulating energies for the whole macrocyclic structure is a result of the increased degrees of freedom observed in structure **68** – compared to previous reports – which are not accounted for accurately using MMFFs force field molecular dynamics. However, the theoretical descriptions did deliver the correct relative minimum energy order for the *E*- and *Z*-isomers and the intrinsic switching of atropisomer stabilities in the different double bond configurations for the macrocycle **68**.

7.11.1.1. Macrocyclic HTI Motor 68

Energies for macrocyclic molecular motor are summarized in Table 33 from lowest to highest energy, tabulated from top to bottom. These energies reproduce experimentally obtained values in the energetic order only.

Table 33 Theoretical obtained lowest energies of macrocyclic molecular motor **68** found from sampling of structures using force field molecular dynamics, followed by DFT calculations at the B3LYP-GD3BJ/6-311G(d,p) IEFPCM (CH_2Cl_2) level of theory. Notice the switch in relative stability for R_a- and S_a-isomers when changing from *E*- to *Z*-double bond configuration.

isomer	G_0 in Hartree	ΔG in Hartree	ΔG in kcal mol^{-1}
68-*E*-(*S*)-(*P*)-(S_a)	-2814.885841	0.0	0.0
68-*Z*-(*S*)-(*P*)-(R_a)	-2814.877436	0.008405	5.3
68-*Z*-(*S*)-(*P*)-(S_a)	-2814.874628	0.011213	7.0
68-*E*-(*S*)-(*M*)-(S_a)	-2814.874405	0.011436	7.2
68-*E*-(*S*)-(*M*)-(R_a)	-2814.874398	0.011443	7.2
68-*E*-(*S*)-(*P*)-(R_a)	-2814.874050	0.011791	7.4

It is noticeable, that despite **68**-*E*-(*S*)-(*M*)-(S_a) having the attachment points of the covalent linker on opposite sides of the benzothiophenone plane as opposed to **68**-*E*-(*S*)-(*M*)-(R_a), both have almost similar energies. From this observation it can be concluded that the length of the tether is long enough to be partly wind around the motor core, leading to a noticeable tilt of the biaryl axis (see chapter 7.4.2) but without imposing any noticeable strain upon the system. This is also observed experimentally from the **68**-*E*-(*S*)-(*M*) → **68**-*E*-(*S*)-(*P*) barrier measurements, which are also almost identical for both atropisomers (see chapter 7.6.1).

7.11.1.2. Reference fragment 80

With the simulated energy profile of macrocyclic molecular motor **68** showing noticeable deviations from experimentally obtained values, another approach was attempted modelling only the motor core without the covalent linker. To this end, the anchoring points of the tether were capped with methoxy groups as shown in Figure 221 leading to eight possible conformations representing all species involved in the dual motor macrocycle motion shown in Figure 182 for one sulfoxide configuration. For reference fragment **80** it was also now possible to simulate transition state energies for THI steps as well as for thermal atropisomerizations and compare these values to experimental counterparts.

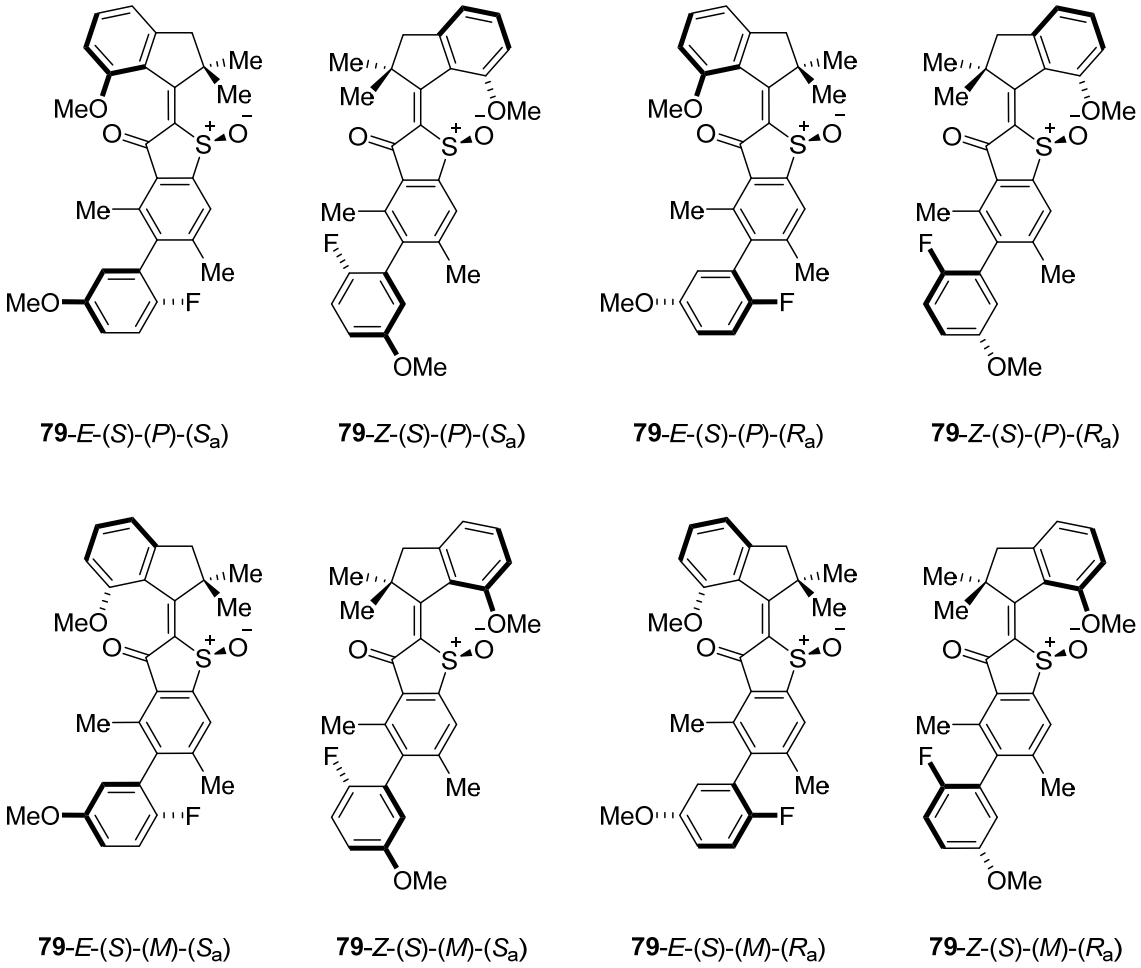

Figure 221 Overview of all eight *S*-configured conformations of molecular motor fragment **80**, representing all conformations involved in the dual motor macrocycle motion of **68** shown in Figure 211.

Minima structures for each isomer depicted in Figure 221 were obtained at the B3LYP/6-311G(d,p) IEFPCM (CH_2Cl_2) level of theory with all the obtained energies including THI transition state energies shown in Table 34.

Table 34 Theoretical obtained minima energies considering stable and metastable conformations as well as THI transition state energies of molecular motor fragment **80**, simulated at the B3LYP/6-311G(d,p) IEFPCM (CH_2Cl_2) level of theory.

isomer	G_0 in Hartree	ΔG in Hartree	ΔG in kcal mol^{-1}
80-*E*-(*S*)-(*P*)-(S_a)	−1920.352834	0.000866	0.5
80-*E*-(*S*)-(*M*)-(S_a)	−1920.349467	0.004233	2.7
TS-**80**-*E*-(*S*)-(*M*/*P*)-(S_a)	−1920.327745	0.021722	13.6
80-*Z*-(*S*)-(*P*)-(S_a)	−1920.353700	0	0.0
80-*Z*-(*S*)-(*M*)-(S_a)	−1920.349104	0.004596	2.9
TS-**80**-*Z*-(*S*)-(*M*/*P*)-(S_a)	−1920.339483	0.009621	6.0
80-*E*-(*S*)-(*P*)-(R_a)	−1920.352289	0.001431	0.9
80-*E*-(*S*)-(*M*)-(R_a)	−1920.349279	0.003010	1.9
TS-**80**-*E*-(*S*)-(*M*/*P*)-(R_a)	−1920.327126	0.022153	13.9
80-*Z*-(*S*)-(*P*)-(R_a)	−1920.353720	0	0.0
80-*Z*-(*S*)-(*M*)-(R_a)	−1920.347926	0.005794	3.6
TS-**80**-*Z*-(*S*)-(*M*/*P*)-(R_a)	−1920.338958	0.008968	5.6

Furthermore, biaryl rotation barriers were also simulated for all clockwise (cw) and counterclockwise (ccw) directions leading to eight additional thermal barriers given in Table 35.

Table 35 Theoretical obtained transition state energies for clockwise (cw) and counter clockwise (ccw) biaryl atropisomerizations of molecular motor fragment **80**, simulated at the B3LYP/6-311G(d,p) IEFPCM (CH_2Cl_2) level of theory.

isomer		G_0 in Hartree	ΔG in Hartree	ΔG in kcal mol^{-1}
TS-**80**-*E*-(*S*)-(*P*)-(S_a/R_a)	CW	−1920.303092	0.049197	30.9
	CCW	−1920.301803	0.050486	31.7
TS-**80**-*Z*-(*S*)-(*P*)-(S_a/R_a)	CW	−1920.304780	0.048940	30.7
	CCW	−1920.304010	0.049710	31.2
TS-**80**-*E*-(*S*)-(*P*)-(R_a/S_a)	CW	−1920.302152	0.050682	31.8
	CCW	−1920.301668	0.051166	32.1
TS-**80**-*Z*-(*S*)-(*P*)-(R_a/S_a)	CW	−1920.303348	0.050372	31.6
	CCW	−1920.303913	0.049807	31.3

With all meaningful energies at hand, a quantitative energy scheme predicted by theory for molecular motor fragment **80** can be drawn, shown in Figure 222. This does represent the expected directionality for such HTI-based molecular motors[154,156–159] with distinct properties such as the **80**-*Z*-(*S*)-(*M*) → **80**-*Z*-(*S*)-(*P*) barrier being lower than the respective **80**-*E*-(*S*)-(*M*) → **80**-*E*-(*S*)-(*P*) barrier. Furthermore,

elusive metastable energies of *M*-helicities are higher than their corresponding *P*-helicity counterparts and most stable ground state isomers possess *Z*-configuration of the double bond.

7.12. Theoretical prediction of directionality

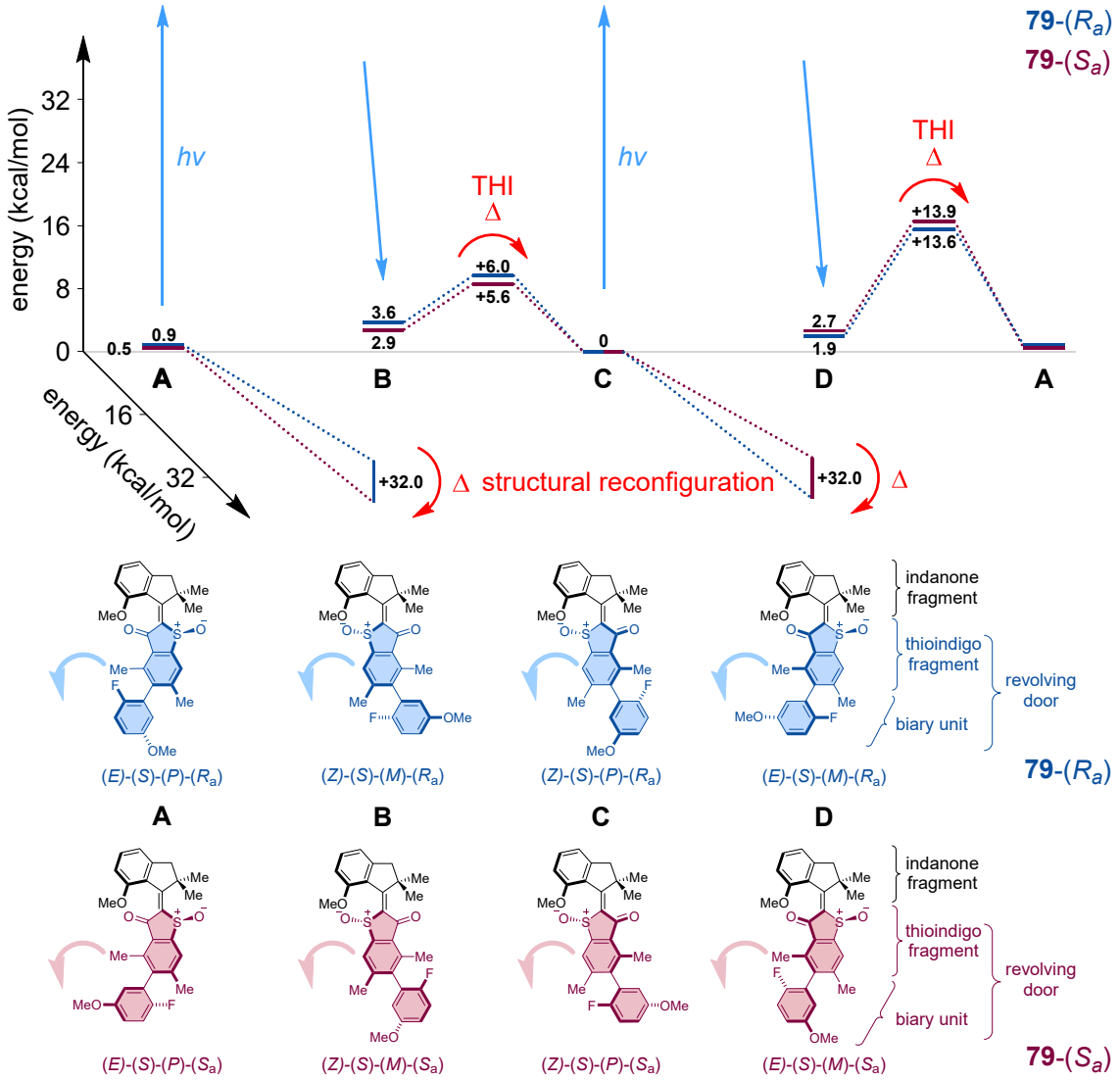

Figure 222 Simulated potential energy profile of HTI-based macrocyclic molecular motor fragments **80**-(R_a) and **80**-(S_a) resembling the experimentally acquired values from the energetic landscape of macrocyclic motors **68**-(R_a) and **68**-(S_a) respectively. The energies were determined at the B3LYP/6-311G(d,p) IEFPCM (CH_2Cl_2) level of theory. Ground state energies, DBI and THI are depicted on the vertical axis and atropisomer rotation barriers namely structural reconfiguration on the diagonal axis. For simplicity only structures with *S*-configured sulfoxide are shown. Adapted with minor format modifications from *J. Am. Chem. Soc.* **2023**, 145, 13081–13088 licensed under CC BY-NC-ND 4.0. Copyright © 2023 The Authors. Published by American Chemical Society.[2]

The two complete quantitative experimentally obtained and simulated energy schemes shown in Figure 210 and 222 respectively can be compared to each other as done in Figure 223.

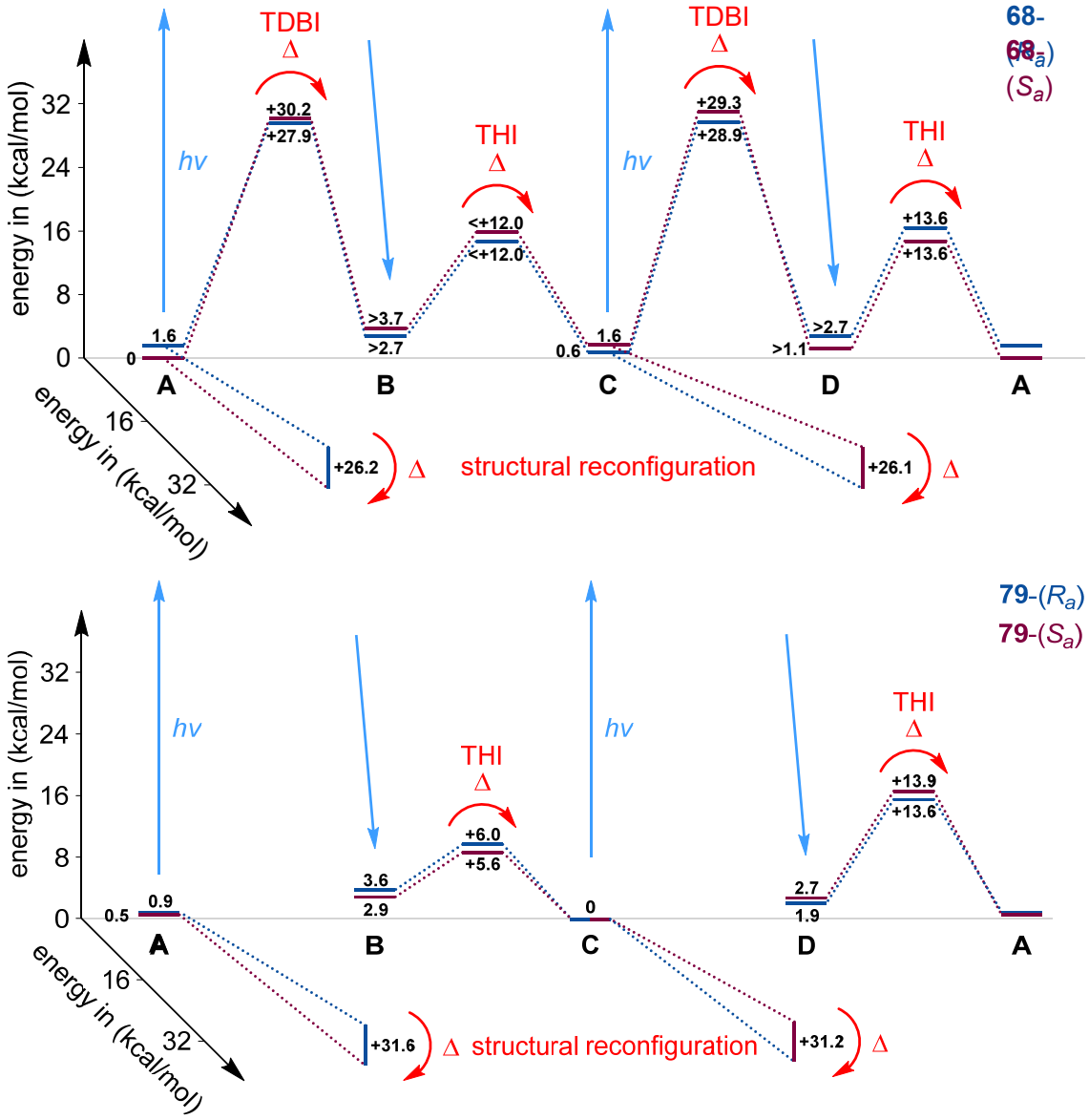

Figure 223 Quantitative comparison of experimentally determined values of macrocyclic molecular motor **68** (top) and simulated values for reference fragment **80** (bottom). Ground state energies, DBI and THI are depicted on the vertical axis and atropisomer rotation barriers namely structural reconfiguration on the diagonal axis. Ground state energies, THI and atropisomer rotation barriers can be quantitatively compared. Very good agreement of values can be found for *E*-(*S*)-(*M*) → *E*-(*S*)-(*P*) barriers with ± 0.3 kcal mol^{-1} and for *Z*-(*S*)-(*M*) → *Z*-(*S*)-(*P*) barriers assuming they are in the same region as other *Z*-(*S*)-(*M*) barriers measured for HTI-based motors. Ground state energies of stable and metastable isomers do also show reasonable agreement between theory and experiment. Only the relative energetic order of minima **A** and **C** and structural reconfiguration steps do show some deviations which are however still within the error margin of DFT calculations. Adapted with minor format modifications from *J. Am. Chem. Soc.* **2023**, 145, 13081–13088 licensed under CC BY-NC-ND 4.0. Copyright © 2023 The Authors. Published by American Chemical Society.[2]

Accurate accordance between theory and experiment were found for **68**-*E*-(*S*)-(*M*) → **68**-*E*-(*S*)-(*P*) THI barriers with a maximum of ± 0.3 kcal mol^{-1} deviation. A similar close match can be found for the **68**-*Z*-(*S*)-(*M*) → **68**-*Z*-(*S*)-(*P*) barrier under the assumption that macrocyclic molecular motor **68** behaves similar to other HTI-based motors[154,156–159] which is indicated by the measured upper bound of approximately <+12.0 kcal mol^{-1}. Ground state energies are also reflected well except for the order of **A** and **C** stabilities and the stability flip between R_a and S_a for **A** and **C**, which might be attributed to the macrocyclization and is therefore not reflected in the non-cyclic fragment **80**. Usually, the **A** configuration is thermodynamically more stable than the **C** isomer and this trend can be reversed in the corresponding macrocycle[158,159] which does therefore not contradict what is observed here.

However, for the metastable isomers **B** and **D** the stability flip between R_a and S_a is accounted for in the theoretical description, but with opposing stability predicted for **80** in comparison to **68**. The order of activation energy barriers was established well from simulations at the B3LYP-GD3BJ/6-311G(d,p) IEFPCM (CH_2Cl_2) level of theory merely the atropisomerization barriers namely the structural reconfiguration steps show some deviation from experimental values. The calculated atropisomerization barriers in **80** are significantly higher than the experimentally found values in **68**. However, the absolute deviations within a maximum of ± 5.4 kcal mol^{-1} for this process are still within reasonable boundaries of energetic predictions from DFT calculations. It is noteworthy that experimentally obtained values rely on a simulation with potential measurement errors as a source for observed deviations as well.

7.13. Conclusion

Taken together, a macrocyclic molecular motor system is presented, which consists of an enlarged revolving door section with an integrated switchable biaryl axis, stable during motor operation at ambient temperatures and below. Through precise adjustment of the biaryl axis barrier *via* steric overcrowding and integration into the revolving door, two independent atropisomer configurations can be obtained, which are each part of one distinctly different unidirectional cycle. Enlargement of the covalent linker chain enables movement of the biaryl-containing enlarged revolving door independently from its macrocyclic connecting tether. This defines the point of rotation during motor operation to be outside of the biaryl fragment. In other words, two different enlarged revolving doors can be established, differeing in the axial chirality of their inherent biaryl axis. Both rotate in the same direction during motor operation but their rotation steps are different with respect to the overall macrocycle structure. The two rotation cycles can be interconverted by highly selective thermal atropisomerizations, at defined states within their individual rotation cycles. In this way, an orthogonal stimulus (i.e. brief heating to 80 °C) introduces another level of control for the unidirectional rotating revolving door which abrogates the conjunct motion, leading to a sole single bond rotation along the biaryl axis, flipping its configuration. During this structural reconfiguration step, the point of rotation lies inside the revolving door, more specifically in the middle of the biaryl axis. Afterwards, the resulting reconfigured macrocycle can operate again as an unidirectional motor, rotating the enlarged revolving door at ambient temperatures and below. The motor rotation mechanism was only affected slightly from this design with respect to operational speed or wavelength dependency, demonstrating two entirely functional unidirectional molecular motor cycles within one macrocyclic machine shown in Figure 224.

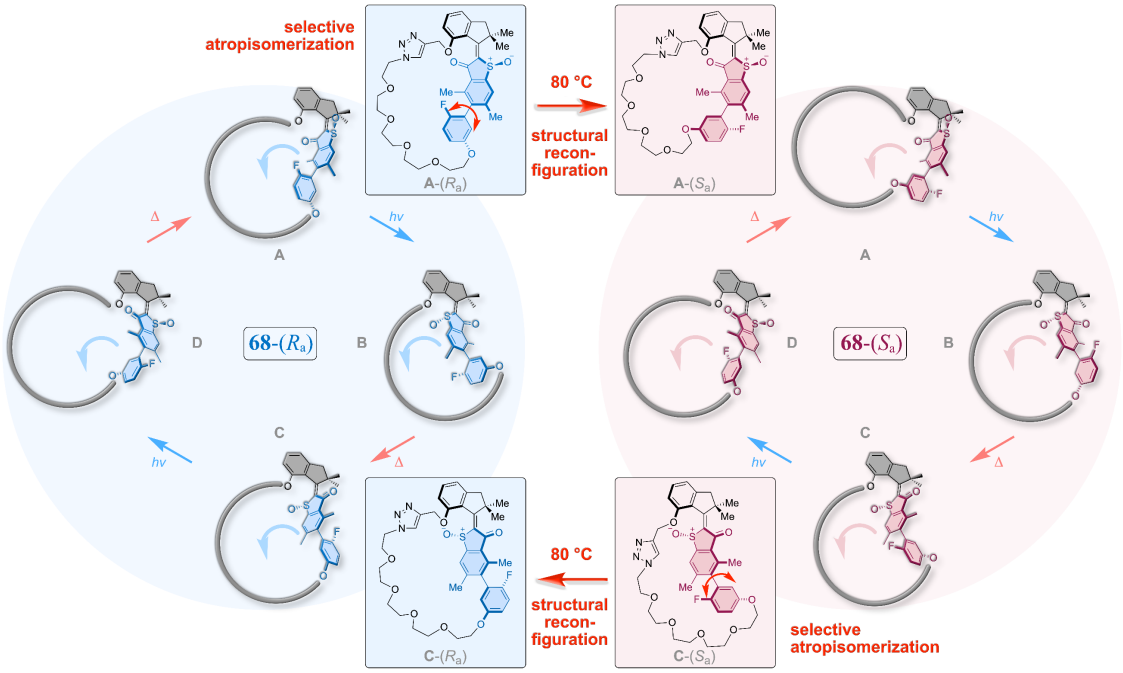

Figure 224 Structural reconfiguration combines macrocyclic molecular motor cycle of **68**-(R_a) with **68**-(S_a). Independent rotation of enlarged revolving doors (blue and red highlighted structures) with identical directionality is achieved in **68**-(R_a) (blue) and **68**-(S_a) (red) within the same macrocyclic framework under illumination with visible light at ambient temperatures. The macrocyclic environment of the embedded molecular motor can be switched from **A**-(R_a) to **A**-(S_a) and from **C**-(S_a) to **C**-(R_a) at elevated temperatures *via* selective atropisomerization, namely structural reconfiguration. Adapted with minor format modifications from *J. Am. Chem. Soc.* **2023**, 145, 13081–13088 licensed under CC BY-NC-ND 4.0. Copyright © 2023 The Authors. Published by American Chemical Society.[2]

To sum this up, separation of biaryl rotation from motor rotation in this system enables two unidirectional independent motor cycles at temperatures below occurrence of thermal atropisomerization. This is achieved at 22 °C by raising the barrier for biaryl rotation in combination with ring size expansion thus tolerating rotation for a significantly enlarged revolving door despite halted atropisomerization. Increased steric bulk led to revolving door enlargement and additionally allowed for structural reconfiguration at elevated temperatures, giving raise to two independent unidirectional motor rotation cycles within one molecular machine. In conclusion, HTI-based macrocyclic molecular motor systems have been expanded upon an additional orthogonal stimulus, enabling structural reprogramming of two unidirectional motor cycles within one molecular machine shown in Figure 224, introducing another level of control attractive for future multi-level operational nanomachinery. This paves the way for even more elaborated concepts of transferring unidirectional motor rotation onto remote entities.

8. Experimental section

8.1. Materials and methods

Reagents and solvents were obtained from *abcr*, *Acros Organics*, *Fluka*, *Merck*, *Sigma-Aldrich* or *TCI* in the qualities *puriss*., *p.a*., or *purum* and used as received. Technical solvents were distilled prior to use for column chromatography and extraction on a rotary evaporator (*Heidolph Laborota* 4000, 4001 and *Vacuubrand CVC 3000*). Reactions were monitored on *Merck* Silica 60 F-254 or *Macherey-Nagel* ALUGRAM® Sil G/UV254 thin layer chromatography (TLC) plates and detection was done by irradiation with UV light (254 nm or 366 nm) to determine retardation factors (R_f).

Flash column chromatography was performed on silica gel (*Merck*, particle size 0.040–0.200 mm, *ACROS*, 0.035–0.070 mm or *Machery-Nagel*, particle size 0.040–0.063 mm) using distilled technical solvents. Automated medium pressure liquid chromatography (MPLC) was performed on *Biotage Isolera One* or *Biotage Selekt* machines using pre-packed silica columns from *Biotage* or *Macherey-Nagel*.

High performance liquid chromatography (HPLC) was performed on a *Shimadzu* HPLC system consisting of a LC-20AP solvent delivery module, a CTO-20A column oven, a SPD-M20A photodiode array UV/Vis detector, and a CBM-20A system controller using a semi preparative CHIRALPAK® IC column (particle size 5 µm) from *Daicel* and HPLC grade solvents (Ethyl acetate, *n*-hexane, and *i*PrOH) from *Sigma-Aldrich*, *VWR*, *ROTH* and *Honeywell*.

^{1}H NMR and ^{13}C NMR spectra were measured on a *JEOL ECX 400* (400 MHz), *Bruker AVANCE NEO HD 400* (400 MHz),[IX] *Varian VNMRS 400* (400 MHz), *Varian VNMRS 600* (600 MHz),[X] or *Bruker AVANCE III HD 800* (800 MHz)[XI] NMR spectrometer at 298 K unless the temperature is indicated otherwise. Deuterated solvents were obtained from *Cambridge Isotope Laboratories*, *Deutero GmbH*, or *Eurisotop* and used without further purification. Chemical shifts (δ) are given relative to tetramethylsilane as an external standard. Residual solvent signals in the ^{1}H and ^{13}C NMR spectra were used as internal reference. $CDCl_3$: δ_H = 7.260 ppm, δ_C = 77.160 ppm; $(CD_3)_2SO$: δ_H = 2.50 ppm, δ_C = 39.52 ppm; CD_2Cl_2: δ_H = 5.320 ppm, δ_C = 54.000 ppm; toluene-d_8: δ_H = 2.080 ppm. Resonance multiplicity is indicated as s (singlet), d (doublet), t (triplet), q (quartet), m (multiplet), and b (broad). Chemical shifts are given in parts per million (ppm) on the delta scale (δ) and the coupling constant values (J) in hertz (Hz).

Electron impact (EI) and atmosperic pressure photoionization (APPI) mass spectra were measured on a *Finnigan MAT95Q*[XIII,XIV] or a *Finnigan MAT90*[XIII,XIV] and a *MicrOTOF II*[XII] spectrometer respectively. Signals are reported in m/z units and the molecular ion is designated as M.

UV/Vis absorption spectra were measured on a *Varian Cary 5000* or on an *Agilent Cary 60* spectrophotometer. The spectra were recorded in quartz cuvettes (1 cm). Spectral grade solvents were obtained from *VWR* and *Merck*. Absorption wavelengths (λ) are reported in nm and the molar attenuation coefficients (ε) in L mol^{-1} cm^{-1}.

Fluorescence spectra were measured on a *Horiba Jobin Yvon FluoroMax-4* spectrofluorometer. The spectra were recorded in quartz cuvettes (1 cm). Spectral grade solvents were obtained from *VWR* and *Merck*. Emission and excitation wavelengths (λ) are reported in nm.

Infrared spectra (ATR) were recorded on a *Nicolet iS5, iD7 ATR* spectrometer. Transmittance values are qualitatively described by wavenumber $\tilde{\nu}$ in cm^{-1} as strong (s), medium (m), weak (w).

Photoisomerization experiments were conducted with continuous irradiation of the solutions in NMR tubes in CD_2Cl_2 or $C_2D_2Cl_2$. Irradiations at 22 °C were conducted using LEDs from *Thorlabs GmbH* and *Roithner Lasertechnik GmbH* (365 nm, 385 nm, 405 nm, 420 nm, 435 nm, 450 nm, 470 nm, 490 nm, 505 nm, 515 nm, 530 nm and 565 nm). QY Φ measurements were performed using instrumental setups from the *Riedle* group.[231,247]

X-ray crystallographic analysis was performed on a *Bruker D8Venture TXS* using molybdenum-Kα-radiation or on a *SuperNova*, *Dual*, Cu at home/near, Atlas diffractometer.

References are given after the compound number or in the respective synthesis part for literature known substances or procedures, which were conducted according to similar methods. Literature known compounds were only characterized using ^{1}H NMR and/or mass spectroscopy.

8.2. Synthesis of compounds from chapter 3

8.2.1. HTI-PA switch 2

HTI-PA **2** was synthesized from commercially available starting materials benzenethiol **3** and 4-bromobenzaldehyde **6** in five steps as shown in Figure 225.

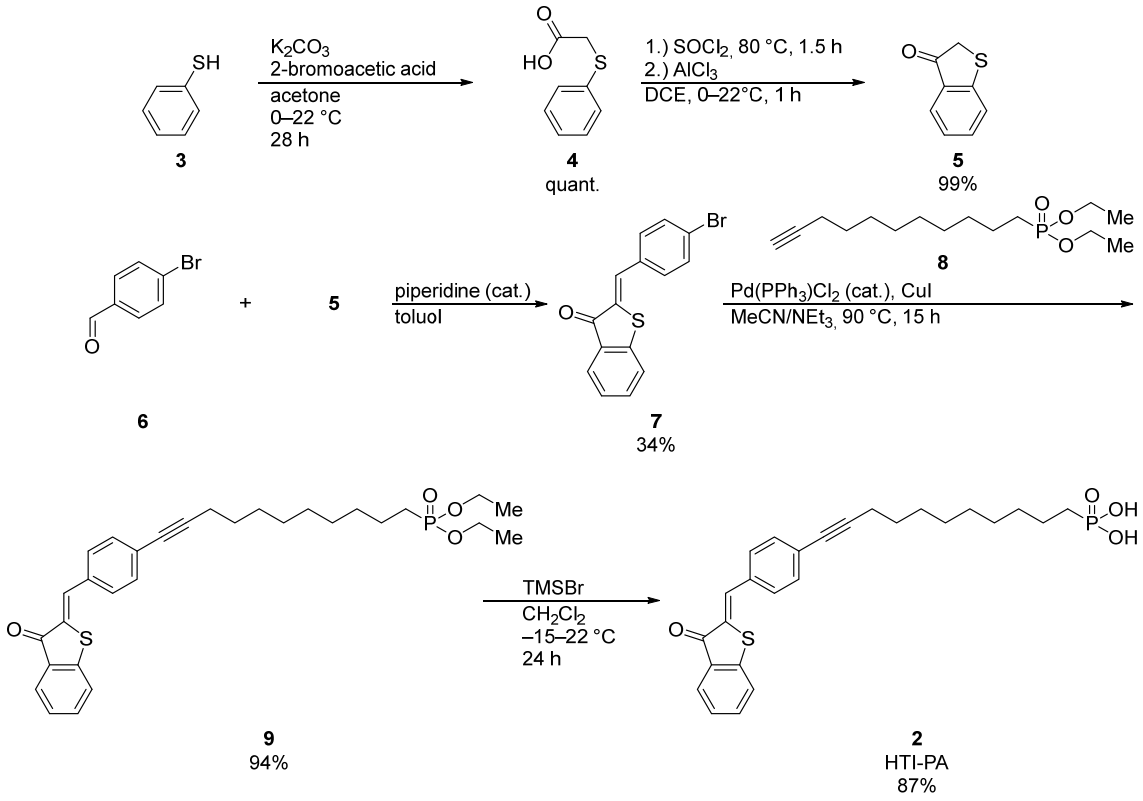

Figure 225 Synthesis of HTI-based HTI-PA **2** for surface attachment starting from commercially available starting material benzenethiol **3** and 4-bromobenzaldehyde **6**.

2-(phenylthio)acetic acid (4)[222]

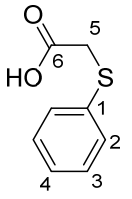

2-Bromoacetic acid (7.61 g, 54.7 mmol, 1.1 equiv.) and potassium carbonate (20.7 g, 150 mmol, 3.0 equiv.) were dissolved in acetone (200 mL, 0.25 M) and cooled to 0 °C. Commercially available benzenethiol **3** (5.51 g, 50.0 mmol, 1.0 equiv.) was added to the clear solution and the reaction mixture was allowed to warm up to 22 °C. After stirring for 28 h the pH was adjusted to 2 with an aqueous HCl

(1.0 M) solution. The aqueous solution was extracted three times with ethyl acetate (200 mL each), the combined organic phases were dried over anhydrous sodium sulfate and the solvent was removed *in vacuo* yielding compound **4** (8.41 g, 49.8 mmol, quantitative conversion) as a white solid.

^{1}H NMR (400 MHz, CD_2Cl_2): δ = 9.39–8.52 (b, 1H, HOC6), 7.48–7.42 (m, 2H, HC2), 7.41–7.33 (m, 2H, HC3), 7.33–7.27 (m, 1H, HC4), 3.74 (s, 2H, H_2C5) ppm.

^{13}C NMR (101 MHz, CD_2Cl_2): δ = 175.62 (C6), 134.63 (C1), 129.86 (C2), 129.15 (C3), 127.15 (C4), 36.40 (C5) ppm.

HR-MS (APPI$^+$, *m*/*z*) $[M]^+$ calc. for $[C_8H_8O_2S]^+$: 168.0245, found: 168.0238.

IR: $\tilde{\nu}$ = 3053 (s), 2988 (s), 2908 (m), 2693 (m), 2583 (m), 2495 (s), 2112 (s), 1942 (s), 1856 (s), 1824 (s), 1790 (s), 1699 (s), 1583 (m), 1573 (m), 1481 (s), 1425 (s), 1390 (s), 1311 (s), 1196 (s), 1092 (m), 1073 (m), 1024 (s), 897 (s), 836 (w), 814 (m), 734 (s), 703 (m), 688 (s), 666 (s), 469 (s), 427 (s) cm^{-1}.

benzo[*b*]thiophen-3(2*H*)-one (5)[154]

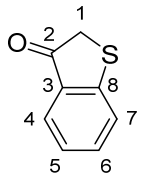

Acetic acid substituted thiol **4** (530 mg, 1.93 mmol, 1.0 equiv.) was dissolved in thionyl chloride (1.26 mL, 17.3 mmol, 9.0 equiv.) and heated at 80 °C for 1.5 h. The remaining thionyl chloride was removed *in vacuo* and the residual solid dissolved in 1,2-dichloroethane (5.00 mL, 2.6 M) before cooling to 0 °C with an ice bath. Then $AlCl_3$ (270 mg, 2.02 mmol, 1.05 equiv.) was added and the suspension stirred for 30 min at 0 °C. After the ice bath was removed, stirring continued for 30 min at 22 °C before the reaction mixture was stopped by transferring to a 2.0 M aqueous HCl/ice mixture (100 mL). The aqueous phase was extracted three times with CH_2Cl_2 (100 mL each), the combined organic layers were dried over anhydrous sodium sulfate, and the solvent was removed *in vacuo*, yielding compound **5** (492 mg, 1.91 mmol, 99%) as a light yellow solid.

^{1}H NMR (400 MHz, CD_2Cl_2): δ = 7.75 (ddd, $^3J_{HH}$ = 7.8 Hz, $^4J_{HH}$ = 1.4 Hz, $^5J_{HH}$ = 0.7 Hz, 1H, HC4), 7.57 (ddd, $^3J_{HH}$ = 8.0, 7.1 Hz, $^4J_{HH}$ = 1.4 Hz, 1H, HC6), 7.46 (dt, $^3J_{HH}$ = 8.0 Hz, $^5J_{HH}$ = 0.8 Hz, 1H, HC7), 7.23 (ddd, $^3J_{HH}$ = 7.9, 7.1 Hz, $^4J_{HH}$ = 0.9 Hz, 1H, HC5), 3.79 (s, 2H, H_2C1) ppm.

^{13}C NMR (101 MHz, CD_2Cl_2): δ = 200.15 (C2), 154.55 (C8), 135.96 (C6), 131.43 (C3), 126.73 (C7), 125.07 (C4 or C5), 124.99 (C4 or C5), 39.68 (C1) ppm.

HR-MS (APPI$^+$, *m*/*z*) [M+H]$^+$ calc. for [C_8H_7OS]$^+$: 151.0212, found: 151.0212.

IR: $\tilde{\nu}$ = 3345 (w), 3056 (w), 2933 (w), 1970 (w), 1944 (w), 1842 (w), 1818 (w), 1689 (s), 1593 (s), 1571 (s), 1478 (w), 1448 (s), 1381 (s), 1337 (w), 1310 (m), 1284 (s), 1222 (m), 1199 (m), 1161 (m), 1115 (m), 1065 (s), 1014 (m), 964 (w), 879 (w), 856 (w), 779 (w), 748 (s), 713 (w), 692 (m), 637 (w), 614 (m), 573 (s), 555 (s), 522 (w), 474 (s), 4067 (s) cm^{-1}.

2-(4-bromobenzylidene)benzo[*b*]thiophen-3(2*H*)-one (7)[90]

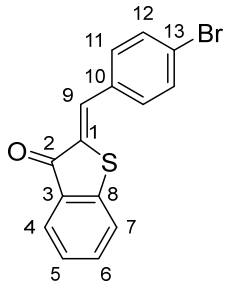

Benzo[*b*]thiophen-3(2*H*)-one **5** (250 mg, 1.66 mmol, 1.0 equiv.) was dissolved in toluene (20.0 mL, 0.083 M) 4-bromobenzaldehyde **6** (310 mg, 2.00 mmol, 1.2 equiv.) and one drop of piperidine were added. The reaction mixture was stirred for 2 h at 100 °C, then cooled to 22 °C, and stopped by addition of a saturated aqueous ammonium chloride solution (20 mL). The aqueous phase was extracted three times with ethyl acetate (200 mL each), the combined organic layers were dried over anhydrous sodium sulfate, and the solvent was removed *in vacuo*. Purification of the crude product was achieved by flash column chromatography (SiO_2, *iso*-hexane:ethyl acetate, 50:1 v/v) yielding compound **7** (170 mg, 0.540 mmol, 34%) as a yellow solid.

***Z*-Isomer**

^{1}H NMR (400 MHz, CD_2Cl_2): δ = 7.91 (ddd, $^3J_{HH}$ = 7.7 Hz, $^4J_{HH}$ = 1.4, 0.7 Hz, 1H, HC4), 7.86 (s, 1H, HC9), 7.67–7.59 (m, 5H, HC6, HC11, HC12), 7.59–7.54 (m, 1H, HC7), 7.34 (ddd, $^3J_{HH}$ = 8.0, 7.2 Hz, $^4J_{HH}$ = 1.1 Hz, 1H, HC5) ppm.

^{13}C NMR (151 MHz, CD_2Cl_2): δ = 188.67 (C2), 146.09 (C8), 135.94 (C6), 133.75 (C10), 132.70 (C12), 132.64 (C11), 132.00 (C9), 131.47 (C1), 130.67 (C3), 127.26 (C4), 126.27 (C5), 124.79 (C13), 124.47 (C7) ppm.

HR-MS (APPI$^+$, *m*/*z*) [M+H]$^+$ calc. for [$C_{15}H_{10}BrOS$]$^+$: 315.9551, found: 315.9553.

IR: $\tilde{\nu}$ = 3063 (m), 2918 (s), 2849 (s), 1736 (w), 1682 (s), 1661 (m), 1583 (s), 1570 (s), 1484 (s), 1448 (s), 1397 (m), 1373 (w), 1313 (w), 1279 (s), 1219 (w), 1201 (w), 1163 (w), 1118 (w), 1066 (s), 1047 (s),

1004 (s), 897 (s), 867 (w), 816 (s), 801 (s), 778 (s), 735 (s), 674 (s), 603 (s), 520 (s), 445 (s), 423 (s) cm^{-1}.

TLC (SiO_2, *iso*-hexane:ethyl acetate, 50:1 v/v): $R_f = 0.49$.

diethyl (11-(4-((3-oxobenzo[b]thiophen-2(3H)-ylidene)methyl)phenyl)undec-10-yn-1-yl)phosphonate (9)

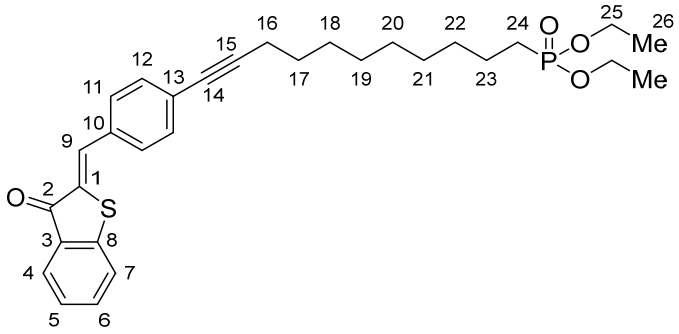

Compound **7** (101 mg, 0.315 mmol, 1.0 equiv.), bis(triphenylphosphine)palladium chloride (23.5 mg, 32.0 µmol, 10 mol%), copper(I) iodide (8.40 mg, 35.0 µmol, 11 mol%), diethyl undec-10-yn-1-ylphosphonate **8** (251 mg, 0.851 mmol, 2.7 equiv.) and anhydrous acetonitrile (2.50 mL, 0.13 M) were suspended in freshly distilled anhydrous triethylamine (5.00 mL, 0.063 M). The reaction mixture was degassed by flushing with a stream of argon for 10 min and then heated at 90 °C for 15 h. After cooling to 22 °C, the reaction was stopped by the addition of silica gel and the volatiles were removed *in vacuo*. Purification of the crude product was achieved by flash column chromatography (SiO_2, *iso*-hexane:ethyl acetate, 1:0 to 0:1 v/v), yielding compound **9** (157 mg, 0.299 mmol, 94%) as a viscous red oil.

***Z*-Isomer**

^{1}H NMR (400 MHz, CD_2Cl_2): δ = 7.89 (ddd, $^3J_{HH}$ = 7.7 Hz, $^4J_{HH}$ = 1.4, 0.7 Hz, 1H, HC4), 7.87 (s, 1H, HC9), 7.65–7.62 (m, 2H, HC11), 7.60 (ddd, $^3J_{HH}$ = 7.9, 7.1 Hz, $^4J_{HH}$ = 1.4 Hz, 1H, HC6), 7.53 (dt, $^3J_{HH}$ = 7.9, $^4J_{HH}$ = 1.0 Hz, 1H, HC7), 7.49–7.46 (m, 2H, HC12), 7.31 (ddd, $^3J_{HH}$ = 8.0, 7.1 Hz, $^4J_{HH}$ = 1.1 Hz, 1H, HC5), 4.13–3.95 (m, 4H, H_2C25), 2.44 (t, $^3J_{HH}$ = 7.1 Hz, 2H, H_2C16), 1.74–1.31 (m, 16H, H_2C17–H_2C24), 1.30 (t, $^3J_{HH}$ = 7.1 Hz, 6H, H_3C26) ppm.

^{13}C NMR (101 MHz, CD_2Cl_2): δ = 188.65 (C2), 146.18 (C8), 135.77 (C6), 133.74 (C10), 132.66 (C9), 132.42 (C12), 131.18 (C11), 130.76 (C3), 128.88 (C1), 127.18 (C4), 126.44 (C13), 126.16 (C5), 124.42 (C7), 94.32 (C15), 80.65 (C14), 61.63 (C25), 30.97 (C18, C19, C20, C21, C22, C23 or C24), 29.68 (C18, C19, C20, C21, C22, C23 or C24), 29.49 (C18, C19, C20, C21, C22, C23 or C24), 29.48 (C18, C19, C20, C21, C22, C23 or C24), 29.31 (C18, C19, C20, C21, C22, C23 or C24), 29.06 (C17), 25.96

(C18, C19, C20, C21, C22, C23 or C24), 22.82 (C18, C19, C20, C21, C22, C23 or C24), 19.89 (C16), 16.71 (C26) ppm.

HR-MS (APPI$^+$, *m*/*z*) $[M+H]^+$ calc. for $[C_{30}H_{38}O_4PS]^+$: 525.2223, found: 525.2230.

IR: $\tilde{\nu}$ = 3434 (s), 3059 (w), 2979 (m), 2926 (s), 2582 (m), 2219 (w), 1677 (s), 1589 (s), 1568 (s), 1543 (w), 1506 (m), 1449 (m), 1409 (w), 1390 (w), 1368 (w), 1310 (w), 1329 (w), 1282 (s), 1225 (s), 1205 (m), 1183 (m), 1162 (m), 1085 (w), 1096 (m), 1050 (s), 1020 (s), 957 (s), 827 (m), 784 (m), 742 (m), 722 (m), 695 (w), 679 (w), 645 (w), 540 (s), 495 (w) cm^{-1}.

TLC (SiO_2, ethyl acetate, 100%): R_f = 0.21.

11-(4-((3-oxobenzo[b]thiophen-2(3H)-ylidene)methyl)phenyl)undec-10-yn-1-ylphosphonic acid (2)[302]

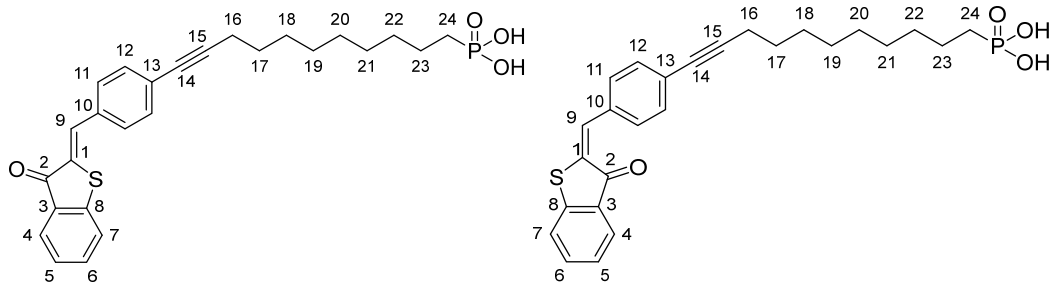

A solution of compound **9** (157 mg, 0.300 mmol, 1.0 equiv.) in anhydrous CH_2Cl_2 (18.0 mL, 0.017 M) was prepared under an argon atmosphere and cooled to –15 °C. Then bromotrimethylsilane (0.600 mL, 4.50 mmol, 15 equiv.) was added dropwise and the reaction mixture was stirred at 22 °C for 24 h. Excess bromotrimethylsilane and other volatiles were removed *in vacuo* with a second cooling trap. The crude product was precipitated from methanol (6 mL) by addition of a few drops of water and washed with *n*-hexane (50 mL), ethyl acetate (50 mL), and CH_2Cl_2 (50 mL), yielding compound **2** (122 mg, 0.260 mmol, 87%) as a yellow-beige colored powder.

***Z*-Isomer**

^{1}H NMR (601 MHz, dimethyl sulfoxide-d_6): δ = 7.90 (s, 1H, HC9), 7.88 (d, $^3J_{HH}$ = 7.7 Hz, 1H, HC4), 7.80 (d, 1H, HC7), 7.78–7.73 (m, 3H, HC11, HC6), 7.54 (d, $^3J_{HH}$ = 8.4 Hz, 2H, HC12), 7.50 (td, $^3J_{HH}$ = 7.4 Hz, $^4J_{HH}$ = 1.0 Hz, 1H, HC5), 2.45 (t, $^3J_{HH}$ = 7.1 Hz, 2H, H_2C16), 1.55 (p, $^3J_{HH}$ = 7.1 Hz, 2H, H_2C17), 1.51–1.44 (m, 4H, H_2C22, H_2C24), 1.43–1.38 (m, 2H, H_2C18), 1.33–1.28 (m, 4H, H_2C19, H_2C23), 1.28–1.24 (m, 4H, H_2C20, H_2C21) ppm.

^{13}C NMR (151 MHz, dimethyl sulfoxide-d_6): δ = 187.86 (C2), 145.09 (C8), 136.44 (C6), 133.20 (C10), 132.37 (C9), 132.22 (C12), 131.18 (C11), 130.33 (C1), 129.63 (C3), 126.87 (C4), 126.61 (C5), 125.48 (C13), 124.82 (C7), 94.48 (C15), 80.62 (C14), 30.21 (d, $^2J_{CP}$ = 16.0 Hz, C23), 28.92 (C20 or C21), 28.79 (C20 or C21), 28.64 (C19), 28.47 (C18), 28.18 (C17), 28.11 (d, $^1J_{CP}$ = 135.7 Hz, C24), 22.86 (d, $^3J_{CP}$ = 4.7 Hz, C22), 18.95 (C16) ppm.

HR-MS (APPI$^+$, *m*/*z*) [M+H]$^+$ calc. for $[C_{26}H_{30}O_4PS]^+$: 469.1597, found: 469.1590.

IR: $\tilde{\nu}$ = 2926 (m), 2848 (w), 2319 (w), 2260 (w), 2225 (w), 2164 (w), 1676 (s), 1589 (s), 1568 (m), 1584 (w), 1505 (m), 1449 (m), 1408 (m), 1285 (m), 1221 (w), 1168 (w), 1116 (m), 1092 (m), 1066 (m), 1053 (m), 998 (s), 947 (s), 897 (m), 827 (m), 780 (w), 742 (s), 723 (w), 688 (w), 622 (w), 533 (w), 522 (w), 340 (s), 423 (s) cm^{-1}.

***E*-Isomer**

^{1}H NMR (601 MHz, dimethyl sulfoxide-d_6): δ = 8.16–8.11 (m, 2H, HC11), 7.79 (dt, $^3J_{HH}$ = 7.8 Hz, $^4J_{HH}$ = 1.1 Hz, 1H, HC4), 7.72–7.70 (m, 2H, HC6 and HC7), 7.62 (s, 1H, HC9), 7.46–7.42 (m, 2H, HC12), 7.37 (ddd, $^3J_{HH}$ = 8.0, 5.5 Hz, $^4J_{HH}$ = 2.6 Hz, 1H, HC5), 2.46 (t, $^3J_{HH}$ = 7.1 Hz, 2H, H_2C16), 1.56 (p, $^3J_{HH}$ = 7.2 Hz, 2H, H_2C17), 1.51–1.39 (m, 6H, H_2C18, H_2C22, H_2C24), 1.34–1.25 (m, 8H, H_2C19, H_2C20, H_2C21, H_2C23) ppm.

^{13}C NMR (151 MHz, dimethyl sulfoxide-d_6): δ = 185.60 (C2), 144.74 (C8), 137.84 (C9), 135.66 (C6), 133.24 (C10), 132.59 (C1), 132.02 (C3), 131.31 (C11), 130.89 (C12), 126.63 (C4), 125.50 (C5), 125.33 (C13), 124.05 (C7), 93.69 (C15), 80.73 (C14), 30.06 (d, $^2J_{CP}$ = 15.8 Hz, C22), 28.78 (C18, C19, C20 or C21), 28.66 (C18, C19, C20 or C21), 28.50 (C18, C19, C20 or C21), 28.34 (C18, C19, C20 or C21), 28.10 (C17), 27.62 (d, $^1J_{CP}$ = 135.8 Hz, C24), 22.78 (d, $^3J_{CP}$ = 4.6 Hz, C23), 18.79 (C16) ppm.

8.3. Synthesis of compounds from chapter 4

8.3.1. Fluorescent HTI switch 11

Fluorescent HTI-based photoswitch **11** was synthesized in one step from commercially available 3-formylbenzoic acid **14** and benzothiophenone **5** shown in Figure 226. Synthesis of benzothiophenone **5** can be found in chapter 8.2.

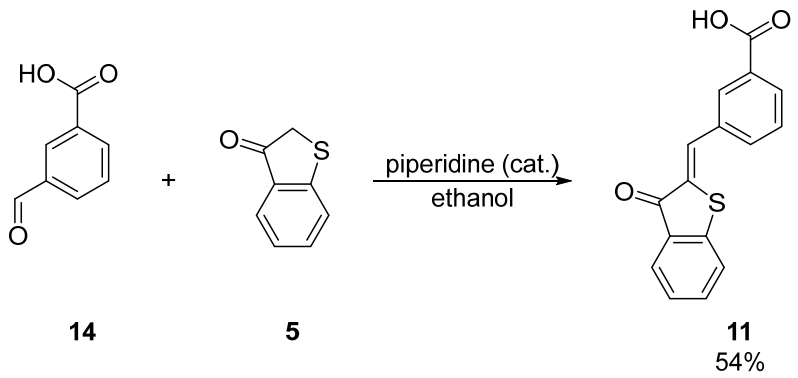

Figure 226 One step synthesis of fluorescent HTI switch **11** from commercially available 3-formylbenzoic acid **14** and benzothiophenone **5**. Synthesis of benzothiophenone **5** can be found in chapter 8.2.

***Z*-3-((3-oxobenzo[b]thiophen-2(3H)-ylidene)methyl)benzoic acid (11)**[235]

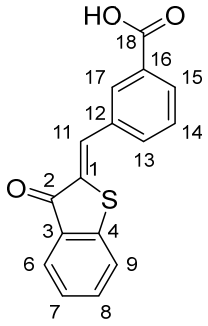

Benzothiophenone **5** (909 mg, 5.9 mmol, 1.0 equiv.) and 3-formylbenzoic acid **14** (1.15 g, 7.69 mmol, 1.3 equiv.) were dissolved in absolute ethanol (32 mL, 0.185 M). Three drops of piperidine were added and the solution was heated at 80 °C for 6 h under an argon atmosphere. After cooling to 22 °C the pH was adjusted to 2 with a 1 M aqueous HCl solution after which diethylether (75 mL) and water (75 mL) were added and the precipitate yielded compound **11** (102 mg, 0.36 mmol, 54%) as a yellow solid.

^{1}H NMR (601 MHz, dimethyl sulfoxide-d_6): δ = 13.40–13.28 (m, 1H, H-OC18), 8.40 (t, ^4J(H,H) = 1.8 Hz, 1H, H-C17), 8.05 (dd, ^3J(H,H) = 7.7 Hz, ^4J(H,H) = 1.7 Hz, 2H, H-C13 and H-C 15), 8.02 (s, 1H, H-C11), 7.91 (dd, ^3J(H,H) = 7.9 Hz, ^4J(H,H) = 1.3 Hz, 1H, H-C6), 7.88 (d, ^3J(H,H) = 7.9 Hz,

1H, H-C9), 7.77 (td, ^{3}J(H,H) = 7.7 Hz, ^{4}J(H,H) = 1.3 Hz, 1H, H-C7), 7.70 (t, ^{3}J(H,H) = 7.7 Hz, 1H, H-C14), 7.44 (td, ^{3}J(H,H) = 7.5 Hz, ^{4}J(H,H) = 0.9 Hz, 1H, H-C8) ppm.

^{13}C NMR (151 MHz, dimethyl sulfoxide-d_6): δ = 187.61 (C2), 166.70 (C18), 144.98 (C3), 136.28 (C7), 135.61 (C13), 134.13 (C12), 131.95 (C11), 131.81 (C16), 130.91 (C15), 130.73 (C1), 130.45 (C17), 129.75 (C14), 129.42 (C4), 126.68 (C6), 126.42 (C8), 124.77 (C9) ppm.

HR-MS (APPI$^+$, *m*/*z*) [M+H]$^+$ calc. for $[C_{16}H_{11}O_3S]^+$: 283.0423, found: 283.0428.

IR: $\tilde{\nu}$ = 3058 (m), 2994 (m), 2878 (m), 2821 (m), 2661 (m), 2615 (m), 2556 (m), 1701 (m), 1685 (s), 1581 (m), 1449 (m), 1415 (m), 1315 (m), 1278 (s), 1208 (m), 1161 (w), 1064 (s), 1049 (s), 928 (w), 908 (w), 867 (w), 774 (w), 751 (s), 734 (s), 671 (s), 659 (m), 568 (w), 531 (s), 484 (m), 422 (m) cm^{-1}.

8.4. Synthesis of compounds from chapter 5

8.4.1. HTI motors 15a–15g

For simplicity only structures with *S*-configured sulfoxide are shown and discussed in the following but racemates with both *S*- and *R*-configured sulfoxide were obtained from synthesis. All realized synthetic transformations necessary for the synthesis of **15a**–**15g** are shown in Figure 227 and residues are defined in Table 36. A sample of already published molecular motor **15d** previously synthesized in the *Dube* group was used for all experimental data generated within this work.[154] Synthesis of benzothiophenone **5** can be found in chapter 8.2 and motor **15h** in chapter 8.5.2.

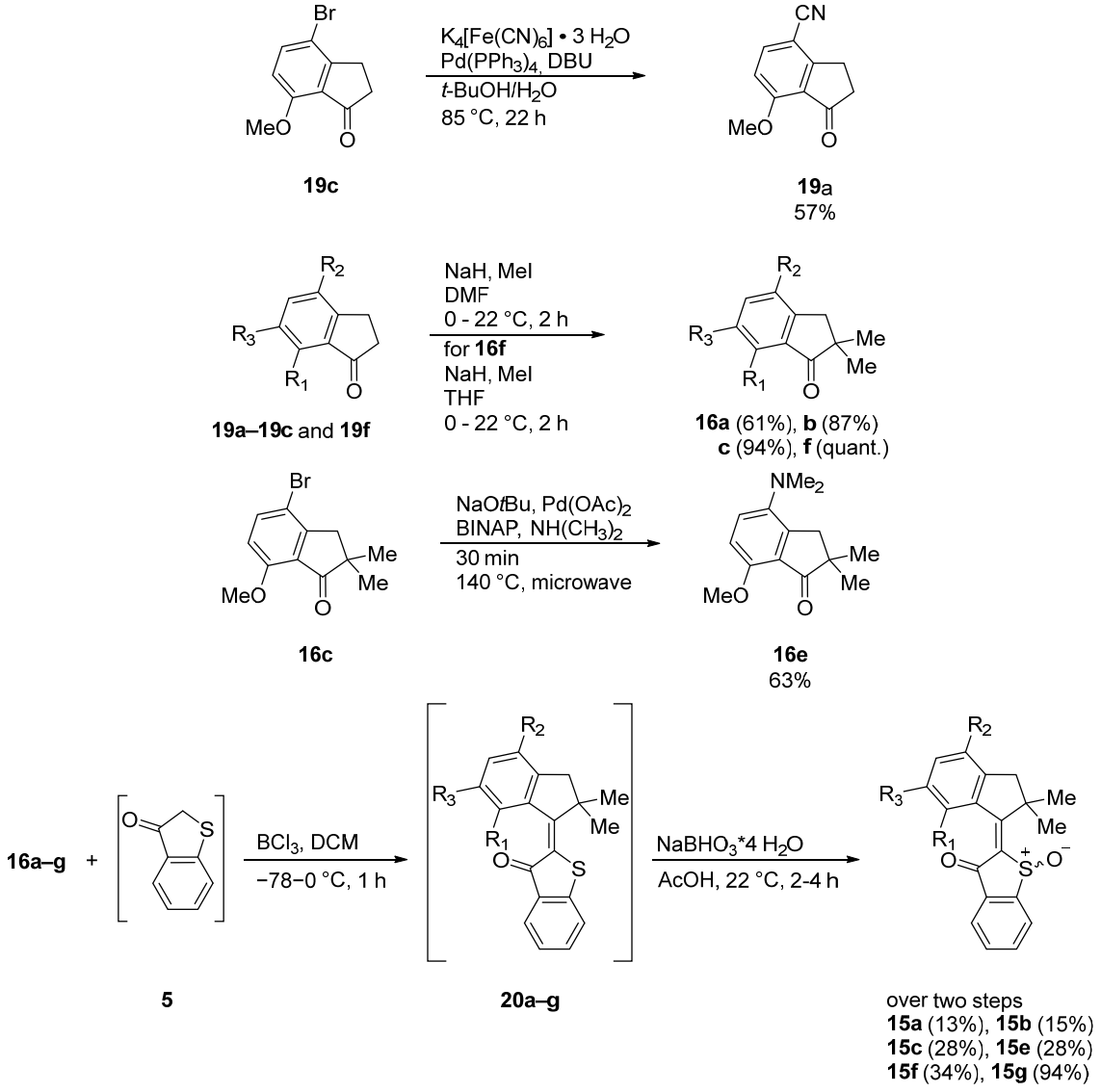

Figure 227 Overview of all synthesized motors **15a**–**15g** except **15d**. Synthesis of benzothiophenone **5** can be found in chapter 8.2 and motor **15h** in chapter 8.5.2.

Table 36 Substitution pattern of HTI-based molecular motors **15a**–**15h** and their corresponding starting materials. Substitution pattern of motor **15d** is only listed for completeness but was not synthesized within this work since a sample previously synthesized in the *Dube* group was used for all experiments. Synthesis of motor **15h** can be found in chapter 8.5.2.

	R_1	R_2	R_3	R_4	R_5
a	OMe	CN	H	H	H
b	OMe	H	H	H	H
c	OMe	Br	H	H	H
d	OMe	OMe	H	H	H
e	OMe	NMe_2	H	H	H
f	H	H	H	H	H
g	H	H	OMe	H	H
h	H	H	OMe	Me	C_7H_6OF

7-methoxy-1-oxo-2,3-dihydro-1*H*-indene-4-carbonitrile (19a)

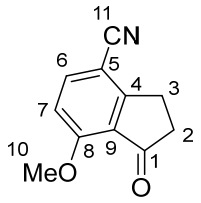

A mixture of tetrakis(triphenylphosphine)palladium(0) (127 mg, 0.100 mmol, 5 mol%), potassium hexacyanoferrate(II) trihydrate (337 mg, 80.0 µmol, 40 mol%) and commercially available 4-bromo-7-methoxy indanone **19c** (483 mg, 2.00 mmol, 1.0 equiv.) in a *tert*-butyl alcohol:water mixture (6.00 mL, 1:1 v/v, 0.30 M) with diazabicycloundecene (0.740 mL, 0.500 mmol, 25 mol%) was prepared under an argon atmosphere. After stirring at 22 °C for 10 min, the mixture was heated to 85 °C for 49 h. The cooled reaction mixture was filtered, rinsed three times with methanol (50 mL each), three times with CH_2Cl_2 (50 mL each), and the solvent of the combined organic layers removed *in vacuo*. Purification of the crude product was achieved by flash column chromatography (SiO_2, *iso*-hexane:ethyl acetate, 1:1 v/v), yielding compound **19a** (212 mg, 1.14 mmol, 57%) as a white solid.

^{1}H NMR (601 MHz, CD_2Cl_2): δ = 7.82 (d, $^3J_{HH}$ = 8.6 Hz, 1H, HC6), 6.90 (d, $^3J_{HH}$ = 8.6 Hz, 1H, HC7), 3.98 (s, 3H, H_3C10), 3.22–3.17 (m, 2H, H_2C3), 2.72–2.65 (m, 2H, H_2C2) ppm.

^{13}C NMR (151 MHz, CD_2Cl_2): δ = 202.34 (C1), 161.73 (C4), 161.50 (C8), 140.17 (C6), 126.35 (C9), 116.88 (C11), 110.71 (C7), 102.78 (C5), 56.73 (C10), 36.65 (C2), 25.47 (C3) ppm.

HR-MS (APPI, *m/z*) $[M+H]^+$ calc. for $[C_{11}H_{10}NO_2]^+$: 188.0706, found: 188.0713.

IR: $\tilde{\nu}$ = 3387 (w), 3083 (m), 3040 (m), 2990 (m), 2949 (w), 2846 (w), 2224 (s), 1699 (s), 1597 (m), 1573 (s), 1492 (s), 1473 (m), 1430 (m), 1339 (m), 1294 (s), 1247 (m), 1222 (s), 1193 (s), 1087 (s), 1023 (s), 999 (s), 941 (w), 891 (w), 830 (s), 705 (s), 657 (s), 612 (s), 544 (s), 499 (s), 434 (s) cm^{-1}.

TLC (SiO_2, *iso*-hexane:ethyl acetate, 1:1 v/v): R_f = 0.27.

7-methoxy-2,2-dimethyl-1-oxo-2,3-dihydro-1*H*-indene-4-carbonitrile (16a)[159]

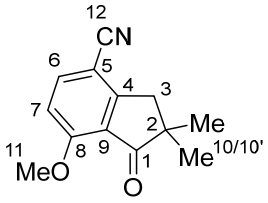

To a solution of compound **19a** (184 mg, 0.978 mmol, 1.0 equiv.) in anhydrous *N*,*N*-dimethylformamide (2.00 mL, 0.49 M) at 0 °C, sodium hydride (105 mg (60% in mineral oil), 2.46 mmol, 2.5 equiv.) was added and the resulting suspension stirred for 20 min at 0 °C. Then iodomethane (0.150 mL, 2.46 mmol, 2.5 equiv.) was added dropwise and the reaction mixture was stirred at 22 °C for 2 h. After addition of a saturated aqueous ammonium chloride solution (50 mL) the aqueous solution was extracted three times with ethyl acetate (40 mL each). The combined organic layers were washed four times with water (100 mL each, to remove residual *N*,*N*-dimethylformamide), twice with a saturated aqueous NaCl solution (60 mL each), dried over anhydrous sodium sulfate, and the solvent removed *in vacuo*. Purification of the crude product was achieved by flash column chromatography (SiO_2, *iso*-hexane:ethyl acetate, 4:1 v/v), yielding compound **16a** (128 mg, 0.593 mmol, 61%) as a white solid.

^{1}H NMR (400 MHz, CD_2Cl_2): δ = 7.83 (d, $^3J_{HH}$ = 8.6 Hz, 1H, HC6), 6.92 (d, $^3J_{HH}$ = 8.6 Hz, 1H, HC7), 3.99 (s, 3H, H_3C11), 3.07 (s, 2H, H_2C3), 1.21 (s, 6H, H_3C10 and H_3C10') ppm.

^{13}C NMR (101 MHz, CD_2Cl_2): δ = 207.00 (C1), 161.91 (C8), 158.83 (C4), 140.26 (C6), 124.49 (C9), 116.97 (C12), 110.85 (C7), 102.77 (C5), 56.74 (C11), 45.95 (C2), 42.03 (C3), 25.35 (C10 and C10') ppm.

HR-MS (APPI, *m/z*) $[M+H]^+$ calc. for $[C_{13}H_{14}NO_2]^+$: 216.1019, found 216.1022.

IR: $\tilde{\nu}$ = 3403 (w), 3093 (w), 3053 (w), 2958 (m), 2871 (w), 2844 (w), 2220 (s), 1996 (w), 1927 (w), 1709 (s), 1598 (s), 1576 (s), 1491 (s), 1463 (s), 1335 (m), 1378 (w), 1337 (w), 1293 (s), 1227 (m), 1190 (m), 1164 (m), 1083 (m), 997 (s), 953 (s), 918 (m), 891 (w), 818 (s), 738 (m), 706 (s), 642 (w), 604 (w), 585 (w), 555 (m), 509 (m), 452 (w), 435 (w) cm^{-1}.

TLC (SiO_2, *iso*-hexane:ethyl acetate, 4:1 v/v): R_f = 0.13.

7-methoxy-2,2-dimethyl-2,3-dihydro-1H-inden-1-one (16b)[158]

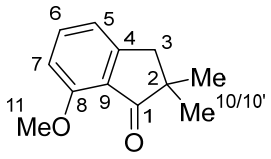

To a solution of compound **19b** (1.06 mg, 6.54 mmol, 1.0 equiv.) in anhydrous *N*,*N*-dimethylformamide (30.0 mL, 0.55 M) at 0 °C, sodium hydride (659 mg (60% in mineral oil), 16.4 mmol, 2.5 equiv.) was added and the resulting suspension stirred for 20 min at 0 °C. Then iodomethane (1.00 mL, 16.4 mmol, 2.5 equiv.) was added dropwise and the reaction mixture was stirred at 22 °C for 2 h. After addition of a saturated aqueous ammonium chloride solution (50 mL) the aqueous solution was extracted three times with ethyl acetate (300 mL each). The combined organic layers were washed four times with water (100 mL each, to remove residual *N*,*N*-dimethylformamide), twice with a saturated aqueous NaCl solution (60 mL each), dried over anhydrous sodium sulfate, and the solvent removed *in vacuo*. Purification of the crude product was achieved by flash column chromatography (SiO_2, *iso*-hexane:ethyl acetate, 12:1 v/v), yielding compound **16b** (1.10 g, 5.70 mmol, 87%) as a white solid.

^{1}H NMR (400 MHz, $CDCl_3$): δ = 7.52 (dd, $^3J_{HH}$ = 8.2, 7.5 Hz, 1H, HC6), 6.96 (dq, $^3J_{HH}$ = 7.5, 0.9 Hz, 1H, HC5), 6.80–6.76 (m, 1H, HC7), 3.95 (s, 3H, HC11), 2.94 (t, $^4J_{HH}$ = 0.9 Hz, 2H, HC3), 1.22 (s, 6H, HC10 and HC10').

HR-MS (APPI, *m/z*) $[M+H]^+$ calc. for $[C_{12}H_{15}O_2]^+$: 190.0989, found 190.0994.

4-bromo-7-methoxy-2,2-dimethyl-2,3-dihydro-1*H*-inden-1-one (16c)[157,241]

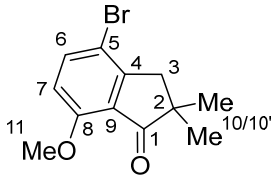

To a solution of compound **19c** (505 mg, 1.46 mmol, 1.0 equiv.) in anhydrous *N*,*N*-dimethylformamide (3.00 mL, 0.49 M) at 0 °C, sodium hydride (153 mg (60% in mineral oil), 3.65 mmol, 2.5 equiv.) was added and the resulting suspension stirred for 20 min at 0 °C. Then iodomethane (0.220 mL, 2.50 mmol, 2.5 equiv.) was added dropwise and the reaction mixture was stirred at 22 °C for 2 h. After addition of a saturated aqueous ammonium chloride solution (50 mL) the aqueous mixture was extracted three times with ethyl acetate (40 mL each). The combined organic phases were washed four times with water (100 mL each, to remove residual *N*,*N*-dimethylformamide), twice with a saturated aqueous NaCl solution (60 mL each), dried over anhydrous sodium sulfate, and the solvent removed *in vacuo*.

Purification of the crude product was achieved by flash column chromatography (SiO_2, *iso*-hexane:ethyl acetate, 1:1 v/v), yielding compound **16c** (371 mg, 1.38 mmol, 94%) as a white solid.

^{1}H NMR (400 MHz, CD_2Cl_2): δ = 7.66 (d, $^3J_{HH}$ = 8.7, 1H, HC6), 6.76 (d, $^3J_{HH}$ = 8.7, 1H, H C7), 3.91 (s, 3H, H_3C11), 2.86 (s, 2H, H_2C3), 1.19 (s, 6H, H_3C10 and H_3C10') ppm.

^{13}C NMR (101 MHz, CD_2Cl_2): δ = 208.17 (C1), 158.16 (C8), 154.07 (C4), 138.96 (C6), 125.50 (C9), 112.13 (C5), 111.86 (C7), 56.31 (C11), 45.84 (C2), 43.84 (C3), 25.50 (C10 and C10') ppm.

HR-MS (APPI, *m/z*) $[M+H]^+$ calc. for $[C_{12}H_{14}BrO_2]^+$: 269.0172, found 269.0176.

IR: $\tilde{\nu}$ = 3417 (w), 3082 (w), 3010 (w), 2969 (m), 2917 (m), 2858 (w), 2836 (w), 2549 (w), 1913 (w), 1715 (s), 1585 (s), 1464 (s), 1455 (s), 1432 (s), 1379 (s), 1359 (m), 1330 (m), 1275 (s), 1234 (m), 1194 (m), 1181 (m), 1221 (m), 1080 (s), 998 (s), 952 (m), 924 (m), 870 (w), 811 (s), 779 (m), 688 (m), 640 (m), 608 (m), 501 (m), 473 (m) cm^{-1}.

TLC (SiO_2, *iso*-hexane:ethyl acetate, 1:1 v/v): R_f = 0.92.

4-(dimethylamino)-7-methoxy-2,2-dimethyl-2,3-dihydro-1H-inden-1-one (16e)[III]

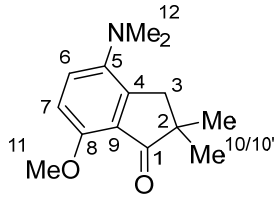

A solution of BINAP (31.6 mg, 50.7 µmol, 15 mol%) and $Pd(OAc)_2$ (6.75 mg, 30.0 µmol, 10 mol%) was stirred in dry toluene (8.00 mL, 0.042 M) at 22 °C for 20 min under an argon atmosphere. Meanwhile compound **16c** (100 mg, 0.340 mmol, 1.0 equiv.) and sodium *tert*-butoxide (168 mg, 1.75 mmol, 5.2 equiv.) were added into a flame dried microwave vial followed by the catalyst solution. Additional *N*,*N*-dimethylformamide (0.950 mL) was added and the reaction mixture was stirred at 140 °C for 30 min under microwave irradiation. The reaction was stopped by addition of a saturated aqueous ammonium chloride solution (50 mL), the aqueous mixture was extracted three times with CH_2Cl_2 (200 mL each), the combined organic phases were dried over anhydrous sodium sulfate, and the solvent removed *in vacuo*. Purification of the crude product was achieved by flash column chromatography (SiO_2, *iso*-hexane:ethyl acetate, 9:1 v/v), yielding compound **16e** (49.4 mg, 1.38 mmol, 63%) as a yellow-green oil.

^{1}H NMR (400 MHz, CD_2Cl_2): δ = 7.16 (d, $^3J_{HH}$ = 8.7 Hz, 1H, HC6), 6.76 (d, $^3J_{HH}$ = 8.6 Hz, 1H, HC7), 3.86 (s, 3H, H_3C11), 2.90 (s, 2H, H_2C3), 2.72 (s, 6H, H_3C12 and H_3C12'), 1.17 (s, 6H, H_3C10 and H_3C10') ppm.

^{13}C NMR (126 MHz, CD_2Cl_2): δ = 209.22 (C1), 153.86 (C8), 148.09 (C4), 145.00 (C5), 124.93 (C6), 124.44 (C9), 110.03 (C7), 56.06 (C11), 45.82 (C2), 44.02 (C12 and C12'), 41.74 (C3), 25.62 (C10 and C10') ppm.

HR-MS (APPI, *m/z*) $[M+H]^+$ calc. for $[C_{14}H_{20}NO_2]^+$: 234.1489, found 234.1489.

TLC (SiO_2, *iso*-hexane:ethyl acetate, 9:1 v/v): R_f = 0.18.

2,2-dimethyl-2,3-dihydro-1H-inden-1-one (16f)

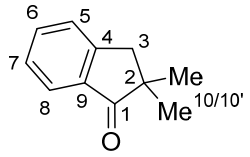

To a solution of compound **19f** (2.10 mg, 15.1 mmol, 1.0 equiv.) in anhydrous tetrahydrofuran (30.0 mL, 0.50 M) at 0 °C, sodium hydride (1.50 g (60% in mineral oil), 37.8 mmol, 2.5 equiv.) was added and the resulting suspension stirred for 20 min at 0 °C. Then iodomethane (2.35 mL, 37.8 mmol, 2.5 equiv.) was added dropwise and the reaction mixture stirred at 22 °C for 2 h. After addition of a saturated aqueous ammonium chloride solution (50 mL) the aqueous mixture was extracted three times with ethyl acetate (300 mL each). The combined organic phases were washed twice with a saturated aqueous NaCl solution (100 mL each), dried over anhydrous sodium sulfate, and the solvent removed *in vacuo*. Purification of the crude product was achieved by flash column chromatography (SiO_2, *iso*-hexane:ethyl acetate, 9:1 v/v), yielding compound **16f** (2.40 g, 15.1 mmol, quantitative conversion) as a white solid.

^{1}H NMR (400 MHz, CD_2Cl_2): δ = 7.70 (ddq, $^3J_{HH}$ = 7.6 Hz, $^4J_{HH}$ = 1.2, 0.6 Hz, 1H, HC5), 7.60 (td, $^3J_{HH}$ = 7.4 Hz, $^4J_{HH}$ = 1.3 Hz, 1H, HC7), 7.45 (dp, $^3J_{HH}$ = 7.7 Hz, $^4J_{HH}$ = 1.0 Hz, 1H, HC8), 7.40–7.35 (m, 1H, HC6), 3.00 (q, $^4J_{HH}$ = 0.8 Hz, 2H H_2C3), 1.20 (s, 6H, H_3C10 and H_3C10').

HR-MS (APPI, *m/z*) $[M+H]^+$ calc. for $[C_{11}H_{13}O]^+$: 161.0961, found 161.0966.

(*E*/*Z*)-7-methoxy-2,2-dimethyl-1-(3-oxobenzo[*b*]thiophen-2(3*H*)-ylidene)-2,3-dihydro-1*H*-indene-4-carbonitrile (20a)[159]

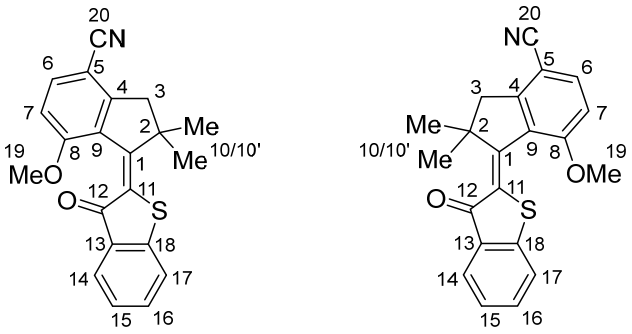

Two separate Schlenk flasks under an argon atmosphere were charged individually with compound **16a** (110 mg, 0.510 mmol, 1.0 equiv.) in anhydrous CH_2Cl_2 (0.130 mL, 2.1 M) in the first flask at 0 °C and compound **5** (82.2 mg, 0.560 mmol, 1.1 equiv.) in anhydrous CH_2Cl_2 (2.80 mL, 0.52 M) in the second flask at −78 °C. Boron trichloride (0.540 mL, 1.0 M in anhydrous CH_2Cl_2, 0.540 mmol, 1.1 equiv.) was added to the flask containing compound **5** and the resulting mixture was immediately taken up into the same syringe and transferred to the second flask containing compound **16a** at 0 °C. The reaction mixture was vigorously stirred for 90 min while warming up to 22 °C and then stopped by transferring to a saturated aqueous ammonium chloride solution (20 mL). The aqueous phase was extracted four times with CH_2Cl_2 (100 mL each), the combined organic layers were dried over anhydrous sodium sulfate, and the solvent was removed *in vacuo*. The crude product was purified by flash column chromatography (SiO2, *iso*-hexane:ethyl acetate, 50:1 v/v), yielding compound **20a** as a red oil, which was used in the next synthetic step without further purification.

HR-MS (APPI, *m/z*) $[M+H]^+$ calc. for $[C_{21}H_{18}NO_2S]^+$: 348.1053, found 348.1056.

TLC (SiO_2, *iso*-hexane:ethyl acetate, 98:2 v/v): R_f = 0.12 and 0.27.

(*E*/*Z*)-2-(7-methoxy-2,2-dimethyl-2,3-dihydro-1*H*-inden-1-ylidene)benzo[*b*]thiophen-3(2*H*)-one (20b)[159]

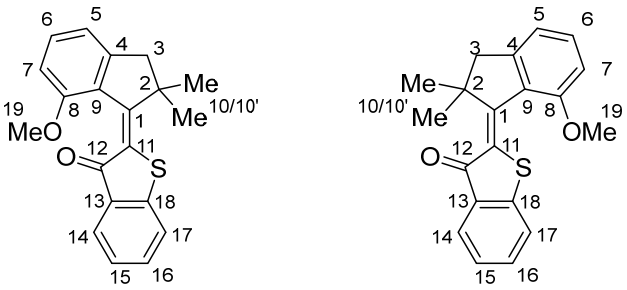

Two separate Schlenk flasks under an argon atmosphere were charged individually with compound **16b** (301 mg, 1.58 mmol, 1.0 equiv.) in anhydrous CH_2Cl_2 (0.300 mL, 5.1 M) in the first flask at 0 °C and compound **5** (248 mg, 1.58 mmol, 1.0 equiv.) in anhydrous CH_2Cl_2 (4.40 mL, 0.36 M) in the second flask at −78 °C. Boron trichloride (1.58 mL, 1.0 M in anhydrous CH_2Cl_2, 1.58 mmol, 1.0 equiv.) was added to the flask containing compound **5** and the resulting mixture was immediately taken up into the same syringe and transferred to the second flask containing compound **16b** at 0 °C. The reaction mixture was vigorously stirred for 90 min while warming up to 22 °C and then stopped by transferring to a saturated aqueous ammonium chloride solution (20 mL). The aqueous phase was extracted four times with CH_2Cl_2 (100 mL each), the combined organic layers were dried over anhydrous sodium sulfate, and the solvent was removed *in vacuo*. The crude product was purified by flash column chromatography (SiO2, *iso*-hexane:ethyl acetate, 95:5 v/v), yielding compound **20b** as a red oil, which was used in the next synthetic step without further purification.

HR-MS (APPI, *m/z*) $[M+H]^+$ calc. for $[C_{20}H_{19}O_2S]^+$: 323.1100, found 323.1104.

TLC (SiO_2, *iso*-hexane:ethyl acetate, 95:5 v/v): R_f = 0.18 and 0.43.

(*E*/*Z*)-2-(4-bromo-7-methoxy-2,2-dimethyl-2,3-dihydro-1*H*-inden-1-ylidene)benzo[*b*]thiophen-3(2*H*)-one (20c)[159]

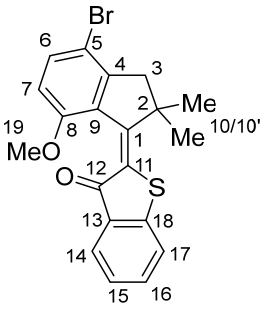

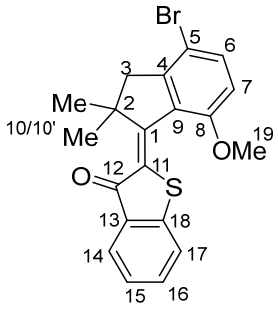

Two separate Schlenk flasks under an argon atmosphere were charged individually with compound **16c** (353 mg, 1.31 mmol, 1.0 equiv.) in anhydrous CH_2Cl_2 (1.00 mL, 2.2 M) in the first flask at 0 °C and compound **5** (217 mg, 1.44 mmol, 1.1 equiv.) in anhydrous CH_2Cl_2 (3.00 mL, 0.52 M) in the second flask at −78 °C. Boron trichloride (1.38 mL, 1.0 M in anhydrous CH_2Cl_2, 1.38 mmol, 1.1 equiv.) was added to the flask containing compound **5** and the resulting mixture was immediately taken up into the same syringe and transferred to the second flask containing compound **16c** at 0 °C. The reaction mixture was vigorously stirred for 90 min while warming up to 22 °C and then stopped by transferring to a saturated aqueous ammonium chloride solution (20 mL). The aqueous phase was extracted four times with CH_2Cl_2 (100 mL each), the combined organic layers were dried over anhydrous sodium sulfate, and the solvent was removed *in vacuo*. The crude product was purified by flash column chromatography (SiO2, *iso*-hexane:ethyl acetate, 96:4v/v), yielding compound **20c** as a red oil, which was used in the next synthetic step without further purification.

HR-MS (APPI, *m/z*) $[M+H]^+$ calc. for $[C_{20}H_{18}BrO_2S]^+$: 401.0205, found 401.0210.

TLC (SiO_2, *iso*-hexane:ethyl acetate, 95:5 v/v): R_f = 0.03 and 0.08.

(*E*/*Z*)-2-(4-(dimethylamino)-7-methoxy-2,2-dimethyl-2,3-dihydro-1*H*-inden-1-ylidene)benzo[*b*]thiophen-3(2*H*)-one (20e)[III]

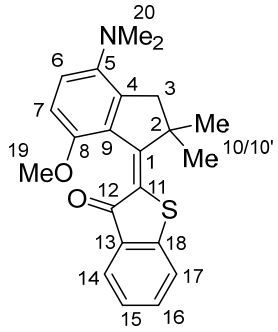

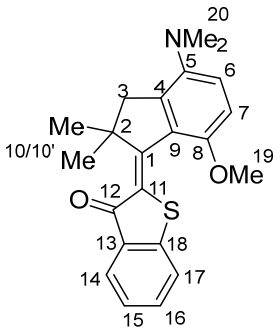

Two separate Schlenk flasks under an argon atmosphere were charged individually with compound **16e** (121 mg, 0.52 mmol, 1.0 equiv.) in anhydrous CH_2Cl_2 (0.400 mL, 2.2 M) in the first flask at 0 °C and compound **5** (85.6 mg, 0.57 mmol, 1.1 equiv.) in anhydrous CH_2Cl_2 (1.20 mL, 0.52 M) in the second flask at −78 °C. Boron trichloride (0.540 mL, 1.0 M in anhydrous CH_2Cl_2, 0.54 mmol, 1.1 equiv.) was added to the flask containing compound **5** and the resulting mixture was immediately taken up into the same syringe and transferred to the second flask containing compound **16e** at 0 °C. The reaction mixture was vigorously stirred for 90 min while warming up to 22 °C and then stopped by transferring to a saturated aqueous ammonium chloride solution (20 mL). The aqueous phase was extracted four times with CH_2Cl_2 (100 mL each), the combined organic layers were dried over anhydrous sodium sulfate, and the solvent was removed *in vacuo*. The crude product was purified by flash column chromatography (SiO2, *iso*-hexane:ethyl acetate, 9:1 v/v), yielding compound **20e** as a red oil, which was used in the next synthetic step without further purification.

HR-MS (APPI, *m/z*) $[M+H]^+$ calc. for $[C_{22}H_{24}NO_2S]^+$: 366.1522, found 366.1529.

TLC (SiO_2, *iso*-hexane:ethyl acetate, 9:1 v/v): $R_f = 0.15$ and 0.36.

(*E*/*Z*)-2-(2,2-dimethyl-2,3-dihydro-1*H*-inden-1-ylidene)benzo[*b*]thiophen-3(2*H*)-one (20f)[159]

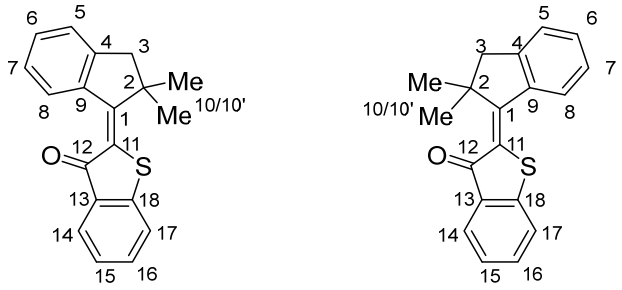

Two separate Schlenk flasks under an argon atmosphere were charged individually with compound **16f** (313 mg, 1.95 mmol, 1.0 equiv.) in anhydrous CH_2Cl_2 (0.800 mL, 2.4 M) in the first flask at 0 °C and compound **5** (295 mg, 1.95 mmol, 1.0 equiv.) in anhydrous CH_2Cl_2 (5.40 mL, 0.36 M) in the second flask at −78 °C. Boron trichloride (1.95 mL, 1.0 M in anhydrous CH_2Cl_2, 1.95 mmol, 1.0 equiv.) was added to the flask containing compound **5** and the resulting mixture was immediately taken up into the same syringe and transferred to the second flask containing compound **16f** at 0 °C. The reaction mixture was vigorously stirred for 90 min while warming up to 22 °C and then stopped by transferring to a saturated aqueous ammonium chloride solution (20 mL). The aqueous phase was extracted four times with CH_2Cl_2 (100 mL each), the combined organic layers were dried over anhydrous sodium sulfate, and the solvent was removed *in vacuo*. The crude product was purified by flash column chromatography (SiO2, *iso*-hexane:ethyl acetate, 99:1 v/v), yielding compound **20f** as a red oil, which was used in the next synthetic step without further purification.

HR-MS (APPI, *m/z*) $[M+H]^+$ calc. for $[C_{20}H_{16}O_2S]^+$: 309.0944, found 309.0952.

TLC (SiO_2, *iso*-hexane:ethyl acetate, 99:1 v/v): $R_f = 0.39$.

(*E*/*Z*)-2-(6-methoxy-2,2-dimethyl-2,3-dihydro-1*H*-inden-1-ylidene)benzo[*b*]thiophen-3(2*H*)-one (20g)[159]

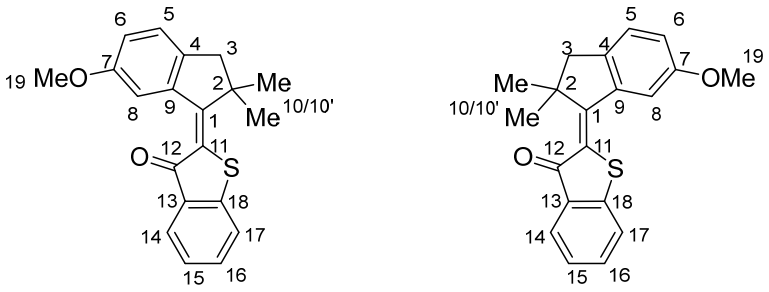

Two separate Schlenk flasks under an argon atmosphere were charged individually with compound **16g** (300 mg, 1.58 mmol, 1.0 equiv.) in anhydrous CH_2Cl_2 (0.800 mL, 2.0 M) in the first flask at 0 °C and compound **5** (237 mg, 1.58 mmol, 1.0 equiv.) in anhydrous CH_2Cl_2 (4.40 mL, 0.36 M) in the second flask at −78 °C. Boron trichloride (1.58 mL, 1.0 M in anhydrous CH_2Cl_2, 1.58 mmol, 1.0 equiv.) was added to the flask containing compound **5** and the resulting mixture was immediately taken up into the same syringe and transferred to the second flask containing compound **16g** at 0 °C. The reaction mixture was vigorously stirred for 90 min while warming up to 22 °C and then stopped by transferring to a saturated aqueous ammonium chloride solution (20 mL). The aqueous phase was extracted four times with CH_2Cl_2 (100 mL each), the combined organic layers were dried over anhydrous sodium sulfate, and the solvent was removed *in vacuo*. The crude product was purified by flash column chromatography (SiO2, *iso*-hexane:ethyl acetate, 95:5 v/v), yielding compound **20g** as a red oil, which was used in the next synthetic step without further purification.

HR-MS (APPI, *m/z*) $[M+H]^+$ calc. for $[C_{22}H_{24}NO_2S]^+$: 323.1100, found 323.1103.

TLC (SiO_2, *iso*-hexane:ethyl acetate, 95:5 v/v): R_f = 0.27 for *Z*-isomer and 0.37 for *E*-isomer.

(*E*/*Z*)-7-methoxy-2,2-dimethyl-1-(1-oxido-3-oxobenzo[*b*]thiophen-2(3*H*)-ylidene)-2,3-dihydro-1*H*-indene-4-carbonitrile (15a)

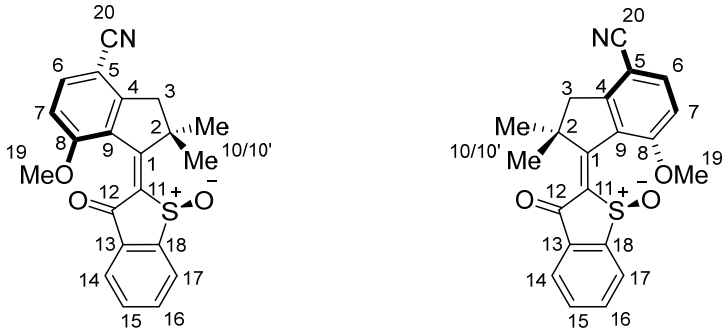

Compound **20a** (54.7 mg, 0.160 mmol, 1.0 equiv.) was dissolved in acetic acid (7.0 mL, 0.023 M of **20a**) and sodium perborate tetrahydrate (100 mg, 0.650 mmol, 4.0 equiv.) was added, subdivided into small portions. The mixture was stirred at 22 °C for 2 h until the reaction was stopped by cautiously transferring to a saturated aqueous sodium bicarbonate solution (100 mL). After extraction of the aqueous solution three times with ethyl acetate (100 mL each), the combined organic phases were washed with a saturated aqueous NaCl solution (100 mL), dried over anhydrous sodium sulfate, and the solvent was removed *in vacuo*. Purification of the crude product was achieved by flash column chromatography (SiO_2, *iso*-hexane:ethyl acetate, 1:1 v/v), yielding compound **15a** (23.4 mg, 64.0 µmol, 13% over two steps) as a yellow solid.

racemic *E*-(*S*)-(*P*)/*E*-(*R*)-(*M*) isomers:

^{1}H NMR (601 MHz, CD_2Cl_2): δ = 8.08 (d, $^3J_{HH}$ = 7.7 Hz, 1H, HC17), 8.00 (dd, $^3J_{HH}$ = 7.6 Hz, $^4J_{HH}$ = 1.2 Hz, 1H, HC14), 7.88 (ddd, $^3J_{HH}$ = 7.8, 7.3 Hz, $^4J_{HH}$ = 1.2 Hz, 1H, HC16), 7.76 (td, $^3J_{HH}$ = 7.5 Hz, 1H, HC15), 7.73 (d, $^3J_{HH}$ = 8.7 Hz, 1H, HC6), 6.91 (d, $^3J_{HH}$ = 8.7 Hz, 1H, HC7), 3.88 (s, 3H, H_3C19), 3.35 (d, ^2J = 15.9 Hz, 1H, HC3), 3.05 (d, ^2J = 15.9 Hz, 1H, H'-C3), 1.99 (s, 3H, H_3C10 or H_3C10'), 1.40 (s, 3H, H_3C10 or H_3C10') ppm.

^{13}C NMR (151 MHz, CD_2Cl_2): δ = 183.17 (C12), 166.62 (C1), 162.16 (C8), 154.45 (C4), 149.75 (C18), 138.34 (C11), 137.47 (C6), 135.66 (C13), 135.62 (C16), 132.89 (C15), 128.81 (C5), 127.32 (C17), 125.36 (C14), 117.56 (C20), 110.79 (C7), 101.46 (C9), 56.12 (C19), 52.89 (C2), 49.23 (C3), 28.12 (C10 or C10'), 26.04 (C10 or C10') ppm.

HR-MS (APPI, *m/z*) $[M+H]^+$ calc. for $[C_{21}H_{18}NO_3S]^+$: 364.1002, found 364.1008.

TLC (SiO_2, *iso*-hexane:ethyl acetate, 1:1 v/v): R_f = 0.04 for *Z*-isomer and 0.14 for *E*-isomer.

(*E*/*Z*)-2-(7-methoxy-2,2-dimethyl-2,3-dihydro-1*H*-inden-1-ylidene)benzo[*b*]thiophen-3(2*H*)-one 1-oxide (15b)

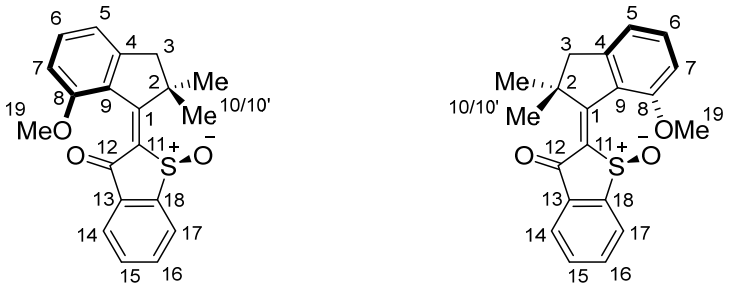

Compound **20b** (138 mg, 0.430 mmol, 1.0 equiv.) was dissolved in acetic acid (7.0 mL, 0.061 M of **20b**) and sodium perborate tetrahydrate (268 mg, 7.71 mmol, 4.0 equiv.) was added, subdivided into small portions. The mixture was stirred at 22 °C for 2 h until the reaction was stopped by cautiously transferring to a saturated aqueous sodium bicarbonate solution (100 mL). After extraction of the aqueous solution three times with ethyl acetate (100 mL each), the combined organic phases were washed with a saturated aqueous NaCl solution (100 mL), dried over anhydrous sodium sulfate, and the solvent was removed *in vacuo*. Purification of the crude product was achieved by flash column chromatography (SiO_2, *iso*-hexane:ethyl acetate, 4:1 to 2:3 v/v), yielding compound **15b** (80.8 mg, 0.240 mmol, 15% over two steps) as a yellow solid.

racemic *E*-(*S*)-(*P*)/*E*-(*R*)-(*M*) isomers:

^{1}H NMR (601 MHz, CD_2Cl_2): δ = 8.06 (d, $^3J_{HH}$ = 7.7 Hz, 1H, HC17), 7.99 (dd, $^3J_{HH}$ = 7.6 Hz, $^4J_{HH}$ = 1.3 Hz, 1H, HC14), 7.85 (td, $^3J_{HH}$ = 7.6 Hz, $^4J_{HH}$ = 1.3 Hz, 1H, HC16), 7.74 (t, $^3J_{HH}$ = 7.5 Hz, 1H, HC15), 7.45 (dd, $^3J_{HH}$ = 8.3, 7.4 Hz, 1H, HC6), 6.95 (d, $^3J_{HH}$ = 7.4 Hz, 1H, HC5), 6.81 (d, $^3J_{HH}$ = 8.3 Hz, 1H, HC7), 3.81 (s, 3H, H_3C19), 3.26 (d, $^2J_{HH}$ = 15.3 Hz, 1H, HC3), 2.84 (d, $^2J_{HH}$ = 15.2 Hz, 1H, H'-C3), 1.94 (s, 3H, H_3C10), 1.38 (s, 3H, H_3C10') ppm.

^{13}C NMR (151 MHz, CD_2Cl_2): δ = 183.12 (C12), 169.57 (C1), 159.44 (C8), 150.76 (C4), 149.50 (C18), 139.89 (C11), 135.92 (C13), 135.08 (C16), 134.52 (C6), 132.63 (C15), 127.96 (C9), 127.13 (C17), 125.16 (C14), 117.31 (C5), 109.41 (C7), 55.38 (C19), 52.76 (C2), 49.98 (C3), 28.31 (C10 or C10'), 26.19 (C10 or C10') ppm.

HR-MS (APPI, *m/z*) $[M+H]^+$ calc. for $[C_{20}H_{19}O_3S]^+$: 339.1049, found 339.1052.

TLC (SiO_2, *iso*-hexane:ethyl acetate, 4:1 v/v): R_f = 0.07.

racemic *Z*-(*S*)-(*P*)/*Z*-(*R*)-(*M*) isomers:

^{1}H NMR (601 MHz, CD_2Cl_2): δ = 8.00 (dt, $^3J_{HH}$ = 7.7 Hz, $^5J_{HH}$ = 0.9 Hz, 1H, HC17), 7.96 (ddd, $^3J_{HH}$ = 7.7 Hz, $^4J_{HH}$ = 1.2 Hz, $^5J_{HH}$ = 0.7 Hz, 1H, HC14), 7.83 (ddd, $^3J_{HH}$ = 7.7, 7.3 Hz, $^4J_{HH}$ = 1.2 Hz, 1H, HC16), 7.72–7.66 (m, 1H, HC15), 7.52 (dd, $^3J_{HH}$ = 8.3, 7.4 Hz, 1H, HC6), 6.97 (ddt, $^3J_{HH}$ = 7.4 Hz, $^4J_{HH}$ = 1.5, 0.8 Hz, 1H, HC5), 6.90 (dd, $^3J_{HH}$ = 8.3 Hz, $^4J_{HH}$ = 1.0 Hz, 1H, HC7), 4.09 (s, 3H, H_3C19), 3.18 (d, $^2J_{HH}$ = 15.9 Hz, 1H, HC3), 2.86 (d, $^2J_{HH}$ = 15.9 Hz, 1H, H'C3), 1.53 (s, 3H, HC10), 1.52 (s, 3H, HC') ppm.

^{13}C NMR (151 MHz, CD_2Cl_2): δ = 185.19 (C12), 170.28 (C9), 157.83 (C8), 151.78 (C4), 150.75 (C18), 143.43 (C11), 136.17 (C13), 135.46 (C6), 135.41 (C17), 132.03 (C15), 126.60 (C16), 125.59 (C9), 124.74 (C14), 117.87 (C7), 109.27 (C5), 55.16 (C19), 52.21 (C2), 50.76 (C3), 28.25 (C10), 25.45 (C10') ppm.

HR-MS (APPI, *m/z*) $[M+H]^+$ calc. for $[C_{20}H_{19}O_3S]^+$: 339.1049, found 339.1052.

TLC (SiO_2, *iso*-hexane:ethyl acetate, 4:1 v/v): R_f = 0.02.

(*E*/*Z*)-2-(4-bromo-7-methoxy-2,2-dimethyl-2,3-dihydro-1*H*-inden-1-ylidene)benzo[*b*]thiophen-3(2*H*)-one 1-oxide (15c)

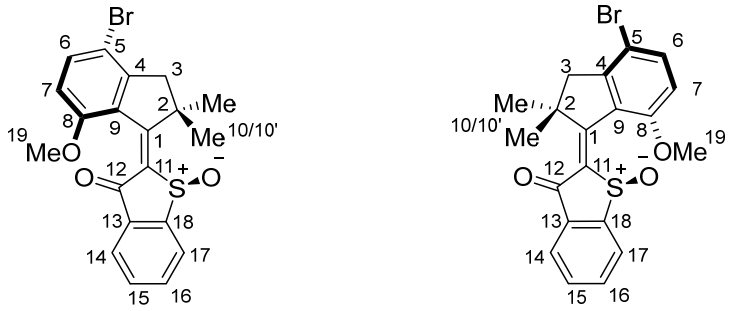

Compound **20c** (251 mg, 0.620 mmol, 1.0 equiv.) was dissolved in acetic acid (31.0 mL, 0.020 M of **20c**) and sodium perborate tetrahydrate (388 mg, 2.50 mmol, 4.0 equiv.) was added, subdivided into small portions. The mixture was stirred at 22 °C for 2 h until the reaction was stopped by cautiously transferring to a saturated aqueous sodium bicarbonate solution (100 mL). After extraction of the aqueous solution three times with ethyl acetate (100 mL each), the combined organic phases were washed with a saturated aqueous NaCl solution (100 mL), dried over anhydrous sodium sulfate, and the solvent was removed *in vacuo*. Purification of the crude product was achieved by flash column chromatography (SiO_2, *iso*-hexane:ethyl acetate, 1:1 v/v), yielding compound **15c** (152 mg, 0.364 mmol, 28% over two steps) as a yellow solid.

racemic *E*-(*S*)-(*P*)/*E*-(*R*)-(*M*) isomers:

^{1}H NMR (601 MHz, CD_2Cl_2): δ = 8.07 (d, $^3J_{HH}$ = 7.7 Hz, 1H, HC17), 7.99 (t, $^3J_{HH}$ = 7.6 Hz, 1H, HC14), 7.85 (td, $^3J_{HH}$ = 7.5 Hz, 2H, HC16), 7.74 (td, $^3J_{HH}$ = 7.5 Hz, 1H, HC15), 7.57 (d, $^3J_{HH}$ = 8.8 Hz, 1H, HC6), 6.75 (dd, $^3J_{HH}$ = 8.8 Hz, 1H, HC7), 3.81 (s, 3H, H_3C19), 3.19 (d, $^2J_{HH}$ = 15.7 Hz, 1H, HC3), 2.90 (d, $^2J_{HH}$ = 15.5 Hz, 2H, H'-C3), 1.97 (s, 3H, H_3C10), 1.40 (s, 3H, H_3C10') ppm.

^{13}C NMR (151 MHz, CD_2Cl_2): δ = 185.19 (C12), 168.52 (C1), 158.70 (C8), 149.60 (C18), 149.46 (C4), 141.21 (C11), 136.44 (C6), 135.81 (C13), 135.37 (C16), 132.82 (C15), 129.31 (C9), 127.23 (C17), 111.78 (C7), 110.35 (C5), 55.75 (C19), 52.04 (C2), 51.09 (C3), 28.32 (C10 or C10'), 26.10 (C10 or C10') ppm.

HR-MS (APPI, *m/z*) $[M+H]^+$ calc. for $[C_{20}H_{17}BrO_3S]^+$: 417.0155, found 417.0159.

TLC (SiO_2, *iso*-hexane:ethyl acetate, 1:1 v/v): R_f = 0.12 for *Z*-isomer and 0.27 for *E*-isomer.

(*E*/*Z*)-2-(4-bromo-7-methoxy-2,2-dimethyl-2,3-dihydro-1*H*-inden-1-ylidene)benzo[*b*]thiophen-3(2*H*)-one 1-oxide (15e)[III]

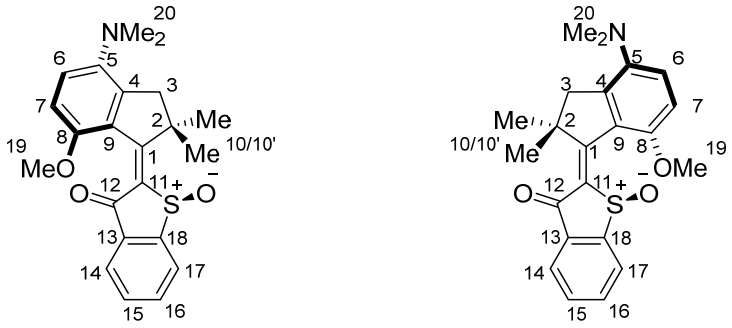

Compound **20e** (35.0 mg, 96.0 mmol, 1.0 equiv.) was dissolved in acetic acid (4.80 mL, 0.020 M of **20e**) and sodium perborate tetrahydrate (59.1 mg, 0.384 mmol, 4.0 equiv.) was added, subdivided into small portions. The mixture was stirred at 22 °C for 2 h until the reaction was stopped by cautiously transferring to a saturated aqueous sodium bicarbonate solution (100 mL). After extraction of the aqueous solution three times with ethyl acetate (20 mL each), the combined organic phases were washed with a saturated aqueous NaCl solution (10 mL), dried over anhydrous sodium sulfate, and the solvent was removed *in vacuo*. Purification of the crude product was achieved by flash column chromatography (SF5 C18, methanol:water, 75:25 v:v), yielding compound **15e** (13.8 mg, 36.0 µmol, 28% over two steps) as a yellow solid. Separation into *E*- and *Z*-isomers was achieved on a CHIRALPAK® ID column (CH_2Cl_2:methanol, 100:0 to 70:30 v:v, at 40 °C).

racemic *E*-(*S*)-(*P*)/*E*-(*R*)-(*M*) isomers:

^{1}H NMR (601 MHz, CD_2Cl_2): δ = 8.22 (d, $^{3}J_{HH}$ = 9.2 Hz, 1H, HC6), 8.08 (d, $^{3}J_{HH}$ = 7.8 Hz, 1H, HC17), 7.99 (d, $^{3}J_{HH}$ = 7.6 Hz, 1H, HC14), 7.87 (td, $^{3}J_{HH}$ = 7.6 Hz, 1.2, 1H, HC16), 7.75 (td, $^{3}J_{HH}$ = 7.5 Hz, 1.0, 1H, HC15), 6.88 (d, $^{3}J_{HH}$ = 9.2 Hz, 1H, HC7), 3.83 (s, 3H, HC19), 3.59 (s, 3H, H_3C20 or H_3C20'), 3.55 (s, 3H, H_3C20 or H_3C20'), 3.47 (s, 2H, H_2C3), 1.99 (s, 3H, H_3C10 or H_3C10'), 1.39 (s, 3H, H_3C10 or H_3C10') ppm.

^{13}C NMR (151 MHz, CD_2Cl_2): δ = 183.40 (C12), 167.00 (C1), 159.12 (C8), 149.63 (C18), 144.58 (C5), 141.44 (C11), 141.07 (C4), 135.77 (C13), 135.48 (C16), 132.82 (C15), 129.63 (C9), 127.26 (C17), 126.18 (C6), 125.30 (C14), 109.94 (C7), 62.87 (C20 or C20'), 62.23 (C20 or C20'), 55.85 (C19), 52.74 (C2), 51.13 (C3), 28.05 (C10 or C10'), 25.93 (C10 or C10').

HR-MS (APPI, *m/z*) $[M+H]^+$ calc. for $[C_{22}H_{24}NO_3S]^+$: 382.1471, found 382.1476.

TLC (SiO_2, *iso*-hexane:ethyl acetate, 1:1 v/v): R_f = 0.36.

racemic *Z*-(*S*)-(*P*)/*Z*-(*R*)-(*M*) isomers:

^{1}H NMR (601 MHz, CD_2Cl_2): δ = 8.32 (d, $^{3}J_{HH}$ = 9.1 Hz, 1H, HC6), 8.00 (dt, $^{3}J_{HH}$ = 7.6 Hz, $^{4}J_{HH}$ = 0.9 Hz, 1H, HC17), 7.97 (dt, $^{3}J_{HH}$ = 7.6 Hz, $^{4}J_{HH}$ = 1.0 Hz, 1H, HC14), 7.85 (td, $^{3}J_{HH}$ = 7.5 Hz, $^{4}J_{HH}$ = 1.2 Hz, 1H, HC16), 7.71 (td, $^{3}J_{HH}$ = 7.5 Hz, $^{4}J_{HH}$ = 1.0 Hz, 1H, HC15), 6.98 (d, $^{3}J_{HH}$ = 9.1 Hz, 1H, HC7), 4.11 (s, 3H, HC19), 3.58 (s, 3H, H_3C20 or H_3C20'), 3.54 (s, 3H, H_3C20 or H_3C20'), 3.44 (d, $^{2}J_{HH}$ = 16.1 Hz, 1H, HC3), 3.35 (d, $^{2}J_{HH}$ = 16.1 Hz, 1H, H'C3), 1.53 (s, 3H, H_3C10), 1.52 (s, 3H, H_3C10') ppm.

^{13}C NMR (151 MHz, CD_2Cl_2): δ = 185.13 (C12), 167.00 (C1), 157.62 (C8), 150.69 (C18), 145.27 (C5), 141.85 (C4), 136.10 (C13), 135.80 (C16), 132.24 (C15), 127.56 (C9), 127.21 (C11), 126.65 (C17), 124.84 (C14), 109.91 (C7), 62.42 (C20 or C21), 61.80 (C20 or C21), 55.72 (C19), 52.43 (C2), 51.70 (C3), 28.18 (C10 or C10'), 25.37 (C10 or C10') ppm.

HR-MS (APPI, *m/z*) $[M+H]^+$ calc. for $[C_{22}H_{24}NO_3S]^+$: 382.1471, found 382.1476.

TLC (SiO_2, *iso*-hexane:ethyl acetate, 9:1 v/v): R_f = 0.15.

(*E*/*Z*)-7-methoxy-2,2-dimethyl-1-(1-oxido-3-oxobenzo[*b*]thiophen-2(3*H*)-ylidene)-2,3-dihydro-1*H*-indene-4-carbonitrile (15f)

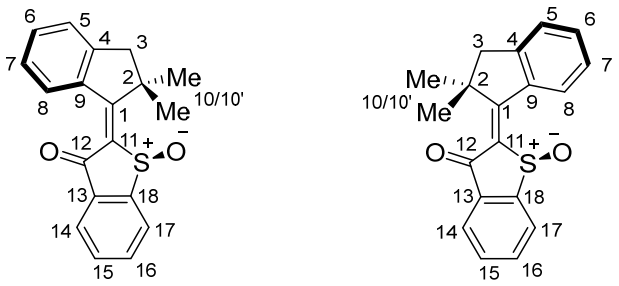

Compound **20f** (108 mg, 0.370 mmol, 1.0 equiv.) was dissolved in acetic acid (17.0 mL, 0.022 M of **20f**) and sodium perborate tetrahydrate (226 mg, 1.47 mmol, 4.0 equiv.) was added, subdivided into small portions. The mixture was stirred at 22 °C for 2 h until the reaction was stopped by cautiously transferring to a saturated aqueous sodium bicarbonate solution (100 mL). After extraction of the aqueous solution three times with ethyl acetate (100 mL each), the combined organic phases were washed with a saturated aqueous NaCl solution (100 mL), dried over anhydrous sodium sulfate, and the solvent was removed *in vacuo*. Purification of the crude product was achieved by flash column chromatography (SiO_2, *iso*-hexane:ethyl acetate, 9:1 to 1:1 v/v), yielding compound **15f** (114 mg, 0.370 mmol, 34% over two steps) as a yellow solid.

racemic *E*-(*S*)-(*P*)/*E*-(*R*)-(*M*) isomers:

^{1}H NMR (601 MHz, CD_2Cl_2): δ = 8.44–8.38 (m, 2H, HC8), 8.05 (dt, $^3J_{HH}$ = 7.7 Hz, $^5J_{HH}$ = 0.9 Hz, 2H, HC17), 8.02 (ddd, $^3J_{HH}$ = 7.7 Hz, $^4J_{HH}$ = 1.2 Hz, $^5J_{HH}$ = 0.7 Hz, 2H, HC14), 7.91–7.86 (m, 2H, HC16), 7.77 (tt, $^3J_{HH}$ = 7.4 Hz, $^4J_{HH}$ = 1.0 Hz, 2H, HC15), 7.48 (td, $^3J_{HH}$ = 7.4 Hz, $^4J_{HH}$ = 1.1 Hz, 1H, HC6), 7.38 (ddt, $^3J_{HH}$ = 7.6 Hz, $^4J_{HH}$ = 1.2 Hz, $^5J_{HH}$ = 0.6 Hz, 2H, HC5), 7.32–7.27 (m, 1H, HC7), 3.24 (d, $^2J_{HH}$ = 15.5 Hz, 2H, HC3), 2.91 (dd, $^2J_{HH}$ = 15.4, 0.7, 3H, H'C3), 1.94 (s, 3H, HC10 or HC10'), 1.50–1.47 (m, 3H, HC10 or HC10'). ppm.

^{13}C NMR (151 MHz, CD_2Cl_2): δ = 184.61 (C12), 176.84 (C1), 150.64 (C4), 148.31 (C18), 137.75 (C9), 135.91 (C16), 135.12 (C13), 133.54 (C6), 133.03 (C15), 131.26 (C8), 127.19 (C11), 126.28 (C7), 126.10 (C14), 125.45 (C5), 52.09 (C2), 50.13 (C3), 29.34 (C10 or C10'), 26.78 (C10 or C10') ppm.

HR-MS (APPI, *m/z*) $[M+H]^+$ calc. for $[C_{21}H_{18}NO_3S]^+$: 309.0944, found 309.0943.

TLC (SiO_2, *iso*-hexane:ethyl acetate, 1:1 v/v): R_f = 0.33.

racemic *Z*-(*S*)-(*P*)/*Z*-(*R*)-(*M*) isomers:

^{1}H NMR (601 MHz, CD_2Cl_2): δ = 8.52 (dt, $^{3}J_{HH}$ = 7.9 Hz, $^{5}J_{HH}$ = 0.9 Hz, 1H, HC8), 8.05 (dt, $^{3}J_{HH}$ = 7.7 Hz, $^{5}J_{HH}$ = 0.9, 1H, HC17), 8.01 (ddd, $^{3}J_{HH}$ = 7.6 Hz, $^{4}J_{HH}$ = 1.2 Hz, $^{5}J_{HH}$ = 0.7 Hz, 1H, HC14), 7.87 (td, $^{3}J_{HH}$ = 7.5 Hz, $^{4}J_{HH}$ = 1.2 Hz, 1H, HC16), 7.77 (td, $^{3}J_{HH}$ = 7.5 Hz, $^{3}J_{HH}$ = 1.0 Hz, 1H, HC15), 7.55 (td, $^{3}J_{HH}$ = 7.4 Hz, $^{4}J_{HH}$ = 1.0 Hz, 1H, HC6), 7.50–7.44 (m, 1H, HC7), 7.41 (dp, $^{3}J_{HH}$ = 7.6 Hz, $^{5}J_{HH}$ = 1.1 Hz, 1H, HC5), 3.22–3.04 (m, 2H, HC3), 1.68 (s, 3H, H_3C10 or H_3C10'), 1.57 (s, 3H, H_3C10 or H_3C10'). ppm.

^{13}C NMR (151 MHz, CD_2Cl_2): δ = 185.97 (C12), 177.62 (C1), 151.97 (C4), 148.78 (C18), 137.74 (C9), 137.06 (C11), 135.81 (C13), 135.71 (C16), 133.74 (C6), 133.12 (C15), 130.69 (C8), 127.95 (C7), 127.36 (C17), 126.09 (C5), 126.02 (C14), 51.23 (C3), 49.93 (C2), 26.47 (C10 or C10'), 25.99 (C10 or C10') ppm.

HR-MS (APPI, *m/z*) $[M+H]^+$ calc. for $[C_{21}H_{18}NO_3S]^+$: 309.0944, found 309.0944.

TLC (SiO_2, *iso*-hexane:ethyl acetate, 1:1 v/v): R_f = 0.28.

(*E*/*Z*)-7-methoxy-2,2-dimethyl-1-(1-oxido-3-oxobenzo[*b*]thiophen-2(3*H*)-ylidene)-2,3-dihydro-1*H*-indene-4-carbonitrile (15g)

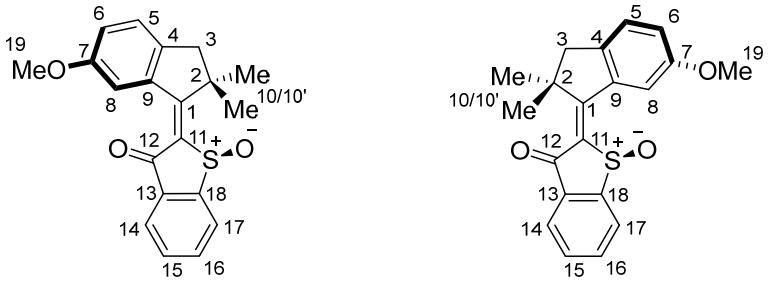

Compound **20g** (102 mg, 0.317 mmol, 1.0 equiv.) was dissolved in acetic acid (16.0 mL, 0.020 M of **20g**) and sodium perborate tetrahydrate (108 mg, 1.39 mmol, 4.5 equiv.) was added, subdivided into small portions. The mixture was stirred at 22 °C for 4 h until the reaction was stopped by cautiously transferring to a saturated aqueous sodium bicarbonate solution (100 mL). After extraction of the aqueous solution three times with ethyl acetate (100 mL each), the combined organic phases were washed with a saturated aqueous NaCl solution (100 mL), dried over anhydrous sodium sulfate, and the solvent was removed *in vacuo*. Purification of crude product was achieved by flash column chromatography (SiO_2, *iso*-hexane:ethyl acetate, 1:1 v/v), yielding compound **15g** (98.7 mg, 0.291 mmol, 94% over two steps) as a yellow solid.

racemic *E*-(*S*)-(*P*)/*E*-(*R*)-(*M*) isomers:

^{1}H NMR (400 MHz, CD_2Cl_2): δ = 8.06–8.03 (m, 1H, HC17), 8.03–8.00 (m, 1H, HC14), 7.99 (d, $^{4}J_{HH}$ = 2.5 Hz, 1H, HC8), 7.91–7.85 (m, 1H, HC16), 7.76 (td, $^{3}J_{HH}$ = 7.5 Hz, $^{4}J_{HH}$ = 1.1 Hz, 1H, HC15), 7.27 (ddt, $^{3}J_{HH}$ = 8.4 Hz, $^{4}J_{HH}$ = 1.2 Hz, $^{5}J_{HH}$ = 0.6 Hz, 1H, HC5), 7.08 (dd, $^{3}J_{HH}$ = 8.3 Hz, $^{4}J_{HH}$ = 2.5 Hz, 1H, HC6), 3.84 (s, 3H, HC19), 3.18 (d, $^{2}J_{HH}$ = 15.3 Hz, 1H, HC3), 2.84 (d, $^{2}J_{HH}$ = 15.3 Hz, 1H, H'C3), 1.92 (s, 3H, HC10 or HC10'), 1.50 (s, 3H, HC10 or HC10') ppm.

^{13}C NMR (126 MHz, CD_2Cl_2): δ = 186.16 (C12), 178.16 (C1), 159.76 (C7), 148.65 (C18), 144.54 (C4), 138.83 (C9), 136.55 (C11), 135.71 (C13), 135.69 (C16), 133.09 (C15), 127.30 (C17), 126.53 (C5), 125.99 (C14), 121.93 (C6), 113.48 (C8), 56.07 (C19), 50.58 (C3), 50.52 (C2), 26.32 (C10), 26.16 (C10') ppm.

HR-MS (APPI, *m/z*) $[M+H]^+$ calc. for $[C_{20}H_{19}O_3S]^+$: 339.1049, found 339.1049.

racemic *Z*-(*S*)-(*P*)/*Z*-(*R*)-(*M*) isomers:

^{1}H NMR (500 MHz, CD_2Cl_2): δ = 8.08 (d, $^{4}J_{HH}$ = 2.4 Hz, 1H, HC8), 8.05 (dt, $^{3}J_{HH}$ = 7.8 Hz, $^{5}J_{HH}$ = 0.9 Hz, 1H, HC17), 8.00 (ddd, $^{3}J_{HH}$ = 7.7 Hz, $^{4}J_{HH}$ = 1.3, $^{5}J_{HH}$ = 0.7 Hz, 1H, HC14), 7.86 (td, $^{3}J_{HH}$ = 7.5 Hz, $^{4}J_{HH}$ = 1.2 Hz, 1H, HC16), 7.79–7.74 (m, 1H, HC15), 7.29 (dq, $^{3}J_{HH}$ = 8.4 Hz, $^{5}J_{HH}$ = 0.9 Hz, 1H, HC5), 7.15 (dd, $^{3}J_{HH}$ = 8.3 Hz, $^{4}J_{HH}$ = 2.4, 1H, HC6), 3.92 (s, 3H, HC19), 3.09 (d, $^{2}J_{HH}$ = 16.2 Hz, 1H, HC3), 3.01 (d, $^{2}J_{HH}$ = 16.3 Hz, 1H, H'C3), 1.66 (s, 3H, HC10 or HC10'), 1.56 (s, 3H, HC10 or HC10') ppm.

^{13}C NMR (126 MHz, CD_2Cl_2): δ = 186.16 (C12), 178.16 (C1), 159.76 (C7), 148.65 (C18), 144.54 (C4), 138.83 (C9), 136.55 (C11), 135.71 (C13), 135.69 (C16), 133.09 (C15), 127.30 (C17), 126.53 (C5), 125.99 (C14), 121.93 (C6), 113.48 (C8), 56.07 (C19), 50.58 (C3), 50.52 (C2), 26.32 (C10), 26.16 (C10') ppm.

HR-MS (APPI, *m/z*) $[M+H]^+$ calc. for $[C_{20}H_{19}O_3S]^+$: 339.1049, found 339.1055.

8.5. Synthesis of compounds from chapter 6

8.5.1. Macrocyclic HTI 33

Macrocyclic HTI machine **33** was constructed combining tetraethylene glycol chain **34** with indanone **35** and benzothiophenone **17**, furnishing macrocycle **33** as shown in Figure 228. Commercially available 6-hydroxy indanone **47**, tetraethylene glycol **36**, and 4-bromo-3,5-dimethylphenol **40** were utilized as starting structures. Building blocks **34** and **17** were prepared according to a previous report and **35** was synthesized through a modification thereof.[2]

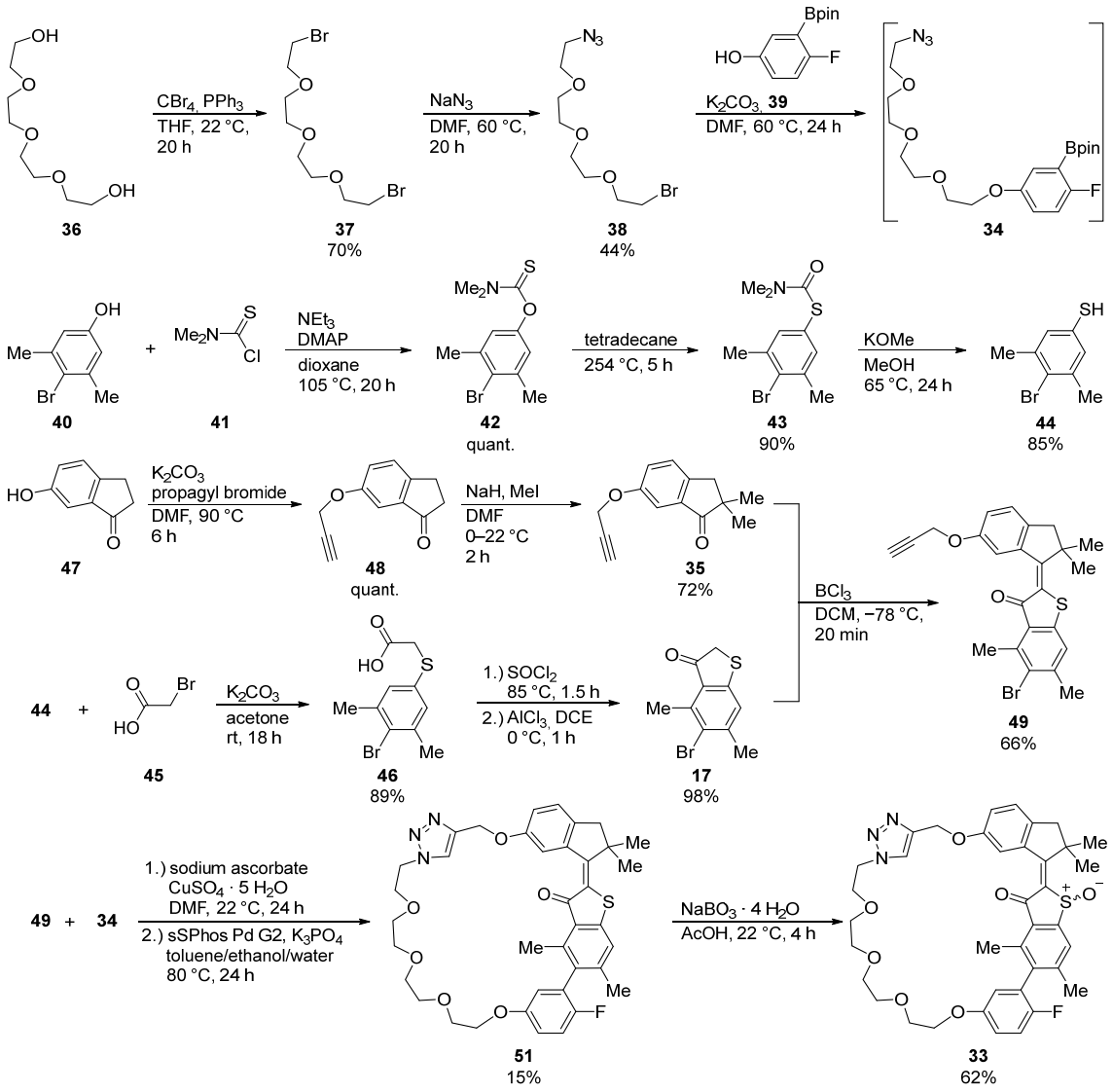

Figure 228 Overview of 14-step synthesis of macrocyclic molecular HTI-based machine **33** starting from commercially available starting materials 6-hydroxy indanone **47**, tetraethylene glycol **36** and 4-bromo-3,5-dimethylphenol **40**. Building blocks **34**, **35** and **17** were prepared individually to assemble HTI **33** in a highly modular fashion.

All molecules successfully synthesized previously and described in literature were only characterized using ^{1}H NMR and HRMS mass spectrometry.[158,159]

_O_-(4-bromo-3,5-dimethylphenyl) dimethylcarbamothioate (42)[159]

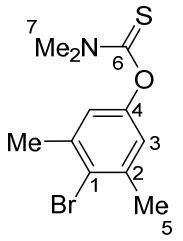

Commercially available 4-Bromo-3,5-dimethylphenol **40** (10.0 g, 49.7 mmol, 1.0 equiv.), dimethylthiocarbamoyl chloride **41** (7.69 g, 62.1 mmol, 1.25 equiv.), 4-dimethylaminopyridine (613 mg, 5.02 mmol, 0.1 equiv.) and triethylamine (13.8 mL, 99.4 mmol, 2.0 equiv.) were dissolved in dioxane (200 mL) and stirred at 105 °C for 20 h. The reaction was stopped by addition of a saturated aqueous ammonium chloride solution (400 mL) and the aqueous solution extracted three times with ethyl acetate (200 mL each). The combined organic phases were washed with a saturated aqueous NaCl solution (200 mL), dried over anhydrous sodium sulfate, and the solvent was removed *in vacuo*. Purification of the crude product was achieved by flash column chromatography (SiO_2, *iso*-hexane:ethyl acetate, 19:1), yielding compound **42** (14.3 g, 49.6 mmol, quantitative conversion) as colorless crystals.

^{1}H NMR (400 MHz, CD_2Cl_2): δ = 6.82 (dd, $^{4}J_{HH}$ = 1.4, 0.7 Hz, 2H, HC3), 3.41 (s, 3H, H_3C7), 3.30 (s, 3H, H_3C7), 2.41 (t, $^{4}J_{HH}$ = 0.7 Hz, 6H, H_3C5) ppm.

HR-MS (APPI, *m/z*) $[M+H]^+$ calc. for $[C_{11}H_{15}BrNOS]^+$: 288.0052, found 288.0045.

_S_-(4-bromo-3,5-dimethylphenyl) dimethylcarbamothioate (43)[159]

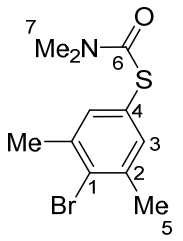

Compound **42** (15.6 g, 54.3 mmol) was suspended in tetradecane (113 mL, 0.48 M) and heated at 200 °C for 5 h in a sand bath. The crude product was purified directly, before completely cooling down to room temperature, by flash column chromatography (SiO_2, *iso*-hexane:ethyl acetate, 9:1 v/v), yielding compound **43** (14.1 g, 48.9 mmol, 90%) as a slightly yellow solid.

^{1}H NMR (400 MHz, CD_2Cl_2): δ = 7.20 (t, $^4J_{HH}$ = 0.7 Hz, 2H, HC3), 3.01 (m, 6H, H_3C7), 2.42 (d, $^4J_{HH}$ = 0.7 Hz, 6H, H_3C5) ppm.

HR-MS (APPI, *m/z*) $[M+H]^+$ calc. for $[C_{11}H_{15}BrNOS]^+$: 288.0052, found 288.0054.

4-bromo-3,5-dimethylbenzenethiol (44)[159]

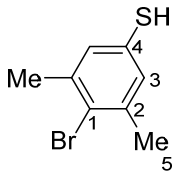

Compound **43** (5.83 g, 20.2 mmol, 1.0 equiv.) and potassium methoxide (1.64 g, 22.2 mmol, 1.1 equiv.) were dissolved in dry methanol (50.0 mL, 0.40 M) and heated at 70 °C for 17 h. The reaction was stopped by addition of a saturated aqueous ammonium chloride solution (50 mL) and the aqueous solution was extracted three times with ethyl acetate (100 mL each). The combined organic phases were washed with a saturated aqueous NaCl solution (100 mL), dried over anhydrous sodium sulfate and the solvent was removed *in vacuo*. Purification of crude product was achieved by flash column chromatography (SiO_2, *iso*-hexane), yielding compound **44** (3.71 g, 17.1 mmol, 85%) as a colorless liquid, containing the disulfide dimer as a minor byproduct.

^{1}H NMR (400 MHz, CD_2Cl_2): δ = 7.01 (t, $^4J_{HH}$ = 0.7 Hz, 2H, HC3), 3.45 (s, 1H, H-S), 2.35 (d, $^4J_{HH}$ = 0.7 Hz, 6H, H_3C5) ppm.

HR-MS (APPI, *m/z*) $[M+H]^+$ calc. for $[C_8H_{10}BrS]^+$: 216.9681, found 216.9677.

2-((4-bromo-3,5-dimethylphenyl)thio)acetic acid (46)[159]

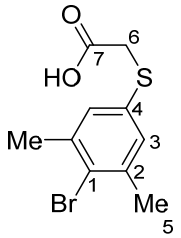

4-bromo-3,5-dimethylbenzenethiol **44** (3.71 g, 17.1 mmol, 1.0 equiv.) was dissolved in acetone (50.0 mL, 0.34 M), bromoacetic acid **45** (2.66 g, 18.8 mmol, 1.1 equiv.) and potassium carbonate (7.09 g, 51.3 mmol, 3.0 equiv.) were added, and the suspension was stirred at 22 °C for 18 h. The reaction mixture was stopped by transferring to an aqueous 2.0 M HCl solution (100 mL) and the aqueous solution was extracted three times with ethyl acetate (100 mL each). The combined organic phases were

washed with a saturated aqueous NaCl solution (100 mL), dried over anhydrous sodium sulfate and the solvent was removed *in vacuo*, yielding compound **46** (4.17 g, 15.2 mmol, 89%) as colorless crystals.

^{1}H NMR (400 MHz, CD_2Cl_2): δ = 7.13 (dd, J_{HH} = 1.3, $^4J_{HH}$ = 0.7 Hz, 2H, HC3), 3.67 (s, 2H, H_2C6), 2.38 (d, $^4J_{HH}$ = 0.7 Hz, 6H, H_3C5) ppm.

HR-MS (APPI, *m/z*) $[M]^+$ calc. for $[C_{10}H_{11}BrO_2S]^+$: 273.9963, found 273.9661.

5-bromo-4,6-dimethylbenzo[*b*]thiophen-3(2*H*)-one (17)[159]

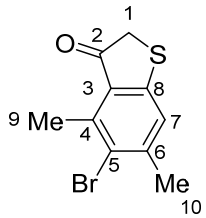

Acetic acid substituted thiol **46** (1.00 g, 3.74 mmol, 1.0 equiv.) was dissolved in thionyl chloride (2.44 mL, 33.7 mmol, 9.0 equiv.) and heated at 80 °C for 4 h. The remaining thionyl chloride was removed *in vacuo* and the residual solid dissolved in 1,2-dichloroethane (10 mL, 0.37 M) before cooling to 0 °C with an ice bath. Then $AlCl_3$ (524 mg, 3.93 mmol, 1.05 equiv.) was added and the suspension stirred for 30 min at 0 °C. After the ice bath was removed, stirring continued for 30 min at 22 °C before the reaction mixture was stopped by transferring to a 2.0 M aqueous HCl/ice mixture (100 mL). The aqueous phase was extracted three times with CH_2Cl_2 (100 mL each), the combined organic layers were dried over anhydrous sodium sulfate, and the solvent was removed *in vacuo*, yielding compound **17** (938 mg, 3.67 mmol, 98%) as a red solid.

^{1}H NMR (400 MHz, CD_2Cl_2): δ = 7.19 (s, 1H, HC7), 3.79 (s, 2H, H_2C1), 2.74 (s, 3H, H_3C9), 2.46 (s, 3H, H_3C10) ppm.

HR-MS (EI^+, *m/z*) $[M]^+$ calc. for $[C_{10}H_9BrOS]^+$: 255.9557, found: 255.9548.

6-(prop-2-yn-1-yloxy)-2,3-dihydro-1*H*-inden-1-one (48)[159]

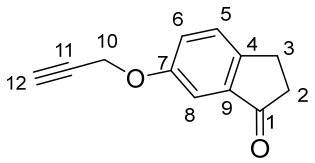

Commercially available 6-hydroxy-1-indanone **47** (909 mg, 6.13 mmol, 1.0 equiv.) was mixed in *N*,*N*-dimethylformamide (41.0 mL, 0.15 M) with potassium carbonate (3.39 g, 24.5 mmol, 4.0 equiv.) and propargyl bromide (0.700 mL, 80% in toluene, 6.13 mmol, 1.0 equiv.). After stirring the mixture for 6 h at 90 °C the reaction was stopped by transferring to water (100 mL). The aqueous solution was extracted three times with ethyl acetate (100 mL each), the combined organic phases washed four times with water (30 mL each, to remove residual *N*,*N*-dimethylformamide), a saturated aqueous NaCl solution (100 mL), and dried over anhydrous sodium sulfate. Removal of the solvent *in vacuo* yielded compound **48** as a colorless liquid (1.12 g, 6.02 mmol, quantitative conversion), which was used in the next synthetic step without further purification.

^{1}H NMR (400 MHz, CD_2Cl_2): δ = 7.45–7.39 (m, 1H, HC8), 7.28–7.20 (m, 2H, HC5, HC6), 4.74 (d, $^4J_{HH}$ = 2.4 Hz, 2H, H_2C10), 3.12–3.03 (m, 2H, H_2C3), 2.71–2.64 (m, 2H, H_2C2), 2.58 (t, $^4J_{HH}$ = 2.4 Hz, 1H, HC12) ppm.

^{13}C NMR (101 MHz, CD_2Cl_2): δ = 206.65 (C1), 157.61 (C7), 149.18 (C9), 138.70 (C4), 128.06 (C8), 124.36 (C6), 106.78 (C5), 78.58 (C11), 75.99 (C12), 56.55 (10), 37.36 (C2), 25.51 (C3) ppm.

HR-MS (EI^+, *m*/*z*) $[M]^+$ calc. for $[C_{12}H_{10}O_2]^+$: 186.0675, found: 186.0674.

IR: $\tilde{\nu}$ = 3922 (w), 3908 (w), 3259 (s), 3245 (s), 3060 (m), 2958 (w), 2924 (s), 2884 (w) 2860 (w), 2114 (s), 2040 (w), 1888 (m), 1796 (w), 1690 (s), 1613 (m), 1583 (w), 1485 (s), 1442 (s), 1397 (m), 1374 (m), 1325 (m), 1275 (s), 1242 (s), 1211 (s), 1167 (s), 1118 (w), 1018 (s), 925 (m), 903 (m), 882 (m), 829 (s), 769 (m), 710 (m), 696 (s), 668 (s), 629 (m), 590 (w), 556 (s), 498 (s), 462 (w) cm^{-1}.

TLC (SiO_2, *iso*-hexane:ethyl acetate, 12:1 v/v): R_f = 0.10.

2,2-dimethyl-6-(prop-2-yn-1-yloxy)-2,3-dihydro-1*H*-inden-1-one (35)[159]

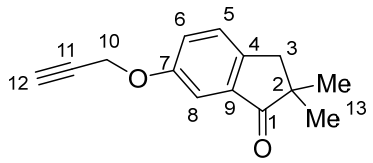

To a solution of compound **48** (627 mg, 3.37 mmol, 1.0 equiv.) in anhydrous *N*,*N*-dimethylformamide (6.00 mL, 0.56 M) at 0 °C, sodium hydride (344 mg (60% in mineral oil), 8.41 mmol, 2.5 equiv.) was added and the resulting suspension stirred for 20 min at 0 °C. Then iodomethane (0.520 mL, 8.41 mmol, 2.5 equiv.) was added dropwise and the reaction mixture was stirred for 2 h at 22 °C. After addition of a saturated aqueous ammonium chloride solution (25 mL) the aqueous solution was extracted three times with ethyl acetate (50 mL each). The combined organic phases were washed four times with water (20 mL each, to remove residual *N*,*N*-dimethylformamide), twice with a saturated aqueous NaCl solution (30 mL each), dried over anhydrous sodium sulfate, and the solvent was removed *in vacuo*. Purification of the crude product was achieved by flash column chromatography (SiO_2, *iso*-hexane:ethyl acetate, 12:1 v/v), yielding compound **35** (521 mg, 2.43 mmol, 72%) as a colorless liquid.

^{1}H NMR (400 MHz, CD_2Cl_2): δ = 7.41–7.33 (m, 1H, HC5), 7.28–7.20 (m, 2H, HC6, HC8), 4.74 (d, $^4J_{HH}$ = 2.4 Hz, 2H, H_2C10), 2.96–2.90 (m, 2H, H_2C3), 2.59 (t, $^4J_{HH}$ = 2.4 Hz, 1H, HC12), 1.20 (s, 6H, H_3C13 and H_3C13') ppm.

^{13}C NMR (101 MHz, CD_2Cl_2): δ = 211.18 (C1), 157.68 (C7), 146.22 (C4), 136.90 (C9), 128.05 (C5), 124.61 (C6), 107.32 (C8), 78.59 (C11), 75.98 (C12), 56.50 (C10), 46.59 (C2), 42.46 (C3), 25.44 (C13) ppm.

HR-MS (EI^+, *m*/*z*) $[M]^+$ calc. for $[C_{14}H_{14}O_2]^+$: 214.0988, found: 214.0986.

IR: $\tilde{\nu}$ = 3367 (w), 3288 (s), 3259 (s), 3061 (w), 3960 (s), 2924 (s), 2866 (m), 2121 (m), 1702 (s), 1614 (m), 1586 (w), 1485 (s), 1444 (m), 1379 (m), 1329 (w), 1304 (s), 1275 (s), 1228 (s), 1182 (m), 1154 (m), 1102 (w), 1019 (s), 924 (m), 883 (w), 863 (w), 824 (m), 770 (m), 673 (s), 626 (s), 544 8m), 468 (m), 430 (m), 403 (m) cm^{-1}.

TLC (SiO_2, *iso*-hexane:ethyl acetate, 12:1 v/v): R_f = 0.29.

(*E*/*Z*)-5-bromo-2-(2,2-dimethyl-6-(prop-2-yn-1-yloxy)-2,3-dihydro-1*H*-inden-1-ylidene)-4,6-dimethylbenzo[*b*]thiophen-3(2*H*)-one (49)[159]

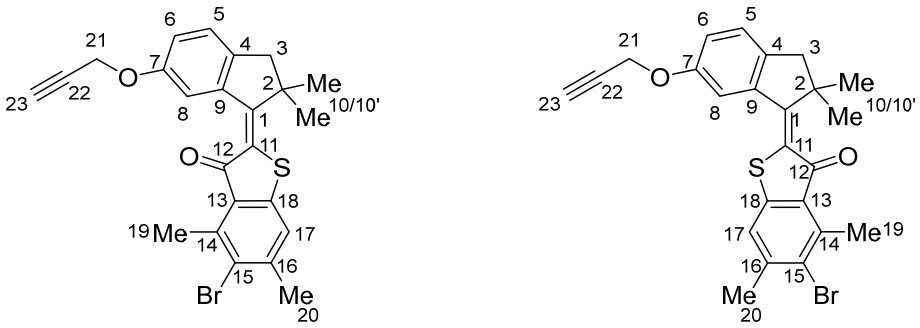

Two separate Schlenk flasks under a nitrogen atmosphere were charged individually with compound **35** (108 mg, 0.505 mmol, 1.0 equiv.) in anhydrous CH_2Cl_2 (0.300 mL, 1.7 M) in the first flask at 0 °C and compound **17** (129 mg, 0.502 mmol, 1.0 equiv.) in anhydrous CH_2Cl_2 (1.50 mL, 0.33 M) in the second flask at −78 °C. Boron trichloride (0.500 mL, 1.0 M in anhydrous CH_2Cl_2, 0.500 mmol, 1.0 equiv.) was added to the flask containing compound **17** and the resulting mixture was immediately taken up into the same syringe and transferred to the second flask containing compound **35** at 0 °C. The reaction mixture was vigorously stirred for 40 min while warming up to 22 °C and then stopped by transferring to a saturated aqueous ammonium chloride solution (20 mL). The aqueous phase was extracted four times with CH_2Cl_2 (40 mL each), the combined organic layers were dried over anhydrous sodium sulfate, and the solvent was removed *in vacuo*. Purification of the crude product was achieved by flash column chromatography (SiO2, *iso*-hexane:ethyl acetate, 50:1 v/v) yielding compound **49** (150 mg, 0.331 mmol, 66%) as a red solid.

^{1}H NMR (600 MHz, CD_2Cl_2): δ = 7.68 (d, $^4J_{HH}$ = 2.3 Hz, 1H, HC8), 7.25 (d, $^3J_{HH}$ = 8.2 Hz, 1H, HC5), 7.23 (d, $^4J_{HH}$ = 1.0 Hz, 1H, HC17), 7.05 (dd, $^3J_{HH}$ = 8.2 Hz, $^4J_{HH}$ = 2.3 Hz, 1H, HC6), 4.78 (d, $^4J_{HH}$ = 2.4 Hz, 2H, H_2C21), 3.01 (d, $^4J_{HH}$ = 1.0 Hz, 2H, H_2C3), 2.85 (s, 3H, H_3C19), 2.63 (t, $^4J_{HH}$ = 2.4 Hz, 1H, HC23), 2.50 (d, $^4J_{HH}$ = 0.8 Hz, 3H, H_3C20), 1.61 (s, 6H, H_3C10 and H_3C10') ppm.

^{13}C NMR (151 MHz, CD_2Cl_2): δ = 188.22 (C12), 162.57 (C4), 157.25 (C7), 145.04 (C16), 144.75 (C11), 143.32 (C9), 141.68 (C1), 141.49 (C13), 128.35 (C14), 126.65 (C15), 126.25 (C5), 126.19 (C18), 122.81 (C17), 119.21 (C6), 113.70 (C8), 78.91 (C22), 75.95 (C23), 56.72 (C21), 50.89 (C3) 49.51 (C2), 25.70 (C10), 25.31 (C20), 18.12 (C19) ppm.

HR-MS (EI^+, *m*/*z*) $[M]^+$ calc. for $[C_{24}H_{21}BrO_2S]^+$: 452.0440, found: 452.0443.

IR: $\tilde{\nu}$ = 3292 (w), 3280 (s), 3265 (s), 2960 (m), 2923 (m), 2176 (w) 2157 (m), 2034 (w), 1998 (w), 1968 (w), 1761 (w), 1707 (s), 1487 (s), 1445 (m), 1380 (w), 1306 (w), 1261 (s), 1236 (s), 1102 (m), 1026 (s), 803 (m) cm^{-1}.

TLC (SiO_2, *iso*-hexane:ethyl acetate, 50:1 v/v): R_f = 0.36 and 0.47.

1-bromo-2-(2-(2-(2-bromoethoxy)ethoxy)ethoxy)ethane (37)[268]

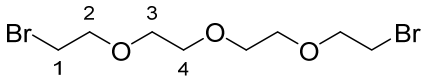

A mixture of commercially available tetraethylene glycol **36** (5.63 mL, 25.7 mmol, 1.0 equiv.) and tetrabromomethane (18.8 g, 56.6 mmol, 2.2 equiv.) in tetrahydrofuran (30.0 mL, 1.2 M) solution was cooled to 0 °C. Then triphenylphosphine (13.5 g, 54.0 mmol, 2.1 equiv.) was added slowly and the resulting mixture was allowed to warm up to 22 °C and stirred 21 h at this temperature. The reaction was stopped by transferring to a saturated aqueous ammonium chloride solution (200 mL) and the aqueous solution was extracted three times with ethyl acetate (200 mL each). The combined organic phases were washed with a saturated aqueous NaCl solution (100 mL), dried over anhydrous sodium sulfate, and the solvent was removed *in vacuo*. Purification of the crude product was achieved by flash column chromatography (SiO_2, *iso*-hexane:ethyl acetate, 3:1 v/v), yielding compound **37** (5.77 g, 18.1 mmol, 70%) as a colorless oil.

^{1}H NMR (400 MHz, CD_2Cl_2): δ = 3.79 (t, $^3J_{HH}$ = 6.1 Hz, 4H, H_2C2), 3.66–3.60 (m, 8H, H_2C3, H_2C4), 3.49 (t, $^3J_{HH}$ = 6.1 Hz, 4H, H_2C1) ppm.

^{13}C NMR (101 MHz, CD_2Cl_2): δ = 71.56 (C2), 70.97 (C4), 70.91 (C3), 31.27 (C1) ppm.

HR-MS (APPI$^+$, *m*/*z*) $[M+H]^+$ calc. for $[C_8H_{17}Br_2O_3]^+$: 318.9539, found: 318.9538.

IR: $\tilde{\nu}$ = 2866 (s), 1735 (w), 1455 (m), 1422 (m), 1350 (s), 1325 (w), 1276 (m), 1247 (m), 1226 (m), 1100 (s), 1040 (m), 1020 (m), 998 (m), 953 (m), 932 (m), 878 (m), 822 (m), 800 (s), 662 (s), 570 (s), 467 (s) cm^{-1}.

TLC (SiO_2, *iso*-hexane:ethyl acetate, 3:1 v/v): R_f = 0.33.

1-azido-2-(2-(2-(2-bromoethoxy)ethoxy)ethoxy)ethane (38)[269]

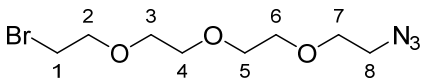

A solution of compound **37** (2.05 g, 6.25 mmol, 1.0 equiv.) and sodium azide (262 mg, 1.87 mmol, 0.6 equiv.) in *N*,*N*-dimethylformamide (4.20 mL, 1.5 M) was stirred for 21 h at 60 °C. The reaction was stopped by addition of water (100 mL) and the aqueous solution extracted three times with ethyl acetate

(100 mL each). The combined organic phases were washed four times with water (50 mL each, to remove residual *N*,*N*-dimethylformamide), a saturated aqueous NaCl solution (100 mL), dried over anhydrous sodium sulfate, and the solvent removed *in vacuo*. Purification of the crude product was achieved by flash column chromatography (SiO_2, *i*Hex:ethyl acetate, 4:1 v/v), yielding compound **38** (386 mg, 1.37 mmol, 44%) as a colorless oil.

^{1}H NMR (400 MHz, CD_2Cl_2): δ = 3.79 (t, $^3J_{HH}$ = 6.1 Hz, 2H, H_2C2), 3.67–3.60 (m, 10H, H_2C3, H_2C4, H_2C5, H_2C6, H_2C7), 3.49 (t, $^3J_{HH}$ = 6.1 Hz, 2H, H_2C1), 3.38 (t, $^3J_{HH}$ = 5.0 Hz, 2H, H_2C8) ppm.

^{13}C NMR (101 MHz, CD_2Cl_2): δ = 71.52 (C2), 71.02 (C4, C5 or C6), 70.98 (C4, C5 or C6), 70.88 (C4, C5 or C6), 70.31 (C3), 70.31 (C7), 51.23 (C8), 31.28 (C1) ppm.

HR-MS (APPI$^+$, *m*/*z*) $[M+H]^+$ calc. for $[C_8H_{17}BrN_3O_3]^+$: 282.0448, found 282.0449.

IR: $\tilde{\nu}$ = 2953 (s), 2924 (s), 2854 (s), 2362 (w), 2189 (w), 2112 (s), 2098 (s), 1742 (m), 1736 (m), 1458 (m), 1444 (m), 1375 (s), 1359 (s), 1276 (m), 1242 (m), 1122 (s), 821 (w) cm^{-1}.

TLC (SiO_2, *iso*-hexane:ethyl acetate, 4:1 v/v): R_f = 0.18.

2-(5-(2-(2-(2-(2-azidoethoxy)ethoxy)ethoxy)ethoxy)-2-fluorophenyl)-4,4,5,5-tetramethyl-1,3,2-dioxaborolane (34)[159]

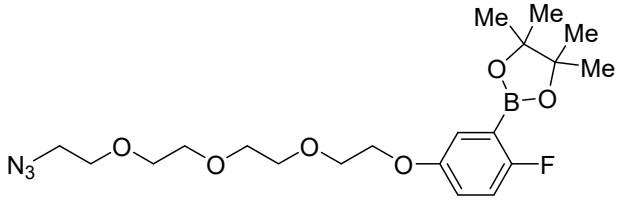

Compound **38** (547 mg, 2.31 mmol, 1.0 equiv.), commercially available 2-fluoro-5-hydroxyphenylboronic acid pinacol ester **39** (543 mg, 2.31 mmol, 1.2 equiv.), and potassium carbonate (585 mg, 8.80 mmol, 4.0 equiv.) were mixed in *N*,*N*-dimethylformamide (7.50 mL, 0.31 M). The suspension was heated to 60 °C for 23 h and the reaction was stopped by transferring to a saturated aqueous sodium bicarbonate solution (100 mL) and the aqueous solution was extracted three times with ethyl acetate (100 mL each). The combined organic phases were washed four times with water (50 mL each to remove remaining *N*,*N*-dimethylformamide), a saturated aqueous NaCl solution (50 mL), and dried over anhydrous sodium sulfate. Removal of the solvent *in vacuo* yielded compound **34** as a colorless liquid, which was used in the next synthetic step without further purification.

HR-MS (APPI$^+$, *m*/*z*) $[M+H]^+$ calc. for $[C_{20}H_{32}{}^{79}BFN_3O_6]^+$: 440.2363, found: 440.2364.

(*E*/*Z*)-5-bromo-2-(6-((1-(2-(2-(2-(2-(4-fluoro-3-(4,4,5,5-tetramethyl-1,3,2-dioxaborolan-2-yl)phenoxy)ethoxy)ethoxy)ethoxy)ethyl)-1*H*-1,2,3-triazol-4-yl)methoxy)-2,2-dimethyl-2,3-dihydro-1*H*-inden-1-ylidene)-4,6-dimethylbenzo[*b*]thiophen-3(2*H*)-one (50)[159]

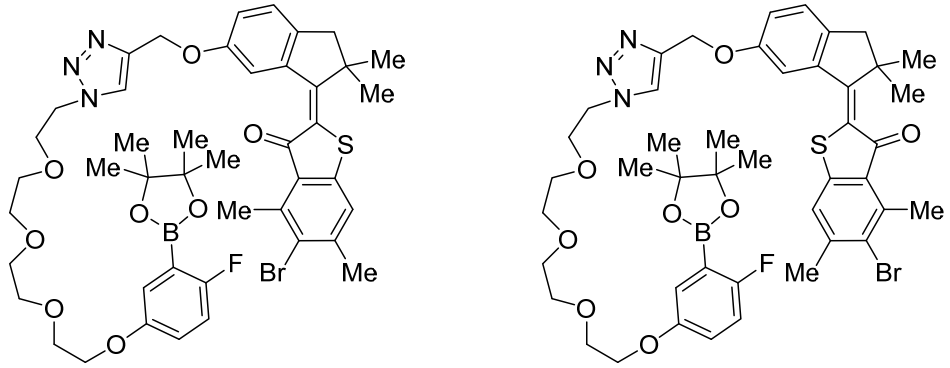

A mixture of HTI **49** (329 mg, 0.73 mmol, 1.0 equiv.), compound **34** (340 mg, 0.770 mmol, 1.1 equiv), sodium ascorbate (19.8 mg, 102 µmol, 14 mol%) and copper(II) sulfate pentahydrate (5.10 mg, 20.0 µmol, 3 mol%) were dissolved in *N*,*N*-dimethylformamide (3.00 mL, 1.4 M) and the resulting solution was stirred for 1 d at 22 °C. After transferring the reaction to a saturated aqueous ammonium chloride solution (75 mL), the aqueous solution was extracted three times with ethyl acetate (75 mL each). The combined organic phases were washed four times with water (30 mL each, to remove residual *N*,*N*-dimethylformamide), a saturated aqueous NaCl solution (75 mL), dried over anhydrous sodium sulfate and the solvent was removed *in vacuo*. The crude product was purified by flash column chromatography (SiO_2, CH_2Cl_2:methanol, 100:0 to 97:3 v/v), yielding compound **50** as a viscous red oil, which was used in the next synthetic step without further purification.

HR-MS (APPI$^+$, *m*/*z*) $[M+H]^+$ calc. for $[C_{44}H_{53}BBrFN_3O_8S]^+$: 892.2808, found: 892.2817.

TLC (SiO_2, CD_2Cl_2:methanol, 99:1 v/v): R_f = 0.04 and 0.20.

(*E*/*Z*)-16-fluoro-24,26,32,32-tetramethyl-22,23,32,33-tetrahydro-31*H*,61*H*-4,9,12,15,18-pentaoxa-6(4,1)-triazola-2(5,2)-benzo[*b*]thiophena-3(1,6)-indena-1(1,3)-benzenacyclooctadecaphan-23-one (51)[77]

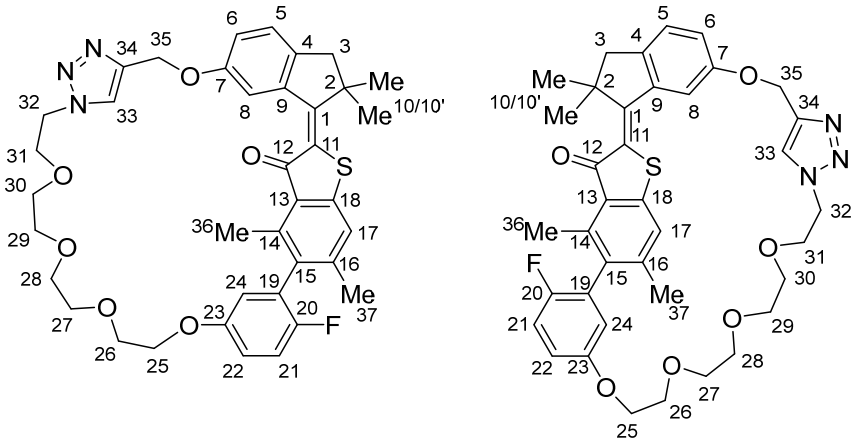

Compound **50** (424 mg, 0.720 mmol, 1.0 equiv.) and potassium phosphate (465 mg, 2.16 mmol, 3.0 equiv.) were dissolved in a mixture of toluene, ethanol, and water (3:3:1, 31.5 mL, 0.023 M) under a nitrogen atmosphere. The reaction mixture was degassed *via* three freeze-pump-thaw cycles, sSPhos Pd G2 (48.0 mg, 60.0 µmol, 8 mol%) added and heated at 80 °C for 24 h. The reaction was stopped by addition of a saturated aqueous ammonium chloride solution (50 mL) at 22 °C and the aqueous reaction mixture was extracted three times with ethyl acetate (50 mL each). The combined organic phases were dried over anhydrous sodium sulfate and the solvent was removed *in vacuo*. Purification of the crude product was achieved by flash column chromatography (SiO_2, CH_2Cl_2:methanol, 50:1 v/v), yielding compound **51** (74.6 mg, 0.110 mmol, 15% over two steps) as an orange solid. Four isomers (two enantiomeric atropisomers for each *E*- and *Z*-isomer) were obtained from HPLC separation using a preparative *Daicel* CHIRALPAK® ID column (*n*-hexane:ethyl acetate, 50:50 to 0:100 v/v, at 40 °C).

racemic *E*-(S_a)/*E*-(R_a)-Isomer:

^{1}H NMR (600 MHz, CD_2Cl_2): δ = 8.47 (d, $^3J_{HH}$ = 2.5 Hz, 1H, HC8), 7.25 (s, 1H, HC17), 7.23 (s, 1H, HC33), 7.18 (dd, $^3J_{HH}$ = 8.3 Hz, $^5J_{HH}$ = 0.6 Hz, 1H, HC5), 7.11 (t, $^3J_{HH}$ = 8.8 Hz, 1H, HC21), 6.95 (d, $^3J_{HH}$ = 2.4 Hz, 1H, HC6), 6.94–6.90 (m, 1H, HC22), 6.65 (ddd, J_{HH} = 5.8, 3.2, 1.6 Hz, 1H, HC24), 5.23–5.18 (m, 2H, HC35), 4.58–4.51 (m, 1H, HC32), 4.46 (m, 1H, HC32), 4.26–4.21 (m, 1H, HC30, HC29, HC28, HC27, HC26 or HC25), 4.05–4.01 (m, 1H, HC30, HC29, HC28, HC27, HC26 or HC25), 3.88–3.82 (m, 1H, HC31), 3.78–3.72 (m, 1H, HC31), 3.65–3.56 (m, 6H, H_2C30, H_2C29, H_2C28, H_2C27, H_2C26 or H_2C25), 3.54–3.49 (m, 2H, H_2C30, H_2C29, H_2C28, H_2C27, H_2C26 or H_2C25), 3.28–3.22 (m, 1H, HC30, HC29, HC28, HC27, HC26 or HC25), 3.21–3.15 (m, 1H, HC30, HC29, HC28, HC27, HC26

or HC25), 3.00 (d, $^{2}J_{HH}$ = 1.4 Hz, 1H, HC3), 2.93 (d, $^{2}J_{HH}$ = 3.1 Hz, 1H, H‘C3), 2.47 (s, 3H, H_3C36), 2.13–2.11 (m, 3H, H_3C37), 1.52 (s, 3H, HC10), 1.50 (s, 3H, H_3C10‘) ppm.

^{13}C NMR (151 MHz, CD_2Cl_2): δ = 189.23 (C12), 161.55 (C1), 158.19 (C9), 156.55 (C7), 155.52 (C23), 154.51 (d, $^{1}J_{CF}$ = 233.2 Hz, C20), 143.77 (C34) 140.95 (C4), 140.50 (C14), 134.19 (C16), 133.85 (C15), 127.78 (C13), 127.63 (C11), 127.62 (d, $^{2}J_{CF}$ = 13.3 Hz, C19), 127.44 (C18), 125.44 (C5), 121.96 (C17), 121.93 (C33), 118.84 (C6), 116.65 (d, $^{3}J_{CF}$ = 19.7 Hz, C21), 116.56 (C24), 114.74 (C22), 112.85 (C8), 71.74 (C30, C29, C28, C27, C26 or C25), 71.38 (C30, C29, C28, C27, C26 or C25), 71.21 (C30, C29, C28, C27, C26 or C25), 71.05 (C32), 70.90 (C30, C29, C28, C27, C26 or C25), 70.82 (C30, C29, C28, C27, C26 or C25), 69.88 (C31), 65.70 (C30, C29, C28, C27, C26 or C25), 61.85 (C35), 50.90 (C3), 49.57 (C2), 26.76 (C10), 26.72 (C10‘), 21.70 (C36), 15.96 (C37) ppm.

HR-MS (APPI$^+$, *m*/*z*) [M+H]$^+$ calc. for $[C_{38}H_{41}FN_3O_6S]^+$: 686.2695, found: 686.2698.

IR: $\tilde{\nu}$ = 2959 (s), 2932 (s), 2850 (s), 2362 (w), 2327 (w), 2152 (w), 2093 (w), 1673 (m), 1606 (w), 1581 (w), 1495 (w), 1480 (m), 1459 (m), 1343 (m), 1307 (m), 1206 (s), 1007 (w), 1072 (m), 1015 (m), 919 (m), 777 (m), 733 (s), 696 (m) cm^{-1}.

TLC (SiO_2, CD_2Cl_2:methanol, 50:1 v/v): R_f = 0.30.

racemic *Z*-(S_a)/*Z*-(R_a)-Isomer:

^{1}H NMR (600 MHz, CD_2Cl_2): δ = 8.52 (d, $^{5}J_{HH}$ = 2.5 Hz, 1H, HC8), 8.17 (s, 1H, HC33), 7.25 (s, 1H, HC17), 7.19 (d, $^{3}J_{HH}$ = 8.3 Hz, 1H, HC6), 7.11 (t, $^{3}J_{HH}$ = 8.9 Hz, 1H, HC21), 7.00 (dd, $^{3}J_{HH}$ = 8.3 Hz, $^{5}J_{HH}$ = 2.5 Hz, 1H, HC5), 6.92 (ddd, $^{3}J_{HH}$ = 9.0 Hz, $^{4}J_{HH}$ = 3.1 Hz, 1H, HC22), 6.73 (dd, $^{4}J_{HH}$ = 3.1 Hz, 1H, HC24), 5.24–5.15 (m, 2H, H_2C35), 4.55–4.44 (m, 2H, H_2C32), 4.21–4.11 (m, 2H, H_2C25), 3.90–3.80 (m, 2H, H_2C31), 3.79–3.75 (m, 2H, H_2C26), 3.63–3.60 (m, 2H, H_2C27), 3.56–3.52 (m, 2H, H_2C28), 3.52 (m, 4H, H_2C29, H_2C30), 3.00 (d, $^{2}J_{HH}$ = 15.6 Hz, 1H, HC3), 2.87 (d, $^{2}J_{HH}$ = 15.7 Hz, 1H, H’C3), 2.50 (s, 3H, H_3C36), 2.17 (s, 3H. H_3C37), 1.58 (s, 3H, H_3C10), 1.44 (s, 3H, H_3C10’) ppm.

^{13}C NMR (151 MHz, CD_2Cl_2): δ = 189.53 (C12), 161.98 (C1), 156.54 (C7), 155.50 (d, $^{4}J_{CF}$ = 1.1 Hz, C23), 154.71 (d, $^{1}J_{CF}$ = 235.7 Hz, C20), 145.34 (C18), 144.56 (C16), 143.75 (C34), 141.66 (C9), 140.37 (C14), 139.33 (C4), 133.98 (C15), 127.77 (C13), 127.56 (C11), 127.43 (d, $^{2}J_{CF}$ = 19.8 Hz, C19), 125.90 (C6), 124.95 (C33), 121.92 (C17), 120.80 (C5), 118.50 (d, $^{3}J_{CF}$ = 3.6 Hz, C24), 116.65 (d, $^{2}J_{CF}$ = 24.4 Hz, C21), 115.77 (d, $^{3}J_{CF}$ = 7.7 Hz, C22), 112.59 (C8), 70.89 (C28), 70.61 (C29), 70.19 (C27), 70.07 (C26), 70.03 (C30), 69.86 (C31), 68.91 (C25), 61.83 (C35), 50.56 (C32), 49.63 (C2), 48.86 (C3), 26.74 (C10), 26.49 (C10’), 21.48 (d, $^{5}J_{CF}$ = 1.4 Hz, C37), 16.59 (C36) ppm.

HR-MS (APPI$^+$, *m*/*z*) [M+H]$^+$ calc. for $[C_{38}H_{41}FN_3O_6S]^+$: 686.2695, found: 686.2693.

IR: $\tilde{\nu}$ = 3339 (m), 3147 (m), 2922 (s), 2851 (s), 2363 (w), 2331 (w), 2250 (w), 2155 (m), 1705 (w), 1654 (m), 1611 (m), 1496 (w), 1465 (m), 1458 (m), 1405 (m), 1356 (w), 1259 (w), 1205 (s), 1003 (w), 1064 (s), 952 (w), 879 (w), 853 (w) cm^{-1}.

TLC (SiO_2, CD_2Cl_2:methanol, 50:1 v/v): R_f = 0.26.

(*E*/*Z*)-16-fluoro-24,26,32,32-tetramethyl-22,23,32,33-tetrahydro-31*H*,61*H*-4,9,12,15,18-pentaoxa-6(4,1)-triazola-2(5,2)-benzo[*b*]thiophena-3(1,6)-indena-1(1,3)-benzenacyclooctadecaphan-23-one 21-oxide (33)[159]

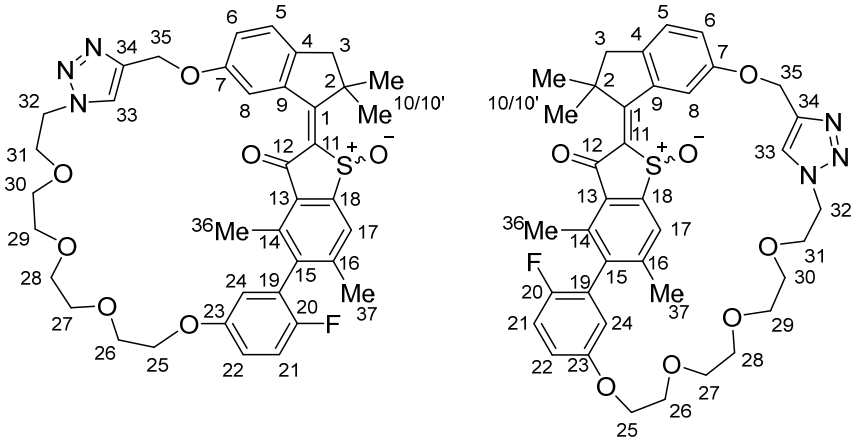

Compound **51** (30.4 mg, 44.3 µmol, 1.0 equiv.) was dissolved in acetic acid (2.50 mL, 0.020 M of **51**) and sodium perborate tetrahydrate (11.3 mg, 73.4 µmol, 1.66 equiv.) was added, subdivided into small portions. The mixture was stirred at 22 °C for 5 h until the reaction was stopped by cautiously transferring to a saturated aqueous sodium bicarbonate solution (50 mL). After extraction of the aqueous solution three times with ethyl acetate (50 mL each), the combined organic phases were washed with a saturated aqueous NaCl solution (50 mL), dried over anhydrous sodium sulfate, and the solvent was removed *in vacuo*. Purification of the crude product was achieved by flash column chromatography (SiO_2, CH_2Cl_2:methanol, 40:1 v/v), yielding compound **33** (20.2 mg, 28.7 µmol, 65%) as a yellow solid. Both *E*-configured atropisomers were obtained from the reaction and separated on a *Macherey-Nagel Nucleosil* SiO_2 column (100% ethyl acetate, at 40 °C). *Z*-configured isomers were obtained after irradiation using 505 nm or 565 nm and HPLC separation using a preparative *Macherey-Nagel Nucleosil* SiO_2 column (100% ethyl acetate, at 40 °C) followed by a preparative *Daicel* CHIRALPAK® IC column (*n*-hexane:ethyl acetate, 50:50 to 0:100 v/v, at 40 °C).

Only (*S*) configured diastereomers are shown in the following for clarity.

racemic *E*-isomers:

33-*E*-I = *E*-(*S*)-(*M*/*P*)-(S_a)/*E*-(*R*)-(*M*/*P*)-(R_a)

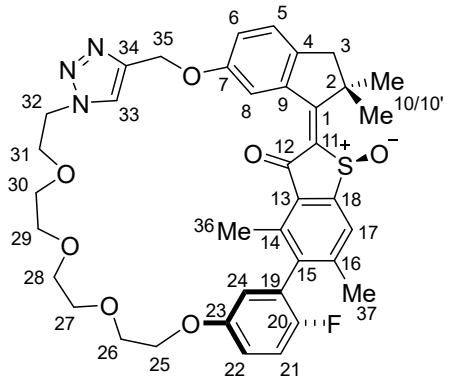

^{1}H NMR (800 MHz, CD_2Cl_2): δ = 7.87 (s, 1H, HC33), 7.83 (s, 1H, HC17), 7.75 (d, $^4J_{HH}$ = 2.5 Hz, 1H, HC8), 7.29 (d, J = 8.2 Hz, 1H, HC5), 7.15 (t, J = 8.8 Hz, 1H, HC21), 7.10 (dd, $^3J_{HH}$ = 8.3 Hz, $^4J_{HH}$ = 2.5 Hz, 1H, HC6), 6.96 (dt, J_{HH} = 9.0, 3.5, 1H, HC22), 6.70 (dd, J_{HH} = 5.8, 3.1, 1H, HC24), 5.17–5.08 (m, 2H, H_2C35), 4.53 (qdd, J=14.3, 6.1, 4.0, 2H, H_2C32), 4.17–4.10 (m, 2H, H_2C25), 3.91–3.84 (m, 2H, H_2C31), 3.78 (dd, J=5.1, 4.1, 2H, H_2C26), 3.62 (dd, J=4.9, 4.1, 2H, H_2C27), 3.57–3.52 (m, 6H, H_2C28, H_2C29 and H_2C30), 3.20 (d, $^2J_{HH}$ = 14.8 Hz, 1H, HC3), 2.81 (d, $^2J_{HH}$ = 14.8 Hz, 1H, H‘C3), 2.53 (s, 3H, H_3C36), 2.30 (s, 3H, H_3C37), 1.94 (s, 3H, H_3C10), 1.44 (s, 3H, H_3C10‘) ppm.

^{13}C NMR (201 MHz, CD_2Cl_2) δ = 185.18 (C12), 174.51 (C11), 156.74(C7), 155.67 (C23), 154.05 (d, $^1J_{CF}$ = 236.9 Hz, C20), 150.13 (C18), 145.95 (C14), 143.63 (C34), 143.33 (C4), 141.37 (C15), 139.94 (C16), 139.40 (C1), 138.85 (C9), 130.53 (C13), 126.79 (d, $^2J_{CF}$ = 20,1 Hz, C19), 126.18 (C5), 125.16 (C17), 124.45 (C33), 121.56 (C6), 117.39 (d, $^3J_{CF}$ = 3.0 Hz, C24), 116.99 (d, $^2J_{CF}$ = 23.8 Hz, C21), 116.01 (d, $^3J_{CF}$ = 7.8 Hz, C22), 114.62 (C8), 71.13 (C27), 71.06 (C30), 70.97 (C29), 70.59 (C28), 70.00 (C26), 69.89 (C31), 68.71 (C25), 62.42 (C35), 52.58 (C2), 50.77 (C32), 49.48 (C3), 29.21 (C10), 26.07 (C10‘), 21.66 (C37), 16.79 (C36) ppm.

^{19}F NMR (377 MHz, CD_2Cl_2): δ = −126.53 (FC20) ppm.

HR-MS (EI^+, *m*/*z*) $[M+H]^+$ calc. for $[C_{38}H_{40}FN_3O_7S]^+$: 701.2566, found: 701.2572.

IR: $\tilde{\nu}$ = 3139 (w), 2926 (s), 2869 (s), 1732 (s), 1673 (s), 1581 (s), 1539 (s), 1494 (s), 1485 (s), 1461 (m), 1373 (w), 1293 (m), 1242 (s), 1228 (s), 1207 (m), 1170 (w), 1143 (s), 1122 (s), 1051 (s), 1035 (s), 1002 (m), 947 (w), 862 (m), 817 (m), 792 (s), 742 (s), 714 (s), 635 (s), 510 (s), 411 (w) cm^{-1}.

TLC (SiO_2, CD_2Cl_2:methanol, 40:1 v/v): R_f = 0.34.

33-*E*-II = *E*-(*S*)-(*M*/*P*)-(*R*$_a$)/*E*-(*R*)-(*M*/*P*)-(*S*$_a$)

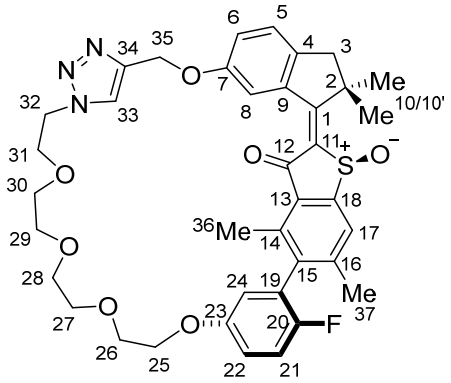

^{1}H NMR (800 MHz, CD_2Cl_2): δ = 8.16 (s, 1H, HC33), 7.88 (d, $^4J_{HH}$ = 2.5 Hz, 1H, HC8), 7.78 (s, 1H, HC17), 7.25 (d, $^3J_{HH}$ = 8.3 Hz, 1H, HC5), 7.15 (t, J_{HH} = 8.8 Hz, 1H, HC21), 7.08 (dd, $^3J_{HH}$ = 8.2 Hz, $^4J_{HH}$ = 2.5 Hz, 1H, HC6), 6.97 (dt, J_{HH} = 9.1 Hz, 3.5 Hz, 1H, HC22), 6.71 (dd, J_{HH} = 5.8 Hz, 3.1 Hz, 1H, HC24), 5.20 (d, J_{HH} = 2.6 Hz, 2H, H_2C35), 4.54–4.42 (m, 2H, H_2C32), 4.20–4.13 (m, 2H, H_2C25), 3.89–3.80 (m, 2H, H_2C31), 3.80–3.74 (m, 2H, H_2C26), 3.62–3.58 (m, 2H, H_2C27), 3.54–3.48 (m, 6H, H_2C28, H_2C29, H_2C30), 3.02 (d, $^2J_{HH}$ = 15.3 Hz, 1H, HC3), 2.95 (d, $^2J_{HH}$ = 15.3 Hz, 1H, H‘C3), 2.53 (s, 3H, H_3C36), 2.29 (s, 3H, H_3C37), 1.75 (s, 3H, H_3C10), 1.65 (s, 3H, H_3C10‘) ppm.

^{13}C NMR (201 MHz, CD_2Cl_2): δ = 188.44 (C12), 174.14 (C11), 156.31 (C7), 155.69 (C23), 154.15 (d, $^1J_{CF}$ = 238.2 Hz, C20), 149.31 (C18), 146.25 (C14), 143.73 (C4), 143.52 (C34), 141.75 (C15), 140.05 (C16), 138.22 (C9), 137.12 (C1), 129.99 (C13), 126.66 (d, $^2J_{CF}$ = 20.1 Hz, C19), 126.35 (C5), 125.70 (C17), 124.81 (C33), 123.12 (C6), 117.68 (C24), 116.93 (d, $^2J_{CF}$ = 23.8 Hz, C21), 116.11 (d, $^3J_{CF}$ = 7.2 Hz, C22), 113.98 (C8), 71.18 (C27), 71.00 (C28), 70.91 (C29), 70.62 (C30), 70.17 (C26), 69.75 (C31), 68.92 (C25), 61.77 (C35), 51.92 (C2), 50.42 (C32), 49.28 (C3), 29.37 (C10), 27.93 (C10’), 21.63 (C37), 16.77 (C36) ppm.

^{19}F NMR (377 MHz, CD_2Cl_2): δ = −126.00 (FC20) ppm.

HR-MS (EI^+, *m*/*z*) $[M+H]^+$ calc. for $[C_{38}H_{40}FN_3O_7S]^+$: 701.2566, found: 701.2572.

IR: $\tilde{\nu}$ = 3150 (w), 2923 (s), 2867 (s), 1733 (s), 1669 (s), 1580 (s), 1536 (m), 1494 (s), 1484 (s), 1459 (m), 1417 (w), 1375 (w), 1297 (m), 1241 (m), 1229 (m), 1205 (m), 1192 (m), 1142 (m), 1104 (m), 1050 (s), 1034 (s), 938 (w), 892 (w), 861 (w), 816 (m), 793 (m), 741 (s), 634 (m), 536 (w) cm^{-1}.

TLC (SiO_2, CD_2Cl_2:methanol, 40:1 v/v): R_f = 0.34.

racemic *Z*-isomers:

33-*Z*-I = *Z*-(*S*)-(*M*/*P*)-(*S*$_a$)/*Z*-(*R*)-(*M*/*P*)-(*R*$_a$)

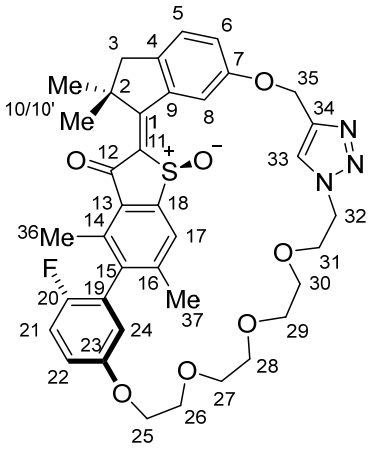

^{1}H NMR (800 MHz, CD_2Cl_2) δ = 8.68 (s, 1H, HC33), 8.50 (d, $^4J_{HH}$ = 2.4 Hz, 1H, HC8), 7.79 (s, 1H, HC17), 7.26 (d, $^3J_{HH}$ = 8.3 Hz, 1H, HC5), 7.18–7.13 (m, 2H, HC6 and HC24), 7.10 (t, J_{HH} = 8.8 Hz, 1H, HC21), 6.96 (ddd, J_{HH} = 9.0, 4.1, 3.1 Hz, 1H, HC22), 5.40 (dd, $^1J_{HH}$ = 88.3 Hz, 14.1, 4H, H_2C35), 4.46 (dt, $^3J_{HH}$ = 6.1 Hz, 3.8, 2H, H_2C32), 4.25 (dt, J_{HH} = 5.6 Hz, 2.8, 2H, H_2C25), 3.74 (ddd, $^1J_{HH}$ = 10.1 Hz, $^3J_{HH}$ = 5.9 Hz, 3.8, 1H, HC31), 3.72 (ddd, $^1J_{HH}$ = 11.3, 5.2, 3.2 Hz, 1H, HC26), 3.68 (ddd, $^1J_{HH}$ = 11.3, 5.2, 3.2 Hz, 1H, HC26), 3.63 (ddd, $^1J_{HH}$ = 10.4 Hz, $^3J_{HH}$ = 6.3 Hz, 3.9, 1H, HC31), 3.53–3.46 (m, 2H, H_2C27), 3.44–3.40 (m, 2H, H_2C30), 3.40–3.36 (m, 1H, HC29), 3.30–3.26 (m, 2H, H_2C28), 3.24 (ddd, J=10.3, 9.0, 4.7, 1H, HC29), 3.12 (d, $^1J_{HH}$ = 16.2 Hz, 1H, HC3) 2.91 (d, $^1J_{HH}$ = 16.1 Hz, 1H, H'C3), 2.52 (s, 3H, H_3C36), 2.26 (s, 3H, H_3C37), 1.57 (s, 3H, H_3C10), 1.54 (s, 3H, H_3C10') ppm.

^{13}C NMR (201 MHz, CD_2Cl_2) δ = 189.16 (C12), 179.36 (C11), 157.84 (C7), 156.64 (C23), 154.80 (C19), 153.62 (C20), 149.74 (C18), 146.11 (C14), 143.96 (C4), 143.08 (C34), 143.03 (C15), 140.22 (C16), 139.65 (C9), 134.23 (C1), 129.84 (C13), 126.90 (C5), 126.09 (C33), 125.98 (C17), 124.80 (C6), 119.54 (d, $^3J_{CF}$ = 7.7 Hz, C22), 118.03 (C24), 116.72 (d, $^2J_{CF}$ = 23.8 Hz, C21), 112.22 (C8), 72.12 (C26), 70.92 (C25), 70.88 (C27), 70.75 (C30), 70.66 (C29), 70.44 (C28), 69.81 (C31), 61.35 (C35), 50.68 (C2), 50.63 (C3), 50.48 (C32), 27.26 (C10), 25.43 (C10'), 21.96 (C37), 16.05 (C36) ppm.

^{19}F NMR (377 MHz, CD_2Cl_2): δ = −126.85 (FC20) ppm.

HR-MS (EI^+, *m*/*z*) $[M+H]^+$ calc. for $[C_{38}H_{40}FN_3O_7S]^+$: 701.2566, found: 701.2572.

IR: $\tilde{\nu}$ = 3285 (w), 3123 (w), 2078 (w), 2958 (m), 2923 (s), 2853 (m), 1752 (m), 1704 (m), 1673 (m), 1599 (s), 1538 (s), 1486 (s), 1427 (m), 1377 (w), 1300 (w), 1275 (w), 1259 (w), 1230 (s), 1167 (w), 1143 (w), 1100 (m), 1052 (m), 1028 (m), 909 (w), 866 (w), 802 (m), 772 (w), 679 (s), 441 (w), 418 (s) cm^{-1}.

TLC (SiO_2, CD_2Cl_2:methanol, 40:1 v/v): R_f = 0.34.

33-*Z*-II = *Z*-(*S*)-(*M*/*P*)-(*R*$_a$)/*Z*-(*R*)-(*M*/*P*)-(*S*$_a$)

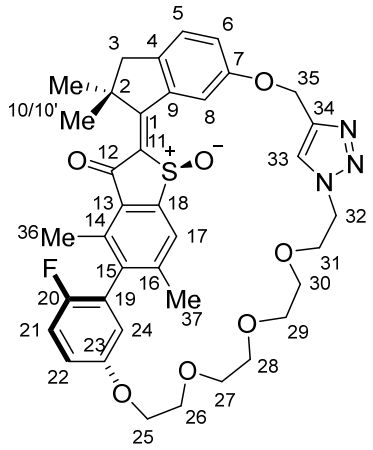

^{1}H NMR (800 MHz, CD_2Cl_2) δ = 8.09 (s, 1H, HC33), 7.98 (d, $^4J_{HH}$ = 2.3 Hz, 1H, HC8), 7.88 (s, 1H, HC17), 7.28 (d, $^3J_{HH}$ = 8.4 Hz, 1H, HC5), 7.20 (dd, $^3J_{HH}$ = 8.4 Hz, $^4J_{HH}$ = 2.3Hz, 1H, HC6), 7.11 (t, $^3J_{HH}$ = 8.7 Hz, 1H, HC21), 7.03 (dd, J_{HH} = 5.8 Hz, 3.1 Hz, 1H, HC24), 6.97 (dt, J_{HH} = 9.1 Hz, 3.6 Hz, 1H, HC22), 5.44–5.37 (m, 3H, H_2C35), 4.59–4.49 (m, 2H, H_2C32), 4.29–4.20 (m, 2H, H_2C25), 3.82 (ddd, J_{HH} = 10.5 Hz, 5.9, 4.9, 1H, HC31), 3.73 (ddd, J_{HH} = 10.2 Hz, 7.0, 4.8, 1H, HC31), 3.70–3.63 (m, 2H, H_2C26), 3.50 (dddd, J=28.6, 10.4, 6.0, 2.9, 2H, H_2C27), 3.40 (dddd, J=40.3, 10.8, 6.1, 2.9, 2H, H_2C28), 3.34–3.26 (m, 2H, H_2C30 or H_2C29), 3.25–3.19 (m, 2H, H_2C30 or H_2C29), 3.09 (d, $^2J_{HH}$ = 16.1 Hz, 1H, HC3), 2.95 (d, $^2J_{HH}$ = 16.1 Hz, 1H, H'C3), 2.52 (s, 3H, H_3C36), 2.28 (s, 3H, H_3C37), 1.67 (s, 3H, H_3C10), 1.52 (s, 3H, H_3C10') ppm.

^{13}C NMR (201 MHz, CD_2Cl_2) δ = 186.87 (C12), 176.84 (C11), 158.05 (C7), 156.63 (C23), 154.22 (d, $^1J_{CF}$ = 238.3 Hz, C20), 148.40 (C18), 145.77 (C14), 145.15 (C4), 143.69 (C34), 142.58 (C15), 140.07 (C16), 138.47 (C9), 136.21 (C1), 130.53 (C13), 127.02 (C5), 126.03 (C17), 124.91 (C6), 124.70 (C33), 119.64 (C22), 119.60 (C19), 117.72 (C24), 116.86 (d, $^1J_{CF}$ = 22.8 Hz, C21), 112.92 (C8), 71.82 (C26), 71.28 (C27), 70.94 (C28), 70.74 (C25), 70.38 (C29 or C30), 70.17 (C29 or C30), 69.99 (C31), 62.52 (C35), 50.66 (C2), 50.60 (C3), 50.58 (C32), 26.41 (C10), 26.18 (C10'), 22.09 (C37), 16.10 (C36) ppm.

^{19}F NMR (377 MHz, CD_2Cl_2): δ = −126.10 (FC20) ppm.

HR-MS (EI^+, *m*/*z*) $[M+H]^+$ calc. for $[C_{38}H_{40}FN_3O_7S]^+$: 701.2566, found: 701.2572.

IR: $\tilde{\nu}$ = 3143 (w), 3079 (w), 2921 (s), 2856 (s), 1732 (m), 1667 (s), 1604 (m), 1579 (s), 1523 (s), 1487 (s), 1456 (m), 1412 (w), 1379 (m), 1299 (w), 1285 (w), 1260 (w), 1221 (s), 1206 (s), 1144 (s), 1104 (s), 1036 (s), 1003 (w), 988 (m), 961 (w), 882 (m), 828 (s), 769 (m), 631 (m) cm^{-1}.

TLC (SiO_2, CD_2Cl_2:methanol, 40:1 v/v): R_f = 0.34.

8.5.2. Non-macrocyclic HTI 15h

Unrestricted HTI motor **15h** was constructed combining benzothiophenone **17** with indanone **52** and biaryl **53**, furnishing motor **15h** as shown in Figure 229. Commercially available 6-hydroxy indanone **47**, 4-bromo-3,5-dimethylphenol **40**, and 2-fluoro-5-hydroxyphenylboronic acid pinacol ester **39** were utilized as starting structures. Building block **17** was prepared according to a previous report and **52** and **53** were synthesized through a modification thereof.[158]

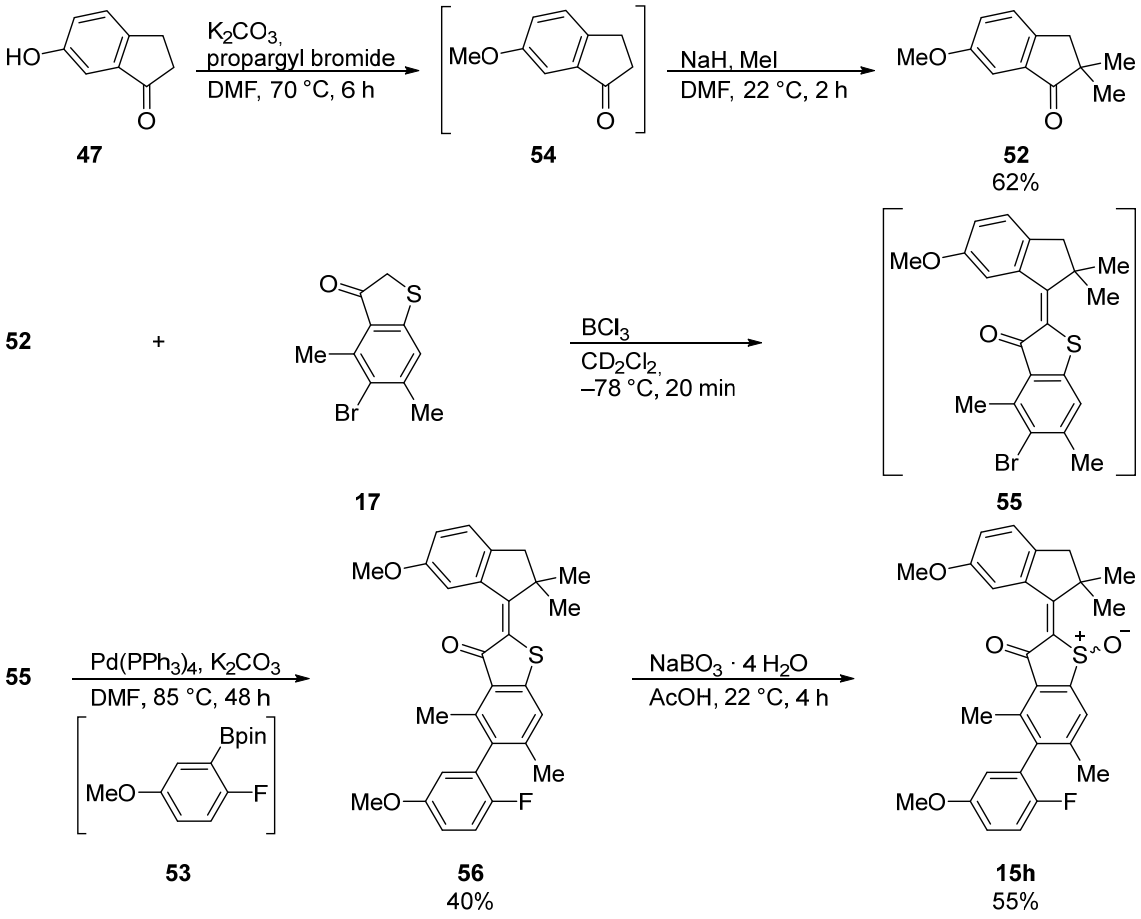

Figure 229 Overview of 5-step synthesis of molecular HTI-based motor **15h** starting from commercially available starting materials 6-hydroxy indanone **47**, and 4-bromo-3,5-dimethylphenol **40**.

6-methoxy-2,3-dihydro-1*H*-inden-1-one (54)

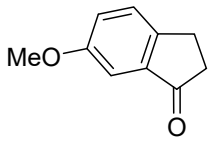

Commercially available 6-hydroxy-1-indanone **47** (1.00 g, 6.75 mmol, 1.0 equiv.), iodomethane (0.630 mL, 10.1 mmol, 1.5 equiv.), and potassium carbonate (3.70 g, 27.0 mmol, 4.0 equiv.) were mixed in *N*,*N*-dimethylformamide (43.0 mL, 0.15 M) and the suspension was heated to 70 °C for 6 h. The reaction was stopped by transferring to a saturated aqueous sodium bicarbonate solution (100 mL) and the aqueous solution was extracted three times with ethyl acetate (100 mL each). The combined organic phases were washed four times with water (30 mL each to remove remaining *N*,*N*-dimethylformamide), a saturated aqueous NaCl solution (100 mL), and dried over anhydrous sodium sulfate. Removal of the solvent *in vacuo* yielded compound **54** as a white solid, which was used in the next synthetic step without further purification.

HR-MS (APPI$^+$, *m*/*z*) $[M+H]^+$ calc. for $[C_{10}H_{11}O_2]^+$: 162.0754, found: 162.0751.

TLC (SiO_2, *iso*-hexane:ethyl acetate, 1:1 v/v): $R_f = 0.60$.

6-methoxy-2,2-dimethyl-2,3-dihydro-1*H*-inden-1-one (52)[159]

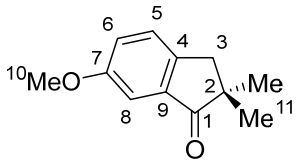

To a solution of compound **54** (775 mg, 4.78 mmol, 1.0 equiv.) in anhydrous *N*,*N*-dimethylformamide (9.50 mL, 0.50 M) at 0 °C, sodium hydride (290 mg (60% in mineral oil), 7.18 mmol, 1.5 equiv.) was added. and the resulting suspension stirred for 20 min at 0 °C. Then iodomethane (0.450 mL, 7.18 mmol, 1.5 equiv.) was added dropwise and the reaction mixture was stirred for 2 h at 22 °C. After addition of a saturated aqueous ammonium chloride solution (25 mL), the aqueous solution was extracted three times with ethyl acetate (50 mL each), and the combined organic phases were washed four times with water (20 mL each, to remove residual *N*,*N*-dimethylformamide), twice with a saturated aqueous NaCl solution (30 mL each), dried over anhydrous sodium sulfate, and the solvent was removed *in vacuo*. Purification of the crude product was achieved by flash column chromatography (SiO_2, *iso*-hexane:ethyl acetate, 9:1 v/v), yielding compound **52** (563 mg, 2.96 mmol, 62%) as a colorless liquid.

^{1}H NMR (500 MHz, CD_2Cl_2): δ = 7.34 (dq, $^3J_{HH}$ = 8.3 Hz, $^4J_{HH}$ = 0.9 Hz, 1H, HC5), 7.19 (dd, $^3J_{HH}$ = 8.3 Hz, $^5J_{HH}$ = 2.6 Hz, 1H, HC6), 7.16 (d, $^5J_{HH}$ = 2.5 Hz, 1H, HC8), 3.83 (s, 3H, H_3C10), 2.92 (d, $^4J_{HH}$ = 0.8 Hz, 2H, H_2C3), 1.20 (s, 6H, H_3C11 and H_3C11') ppm.

^{13}C NMR (126 MHz, CD_2Cl_2): δ = 211.39 (C1), 159.91 (C7), 145.39 (C4), 136.92 (C9), 127.81 (C5), 124.16 (C6), 105.85 (C8), 56.00 (C10), 46.57 (C2), 42.45 (C3), 25.46 (C11) ppm.

HR-MS (APPI$^+$, *m*/*z*) $[M+H]^+$ calc. for $[C_{12}H_{15}O_2]^+$: 191.1067, found: 191.1064.

IR: $\tilde{\nu}$ = 3400 (w), 3058 (w), 3001 (w), 2958 (s), 2924 (s), 2864 (m), 2835 (m), 1778 (w), 1704 (s), 1616 (m), 1585 (w), 1489 (s), 1464 (s), 1429 (s), 1379 (w), 1359 (w), 1334 (w), 1305 (m), 1276 (s), 1241 (s), 1153 (m), 1097 (w), 1027 (s), 1004 (s), 886 (m), 862 (m), 823 (m), 772 (s), 706 (w), 689 (w), 617 (w), 549 (w), 501 (w) cm^{-1}.

TLC (SiO_2, *iso*-hexane:ethyl acetate, 9:1 v/v): R_f = 0.50.

2-(2-fluoro-5-methoxyphenyl)-4,4,5,5-tetramethyl-1,3,2-dioxaborolane (53)

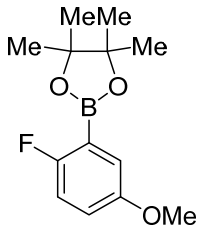

Commercially available 2-fluoro-5-hydroxyphenylboronic acid pinacol ester **39** (503 mg, 2.1 mmol, 1.0 equiv.), iodomethane (0.200 mL, 3.15 mmol, 1.5 equiv.), and potassium carbonate (1.17 g, 8.40 mmol, 4.0 equiv.) were mixed in *N*,*N*-dimethylformamide (14.0 mL, 0.15 M) and the suspension heated to 70 °C for 18 h. The reaction was stopped by transferring to a saturated aqueous sodium bicarbonate solution (100 mL) and the aqueous solution was extracted three times with ethyl acetate (100 mL each). The combined organic phases were washed four times with water (30 mL each to remove remaining *N*,*N*-dimethylformamide), a saturated aqueous NaCl solution (100 mL), and dried over anhydrous sodium sulfate. Removal of the solvent *in vacuo* yielded compound **53** as a white solid, which was used in the next synthetic step without further purification.

HR-MS (APPI$^+$, *m*/*z*) $[M]^+$ calc. for $[C_{13}H_{18}BFO_3]^+$: 252.1333, found: 252.1328.

TLC (SiO_2, *iso*-hexane:ethyl acetate, 1:1 v/v): R_f = 0.91.

(*E*/*Z*)-5-bromo-2-(6-methoxy-2,2-dimethyl-2,3-dihydro-1*H*-inden-1-ylidene)-4,6-dimethylbenzo[*b*]thiophen-3(2*H*)-one (55)[159]

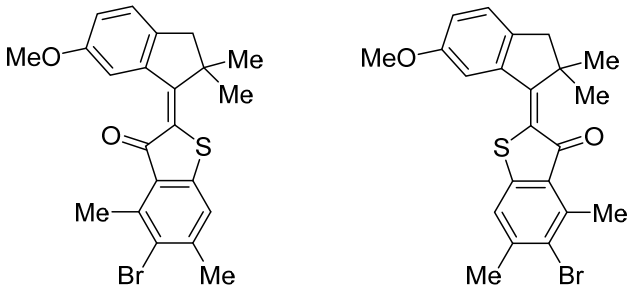

Two separate Schlenk flasks under a nitrogen atmosphere were charged individually with compound **52** (500 mg, 2.63 mmol, 1.0 equiv.) in anhydrous CH_2Cl_2 (5.10 mL, 0.52 M) in the first flask at 0 °C and compound **17** (679 mg, 2.63 mmol, 1.0 equiv.) in anhydrous CH_2Cl_2 (1.20 mL, 2.1 M) in the second flask at −78 °C. Boron trichloride (2.63 mL, 1.0 M in anhydrous CH_2Cl_2, 2.63 mmol, 1.0 equiv.) was added to the flask containing compound **17** and the resulting mixture was immediately taken up into the same syringe and transferred to the second flask containing compound **52** at 0 °C. The reaction mixture was vigorously stirred for 40 min while warming up to 22 °C and then stopped by transferring to a saturated aqueous ammonium chloride solution (70 mL). The aqueous phase was extracted four times with CH_2Cl_2 (70 mL each), the combined organic layers were dried over anhydrous sodium sulfate, and the solvent was removed *in vacuo*. The crude product was purified by flash column chromatography (SiO_2, *iso*-hexane:ethyl acetate, 50:1 v/v), yielding compound **55** as a red solid, which was used in the next synthetic step without further purification.

HR-MS (APPI$^+$, *m*/*z*) $[M+H]^+$ calc. for $[C_{22}H_{22}BrO_2S]^+$: 429.0518, found: 429.0517.

TLC (SiO_2, *iso*-hexane:ethyl acetate, 50:1 v/v): R_f = 0.22 and 0.28.

(*E*/*Z*)-5-(2-fluoro-5-methoxyphenyl)-2-(6-methoxy-2,2-dimethyl-2,3-dihydro-1*H*-inden-1-ylidene)-4,6-dimethylbenzo[*b*]thiophen-3(2*H*)-one (56)

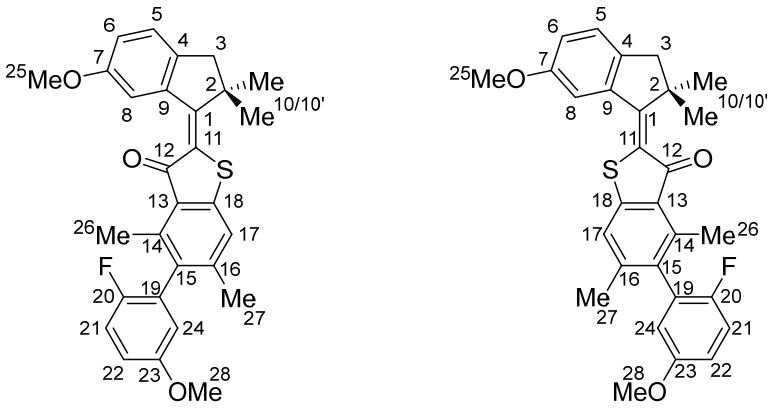

Compound **55** (318 mg, 0.740 mmol, 1.0 equiv.), 3-methoxyphenylboronic acid pinacol ester **53** (204 mg, 0.810 mmol, 1.1 equiv.) and potassium phosphate (309 mg, 2.22 mmol, 3.0 equiv.) were mixed in anhydrous *N*,*N*-dimethylformamide (7.40 mL, 0.10 M) under a nitrogen atmosphere. After addition of tetrakis(triphenylphosphane)palladium(0) (42.5 mg, 37.0 µmol, 5 mol%) the suspension was heated at 85 °C for 48 h. The reaction was stopped by addition of a saturated aqueous ammonium chloride solution (50 mL) at 22 °C and the aqueous mixture was extracted three times with ethyl acetate (50 mL each). The combined organic phases were dried over anhydrous sodium sulfate and the solvent was removed *in vacuo*. Purification of the crude product was achieved by flash column chromatography (SiO_2, *iso*-hexane:ethyl acetate, 50:1 v/v), yielding compound **56** (155 mg, 0.330 mmol, 40%) as an orange solid. Four isomers (two enantiomeric atropisomers for each *E*- and *Z*-isomer) were obtained from HPLC separation using a preparative *Daicel* CHIRALPAK® ID column (*n*-hexane:ethyl acetate, 80:20 to 75:25 v/v, at 40 °C).

racemic *E*-Isomer:

^{1}H NMR (600 MHz, CD_2Cl_2): δ = 8.47 (d, $^4J_{HH}$ = 2.5 Hz, 1H, HC8), 7.23 (s, 1H, HC17), 7.18 (dd, $^3J_{HH}$ = 8.3 Hz, 1H, HC5), 7.11 (t, $^3J_{HH}$ = 8.9 Hz, 1H, HC21), 6.95 (dd, $^3J_{HH}$ = 8.3 Hz, $^4J_{HH}$ = 2.5 Hz, 1H, HC6), 6.92 (ddd, $^3J_{HH}$ = 9.0, ^4J(H,F) = 4.0 Hz, $^4J_{HH}$ = 3.2, 1H, HC22), 6.65 (dd, $^4J_{HH}$ = 5.8 Hz, $^4J_{HH}$ = 3.2 Hz, 1H, HC24), 3.82 (s, 3H, H_3C25), 3.79 (s, 3H, H_3C28), 2.93 (s, 2H, H_2C3), 2.47 (s, 3H, H_3C26), 2.12 (s, 3H, H_3C27), 1.50 (s, 3H, H_3C10), 1.26 (s, 3H, H_3C10').

^{13}C NMR (151 MHz, CD_2Cl_2): δ = 189.23 (C12), 161.56 (C1), 158.20 (C7), 156.38 (C23), 155.62 (C20), 145.16 (C18), 144.33 (C16), 140.96 (C4), 140.51 (C14), 139.45 (C9), 133.86 (C15), 127.66 (C13), 127.54 (C11), 127.44 (C19), 125.44 (C5), 121.96 (C17), 118.85 (C6), 116.59 (C21), 116.56 (C24), 114.79 (C22), 112.86 (C8), 56.16 (C28), 55.81 (C25), 48.91 (C3), 30.10 (C10), 26.77 (C10'), 26.72 (C2), 21.70 (C27), 15.97 (C26).

^{19}F NMR (377 MHz, CD_2Cl_2): δ = −126.84 (FC20) ppm.

HR-MS (APPI$^+$, *m*/*z*) [M+H]$^+$ calc. for $[C_{29}H_{28}FO_3S]^+$: 475.1738, found: 475.1737.

IR: $\tilde{\nu}$ = 3084 (w), 2991 (w), 2945 (s), 2917 (s), 2852 (m), 2831 (m), 1655 (s), 1601 (m), 1577 (s), 1513 (m), 1485 (s), 1448 (s), 1375 (m), 1288 (m), 1261 (m), 1249 (s), 1205 (s), 1174 (s), 1114 (w), 1032 (s), 956 (m), 856 (m), 812 (m), 786 (m), 748 (w), 595 (s) cm^{-1}.

TLC (SiO_2, *iso*-hexane:ethyl acetate, 50:1 v/v): R_f = 0.33.

racemic *Z*-Isomer:

^{1}H NMR (400 MHz, CD_2Cl_2): δ = 7.65 (d, $^4J_{HH}$ = 2.3 Hz, 1H, HC8), 7.28–7.24 (m, 1H, HC17), 7.24–7.20 (m, 1H, HC5), 7.12 (t, $^3J_{HH}$ = 8.9 Hz, 1H, HC21), 6.99 (dd, $^3J_{HH}$ = 8.3 Hz, $^4J_{HH}$ = 2.3 Hz, 1H, HC6), 6.92 (ddd, $^3J_{HH}$ = 9.0 Hz, $^4J_{HH}$ = 3.2 Hz, 1H, HC22), 6.66 (dd, J_{HH} = 5.9 Hz, $^4J_{HH}$ = 3.1, 1H, HC24), 3.90 (s, 3H, H_3C25), 3.80 (s, 3H, H_3C28), 3.00 (s, 2H, H_2C3), 2.46 (s, 3H, H_3C26), 2.13 (s, 3H, H_3C27), 1.62 (s, 6H, H_3C10 and H_3C10') ppm.

^{13}C NMR (126 MHz, CD_2Cl_2): δ = 189.18 (C12), 162.10 (C1), 159.39 (C7), 156.40 (C23), 154.51 (C20), 145.73 (C18), 144.17 (C16), 142.22 (C4), 141.80 (C9), 140.29 (C14), 134.20 (C15), 127.58 (C19), 127.49 (C13), 126.23 (C11), 126.11 (C5), 122.08 (C17), 118.28 (C6), 116.66 (C21), 116.60 (C24), 114.78 (C22), 112.37 (C8), 56.15 (C29), 55.99 (C25), 50.92 (C3), 49.35 (C2), 25.90 (C10), 25.74 (C10'), 21.69 (C27), 15.95 (C26) ppm.

^{19}F NMR (377 MHz, CD_2Cl_2): δ = −126.74 (FC20) ppm.

HR-MS (APPI$^+$, *m*/*z*) [M+H]$^+$ calc. for $[C_{29}H_{28}FO_3S]^+$: 475.1738, found: 475.1737.

IR: $\tilde{\nu}$ = 2945 (s), 2922 (s), 2358 (m), 1656 (s), 1601 (m), 1583 (s), 1522 (m), 1487 (s), 1458 (s), 1376 (m), 1288 (m), 1261 (m), 1249 (s), 1208 (s), 1147 (s), 1120 (w), 1037 (s), 993 (m), 946 (m), 855 (m), 814 (m), 716 (w), 667 (w), 423 (s) cm^{-1}.

TLC (SiO_2, *iso*-hexane:ethyl acetate, 50:1 v/v): R_f = 0.29.

(*E*/*Z*)-5-(2-fluoro-5-methoxyphenyl)-2-(6-methoxy-2,2-dimethyl-2,3-dihydro-1*H*-inden-1-ylidene)-4,6-dimethylbenzo[*b*]thiophen-3(2*H*)-one 1-oxide (15h)[159]

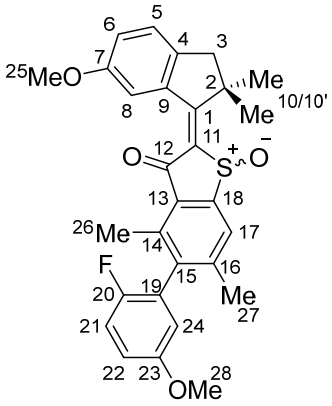

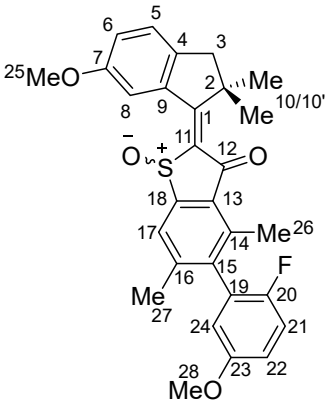

Compound **56** (155 mg, 0.330 mmol, 1.0 equiv.) was dissolved in acetic acid (15.1 mL, 0.02 M of **56**) and sodium perborate tetrahydrate (101 mg, 0.660 mmol, 2.0 equiv.) was added, subdivided into small portions. The mixture was stirred at 22 °C for 3.5 h until the reaction was stopped by cautiously transferring to a saturated aqueous sodium bicarbonate solution (100 mL). After extraction of the aqueous solution three times with ethyl acetate (100 mL each), the combined organic phases were washed with a saturated aqueous NaCl solution (100 mL), dried over anhydrous sodium sulfate, and the solvent was removed *in vacuo*. Purification of the crude product was achieved by flash column chromatography (SiO_2, *iso*-hexane:ethyl acetate, 3:2 v/v), yielding compound **15h** (88.5 mg, 0.180 mmol, 55%) as a yellow solid. Four diastereomeric isomers (with differently configured sulfoxide stereocenter, biaryl chiral axis, and *E*- or *Z*-configuration of the double bond) could be separated from the product mixture *via* HPLC separation using a Diacel CHIRALPAK® ID column (*n*-hexane:ethyl acetate, 50:50 to 30:70 v/v, at 40 °C).

Only (*S*) configured diastereomers are shown in the following for clarity.

racemic *E*-isomers:

15h-*E*-(*S*)-(S_a)/15h-*E*-(*R*)-(R_a)

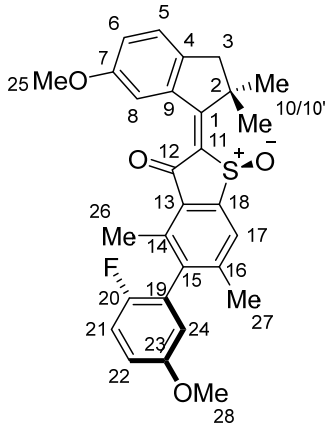

^{1}H NMR (601 MHz, CD_2Cl_2): δ = 7.86 (d, ^4J = 2.5 Hz, 1H, HC8), 7.82–7.78 (m, 1H, HC17), 7.26 (dp, J = 8.31, 1H, HC5), 7.15 (t, ^3J = 8.9 Hz, 1H, HC21), 7.05 (dd, ^3J = 8.3 Hz, ^4J = 2.5 Hz, 1H, HC6), 6.96 (ddd, ^3J = 9.1 Hz, J = 4.0 Hz, ^4J = 3.2 Hz, 1H, HC22), 6.65 (dd, J = 5.8 Hz, ^4J = 3.1 Hz, 1H, HC24), 3.81 (s, 3H, H_3C25), 3.81 (s, 3H, H_3C28), 3.14 (d, ^2J = 15.2 Hz, 1H, HC3), 2.85 (m, ^2J = 15.2 Hz, 1H, H'C3), 2.52 (s, 3H, H_3C26), 2.26 (s, 3H, H_3C27), 1.89 (s, 3H, H_3C10), 1.52 (s, 3H, H_3C10').

^{13}C NMR (151 MHz, CD_2Cl_2): δ = 186.17 (C12), 174.94 (C1), 158.03 (C7), 156.59 (C23), 154.01 (d, $^1J_{CF}$ = 236.7 Hz, C20), 149.19 (C18), 145.92 (C16), 142.94 (C4), 141.53 (C15), 140.15 (C13), 138.69 (C9), 137.70 (C11), 130.11 (C14), 126.83 (d, $^2J_{CF}$ = 19.7 Hz, C19), 125.83 (C5), 125.70 (C17), 120.92 (C6), 116.92 (d, $^1J_{CF}$ = 24.0 Hz, C21), 115.81 (d, $^2J_{CF}$ = 3.4 Hz, C24), 115.30 (d, $^1J_{CF}$ = 7.8 Hz, C22), 114.45 (C8), 56.22 (C28), 55.86 (C25), 52.37 (C3), 49.41 (C2), 29.49 (C10), 27.06 (C10'), 21.88 (C26), 16.18 (C27).

^{19}F NMR (377 MHz, CD_2Cl_2): δ = −127.11 (FC20) ppm.

HR-MS (ESI^+, m/z) $[M+H]^+$ calc. for $[C_{29}H_{28}FO_4S]^+$: 491.1687, found: 491.1683.

IR: $\tilde{\nu}$ = 3310 (w), 3153 (w), 2954 (w), 2917 (s), 2849 (s), 2359 (w), 1736 (w), 1662 (s), 1582 (w), 1559 (w), 1527 (w) 1496 (m), 1463 (m), 1405 (w), 1379 (w), 1296 (w), 1250 (w), 1206 (s), 1143 (w), 1123 (w), 1064 (w), 1032 (m), 948 (w), 851 (w), 717 (w), 418 (s) cm^{-1}.

TLC (SiO_2, *iso*-hexane:ethyl acetate, 3:2 v/v): R_f = 0.39.

15h-*E*-(*S*)-(*R*$_a$)/15h-*E*-(*R*)-(*S*$_a$)

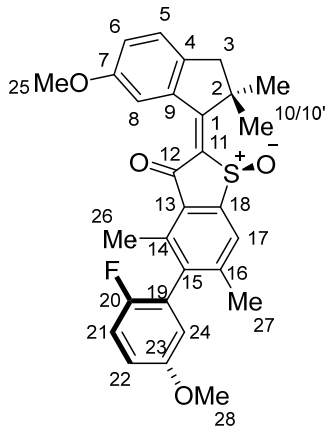

^{1}H NMR (601 MHz, CD_2Cl_2): δ = 7.82 (d, ^4J = 2.5 Hz, 1H, HC8), 7.81–7.78 (m, 1H, HC17), 7.28–7.23 (m, 1H, HC5), 7.16 (t, ^3J = 8.9 Hz, 1H, HC21), 7.04 (dd, ^3J = 8.3 Hz, ^4J = 2.5 Hz, 1H, HC6), 6.96 (ddd, ^3J = 9.1 Hz, J = 4.0 Hz, ^4J = 3.2 Hz, 1H, HC22), 6.62 (dd, J = 5.8 Hz, ^4J = 3.1 Hz, 1H, HC24), 3.81 (s, 3H, H_3C25), 3.80 (s, 3H, H_3C28), 3.16 (d, ^2J = 15.1 Hz, 1H, HC3), 2.83 (d, ^2J = 15.1 Hz, 1H, H'C3), 2.50 (s, 3H, H_3C26), 2.25 (s, 3H, H_3C27), 1.91 (s, 3H, H_3C10), 1.49 (s, 3H, H_3C10').

^{13}C NMR (151 MHz, CD_2Cl_2): δ = 185.81 (C12), 174.95 (C1), 158.00 (C7), 156.54 (C23), 154.97 (d, $^1J_{CF}$ = 236.9 Hz, C20), 149.22 (C18), 145.93 (C16), 142.89 (C4), 141.50 (C15), 140.00 (C14), 138.73 (C9), 137.93 (C11), 130.24 (C13), 126.88 (d, $^2J_{CF}$ = 19.5 Hz, C19), 125.83 (C6), 125.62 (C17), 120.99 (C5), 116.97 (d, $^1J_{CF}$ = 24.3 Hz, C21), 115.87 (d, $^2J_{CF}$ = 3.3 Hz, C24), 115.24 (d, $^1J_{CF}$ = 7.7 Hz, C22), 114.31 (C8), 56.20 (C28), 55.85 (C25), 52.45 (C2), 49.42 (C3), 29.47 (C10), 26.76 (C10'), 21.84 (C26), 16.29 (C27).

^{19}F NMR (377 MHz, CD_2Cl_2): δ = −126.76 (FC20) ppm.

HR-MS (ESI$^+$, *m*/*z*) $[M+H]^+$ calc. for $[C_{29}H_{28}FO_4S]^+$: 491.1687, found: 491.1683.

IR: $\tilde{\nu}$ = 3435 (w), 2955 (m), 2926 (m), 2848 (m), 2166 (w), 1673 (s), 1582 (s), 1538 (s), 1492 (s) 1488 (s), 1464 (m), 1419 (w), 1378 (w), 1293 (m), 1251 (m), 1117 (w), 1207 (s), 1152 (m), 1056 (m), 1034 (s), 954 (w), 862 (m), 816 (m), 792 (w), 740 (w), 712 (w) cm^{-1}.

TLC (SiO_2, *iso*-hexane:ethyl acetate, 3:2 v/v): R_f = 0.39.

racemic *Z*-isomers:

15h-*Z*-(*S*)-(S_a)/15h-*Z*-(*R*)-(R_a)

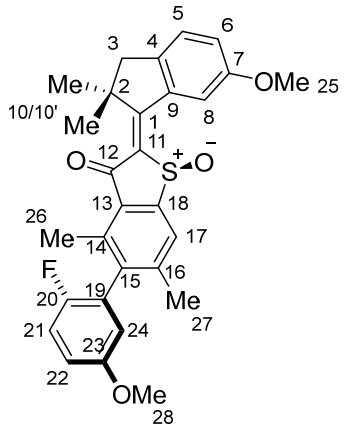

^{1}H NMR (601 MHz, CD_2Cl_2): δ = 8.09 (d, ^4J = 2.3 Hz, 1H, HC8), 7.80–7.77 (m, 1H, HC17), 7.28 (dq, ^3J = 8.4 Hz, J = 0.9 Hz, 1H, HC5), 7.15 (t, ^3J = 8.9 Hz, 1H, HC21), 7.13 (dd, ^3J = 8.4 Hz, ^4J = 2.4 Hz, 1H, HC6), 6.96 (ddd, ^3J = 9.1 Hz, J = 4.0 Hz, ^4J = 3.2 Hz, 1H, HC22), 6.65 (dd, J = 5.8 Hz, ^4J = 3.1 Hz, 1H, HC24), 3.93 (s, 3H, H_3C25), 3.80 (s, 3H, H_3C28), 3.03 (d, ^2J = 16.2 Hz, 1H, HC3), 3.04 (d, ^2J = 16.2 Hz, 1H, H'C3), 2.50 (s, 3H, H_3C26), 2.24 (s, 3H, H_3C27), 1.64 (s, 3H, H_3C10), 1.55 (s, 3H, H_3C10').

^{13}C NMR (151 MHz, CD_2Cl_2): δ = 188.07 (C12), 176.45 (C1), 159.70 (C7), 156.61 (C23), 153.96 (d, $^1J_{CF}$ = 236.5 Hz, C20), 149.68 (C18), 145.83 (C16), 143.67 (C4), 141.72 (C15), 140.10 (C14), 139.33 (C9), 136.76 (C11), 130.41 (C13), 126.78 (d, $^2J_{CF}$ = 19.6 Hz, C19), 126.46 (C5), 125.96 (C17), 121.47 (C6), 116.91 (d, $^2J_{CF}$ = 24.0 Hz, C21), 115.74 (d, $^3J_{CF}$ = 3.3 Hz, C24), 115.40 (d, $^1J_{CF}$ = 7.8 Hz, C22), 113.31 (C8), 56.21 (C28), 56.12 (C25), 50.51 (C3), 50.46 (C2), 26.63 (C10), 26.31 (C10'), 21.83 (C27), 16.10 (C26).

^{19}F NMR (377 MHz, CD_2Cl_2): δ = −127.17 (FC20) ppm.

HR-MS (ESI^+, m/z) $[M+H]^+$ calc. for $[C_{29}H_{28}FO_4S]^+$: 491.1687, found: 491.1680.

IR: $\tilde{\nu}$ = 3359 (s), 3186 (m), 3001 (w), 2956 (w), 2922 (s), 2851 (s), 2360 (w), 2335 (w), 1659 (s) 1632 (s), 1582 (w), 1539 (w), 1496 (m), 1468 (m), 1423 (w), 1411 (w), 1294 (w), 1206 (m), 1142 (w), 1035 (s), 861 (w), 818 (w), 711 (w), 643 (w), 408 (s) cm^{-1}.

TLC (SiO_2, *iso*-hexane:ethyl acetate, 3:2 v/v): R_f = 0.26.

15h-*Z*-(*S*)-(*R*$_a$)/15h-*Z*-(*R*)-(*S*$_a$)

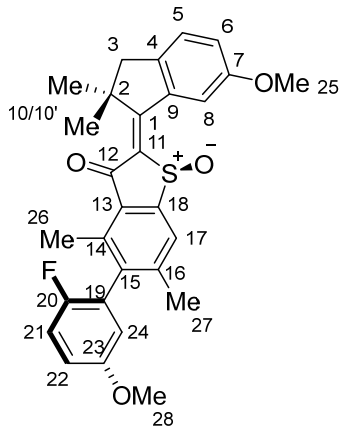

^{1}H NMR (601 MHz, CD_2Cl_2): δ = 8.06 (d, ^4J = 2.3 Hz, 1H, HC8), 7.79 (p, J = 0.67 Hz, 1H, HC17), 7.28 (dq, ^3J = 8.4 Hz, J = 0.9 Hz, 1H, HC5), 7.16 (t, ^3J = 8.9 Hz, 1H, HC21), 7.13 (dd, ^3J = 8.4 Hz, ^4J = 2.4 Hz, 1H, HC6), 6.96 (ddd, ^3J = 9.1 Hz, J = 4.0 Hz, ^4J = 3.2 Hz, 1H, HC22), 6.62 (dd, J = 5.8 Hz, ^4J = 3.2 Hz, 1H, HC24), 3.93 (s, 3H, H_3C25), 3.80 (s, 3H, H_3C28), 3.06 (d, ^2J = 16.1 Hz, 1H, HC3), 3.00 (d, ^2J = 16.1 Hz, 1H, H'C3), 2.50 (s, 3H, H_3C26), 2.24 (s, 3H, H_3C27), 1.64 (s, 3H, H_3C10), 1.55 (s, 3H, H_3C10').

^{13}C NMR (151 MHz, CD_2Cl_2): δ = 188.07 (C12), 176.45 (C1), 159.70 (C7), 156.61 (C23), 153.96 (d, $^1J_{CF}$ = 236.5 Hz, C20), 149.68 (C18), 145.83 (C16), 143.67 (C4), 141.72 (C15), 140.10 (C14), 139.33 (C9), 136.76 (C11), 130.41 (C13), 126.78 (d, $^2J_{CF}$ = 19.6 Hz, C19), 126.46 (C5), 125.96 (C17), 121.47 (C6), 116.91 (d, $^2J_{CF}$ = 24.0 Hz, C21), 115.74 (d, $^3J_{CF}$ = 3.3 Hz, C24), 115.40 (d, $^1J_{CF}$ = 7.8 Hz, C22), 113.31 (C8), 56.21 (C28), 56.12 (C25), 50.51 (C3), 50.46 (C2), 26.63 (C10), 26.31 (C10'), 21.83 (C27), 16.10 (C26).

^{19}F NMR (377 MHz, CD_2Cl_2): δ = −126.53 (FC20) ppm.

HR-MS (ESI^+, *m*/*z*) $[M+H]^+$ calc. for $[C_{29}H_{28}FO_4S]^+$: 491.1687, found: 491.1689.

IR: $\tilde{\nu}$ = 3433 (m), 2961 (m), 2929 (w), 2866 (w), 2836 (w), 1673 (s), 1606 (w), 1582 (w), 1536 (s), 1491 (s), 1463 (w), 1421 (s), 1378 (w), 1292 (s), 1251 (m), 1228 (m), 1203 (s), 1145 (m), 1121 (w), 1067 (w), 1032 (s), 991 (w), 953 (m), 918 (w), 878 (m), 816 (m), 718 (m), 618 (w), 563 (w) cm^{-1}.

TLC (SiO_2, *iso*-hexane:ethyl acetate, 3:2 v/v): R_f = 0.26.

8.6. Synthesis of compounds from chapter 7

8.6.1. Macrocyclic HTI 68

Macrocyclic HTI motor **68** was constructed combining benzothiophenone **17** with pentaethylene glycol chain **69** and indanone **70**, furnishing macrocyclic motor **68** as shown in Figure 230. Commercially available 4-bromo-3,5-dimethylphenol **40**, 7-hydroxy indanone **74** and pentaethylene glycol **71** were utilized as starting structures. Building block **17** and **70** were prepared according to a previous report and **69** was synthesized through a modification thereof. [158,159]

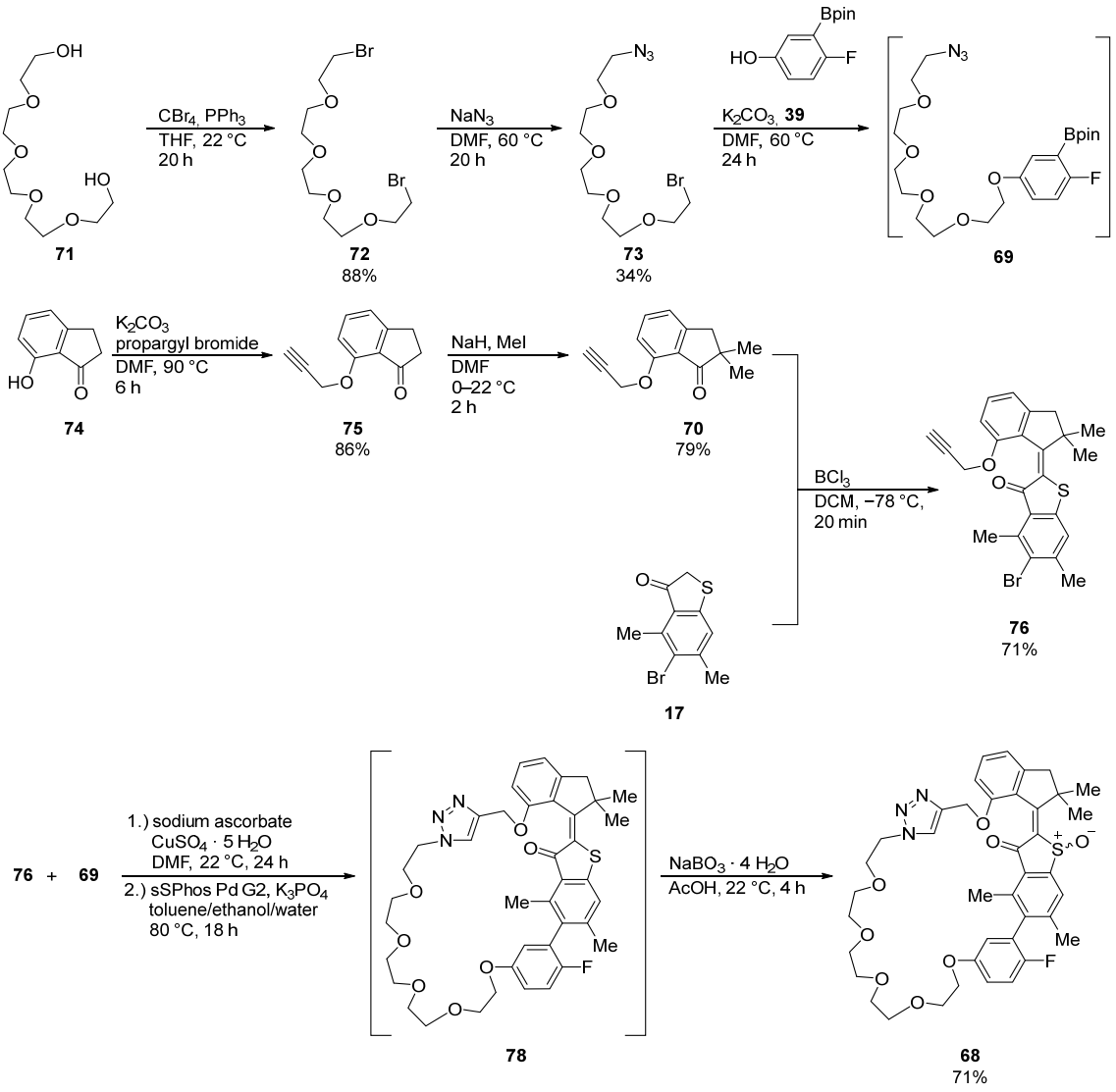

Figure 230 Overview of 9-step synthesis of macrocyclic molecular motor **68** starting from commercially available starting materials pentaethylene glycol **71**, 4-bromo-3,5-dimethylphenol **40**, and 7-hydroxy indanone **74**. Synthetic route to benzothiophenone **17** is elaborated in chapter 8.5.

All molecules successfully synthesized previously and described in literature were only characterized using ^{1}H NMR and HRMS mass spectrometry.[158,159]

7-(prop-2-yn-1-yloxy)-2,3-dihydro-1*H*-inden-1-one (75)[159]

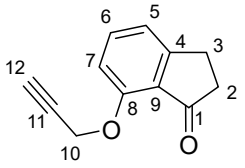

Commercially available 7-hydroxy-1-indanone **74** (1.00 g, 6.75 mmol, 1.0 equiv.), propargyl bromide (0.760 mL, 80% in toluene, 6.75 mmol, 1.0 equiv.), and potassium carbonate (3.73 g, 27.0 mmol, 4.0 equiv.) were mixed in *N*,*N*-dimethylformamide (45.0 mL, 0.15 M) and the suspension was heated to 90 °C for 6 h. The reaction was stopped by transferring to water (100 mL) and the aqueous solution was extracted three times with ethyl acetate (100 mL each). The combined organic phases were washed four times with water (30 mL each to remove remaining *N*,*N*-dimethylformamide), a saturated aqueous NaCl solution (100 mL), and dried over anhydrous sodium sulfate. Removal of the solvent *in vacuo* yielded compound **75** (1.08 g, 5.80 mmol, 86%) as a colorless liquid, which was used in the next synthetic step without further purification.

^{1}H NMR (400 MHz, $CDCl_3$): δ = 7.53 (dd, $^{3}J_{HH}$ = 8.2, 7.6 Hz, 1H, HC6), 7.09 (dd, $^{3}J_{HH}$ = 7.6 Hz, $^{4}J_{HH}$ = 0.9 Hz, 1H, HC5), 6.91 (dd, $^{3}J_{HH}$ = 8.2, $^{4}J_{HH}$ = 0.8 Hz, 1H, HC7), 4.84 (d, J_{HH} = 2.4 Hz, 2H, H_2C10), 3.10–3.04 (m, 2H, H_2C2), 2.64–2.58 (m, 3H, H_2C3 and HC12) ppm.

HR-MS (APPI^{+}, *m*/*z*) $[M+H]^{+}$ calc. for $[C_{12}H_{11}O_2]^{+}$: 187.0754, found: 187.0753.

2,2-dimethyl-7-(prop-2-yn-1-yloxy)-2,3-dihydro-1*H*-inden-1-one (70)[159]

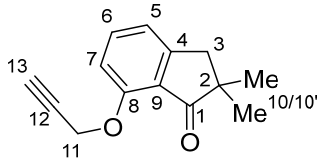

To a solution of compound **75** (1.08 mg, 5.80 mmol, 1.0 equiv.) in anhydrous *N*,*N*-dimethylformamide (12.0 mL, 0.5 M) at 0 °C, sodium hydride (580 mg (60% in mineral oil), 15.0 mmol, 2.5 equiv.) was added and the resulting suspension stirred for 20 min at 0 °C. Then iodomethane (0.900 mL, 14.5 mmol,

2.5 equiv.) was added dropwise and the reaction mixture was stirred for 2 h at 22 °C. After addition of a saturated aqueous ammonium chloride solution (50 mL) the aqueous solution was extracted three times with ethyl acetate (100 mL each). The combined organic phases were washed four times with water (40 mL each, to remove residual *N*,*N*-dimethylformamide), twice with a saturated aqueous NaCl solution (60 mL each), dried over anhydrous sodium sulfate, and the solvent was removed *in vacuo*. Purification of the crude product was achieved by flash column chromatography (SiO_2, *iso*-hexane:ethyl acetate, 12:1 v/v), yielding compound **70** (982 mg, 4.58 mmol, 79%) as a colorless liquid.

^{1}H NMR (400 MHz, $CDCl_3$): δ = 7.53 (dd, $^3J_{HH}$ = 8.2, 7.6 Hz, 1H, HC6), 7.03–7.00 (m, 1H, HC5), 6.96 (dd, $^3J_{HH}$ = 8.2, $^4J_{HH}$ = 0.8 Hz, 1H, HC7), 4.86 (d, J_{HH} = 2.4 Hz, 2H, H_2C11), 2.95 (m, 2H, H_2C3), 2.52 (t, J_{HH} = 2.4 Hz, 1H, HC13), 1.22 (s, 6H, H_3C10 and H_3C10') ppm.

HR-MS ($APPI^+$, *m*/*z*) $[M+H]^+$ calc. for $[C_{14}H_{15}O_2]^+$: 215.1067, found: 215.1068.

(*E*/*Z*)-5-bromo-2-(2,2-dimethyl-7-(prop-2-yn-1-yloxy)-2,3-dihydro-1*H*-inden-1-ylidene)-4,6-dimethylbenzo[*b*]thiophen-3(2*H*)-one (76)[159]

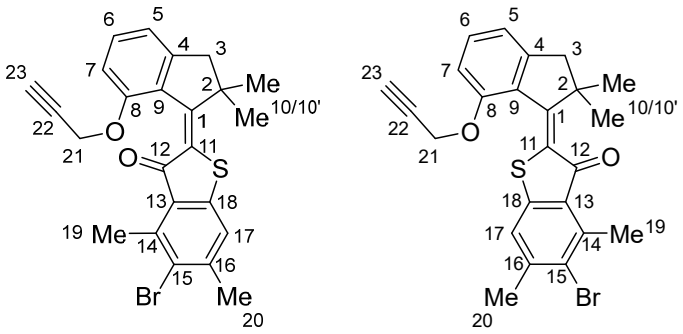

Two separate Schlenk flasks under a nitrogen atmosphere were charged individually with compound **70** (139 mg, 0.650 mmol, 1.0 equiv.) in anhydrous CH_2Cl_2 (0.300 mL, 2.2 M) in the first flask at 0 °C and compound **17** (167 mg, 0.650 mmol, 1.0 equiv.) in anhydrous CH_2Cl_2 (1.50 mL, 0.43 M) in the second flask at −78 °C. Boron trichloride (0.650 mL, 1.0 M in anhydrous CH_2Cl_2, 0.650 mmol, 1.0 equiv.) was added to the flask containing compound **17** and the resulting mixture was immediately taken up into the same syringe and transferred to the second flask containing compound **70** at 0 °C. The reaction mixture was vigorously stirred for 20 min while warming up to 22 °C and then stopped by transferring to a saturated aqueous ammonium chloride solution (30 mL). The aqueous phase was extracted four times with CH_2Cl_2 (50 mL each), the combined organic layers were dried over anhydrous sodium sulfate, and the solvent was removed *in vacuo*. Purification of the crude product was achieved by flash column chromatography (SiO2, *iso*-hexane:ethyl acetate, 50:1 v/v), yielding compound **76** (210 mg, 0.460 mmol, 71%) as a red solid.

^{1}H NMR (400 MHz, $CDCl_3$): δ = 7.33 (dd, $^3J_{HH}$ = 8.3, 7.4 Hz, 1H, HC6), 7.23–7.22 (m, 1H, HC17), 6.94 (dd, $^3J_{HH}$ = 7.4 Hz, $^4J_{HH}$ = 1.0 Hz, 1H, HC5), 6.86 (dd, $^3J_{HH}$ = 8.3, 0.8 Hz, 1H, HC7), 4.71 (d, J_{HH} = 2.4 Hz, 2H, H_2C21), 3.17 (d, J_{HH} = 15.4 Hz, 1H, H_2C3), 2.87 (d, J_{HH} = 0.5 Hz, 3H, H_3C19), 2.75 (d, J_{HH} = 15.4 Hz, 1H, H_2C3), 2.49 (d, J_{HH} = 0.7 Hz, 3H, H_3C20), 2.47 (t, J_{HH} = 2.4 Hz, 1H, HC23), 1.66 (s, 3H, H_3C10), 1.18 (s, 3H, H_3C10') ppm.

HR-MS (APPI$^+$, *m*/*z*) $[M+H]^+$ calc. for $[C_{24}H_{22}BrO_2S]^+$: 453.0519, found: 453.0518.

1,14-dibromo-3,6,9,12-tetraoxatetradecane (72)[159]

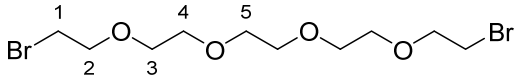

A mixture of commercially available pentaethylene glycol **71** (2.00 mL, 9.45 mmol, 1.0 equiv.) and tetrabromomethane (6.90 g, 20.8 mmol, 2.2 equiv.) in tetrahydrofuran (12.0 mL, 0.79 M) solution was cooled to 0 °C. Then triphenylphosphine (5.22 g, 19.8 mmol, 2.1 equiv.) was added slowly and the resulting mixture was allowed to warm up to 22 °C and stirred 20 h at this temperature. The reaction was stopped by transferring to a saturated aqueous ammonium chloride solution (100 mL) and the aqueous solution was extracted three times with ethyl acetate (100 mL each). The combined organic phases were washed with a saturated aqueous NaCl solution (50 mL), dried over anhydrous sodium sulfate, and the solvent was removed *in vacuo*. Purification of the crude product was achieved by flash column chromatography (SiO_2, *iso*-hexane:ethyl acetate, 2:1 v/v), yielding compound **72** (3.04, 8.34 mmol, 88%) as a colorless oil.

^{1}H NMR (400 MHz, $CDCl_3$): δ = 3.81 (t, $^3J_{HH}$ = 6.3 Hz, 4H, H_2C2), 3.71–3.62 (m, 12H, H_2C3, H_2C4, H_2C5), 3.47 (t, $^3J_{HH}$ = 6.3 Hz, 4H, H_2C1) ppm.

^{13}C NMR (101 MHz, $CDCl_3$): δ = 71.36 (C2), 70.82 (C3, C4 or C5), 70.75 (C3, C4 or C5), 70.70 (C3, C4 or C5), 30.45 (C1) ppm.

HR-MS (ESI$^+$, *m*/*z*) $[M+Na]^+$ calc. for $[C_{10}H_{20}Br_2NaO_4]^+$: 384.9621, found: 384.9627.

IR: $\tilde{\nu}$ = 2922 (s), 2854 (m), 2153 (w), 2028 (s), 1737 (m), 1454 (m), 1350 (m), 1277 (m), 1246 (m), 1107 (s), 942 (w), 457 (w) cm^{-1}.

TLC (SiO_2, *iso*-hexane:ethyl acetate, 2:1 v/v): R_f = 0.18.

1-azido-14-bromo-3,6,9,12-tetraoxatetradecane (73)[159]

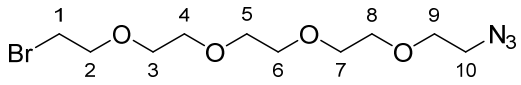

A solution of compound **72** (3.04 g, 8.34 mmol, 1.0 equiv.) and sodium azide (325 mg, 5.00 mmol, 0.6 equiv.) in *N*,*N*-dimethylformamide (5.60 mL, 1.5 M) was stirred for 25 h at 60 °C. The reaction was stopped by addition of water (150 mL) and the aqueous solution extracted three times with ethyl acetate (150 mL each). The combined organic phases were washed four times with water (75 mL each, to remove residual *N*,*N*-dimethylformamide), a saturated aqueous NaCl solution (150 mL), dried over anhydrous sodium sulfate, and the solvent removed *in vacuo*. Purification of the crude product was achieved by flash column chromatography (SiO_2, *i*Hex:ethyl acetate, 1:1 v/v), yielding compound **73** (924 mg, 2.84 mmol, 34%) as a colorless oil.

^{1}H NMR (400 MHz, CD_2Cl_2): δ = 3.78 (t, $^3J_{HH}$ = 6.1 Hz, 2H, H_2C2), 3.68–3.57 (m, 14H, H_2C3, H_2C4, H_2C5, H_2C6, H_2C7, H_2C8, H_2C9), 3.48 (t, $^3J_{HH}$ = 6.1, 2H, H_2C1), 3.37 (t, $^3J_{HH}$ = 5.1, 2H, H_2C10) ppm.

^{13}C NMR (101 MHz, CD_2Cl_2): δ = 71.49 (C2), 70.99 (C3, C4, C5, C6, C7 or C8), 70.95 (C3, C4, C5, C6, C7 or C8), 70.94 (C3, C4, C5, C6, C7 or C8), 70.89 (C3, C4, C5, C6, C7 or C8), 70.85 (C3, C4, C5, C6, C7 or C8), 70.83 (C3, C4, C5, C6, C7 or C8), 70.25 (C9), 51.18 (C10), 31.22 (C1). ppm.

HR-MS (APPI$^+$, *m*/*z*) $[M+H]^+$ calc. for $[C_{10}H_{21}BrN_3O_4]^+$: 326.0710, found: 326.0710.

IR: $\tilde{\nu}$ = 2864 (s), 2096 (s), 1442 (m), 1348 (m), 1279 (s), 1250 (m), 1186 (w), 1109 (s), 1038 (m), 996 (m), 939 (m), 852 (m), 662 (m), 610 (w), 569 (m), 555 (m), 505 (w) cm^{-1}.

TLC (SiO_2, *iso*-hexane:ethyl acetate, 1:1 v/v): R_f = 0.45.

2-(5-((14-azido-3,6,9,12-tetraoxatetradecyl)oxy)-2-fluorophenyl)-4,4,5,5-tetramethyl-1,3,2-dioxaborolane (69)[159]

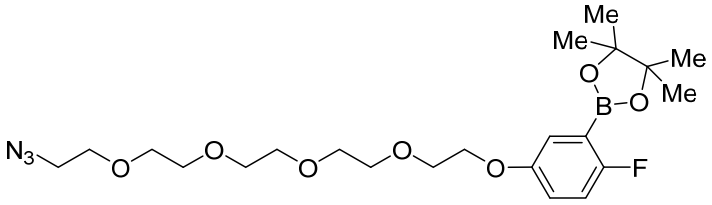

Compound **73** (282 mg, 0.860 mmol, 1.0 equiv.), commercially available 2-fluoro-5-hydroxyphenylboronic acid pinacol ester **39** (221 mg, 0.930 mmol, 1.1 equiv.), and potassium carbonate (427 mg, 3.08 mmol, 3.6 equiv.) were mixed in *N*,*N*-dimethylformamide (3.00 mL, 0.29 M). The

suspension was heated to 60 °C for 23 h and the reaction was stopped by transferring to a saturated aqueous sodium bicarbonate solution (50 mL). The aqueous solution was extracted three times with ethyl acetate (50 mL each) and the combined organic phases were washed four times with water (25 mL each to remove remaining *N*,*N*-dimethylformamide), a saturated aqueous NaCl solution (25 mL), and dried over anhydrous sodium sulfate. Removal of the solvent *in vacuo* yielded compound **69** as a colorless liquid, which was used in the next synthetic step without further purification.

HR-MS (APPI$^+$, *m*/*z*) $[M+H]^+$ calc. for $[C_{23}H_{35}BFN_3O_7]^+$: 484.2625, found: 484.2625.

5-bromo-2-(7-((1-(14-(4-fluoro-3-(4,4,5,5-tetramethyl-1,3,2-dioxaborolan-2-yl)phenoxy)-3,6,9,12-tetraoxatetradecyl)-1*H*-1,2,3-triazol-4-yl)methoxy)-2,2-dimethyl-2,3-dihydro-1*H*-inden-1-ylidene)-4,6-dimethylbenzo[*b*]thiophen-3(2*H*)-one (77)[159]

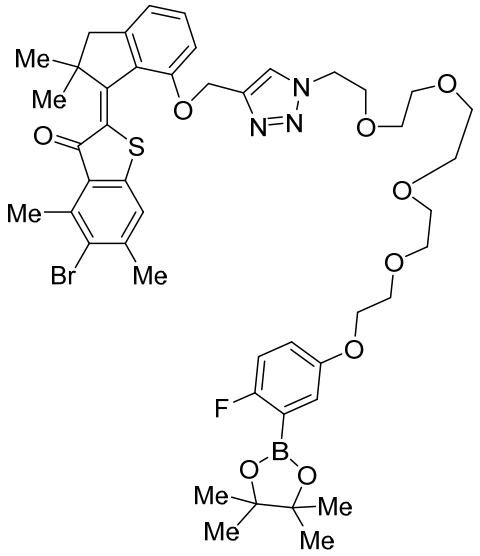

A mixture of HTI **76** (303 mg, 0.66 mmol, 1.0 equiv.), compound **69** (353 mg, 0.730 mmol, 1.05 equiv), sodium ascorbate (31.7 mg, 160 µmol, 24 mol%) and copper(II) sulfate pentahydrate (11.9 mg, 47.6 µmol, 3 mol%) were dissolved in *N*,*N*-dimethylformamide (3.30 mL, 0.20 M) and the resulting solution was stirred for 1 d at 22 °C. After transferring the reaction to a saturated aqueous ammonium chloride solution (75 mL), the aqueous solution was extracted three times with ethyl acetate (75 mL each). The combined organic phases were washed four times with water (30 mL each, to remove residual *N*,*N*-dimethylformamide), a saturated aqueous NaCl solution (75 mL), dried over anhydrous sodium sulfate and the solvent was removed *in vacuo*. The crude product was purified by flash column chromatography (SiO_2, CH_2Cl_2:methanol, 100:0 to 97:3 v/v), yielding compound **77** as a viscous red oil, which was used in the next synthetic step without further purification.

HR-MS (APPI$^+$, *m*/*z*) [M+Na]$^+$ calc. for [$C_{46}H_{56}BBrFN_3NaO_9S$]$^+$: 958.2890, found: 958.2886.

TLC (SiO_2, CH_2Cl_2:methanol, 97:3 v/v): R_f = 0.23 and 0.33.

(*E*/*Z*)-16-fluoro-24,26,32,32-tetramethyl-22,23,32,33-tetrahydro-31*H*,61*H*-4,9,12,15,18,21-hexaoxa-6(4,1)-triazola-2(5,2)-benzo[*b*]thiophena-3(1,7)-indena-1(1,3)-benzenacyclohenicosaphan-23-one (78)[77]

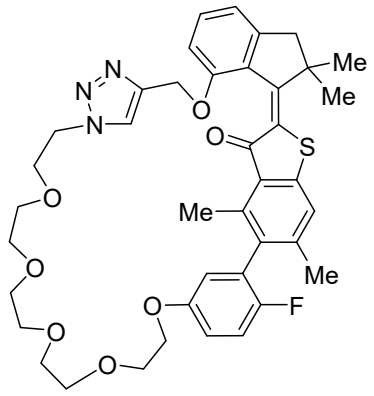

Crude compound **77** (620 mg, 0.662 mmol (assuming pure product), 1.0 equiv.) and potassium phosphate (425 mg, 1.99 mmol, 3.0 equiv.) were dissolved in a mixture of toluene, ethanol, and water (3:3:1, 31.5 mL, 0.021 M) under a nitrogen atmosphere. The reaction mixture was degassed *via* three freeze-pump-thaw cycles, sSPhos Pd G2 (43.7 mg, 53.0 mmol, 8 mol%) added and heated at 80 °C for 24 h. The reaction was stopped by addition of a saturated aqueous ammonium chloride solution (50 mL) at 22 °C and the aqueous mixture was extracted three times with ethyl acetate (50 mL each). The combined organic phases were dried over anhydrous sodium sulfate and the solvent was removed *in vacuo*. The crude product was purified by flash column chromatography (SiO_2, CH_2Cl_2:methanol, 100:1 to 50:1 v/v), yielding compound **78** as an orange solid, which was used in the next synthetic step without further purification.

HR-MS (APPI$^+$, *m*/*z*) [M+H]$^+$ calc. for [$C_{40}H_{45}FN_3O_7S$]$^+$: 730.2957, found: 730.2967.

TLC (SiO_2, CH_2Cl_2:methanol, 97:3 v/v): R_f = 0.27.

(*E*/*Z*)-16-fluoro-24,26,32,32-tetramethyl-22,23,32,33-tetrahydro-31*H*,61*H*-4,9,12,15,18,21-hexaoxa-6(4,1)-triazola-2(5,2)-benzo[*b*]thiophena-3(1,7)-indena-1(1,3)-benzenacyclohenicosaphan-23-one 21-oxide (68)[159]

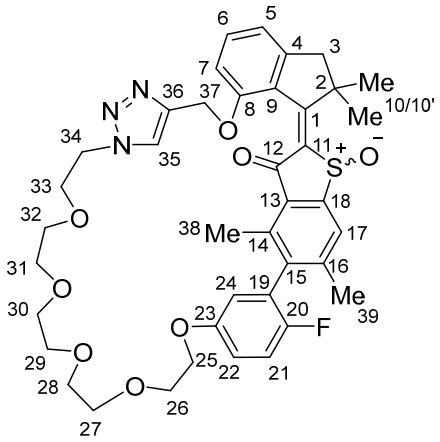

Compound **78** (89.7 mg, 123 µmol (assuming pure product), 1.0 equiv.) was dissolved in acetic acid (5.60 mL, 0.022 M of **78**) and sodium perborate tetrahydrate (30.2 mg, 185 µmol, 1.5 equiv.) was added, subdivided into small portions. The mixture was stirred at 22 °C for 5 h until the reaction was stopped by cautiously transferring to a saturated aqueous sodium bicarbonate solution (100 mL). After extraction of the aqueous solution three times with ethyl acetate (100 mL each), the combined organic phases were washed with a saturated aqueous NaCl solution (100 mL), dried over anhydrous sodium sulfate, and the solvent was removed *in vacuo*. Purification of the crude product was achieved by flash column chromatography (SiO_2, CH_2Cl_2:methanol, 40:1 v/v), yielding compound **68** (65.0 mg, 87.1 µmol, 13% over three steps) as a yellow solid. Both *E*-configured atropisomers were obtained from the reaction and separated on a *Macherey-Nagel Nucleosil* SiO_2 column (100% ethyl acetate, at 40 °C). *Z*-configured isomers were obtained after irradiation with a 470 nm LED followed by HPLC separation using a *Macherey-Nagel Nucleosil* SiO_2 column (100% ethyl acetate, at 40 °C) and a *Daicel* CHIRALPAK® IB-N column (*n*-hexane:ethyl acetate, 50:50 to 0:100 v/v, at 40 °C) or a CHIRALPAK® IC column (*n*-hexane:ethyl acetate, 50:50 to 0:100 v/v, at 40 °C).

Only (*S*) configured diastereomers are shown in the following for clarity.

racemic *E*-isomers:

68-*E*-(*S*)-(*P*)-(R_a)/68-*E*-(*R*)-(*M*)-(S_a) = A-(R_a)

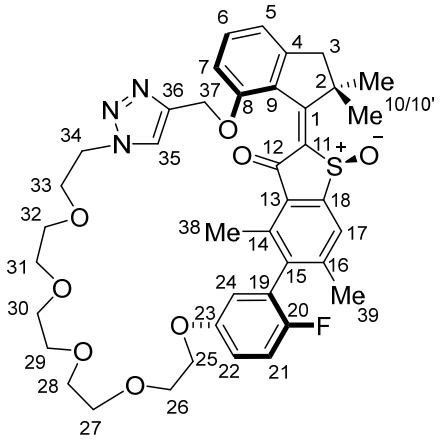

^{1}H NMR (601 MHz, CD_2Cl_2): δ = 8.24 (s, 1H, HC35), 7.81 (s, 1H, HC17), 7.28 (t, $^3J_{HH}$ = 7.8 Hz, 1H, HC6), 7.12 (m, 1H, HC21), 6.95 (ddd, J_{HH} = 9.1, 3.9, 3.1 Hz, 1H, HC22), 6.92 (d, $^3J_{HH}$ = 7.3 Hz, 1H, HC5), 6.66 (m, 2H, HC7 and HC24), 5.35–5.33 (m, 2H, H_2C37), 4.56 (dt, $^2J_{HH}$ = 13.8, J_{HH} = 6.2 Hz, 1H, HC34), 4.39 (dt, $^2J_{HH}$ = 13.7 Hz, J_{HH} = 6.6, 1H, HC34), 4.11 (m, H_2C25), 3.86–3.71 (m, 4H, H_2C33 and H_2C26, H_2C27, H_2C28, H_2C29 or H_2C30), 3.65 (dd, J_{HH} = 5.4, 3.3 Hz, 2H, H_2C26, H_2C27, H_2C28, H_2C29 or H_2C30), 3.61–3.43 (m, 10H, H_2C26, H_2C27, H_2C28, H_2C29 or H_2C30), 3.23 (d, $^2J_{HH}$ = 15.0 Hz, 1H, HC3), 2.81 (d, $^2J_{HH}$ = 15.1 Hz, 1H, H‘C3), 2.42 (s, 3H, H_3C38), 2.26 (s, 3H, H_3C39), 1.96 (s, 3H, H_3C10), 1.36 (s, 3H, H_3C10‘) ppm.

^{13}C NMR (151 MHz, CD_2Cl_2): δ = 184.59 (C12), 167.76 (C1), 156.97 (C8), 155.43 (C23), 153.75 (d, $^1J_{CF}$ = 237.2 Hz, C20), 150.88 (C4), 149.38 (C18), 145.27 (C16), 144.43 (C36), 140.77 (C15), 140.31 (C11), 138.37 (C14), 133.85 (C6), 131.34 (C13), 127.62 (C9), 126.52 (d, $^1J_{CF}$ = 19.3 Hz, C19), 125.31 (C17), 124.34 (C35), 117.49 (C5), 116.69 (d, $^1J_{CF}$ = 23.8 Hz, C21), 116.56 (d, $^1J_{CF}$ = 3.1 Hz, C24), 115.24 (d, $^1J_{CF}$ = 7.7 Hz, C22), 110.88 (C7), 70.98 (C26, C27, C28, C29, C30 or C31), 70.82 (C26, C27, C28, C29, C30 or C31), 70.71 (C26, C27, C28, C29, C30 or C31), 70.65 (C32), 70.59 (C26, C27, C28, C29, C30 or C31), 70.31 (C26, C27, C28, C29, C30 or C31), 69.68 (C26, C27, C28, C29, C30 or C31), 69.51 (C33), 68.26 (C25), 63.30 (C37), 52.88 (C2), 49.80 (C34), 49.77 (C3), 28.24 (C10), 26.18 (C10‘), 22.99 (C39), 21.49 (C38) ppm.

^{19}F NMR (377 MHz, CD_2Cl_2): δ = −125.93 (FC20) ppm.

HR-MS (APPI$^+$, m/z) $[M+H]^+$ calc. for $[C_{40}H_{45}FN_3O_8S]^+$: 746.2906, found: 746.2907.

IR: $\tilde{\nu}$ = 2959 (s), 2924 (s), 2871 (s), 1677 (m), 1583 (s), 1551 (m), 1497 (m), 1475 (m) 1458 (m), 1377 (s), 1363 (s), 1297 (s), 1274 (m), 1228 (w), 1207 (w), 1124 (m), 1050 (s), 998 (s), 950 (m), 845 (m), 817 (m), 793 (m), 426 (m) cm^{-1}.

TLC (SiO_2, *iso*-hexane:*i*Pr, 1:1 v/v): R_f = 0.06.

68-*E*-(*S*)-(*P*)-(S_a)/68-*E*-(*R*)-(*M*)-(R_a) = A-(S_a)

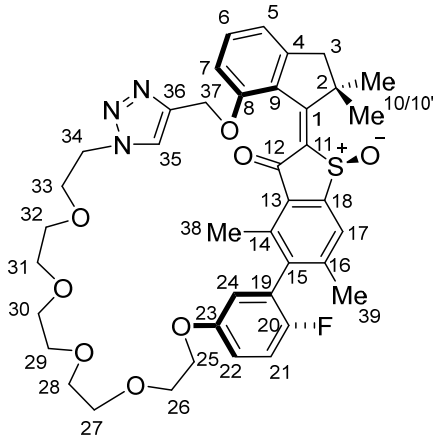

^{1}H NMR (601 MHz, CD_2Cl_2): δ = 7.80 (s, 1H, HC17), 7.66 (s, 1H, HC35), 7.42 (dd, J_{HH} = 8.3, 7.4 Hz, 1H, HC6), 7.12 (m, 2H, HC7 and HC21), 7.00–6.93 (m, 2H, HC5 and HC22), 6.84 (dd, J_{HH} = 5.8, 3.1 Hz, 1H, HC24), 5.29–5.18 (m, 2H, H_2C37), 4.44–4.36 (m, 1H, HC34), 4.30 (dt, J_{HH} = 14.3, 4.9 Hz, 1H, HC34), 4.22–4.16 (m, 2H, H_2C25), 3.85 (td, J_{HH} = 4.1, 1.1 Hz, 2H, H_2C26), 3.82–3.77 (m, 2H, H_2C33), 3.70–3.66 (m, 2H, H_2C27), 3.63–3.57 (m, 2H, H_2C28), 3.57–3.46 (m, 8H, H_2C29, H_2C30, H_2C31 and H_2C32), 3.27 (d, $^2J_{HH}$ = 15.1 Hz, 1H, HC3), 2.81 (d, $^2J_{HH}$ = 15.1 Hz, 1H, H‘C3), 2.39 (s, 3H, H_3C38), 2.25 (s, 3H, H_3C39), 1.94 (s, 3H, H_3C10), 1.35 (s, 3H, H_3C10’) ppm.

^{13}C NMR (151 MHz, CD_2Cl_2): δ = 184.28 (C12), 168.08 (C1), 158.27 (C8), 155.81 (C23), 154.13 (d, $^1J_{CF}$ = 236.8 Hz, C20), 150.60 (C4), 150.10 (C11), 144.92 (C16), 143.87 (C36), 140.97 (C15), 140.49 (C18), 139.30 (C14), 134.06 (C6), 130.97 (C13), 128.65 (C9), 126.92 (d, $^2J_{CF}$ = 19.2 Hz, C19), 125.39 (C17), 124.57 (C35), 118.01 (C5), 116.99 (d, $^3J_{CF}$ = 3.0 Hz, C24), 116.82 (d, $^2J_{CF}$ = 24.2 Hz, C21), 115.80 (d, $^2J_{CF}$ = 7.6 Hz, C22), 111.71 (C7), 71.23 (C27), 71.09 (C31), 71.00 (C30), 70.97 (C28), 70.93 (C29), 70.77 (C32), 70.06 (C26), 69.82 (C33), 68.69 (C25), 63.21 (C37), 52.86 (C2), 50.70 (C34), 50.12 (C3), 28.31 (C10’), 26.27 (C10), 21.75 (C39), 16.09 (C38) ppm.

^{19}F NMR (377 MHz, CD_2Cl_2): δ = −126.90 (FC20) ppm.

HR-MS ($APPI^+$, m/z) $[M+H]^+$ calc. for $[C_{40}H_{45}FN_3O_8S]^+$: 746.2906, found: 746.2908.

IR: $\tilde{\nu}$ = 2959 (s), 2923 (s), 2867 (s), 2362 (w), 1740 (w), 1675 (m), 1584 (s), 1555 (m), 1497 (m), 1475 (m) 1436 (m), 1378 (s), 1261 (m), 1191 (w), 1144 (w), 1099 (m), 1053 (s), 948 (s), 838 (m), 793 (m), 775 (w), 793 (w), 695 (w) cm^{-1}.

TLC (SiO_2, *iso*-hexane:*i*Pr, 1:1 v/v): R_f = 0.06.

racemic *Z*-isomers:

68-*Z*-(*S*)-(*P*)-(R_a)/68-*Z*-(*R*)-(*M*)-(S_a) = C-(R_a)

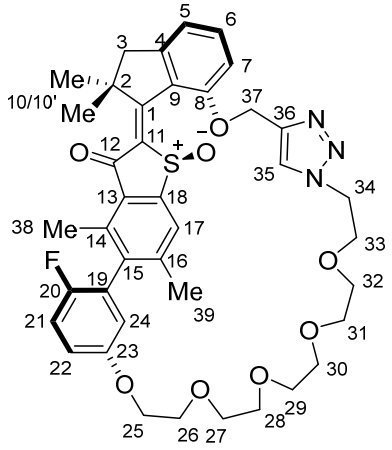

^{1}H NMR (601 MHz, CD_2Cl_2): δ = 7.87 (s, 1H, HC35), 7.72 (s, 1H, HC17), 7.54 (dd, $^3J_{HH}$ = 8.3, 7.4 Hz, 1H, HC6), 7.13 (t, J_{HH} = 8.8 Hz, 1H, HC21), 7.08 (d, $^3J_{HH}$ = 8.3, 1H, HC7), 7.03–7.00 (m, 1H, HC5), 6.95 (ddd, J_{HH} = 9.0, 4.0 Hz, $^4J_{HH}$ = 3.1 Hz, 1H, HC22), 6.75 (dd, J_{HH} = 5.9 Hz, $^4J_{HH}$ = 3.1 Hz, 1H, HC24), 5.46–5.32 (m, 2H, H_2C37), 4.54–4.43 (m, 2H, H_2C34), 4.18–4.14 (m, 2H, H_2C25), 3.79–3.76 (m, 2H, H_2C26), 3.76–3.71 (m, 2H, H_2C33), 3.66–3.61 (m, 2H, H_2C27), 3.55 (ddd, J=5.3, 2.8, 1.3, 2H, H_2C28), 3.53 (t, J_{HH} = 4.5 Hz, 2H, H_2C30), 3.47–3.42 (m, 2H, H_2C31), 3.34–3.25 (m, 4H, H_2C29 and H_2C32), 3.18 (d, $^2J_{HH}$ = 15.8 Hz, 1H, HC3), 2.84 (d, $^2J_{HH}$ = 15.8 Hz, 1H, H'C3), 2.47 (s, 3H, H_3C38), 2.22 (s, 3H, H_3C39), 1.51 (s, 3H, H_3C10), 1.49 (s, 3H, H_3C10') ppm.

^{13}C NMR (151 MHz, CD_2Cl_2): δ = 186.00 (C12), 168.08 (C1), 156.74 (C8), 155.84 (C23), 155.01 (d, $^1J_{CF}$ = 237.7 Hz, C20), 151.53 (C4), 151.49 (C18), 145.44 (C16), 144.13 (C11), 142.95 (C36), 140.70 (C15), 138.68 (C14), 134.92 (C6), 131.47 (C13), 126.89 (d, $^2J_{CF}$ = 20.2 Hz, C19), 126.20 (C9), 125.17 (C35), 124.78 (C17), 118.44 (C5), 118.10 (C24), 116.96 (C21), 116.78 (d, $^3J_{CF}$ = 7.1 Hz, C22), 110.41 (C7), 71.52 (C27), 70.98 (C31), 70.89 (C30), 70.86 (C28), 70.74 (C32 or C29), 70.57 (C32 or C29), 69.83 (C26), 69.71 (C33), 69.25 (C25), 63.03 (C37), 52.12 (C2), 50.80 (C3), 50.59 (C34), 28.34 (C10'), 25.73 (C10), 21.81 (C39), 16.32 (C38) ppm.

^{19}F NMR (377 MHz, CD_2Cl_2): δ = −125.96 (FC20) ppm.

HR-MS (APPI$^+$, m/z) $[M+H]^+$ calc. for $[C_{40}H_{45}FN_3O_8S]^+$: 746.2906, found: 746.2905.

IR: $\tilde{\nu}$ = 2922 (s), 2866 (s), 1737 (w), 1668 (s), 1582 (s), 1541 (s), 1496 (m), 1473 (m), 1457 (m), 1264 (m), 1228 (w), 1190 (w), 1169 (w), 1043 (s), 1107 (s), 1046 (s), 954 (m), 938 (m), 822 (m), 771 (m), 545 (w), 528 (w) cm^{-1}.

TLC (SiO_2, *iso*-hexane:*i*Pr, 1:1 v/v): R_f = 0.06.

68-*Z*-(*S*)-(*P*)-(S_a)/68-*Z*-(*R*)-(*M*)-(R_a) = C-(S_a)

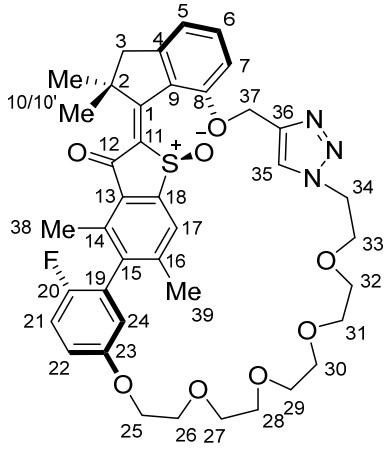

^{1}H NMR (601 MHz, CD_2Cl_2): δ = 8.66 (s, 1H, HC35), 7.77–7.74 (m, 1H, HC17), 7.38 (dd, $^3J_{HH}$ = 8.3, 7.4 Hz, 1H, HC6), 7.10 (m, 1H, HC21), 6.98–6.95 (m, 1H, HC22), 6.95–6.91 (m, 2H, HC5 and HC24), 6.84 (d, $^3J_{HH}$ = 8.3 Hz, 1H, HC7), 5.65–5.56 (m, 2H, H_2C37), 4.61–4.45 (m, 2H, H_2C34), 4.37–4.16 (m, 2H, H_2C25), 3.88–3.77 (m, 3H, H_2C33 and HC32), 3.73–3.64 (m, 2H, H_2C26), 3.64 –3.40 (m, 11H, H_2C27, H_2C28, H_2C29, H_2C30, H_2C31 and HC32), 3.15 (d, $^2J_{HH}$ = 15.8 Hz, 1H, HC3), 2.86 (d, $^2J_{HH}$ = 15.8 Hz, 1H, H'C3), 2.50 (s, 3H, H_3C38), 2.27 (s, 3H, H_3C39), 1.54 (s, 3H, H_3C10), 1.52 (s, 3H, H_3C10') ppm.

^{13}C NMR (151 MHz, CD_2Cl_2): δ = 187.21 (C12), 168.16 (C1), 156.21 (C23), 155.86 (C8), 154.23 (d, $^1J_{CF}$ = 237.6 Hz, C20), 151.60 (C4), 150.99 (C18), 145.48 (C16), 143.93 (C36), 143.35 (C11), 140.80 (C15), 138.54 (C14), 134.75 (C6), 131.70 (C13), 126.30 (d, $^2J_{CF}$ = 19.6 Hz, C19), 126.09 (C9), 125.68 (C35), 125.35 (C17), 119.18 (d, $^3J_{CF}$ = 7.7 Hz, C22), 117.94 (C5), 117.44 (d, $^3J_{CF}$ = 3.5 Hz, C24), 116.72 (d, $^2J_{CF}$ = 24.1 Hz, C21), 111.02 (C7), 71.68 (C26), 71.47 (C27), 70.92 (C28, C29 or C30), 70.56 (C28, C29 or C30), 70.34 (C28, C29 or C30 and C31), 70.07 (C32), 69.77 (C25), 69.76 (C33), 62.97 (C37), 51.93 (C2), 50.88 (C3), 50.45 (C34), 28.30 (C10'), 25.97 (C10), 22.24 (C39), 16.05 (C38) ppm.

^{19}F NMR (377 MHz, CD_2Cl_2): δ = −126.16 (FC20) ppm.

HR-MS (APPI$^+$, m/z) $[M+H]^+$ calc. for $[C_{40}H_{45}FN_3O_8S]^+$: 746.2906, found: 746.2914.

IR: $\tilde{\nu}$ = 2955 (s), 2921 (s), 2851 (s), 2359 (m), 1736 (w), 1668 (s), 1582 (s), 1542 (m), 1496 (m), 1473 (m) 1458 (m), 1378 (s), 1298 (s), 1270 (m), 1228 (w), 1202 (m), 1144 (m), 1108 (m), 1049 (s), 951 (s), 823 (m), 773 (m), 525 (m) cm^{-1}.

TLC (SiO_2, *iso*-hexane:*i*Pr, 1:1 v/v): R_f = 0.06.

9. References

[1] B. L. Regen-Pregizer, A. Ozcelik, P. Mayer, F. Hampel, H. Dube, *Nat. Commun.* **2023**, *14*, 4595.

[2] B. L. Regen-Pregizer, H. Dube, *J. Am. Chem. Soc.* **2023**, *145*, 13081–13088.

[3] K. Kinbara, T. Aida, *Chem. Rev.* **2005**, *105*, 1377–1400.

[4] G. Saper, H. Hess, *Chem. Rev.* **2020**, *120*, 288–309.

[5] R. Bocanegra, G. A. Ismael Plaza, C. R. Pulido, B. Ibarra, *Comput. Struct. Biotechnol. J.* **2021**, *19*, 2057–2069.

[6] R. D. Vale, R. A. Milligan, *Science* **2000**, *288*, 88–95.

[7] H. Noji, R. Yasuda, M. Yoshida, K. Kinosita, *Nature* **1997**, *386*, 299–302.

[8] P. D. Boyer, *Angew. Chem. Int. Ed.* **1998**, *37*, 2296–2307.

[9] J. E. Walker, *Angew. Chem. Int. Ed.* **1998**, *37*, 2308–2319.

[10] J. R. Knowles, *Annu. Rev. Biochem.* **1980**, *49*, 877–919.

[11] J.-P. Sauvage, *Angew. Chem. Int. Ed.* **2017**, *56*, 11080–11093.

[12] J. F. Stoddart, *Angew. Chem. Int. Ed.* **2017**, *56*, 11094–11125.

[13] B. L. Feringa, *Angew. Chem. Int. Ed.* **2017**, *56*, 11060–11078.

[14] S. Kassem, T. van Leeuwen, A. S. Lubbe, M. R. Wilson, B. L. Feringa, D. A. Leigh, *Chem. Soc. Rev.* **2017**, *46*, 2592–2621.

[15] S. Krause, B. L. Feringa, *Nat. Rev. Chem.* **2020**, *4*, 550–562.

[16] R. Costil, M. Holzheimer, S. Crespi, N. A. Simeth, B. L. Feringa, *Chem. Rev.* **2021**, *121*, 13213–13237.

[17] H. A. Wegner, *Angew. Chem. Int. Ed.* **2012**, *51*, 4787–4788.

[18] J. Wachtveitl, A. Zumbusch, *ChemBioChem* **2011**, *12*, 1169–1170.

[19] S. Samanta, A. A. Beharry, O. Sadovski, T. M. McCormick, A. Babalhavaeji, V. Tropepe, G. A. Woolley, *J. Am. Chem. Soc.* **2013**, *135*, 9777–9784.

[20] A. M. Smith, M. C. Mancini, S. Nie, *Nat. Nanotechnol.* **2009**, *4*, 710–711.

[21] Fritzsche, *J. Prakt. Chem.* **1867**, *101*, 333–343.

[22] N. Koumura, R. W. J. Zijlstra, R. A. van Delden, N. Harada, B. L. Feringa, *Nature* **1999**, *401*, 152–155.

[23] W. Albert. Noyes, L. S. Kassel, *Chem. Rev.* **1926**, *3*, 199–225.

[24] H. D. Roth, *Angew. Chem. Int. Ed.* **1989**, *28*, 1193–1207.

[25] S. W. Benson, *J. Chem. Educ.* **1965**, *42*, 502.

[26] G. S. Hartley, *Nature* **1937**, *140*, 281–281.

[27] J. Twilton, C. (Chip) Le, P. Zhang, M. H. Shaw, R. W. Evans, D. W. C. MacMillan, *Nat. Rev. Chem.* **2017**, *1*, 1–19.

[28] T. Bach, J. P. Hehn, *Angew. Chem. Int. Ed.* **2011**, *50*, 1000–1045.

[29] D. Villarón, S. J. Wezenberg, *Angew. Chem. Int. Ed.* **2020**, *59*, 13192–13202.

[30] R. Siewertsen, H. Neumann, B. Buchheim-Stehn, R. Herges, C. Näther, F. Renth, F. Temps, *J. Am. Chem. Soc.* **2009**, *131*, 15594–15595.

[31] M. N. Chaur, D. Collado, J.-M. Lehn, *Chem. Eur. J.* **2011**, *17*, 248–258.

[32] C. Petermayer, H. Dube, *Acc. Chem. Res.* **2018**, *51*, 1153–1163.

[33] S. Wiedbrauk, H. Dube, *Tetrahedron Lett.* **2015**, *56*, 4266–4274.

[34] M. W. H. Hoorens, M. Medved', A. D. Laurent, M. Di Donato, S. Fanetti, L. Slappendel, M. Hilbers, B. L. Feringa, W. Jan Buma, W. Szymanski, *Nat. Commun.* **2019**, *10*, 2390.

[35] S. Thumser, L. Köttner, N. Hoffmann, P. Mayer, H. Dube, *J. Am. Chem. Soc.* **2021**, *143*, 18251–18260.

[36] G. Berkovic, V. Krongauz, V. Weiss, *Chem. Rev.* **2000**, *100*, 1741–1754.

[37] L. Wimberger, S. K. K. Prasad, M. D. Peeks, J. Andréasson, T. W. Schmidt, J. E. Beves, *J. Am. Chem. Soc.* **2021**, *143*, 20758–20768.

[38] M. Irie, *Chem. Rev.* **2000**, *100*, 1685–1716.

[39] M. Irie, T. Fukaminato, K. Matsuda, S. Kobatake, *Chem. Rev.* **2014**, *114*, 12174–12277.

[40] G. S. Hammond, N. J. Turro, A. Fischer, *J. Am. Chem. Soc.* **1961**, *83*, 4674–4675.

[41] W. G. Dauben, R. L. Cargill, *Tetrahedron* **1961**, *15*, 197–201.

[42] J. Orrego-Hernández, A. Dreos, K. Moth-Poulsen, *Acc. Chem. Res.* **2020**, *53*, 1478–1487.

[43] S. Helmy, F. A. Leibfarth, S. Oh, J. E. Poelma, C. J. Hawker, J. Read de Alaniz, *J. Am. Chem. Soc.* **2014**, *136*, 8169–8172.

[44] M. M. Lerch, S. J. Wezenberg, W. Szymanski, B. L. Feringa, *J. Am. Chem. Soc.* **2016**, *138*, 6344–6347.

[45] H. Goerner, C. Fischer, S. Gierisch, J. Daub, *J. Phys. Chem.* **1993**, *97*, 4110–4117.

[46] A. U. Petersen, M. Jevric, J. Elm, S. T. Olsen, C. G. Tortzen, A. Kadziola, K. V. Mikkelsen, M. B. Nielsen, *Org. Biomol. Chem.* **2016**, *14*, 2403–2412.

[47] H. Stobbe, *Ber. Dtsch. Chem. Ges.* **1905**, 3673–3682.

[48] Y. Yokoyama, *Chem. Rev.* **2000**, *100*, 1717–1740.

[49] D. Lachmann, R. Lahmy, B. König, *Chem. Eur. J.* **2019**, *2019*, 5018–5024.

[50] J. C. Splitstoser, T. D. Dillehay, J. Wouters, A. Claro, *Sci. Adv.* **2016**, *2*, e1501623.

[51] A. Baeyer, *Ber. Dtsch. Chem. Ges.* **1883**, 2188–2204.

[52] J. Pina, D. Sarmento, M. Accoto, P. L. Gentili, L. Vaccaro, A. Galvão, J. S. Seixas de Melo, *J. Phys. Chem. B* **2017**, *121*, 2308–2318.

[53] C. Petermayer, S. Thumser, F. Kink, P. Mayer, H. Dube, *J. Am. Chem. Soc.* **2017**, *139*, 15060–15067.

[54] L. A. Huber, P. Mayer, H. Dube, *ChemPhotoChem* **2018**, *2*, 458–464.

[55] C.-Y. Huang, A. Bonasera, L. Hristov, Y. Garmshausen, B. M. Schmidt, D. Jacquemin, S. Hecht, *J. Am. Chem. Soc.* **2017**, *139*, 15205–15211.

[56] Š. Budzák, J. Jovaišaitė, C.-Y. Huang, P. Baronas, K. Tulaitė, S. Juršėnas, D. Jacquemin, S. Hecht, *Chem. Eur. J.* **2022**, *28*, 1521–3765.

[57] P. Friedländer, *Chem. Ber.* **1906**, 1060–1066.

[58] E. I. Stearns, *J. Opt. Soc. Am.* **1942**, *32*, 282–284.

[59] G. M. Wyman, W. R. Brode, *J. Am. Chem. Soc.* **1951**, *73*, 1487–1493.

[60] D. A. Rogers, J. D. Margerum, G. M. Wyman, *J. Am. Chem. Soc.* **1957**, *79*, 2464–2468.

[61] M. A. Mostoslavskii, V. A. Izmail'skii, *Ukr. Khem. Zh.* **1961**, *27*, 234–237.

[62] M. A. Mostoslavskii, M. D. Kravchenko, *Chem. Heterocycl. Compd.* **1970**, *4*, 45–47.

[63] A. V. Popova, S. P. Bondarenko, M. S. Frasinyuk, *Chem. Heterocycl. Compd.* **2019**, *55*, 285–299.

[64] L. Köttner, F. Wolff, P. Mayer, E. Zanin, H. Dube, *J. Am. Chem. Soc.* **2024**, *146*, 1894–1903.

[65] K. Ichimura, T. Seki, T. Tamaki, T. Yamaguchi, *Chem. Lett.* **1990**, *19*, 1645–1646.

[66] V. Josef, F. Hampel, H. Dube, *Angew. Chem. Int. Ed.* **2022**, *61*, 1521–3773.

[67] T. Lougheed, V. Borisenko, T. Hennig, K. Rück-Braun, G. A. Woolley, *Org. Biomol. Chem.* **2004**, *2*, 2798–2801.

[68] S. Herre, T. Schadendorf, I. Ivanov, C. Herrberger, W. Steinle, K. Rück-Braun, R. Preissner, H. Kuhn, *ChemBioChem* **2006**, *7*, 1089–1095.

[69] T. Cordes, B. Heinz, N. Regner, C. Hoppmann, T. E. Schrader, W. Summerer, K. Rück-Braun, W. Zinth, *ChemPhysChem* **2007**, *8*, 1713–1721.

[70] D. V. Berdnikova, *Beilstein J. Org. Chem.* **2019**, *15*, 2822–2829.

[71] D. V. Berdnikova, *Chem. Commun.* **2019**, *55*, 8402–8405.

[72] A. Sailer, F. Ermer, Y. Kraus, F. H. Lutter, C. Donau, M. Bremerich, J. Ahlfeld, O. Thorn-Seshold, *ChemBioChem* **2019**, *20*, 1305–1314.

[73] A. Sailer, J. C. M. Meiring, C. Heise, L. N. Pettersson, A. Akhmanova, J. Thorn-Seshold, O. Thorn-Seshold, *Angew. Chem. Int. Ed.* **2021**, *60*, 23695–23704.

[74] L. Finlayson, I. R. M. Barnard, L. McMillan, S. H. Ibbotson, C. T. A. Brown, E. Eadie, K. Wood, *J. Photochem. Photobiol.* **2022**, *98*, 974–981.

[75] M. Guentner, E. Uhl, P. Mayer, H. Dube, *Chem. Eur. J.* **2016**, *22*, 16433–16436.

[76] S. Wiedbrauk, T. Bartelmann, S. Thumser, P. Mayer, H. Dube, *Nat. Commun.* **2018**, *9*, 1456.

[77] T. Bartelmann, F. Gnannt, M. Zitzmann, P. Mayer, H. Dube, *Chem. Sci.* **2021**, *12*, 3651–3659.

[78] F. Kink, M. P. Collado, S. Wiedbrauk, P. Mayer, H. Dube, *Chem. Eur. J.* **2017**, *23*, 6237–6243.

[79] M. Zitzmann, F. Hampel, H. Dube, *Chem. Sci.* **2023**, *14*, 5734–5742.

[80] M. Sacherer, F. Hampel, H. Dube, *Nat. Commun.* **2023**, *14*, 4382.

[81] K. Kuntze, J. Viljakka, M. Virkki, C.-Y. (Dennis) Huang, S. Hecht, A. Priimagi, *Chem. Sci.* **2023**, *14*, 2482–2488.

[82] J. E. Zweig, T. R. Newhouse, *J. Am. Chem. Soc.* **2017**, *139*, 10956–10959.

[83] A. Gernet, A. El Rhaz, L. Jean, *Chem. Eur. J.* **2023**, e202301160.

[84] A. Gerwien, B. Jehle, M. Irmler, P. Mayer, H. Dube, *J. Am. Chem. Soc.* **2022**, *144*, 3029–3038.

[85] A. Gerwien, M. Schildhauer, S. Thumser, P. Mayer, H. Dube, *Nat. Commun.* **2018**, *9*, 2510.

[86] F. Kohl, A. Gerwien, F. Hampel, P. Mayer, H. Dube, *J. Am. Chem. Soc.* **2022**, *144*, 2847–2852.

[87] G. Moncelsi, L. Escobar, H. Dube, P. Ballester, *Chem. Asian J.* **2018**, *13*, 1632–1639.

[88] T. Cordes, T. Schadendorf, B. Priewisch, K. Rück-Braun, W. Zinth, *J. Phys. Chem. A* **2008**, *112*, 581–588.

[89] T. Cordes, T. Schadendorf, K. Rück-Braun, W. Zinth, *Chem. Phys. Lett.* **2008**, *455*, 197–201.

[90] B. Maerz, S. Wiedbrauk, S. Oesterling, E. Samoylova, A. Nenov, P. Mayer, R. de Vivie-Riedle, W. Zinth, H. Dube, *Chem. Eur. J.* **2014**, *20*, 13984–13992.

[91] S. Wiedbrauk, B. Maerz, E. Samoylova, P. Mayer, W. Zinth, H. Dube, *J. Phys. Chem. Lett.* **2017**, *8*, 1585–1592.

[92] S. Wiedbrauk, B. Maerz, E. Samoylova, A. Reiner, F. Trommer, P. Mayer, W. Zinth, H. Dube, *J. Am. Chem. Soc.* **2016**, *138*, 12219–12227.

[93] D. V. Berdnikova, B. M. Kriesche, T. Paululat, T. S. Hofer, *Chem. Eur. J.* **2022**, *28*, e202202752.

[94] L. Köttner, E. Ciekalski, H. Dube, *Angew. Chem. Int. Ed.* **2023**, *62*, e202312955.

[95] M. Sacherer, S. Gracheva, H. Maid, C. Placht, F. Hampel, H. Dube, *J. Am. Chem. Soc.* **2024**, *146*, 9575–9582.

[96] R. P. Feynman, *Eng. Sci.* **1960**, *23*, 22–36.

[97] T. R. Kelly, H. De Silva, R. A. Silva, *Nature* **1999**, *401*, 150–152.

[98] T. R. Kelly, M. C. Bowyer, K. V. Bhaskar, D. Bebbington, A. Garcia, F. Lang, M. H. Kim, M. P. Jette, *J. Am. Chem. Soc.* **1994**, *116*, 3657–3658.

[99] T. R. Kelly, I. Tellitu, J. P. Sestelo, *Angew. Chem. Int. Ed.* **1997**, *36*, 1866–1868.

[100] T. R. Kelly, J. P. Sestelo, I. Tellitu, *J. Org. Chem.* **1998**, *63*, 3655–3665.

[101] T. R. Kelly, R. A. Silva, H. De Silva, S. Jasmin, Y. Zhao, *J. Am. Chem. Soc.* **2000**, *122*, 6935–6949.

[102] N. P. M. Huck, W. F. Jager, B. de Lange, B. L. Feringa, *Science* **1996**, *273*, 1686–1688.

[103] N. Harada, N. Koumura, B. L. Feringa, *J. Am. Chem. Soc.* **1997**, *119*, 7256–7264.

[104] W. R. Browne, B. L. Feringa, *Nat. Nanotechnol.* **2006**, *1*, 25–35.

[105] E. R. Kay, D. A. Leigh, F. Zerbetto, *Angew. Chem. Int. Ed.* **2007**, *46*, 72–191.

[106] S. Erbas-Cakmak, D. A. Leigh, C. T. McTernan, A. L. Nussbaumer, *Chem. Rev.* **2015**, *115*, 10081–10206.

[107] A. Mondal, R. Toyoda, R. Costil, B. L. Feringa, *Angew. Chem. Int. Ed.* **2022**, *61*, e202206631.

[108] J. A. Spudich, *Nat. Rev. Mol. Cell Biol.* **2001**, *2*, 387–392.

[109] S. M. Block, *Biophys. J.* **2007**, *92*, 2986–2995.

[110] N. J. Carter, R. A. Cross, *Nature* **2005**, *435*, 308–312.

[111] G. Bhabha, G. T. Johnson, C. M. Schroeder, R. D. Vale, *Trends Biochem. Sci.* **2016**, *41*, 94–105.

[112] P. D. Boyer, *Annu. Rev. Biochem.* **1997**, *66*, 717–749.

[113] M. Forgac, *Nat. Rev. Mol. Cell Biol.* **2007**, *8*, 917–929.

[114] H. C. Berg, *Annu. Rev. Biochem.* **2003**, *72*, 19–54.

[115] M. Piccolino, *Nat. Rev. Mol. Cell Biol.* **2000**, *1*, 149–152.

[116] E. Nogales, N. Grigorieff, *J. Cell Biol.* **2001**, *152*, F1–F10.

[117] H. L. Tierney, C. J. Murphy, A. D. Jewell, A. E. Baber, E. V. Iski, H. Y. Khodaverdian, A. F. McGuire, N. Klebanov, E. C. H. Sykes, *Nat. Nanotechnol.* **2011**, *6*, 625–629.

[118] M. von Delius, E. M. Geertsema, D. A. Leigh, *Nat. Chem.* **2010**, *2*, 96–101.

[119] M. von Delius, E. M. Geertsema, D. A. Leigh, D.-T. D. Tang, *J. Am. Chem. Soc.* **2010**, *132*, 16134–16145.

[120] M. J. Barrell, A. G. Campaña, M. von Delius, E. M. Geertsema, D. A. Leigh, *Angew. Chem. Int. Ed.* **2011**, *50*, 285–290.

[121] B. Lewandowski, G. De Bo, J. W. Ward, M. Papmeyer, S. Kuschel, M. J. Aldegunde, P. M. E. Gramlich, D. Heckmann, S. M. Goldup, D. M. D'Souza, A. E. Fernandes, D. A. Leigh, *Science* **2013**, *339*, 189–193.

[122] C. Cheng, P. R. McGonigal, S. T. Schneebeli, H. Li, N. A. Vermeulen, C. Ke, J. F. Stoddart, *Nat. Nanotechnol.* **2015**, *10*, 547–553.

[123] G. Ragazzon, M. Baroncini, S. Silvi, M. Venturi, A. Credi, *Nat. Nanotechnol.* **2015**, *10*, 70–75.

[124] W. L. Mock, K. J. Ochwat, *J. Phys. Org. Chem.* **2003**, *16*, 175–182.

[125] S. P. Fletcher, F. Dumur, M. M. Pollard, B. L. Feringa, *Science* **2005**, *310*, 80–82.

[126] B. J. Dahl, B. P. Branchaud, *Tetrahedron Lett.* **2004**, *45*, 9599–9602.

[127] G. Bringmann, A. J. Price Mortimer, P. A. Keller, M. J. Gresser, J. Garner, M. Breuning, *Angew. Chem. Int. Ed.* **2005**, *44*, 5384–5427.

[128] B. S. L. Collins, J. C. M. Kistemaker, E. Otten, B. L. Feringa, *Nat. Chem.* **2016**, *8*, 860–866.

[129] Y. Zhang, Z. Chang, H. Zhao, S. Crespi, B. L. Feringa, D. Zhao, *Chem* **2020**, *6*, 2420–2429.

[130] S. Borsley, E. Kreidt, D. A. Leigh, B. M. W. Roberts, *Nature* **2022**, *604*, 80–85.

[131] D. A. Leigh, J. K. Y. Wong, F. Dehez, F. Zerbetto, *Nature* **2003**, *424*, 174–179.

[132] S. Borsley, D. A. Leigh, B. M. W. Roberts, *Angew. Chem. Int. Ed.* **2024**, *63*, e202400495.

[133] R. D. Astumian, *Science* **1997**, *276*, 917–922.

[134] R. Ait-Haddou, W. Herzog, *Cell Biochem. Biophys.* **2003**, *38*, 191–213.

[135] A. Coskun, M. Banaszak, R. D. Astumian, J. F. Stoddart, B. A. Grzybowski, *Chem. Soc. Rev.* **2011**, *41*, 19–30.

[136] M. R. Wilson, J. Solà, A. Carlone, S. M. Goldup, N. Lebrasseur, D. A. Leigh, *Nature* **2016**, *534*, 235–240.

[137] J. V. Hernández, E. R. Kay, D. A. Leigh, *Science* **2004**, *306*, 1532–1537.

[138] L. Greb, J.-M. Lehn, *J. Am. Chem. Soc.* **2014**, *136*, 13114–13117.

[139] J.-M. Lehn, *Chem. Eur. J.* **2006**, *12*, 5910–5915.

[140] G. Haberhauer, *Angew. Chem. Int. Ed.* **2011**, *50*, 6415–6418.

[141] A. Gerwien, P. Mayer, H. Dube, *J. Am. Chem. Soc.* **2018**, *140*, 16442–16445.

[142] A. Gerwien, P. Mayer, H. Dube, *Nat. Commun.* **2019**, *10*, 4449.

[143] N. Koumura, E. M. Geertsema, A. Meetsma, B. L. Feringa, *J. Am. Chem. Soc.* **2000**, *122*, 12005–12006.

[144] N. Ruangsupapichat, M. M. Pollard, S. R. Harutyunyan, B. L. Feringa, *Nat. Chem.* **2011**, *3*, 53–60.

[145] D.-H. Qu, B. L. Feringa, *Angew. Chem. Int. Ed.* **2010**, *49*, 1107–1110.

[146] P. Štacko, J. C. M. Kistemaker, T. van Leeuwen, M.-C. Chang, E. Otten, B. L. Feringa, *Science* **2017**, *356*, 964–968.

[147] T. van Leeuwen, W. Danowski, S. F. Pizzolato, P. Štacko, S. J. Wezenberg, B. L. Feringa, *Chem. Eur. J.* **2018**, *24*, 81–84.

[148] A. Faulkner, T. van Leeuwen, B. L. Feringa, S. J. Wezenberg, *J. Am. Chem. Soc.* **2016**, *138*, 13597–13603.

[149] T. van Leeuwen, J. Pol, D. Roke, S. J. Wezenberg, B. L. Feringa, *Org. Lett.* **2017**, *19*, 1402–1405.

[150] S. F. Pizzolato, P. Štacko, J. C. M. Kistemaker, T. van Leeuwen, E. Otten, B. L. Feringa, *J. Am. Chem. Soc.* **2018**, *140*, 17278–17289.

[151] S. F. Pizzolato, P. Štacko, J. C. M. Kistemaker, T. van Leeuwen, B. L. Feringa, *Nat. Catal.* **2020**, *3*, 488–496.

[152] A. Cnossen, L. Hou, M. M. Pollard, P. V. Wesenhagen, W. R. Browne, B. L. Feringa, *J. Am. Chem. Soc.* **2012**, *134*, 17613–17619.

[153] J.-J. Yu, L.-Y. Zhao, Z.-T. Shi, Q. Zhang, G. London, W.-J. Liang, C. Gao, M.-M. Li, X.-M. Cao, H. Tian, B. L. Feringa, D.-H. Qu, *J. Org. Chem.* **2019**, *84*, 5790–5802.

[154] M. Guentner, M. Schildhauer, S. Thumser, P. Mayer, D. Stephenson, P. J. Mayer, H. Dube, *Nat. Commun.* **2015**, *6*, 8406.

[155] R. Wilcken, M. Schildhauer, F. Rott, L. A. Huber, M. Guentner, S. Thumser, K. Hoffmann, S. Oesterling, R. de Vivie-Riedle, E. Riedle, H. Dube, *J. Am. Chem. Soc.* **2018**, *140*, 5311–5318.

[156] L. A. Huber, S. Thumser, K. Grill, D. Voßiek, N. N. Bach, P. Mayer, H. Dube, *Chem. Eur. J.* **2021**, *27*, 10758–10765.

[157] N. N. Bach, V. Josef, H. Maid, H. Dube, *Angew. Chem. Int. Ed.* **2022**, *61*, e202201882.

[158] E. Uhl, P. Mayer, H. Dube, *Angew. Chem. Int. Ed.* **2020**, *59*, 5730–5737.

[159] E. Uhl, S. Thumser, P. Mayer, H. Dube, *Angew. Chem. Int. Ed.* **2018**, *57*, 11064–11068.

[160] L. Reißenweber, E. Uhl, F. Hampel, P. Mayer, H. Dube, *J. Am. Chem. Soc.* **2024**, *146*, 23387–23397.

[161] K. Grill, H. Dube, *J. Am. Chem. Soc.* **2020**, *142*, 19300–19307.

[162] P. Biswas, A. Ozcelik, M. Hartinger, F. Hampel, H. Dube, *Res. Sq.* **2024**.

[163] J. M. R. Parrondo, B. J. de Cisneros, *Appl. Phys. A* **2002**, *75*, 179–191.

[164] V. Serreli, C.-F. Lee, E. R. Kay, D. A. Leigh, *Nature* **2007**, *445*, 523–527.

[165] M. Alvarez-Pérez, S. M. Goldup, D. A. Leigh, A. M. Z. Slawin, *J. Am. Chem. Soc.* **2008**, *130*, 1836–1838.

[166] A. Carlone, S. M. Goldup, N. Lebrasseur, D. A. Leigh, A. Wilson, *J. Am. Chem. Soc.* **2012**, *134*, 8321–8323.

[167] P. Reimann, *Phys. Rep.* **2002**, *361*, 57–265.

[168] M. N. Chatterjee, E. R. Kay, D. A. Leigh, *J. Am. Chem. Soc.* **2006**, *128*, 4058–4073.

[169] R. A. Bissell, E. Córdova, A. E. Kaifer, J. F. Stoddart, *Nature* **1994**, *369*, 133–137.

[170] N. Armaroli, V. Balzani, J.-P. Collin, P. Gaviña, J.-P. Sauvage, B. Ventura, *J. Am. Chem. Soc.* **1999**, *121*, 4397–4408.

[171] R. Ballardini, V. Balzani, W. Dehaen, A. E. Dell'Erba, F. M. Raymo, J. F. Stoddart, M. Venturi, *Eur. J. Org. Chem.* **2000**, *2000*, 591–602.

[172] W. J. Stockerl, L. Reißenweber, A. Gerwien, N. N. Bach, S. Thumser, P. Mayer, R. M. Gschwind, H. Dube, *Chem. Eur. J.* **2024**, *30*, e202302267.

[173] P. L. Anelli, N. Spencer, J. F. Stoddart, *J. Am. Chem. Soc.* **1991**, *113*, 5131–5133.

[174] Y. Feng, M. Ovalle, J. S. W. Seale, C. K. Lee, D. J. Kim, R. D. Astumian, J. F. Stoddart, *J. Am. Chem. Soc.* **2021**, *143*, 5569–5591.

[175] W. D. Hounshell, C. A. Johnson, A. Guenzi, F. Cozzi, K. Mislow, *Proc. Natl. Acad. Sci. U.S.A.* **1980**, *77*, 6961–6964.

[176] H. Iwamura, K. Mislow, *Acc. Chem. Res.* **1988**, *21*, 175–182.

[177] A. Gakh, R. A. Sachleben, J. C. Bryan, *Chem. Tech.* **1997**, 26–33.

[178] D. K. Frantz, A. Linden, K. K. Baldridge, J. S. Siegel, *J. Am. Chem. Soc.* **2012**, *134*, 1528–1535.

[179] H. H. Lin, A. Croy, R. Gutierrez, C. Joachim, G. Cuniberti, *J. Phys. Commun.* **2019**, *3*, 025011.

[180] S. Pérez-Estrada, B. Rodríguez-Molina, E. F. Maverick, S. I. Khan, M. A. Garcia-Garibay, *J. Am. Chem. Soc.* **2019**, *141*, 2413–2420.

[181] I. Liepuoniute, M. J. Jellen, M. A. Garcia-Garibay, *Chem. Sci.* **2020**, *11*, 12994–13007.

[182] S. Abid, Y. Gisbert, M. Kojima, N. Saffon-Merceron, J. Cuny, C. Kammerer, G. Rapenne, *Chem. Sci.* **2021**, *12*, 4709–4721.

[183] M. J. Jellen, I. Liepuoniute, M. Jin, C. G. Jones, S. Yang, X. Jiang, H. M. Nelson, K. N. Houk, M. A. Garcia-Garibay, *J. Am. Chem. Soc.* **2021**, *143*, 7740–7747.

[184] Y. Gisbert, S. Abid, C. Kammerer, G. Rapenne, *Chem. Eur. J.* **2021**, *27*, 12019–12031.

[185] A. Gerwien, F. Gnannt, P. Mayer, H. Dube, *Nat. Chem.* **2022**, *14*, 670–676.

[186] M. K. J. ter Wiel, R. A. van Delden, A. Meetsma, B. L. Feringa, *Org. Biomol. Chem.* **2005**, *3*, 4071–4076.

[187] A. S. Lubbe, N. Ruangsupapichat, G. Caroli, B. L. Feringa, *J. Org. Chem.* **2011**, *76*, 8599–8610.

[188] F. Gnannt, A. Gerwien, H. Dube, *Angew. Chem. Int. Ed.* **2024**, *63*, e202405299.

[189] E. M. Arpa, S. Stafström, B. Durbeej, *Chem. Eur. J.* **2024**, *30*, e202303191.

[190] Q. Li, G. Fuks, E. Moulin, M. Maaloum, M. Rawiso, I. Kulic, J. T. Foy, N. Giuseppone, *Nat. Nanotechnol.* **2015**, *10*, 161–165.

[191] J. T. Foy, Q. Li, A. Goujon, J.-R. Colard-Itté, G. Fuks, E. Moulin, O. Schiffmann, D. Dattler, D. P. Funeriu, N. Giuseppone, *Nat. Nanotechnol.* **2017**, *12*, 540–545.

[192] Y. Liu, Q. Zhang, S. Crespi, S. Chen, X.-K. Zhang, T.-Y. Xu, C.-S. Ma, S.-W. Zhou, Z.-T. Shi, H. Tian, B. L. Feringa, D.-H. Qu, *Angew. Chem. Int. Ed.* **2021**, *60*, 16129–16138.

[193] M. Kathan, S. Crespi, N. O. Thiel, D. L. Stares, D. Morsa, J. de Boer, G. Pacella, T. van den Enk, P. Kobauri, G. Portale, C. A. Schalley, B. L. Feringa, *Nat. Nanotechnol.* **2022**, *17*, 159–165.

[194] M. Kathan, S. Crespi, A. Troncossi, C. N. Stindt, R. Toyoda, B. L. Feringa, *Angew. Chem. Int. Ed.* **2022**, *61*, e202205801.

[195] R. Dorel, C. Miró, Y. Wei, S. J. Wezenberg, B. L. Feringa, *Org. Lett.* **2018**, *20*, 3715–3718.

[196] C. Gao, A. Vargas Jentzsch, E. Moulin, N. Giuseppone, *J. Am. Chem. Soc.* **2022**, *144*, 9845–9852.

[197] N. Katsonis, T. Kudernac, M. Walko, S. J. van der Molen, B. J. van Wees, B. L. Feringa, *Adv. Mater.* **2006**, *18*, 1397–1400.

[198] Arramel, T. C. Pijper, T. Kudernac, N. Katsonis, M. van der Maas, B. L. Feringa, B. J. van Wees, *Nanoscale* **2013**, *5*, 9277–9282.

[199] G. Srivastava, P. Štacko, J. I. Mendieta-Moreno, S. Edalatmanesh, J. C. M. Kistemaker, G. H. Heideman, L. Zoppi, M. Parschau, B. L. Feringa, K.-H. Ernst, *ACS Nano* **2023**, *17*, 3931–3938.

[200] R. A. van Delden, M. K. J. ter Wiel, M. M. Pollard, J. Vicario, N. Koumura, B. L. Feringa, *Nature* **2005**, *437*, 1337–1340.

[201] G. T. Carroll, G. London, T. F. Landaluce, P. Rudolf, B. L. Feringa, *ACS Nano* **2011**, *5*, 622–630.

[202] N. Katsonis, M. Lubomska, M. M. Pollard, B. L. Feringa, P. Rudolf, *Prog. Surf. Sci.* **2007**, *82*, 407–434.

[203] W. R. Browne, B. L. Feringa, *Annu. Rev. Phys. Chem.* **2009**, *60*, 407–428.

[204] Q. Shen, L. Wang, S. Liu, Y. Cao, L. Gan, X. Guo, M. L. Steigerwald, Z. Shuai, Z. Liu, C. Nuckolls, *Adv. Mater.* **2010**, *22*, 3282–3287.

[205] H. Zhang, X. Guo, J. Hui, S. Hu, W. Xu, D. Zhu, *Nano Lett.* **2011**, *11*, 4939–4946.

[206] M. Kim, N. S. Safron, C. Huang, M. S. Arnold, P. Gopalan, *Nano Lett.* **2012**, *12*, 182–187.

[207] O. Ivashenko, J. T. van Herpt, B. L. Feringa, P. Rudolf, W. R. Browne, *Langmuir* **2013**, *29*, 4290–4297.

[208] M. Gobbi, S. Bonacchi, J. X. Lian, A. Vercouter, S. Bertolazzi, B. Zyska, M. Timpel, R. Tatti, Y. Olivier, S. Hecht, M. V. Nardi, D. Beljonne, E. Orgiu, P. Samorì, *Nat. Commun.* **2018**, *9*, 2661.

[209] H. Qiu, S. Ippolito, A. Galanti, Z. Liu, P. Samorì, *ACS Nano* **2021**, *15*, 10668–10677.

[210] Y. Wang, D. Iglesias, S. M. Gali, D. Beljonne, P. Samorì, *ACS Nano* **2021**, *15*, 13732–13741.

[211] K. Hoffmann, P. Mayer, H. Dube, *Org. Biomol. Chem.* **2019**, *17*, 1979–1983.

[212] K. Hoffmann, Hemithioindigo-basierte molekulare Motoren und deren supramolekulare Anwendungen, Ph.D. Thesis, Ludwig-Maximilians-Universität München, **2023**.

[213] G. London, G. T. Carroll, T. F. Landaluce, M. M. Pollard, P. Rudolf, B. L. Feringa, *Chem. Commun.* **2009**, 1712–1714.

[214] G. London, G. T. Carroll, B. L. Feringa, *Org. Biomol. Chem.* **2013**, *11*, 3477–3483.

[215] J. Vachon, G. T. Carroll, M. M. Pollard, E. M. Mes, A. M. Brouwer, B. L. Feringa, *Photochem. Photobiol. Sci.* **2014**, *13*, 241–246.

[216] A. Jedaa, M. Burkhardt, U. Zschieschang, H. Klauk, D. Habich, G. Schmid, M. Halik, *Org. Electron.* **2009**, *10*, 1442–1447.

[217] B. Zhao, Z. Gan, M. Johnson, E. Najafidehaghani, T. Rejek, A. George, R. H. Fink, A. Turchanin, M. Halik, *Adv. Funct. Mater.* **2021**, *31*, 2105444.

[218] M. Salinas, C. M. Jäger, A. Y. Amin, P. O. Dral, T. Meyer-Friedrichsen, A. Hirsch, T. Clark, M. Halik, *J. Am. Chem. Soc.* **2012**, *134*, 12648–12652.

[219] W. H. Lee, Y. D. Park, *Adv. Mater. Interfaces* **2018**, *5*, 1700316.

[220] Y. Zhao, S. Bertolazzi, P. Samorì, *ACS Nano* **2019**, *13*, 4814–4825.

[221] A. R. Brill, A. Kafri, P. K. Mohapatra, A. Ismach, G. de Ruiter, E. Koren, *ACS Appl. Mater. Interfaces* **2021**, *13*, 32590–32597.

[222] M. Zarei, M. Mohamadzadeh, *Tetrahedron* **2011**, *67*, 5832–5840.

[223] Martin. Karplus, *J. Am. Chem. Soc.* **1963**, *85*, 2870–2871.

[224] A. C. Wang, A. Bax, *J. Am. Chem. Soc.* **1996**, *118*, 2483–2494.

[225] F. Li, J. H. Lee, A. Grishaev, J. Ying, A. Bax, *ChemPhysChem* **2015**, *16*, 572–578.

[226] M. Botella, I. Ema, J. San Fabián, J. M. García de la Vega, *Int. J. Quantum Chem.* **2022**, *122*, e26979.

[227] M. J. Minch, *Concepts Magn. Reson.* **1994**, *6*, 41–56.

[228] T. Turney, Q. Pan, L. Sernau, I. Carmichael, W. Zhang, X. Wang, R. J. Woods, A. S. Serianni, *J. Phys. Chem. B* **2017**, *121*, 66–77.

[229] U. R. Couto, A. Navarro-Vázquez, C. F. Tormena, *Magn. Reson. Chem.* **2019**, *57*, 939–945.

[230] L. Köttner, M. Schildhauer, S. Wiedbrauk, P. Mayer, H. Dube, *Chem. Eur. J.* **2020**, *26*, 10712–10718.

[231] U. Megerle, R. Lechner, B. König, E. Riedle, *Photochem. Photobiol. Sci.* **2010**, *9*, 1400–1406.

[232] B. Wang, G. Di Carlo, R. Turrisi, L. Zeng, K. Stallings, W. Huang, M. J. Bedzyk, L. Beverina, T. J. Marks, A. Facchetti, *Chem. Mater.* **2017**, *29*, 9974–9980.

[233] D. H. Lee, T. Park, T. Jeong, Y. Jung, J. Park, N. Joo, U. Won, H. Yoo, *Front. Mater.* **2023**, *10*.

[234] B. S. Morozov, A. S. Oshchepkov, I. Klemt, A. M. Agafontsev, S. Krishna, F. Hampel, H.-G. Xu, A. Mokhir, D. Guldi, E. Kataev, *JACS Au* **2023**, *3*, 964–977.

[235] D. C. Young, T. R. Bailey, *Methods for Treating or Preventing Viral Infections and Associated Diseases*, **2001**, US6316492B1.

[236] R. Iino, K. Kinbara, Z. Bryant, *Chem. Rev.* **2020**, *120*, 1–4.

[237] K. Grill, H. Dube, *J. Am. Chem. Soc.* **2020**, *142*, 19300–19307.

[238] L. Pfeifer, N. V. Hoang, S. Crespi, M. S. Pshenichnikov, B. L. Feringa, *Sci. Adv.* **2022**, *8*, eadd0410.

[239] A. Guinart, M. Korpidou, D. Doellerer, G. Pacella, M. C. A. Stuart, I. A. Dinu, G. Portale, C. Palivan, B. L. Feringa, *Proc. Natl. Acad. Sci. U.S.A.* **2023**, *120*, e2301279120.

[240] E. Uhl, Integrated hemithioindigo based molecular motors - transmission of directional motion and potential energy, Ph.D. Thesis, Ludwig-Maximilians-Universität München, **2021**.

[241] Q. Ling, Y. Huang, Y. Zhou, Z. Cai, B. Xiong, Y. Zhang, L. Ma, X. Wang, X. Li, J. Li, J. Shen, *Bioorg. Med. Chem.* **2008**, *16*, 7399–7409.

[242] D. Zhang, H. Sun, L. Zhang, Y. Zhou, C. Li, H. Jiang, K. Chen, H. Liu, *Chem. Commun.* **2012**, *48*, 2909–2911.

[243] N. N. Bach, Molecular Machines Based on Hemithioindigo, Ph.D. Thesis, Ludwig-Maximilians-Universität München, **2023**.

[244] S. K. Cushing, M. Li, F. Huang, N. Wu, *ACS Nano* **2014**, *8*, 1002–1013.

[245] S. K. Cushing, W. Ding, G. Chen, C. Wang, F. Yang, F. Huang, N. Wu, *Nanoscale* **2017**, *9*, 2240–2245.

[246] Z. Man, Z. Lv, Z. Xu, M. Liu, J. He, Q. Liao, J. Yao, Q. Peng, H. Fu, *J. Am. Chem. Soc.* **2022**, *144*, 12652–12660.

[247] H. Volfova, Q. Hu, E. Riedle, *EPA Newsletter* **2019**, 51–69.

[248] M. M. Pollard, M. Klok, D. Pijper, B. L. Feringa, *Adv. Funct. Mater.* **2007**, *17*, 718–729.

[249] C. Fang, B. Oruganti, B. Durbeej, *RSC Adv.* **2014**, *4*, 10240–10251.

[250] N. Koumura, E. M. Geertsema, M. B. van Gelder, A. Meetsma, B. L. Feringa, *J. Am. Chem. Soc.* **2002**, *124*, 5037–5051.

[251] D. Pijper, R. A. van Delden, A. Meetsma, B. L. Feringa, *J. Am. Chem. Soc.* **2005**, *127*, 17612–17613.

[252] M. K. J. ter Wiel, R. A. van Delden, A. Meetsma, B. L. Feringa, *J. Am. Chem. Soc.* **2003**, *125*, 15076–15086.

[253] J. Vicario, A. Meetsma, B. L. Feringa, *Chem. Commun.* **2005**, 5910–5912.

[254] T. Fernández Landaluce, G. London, M. M. Pollard, P. Rudolf, B. L. Feringa, *J. Org. Chem.* **2010**, *75*, 5323–5325.

[255] D. Roke, S. J. Wezenberg, B. L. Feringa, *Proc. Natl. Acad. Sci. U.S.A.* **2018**, *115*, 9423–9431.

[256] M. M. Pollard, A. Meetsma, B. L. Feringa, *Org. Biomol. Chem.* **2008**, *6*, 507–512.

[257] M. Klok, N. Boyle, M. T. Pryce, A. Meetsma, W. R. Browne, B. L. Feringa, *J. Am. Chem. Soc.* **2008**, *130*, 10484–10485.

[258] A. A. Kulago, E. M. Mes, M. Klok, A. Meetsma, A. M. Brouwer, B. L. Feringa, *J. Org. Chem.* **2010**, *75*, 666–679.

[259] M. Schildhauer, F. Rott, S. Thumser, P. Mayer, R. de Vivie-Riedle, H. Dube, *ChemPhotoChem* **2019**, *3*, 365–371.

[260] I. Schapiro, M. Gueye, M. Paolino, S. Fusi, G. Marchand, S. Haacke, M. E. Martin, M. Huntress, V. P. Vysotskiy, V. Veryazov, J. Léonard, M. Olivucci, *Photochem. Photobiol. Sci.* **2019**, *18*, 2259–2269.

[261] E. Gruber, A. M. Kabylda, M. B. Nielsen, A. P. Rasmussen, R. Teiwes, P. A. Kusochek, A. V. Bochenkova, L. H. Andersen, *J. Am. Chem. Soc.* **2022**, *144*, 69–73.

[262] M. Filatov, M. Paolino, S. K. Min, C. H. Choi, *Chem. Commun.* **2019**, *55*, 5247–5250.

[263] J. Wang, B. Oruganti, B. Durbeej, *Org. Lett.* **2020**, *22*, 7113–7117.

[264] M. Paolino, T. Giovannini, M. Manathunga, L. Latterini, G. Zampini, R. Pierron, J. Léonard, S. Fusi, G. Giorgi, G. Giuliani, A. Cappelli, C. Cappelli, M. Olivucci, *J. Phys. Chem. Lett.* **2021**, *12*, 3875–3884.

[265] J. Bauer, L. Hou, J. C. M. Kistemaker, B. L. Feringa, *J. Org. Chem.* **2014**, *79*, 4446–4455.

[266] R. Wilcken, L. Huber, K. Grill, M. Guentner, M. Schildhauer, S. Thumser, E. Riedle, H. Dube, *Chem. Eur. J.* **2020**, *26*, 13507–13512.

[267] M. Filatov(Gulak), M. Paolino, R. Pierron, A. Cappelli, G. Giorgi, J. Léonard, M. Huix-Rotllant, N. Ferré, X. Yang, D. Kaliakin, A. Blanco-González, M. Olivucci, *Nat. Commun.* **2022**, *13*, 6433.

[268] S. Gunzenhauser, E. Biala, P. Strazewski, *Tetrahedron Lett.* **1998**, *39*, 6277–6280.

[269] F. Gallo, B. Korsak, C. Mueller, T. Hechler, A. Pahl, M. Kulke, W. Simon, C. Lutz, *Psma-Targeting Amanitin Conjugates*, **2019**, WO2019057964A1.

[270] C. Karunakaran, R. Kamalam, *J. Chem. Soc., Perkin Trans. 2* **2002**, 2011–2018.

[271] C. Petermayer, H. Dube, *J. Am. Chem. Soc.* **2018**, *140*, 13558–13561.

[272] C. P. Petermayer, Development and Characterization of Novel Indigoid Chromophores, Photoswitches and Molecular Machinery, Ph.D. Thesis, Ludwig-Maximilians-Universität München, **2019**.

[273] G. Marchand, J. Eng, I. Schapiro, A. Valentini, L. M. Frutos, E. Pieri, M. Olivucci, J. Léonard, E. Gindensperger, *J. Phys. Chem. Lett.* **2015**, *6*, 599–604.

[274] B. Oruganti, J. Wang, B. Durbeej, *Int. J. Quantum Chem.* **2018**, *118*, e25405.

[275] K. Opron, Z. F. Burton, *Science* **2019**, *20*, 40.

[276] J. Michl, E. C. H. Sykes, *ACS Nano* **2009**, *3*, 1042–1048.

[277] B. Rodríguez-Molina, N. Farfán, M. Romero, J. M. Méndez-Stivalet, R. Santillan, M. A. Garcia-Garibay, *J. Am. Chem. Soc.* **2011**, *133*, 7280–7283.

[278] D. R. S. Pooler, A. S. Lubbe, S. Crespi, B. L. Feringa, *Chem. Sci.* **2021**, *12*, 14964–14986.

[279] A. B. Kolomeisky, M. E. Fisher, *Annu. Rev. Phys. Chem.* **2007**, *58*, 675–695.

[280] R. Eelkema, M. M. Pollard, J. Vicario, N. Katsonis, B. S. Ramon, C. W. M. Bastiaansen, D. J. Broer, B. L. Feringa, *Nature* **2006**, *440*, 163–163.

[281] A. Cnossen, J. C. M. Kistemaker, T. Kojima, B. L. Feringa, *J. Org. Chem.* **2014**, *79*, 927–935.

[282] T. Orlova, F. Lancia, C. Loussert, S. Iamsaard, N. Katsonis, E. Brasselet, *Nat. Nanotechnol.* **2018**, *13*, 304–308.

[283] D. Dattler, G. Fuks, J. Heiser, E. Moulin, A. Perrot, X. Yao, N. Giuseppone, *Chem. Rev.* **2020**, *120*, 310–433.

[284] F. Xu, B. L. Feringa, *Adv. Mater.* **2023**, *35*, 2204413.

[285] B. K. Pathem, S. A. Claridge, Y. B. Zheng, P. S. Weiss, *Annu. Rev. Phys. Chem.* **2013**, *64*, 605–630.

[286] Q. Li, H. Qian, B. Shao, R. P. Hughes, I. Aprahamian, *J. Am. Chem. Soc.* **2018**, *140*, 11829–11835.

[287] Q.-Z. Yang, Z. Huang, T. J. Kucharski, D. Khvostichenko, J. Chen, R. Boulatov, *Nat. Nanotechnol.* **2009**, *4*, 302–306.

[288] N. Regner, T. T. Herzog, K. Haiser, C. Hoppmann, M. Beyermann, J. Sauermann, M. Engelhard, T. Cordes, K. Rück-Braun, W. Zinth, *J. Phys. Chem. B* **2012**, *116*, 4181–4191.

[289] O. Babii, S. Afonin, L. V. Garmanchuk, V. V. Nikulina, T. V. Nikolaienko, O. V. Storozhuk, D. V. Shelest, O. I. Dasyukevich, L. I. Ostapchenko, V. Iurchenko, S. Zozulya, A. S. Ulrich, I. V. Komarov, *Angew. Chem. Int. Ed.* **2016**, *55*, 5493–5496.

[290] E. Nieland, J. Voss, A. Mix, B. M. Schmidt, *Angew. Chem. Int. Ed.* **2022**, *61*, e202212745.

[291] L. Albert, J. Nagpal, W. Steinchen, L. Zhang, L. Werel, N. Djokovic, D. Ruzic, M. Hoffarth, J. Xu, J. Kaspareit, F. Abendroth, A. Royant, G. Bange, K. Nikolic, S. Ryu, Y. Dou, L.-O. Essen, O. Vázquez, *ACS Cent. Sci.* **2022**, *8*, 57–66.

[292] Z.-T. Shi, Y.-X. Hu, Z. Hu, Q. Zhang, S.-Y. Chen, M. Chen, J.-J. Yu, G.-Q. Yin, H. Sun, L. Xu, X. Li, B. L. Feringa, H.-B. Yang, H. Tian, D.-H. Qu, *J. Am. Chem. Soc.* **2021**, *143*, 442–452.

[293] L. A. Huber, K. Hoffmann, S. Thumser, N. Böcher, P. Mayer, H. Dube, *Angew. Chem. Int. Ed.* **2017**, *56*, 14536–14539.

[294] S. Hoops, S. Sahle, R. Gauges, C. Lee, J. Pahle, N. Simus, M. Singhal, L. Xu, P. Mendes, U. Kummer, *Bioinform.* **2006**, *22*, 3067–3074.

[295] E. M. Geertsema, S. J. van der Molen, M. Martens, B. L. Feringa, *Proc. Natl. Acad. Sci. U.S.A.* **2009**, *106*, 16919–16924.

[296] T. Bruhn, A. Schaumlöffel, Y. Hemberger, G. Bringmann, *Chirality* **2013**, *25*, 243–249.

[297] T. Bruhn, A. Schaumlöffel, Y. Hemberger, G. Pecitelli, SpecDis version 1.71, Berlin, Germany, **2017**.

[298] M. J. Frisch, G. W. Trucks, H. B. Schlegel, G. E. Scuseria, M. A. Robb, J. R. Cheeseman, G. Scalmani, V. Barone, G. A. Petersson, H. Nakatsuji, X. Li, M. Caricato, A. V. Marenich, J. Bloino, B. G. Janesko, R. Gomperts, B. Mennucci, H. P. Hratchian, J. V. Ortiz, A. F. Izmaylov, J. L. Sonnenberg, Williams, F. Ding, F. Lipparini, F. Egidi, J. Goings, B. Peng, A. Petrone, T. Henderson, D. Ranasinghe, V. G. Zakrzewski, J. Gao, N. Rega, G. Zheng, W. Liang, M. Hada, M. Ehara, K. Toyota, R. Fukuda, J. Hasegawa, M. Ishida, T. Nakajima, Y. Honda, O. Kitao, H. Nakai, T. Vreven, K. Throssell, J. A. Montgomery Jr., J. E. Peralta, F. Ogliaro, M. J. Bearpark, J. J. Heyd, E. N. Brothers, K. N. Kudin, V. N. Staroverov, T. A. Keith, R. Kobayashi, J. Normand, K. Raghavachari, A. P. Rendell, J. C. Burant, S. S. Iyengar, J. Tomasi, M. Cossi, J. M. Millam, M. Klene, C. Adamo, R. Cammi, J. W. Ochterski, R. L. Martin, K. Morokuma, O. Farkas, J. B. Foresman, D. J. Fox, **2016**.

[299] Schrödinger Release 2019-2: MacroModel, Schrödinger, LLC, New York, NY, **2019**.

[300] Schrödinger Release 2019-2: Maestro, Schrödinger, LLC, New York, NY, **2019**.

[301] T. A. Halgren, *J. Comput. Chem.* **1999**, *20*, 720–729.

[302] J. E. Wittmann, L. M. S. Stiegler, C. Henkel, J. Träg, K. Götz, T. Unruh, D. Zahn, A. Hirsch, D. Guldi, M. Halik, *Adv. Mater. Interfaces* **2019**, *6*, 1801930.